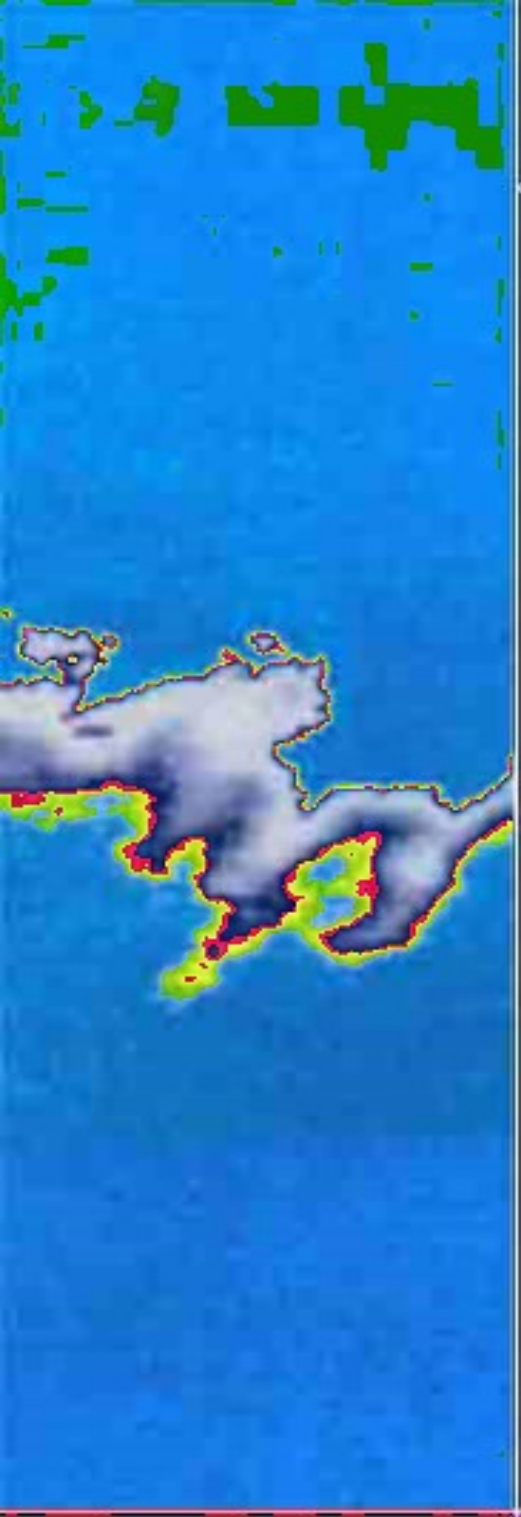

SECOND EDIT

Turbul
Shear
in
Super

Turbulent Shear Layers in Supersonic Flow

Second Edition

Alexander J. Smits Jean-Paul Dussauge

Turbulent Shear Layers in Supersonic Flow

Second Edition

With 171 Illustrations

Springer

Alexander J. Smits
Department of Mechanical Engineering
Princeton University
Princeton, NJ 08544
USA
asmits@princeton.edu

Jean-Paul Dussauge
Institut de Recherche
Sur les Phénomènes Hors Équilibre
Unité Mixte Université d'Aix-Marseille I et II
CNRS No. 138
Marseille 13003
France
jean-paul.dussauge@polytech.univ-mrs.fr

Cover illustration: Rayleigh scattering images of a turbulent boundary layer in side view. From M. W. Smith, "Flow visualization in supersonic turbulent boundary layers," PhD. Thesis, Princeton University 1989. With permission of the author.

Library of Congress Control Number: 2005926765

ISBN-10: 0-387-26140-0 e-ISBN 0-387-26305-5
ISBN-13: 978-0387-26140-9

Printed on acid-free paper.

© 2006 Springer Science+Business Media, Inc. © 1996 AIP Press
All rights reserved. This work may not be translated or copied in whole or in part without the written permission of the publisher (Springer Science+Business Media, Inc., 233 Spring Street, New York, NY 10013, USA), except for brief excerpts in connection with reviews or scholarly analysis. Use in connection with any form of information storage and retrieval, electronic adaptation, computer software, or by similar or dissimilar methodology now known or hereafter developed is forbidden.
The use in this publication of trade names, trademarks, service marks, and similar terms, even if they are not identified as such, is not to be taken as an expression of opinion as to whether or not they are subject to proprietary rights.

Printed in the United States of America. (MVY)

9 8 7 6 5 4 3 2 1

springeronline.com

Preface to the Second Edition

Since 1996, when this book first appeared, a number of new experiments and computations have significantly advanced the field. In particular, direct numerical simulations at reasonable Reynolds numbers have started to provide a new and important level of insight into the behavior of compressible turbulent flows. These recent advances provided the primary motivation for preparing a second edition. We have also taken the opportunity to rearrange some of the older material, add some explanatory text, and correct mistakes and omissions. We are particularly grateful to Drs. Sheng Xu and Jonathan Poggie for helping to identify many of these corrections.

Preface to the First Edition

The aims of this book are to bring together the most recent results on the behavior of turbulent boundary layers at supersonic speed and to present some conclusions regarding our present understanding of these flows. By doing so, we hope to give the reader a general introduction to the field, whether they be students or practicing research engineers and scientists, and to help provide a basis for future work in this area. Most textbooks on turbulence or boundary layers contain some background on turbulent boundary layers in supersonic flow, but the information is usually rather cursory, or it is out of date. Only one, by Kutateladze and Leont'ev (1964), addresses the specific issue of turbulent boundary layers in compressible gases, but it focuses largely on solutions of the integral equations of motion, and it is not much concerned with the turbulence itself. Some aspects of turbulence are addressed by Cousteix (1989), but only one chapter is devoted to this topic, and his review, although very useful, is not exhaustive. The scope of the present book is considerably wider in that we are concerned with physical descriptions of turbulent shear-layer behavior, and the response of the mean flow and turbulence to a wide variety of perturbations. For example, in addition to turbulent mixing layers, we will consider boundary layers on flat plates, with and without pressure gradient, on curved walls, and the interaction of boundary layers with shock waves, in two and three dimensions.

Considerable progress has recently been made in developing our understanding of such flows. This progress has largely been driven by experimental work, although numerical simulations of compressible flows have also made significant contributions. Except for the most recent work, the data are readily available from the compilations edited by Fernholz and Finley (1976, 1980, 1981), Fernholz et al. (1989) and Settles and Dodson (1991), and the quantity of relatively new experimental information presented there is impressive. The recent focus on hypersonic flight has also stimulated extensive computational work, and the reviews by Délery and Marvin (1986) and Lele (1994) give a good impression of what is currently possible. Despite these efforts, the full matrix of possibilities defined by Mach number, Reynolds number, pressure gradient, heat transfer, surface condition, and flow geometry is still very sparsely populated and a great deal of further work needs to be done. One clear message from the failure of the most recent hypersonic flight ini-

tiative is that to make substantial progress in improving the understanding of high-speed turbulent flows we need a concerted, broadly based effort in experimental and computational research.

Presently, we are beginning to form a reasonably coherent picture of high-speed boundary layer behavior, particularly in terms of the structure of turbulence, and its response to pressure gradients and its interaction with shock waves. It seemed to us that this was an opportune time to try to bring together the efforts of different research groups, and to present the sum of our present knowledge as a unified picture. We recognize that the details of the picture may change as new insights become available, and we hope that this volume may serve to stimulate such insights.

Our primary focus is on how the effects of compressibility influence turbulent shear-layer behavior, with a particular emphasis on boundary layers. We have restricted ourselves to boundary layers where the freestream is supersonic, and transonic and hypersonic flows are not considered in detail. Without being too precise, we are generally dealing with boundary layers where the freestream Mach number is greater than 1.5, and less than 6. The low Mach number limit is set to reduce the complexities introduced by having large regions of mixed subsonic and supersonic flow, and the high Mach number limit is set to avoid the presence of real gas and low density effects. Moreover, we will restrict ourselves to fully turbulent flows and the problems of stability and transition at high speed will not be discussed. These problems are numerous and important, and they deserve a separate treatment.

Even within these bounds, there exists a rich field of experience, and in Chapter 1 we have tried to give an overview of the complexities that occur in compressible turbulent flows. The equations of motion are discussed in Chapter 2, and the mean equations for turbulent flow are given in Chapter 3, primarily to develop some useful scaling and order-of-magnitude arguments. As further background, a number of concepts important to the understanding of compressible turbulence are introduced in Chapter 4, with a particular emphasis on the development of rapid distortion approximations. Morkovin's hypothesis and Reynolds Analogies are discussed in Chapter 5. Chapter 6 is concerned with the behavior of mixing layers, and Chapters 7 and 8, respectively, deal with the mean flow and turbulence structure of zero pressure gradient boundary layers. The behavior of more complex flows, with pressure gradients and surface curvature, is considered in Chapter 9, where we also illustrate how rapid distortion approximations can give some useful insight into the behavior of these flows. When the flow is compressed rapidly, shock waves appear, and shock boundary layer interactions in two- and three-dimensional flows are the subject of Chapter 10, where we discuss the role of shock wave unsteadiness and the consequences of separation. Throughout the book, we have tried to emphasize some of the possibilities for future development, including guidelines for future experiments, the prospects for computational work, tur-

bulence modeling, and rapid distortion approaches. Chapters 2 and 3, and to some extent Chapters 4, 5, and 7, treat some basic elements in the description of compressible turbulent flows. Although much of this work is available elsewhere, we felt it would be useful to address the elementary properties of these flows in a systematic manner, especially for newcomers to the field. The other chapters are more specialized, and are probably more suitable for readers who have some previous expertise.

No book gets published without a great deal of help along the way. We would like to thank the U.S. Air Force Office of Scientific Research, the Army Research Office, ONR, ARPA, NASA Headquarters, NASA Langley Research Center, NASA Lewis Research Center, CNRS, ONERA, Project Hermès, and DRET for supporting our own research work in this area. The NASA/Stanford Center for Turbulence Research supported a series of lectures by AJS that planted the idea for this book. NATO-AGARD encouraged us to review the data in several publications, and that work was invaluable in getting us started here. Finally, there are a number of individuals who helped us along the way. To Katepalli Sreenivasan, Dennis Bushnell and Lisa Goble we express our sincere thanks. To Hans Fernholz, John Finley, Eric Spina and Randy Smith we extend special thanks for allowing us to adapt their work liberally. Jean Cousteix and John Finley were especially helpful with many detailed comments. To our wives and families go the greatest debt, for freely granting us the time it took to get this done. AJS would like to dedicate his efforts to his parents, Ben Smits and Truus Schoof-Smits, who passed away before this book could be completed.

Contents

Chapter 1

Introduction

1.1 Preliminary Remarks

The history of research in turbulent compressible flows is somewhat checkered, in that changes in national and international priorities have had a large impact on the continuity of effort. The high level of activity that lasted from the end of World War II to about 1965 was largely driven by the wish to fly at supersonic speeds, and the need to solve the hypersonic re-entry problem. Once these aims were met, the general level of urgency diminished considerably, and further efforts became severely reduced in scope. Recently, we saw another upsurge in activity, driven mainly by a new set of national priorities such as the desire to fly at hypersonic speeds, and the projected need for a low-cost supersonic transport aircraft. The failure of the hypersonic flight program came largely because it is not yet possible to design any airplane, let alone a hypersonic airplane, using computational fluid dynamics alone. Much of the fundamental knowledge required to attain hypersonic flight was not available, and the codes could not predict transition, turbulence, and supersonic combustion with sufficient accuracy. If hypersonic flight is to become a reality, generic hypersonic research will need to receive considerable additional attention. Similarly, to make supersonic flight commercially attractive, significant levels of new research will be required to improve fuel efficiency, reduce pollution (in particular the ozone depletion), and minimize noise levels. A better understanding of compressibility effects on turbulence will have a crucial impact on the development of answers to these engineering challenges.

The flow over an actual vehicle in a real fluid is complex at any speed. Boundary layers form which may be laminar or turbulent, and the point where the laminar-to-turbulent transition takes place will vary within the flight envelope. The surfaces of the vehicle are usually curved in at least one direction, the surface area is continually changing in the streamwise direction, and pressure gradients generally act in three directions simultaneously. Significant regions of three-dimensional flow can therefore occur, and regions of separated flow

may develop, with the appearance of free shear layers. Downstream of the vehicle, and inside the propulsion system, jets, wakes, and mixing layers can usually be found, and their interaction with each other and with the boundary layer on the vehicle surface can produce extremely complex flows.

When a vehicle is traveling at high speed, so that the freestream Mach number is greater than one, additional effects come into play. The kinetic energy of the motion now constitutes a significant fraction of the total energy contained in the fluid. Within the shear layers, therefore, viscous dissipation becomes important in the mean kinetic energy balance. Significant temperature gradients occur across shear layers even under adiabatic flow conditions (that is, there is no heat transfer to the fluid). As a result, when a turbulent shear layer develops in supersonic flow, mean density gradients exist in addition to mean velocity gradients and the turbulent field consists of pressure, density and velocity fluctuations. Energy is continually transferred among these modes, and the transport mechanisms are therefore more complex than those encountered in constant property flows. In some parts of the flow, the relative speed of adjacent turbulent motions may be transonic or supersonic, and local compression waves and shock waves can affect the turbulence evolution. The density depends on the pressure and temperature, and vorticity can be produced through baroclinic torques. The heat transfer across the layer cannot be neglected in most practical applications, and the temperature field interacts directly with the velocity field. When pressure gradients are present, the compression and dilatation of fluid elements will be important in addition to the usual effects of pressure gradient as we understand them from our experience of incompressible flows. Perhaps most important, shock waves can occur that may cause separation, strongly unsteady flows, and local regions of intense heat transfer. If the Mach number is high enough, turbulence energy can be transported by sound radiation and dissipated by local shock formation.

Of course, the general behavior of turbulent shear layers is not well understood, even in subsonic flow, and the evolution of a shear layer in supersonic flows is considerably more complex. For example, we have at present a reasonably complete description of the two-dimensional, incompressible, flat plate turbulent boundary layer. At supersonic speeds, we are only starting to develop a similar description of the boundary layer structure, and the picture is not nearly as complete as in the case of incompressible flow. Nevertheless, progress has been made, as we try to make clear. In mixing layers, we know that compressibility can severely reduce the spreading rate, which implies a reordering of the flow structure. The reasons are not entirely clear, but several conjectures exist, as we discuss. Probably the most dramatic effects of compressibility on turbulence are seen in the response of turbulent motions to strong pressure gradients, or their interaction with shock waves. Here we have no simple analogue with a "similar" incompressible flow. For instance, longitudinal pressure gradients in a compressible flow will cause the compression

or dilatation of vortex tubes, thereby enhancing or reducing pressure fluctuations and the longitudinal component of the velocity fluctuations. When shock waves are present in wall-bounded flows, separation will occur if the shock is strong enough (a phenomenon that can be understood from subsonic experience), but strong pressure gradients may cause the wall friction and heat transfer to increase (observations that are in direct contrast to subsonic experience). Even if the shock is not strong enough to cause separation there can exist a strong coupling between the shock and the turbulence, and the distortions of the shock sheet and its unsteady motion have been widely observed. Understanding the shock motion and the resultant unsteady heat transfer and pressure loading is of great importance in many aerodynamic flows.

In a sense, our progress in understanding can be measured by our ability to predict the flow, but "prediction" is an ambiguous concept. Understanding assumes that some rationale has been constructed to describe a physical process. Prediction can be the result of some interpolation procedure, which may be largely empirical without any deep physical understanding. For example, it is possible in many flow configurations, even when they are very complex, to predict the wall-pressure, heat-transfer, and skin-friction distributions with a reasonable degree of accuracy, using simple mixing length or algebraic eddy viscosity models. As long as the flow does not depart dramatically from previous experience we can have a reasonable level of confidence in the prediction, because in many aspects these simple models represent data correlations. In contrast, it is now possible to perform Direct Numerical Simulations (DNS) for some low Reynolds number flows without any explicit modeling. Here we obtain the entire three-dimensional, compressible, time-dependent flowfield. Yet neither the empirically based prediction method, nor the full DNS results allow us to claim that we understand the flowfield. In the first case, a closer examination of the predicted flowfield usually reveals that mixing length or eddy viscosity concepts are inadequate to represent accurately flowfield data such as the mean velocity profile or the Reynolds stress distributions, reflecting the fact that these models do not capture some of the essential flow physics. In the second case, DNS provides us with such an enormous amount of information that our immediate response is to look for relatively simple concepts or models that represent the database in a more organized and comprehensible fashion; exactly the process we follow in interpreting the far more limited data sets generated by experiment.

It is this development of working models that represents one of the fundamental aims of turbulence research, to help reduce the complexity of the actual flowfield dynamics to a simpler set of modeled flow phenomena, without sacrificing any important physical mechanisms. For example, the widespread search for "coherent" structures in turbulent flows is driven mainly by the belief that it may be possible to represent the essential dynamics of a turbulent flowfield by a small set of representative "events" whose generation-dissipation cycle

can be described, and whose interaction is understood. As Sreenivasan (1989) suggests, "even a highly successful model does not account for every detail, but two of its hallmarks are wide applicability and well-understood limitations."

As stated in the Preface to the First Edition, the specific aims of this book are to bring together the most recent results of research on the behavior of turbulent shear layers at supersonic speed, and to present some conclusions regarding our present understanding of these flows (that is, to develop the "models" referred to by Sreenivasan). The main emphasis is on the behavior of turbulent boundary layers and mixing layers. Two- and three-dimensional boundary layers are considered, as well as shock wave-boundary layer interactions, separated flows, and flows with favorable and adverse pressure gradients and with streamline curvature. We have restricted ourselves to supersonic flows, and therefore we do not consider flows where it would be necessary to take account of chemical reactions or nonequilibrium effects, and we assume throughout that the test gas is a perfect gas with constant specific heats.

By way of introduction, we now consider some aspects of compressible turbulent flows to illustrate the range of phenomena that may be encountered. These phenomena are discussed in the context of four particular examples: the behavior of a zero pressure gradient, flat plate boundary layer; the structure of a mixing layer as a function of Mach number; the interaction of freestream turbulence with a shock wave; and a shock wave-boundary layer interaction generated by a compression corner. Finally, we give a brief discussion of measurement techniques for turbulence in compressible flows for the purpose of assessing the uncertainties and errors present in the data, and provide a short description of nonintrusive techniques for quantitative flow visualization in high-speed flows.

1.2 Flat Plate Turbulent Boundary Layers

Figure 1.1 shows two sets of air boundary layer profiles at about the same Reynolds number, one set measured on an adiabatic wall, the other measured on an isothermal wall. The momentum thickness Reynolds number Re_θ ($= \rho_e U_e \theta / \mu_e$) is approximately 9500, where U_e is the freestream velocity, and the viscosity and density are evaluated at the freestream temperature. The temperature of the air increases near the wall, even for adiabatic walls, because the dissipation of kinetic energy by friction is an important source of heat in supersonic shear layers. This leads to a low-density, high-viscosity region near the wall. Somewhat surprisingly, the velocity, temperature, and mass flux profiles for the two flows given in Figure 1.1 look very much the same, even though the boundary conditions, Mach numbers, and heat-transfer parameters differ considerably. The velocity profiles in the outer region, in fact, follow a 1/7th power-law distribution quite well, just as a subsonic velocity profile would at this Reynolds number. With increasing Mach number, however, the elevated

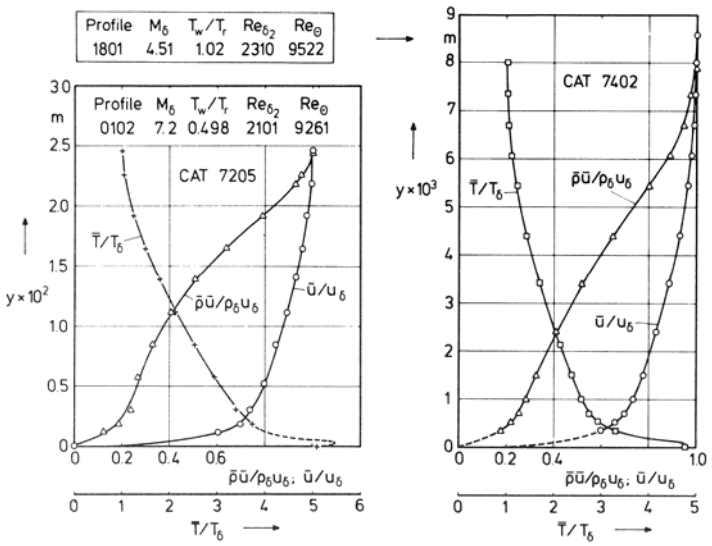

Figure 1.1. Turbulent boundary layer profiles in air ($T_\delta = T_e$). From Fernholz and Finley (1980), where catalogue numbers are referenced. (Reprinted with permission of the authors and AGARD/NATO.)

temperature near the wall means that the bulk of the mass flux is increasingly found toward the outer edge of the layer. This effect is emphasized even more in the boundary layer profiles shown in Figure 1.2, where the freestream Mach number M_e was 10 for a helium flow on an adiabatic wall. For this case, the temperature ratio between the wall and the boundary layer edge was about 30.

If the total temperature T_0 was constant across the layer, then from the definition of the total temperature ($T_0 \equiv T + u^2/2C_p$), we see that there is a very simple relationship between the temperature T and the velocity u. Because there is never an exact balance between frictional heating and conduction (unless the Prandtl number equals one), the total temperature is not quite constant even in an adiabatic flow, and the wall temperature depends on the recovery factor r (see Chapter 5 for further details). Hence, for a perfect gas:

$$\frac{T_w}{T_e} = 1 + r\frac{\gamma - 1}{2}M_e^2,$$

where the subscript w denotes conditions at the wall, and the subscript e denotes conditions at the edge of the boundary layer, that is, in the local freestream, so that the edge Mach number M_e is given by $u_e/\sqrt{\gamma RT_e}$. Since $r \approx 0.9$ for a zero pressure gradient turbulent boundary layer, the temperature

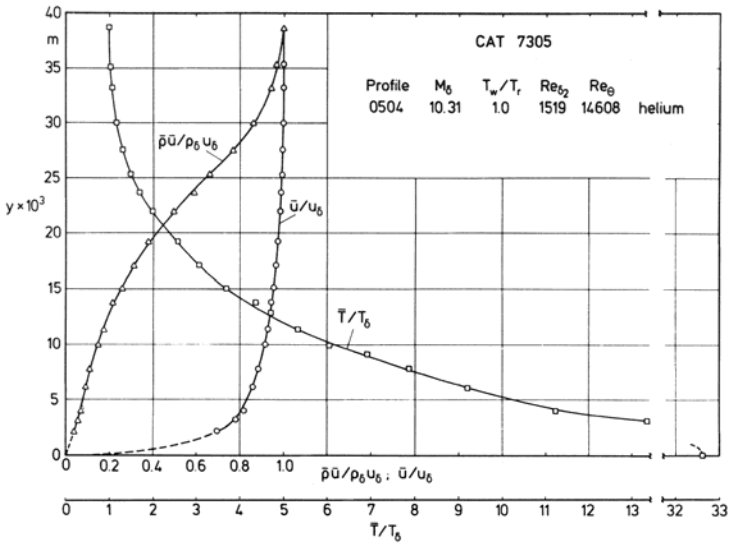

Figure 1.2. Turbulent boundary layer profiles in helium ($T_\delta = T_e$). Figure from Fernholz and Finley (1980), where catalogue numbers are referenced. Original data from Watson et al. (1973). (Reprinted with permission of the authors and AGARD/NATO.)

at the wall in an adiabatic flow is nearly equal to the freestream total temperature. For example, at a freestream Mach number of 3, the ratio $T_w/T_0 = 0.93$.

The static temperature, however, can vary significantly through the layer, and as a result the fluid properties are far from constant. To the boundary layer approximation, the static pressure across the layer is constant, as in subsonic flow, and therefore for both examples shown in Figure 1.1 the density varies by about a factor of 5. The viscosity varies by somewhat less than that: if we assume a power law to express the temperature dependence of viscosity, for instance $(\mu/\mu_e) = (T/T_e)^{0.76}$ (see Section 2.2), then the viscosity varies by a factor of 3.4. Because the density increases and the viscosity decreases with distance from the wall, the kinematic viscosity decreases by a factor of about 17 across the layer. It is therefore difficult to assign a single Reynolds number to describe the state of the boundary layer. Of course, even in a subsonic boundary layer the Reynolds number varies through the layer because the length scale near the wall depends on the distance from the wall. But here the variation is more complex in that the nondimensionalizing fluid properties also change with wall distance. One consequence is that the relative thickness of the viscous sublayer depends not only on the Reynolds number, but also on the Mach number and heat-transfer rate because these will influence the

distribution of the fluid properties. At very high Mach numbers, the whole layer may become viscous-dominated.

A number of characteristic Reynolds numbers may be defined for compressible turbulent boundary layers. For example, for the boundary layer described in Figure 1.2, a Reynolds number based on freestream fluid properties ($Re_\theta = \rho_e u_e \theta/\mu_e = 14,608$) suggests a fully turbulent flow, but a Reynolds number based on fluid properties evaluated at the wall temperature ($= \rho_w u_e \theta/\mu_w = 68$) indicates that low Reynolds number effects will undoubtedly be important. Fernholz and Finley (1980) proposed another useful Reynolds number to describe supersonic boundary layers, $Re_{\delta 2}$, defined by the ratio of the highest momentum flux ($=\rho_e u_e^2$) to the maximum shear stress ($=\tau_w$). Using the estimate for τ_w given by $\mu_w u_e/\theta$, we have $Re_{\delta 2} = \rho_e u_e \theta/\mu_w$. For adiabatic and heated walls, Re_θ is always greater than $Re_{\delta 2}$. For the profile shown in Figure 1.2 they differ by a factor of almost 10. We see that any comparisons we try to make between subsonic and supersonic boundary layers must take into account the variations in fluid properties, which may be strong enough to lead to unexpected physical phenomena.

In fact, subsonic experience is not very helpful in understanding the effects of fluid property variations because the temperature gradients experienced in supersonic boundary layers can be so severe. An "equivalent" subsonic boundary layer experiment with a similarly strong temperature distribution would inevitably be influenced by buoyancy effects, whereas buoyancy effects in supersonic flows are almost always negligible. Even if the plate were oriented vertically, the buoyancy force present in the subsonic case would accelerate the flow and the acceleration would occur in a manner quite different from an imposed longitudinal pressure gradient because the buoyancy force will vary with the distance from the wall. Similar limitations would not apply to a numerical simulation, because the buoyancy force could simply be switched off, and a simulation of a turbulent boundary layer on a strongly heated plate (in zero gravity) could provide valuable data to help understand the effects of variable fluid properties.

Despite the difficulties introduced by variable fluid properties, some simple scaling arguments can be made to help connect supersonic and subsonic data. Take, for example, the behavior of the wall friction. Probably the most widely recognized influence of Mach number on turbulent boundary layer behavior is the observation that at a constant Reynolds number the skin-friction coefficient decreases as the Mach number increases (see Figure 1.3). What at first sight appears to be a rather provocative result can be explained largely in terms of the fluid property variations across the boundary layer. The skin-friction coefficient C_f and the Reynolds number Re_x are by definition based on the fluid properties at the freestream temperature. It can be argued that the friction at the wall is much more likely to scale with the conditions at the wall than with conditions in the freestream. Qualitatively, this argument seems quite

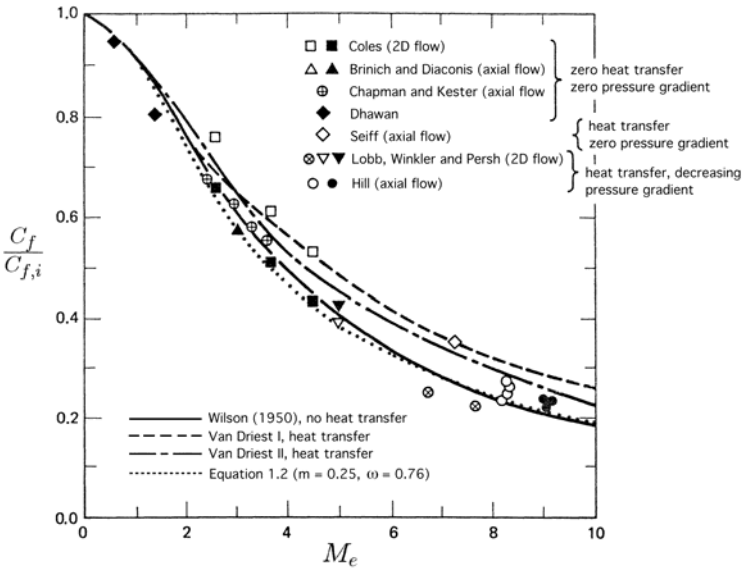

Figure 1.3. C_f versus Mach number, with and without heat transfer. The value of Re_x is approximately constant at 10^7 for all the data. Equation 1.2 based on boundary layer thickness, with $m = 0.25$ and $\omega = 0.76$, is given by the dotted line. (Adapted from Hill (1956), with permission.)

reasonable: as the temperature near the wall increases, the density decreases and the skin friction should also decrease, which it does. If we then assume that the skin-friction coefficient in a supersonic flow still varies with Reynolds number in the same way it does in a subsonic flow, except that the skin-friction coefficient and the Reynolds number should be defined in terms of the fluid properties evaluated at the wall temperature, the Mach-number-dependence is no longer explicitly present. For example, for an incompressible isothermal flow we have approximately a power-law dependence given by:

$$C_{f,i} = K \left(\frac{\rho_e u_e \lambda_i}{\mu_e} \right)^{-m}, \tag{1.1}$$

where K is a constant, and λ_i is a length scale for the incompressible flow, such as the distance from the origin of the boundary layer x, the boundary layer thickness δ, or the momentum thickness θ. If we assume that the same relation holds for a compressible boundary layer, provided that ρ and μ are taken at the wall conditions, we expect that

$$\frac{\tau_w}{\frac{1}{2}\rho_w u_e^2} = K \left(\frac{\lambda_i}{\lambda_c} \right)^{-m} \left(\frac{\rho_w u_e \lambda_c}{\mu_w} \right)^{-m},$$

so that

$$C_f \equiv \frac{\tau_w}{\frac{1}{2}\rho_e u_e^2} = K\left(\frac{\rho_w}{\rho_e}\right)\left(\frac{\lambda_i}{\lambda_c}\right)^{-m}\left(\frac{\rho_w u_e \lambda_c}{\mu_w}\right)^{-m}.$$

That is,

$$C_f = C_{f,i}\left(\frac{\lambda_i}{\lambda_c}\right)^{-m}\left(\frac{T_e}{T_w}\right)^{1-(\omega+1)m}, \tag{1.2}$$

where it was assumed that the viscosity follows a power law relation such as $\mu_w/\mu_e = (T_w/T_e)^\omega$. Here λ_c is the corresponding length scale for compressible flow. If we use x, the ratio $\lambda_i/\lambda_c = 1$, and for a one-seventh power law on the velocity, $m = 0.2$ (see Section 7.6). This simple scheme seems to describe the data trend quite well, although the prediction is somewhat low. If we use δ, experiments show that at a constant Re_x, $\delta_i/\delta_c \approx 1$, but now $m = 0.25$ for a one-seventh power law. This correlation was first suggested by Hinze (1975), and the agreement with the data is better than before (see the dotted line in Figure 1.3). If we choose the momentum thickness instead, $m = 0.25$, and by using the momentum integral equation $d\theta/dx = C_f/2$ we find that for an isothermal wall at a fixed Re_x:

$$\frac{\theta_c}{\theta_i} = \left(\frac{T_e}{T_w}\right)^{\frac{1-(\omega+1)m}{1+m}}, \tag{1.3}$$

which gives skin-friction values near the high end of the data range. Despite the differences, these trends argue that the "correct" Reynolds number for supersonic turbulent boundary layers is that based on fluid properties evaluated at the wall temperature, rather than Re_θ or $Re_{\delta 2}$. This issue is considered further in Chapter 7.

More elaborate schemes may be devised to improve the correlation of the data. One popular approach is the concept of an *intermediate temperature* or *reference temperature*, that is, fluid properties are not evaluated at the wall temperature but at some temperature between the value at the wall and that in the freestream (Rubesin and Johnson, 1949; Monaghan, 1955). Although originally proposed as a convenient concept for data correlation, Dorrance (1962) showed that for a laminar boundary layer the reference temperature corresponds approximately to the velocity averaged temperature (see also van Oudheusden (1997)). Underlying these efforts is the belief that compressibility effects (such as the influence of the pressure field, and nonlinearities such as local, instantaneous shock waves) may not have a strong effect on turbulent boundary layers, at least at nonhypersonic speeds. The effects of Mach number may be essentially passive: apart from changing the local fluid properties the dynamic effects could well be small. This concept was first described by Morkovin (1962), and it is widely known as Morkovin's hypothesis (see Section 5.2 for further details).

As can be seen in Figure 1.3, this particular approach seems to work well for relating the supersonic skin-friction behavior to the subsonic behavior. What

about the mean velocity distribution? Here, a great deal of effort has been spent on establishing a relationship between the local velocity and temperature, either by empirical means or by manipulation of the energy equation, with the aim of deriving a "compressibility transformation" such that the supersonic velocity profile, when plotted in the appropriately transformed coordinates, will collapse on the curve established for subsonic flows. This is an important consideration, especially in the region near the wall where simple power laws are no longer useful. An extensive discussion of this approach was given by Coles (1962), and it is considered in some detail in Chapter 7. A widely used transformation was developed by van Driest (1951) who was able to integrate the mean energy equation under a set of reasonably restrictive assumptions and use the resulting temperature-velocity relationship to define a transformed velocity that takes account of the fluid property variations across the layer. As pointed out by Bushnell et al. (1969) this transformation appears to collapse zero pressure gradient turbulent boundary layer data at Mach numbers up to 12, and the constants in the logarithmic law appear unchanged from their subsonic values (see Chapter 7).

In addition, by using an integral momentum balance it is possible to use this compressibility transformation to predict the skin-friction variation with Mach number. This represents a more complete description of the skin-friction behavior than the one given by Equation 1.2, and the analyses presented by van Driest for flows with and without heat transfer appear to correlate well with existing data (see Figure 1.3).

What about the turbulence? Flow visualizations of supersonic turbulent boundary layers using Rayleigh scattering show boundary layer cross-sections that look remarkably similar to cross-sections obtained in subsonic boundary layers using smoke flow visualization (see Figure 1.4). The simplest quantitative comparison between the turbulence behavior in subsonic and supersonic boundary layers is to compare the distributions of mean square of the streamwise velocity fluctuations $\overline{u'^2}$. When normalized by u_τ^2 $(= \tau_w/\rho_w)$, there is a clear decrease in fluctuation level with increasing Mach number (see Figure 1.5). However, if the streamwise normal stress $\rho\overline{u'^2}$ is normalized by the wall shear stress τ_w, as suggested by Morkovin, the Mach number dependence is no longer evident (see Figure 1.2). The remaining scatter near the wall is probably due to probe resolution difficulties (see Section 1.7.1). Thus the density transformation ρ/ρ_w seems to collapse the turbulence intensities. This result is not immediately obvious, but in Chapters 4 and 8 we give some largely empirical arguments why this should work. The major point to be made here is that a scaling which incorporates the variations in fluid properties (in this case the density) effectively removes the explicit Mach number dependence.

In contrast to the success of Morkovin's scaling for the turbulence intensities, an inspection of other turbulence properties reveals characteristics that cannot be collapsed by a simple density scaling. For example, it is generally

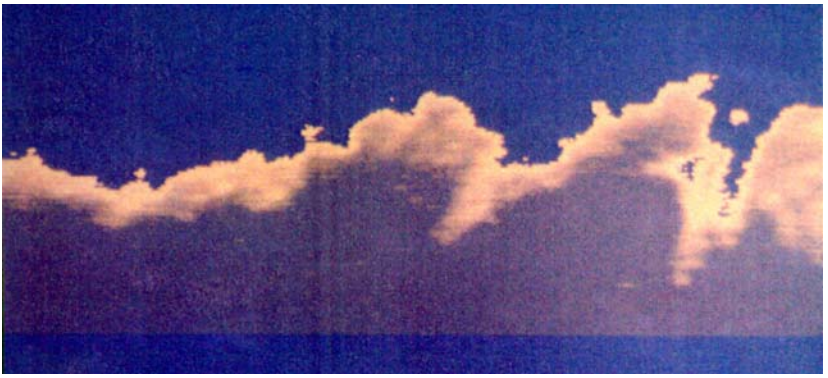

Figure 1.4. Flow visualization of supersonic turbulent boundary layers using Rayleigh scattering (the technique is described in Section 1.7.4). Flow is from left to right. The freestream Mach number is 2.5, and R_θ is about 25,000. (Figure from Smith and Smits (1995). Copyright 1995, Springer-Verlag. Reprinted with permission.)

believed that the intermittency profile is fuller than the corresponding subsonic profile (see, for example, Owen et al. (1975) and Robinson (1986)). In addition, Smits et al. (1989) found that space-time correlations indicate that the (nondimensional) spanwise scales in subsonic and supersonic boundary layers were almost identical but that the (nondimensional) streamwise scales

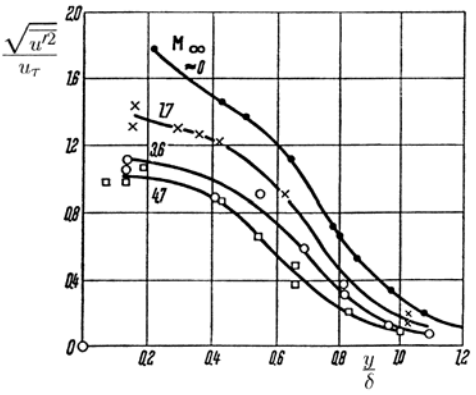

Figure 1.5. Distribution of turbulent velocity fluctuations in boundary layers. Measurements are from Kistler (1959) and Klebanoff (1955). (Figure from Schlichting (1979). Copyright 1979, The McGraw-Hill Companies. Reproduced with permission.

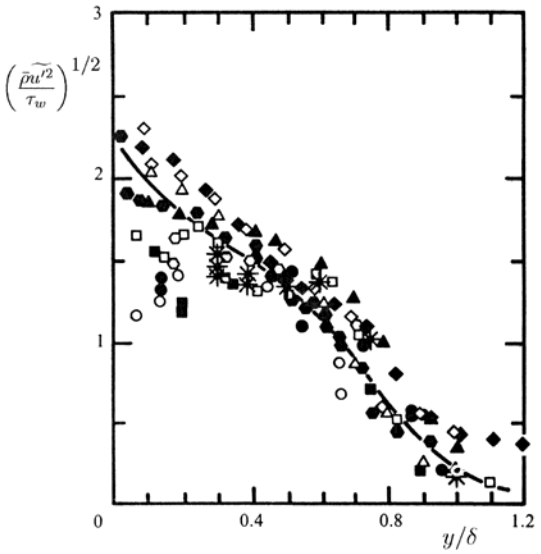

Figure 1.6. Velocity fluctuation intensity in supersonic boundary layers: ∗, Dussauge and Gaviglio (1987); ⭘, $M = 1.72$; ●, $M = 3.56$; ○, $M = 4.67$, Kistler (1959); △, hot wire; ◇, laser, $M = 2.9$, Johnson and Rose (1975); ▲, $M = 2.9$, Smits et al. (1989); ■, $M = 2.32$, Eléna and Lacharme (1988); □, $M = 2.3$, Debiève (1983); ⬣, $M = 2.32$, Eléna and Gaviglio (1993); ◆, $M = 3$, Yanta and Crapo (1976). (Figure taken from Dussauge and Gaviglio (1987). Copyright 1987, Cambridge University Press. Reprinted with permission.)

in Alving's subsonic flow were about twice the size of those in a Mach 2.9 supersonic flow (see Figures 8.39, 8.37, and 8.38).

How can we explain these differences? Are they indications of "true" compressibility effects, that is, dynamic effects due to significant levels of pressure and density fluctuations, or can they also be explained on the basis of fluid property variations? A crucial parameter is the Mach number associated with the turbulent fluctuations, M': if M' approaches unity we expect direct compressibility effects to become important. Local shock waves called *shocklets* would appear, and the fluctuating pressure would become important, not just in the usual pressure strain term in the Reynolds averaged equations but as a significant part of the total turbulent kinetic energy budget. We should note here the distinction between the *fluctuation Mach number* or *turbulence Mach number* M_t, which is the Mach number found using the velocity fluctuation and the mean speed of sound, and the *fluctuating Mach number* M', which takes into account that the local speed of sound also fluctuates. The value of M_t may give a more accurate representation of compressibility effects, at

least in boundary layer flows, although M' turns out to be a useful parameter also. These issues are discussed in more detail in Chapters 3 and 4, but it is worth noting that $M' > M_t$ for adiabatic flows, and they are functions of Mach and Reynolds numbers. If we take $M' = 0.3$ as the point where compressibility effects become important for the turbulence behavior, we expect that for adiabatic boundary layers at reasonable Reynolds numbers this point will be reached with a freestream Mach number of about 4 or 5. As the freestream Mach number increases, the temperature fluctuations become more significant than the velocity fluctuations. The maximum value of M' shifts away from the wall with increasing Mach number, and in hypersonic flows the maximum value can be located near the edge of the layer.

Until recently, one of the major difficulties in studying these problems in boundary layers is that we did not have a general understanding of Reynolds number scaling, and it was therefore difficult to distinguish between Mach and Reynolds number effects. Most of our understanding of boundary layer structure is based on studies of the "canonical" boundary layer, that is, one developing on a flat, adiabatic plate, in a zero pressure gradient, under incompressible flow conditions. Most of these studies were performed at low Reynolds numbers, so that the inner layer occupied a significant fraction of the total boundary layer, and laboratory measurements could be obtained with sufficient resolution. It is doubtful that models for boundary layer structure derived from such studies will apply unchanged to a wider range of flow conditions. In particular, how can the effects of Mach and Reynolds numbers be incorporated? We are still a long way from a general answer to this question but some progress has been made, as discussed in Chapters 7 and 8.

1.3 Propagation of Pressure Fluctuations

Another remarkable feature of supersonic shear flows is how information, such as a change in pressure, is transmitted. How does the flowfield "know" that an "event" or some other kind of perturbation has occurred? This propagation of information without mass transport is directly connected to the nature of the pressure field.

Some examples can be used to describe the problem and to illustrate some of the differences between high-speed and low-speed flows. Consider a source emitting small-amplitude pressure waves in a uniform, low-speed stream. The wave fronts are spherical (or circular in a plane) and the acoustic rays, which are normal to the wave fronts, are pointing outwards from the source in all directions. When the flow is supersonic, perturbations travel only along characteristic directions, and the perturbations are called *Mach waves*. In a given plane, under uniform flow conditions, the Mach waves are straight lines inclined to the flow direction at an angle given by the local Mach number ($= \sin^{-1}(1/M)$). In a given plane, two waves are emitted (a left-running

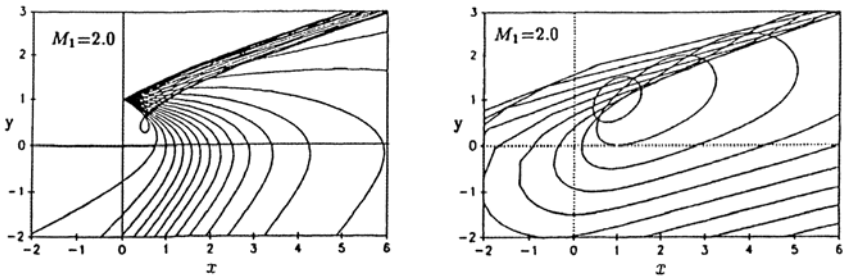

Figure 1.7. Ray paths (left) and wave fronts (right) in a shear layer with a hyperbolic tangent profile where the external Mach numbers are 3 and 1. The source is located at $y = 1$, where the Mach number is 2. The results are presented in the frame of reference of the observer located at $y = 0$, and for which $U = 0$. (From Papamoschou (1991), with the author's permission.)

wave and a right-running wave), so that the information about an event occurring at a given point can only be felt within an angular sector in the plane, originating at the point and lying in the downstream direction. In three dimensions, the sectors make up a Mach cone. Similarly, a given point in the flow can receive information from only a limited portion of space defined by an angular sector or Mach cone originating at the point and lying in the upstream direction. Obviously, information cannot propagate in the upstream direction in supersonic flows as it does at low speeds.

Less trivial is the question of the transmission of information (that is, the propagation of pressure perturbations) at high speed in an inhomogeneous medium. This problem has been examined by Papamoschou (1990, 1991, 1993) for the case of perturbations propagating through a free shear layer. For the sake of simplicity and to characterize the effects of high speed only, he considered the case of constant sound speed (that is, constant temperature) in a shear layer that was not developing in the longitudinal direction. He also neglected the scattering and the absorption of sound by the shear layer. Papamoschou obtained an approximation valid for wavelengths that were small compared to the thickness of the shear layer which illustrates some of the possible effects of compressibility. An example is given in Figure 1.7. An observer located within the shear layer receives pressure information principally from the upstream flow, but there is some possibility—although limited—for backwards propagation of information. Transmission of information in the transverse direction is less affected. For example, the Mach cone is distorted by the presence of the mean velocity profile: this was expected, because pressure waves travel at the speed of sound with respect to the medium, and the medium is moving at velocities of the order of the speed of sound. Thus, in nonuniform flow, the cone of influence can be strongly distorted.

Morkovin (1987) considered the cross-flow communication crucial for the analysis of stability problems in high-speed shear layers (the work by, for example, Mack (1984)). In the case of turbulent shear layers, the theory for such interpretations does not yet exist. However, if the large-scale structures found in shear flows are the results of the most amplified modes, it may be suspected that their dynamics will be also affected by such phenomena: if the direction of acoustic propagation is limited by compressibility, communication between different parts of the flow may become less efficient and produce less amplification of the perturbation. Finally, from the point of view of statistical analysis of fully developed turbulence, the pressure field associated with turbulent eddies probably has a very different nature in high-speed flow than it does in low-speed flow, and this may affect global properties such as the turbulent transport, even in boundary layers. So it is possible that compressibility effects may play a role in the turbulence behavior even at nonhypersonic Mach numbers.

1.4 Mixing Layers

The behavior of mixing layers has significant implications for the understanding of compressible turbulent flows. In particular, it has been widely observed that the growth rate of mixing layers decreases dramatically with increasing Mach number. The curve shown in Figure 1.8 is based on data presented at a conference held at NASA Langley Research Center in 1972, and it indicates that the growth rate of a free shear layer at Mach 3 is reduced by a factor of three when compared to its incompressible growth rate, whereas at Mach 8 it is reduced by a factor greater than five. Clearly, it is of great interest to determine why the growth rate is so strongly reduced by increasing the Mach number. For instance, to propel an aircraft at hypersonic speeds, it is likely that the combustion will need to occur at supersonic speeds. This supersonic combustion ramjet or "scramjet" must mix the fuel and oxidizer and initiate combustion within the length of the engine. Because the gases will be moving at supersonic speed within the engine, and the length of the engine is limited by reasons of weight, efficient mixing is essential. Although there is some evidence that initial conditions can have a first-order effect on the development of mixing layers (Bell and Mehta, 1990), the reduced growth rate of fully developed compressible mixing layers needs to be understood.

In the discussion of boundary layers we saw that the most obvious effect of compressibility was to impose a temperature gradient across the layer, so that the density and viscosity varied with distance from the wall. Direct compressibility effects seemed to be of second-order importance, at least at supersonic Mach numbers, because the fluctuating Mach numbers were small. In mixing layers, it appears that density variations and Mach number differences are both important. For example, Brown and Roshko (1974) observed that changing

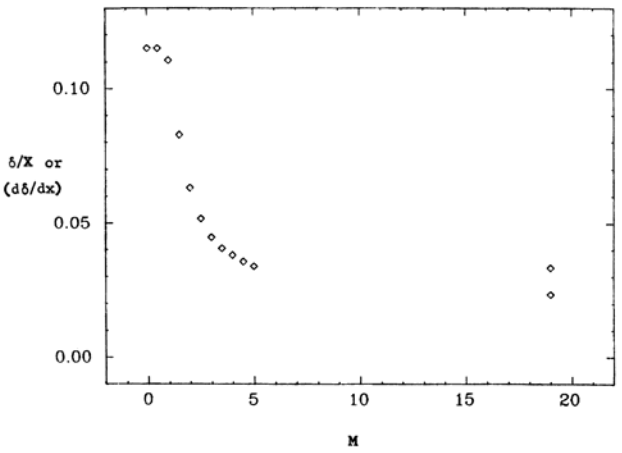

Figure 1.8. The "Langley curve," showing the growth rate of mixing layers as a function of Mach number. From Kline et al. (1981), based on the data presented by Birch and Eggers (1972). (Reprinted with permission of the Thermosciences Division, Department of Mechanical Engineering, Stanford University.)

the density ratio across a subsonic mixing layer by a factor of seven reduced its growth rate by about 30%. In contrast, a high-speed mixing layer where the Mach number difference results in a similar density ratio has a growth rate of only about one-quarter of its incompressible value (see Figure 6.2). Direct compressibility effects seem to have a first-order influence on the behavior of mixing layers, in contrast to the case of boundary layers. For a review of the effects of density variations on turbulence and turbulent shear flow, see Chassaing et al. (2002).

We expect differences between compressible and incompressible flows to occur when eddies are in transonic or supersonic motion relative to each other. The momentum and energy budgets will be affected not just by fluid property variations but by the exchange of momentum and energy among the vorticity, sound, and entropy modes (related mainly to rotational velocity, pressure, and temperature fluctuations, respectively). Again we need some measure of the Mach number of the turbulence. We are concerned with a mixing layer between a high-speed side and a low-speed side, so the most relevant Mach number is therefore not the external Mach numbers, or even the Mach number difference, but the Mach number based on the motion of the large-scale motions relative to the freestream flows on either side of the mixing layer. This *convective Mach number* M_c is defined by $M_c = \Delta U/(a_1 + a_2)$ for isentropic flows. Simply put, M_c expresses the convection velocity of the large-scale motions relative to the average sound speed (see Bogdanoff (1983),

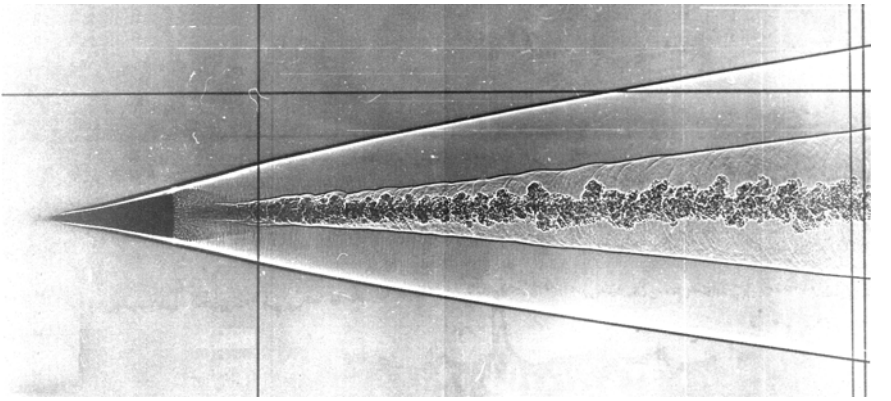

Figure 1.9. Flowfield generated by a conical projectile made visible using shadowgraphy. The corresponding Mach number and freestream Reynolds number based on model length are 5.6 and 4.7×10^6. Note the shocklets and other acoustic disturbances emanating from the structures in the wake. (Photograph provided by T. Canning, NASA-Ames Research Center.)

Norman and Winkler (1985), Papamoschou (1986), and Papamoschou and Roshko (1988)). As M_c approaches unity, we would expect to see shocklets form in the regions where the relative motion between large-scale motions is supersonic.

The analysis by Hussaini et al. (1985) shows that when a two-dimensional vortex is suddenly placed in a supersonic flow, a bow shock forms. The vorticity generated as a result of the curved shock reverses the sign of the vorticity in one half of the vortex while increasing the strength of the other half. The original vortex is effectively split into two smaller parts of opposite sign, and Hussaini et al. postulated that this mechanism might provide an explanation for the effects of shocklets, such as those observed in the near wake of objects moving at supersonic speeds (see Figure 1.9).

The subsonic mixing layer is defined in terms of two well-defined structures: the large-scale transverse eddies or spanwise "rollers" and the longitudinal "hairpin" vortices in the region between the large-scale roll-ups (see Figure 1.10). Experiments show that the structure of the organized motions in mixing layers changes with Mach number (Elliott and Samimy, 1990; Clemens and Mungal, 1991, 1995). As the convective Mach number increases, the familiar subsonic structure of the mixing layer disappears and the features become much more random and three-dimensional (see Figure 1.11).

Similar results have been obtained by direct numerical simulations (see, for example, Sandham and Reynolds (1991), Chen (1991), and Pantano and Sarkar (2002)), which supports the suggestion that the structure of the high Reynolds number turbulent flow in the mixing layer is closely linked to the

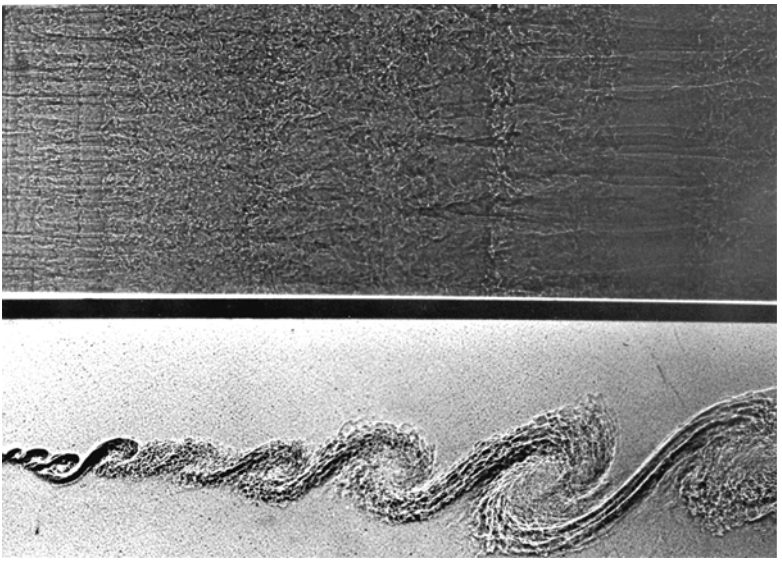

Figure 1.10. Shadowgraphs showing subsonic mixing-layer structure. Top: plan view; Bottom: side view. Flow is from left to right. (From Konrad (1977), as reproduced in Bernal and Roshko (1986). Copyright 1986, Cambridge University Press. Reprinted with permission of the authors and publisher.)

stability of the low Reynolds number, initially laminar flow. The similarities may not be sufficient for reliable quantitative results, but they are useful for understanding how the structures evolve and control mixing, as the convective Mach number increases. Chen (1991), for instance, has shown the effect on the scalar concentration distributions across the layer (see Figure 1.12). At low convective Mach number the spanwise rollers bring the fluid from the high- and low-speed sides into the center, and the concentration profiles show a well-defined peak at the center. At higher convective Mach numbers, the presence of three-dimensional Λ-shaped vortices lead to local upwash and downwash regions that create pockets of partially mixed fluid near the tips of the vortices. As a result, at a given position in the layer, the instantaneous concentration profiles show two preferred mixture fractions, and a peak develops on the centerline (see also Figure 6.14).

1.5 Shock-Turbulence Interaction

The third example of a turbulent compressible flow is the interaction between a shock wave and freestream turbulence. The shadowgraph shown in Figure 1.13 illustrates what can happen. We see how the bow shock formed ahead of a

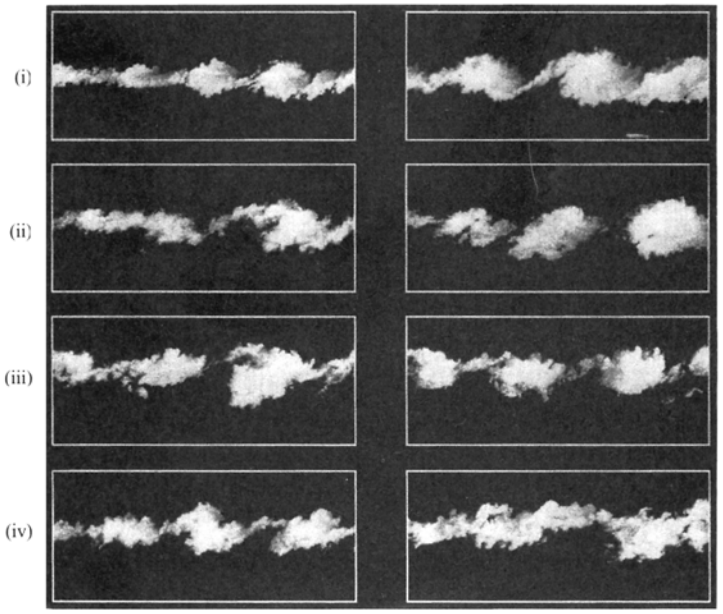

Figure 1.11. Supersonic mixing-layer structure as a function of increasing convective Mach number: (i) $M_c = 0.28$, (ii) $M_c = 0.42$, (iii) $M_c = 0.50$, (iv) $M_c = 0.62$. Two views are given at each Mach number. The visualization is by planar laser Mie scattering from a seeded alcohol fog. (From Clemens and Mungal (1995). Copyright 1995, Cambridge University Press. Reprinted with permission.)

sphere moving at Mach 3 reflects off a perforated plate and passes through the turbulent wake of the sphere. This is an example of the interaction between relatively intense turbulence (typical of a near wake), and a rather weak shock (the shock strength diminishes downstream because the area of the shock sheet increases approximately conically). The interaction with the turbulent wake produces undulations in the shock surface, and these "waves" appear to propagate along the shock. The image of the shock is less clear within the wake, probably because it is distorted in a three-dimensional sense. Shadowgraphs are sensitive to the second derivative of the density gradient, integrated along the light path. Along the upper edge of the wake, the distortion of the first reflected shock appears to match the shape of the large-scale motion that has just passed through it. The interaction between the shock and the turbulence is clearly unsteady, and the shock position is a function of time. Figure 1.13 also illustrates the offset between the upper and lower portions of the shock corresponding to the Mach number gradient across the wake, the slow growth of the wake (as might be expected from the discussion in Section 1.4), the

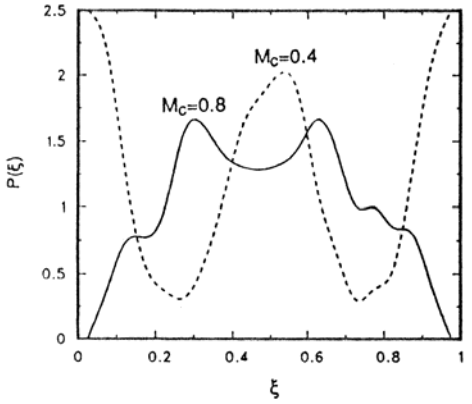

Figure 1.12. The conserved scalar probability distribution versus mixture fraction ξ, on the centerline a free shear layer, at a Reynolds number based on initial vorticity thickness and velocity difference of 1600. (From Chen (1991), with the author's permission.)

acoustic waves emanating from the perforations in the plate, and the acoustic waves originating from the turbulence in the near wake (this phenomenon was more clearly shown in Figure 1.9).

There have been several experiments performed to study the interaction of a shock with turbulence without the complexities introduced by flows such as that shown in Figure 1.13. Debiève and Lacharme (1985), for example, placed an air injector upstream of the throat to generate homogeneous, nearly isotropic turbulence in the freestream of a Mach 2.3 flow, with an *rms* intensity of a little over 1%. A 6° compression corner located on the floor of the wind tunnel was used to generate an oblique shock with a pressure ratio of 1.43, and a density ratio of 1.29 (see Figure 1.14). Therefore the shock was stronger but the turbulence was weaker than for the case shown in Figure 1.13.

In the region of the interaction, a threefold increase was seen in the level of the temperature and velocity fluctuations, but further downstream the residual amplification of, say, the *rms* velocity fluctuations was only about 25%. The large increase in the region of the interaction appeared to be due to the distortion of the shock caused by the incoming turbulence. Along a line in the direction of the incoming flow, the shock moved back and forth, with an amplitude similar to the scales of the incoming turbulence. In this region, the oscillating shock makes a significant contribution to the *rms* velocity perturbation level measured by the hot-wire. Well downstream of the interaction, beyond the range of shock motion, a residual amplification remained but at a much lower level. A rapid distortion analysis developed by Debiève et al.

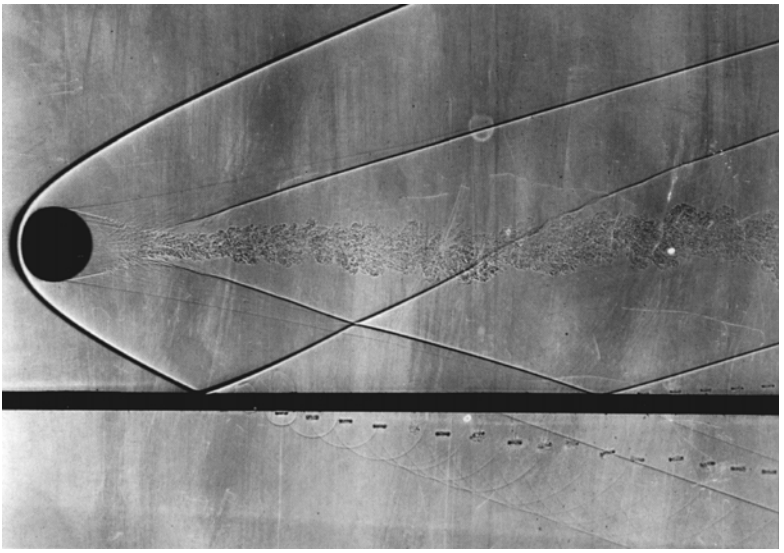

Figure 1.13. Sphere flying over a perforated plate. (Shadowgraph provided by U.S. Army Ballistic Research Laboratory.)

(1982) was used to estimate the turbulence levels throughout the interaction (see Section 4.4.5). This linearized analysis provides a relationship between the upstream and downstream Reynolds stress tensors in terms of the shock strength and its direction. For the most part, it appeared that the evolution of the turbulence could be adequately described by this analysis without recourse to a dynamic "pumping" mechanism due to externally driven shock oscillation (Anyiwo and Bushnell, 1982), where the unsteadiness itself may contribute to the turbulence energy. So the shock causes a "permanent" amplification of the turbulence levels, which seems independent of the shock unsteadiness, and we will show that this may be a general feature of shock wave turbulence interactions. We also show that analyses based on rapid distortion concepts can often be used to gain some quantitative insight into these rapidly perturbed flows.

1.6 Shock Wave-Boundary Layer Interaction

A common example of a shock wave-boundary layer interaction is given by the flow over a wing in transonic flight. As the Mach number of the incoming flow increases to values of about 0.8, a region of supersonic flow may appear on the upper surface of the wing where the flow is accelerated in the region of decreasing pressure. The zone of supersonic flow is usually terminated by

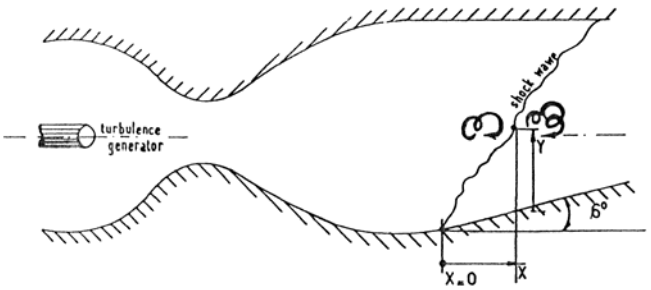

Figure 1.14. Experimental arrangement for the experiment by Debiève and Lacharme (1985). (Copyright 1985, Springer-Verlag. Reprinted with permission.)

a shock located just downstream of the point where the pressure starts to rise, and the strength of the shock and the size of the supersonic flow region depend on the incoming Mach number, the angle of attack, and the shape of the airfoil. The shock can impose a severe pressure gradient on the underlying boundary layer, and it may cause the boundary layer to separate. The shock structure inside the boundary layer then becomes very complex as the flow adjusts to the Mach number gradient across the layer and the presence of a significant sonic region close to the surface (some beautiful images of transonic interactions are given by Van Dyke (1982)). Because the flow downstream of the shock is subsonic, disturbances originating at the trailing edge or in the wake can propagate upstream, and the boundary conditions on the shock may be unsteady. The shock may then move back and forth over the surface of the airfoil with dramatic effects on the lift and drag characteristics, and produce large fluctuating loads on the aircraft structure. This highly unsteady shock wave-boundary layer interaction, and the consequent loss of control of the airplane, led to a number of fatal accidents during the early attempts to break the sound barrier.

This particular type of interaction is not usually found on wings in supersonic flight because the terminating shock moves to the trailing edge as the Mach number increases and the entire flow over the wing (outside the boundary layer) is supersonic. However, shocks and expansions will appear wherever the flow is turned abruptly and an interaction with the boundary layer will result. For example, when a control surface is deployed so that the flow is turned with concave streamline curvature, a *compression corner* interaction occurs. The shock may also be generated by fins, struts, or guide vanes, and the interaction with the boundary layer is usually three-dimensional. In internal flows, it is possible that the shock generated by one deflection surface causes an *incident-shock* or *reflected-shock* interaction on another surface. Some of the configurations used to study two- and three-dimensional shock wave-boundary

layer interactions in the laboratory are illustrated in Figure 10.2.

Shadowgraph visualizations of some two-dimensional compression-corner interactions at a Mach number of 2.9 are shown in Figure 1.15. At all Mach numbers, there exists a subsonic portion of the boundary layer near the wall, which can occupy a significant fraction of the total thickness at low Mach numbers. The demarcation between the subsonic and supersonic parts of the mean profile is called the *sonic line*. When the boundary layer encounters the compression corner, one or more shocks form in the supersonic part of the flow, and the resulting flowfield is the product of the interaction between this shock system and the incoming boundary layer. Within the interaction, large gradients in static pressure, skin friction, and mass flow rate occur, and the sonic line moves away from the surface. If the turning angle is large enough the pressure rise can cause the flow to separate. As we show in Section 9.4, it is possible for the skin-friction and heat-transfer coefficients downstream of the interaction to *exceed* the upstream value by a considerable amount. The interaction is inherently unsteady, which appears to be true for all shock-turbulence interactions, and the shock moves at a relatively low speed back and forth in the streamwise direction. As a result, large-amplitude pressure and heat-transfer fluctuations occur on the wall, which may lead to structural and thermal fatigue problems (Settles et al., 1979; Dolling and Murphy, 1983).

The visualizations shown in Figure 1.15 suggest that the turbulent mixing appears to be considerably enhanced across the shock and that the amplification increases with shock strength. The incursions of freestream fluid appear to become much deeper, suggesting that the length scales of the turbulent motions have correspondingly increased. At the smallest corner angle the shock remains quite distinct almost to the surface, but as the corner angle increases the shock appears to fan out and break into a system of compression waves that start well ahead of the corner. Shadowgraphs, however, represent a spatial average across the flow and do not give a good indication of the behavior in any given streamwise plane. Muck et al. (1985) found that in addition to its motion in the streamwise direction, the shock front is wrinkled in the spanwise direction. The work by Smith et al. (1991) and Poggie et al. (1992) indicates that the shock can also split in the spanwise direction, leading to a highly three-dimensional distortion of the shock front (see Section 10.2). Dolling and Murphy (1983) showed that the mean wall pressure begins to rise well ahead of the average shock position because of this unsteady motion of the shock. This *upstream influence* is seen in the wall-pressure distributions (Figure 1.16) and it increases with corner angle, indicating that the unsteadiness of the shock system becomes more important as the shock strength increases. This figure also indicates that only part of the total compression and turning occurs across the wave system, and compression and streamline curvature continue for several boundary layer thicknesses downstream of the corner.

As far as the turbulence behavior is concerned, we could anticipate from

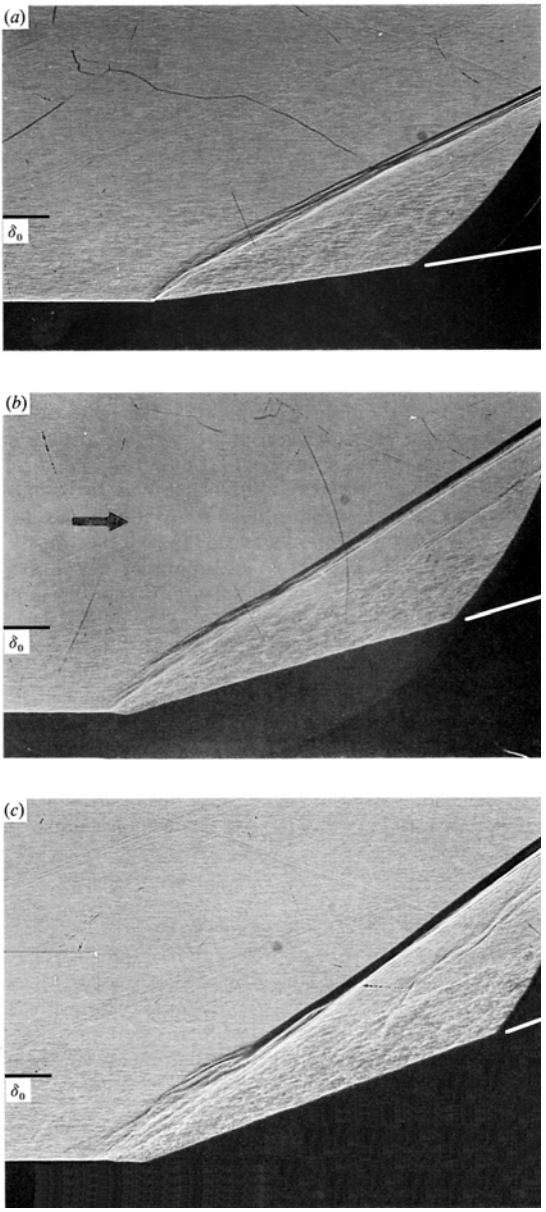

Figure 1.15. Shadowgraphs of compression corner interactions at a Mach number of 2.9 with turning angles of 8°, 16°, and 20°. The curved boundaries on the left and right of the pictures are the edges of the circular window, not parts of the model. (From Settles et al. (1979). Copyright 1979, AIAA. Reprinted with permission.)

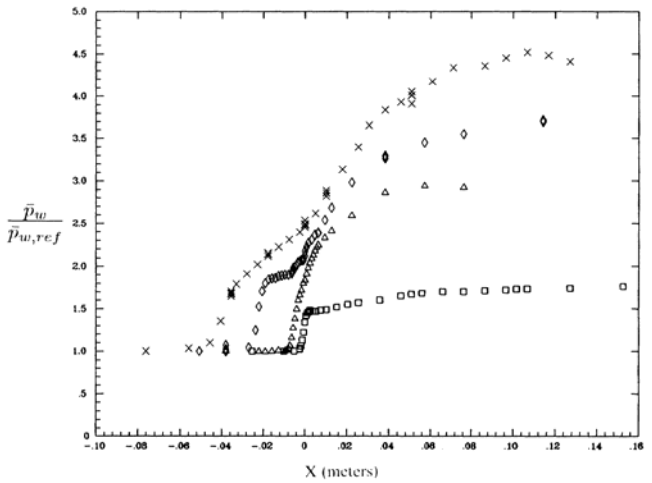

Figure 1.16. Pressure distributions in compression corner interactions at $M = 2.9$: □, 8°; △, 16°; ◇, 20°; ×, 24°. The pressures are normalized by the value of the wall pressure measured upstream of the interaction, and the distance x is measured from the start of the compression corner. (From Settles et al. (1979). Copyright 1979, AIAA. Reprinted with permission.)

the shadowgraphs shown in Figure 1.15 that the turbulence levels in the interaction would be strongly amplified. The hot-wire measurements for the Mach 2.9 compression corners indicate that the mass flux fluctuation intensity, for example, can increase by factors of 4 to 15, and the amplification of the mass weighted shear stress is even greater (Smits and Muck, 1987).

1.7 Measurement Techniques

The subject of measurement techniques for turbulence in compressible flows deserves another text, and it cannot be summarized adequately here. However, it is important to understand some of the limitations and restrictions on the data before studying scaling laws and turbulence structure, and in the brief discussion of experimental techniques that follows we concentrate on issues of accuracy. References are given wherever possible so the interested reader can pursue the subject in greater depth.

1.7.1 Hot Wire Anemometry

Hot-wire anemometry has been the most common measurement technique for obtaining turbulence data in supersonic flows, and it is still widely used. There

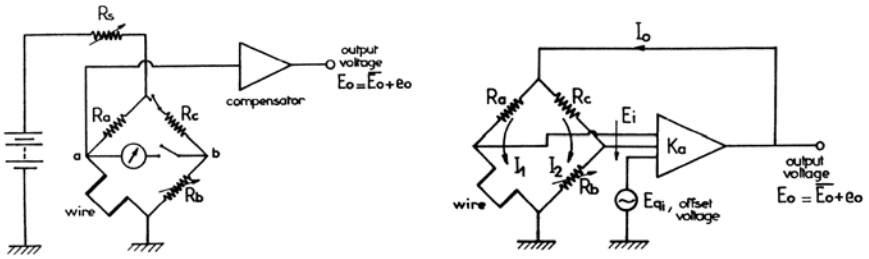

Figure 1.17. Hot-wire anemometer schematics: (a) constant current mode, (b) constant temperature mode. (From Smits and Dussauge (1989). Reprinted with permission of the authors and AGARD/NATO.)

are two main types of hot-wire anemometer: the constant current and the constant temperature type (see Figure 1.17). A third system, the constant voltage anemometer has recently been developed (see, for example, Kegerise and Spina (2000a,b)), but its operation shares many features with the constant current system, and it is not described here.

In the constant current system, the wire filament is heated using a constant current source, and variations in heat transfer produce fluctuations in wire resistance. There is no feedback loop, and the frequency response is extended beyond the limits of the wire thermal inertia by using a compensating network. In the constant temperature mode of operation, a feedback loop is used to keep the wire temperature (and resistance) constant, and variations in heat transfer produce fluctuations in the wire current. The main advantage of the constant temperature system is that the feedback loop automatically compensates the frequency response for the thermal lag of the wire filament.

The probes used in supersonic flow differ somewhat from those used in subsonic flow for reasons of design and strength. It is important, for example, to taper the prongs and use a wedge-shaped body to minimize aerodynamic interference, and the prongs are usually kept short to reduce vibrations and deflections under load. For crossed wires, shocks emanating from one wire and its supports may interfere with the other wire, and care must be taken to avoid this interference at all Mach numbers.

The length of the active filament ℓ is usually between 0.5 and 2 mm, and the diameter d ranges from 1 to 5 μm. If the wire is too long, the spatial resolution deteriorates. If the ℓ/d ratio is too small, the temperature distribution along the wire is highly nonuniform, and heat conduction to the stubs and prongs can be significant. If the ℓ/d ratio is too large, wire breakages are more common. Clearly, choosing the optimum length and diameter is a compromise that is strongly influenced by the flow characteristics.

For a wire oriented at right angles to the direction of a supersonic flow,

a detached bow shock forms, and the front face of the wire is exposed to subsonic flow downstream of this nearly normal shock. Because the major part of the heat transfer occurs by convection over the front surface area of the filament, it is a good approximation for reasonable Reynolds numbers ($Re > 10$) to neglect the sensitivity of the heat transfer to Mach number outside the transonic regime (that is, outside the range $0.8 < M < 1.2$) (Kovasznay, 1953, 1954; Morkovin, 1956, 1962; Gaviglio, 1978). When the effects due to Knudsen number, Mach number, and low Reynolds number can be neglected, the wire-voltage fluctuation is due to variations in mass flux $(\rho u)'$ and total temperature T_0'. It is also possible to measure pressure fluctuations if the flowfield is isentropic (see Laufer, 1961). The relative sensitivity to $(\rho u)'$ and T_0' is a strong function of the overheat ratio, a_w, which is the nondimensional temperature of the wire relative to the wire recovery temperature. At low overheats, the output is primarily sensitive to T_0', and if the overheat is low enough the sensitivity to $(\rho u)'$ can be neglected. Vice versa, at high overheats, the output is primarily sensitive to fluctuations in mass flux, and if the overheat ratio is high enough the contribution to the signal from T_0' may be small enough to be neglected.

To measure the turbulent stresses, further assumptions are required. By operating at different overheat ratios and time averaging, it is possible to obtain $\overline{(\rho u)^2}$, $\overline{(\rho u)\,T_0'}$, and $\overline{T_0'^2}$. If pressure fluctuations are small, $\overline{u'^2}$, $\overline{u'T'}$, and $\overline{T'^2}$ may be found using the definition of total temperature and the equation of state (Kovasznay, 1953). By using the same procedure within fixed frequency bands, it is possible to obtain the spectral distribution of velocity and temperature (see, for example, Bestion (1982)).

This approach is suitable only for the constant current system. For the constant temperature system at low overheat ratios, small fluctuations in total temperature can cause large relative changes in overheat ratio and serious nonlinearities can occur (Smits et al., 1983a). Moreover, the frequency response for T_0' deteriorates rapidly as a_w decreases. However, when T_0' is small, both systems can be used at high overheat to measure the instantaneous mass flux variations directly, and then the Strong Reynolds Analogy can be used to find the instantaneous velocity fluctuation, as long as the pressure fluctuations are negligible (see Section 5.2). In addition, a constant current anemometer operated at a very low overheat can be used to measure T_0' directly.

Smits and Dussauge (1989) pointed out that the calibration of a normal wire in supersonic flow at high Reynolds numbers is a relatively robust procedure. When the Reynolds number is small, or when the Mach number is in the transonic regime, however, additional calibrations are required (Morkovin, 1956; Horstman and Rose, 1977; Rong et al., 1985; Barre et al., 1992; Dupont and Debiève, 1992).

For inclined wires, if it is assumed that the wire heat transfer depends on an "effective" mass flux which is geometrically related to the longitudinal mass

flux, it follows that the ratio of the angular flow sensitivity to the streamwise flow sensitivity ξ is only a function of wire angle. The analysis by Reshotko and Beckwith (1958) for an infinitely long wire supports this hypothesis as long as the Mach number in the direction normal to the wire is outside the transonic range. The analysis also indicates that ξ increases by a factor of about 2 as the Mach number increases from about 0.8 to 1.2, and the experiments by Smits and Muck (1984) confirmed this result. In contrast, Gaviglio et al. (1981), Bestion (1982), and Bonnet and Knani (1986) found that for probes of a slightly different construction ξ depended strongly on the overheat ratio. Also, Bonnet and Knani reported that for some short wires ξ was similar to that observed in subsonic flows, whereas for other wires ξ was about twice the subsonic value, as predicted by Reshotko and Beckwith. They suggested that small differences in aerodynamic interference may have been responsible. In any case, if the angular sensitivity is calibrated over the range of conditions experienced in the experiment no particular assumptions about the heat transfer law are required.

An important consideration is the dynamic range of the instrument. The wire filament has a thermal inertia determined by its volume, specific heat capacity, and the rate of heat transfer. A wire without end conduction behaves as a simple pole with a time constant T_w, and a typical value for $1/2\pi T_w$ is 400 to 800 Hz. The frequency content of the turbulent fluctuations is very much higher, and the response must be compensated electronically to resolve the entire frequency content. For example, to measure $\overline{u'^2}$ in a boundary layer to within 10% accuracy, Kistler (1959) suggested that the upper frequency response of the system f_s must exceed $5u_e/\delta$, where u_e is the freestream velocity and δ is the boundary layer thickness. This criterion ignores the Reynolds number and Mach number dependence of the frequency content, as well as the variation with distance from the wall. In the wall region a better criterion is perhaps given by $f_s > u_e/y$. Even if this frequency response is achieved, these criteria apply to *rms* measurements, and the shape of the high frequency end of the spectrum will still be distorted. Furthermore, the bandwidth required for the measurement of the transverse velocity fluctuation v' is even greater because the v'-spectrum is broader than the u'-spectrum (Gaviglio et al., 1981).

In the constant temperature system, the compensation for thermal lag is achieved automatically by the use of feedback. For maximum frequency response, a symmetrical bridge must be used, and careful tuning is required. Bridge inductance and capacitance, cable length, and feedback amplifier characteristics all need to be adjusted carefully (see Perry (1982) and Watmuff (1995)). Injecting a square-wave voltage perturbation into the bridge appears to be a reliable technique for setting the frequency response, at least at reasonable overheat ratios, that is, greater than about 0.2. (Bonnet and Alziary de Roquefort, 1980).

In the constant current system, the compensation is achieved using a net-

work that approximates a simple zero with time constant T_c, and T_c is adjusted until it matches the wire time constant T_w. This adjustment requires great precision because a small mismatch causes a step in the frequency response of magnitude $(1 - T_w/T_c)$ at a frequency near $1/T_w$. The adjustment is usually performed at each operating point by injecting a square-wave current perturbation across the bridge. Several factors limit the accuracy of this process. First, end-conduction effects can be important (see below). To minimize these effects, the frequency of current injection should be much greater than $1/T_s$. Second, current perturbations are not equivalent to velocity or temperature perturbations. Differences can occur if the bridge is not perfectly balanced, or if stray bridge inductances are present (Smits, 1974; Perry, 1982). Third, the current perturbation must be small enough to avoid nonlinearities, yet large enough to make the signal clearly visible over the background turbulence. Phase-averaging and autocorrelation methods have been used to overcome this difficulty (Arzoumanian and Debiève, 1990): without these refinements, repeatability tests show that the mismatch between T_w and T_s is typically less than 5% (representing 10% error in the mean square voltage output).

End-conduction effects may be important for short wires ($\ell/d < 200$). There is heat conduction to the supports, and the temperature distribution along the wire is no longer uniform. Heat conduction along the wire and through the prongs modifies the frequency response of the sensor. Steps in the Bode diagram can occur similar to those arising from inaccurate compensation, and they can cause errors in measuring variances, spectra, and correlations. End-conduction effects can also introduce phase differences between sensors, and the influence on space-time correlations can be significant. These effects depend strongly on the geometry of the probe and the boundary conditions on the wire, and probes of the soldered design will behave differently from those of the welded design. End conduction effects also depend on the mode of operation and the overheat ratio. They are particularly difficult to control, and it is always difficult to estimate the resulting error in hot-wire measurements. For the constant temperature system in an incompressible flow, Perry et al. (1979) found that the resulting error in *rms* turbulence level can be as high as 10%. In general, these effects are difficult to predict, but because they do not appear to be systematic, repeating the same measurement using different probes can help to establish the error band. It is not clear that these results apply to a supersonic flow, but it seems reasonable to suppose that similar effects can occur and that caution is required. For constant current operation, the phenomenon has been studied in subsonic and supersonic flow (Smits, 1974; Smits et al., 1978; Mougnangola, 1986), and the effects depend critically on the boundary conditions applied at the point where the filament joins the support.

Spatial Resolution Effects

In estimating the uncertainties in hot-wire data, the effects of spatial averaging on turbulence measurements are particularly important. The velocity measured by a hot wire is a spatial average along the sensor length, and it is a weighted average because the temperature distribution along the wire is not uniform. If the velocity variation along the sensor is large, the averaging is also likely to be influenced by the nonlinearity of the probe calibration. Thus eddies that have scales smaller than the length of the wire will not be accurately resolved. Not all components of the three-dimensional spectrum are filtered equally: for example, the attenuation of the turbulence intensity as measured by a single-wire probe is determined by the relative magnitude of the wave number parallel to the probe. Because the spatial filtering of the wire is applied to the three-dimensional spectrum, it will not necessarily remove all the disturbances with a wavelength smaller than the wire length (Blackwelder and Harotinidis, 1983; Ewing et al., 1995). However, measurements of energy spectra and turbulence statistics can be affected dramatically by inadequate spatial resolution and thereby alter the apparent scaling behavior of the data: wire length effects can easily obscure Reynolds number effects (Perry et al., 1986; Klewicki and Falco, 1990). Although this problem is a familiar one, there is no special theory for supersonic flows. In supersonic flows that are approximately self-preserving, the turbulence characteristics are broadly similar to those observed in subsonic flows, and it should be possible to estimate the effects of spatial averaging by using the results obtained there.

As pointed out by Smith (1994), Uberoi and Kovasznay (1953) developed the first technique for calculating the effect of spatial averaging on energy spectra. Wyngaard (1968, 1969) extended this work and developed a framework for correcting measured energy spectra to account for the attenuation at high frequencies (or high wave numbers). Wyngaard showed that when using normal wire probes, measurements of the energy spectra begin to show significant attenuation at wave numbers $k_1 l > 1$ for wires of length $l/\eta = 1$ (l is the wire length, k_1 is the longitudinal wave number and η is the Kolmogorov length-scale). For longer wires, the effects are more severe and begin at lower wave numbers. For crossed-wires, the issue is even more complicated, because the spacing of the two wires and the cross talk between them are further sources of error.

Ligrani and Bradshaw (1987) studied wire length effects on turbulence measurements in the near-wall region ($y^+ \approx 17$) of turbulent boundary layers. They found that adequate resolution ($\pm 4\%$) of turbulence statistics (mean squared values and higher order moments) requires probe dimensions of $l/d > 200$, and $l^+ = lu_\tau/\nu < 20$, where u_τ is the friction velocity. They also found that adequate resolution of the high wave number end of the energy spectra appears to require $l^+ < 5$. Browne et al. (1988) proposed much more stringent criteria: they suggested that for accurate measurements ($\pm 4\%$) of

turbulence statistics, crossed-wire probes should have dimensions $l/\eta < 5$ and $L/\eta < 3$ (L is the distance between the two wires of a crossed-wire probe). Similarly, Klewicki and Falco (1990) indicated that for accurate measurements of velocity derivatives (both spatial and temporal), the wires should be spaced only a few Kolmogorov lengths apart at most.

For high Reynolds number laboratory flows, η is very small, and these restrictions are extremely difficult to meet, particularly when it is necessary to maintain $l/d > 200$ to minimize end-conduction effects. Fernholz and Finley (1996) point out that high Reynolds number experiments using hot wires therefore need to be made in large wind tunnels where the Reynolds number is a consequence of large physical scale and development length rather than high velocity, so as to take advantage of the smallest wires available, with minimum diameters of about 0.6 μm.

Some examples of the effects of spatial filtering are given in Chapter 8. In particular, Figure 8.8 illustrates the effects of spatial filtering on turbulence levels. The maximum value of $\overline{u'^2}/u_\tau^2$ is clearly seen to decrease as the dimensionless wire length l^+ increases. This trend is shown even more clearly by the results of Ligrani and Bradshaw (1987), given in Figure 8.9, where the maximum value of $\overline{u'^2}/u_\tau^2$ increases from 2 to 2.8 as l^+ decrease from 60 to 3.

The effect of sensor-wire separation of one viscous length on the synthetic response of an X-wire probe was investigated by Moin and Spalart (1987). They found that even this small separation led to an overestimation of the $\sqrt{\overline{v'^2}}$ component of more than 10% near the wall, because of the presence of strong velocity gradients in the near-wall region. Park and Wallace (1993) have computed the influence on an X-array, and found that for $L^+ = 9$ at $y^+ = 30$ the $\sqrt{\overline{v'^2}}$ value was about 40% high, and $\overline{u'v'}$ was about 3% low. With $L^+ = 2.3$ the corresponding values were 3% and 5%. These calculations indicate that we can expect the error in $\sqrt{\overline{v'^2}}$ to be larger than the error in $\overline{u'v'}$, and that it will increase with L^+, at least in the near-wall region.

Measurement Accuracy

The accuracy of hot-wire measurements in supersonic flow depends on the limits set by the instrument itself, and on the care exercised by the operator. The effect of an uncalibrated operator on the measurement is unknown, of course, but some recommendations can be made to reduce operator bias. Probably the single best method to determine the confidence limits on the measurements is to repeat the measurement. For example, to check on drift, a measurement at a given point in the flow should be repeated at a different time. If at all possible, calibrations should be performed before and after each profile, and the wire performance should be checked against a known flow (for example, a well-documented zero pressure gradient turbulent boundary layer). Furthermore, the entire set of results should be repeated using a different wire,

anemometer, and operator.

Given that operator bias can be removed, the remaining uncertainties can be determined with reasonable precision. Random errors are introduced by the uncertainties in the calibration and measurement procedures, the possibility of drift in the calibration constants and the presence of end-conduction effects. Systematic errors included neglecting the total temperature fluctuations and the effects of the limited spatial and temporal resolution.

The uncertainties are considerably higher than those found in subsonic flows, where the uncertainties on measurements of $\overline{u'^2}$ and $\overline{u'v'}$ are typically $\pm 5\%$ and $\pm 10\%$, respectively. For supersonic flows, Smits and Dussauge (1989) estimated typical uncertainty levels for two particular flows. In the first example, a normal wire was used in the constant temperature mode at high overheat ratio to measure $\sqrt{\overline{u'^2}}/\overline{U}$ in a boundary layer at Mach 2.84. At $y/\delta = 0.4$, the uncertainty was estimated to lie between -7% and -25%. In the second example, the same quantity was measured in a Mach 1.76 boundary layer using constant current anemometry operated at 14 overheat ratios. At the same location, the error was estimated to lie between $+3\%$ and $+17\%$. It appears that the true value of $\sqrt{\overline{u'^2}}/\overline{U}$ lies between the values obtained by the two systems.

1.7.2 Laser-Doppler Velocimetry

Johnson (1989) summarized the principal advantages of Laser-Doppler Velocimetry (LDV) over hot-wire anemometry as (i) unambiguous signal interpretation (it senses velocity only) and (ii) nonintrusiveness. LDV is also capable of making measurements of the streamwise and normal components of velocity in regions close to a solid surface. The primary disadvantage of the technique is that it measures the velocities of micron-sized particles rather than the velocity of the flow itself. This usually means that the flow must be seeded with particles, and if they are not sufficiently small they will not follow the flow accurately. This problem is particularly severe in regions of strong velocity gradients, as found near the wall and in shock wave-boundary layer interactions. On the other hand, if the particles are too small, the signal on the photodetector has a poor signal-to-noise ratio, which contributes to the uncertainty in the measurement. Additional difficulties arise if the particles are not uniformly distributed, and it is important to ensure that the method of seeding does not disturb the flow (Eléna, 1989).

The most common laser-Doppler velocimeter in use for supersonic turbulence measurements is the *dual-beam* or *fringe* optical arrangement with forward-scatter light collection and burst-counter signal processing (see Figure 1.18). The dual-beam, burst-counter approach is well suited to high-speed flows where particle densities are usually low (Johnson, 1989). What is also not often appreciated is that the burst-counter approach effectively improves

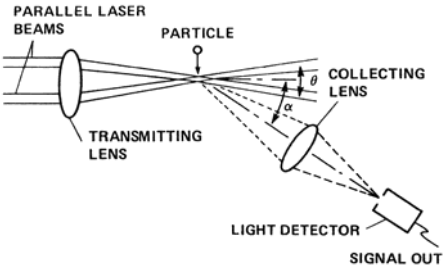

Figure 1.18. Schematic of dual-beam laser-Doppler anemometer. (From Johnson (1989). Reprinted with permission of the author and AGARD/NATO.)

the spatial resolution of the method because the integration over the measurement volume is set by the cross-sectional dimensions of the measurement volume, not its length. Because the signal is obtained from one particle at a time, the length of the volume is not a factor as long as the flow is statistically two-dimensional in that direction. Typically, therefore, the spatial resolution of the LDV technique is of the order of 200 μm in all directions, compared to a hot-wire where it is difficult to obtain a wire-length less than 500 μm. On the other hand, the burst-counter technique can only give statistical properties since the signal is discrete, and the time between bursts of data relatively large (typically of the order of 1 ms). Time histories cannot be obtained, and it is impractical to use LDV to obtain space-time correlations in a high-speed flow.

To assess the accuracy of turbulence statistics obtained using laser-Doppler velocimetry, the primary issues are the effects of particle lag, the uncertainties due to low signal-to-noise ratios, the seeding problem, sampling bias, and angular bias.

The response of a particle to a change in fluid velocity is usually expressed in terms of a time constant. If it is assumed that the Reynolds number of the particle is of order one or less, Stokes's law can be used to find a time constant τ_s for the response of a particle to a sudden change in fluid velocity. Then:

$$\tau_s = \frac{\rho_p d_p^2}{18\mu_g},$$

where ρ_p and d_p are the particle density and diameter, respectively, and μ_g is the fluid viscosity (for a more detailed description of the particle response see Tedeschi (1993)). Typical roll-off frequencies f_{3db} and response distances x_c $(= U\tau_s)$ for a Mach 3 flow are given in Table 1.1. The response was calculated for a step-change in fluid velocity. This is a relevant estimate for shock wave-boundary layer interactions, but may be overly pessimistic for flows with relatively low turbulence levels and where the flow parameters change slowly, as in zero pressure gradient turbulent boundary layers. The scattered

d_p (μm)	f_{3dB} (kHz)	x_c (mm)
5.0	0.9	110
2.0	5.4	18
1.0	22	4.4
0.5	86	1.1
0.3	239	0.4

Table 1.1. Particle response based on Stokes's drag law for $M_e = 3$, $T_0 = 293°$K, and particles with a specific gravity of 1. (From Johnson (1989). Reprinted with permission of the author and AGARD/NATO.)

light intensity is a very strong function of particle diameter, and the intensities fall off rapidly for particle diameters below 1μm. As the particles get smaller, the signal-to-noise ratio decreases significantly and this places a practical limit on the minimum particle diameter of about 1 μm.

The signal-to-noise ratio also depends on the residence time of the particle in the measurement volume. As the speed of the flow increases, the residence time is reduced, and the signal-to-noise ratio decreases. So the need for smaller particles reduces the scattered light intensity, and the higher speeds require an increased bandwidth, both of which result in a reduced signal-to-noise ratio. Stray light is also a problem, one which is particularly troublesome when taking measurements near a solid surface, that is, in the near-wall region.

Seeding a supersonic flow is often difficult, and the quality of the measurements obtained by LDV depends greatly on the method of seeding the flow. As Eléna (1989) pointed out, it is essential that the flow upstream of the measuring point remain undisturbed by the introduction of the particles. For example, Eléna et al. (1985) showed that when an injector is used, its wake can perturb the flow significantly, even when the speed of the injection was equal to the flow speed. Eléna et al. also studied injection at the wall and found that the resulting wall jet can also disturb the boundary layer developing on the wall, even when the injection point is placed upstream of the throat. The results showed that the differences between the jet velocity and the local freestream velocity must be less than 5% to avoid significant errors in the turbulence measurements.

Finally, a number of different bias errors can occur to reduce the quality of the data. Filter bias is caused by incorrect adjustment of the bandpass filters used to improve the signal-to-noise ratio. Gradient bias is due to the fact the velocity varies throughout the measurement volume, particularly in the wall-normal direction for a boundary layer. This error can be reduced by minimizing the dimension of the measurement volume in the direction of the maximum velocity gradient. Velocity bias occurs when there is a correlation

between the number of particles passing through the volume and the velocity of the particles. This is the expected case when the seeding is uniform and the mean interval between samples is less than, or of the same order as, an integral time scale. In supersonic flows, the seeding is never uniform, and the data density is always very low, and velocity bias does not seem to be a serious limitation (Deleuze and Eléna, 1995). Angular bias is related to the number of fringes crossed by the particle in its flight through the measurement volume, and it can produce significant errors when the number of fringes is small. The problem is of particular concern for the accuracy of two-component systems (Eléna, 1989). When the measurement volume contains just enough fringes for validation by the counter, validation occurs only for the particles that have a velocity direction close to the direction normal to the fringes. The velocities that are sampled are only those which have directions that lie within a cone, and the size of the cone is small when the number of fringes is only a little larger than the number required for validation. For a two-component system, the overlap angle that characterizes the useful cross-section for simultaneous validation approaches zero. Angular bias can be reduced by using a Bragg cell to increase the number of fringes by frequency shifting, but in supersonic flows where the measured Doppler frequencies are already very high, this solution is not always possible. Lacharme (1984) showed that a decrease in $\overline{v'^2}$ is expected when the fluctuations are significant. This was also found to be the case for $\overline{u'^2}$ when the correlation coefficient R_{uv} is close to one. Eléna et al. (1985) suggested that the low values of $-\overline{u'v'}$ observed in many LDV measurements near the wall are also related to the effects of angular bias.

Overall accuracy can be difficult to establish for a given experiment and LDV system. Typical of the high-quality LDV data in the literature are the studies by Johnson and Rose (1975) and Deleuze and Eléna (1995) in zero pressure gradient boundary layers at Mach numbers of 2.9 and 2.3, respectively. From an inspection of their results, it seems possible to measure $\overline{u'^2}$ with an accuracy of about $\pm 15\%$ of its peak value, and $\overline{u'v'}$ within $\pm 20\%$ of its peak value, which is comparable to what has been achieved using hot-wires.

1.7.3 Fluctuating Wall Pressure Measurements

A comprehensive review of fluctuating wall pressure measurements was given by Dolling and Dussauge (1989), and it is not repeated here. We consider only the accuracy and the type of data obtained, and the implications for turbulence studies. It should be said immediately that wall pressure data in supersonic flows typically suffer from severe spatial and temporal filtering. Considerable work has been done to analyze the performance of pressure transducers in subsonic flows, but no special analyses have been developed for supersonic flows. However, because the statistical nature of the pressure signal in zero pressure gradient boundary layers seems to be independent of Mach number (at least

at supersonic speeds), it is reasonable to suppose that similar considerations apply. On that basis, Corcos (1963) showed that f_R, the roll-off frequency of a transducer of diameter d, is approximately given by $U_c/\pi d$ (U_c is the convection velocity of the pressure disturbances). If f_R is constrained to be larger than $5u_e/\delta$, as it was for a hot-wire, then

$$d < \frac{1}{5\pi}\frac{U_c}{u_e}. \tag{1.4}$$

If we assume that U_c is typical of near-wall motions, then it is rather small, so that, for example, $U_c \approx 0.6u_e$. Hence, $d < 0.04\delta$, which gives an outer layer scaling for the acceptable transducer size.

It can also be argued that the wall pressure fluctuations depend on some volume surrounding the measurement point, but that they are mainly influenced by the wall region. In other words, they should follow an inner layer scaling. On the basis of subsonic flow experience, we expect that

$$d < 20\nu_w/u_\tau \qquad \text{and} \qquad f > u_\tau^2\big/\nu_w \tag{1.5}$$

(Schewe, 1983). When $\delta u_\tau/\nu_w > 500$, that is, for high Reynolds number flows, the first condition can be met, but not the second, because the smallest available transducers are generally several orders of magnitude too large.

In addition, the frequency response of a transducer designed with a cavity is punctuated by a number of strong peaks corresponding to the natural resonances of the cavity. The harmonics of the dominant resonance are felt at frequencies as low as one-tenth of the dominant frequency, which in most applications overlaps the pressure spectrum. Filtering will obviously remove the resonances, but it can remove some of the signal energy at the same time. It is difficult to measure frequencies above 50 to 100 kHz under any circumstance. As a result of the limited spatial and temporal resolution, the magnitude of the pressure fluctuation level is likely to be severely underestimated in most high-speed experiments, and the spectrum is difficult to interpret when, for example, the shear layer is thin and the energy spectrum covers a range where resonant peaks appear in the data.

Dolling and Dussauge (1989) pointed out that spatial integration *reduces* the standard deviation, but by reducing the contribution of the weakly correlated high frequencies, it *increases* the autocorrelation and two-point correlations. Spurious noise sources, such as tunnel vibration, increase the *rms* value, but should not affect the two-point correlation unless the source of the noise is moving coherently, as might be the case with large-scale variations in tunnel conditions. Electronic noise also increases the standard deviation, but because its time scale is typically very small (high frequencies dominate) the correlations are generally reduced as a result.

Despite these problems, wall pressure data can still be valuable for studying high-speed turbulent flows. Correlation data are less susceptible to error than

measurements of the absolute fluctuation levels themselves, although phase errors between transducers can be a problem, just as they are when using multiple hot-wires. In the study of unsteady shock motion, wall pressure transducers have been indispensable, and they have given much useful data on the range of shock motion and typical shock velocities. They have also been widely used to provide a sampling criterion for measurements that were ensemble averaged on the basis of shock position (see Chapter 10), and this work has given new insights on the mechanisms driving the shock motion.

1.7.4 Flow Imaging

Schlieren and shadowgraph photography have always been important tools for visualizing supersonic flow. The main disadvantage is the spatial integration, so that it is difficult to obtain information about turbulence (for a more detailed description of shadowgraph, schlieren, and other visualization methods, see Merzkirch (1988) and Smits and Lim (2000)). Nevertheless, images of boundary layers obtained on bodies-of-revolution (where the spatial integration is minimized) show marked and regular striations in the layer, leaning downstream at a characteristic angle of 40° to 60° (see, for example, Figure 8.25). Also, James (1958) presented some astonishing shadowgraphs of the flow over bodies-of-revolution over a wide range of Mach numbers, Reynolds numbers, and heat transfer rates. These early images clearly show intermittent transition to turbulence similar to the turbulent spots observed in subsonic flow. In addition, Smith and Smits (1988) and (1995) adapted the schlieren technique with an innovative knife edge design to study turbulence on flat plates, and they were able to determine the convection velocity of the features that had strong density gradients. Focusing schlieren (Weinstein, 1993) avoids some of the effects of integration, and Garg and Settles (1998) have successfully used a similar technique to measure convection velocities of the large-scale motions in a boundary layer at Mach 3.

It is clear, however, that schlieren and shadowgraph methods are not well suited to the study of turbulence. In that respect, planar-laser Mie scattering is more useful. In one version, akin to the vapor-screen method (McGregor, 1961), water vapor in the air is used as a scattering medium. The water vapor, which may be naturally occurring or enhanced by seeding, condenses in regions of low temperature, and it can be made visible using a pulsed laser sheet to give instantaneous cross-sections of the flow similar to those obtained using smoke in air at subsonic speeds. Alternatively, alcohol or acetone is introduced into the flow, typically through a small hole in the wall. The shearing action of the air flow produces small droplets, of diameters in the range of several μm, and these can then be made visible in the same way. An example showing visualizations in mixing layers was given in Figure 1.11, and Smith and Smits (1995) obtained boundary layer images in planes normal to

the wall (see Figure 8.27). Thurow et al. (2000) have used a similar technique in combination with a MHz-rate laser and camera system to obtain short movies of the evolution of large-scale structures in a Mach 1.3 jet.

Planar Laser-Induced Fluorescence (PLIF) is another technique where a tracer is used to make the flow visible. Different tracers can be used, depending on the flow. For example, in combusting flows, OH marks the temperature well, and in high-temperature flows sodium can produce very strong signals (Zimmermann and Miles, 1980). Acetone is another important seeding species for PLIF, and has been extensively used in studies of mixing layer (see, for example Rossmann et al., 2002). Nitric oxide is another example, and Rossmann et al. (2002) used it to measure the instantaneous mixture-fraction field of a hypersonic two-dimensional mixing layer.

Raman Excitation plus Laser-Induced Electronic Fluorescence (RELIEF) is a technique that avoids a tracer and provides velocity by using a tagging laser to excite oxygen molecules into a long-lived state and an interrogation laser to induce fluorescence, and it is similar to the hydrogen-bubble technique for water flows (see Miles et al. (1987, 1989)).

The rapid development of laser-based diagnostics has also made it possible to obtain instantaneous, quantitative flowfield data, rather than pointwise data as obtained using hot-wire anemometry or LDV. One technique that has made considerable impact is planar Rayleigh scattering, first developed by Smith et al. (1989). Cross-sectional images of the air density can be obtained by direct Rayleigh scattering, and because the illumination is provided by a pulsed laser, the images are frozen in time. An example is given in Figure 1.4. The disadvantage of the method is that the presence of water in the air can have a strong effect on the interpretation of the image, even when the water concentration is extremely low (parts per million). Upstream of the nozzle, where it is in the form of water vapor, its Rayleigh cross-section is smaller than air. However, as the flow expands through the nozzle, the water molecules can agglomerate into very small ice clusters, of the order of 30 nm in diameter (Wegener and Stein, 1968). When the clusters are present in sufficient numbers, they can dominate the Rayleigh signal. Under these conditions, the images obtained in air give the density of the ice clusters, rather than the density of the air. The cluster density is a function of temperature, and it appears that there is a threshold temperature below which the cluster concentration is approximately constant, and above which the clusters rapidly disappear (Nau, 1995). In the outer part of the layer shown in Figure 1.4, the particle density is still a measure of the air density, but as the wall is approached and the temperature increases the particles return to the vapor phase and the signal level drops. There are two main consequences. Resolution is lost near the wall (the level depends on the Mach number, the total temperature, and the wall temperature), and strong shocks become visible as lines separating bright zones (low temperature) from dark zones (high temperature), whereas if the

Rayleigh signal were a true measure of the air density, the signal levels should rise, not fall through the shock. These complications can be avoided by operating with pure gases such as nitrogen, or by operating at very low stagnation temperatures (Smith et al., 1991).

It is still possible to obtain interesting results, even in the regime where ice clusters are a problem (Poggie et al., 2004). As a flow visualization tool, it has given very useful insights into the outer layer structure of turbulent jets and boundary layers, and the structure of two- and three-dimensional shock wave-boundary layer interactions. It might also be expected that spatial correlation measurements obtained using Rayleigh scattering should be less sensitive to the variable particle density, and the results obtained by Smith (1989) and Poggie (1995) give results that compare very well with hot-wire data.

In Filtered Rayleigh Scattering (FRS), a molecular filter is used to band-pass the Rayleigh signal, and by sweeping the laser over a range of frequencies it is possible to obtain, in a given plane, the flow velocity, density and temperature (Miles et al., 1992). For flow visualization it has the attractive feature of allowing background suppression by using the molecular filter to eliminate the signal from the stationary wall which has zero Doppler-shift (Forkey et al., 1994).

In low density flows, the naturally ocurring water content in the air supply may not provide a detectable Rayleigh signal, and the molecular signal may also be too weak. Under these circustances, it is sometimes useful to seed the flow with carbon dioxide. Baumgartner (1997) used this method to visualize the structure of a Mach 8 turbulent boundary layer, and Wu (2000) found that under these experimental conditions the upper limit on the average cluster diameter was only about 20 nm. Also, Erbland (2000) estimated that the sublimation time is of order of 10 μs, whereas the condensation time is probably 60 times longer, implying that the visualizations actually represent a history of all of the fluid particles that were "tagged" by sublimation in the higher temperature flow near the wall.

By using two cameras and a single laser, Cogne et al. (1993), Forkey et al. (1993), and Poggie (1995) were able to document the evolution of turbulent large-scale motions in boundary layers, and their interaction with shock waves (see Figures 1.19, 10.7, and 10.13). Lempert et al. (1997) developed a MHz-rate FRS system by combining a pulse-burst laser system with an ultra-fast framing camera. The system captures short FRS movies (typically 30 consecutive frames), and it has been used to study shock motion and distortion in shock wave-boundary layer interactions (Lempert et al., 1997), high-speed jets (Thurow et al., 2000), transition to turbulence on an elliptic cone (Huntley and Smits, 2000), hypersonic boundary layer structure (Auvity et al., 2001), and shock wave-boundary layer interactions (Bookey et al. 2005a,b) (see also Figures 10.7 and 10.8).

In the last ten years or so, Particle Imaging Velocimetry (PIV) has become

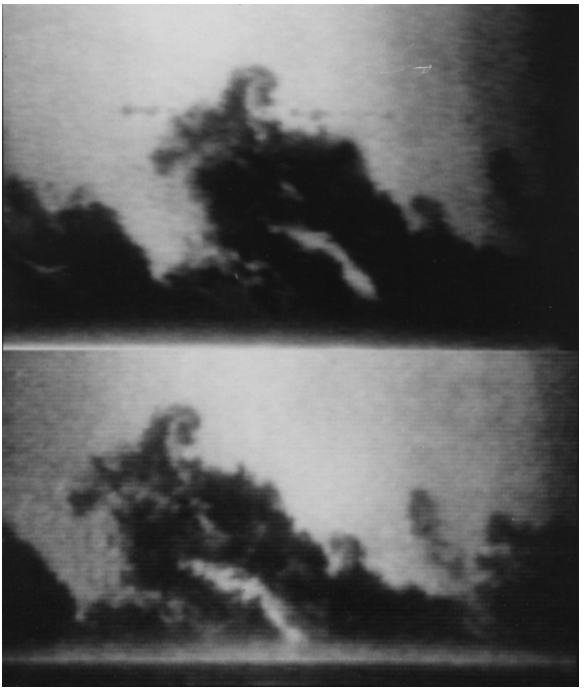

Figure 1.19. Double-pulsed Rayleigh images from a Mach 3 turbulent boundary layer ($Re_\theta = 80,000$, $R_{\delta 2} = 35,000$). Top: time $= t$. Bottom: time $= t + 20$ μs. The flow is from left to right. (Figure from Cogne et al. (1993). Reprinted with permission of ASME.)

a standard tool for studying low-speed fluid flows (see, for example, Gharib's chapter in Smits and Lim (2000)). In PIV, small particles are used to seed the flow, and flow velocities are derived from time-of-flight measurements of the particles. The advantage of PIV over LDV is that PIV gives information in two and even three dimensions, and permits the direct measurement of velocity gradients and vorticity. The disadvantages of the two techniques are similar, in that they are both limited by particle response times and seeding difficulties, and these restrictions are particularly problematic in high-speed flows where shcoks are present. Additional difficulties are related to laser illumination, and the speed and sensitivity of the camera(s). Typically, small particles and short exposure times must be used, which both conspire to reduce the signal intensity. Nevertheless, improvements in hardware have led to a number of interesting applications, including studies of supersonic jets (Lou, 2003) and flow over a sphere at Mach 6 (Scarano and Haertig, 2003). The state of the art is well illustrated by Figure 1.20, showing velocity vectors in a high-speed jet. In this experiment, stereoscopic PIV was used to measure all three velocity

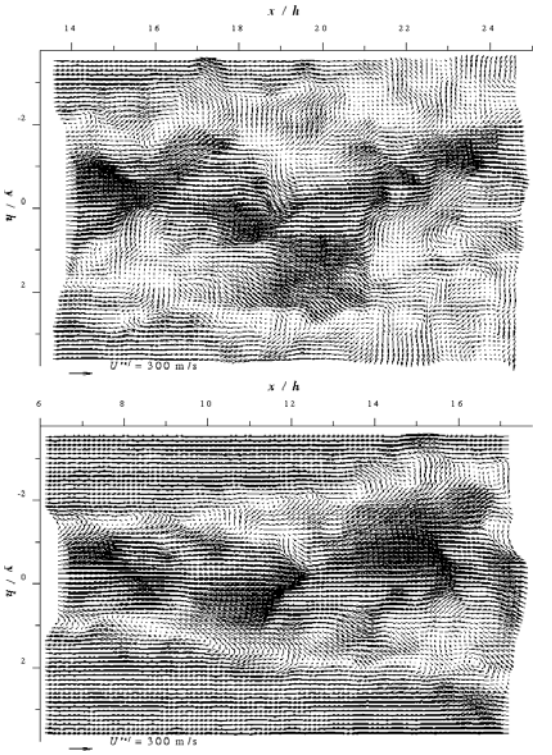

Figure 1.20. Instantaneous velocity vectors in a Mach 1.44 jet, measured using PIV. (Alkislar et al., 2003. Courtesy of the authors.)

components in a single plane (Alkislar et al., 2000, 2003).

1.8 Summary

We have tried to indicate some of the more interesting features of free shear layers and boundary layers in high-speed flow. It is clear that free shear layers are strongly affected by compressibility. Their structure appears to become less organized and more three-dimensional with increasing Mach number, and as a consequence the spreading rate is significantly reduced. For the boundary layer on a flat plate with a zero pressure gradient, the effect of increasing Mach number seems primarily to change the scaling behavior through changes in fluid temperature, although some aspects of the turbulence structure are changed in ways that are difficult to ascribe to fluid property variations alone. In contrast, the propagation of pressure disturbances in supersonic flows is clearly different from that in subsonic experience, and in some cases leads

to a behavior that is counter intuitive. When shock waves are present, the flow response can become extremely complex. Turbulence levels are strongly amplified, the shock becomes unsteady, and the flow may separate.

We have also seen some of the difficulties encountered in experimental studies of supersonic turbulent flows. Most of the turbulence data available in the literature were obtained using hot-wire anemometry, and the uncertainty levels are considerably higher than the levels observed in similar experiments in subsonic flow. In particular, it is difficult to obtain accurate measurements near the wall because the spatial resolution is generally inadequate, and because the Mach number becomes transonic in this region the Mach number dependence of the sensitivity needs to be taken into account. This is an especially difficult problem for crossed-wire measurements. The LDV data are subject to comparable limitations, primarily because of the conflicting requirements on particle size: the particles must be small enough to follow the flow faithfully, and large enough to produce a high signal-to-noise ratio. We saw that these requirements usually cannot be met simultaneously. Accurate wall pressure measurements are also difficult to make, principally because of the poor spatial and temporal resolution encountered in most supersonic applications.

Despite these measurement difficulties, it is possible to obtain useful and important data. Hot-wires, when used with care, can give reasonably reliable indications of turbulence levels and correlations. LDV data can give very good results, particularly for two-component velocity data, and wall pressure transducers are able to give valuable information on shock motion and pressure-correlations. Combined with a range of ingenious flow visualization techniques, and innovative, nonintrusive, quantitative laser-based diagnostics, in addition to the growing usefulness of PIV methods in high-speed flows, the situation has never been better for the experimentalist.

Chapter 2

Equations of Motion

Here, we consider the equations of motion briefly, primarily for the sake of completeness, and to establish a consistent notation. Full derivations can be found in a number of places, notably in Batchelor (1967) and Currie (1974).

We consider only flows of compressible gases where the continuum hypothesis is valid. That is, the smallest volume of interest (a fluid element) will always contain a sufficient number of molecules for statistical averages to be meaningful. The continuum hypothesis fails when the mean free path is comparable to the smallest significant dimension. This can happen under normal temperatures and pressures when the body dimensions are very small, as for the flow around a very thin wire, such as the sensitive element of a hot-wire probe where typical diameters range from 1 to 5 μm, or at very high altitudes, where the densities are very small and the mean free path can be very large. The relevant nondimensional quantity is the Knudsen number, which is the ratio of the mean free path λ to a typical flow dimension. When the Knudsen number exceeds unity we expect rarified gas effects to become important. For a hot-wire in a supersonic flow, the Knudsen number for the wire filament is about 0.2 at normal temperatures and pressures, and for the region occupied by the shock wave it approaches unity. It is difficult to justify the continuum hypothesis within the shock because for shocks of moderate strength the thickness is equal to a few mean free paths in the downstream gas. Nevertheless, the equations of motion for a continuum gas predict shock structures that agree well with experiment. For the flow over the filament itself, however, slip-flow effects associated with a breakdown in the continuum hypothesis have been observed when the Knudsen number based on the filament diameter is of order 0.1 (Davis and Davies, 1972). For laminar boundary layer flows over a vehicle, the ratio of the mean free path to the boundary layer thickness δ can be expressed in terms of the Mach and Reynolds numbers:

$$\frac{\lambda}{\delta} \simeq \frac{M}{\sqrt{Re}}$$

(Kuethe and Schetzer, 1967), indicating that the continuum approximation

will break down at high Mach numbers and low Reynolds numbers, conditions that are typically experienced only in the upper reaches of the atmosphere.

When Knudsen number effects are negligible, and the flow behavior can be described in term of its macroscopic properties such as its pressure, density, and velocity, the flow of a compressible fluid is described completely by the continuity, momentum, and energy equations, together with an equation of state and a suitable set of boundary conditions.

2.1 Continuity

For a compressible fluid the continuity equation is given by:

$$\frac{\partial \rho}{\partial t} + \nabla \cdot \rho \mathbf{V} = 0 \tag{2.1}$$

or

$$\nabla \cdot \mathbf{V} = -\frac{1}{\rho}\frac{D\rho}{Dt}. \tag{2.2}$$

Here $\mathbf{V} = u\mathbf{i} + v\mathbf{j} + w\mathbf{k}$ is the velocity and ρ is the density. The total derivative D/Dt represents the rate of change of density following a particle of fluid in an Eulerian system. A fluid particle has a fixed mass m, and therefore a variable volume. In terms of the volume v $(= m/\rho)$,

$$-\frac{1}{\rho}\frac{D\rho}{Dt} = -\frac{v}{m}\frac{D\left(v/m\right)}{Dt} = \frac{1}{v}\frac{Dv}{Dt}, \tag{2.3}$$

and so the divergence of the velocity is equal to the fractional rate of change of volume of a fluid element of given mass. This is called the rate of dilatation, or simply the dilatation. In tensor notation we have:

$$\frac{\partial \rho}{\partial t} + \frac{\partial \rho u_j}{\partial x_j} = 0. \tag{2.4}$$

2.2 Momentum

The momentum equation for a compressible fluid is given by:

$$\rho\frac{\partial u_i}{\partial t} + \rho u_j \frac{\partial u_i}{\partial x_j} = \frac{\partial \tau_{ij}}{\partial x_j}, \tag{2.5}$$

where τ_{ij} is the (symmetric) stress tensor representing the effects of surface forces (buoyancy forces as well as other body forces have been neglected because they are rarely important in high-speed flows). The three diagonal components of τ_{ij} are the normal stresses and the six off-diagonal components are the tangential or shearing stresses. Note that the surface stresses will only

contribute to the fluid acceleration when their gradients are nonzero. When $\partial\tau_{ij}/\partial x_i = 0$, the effect of surface forces on a material element of fluid is to tend to deform it without changing its momentum.

The stress tensor in a fluid at rest (or in rigid body motion) must be isotropic (see, for example, Batchelor (1967)), and the contribution to the force per unit area exerted on the surface of a control volume with a unit normal vector $\mathbf{n}$ is $\frac{1}{3}\tau_{ij}n_j$. That is, $\tau_{ij} = -p\delta_{ij}$, where $p\left(= -\frac{1}{3}\tau_{ii}\right)$ is called the static-fluid pressure and it acts equally in all directions. The static-fluid pressure is the same as the thermodynamic pressure, which is the pressure measured in a system in equilibrium, and it is a state variable. A negative sign is included because the outward-facing normal of any control volume is defined as a positive vector and by convention a positive pressure is taken to be compressive. The stress tensor in a fluid at rest must therefore be of the form

$$\tau_{ij} = -p\delta_{ij} + d_{ij}, \tag{2.6}$$

where d_{ij} depends on the motion of the fluid only and it is called the shear stress tensor, or the deviatoric stress tensor.

The instantaneous relative velocities in the neighborhood of a point in the fluid are given by the velocity gradient tensor $\partial u_i/\partial x_j$. This tensor describes the motion of all neighboring points. In other words, $\partial u_i/\partial x_j$ describes how an infinitesimal fluid particle deforms in time, and it provides a complete description of the relative state of motion at that point. The velocity gradient tensor can be split into two parts, a rate-of-strain tensor S_{ij} and a rate-of-rotation tensor R_{ij}:

$$\frac{\partial u_i}{\partial x_j} = S_{ij} + R_{ij}, \tag{2.7}$$

where

$$S_{ij} = \tfrac{1}{2}\left(\frac{\partial u_i}{\partial x_j} + \frac{\partial u_j}{\partial x_i}\right) \quad \text{and} \quad R_{ij} = \tfrac{1}{2}\left(\frac{\partial u_i}{\partial x_j} - \frac{\partial u_j}{\partial x_i}\right). \tag{2.8}$$

We see that S_{ij} describes the deformation of a fluid element, whereas R_{ij} describes the instantaneous rate-of-rotation of the fluid element if it were to rotate as a rigid body without deformation. Note that the instantaneous angular velocity is given by ω_k where $R_{ij} = \varepsilon_{ijk}\omega_k$. The vector $\vec{\omega}$ is related to the vorticity $\mathbf{\Omega}$ by $\vec{\omega} = \frac{1}{2}\nabla \times \mathbf{V} = \frac{1}{2}\mathbf{\Omega}$.

The rate-of-strain tensor is the only part of the velocity gradient tensor governed by relative motions among fluid particles. The simplest stress-strain rate relationship is a linear one, and fluids that follow this relationship are called Newtonian. For isotropic Newtonian fluids, the shear stress tensor becomes

$$d_{ij} = \lambda S_{kk}\delta_{ij} + 2\mu S_{ij} \tag{2.9}$$

(see, for example, Currie (1974)), where μ and λ are constants: μ is the dynamic viscosity, and λ is usually written in terms of the bulk viscosity

μ'', where $\mu'' = \lambda + \frac{2}{3}\mu$. The viscosity coefficients relate the shear stress tensor to the rate-of-strain tensor. They are material properties of a fluid, and may be directly related to the molecular interactions that occur inside the fluid. They may therefore be considered as thermodynamic properties in the macroscopic sense, varying with pressure and temperature. They are proper scalars, independent of direction. Hence:

$$\tau_{ij} = -p\delta_{ij} + \mu'' S_{kk}\delta_{ij} + 2\mu\left(S_{ij} - \tfrac{1}{3}S_{kk}\delta_{ij}\right). \tag{2.10}$$

This is the constitutive equation for stress in a Newtonian fluid. The linear dependence holds over a surprising variety of conditions for compressible and incompressible fluids, and it is assumed to describe all the flows considered here.

In a fluid at rest only normal stresses are exerted, and the normal stress is independent of the direction of the surface element across which it acts. We see that in a fluid in motion both the normal and the tangential stresses depend on viscosity.

The dynamic viscosity of a gas is the result of momentum exchange among molecules with the same average molecular velocities but with different bulk velocities. Because the interactions will occur within a distance comparable to the mean free path, the dynamic viscosity must depend on the average molecular speed, the number density and the mean free path. The magnitude is very small but the associated stress μS_{ij} can take large values, especially near a solid wall where the velocity gradients are large. Also, as the temperature of the gas increases, the number of collisions will increase and therefore the dynamic viscosity will increase with temperature. It is nearly independent of pressure. The variation with temperature, between 150°K to 500°K, may be approximated by the formula

$$\frac{\mu}{\mu_0} = \left(\frac{T}{T_0}\right)^{0.76}. \tag{2.11}$$

For a wider range of temperatures, between 100°K and 1900°K, Sutherland's formula is more accurate:

$$\frac{\mu}{\mu_0} = \frac{T_0 + 110.3}{T + 110.3}\left(\frac{T}{T_0}\right)^{3/2} \tag{2.12}$$

(Ames Research Staff, 1953).

With respect to the bulk viscosity, we can introduce the *mechanical* pressure $\overline{p}$ which is the pressure measured in a moving fluid. That is,

$$p - \overline{p} = \mu'' \frac{\partial u_k}{\partial x_k} = \mu'' \nabla \cdot \mathbf{V}.$$

Now $\overline{p} = -\frac{1}{3}\tau_{ii}$, which defines the mechanical pressure in a moving fluid (naturally, for a fluid at rest, $\overline{p} = p$). The mechanical pressure in a moving fluid

differs from the thermodynamic pressure by a term proportional to the volumetric dilatation with a coefficient of proportionality called the bulk viscosity. Note that for an incompressible fluid we need not consider the bulk viscosity—it only becomes important for compressible fluid flow.

The pressure $\overline{p}$ is a measure of the *translational* energy of the molecules only, whereas the thermodynamic pressure is a measure of the *total* energy, which includes vibrational and rotational modes as well as the translational modes. Different modes have different relaxation times, so that energy may be transferred between modes, and the bulk viscosity is a measure of this transfer. For a monatomic gas the only mode of molecular energy is translational and the bulk viscosity is always zero. For polyatomic gases the bulk viscosity is never zero, and in fact it may be orders of magnitude larger than the dynamic viscosity (see, for example, Thompson (1972)). For instance, during the passage of a polyatomic gas through a shock wave, the vibrational modes of energy of the molecules are excited at the expense of the translational modes, so that the bulk viscosity of the gas will be nonzero. However, the stress associated with the bulk viscosity is $\mu''\nabla \cdot \mathbf{V}$, and in many cases of interest the stress is small enough to be neglected (this is usually called Stokes's hypothesis). Here, we assume that $\mu''\nabla \cdot \mathbf{V}$ is negligible.

The final form of the momentum equation, known as the Navier-Stokes equation, is given by:

$$\rho\frac{\partial u_i}{\partial t} + \rho u_j\frac{\partial u_i}{\partial x_j} = -\frac{\partial p}{\partial x_i} + \frac{\partial}{\partial x_j}\left(\mu\left(\frac{\partial u_i}{\partial x_j} + \frac{\partial u_j}{\partial x_i} - \tfrac{2}{3}\frac{\partial u_k}{\partial x_k}\delta_{ij}\right)\right). \qquad (2.13)$$

We now have two equations, the continuity and momentum equations—Equations 2.5 and 2.13, respectively—with three unknowns: p, u_i, and ρ (it is assumed that μ is a known function of the state variables).

For a flow in thermodynamic equilibrium, an extra equation is provided by the equation of state. For the flows considered here it is assumed that the pressure, temperature and density are related to each other by the ideal gas law; that is,

$$p = \rho RT, \qquad (2.14)$$

where R is the gas constant ($= 287.03\ \mathrm{m^2 s^2 K}$ for air). We are interested in systems where velocity, temperature, and pressure gradients are present, systems that may not be in perfect equilibrium. When the rates of change are large, the flow does not have time to achieve local equilibrium, and then the equations of state will contain time as a variable. Lagging internal processes such as dissociation, ionization, evaporation, chemical reactions, and the transfer of energy between molecular modes are called relaxation processes. We have already indicated how the transfer of energy among molecular modes can give rise to a nonzero bulk viscosity coefficient. Nevertheless, variables of state can still be used if the rates of change are not too large. If we restrict our attention to the flow of nonhypersonic continuum gases, and we do not consider the flow

inside shock waves, the experimental evidence suggests that the assumption of thermodynamic equilibrium appears to be reasonable.

To close this system of equations we need to consider the energy of the system.

2.3 Energy

The energy equation for a compressible fluid may be written as:

$$\rho\frac{\partial}{\partial t}\left(e+\tfrac{1}{2}V^2\right)+\rho u_j\frac{\partial}{\partial x_j}\left(e+\tfrac{1}{2}V^2\right)=\frac{\partial \tau_{ij}u_i}{\partial x_j}-\frac{\partial q_i}{\partial x_i}, \tag{2.15}$$

where $V^2=u^2+v^2+w^2$. The left-hand side represents the rate of change of the total energy per unit volume following a fluid particle, and the right-hand side is the sum of the rate of work done on the fluid by the surface forces and the rate of heat added to the fluid by conduction. The work done by the body forces is neglected because buoyancy effects are rarely important in high-speed flows, and temperature differences are assumed to be small enough to neglect radiative heat transfer.

The total energy is the sum of the internal energy e and the kinetic energy of the bulk motion $\frac{1}{2}V^2$. The internal energy is a measure of the energy contained in the translational, rotational and vibrational motions of the gas molecules (as well as electron energies), and it is a state variable. It is Galilean invariant (that is, it is independent of translational motion of the observer) whereas the kinetic energy of the bulk motion is not. (Note that any term involving the absolute value of the velocity will depend on the observer, whereas terms that depend on velocity differences will not.)

The rate of work done by the surface forces may be written as:

$$\frac{\partial \tau_{ij}u_i}{\partial x_j}=u_i\frac{\partial \tau_{ij}}{\partial x_j}+\tau_{ij}\frac{\partial u_i}{\partial x_j}. \tag{2.16}$$

The first part on the right-hand side arises from small differences in stresses on opposite sides of a fluid element, and it contributes to the gain in kinetic energy of the bulk motion of the fluid. The second part is associated with small differences in velocity on opposite sides of the fluid element, and it represents the rate of work done in deforming the element without a change in its bulk velocity. The work done in deforming the element is the only work term that contributes to an increase in the internal energy.

By convention, $\mathbf{q}$ is the conductive heat flux leaving the fluid element (the rate of heat outflow per unit area). Heat conduction contributes to the change in internal energy of the fluid, and makes no contribution to the kinetic energy of the bulk motion. It is assumed that the heat flux is given by the Fourier

heat conduction relationship:

$$q_j = -k\frac{\partial T}{\partial x_j}. \tag{2.17}$$

This is a constitutive equation in that it relates a heat flux to a temperature gradient. A single coefficient of proportionality, the heat conductivity k, is used, which is a property of the fluid and depends on the temperature and pressure.

For many applications it is more useful to express the energy equation in terms of the enthalpy h, where $h = e + p/\rho$, or the stagnation enthalpy, or the total enthalpy h_0, where

$$h_0 = h + \tfrac{1}{2}V^2. \tag{2.18}$$

For constant pressure flows, the enthalpy and total enthalpy have conservation properties that make them attractive variables to use. By using the continuity equation, we can write an equation for the total enthalpy:

$$\rho\frac{\partial h_0}{\partial t} + \rho u_j\frac{\partial h_0}{\partial x_j} = \frac{\partial p}{\partial t} - \frac{\partial q_i}{\partial x_i} + \frac{\partial d_{ij}u_i}{\partial x_j}. \tag{2.19}$$

We see that the total enthalpy can change only through the actions of heat transfer, unsteady pressure variations, or diffusion of kinetic energy by viscosity. Hence the total enthalpy is constant for the flow of a frictionless nonconducting fluid with a steady pressure distribution. Even for a turbulent boundary layer in the steady flow of air, it is a matter of observation that the total enthalpy is nearly constant if there is no heat transfer.

For one-dimensional steady flow, Equations 2.18 and 2.19 are equivalent, and 2.18 is usually called the one-dimensional energy equation. Under these conditions, Equation 2.19 can be integrated between two positions along a streamline, and the total enthalpy will have the same value at these two points if the gradients of velocity and temperature vanish at these locations (see, for example, Batchelor (1967)). This result is particularly useful when considering shock waves or other discontinuities in the flow. The total enthalpy within the shock can vary along a streamline but its value will be the same at all points that lie outside the shock. In other words, the increase and decrease of h_0 along the streamline due to viscous forces and heat conduction exactly cancel over the particular range covered by the shock. Of course, the entropy always increases.

An equation for the enthalpy may be obtained by using the momentum equation to simplify Equation 2.19. Hence,

$$\rho\frac{\partial h}{\partial t} + \rho u_j\frac{\partial h}{\partial x_j} = \frac{\partial p}{\partial t} + u_j\frac{\partial p}{\partial x_j} - \frac{\partial q_i}{\partial x_i} + d_{ij}\frac{\partial u_i}{\partial x_j}. \tag{2.20}$$

The last term on the right-hand side involves the viscous stresses and it is usually called the dissipation function $\mathbf{\Phi}$ (= dissipation rate per unit volume).

The dissipation function represents that part of the viscous work going into deformation, rather than acceleration of the fluid particle. If we assume Stokes's hypothesis,

$$\Phi = d_{ij}\frac{\partial u_j}{\partial x_i} = \tfrac{1}{2}\mu\left(\frac{\partial u_i}{\partial x_j} + \frac{\partial u_j}{\partial x_i}\right)^2, \tag{2.21}$$

and we see that $\mathbf{\Phi}$ is always positive.

To write the energy equation in terms of temperature, it is usually assumed that the gas is a perfect gas with constant specific heats. That is, $h = C_pT$ and $h_0 = C_pT_0$, where T_0 is called the *stagnation* or *total temperature*. Then,

$$\rho C_p\frac{DT}{Dt} = \frac{Dp}{Dt} - \frac{\partial q_i}{\partial x_i} + \mathbf{\Phi}, \tag{2.22}$$

which shows that the temperature of a fluid particle can change by variations in pressure in the direction of the flow, by heat transfer, and by dissipation of kinetic energy by viscosity and thermal conduction.

The energy equation can also be written in terms of entropy. Entropy is another useful parameter primarily because it may also be taken as constant in many flows. By writing the enthalpy in terms of the entropy,

$$Tds = dh - \frac{1}{\rho}dp,$$

we obtain

$$\rho T\frac{Ds}{Dt} = -\frac{\partial q_i}{\partial x_i} + \mathbf{\Phi}. \tag{2.23}$$

That is,

$$\frac{Ds}{Dt} = \frac{\mathbf{\Phi}}{\rho T} + \frac{1}{\rho T}\frac{\partial}{\partial x_j}\left(k\frac{\partial T}{\partial x_j}\right). \tag{2.24}$$

The heat conduction term can be written as the sum of a flux term (that is, a divergence of a temperature gradient), and a term that is quadratic in temperature gradients (positive definite). That is,

$$\frac{Ds}{Dt} - \frac{1}{\rho}\frac{\partial}{\partial x_j}\left(k\frac{\partial \ln T}{\partial x_j}\right) = \frac{\mathbf{\Phi}}{\rho T} + \frac{k}{\rho T^2}\left(\frac{\partial T}{\partial x_j}\right)^2. \tag{2.25}$$

The left-hand side is the sum of a rate of change of entropy per unit mass, plus the net outflow of entropy per unit mass. The right-hand side is zero for a reversible process, and positive for an irreversible process, so that it represents the rate of entropy production per unit mass. It depends on the square of velocity and temperature gradients, and therefore, if the gradients are small, the entropy is changed only by heat conduction.

When there is no heat conduction, the flow is called *adiabatic*. Sometimes, in considering the flow in and out of a control volume, the flow is called adiabatic if there is no heat conduction across the boundaries of the control volume.

When there is no heat conduction and the entropy production (called dissipation) is also negligible, then the flow is *isentropic*. A flow is called *homentropic* if this is true for all particles. For an isentropic flow of a simple system (such as a perfect gas), any state variable can be expressed as a unique function of any one other state variable. Isentropic flows are therefore *barotropic*, that is, density is only a function of pressure. Furthermore, $dh = dp/\rho$, and p varies as ρ^γ (for a perfect gas with constant specific heats).

2.4 Summary

The equations of motion for a compressible, viscous, heat-conducting fluid are:

$$\frac{\partial \rho}{\partial t} + \frac{\partial \rho u_i}{\partial x_i} = 0, \tag{2.26}$$

$$\rho \frac{\partial u_i}{\partial t} + \rho u_j \frac{\partial u_i}{\partial x_j} = -\frac{\partial p}{\partial x_i} + \frac{\partial d_{ij}}{\partial x_j}, \tag{2.27}$$

$$\rho \frac{\partial h}{\partial t} + \rho u_j \frac{\partial h}{\partial x_j} = \frac{Dp}{Dt} - \frac{\partial}{\partial x_i}\left(k \frac{\partial T}{\partial x_i}\right) + d_{ij} \frac{\partial u_i}{\partial x_j}, \tag{2.28}$$

which are, respectively, the continuity, momentum, and energy equations. The deviatoric stress tensor d_{ij} is given by

$$d_{ij} = \mu \left(\frac{\partial u_i}{\partial x_j} + \frac{\partial u_j}{\partial x_i} - \tfrac{2}{3} \frac{\partial u_k}{\partial x_k} \delta_{ij} \right). \tag{2.29}$$

With the addition of an equation of state and the known variation of viscosity and thermal conductivity with temperature and pressure, this is a complete set of equations describing compressible fluid flow, provided that: the continuum hypothesis holds, the fluid particles are in local thermodynamic equilibrium, body forces can be neglected, the fluid is Newtonian, heat conduction follows Fourier's law, and radiative heat transfer can be neglected.

The general formulation of boundary conditions in compressible flow is a specialized topic that is not addressed here, and we only consider the specific conditions introduced by the presence of a wall. The no-slip condition means that the fluid in contact with a solid surface has no relative velocity with respect to the surface. That is, at the wall

$$\mathbf{V} = \mathbf{V}_w. \tag{2.30}$$

When there is heat transfer from the surface, there is an analogue to the no-slip condition in that the temperature of the fluid in contact with the solid surface has the same temperature as the surface itself. That is,

$$T = T_{surface}. \tag{2.31}$$

Alternatively, the heat flux must be specified:

$$k\frac{\partial T}{\partial n} = q_w, \tag{2.32}$$

where q_w is the heat flux from the surface to the fluid and n is the direction normal to the surface.

The no-slip condition breaks down at scales comparable to the mean free path of the molecules, and therefore the assumption of continuum flow generally implies that the no-slip condition holds. Under certain conditions, the no-slip condition may break down, even if the fluid still behaves as a continuum. These conditions are usually only found at high Mach numbers, where $U_{slip}/U_\infty \approx MC_f$. A further discussion of the no-slip condition is given by White (1991), and a fascinating historical note may be found in Goldstein (1938), p. 676.

2.5 Compressible Couette Flow

To illustrate the use of the equations of motion, and to introduce some of the concepts encountered in compressible viscous flows, we consider compressible, laminar Couette flow in some detail. The flow configuration is shown in Figure 2.1. Air flows between two parallel plates, where the upper plate moves at a constant velocity u_e relative to the lower plate. By the no-slip condition, the velocity of the air in contact with the upper plate is also u_e relative to the air in contact with the lower plate. The other boundary conditions are as shown. The temperature of the upper and lower plates are T_e and T_w, respectively, and there is a heat flux q_w from the lower plate into the flow and a shear stress τ_w also acts on the lower plate. The flow is two-dimensional so that $\partial/\partial z = 0$; it is fully-developed so that $\partial/\partial x = 0$, and it is steady so that $\partial/\partial t = 0$. We assume that the gas has constant specific heats.

The continuity equation gives:

$$\frac{\partial \rho v}{\partial y} = 0, \tag{2.33}$$

where $\mathbf{V} = u\mathbf{i} + v\mathbf{j} + w\mathbf{k}$. Hence, $v = 0$ by symmetry, and the flow is parallel.

The momentum equation gives:

$$\frac{\partial \tau_{12}}{\partial y} = 0; \qquad \text{that is,} \qquad \frac{\partial}{\partial y}\left(\mu\frac{\partial u}{\partial y}\right) = 0. \tag{2.34}$$

Therefore the shear stresses and pressure are constant throughout the flowfield. If the flow were incompressible, the viscosity would be constant and Equation 2.34 could be integrated to show that the velocity profile is linear.

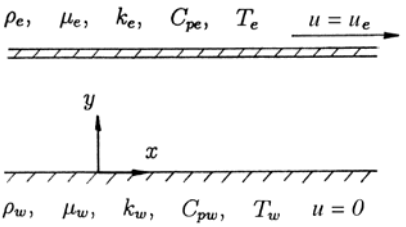

Figure 2.1. Notation for compressible Couette flow.

When the flow is compressible, variations in temperature will produce variations in viscosity, and we need to solve for the temperature distribution before Equation 2.34 can be integrated.

The energy equation gives:

$$\frac{\partial}{\partial y}\left(\mu\, u\frac{\partial u}{\partial y} + k\frac{\partial T}{\partial y}\right) = 0. \tag{2.35}$$

That is, the diffusion of kinetic energy and heat are in equilibrium. If we write the energy equation in terms of the enthalpy, we find:

$$\Phi - \frac{\partial q_i}{\partial x_i} = 0. \tag{2.36}$$

That is, the dissipation and the heat flux are in equilibrium. In fact, the two relations give the same result because:

$$\frac{\partial u_i \tau_{ij}}{\partial x_j} = \Phi + u_i \frac{\partial \tau_{ij}}{\partial x_j}$$

and the viscous stress is constant. It follows that in this fully developed flow the temperature distribution depends only on how the kinetic energy is dissipated and how the heat is diffused.

Integrating Equation 2.35 from the lower wall outwards gives:

$$\mu\, u\frac{\partial u}{\partial y} + \frac{\mu C_p}{P}\frac{\partial T}{\partial y} = -q_w.$$

Here we have introduced the Prandtl number $P = \mu C_p/k$. By using the fact that the stress is constant and by assuming that the Prandtl number is constant (this is a good approximation for many gases) we find that:

$$\frac{\partial}{\partial y}\left(C_p T + \tfrac{1}{2} P u^2\right) = -P\frac{q_w}{\tau_w}\frac{\partial u}{\partial y}.$$

By further integration:

$$C_p\,(T - T_w) + \frac{1}{2}Pu^2 = -P\frac{q_w}{\tau_w}u, \tag{2.37}$$

and using the boundary conditions at the upper wall, we obtain:

$$T_w = T_e + \frac{P}{C_p}\left(\tfrac{1}{2}u_e^2 + \frac{q_w}{\tau_w}u_e\right). \tag{2.38}$$

Consider the case where the lower wall is adiabatic ($q_w = 0$). Here,

$$T_w = T_r = T_e + \tfrac{1}{2}\frac{Pu_e^2}{C_p} = T_e\left(1 + P\frac{\gamma - 1}{2}M_e^2\right),$$

where M_e is the Mach number based on the velocity and temperature of the upper wall, and T_r is called the *recovery temperature* or *adiabatic wall temperature.* Because the velocity of the air in contact with the lower wall is zero, T_w is equal to the total temperature at that point. The total temperature at the upper wall is $T_{0e} = T_e + \frac{1}{2}u_e^2/C_p$. We see that if the Prandtl number is not equal to one, the temperature of the stationary wall is not equal to the total temperature at the upper boundary: the kinetic energy is not exactly "recovered" in the form of heat at the lower boundary. The ratio of the recovered energy to the external energy is called the recovery factor r, where

$$r = \frac{T_r - T_e}{T_{0e} - T_e}. \tag{2.39}$$

In the case of laminar Couette flow, the recovery factor is simply equal to the Prandtl number. Note that when the Prandtl number is less than one (for air $P = 0.72$ at NTP), the temperature of the stationary wall is lower than the total temperature evaluated at the moving boundary.

Equation 2.38 gives the solution for the heat transfer from the lower wall:

$$q_w = \frac{\tau_w C_p}{Pu_e}\,(T_w - T_r)\,, \tag{2.40}$$

which shows that the heat transfer is proportional to the temperature difference $T_w - T_r$, and not $T_w - T_e$ as in low-speed flows. Also, we see that the heat transfer is proportional to the wall shear. That is, for the lower wall,

$$C_h = \frac{1}{2P}C_f, \tag{2.41}$$

where

$$C_f = \frac{\tau_w}{\frac{1}{2}\rho_e u_e^2} \qquad \text{and} \qquad C_h = \frac{q_w}{\rho_e u_e C_p\,(T_w - T_r)}.$$

C_f is the skin-friction coefficient and C_h is the heat-transfer coefficient, or *Stanton number*. Relationships such as Equation 2.41 which connect the heat-transfer and skin-friction coefficients are called Reynolds analogueies, and the ratio $s = 2C_h/C_f$ is called the Reynolds Analogy Factor.

We can find the skin-friction coefficient by integrating the momentum equation (Equation 2.34). If we assume that the viscosity is proportional to the temperature (the actual variation is given by Equations 2.11 and 2.12), we obtain:

$$C_f = \frac{1}{R_e}\left(1 + \frac{T_w}{T_e} + \tfrac{2}{3}P\left(\gamma - 1\right)M^2\right). \tag{2.42}$$

For compressible Couette flow, the skin-friction coefficient increases with heating and Mach number (this is not necessarily true for other wall-bounded flows such as boundary layer flows).

In addition, we obtain from Equations 2.37 and 2.38:

$$\frac{T}{T_e} = \frac{T_w}{T_e} + \frac{T_r - T_w}{T_e}\left(\frac{u}{u_e}\right) - \frac{\gamma - 1}{2}PM_e^2\left(\frac{u}{u_e}\right)^2. \tag{2.43}$$

This temperature-velocity relationship, derived for compressible Couette flow, is often used in the analysis of laminar and turbulent wall-bounded flows by replacing the Prandtl number in Equation 2.43 with the recovery factor appropriate to those flows. In that form, it is often called the Crocco relation or Crocco's law (see Chapter 5 for further details).

One conclusion we can draw from this example is that in the absence of pressure gradients the kinetic energy of a supersonic flow is of such magnitude that when it is transformed into heat and redistributed in space by molecular diffusion significant temperature variations can occur. This can also be understood from the definition of Mach number: $M = u\big/\sqrt{\gamma RT}$. Here the numerator (squared) is proportional to the kinetic energy and the denominator (squared) is proportional to the internal energy. When the Mach number is of order unity the two forms of energy are of the same order of magnitude, and changes in the kinetic energy will result in changes in the temperature and its distribution in space.

2.6 Vorticity

Equations 2.26 to 2.28 represent a complete set of equations describing compressible fluid flow. However, the concept of vorticity can be very useful for gaining further insight, especially in turbulent flows where rotational fluid is often distributed in space in rather compact forms such as vortex tubes and sheets.

For a compressible fluid, the vorticity transport equation is written in terms of the specific vorticity $\boldsymbol{\Omega}/\rho$. By taking the curl of the momentum equation,

we obtain:

$$\begin{aligned}\frac{\partial\left(\Omega_k/\rho\right)}{\partial t}+u_j\frac{\partial\left(\Omega_k/\rho\right)}{\partial x_j} &= \frac{\Omega_j}{\rho}\frac{\partial u_k}{\partial x_j}+\frac{1}{\rho^3}\nabla\rho\times\nabla p \\ &+ \frac{1}{\rho}\varepsilon_{ijk}\frac{\partial^2}{\partial x_i\partial x_j}\left(\mu\left(\frac{\partial u_i}{\partial x_j}+\frac{\partial u_j}{\partial x_i}\right)\right). \quad (2.44)\end{aligned}$$

The first term on the right-hand side of Equation 2.44 is sometimes called the *stretching and tilting* term: part of this term describes the exchange of vorticity between components because of the rotation of vortex lines due to presence of velocity gradients; another part gives the rate of change of vorticity due to stretching of vortex lines. The third term on the right-hand side represents the rate of change of vorticity due to molecular diffusion. The second term is the baroclinic term and it is of particular interest here because it can be an important source term for vorticity in compressible flows. We see from the baroclinic term that in a compressible flow the pressure still appears in the vorticity transport equation. If the density is only a function of pressure, pressure and density gradients are always parallel, and this term does not contribute to the vorticity transport. Under these conditions, the pressure force acting on a fluid element will pass through the center of gravity of the fluid element and no moment results (see Figure 2.2). The flow is then called *barotropic* (for example, isentropic flow of a perfect gas). If the pressure gradients are not parallel to the density gradients, there is a contribution to the rate of change of vorticity: the pressure force does not pass through the center of gravity, a moment about the center of gravity exists, and the rotation vector will change with time. The flow is called *nonbarotropic*.

When the flow is inviscid, barotropic, and two-dimensional, the right-hand side is zero, and the specific vorticity remains constant following a fluid particle: for example, if the flow was initially irrotational, it remains irrotational. So vorticity can change by stretching and tilting, barotropic torques, and viscous diffusion.

A useful result for inviscid compressible flows may be obtained directly from the momentum equation:

$$\frac{\partial\mathbf{V}}{\partial t}+\left(\mathbf{V}\cdot\nabla\right)\mathbf{V}=-\frac{1}{\rho}\nabla p. \quad (2.45)$$

That is,

$$\frac{\partial\mathbf{V}}{\partial t}+\nabla\frac{1}{2}V^2-\mathbf{V}\times\boldsymbol{\Omega}=-\frac{1}{\rho}\nabla p. \quad (2.46)$$

When the pressure is eliminated in terms of the entropy and enthalpy, we obtain Crocco's equation for inviscid flows with no body forces:

$$\mathbf{V}\times\boldsymbol{\Omega}+T\nabla s=\nabla\left(h+\frac{1}{2}V^2\right)+\frac{\partial\mathbf{V}}{\partial t}. \quad (2.47)$$

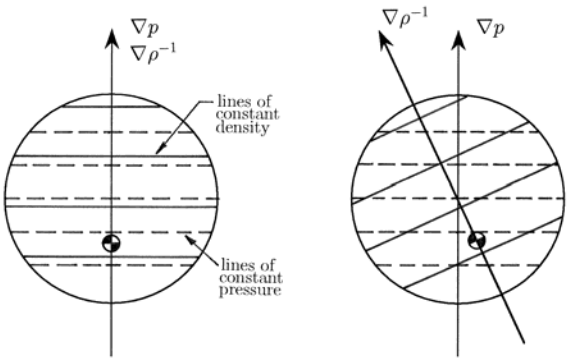

Figure 2.2. Generation of vorticity through baroclinic torques.

If the flow is steady and adiabatic,

$$\mathbf{V} \times \mathbf{\Omega} + T\nabla s = \nabla h_0 \tag{2.48}$$

and the total enthalpy will be constant along each streamline. Hence ∇h_0 is a vector that is perpendicular to the streamlines. Because $\mathbf{V} \times \mathbf{\Omega}$ is also perpendicular to the streamlines, the remaining vector $T\nabla s$ is also. Equation 2.48 can then be written in scalar form:

$$V\Omega + T\frac{ds}{dn} = \frac{dh_0}{dn}. \tag{2.49}$$

where $V = |\mathbf{V}|$, $\Omega = |\mathbf{\Omega}|$, and n is the coordinate perpendicular to the streamlines. Crocco's equation shows that when the total enthalpy is constant everywhere, the vorticity in a homentropic flow must be zero. More interestingly, as a flow passes through a curved shock, the total enthalpy remains constant but the entropy will increase by an amount that depends on the local strength of the shock. Therefore an initially irrotational flow will acquire vorticity proportional to the entropy gradient generated by the curved shock. This is another example of the production of vorticity by baroclinic torques: the term $T\nabla s$ in Equation 2.48 corresponds to the baroclinic term in the vorticity transport equation.

There are a number of other useful properties of vorticity and circulation in inviscid compressible flow. For example, the circulation Γ is defined as:

$$\Gamma = \oint \mathbf{V} \cdot d\ell, \tag{2.50}$$

where counterclockwise contour integration is taken to be positive. That is, the circulation contained within a closed contour in a body of fluid is defined as the integral around the contour of the velocity vector which is locally tangential

to the contour itself. In the absence of shocks and other discontinuities, we can use Stokes's theorem, so that:

$$\Gamma = \iint \mathbf{\Omega} \cdot \mathbf{n} \; dS. \tag{2.51}$$

So the circulation can also be expressed as an area integral of the vorticity component normal to the surface enclosed by the contour, as it is in incompressible flow.

From the definition of vorticity, we have as a vector identity

$$\nabla \cdot \mathbf{\Omega} = \nabla \cdot \nabla \times \mathbf{V} = \mathbf{0}. \tag{2.52}$$

That is, there are no sources or sinks of vorticity inside the fluid, and vorticity can only be generated at the boundaries of the fluid. Therefore vortex tubes must close on themselves or terminate on the boundaries, which may be either a solid surface, or in a compressible flow, a shock wave (because it can be a source of vorticity). Furthermore, in the absence of sources or sinks of vorticity:

$$\iiint \nabla \cdot \mathbf{\Omega} \; d\upsilon = \iint \mathbf{n} \cdot \mathbf{\Omega} \; dS. \tag{2.53}$$

A vortex tube is a tube defined by vortex lines (lines which are tangent to the local vorticity vector). There is no flux of vorticity normal to the surface of the vortex tube, and Equation 2.53 shows that the flux of vorticity along the vortex tube is constant, that is, the circulation around a vortex tube in an inviscid flow is constant. This result, known as Helmholtz's theorem, will hold for compressible and incompressible flows because it is based on the vector identity given in Equation 2.52. Because the circulation remains constant along the length of the vortex tube, the vorticity will increase if the area decreases. What about the rate of change of the circulation as the vortex tube moves? Consider the circulation about a fluid circuit, that is, a circuit defined by fluid particles of fixed identity. We need to find $D\Gamma/Dt$, where the symbol D/Dt is understood to be the rate of change following a fluid circuit. For an inviscid fluid, the momentum equation can be used to show that:

$$\frac{D\Gamma}{Dt} = -\oint \frac{\delta p}{\rho}, \tag{2.54}$$

where δp is the pressure difference between adjacent fluid particles on the closed contour (see Batchelor (1967)). If the fluid is also barotropic (so that the pressure is only a function of density), the right-hand side of Equation 2.54 is zero, and the circulation around any closed material curve is invariant. This is Kelvin's theorem, and it will apply to compressible and incompressible flows as long as the flow is barotropic. Using the definition of circulation, we can also write

$$\frac{D}{Dt}\left(\iint \mathbf{n} \cdot \mathbf{\Omega} \; dS\right) = 0.$$

Thus the flux of vorticity across an open material surface is invariant.

For an inviscid barotropic flow we can therefore make the following observations: If at some instant the flow is without vorticity (such that the circulation around any contour is zero), Kelvin's theorem states that the circulation must remain without vorticity at any future time. In particular, a fluid initially at rest has no vorticity, and must remain without vorticity; vortex tubes are in some sense permanent: a vortex tube specified at an initial instant by the vortex lines that intersect a given closed curve in the fluid has a continuing identity. We may say that in a barotropic inviscid fluid a vortex tube moves with the fluid and its strength remains constant. Because the fluid making up the vortex tube retains its identity as the vortex tube moves and deforms, we must conserve mass. In an incompressible flow, therefore, stretching a vortex tube will inevitably increase its vorticity because the cross-sectional area will always decrease. In a compressible flow, we need to know how the density varies before we can say what is happening to the vorticity: it was clear from the vorticity transport equation that we need to consider the specific vorticity.

Finally, it is important to understand how the velocity field induced by a vortex is affected by compressibility, that is, under what conditions does the usual Biot-Savart law for incompressible flow break down. This requires a consideration of turbulence Mach numbers and fluctuating divergence, and therefore the discussion is deferred until Chapter 4.

Chapter 3

Equations for Turbulent Flow

3.1 Definition of Averages

The complexity of the equations of motion is obvious. Even for incompressible flows, the fact that the velocity and pressure vary with time and cover a wide range of spatial scales precludes the prospect of a general analytical approach. When the flow is compressible, the temperature and density become additional variables, and the flow states become even more complex. The complete problem can only be studied by experiment, or by direct numerical simulations. Direct numerical simulations for compressible turbulent flows have made great strides in recent years, as has the work in large-eddy simulation (Lesieur et al., 1992), but because of practical limits on computer memory and processing speed these computations are currently only possible at Reynolds numbers typical of transitional flows. At Reynolds numbers corresponding to high-speed flight, analytical or numerical approaches have generally sought to reduce the amount of information contained in the solutions of the Navier-Stokes equations by considering only the statistical properties of the flowfield. The equations of motion are then written in terms of the magnitudes of mean quantities. This operation by itself does not present any major difficulties, but the resulting expressions contain more unknowns than there are equations. This is the well-known closure problem. To "close" the set of equations some empirical input is required, and the process of providing this input is called turbulence modeling.

The mean quantities appearing in the equations can be found by ensemble averaging (for flows where long-term variations occur in the flow state) or by time averaging (where such long-term variations are absent). The definition of the ensemble average $\hat{f}$ is

$$\hat{f} \equiv \lim_{N \to \infty} \frac{1}{N} \sum_{1}^{N} n f_n,$$

where f is taken at a given position and time, and N is the rank of the

ensemble (that is, the number of data points taken). In the case where the flow is statistically steady, which is the case for most of the practical examples considered here, it is possible to use the *ergodic hypothesis* to replace the ensemble averages by time averages (Hinze, 1975). If T is the mean integration time, where T is sufficiently long for the mean to be stationary, then the time average $\overline{f}$ is defined by:

$$\overline{f} \equiv \lim_{T\to\infty} \frac{1}{T} \int_t^{t+T} f dt.$$

A number of simple rules govern this averaging procedure. For two arbitrary variables f and g we have:

$$\overline{(f+g)} = \overline{f} + \overline{g}, \qquad \overline{\overline{f}} = \overline{f}, \qquad \overline{f \cdot \overline{g}} = \overline{f} \cdot \overline{g},$$

where the mean is represented by an overbar. In addition, we assume that the variables are sufficiently regular so that the operations of differentiation, integration, and averaging may be inverted in order. That is,

$$\overline{\frac{\partial f}{\partial x_i}} = \frac{\partial \overline{f}}{\partial x_i}, \qquad \overline{\int f d\upsilon} = \int \overline{f} d\upsilon,$$

$$\text{and} \qquad w = \overline{w} + w'' \qquad \text{with} \qquad \overline{w''} = 0,$$

where the double prime denotes a fluctuation from the (temporal) mean. This procedure is usually called Reynolds averaging, and the fluctuations are centered; that is, their mean is zero.

For compressible flows, Reynolds averaging can be used, but it is possible to simplify the resulting equations instead by using mass averaged variables in a procedure often called Favre averaging (Mieghem, 1949; Favre, 1965, 1976). Here we define:

$$w = \tilde{w} + w'$$

with

$$\bar{\rho}\tilde{w} = \overline{\rho w},$$

so that

$$\overline{\rho w'} = 0.$$

The tilde denotes the mass weighted average, and the single prime denotes a fluctuation from the mass averaged mean. In this case, $\overline{w'} \neq 0$. Because the fluctuations are no longer centered, certain statistical results become difficult to interpret. For example, the variances and covariances of two variables no longer obey Schwartz's inequality and therefore a correlation coefficient can take a value greater than one. However, this decomposition has a great advantage in that most of the resulting equations have much simpler forms than the corresponding Reynolds averaged equations.

3.1.1 Turbulent Averages

Because Favre averaging leads to a simpler notation, the mass averaged forms of the equations have been used almost exclusively for the computation of compressible flows. It is worth remembering that it is simply a convenient notation: no formal simplifications result. We show in Section 3.2 that in the continuity equation there is a physically important reason for preferring Favre averages. In the momentum and energy equations, however, terms such as the viscous terms and the dissipation terms are actually more complicated and less amenable to physical interpretation when expressed in mass averaged form.

Because we are concerned with the statistical analysis of turbulent flows, it is important to know which one of the decompositions is more physically correct in formulating models and closure hypotheses. For example, in using a gradient diffusion hypothesis do we use Reynolds averages or Favre averages? Which variables must be used in defining a mixing length? There are no clearcut answers to such questions, but closure relations are often the result of interpolation schemes: they are always approximations of some kind, and very often the uncertainties associated with the models are similar or possibly greater than the differences between the two decompositions. In the same spirit, it is often difficult to know what kind of averaging is performed by a measuring instrument. Is the velocity derived from Pitot tube measurements closer to a mass averaged value, or a Reynolds averaged value? Again, there is no obvious answer. Similarly, when a hot-wire is operated at high resistance ratio it is primarily sensitive to the fluctuating mass flux (see Section 1.7.1), but the assumptions required to obtain the instantaneous velocity or its mass weighted equivalent can lead to greater uncertainty in the data analysis than the differences that arise by using either of the two decompositions.

We can make some of these statements more precise by comparing the two types of averages and the relationships between them. We only discuss some of the simpler relationships, and more complete presentations are given by Favre (1976) and Cebeci and Smith (1974). As before, the single prime denotes a fluctuation weighted by the mass, and the double prime a fluctuation in the Reynolds decomposition. Consider the identity:

$$w = \tilde{w} + w' = \bar{w} + w''.$$

By multiplying by the density and taking the mean, we obtain:

$$\bar{\rho}\tilde{w} = \bar{\rho}\bar{w} + \overline{\rho w''} = \bar{\rho}\bar{w} + \overline{\rho' w''}. \tag{3.1}$$

Hence the difference between the mean quantities $\tilde{w}$ and $\bar{w}$ is given by:

$$\tilde{w} - \bar{w} = \frac{\overline{\rho' w''}}{\bar{\rho}}. \tag{3.2}$$

This difference is a mean quantity which in general depends on the strength of the mean flow gradients. The difference between the fluctuations w' and w'' is also a mean quantity:

$$w' - w'' = \frac{\overline{\rho' w''}}{\bar{\rho}}. \tag{3.3}$$

The distinction between the two decompositions therefore depends on the correlation of the variable w with the density, which in turn will depend on the particular flow under consideration. By way of example we can evaluate this difference for the velocity fluctuations in a boundary layer on an adiabatic flat plate. In Section 5.2, we show that in these flows the fluctuations in density and velocity are connected by the approximate relations:

$$\frac{\sqrt{\overline{\rho'^2}}}{\bar{\rho}} = (\gamma - 1)\, M^2 \frac{\sqrt{\overline{u'^2}}}{\overline{u}} \tag{3.4}$$

and

$$R_{\rho u} = \frac{-\overline{\rho' u'}}{\sqrt{\overline{\rho'^2}}\sqrt{\overline{u'^2}}} \approx 0.8, \tag{3.5}$$

where $R_{\rho u}$ is the correlation coefficient between the velocity and density fluctuations (Equations 3.4 and 3.5 represent one form of the Strong Reynolds Analogy). To simplify the notation we sometimes use the single prime in the statistical quantities, as we did in Equation 3.4. In that case the overbar denotes a Reynolds averaged quantity, and the tilde a mass averaged quantity, and there should be no confusion. Also, we generally adopt the convention $\mathbf{V} = u\mathbf{i} + v\mathbf{j} + w\mathbf{k}$, where u is the velocity in the streamwise direction, v is in the wall-normal direction and w is in the spanwise direction. Using Equation 3.2 we find:

$$\frac{\tilde{u} - \overline{u}}{\overline{u}} = R_{\rho u}\, (\gamma - 1)\, M_t^2,$$

where $M_t = \sqrt{\overline{u'^2}} \big/ \bar{a}$ is the turbulence Mach number (see also Section 4.5). A typical maximum value for M_t in an adiabatic boundary layer with a freestream Mach number of 3 is about 0.2 (see Figure 7.1), which leads to a maximum difference between $\tilde{u}$ and $\overline{u}$ that is less than 1.5%. For a strongly cooled wall flow at Mach 7.2 (Owen and Horstman, 1972), the maximum value of M_t is about 0.4, which gives a maximum difference between $\tilde{u}$ and $\bar{u}$ of about 5%, if Equation 3.4 still holds for this case. It seems that for constant pressure adiabatic boundary layers the differences between the conventional means and the mass weighted means are small for boundary layer flows with Mach numbers less than about 5. In mixing layers or jets, where M_t can take large values even at relatively low Mach numbers, the differences between Favre averaged and Reynolds averaged variables may become important at much lower Mach numbers.

Finally, consider some of the terms in the equations that contain a mixture of the two types of variables. For example, terms such as $\overline{\rho' u_i'}$ and $\overline{p' u_i'}$ that appear in the turbulent kinetic energy equation are formed by combining ρ' and p', that are variables which have a zero mean, and u_i', that does not. As it turns out, these variables have the same value, regardless of the decomposition used. For example, if we begin with Equation 3.3 for the velocity fluctuation, multiply both sides by a centered fluctuation c'', and take the mean, we obtain:

$$\overline{c'' u_i'} - \overline{c'' u_i''} = \overline{c'' \frac{\overline{\rho' u_i''}}{\bar{\rho}}} = -\overline{c''} \frac{\overline{\rho' u_i''}}{\bar{\rho}} = 0.$$

That is,

$$\overline{c'' u_i'} = \overline{c'' u_i''}.$$

Because these variables have values that are independent of the preferred decomposition, we can choose one decomposition to model the terms and then use the result in the other decomposition.

In what follows, we generally choose whichever approach leads to the simplest representation. As we have seen, the connections between the two representations are easily made, and in practical terms the differences between corresponding variables are usually small for boundary layers in nonhypersonic Mach numbers.

3.2 Equations for the Mean Flow

The full equations in Reynolds averaged and mass averaged form are given by Cebeci and Smith (1974). Here we consider the continuity and momentum equations, the energy equation, and the turbulence kinetic energy. Note that the mean density and pressure are always expressed in terms of a Reynolds average, and that ρ' and p' are used to denote fluctuations with respect to $\bar{\rho}$ and $\bar{p}$.

3.2.1 Continuity

The Reynolds averaged form is:

$$\frac{\partial \bar{\rho}}{\partial t} + \frac{\partial}{\partial x_j} \left(\overline{\rho u_j} + \overline{\rho' u_j''} \right) = 0, \tag{3.6}$$

and the mass averaged form is:

$$\frac{\partial \bar{\rho}}{\partial t} + \frac{\partial \bar{\rho} \tilde{u}_j}{\partial x_j} = 0. \tag{3.7}$$

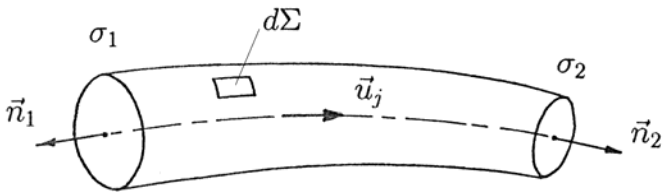

Figure 3.1. Control volume for mass conservation.

The equations show that $\tilde{u}_j$ is the mean velocity of mass transport, which is not true for $\overline{u_j}$. To illustrate the difference, consider the steady flow through the control volume shown in Figure 3.1. Here, $\tilde{u}_j$ is tangential to surface Σ and normal to the cross-sectional areas σ_1 and σ_2. Because the flow is steady, $\partial\bar{\rho}/\partial t = 0$, and Equation 3.6 can be integrated over the volume defined by these surfaces. Using the divergence theorem we obtain the Reynolds averaged form:

$$\int \overline{\rho' u_j''}\ n_j d\Sigma - \int \left(\overline{\rho}\,\overline{u_j} + \overline{\rho' u_j''}\right)\ n_1 d\sigma_1 + \int \left(\overline{\rho}\,\overline{u_j} + \overline{\rho' u_j''}\right)\ n_2 d\sigma_2 = 0.$$

The integrals over surfaces σ_1 and σ_2 represent the mass flow entering and leaving the control volume. Note that the surface Σ is not the surface of a stream tube because the mass flow across it, $\int \overline{\rho' u_j''}\ n_j d\Sigma$, is nonzero. This conceptual difficulty does not occur if the same calculation is performed using a control volume where Σ is tangential to $\tilde{u}_j$, and normal to the cross-sections σ_1 and σ_2. Then the mass averaged form is:

$$\int \bar{\rho}\tilde{u}_j\ n_1 d\sigma_1 - \int \bar{\rho}\tilde{u}_j\ n_2 d\sigma_2 = 0.$$

Because there is no mass flow across surface Σ it represents a stream tube, and therefore $\tilde{u}_j$ is the mean mass transport velocity.

3.2.2 Momentum

The Reynolds averaged form of the momentum equation is:

$$\begin{aligned}\frac{\partial}{\partial t}\left(\overline{\rho}\,\overline{u_i} + \overline{\rho' u_i''}\right) + \frac{\partial}{\partial x_j}\left(\overline{\rho}\,\overline{u_i}\,\overline{u_j} + \overline{u_i}\,\overline{\rho' u_j''}\right)& \\ = -\frac{\partial \bar{p}}{\partial x_i} + \frac{\partial}{\partial x_j}\left(\bar{\tau}_{ij} - \overline{u_j}\,\overline{\rho' u_i''} - \overline{\rho}\,\overline{u_i'' u_j''} - \overline{\rho' u_i'' u_j''}\right),& \qquad (3.8)\end{aligned}$$

and the mass averaged form is:

$$\frac{\partial \bar{\rho}\tilde{u}_i}{\partial t} + \frac{\partial \bar{\rho}\tilde{u}_i\tilde{u}_j}{\partial x_j} = -\frac{\partial \bar{p}}{\partial x_i} + \frac{\partial}{\partial x_j}\left(\bar{\tau}_{ij} - \overline{\rho u_i' u_j'}\right). \qquad (3.9)$$

Similar remarks to those made regarding the continuity equation can be made here. Because mass conservation is inherent in the use of $\tilde{u}_j$, the mass averaged equation is simpler. Moreover, the term $\overline{u_j}\overline{\rho' u_i''}$ in the friction term of Equation 3.8 does not appear in the mass averaged form and as a result Equation 3.9 is very similar in form to the momentum equation for incompressible flows. The Reynolds stress in mass averaged variables is simply $\sigma_{ij} = \widetilde{u_i' u_j'} = \overline{\rho u_i' u_j'}\big/\bar{\rho}$. The difference between this term and $\overline{\rho} \overline{u_i'' u_j''}$ is mainly due to the term $\overline{u_j}\overline{\rho' u_i''}$, because the triple velocity correlation is expected to be an order of magnitude smaller than the other stress terms in Equation 3.8. The term $\overline{u_j}\overline{\rho' u_i''}$ is of the same order as the other terms, and cannot be neglected (Spina et al., 1994). However, the corresponding production term in the turbulent kinetic energy equation is at least two orders of magnitude smaller than the production due to $\overline{\rho} \overline{u_i'' u_j''}$, and it is not important for the energy flow in a compressible boundary layer.

At hypersonic Mach numbers, it is possible that the triple correlation $-\overline{\rho' u_i'' v_j''}$ may become comparable to the "incompressible" Reynolds shear stress, $\overline{\rho} \overline{u_i'' u_j''}$, because $\rho'/\overline{\rho} \sim M^2 u''/U$. Owen (1990) evaluated the various contributions to the "compressible" Reynolds shear stress at Mach 6 through simultaneous use of two-component LDV and a normal hot-wire. His results indicate that $-\overline{\rho' u_i'' v_j''}$ is negligible compared to $\overline{\rho} \overline{u_i'' u_j''}$. Even though density fluctuations increase with the square of the Mach number, it should be remembered that the main contribution to the Reynolds shear stress occurs in the region where the local Mach number is small compared to the freestream value, so this "hypersonic effect" may only be important at very high freestream Mach numbers.

3.2.3 Energy

The total enthalpy is given by:

$$h_0 = h + \tfrac{1}{2} u_i u_i. \tag{3.10}$$

Using the definitions given earlier, we have:

$$\tilde{h}_0 = \tilde{h} + \tfrac{1}{2} \frac{\overline{\rho u_i u_i}}{\bar{\rho}}.$$

That is,

$$\tilde{h}_0 = \tilde{h} + \tfrac{1}{2} \tilde{u}_i \tilde{u}_i + \tfrac{1}{2} \frac{\overline{\rho u_i' u_i'}}{\bar{\rho}}, \tag{3.11}$$

where $\tilde{h}_0 = \overline{\rho h_0}\big/\bar{\rho}$, and $\tilde{h} = \overline{\rho h}\big/\bar{\rho}$. Using these definitions in Equation 2.19, we obtain:

$$\frac{\partial \bar{\rho} \tilde{h}_0}{\partial t} + \frac{\partial \bar{\rho} \tilde{u}_j \tilde{h}_0}{\partial x_j} = \frac{\partial \bar{p}}{\partial t} + \frac{\partial}{\partial x_j} \left(-\overline{\rho u_j' h_0'} + \overline{u_i d_{ij}} - \overline{q_j} \right).$$

It is often useful to expand the stagnation enthalpy in terms of the velocity and temperature. Hence:

$$h_0' = h' + \tilde{u}_i u_i' + \tfrac{1}{2}\left(u_i' u_i' - \frac{\overline{\rho u_i' u_i'}}{\bar{\rho}}\right) \tag{3.12}$$

and finally:

$$\begin{aligned}\frac{\partial \bar{\rho}\tilde{h}_0}{\partial t} + \frac{\partial \bar{\rho}\tilde{u}_j\tilde{h}_0}{\partial x_j} = \frac{\partial \bar{p}}{\partial t} \quad &+ \quad \frac{\partial}{\partial x_j}\left(\tilde{u}_i\overline{d_{ij}} + \overline{u_i' d_{ij}} - \tilde{u}_i\bar{\rho}\overline{u_i' u_j'} - \tfrac{1}{2}\overline{\rho u_i' u_i' u_j'}\right) \\ &- \quad \frac{\partial}{\partial x_j}\left(\overline{q_j} + \overline{\rho u_j' h'}\right). \end{aligned} \tag{3.13}$$

3.2.4 Turbulent Kinetic Energy

The Reynolds averaged form is:

$$\begin{aligned}\frac{\partial}{\partial t}\left(\tfrac{1}{2}\overline{\rho u_i'' u_i''}\right) + \frac{\partial}{\partial x_i}\left(\overline{u_j}\tfrac{1}{2}\overline{\rho u_i'' u_i''}\right) &= -\bar{\rho}\overline{u_i'' u_j''}\frac{\partial \overline{u_i}}{\partial x_j} \\ &- \overline{u_j}\overline{\rho' u_i''}\frac{\partial \overline{u_i}}{\partial x_j} + \overline{p'\frac{\partial u_j''}{\partial x_j}} - \frac{\partial}{\partial x_j}\left(\overline{p' u_j''} + \tfrac{1}{2}\overline{\rho u_i'' u_i'' u_j''}\right) \\ &- \text{ viscous diffusion} - \text{dissipation}, \end{aligned} \tag{3.14}$$

and the mass averaged form is:

$$\begin{aligned}\frac{\partial}{\partial t}\left(\tfrac{1}{2}\overline{\rho u_i' u_i'}\right) + \frac{\partial}{\partial x_i}\left(\overline{u_j}\tfrac{1}{2}\overline{\rho u_i' u_i'}\right) &= -\overline{\rho u_i' u_j'}\frac{\partial \tilde{u}_i}{\partial x_j} \\ &- \frac{\overline{\rho' u_i'}}{\bar{\rho}}\frac{\partial \bar{p}}{\partial x_i} + \overline{p'\frac{\partial u_j'}{\partial x_j}} - \frac{\partial}{\partial x_j}\left(\overline{p' u_j'} + \tfrac{1}{2}\overline{\rho u_i' u_i' u_j'}\right) \\ &- \text{viscous diffusion} - \text{dissipation}. \end{aligned} \tag{3.15}$$

The turbulent kinetic energy equations appear very similar, if one excludes the extra convection terms introduced by the Reynolds decomposition. However, the Reynolds averaged form contains the relative acceleration $\overline{u_j}\overline{\rho' u_i''}\,(\partial \overline{u_i}/\partial x_j)$ which represents the work per unit time required to accelerate a fluid particle of a given mass. This term does not appear in the mass averaged form, but its place is taken by $\overline{\rho' u_i'}\,(\partial \bar{p}/\partial x_i)$. That is, in the absence of friction it is the pressure gradient that produces the force to accelerate the flow. The Favre averaged form is simpler in its interpretation, in that the pressure gradient term disappears in constant pressure flows, whereas the relative acceleration term in the Reynolds averaged equation does not.

The closure problem is also evident from the above equations: the equations for the mean flow contain second-order mean products of fluctuating

quantities, and the equations for the second-order quantities contain third-order products. Equations for the third-order products can also be derived from the Navier-Stokes equations but these will contain fourth-order products, and so on. If the Reynolds stress equations are to be useful, then at some point the equations need to be closed; that is, the highest-order products need to be expressed in terms of lower-order products ($\overline{\rho u_i' u_i' u_j'}$ in terms of $\overline{\rho u_i' u_i'}$, for example) so that the number of equations equals the number of unknowns. In this process of turbulence modeling, most attention has been focused on the turbulence kinetic energy $\frac{1}{2}\overline{\rho q^2}$ $\left(= \overline{\rho u_i' u_i'}\right)$, despite the fact that the turbulent kinetic energy does not appear in any of the mean momentum equations. There are two main reasons for this: there are more data available on the behavior of the terms appearing in the turbulent kinetic energy equation, compared to the equations for the components of the Reynolds stress tensor, and the redistribution term $\overline{p'\left(\partial u_j' \big/ \partial x_j\right)}$ vanishes in an incompressible flow.

3.3 Thin Shear Layer Equations

Thin shear layers are flows where the characteristic scale in the cross-stream direction is much smaller than the characteristic scale in the streamwise direction. As a consequence, derivatives of mean quantities taken in the direction across the flow are always much larger than similar derivatives taken in the freestream direction. Typical examples include mixing layers, jets, wakes and boundary layers where the pressure gradients are not too large. For this class of flows, we can derive a set of approximate equations that are useful for the understanding of compressible turbulent shear layers.

From a mathematical viewpoint, it is always a risky procedure to simplify equations before solving them: any simplification will mean that the general solution cannot be obtained. However, the complexity of the original equations is so extensive that it is not possible to find the general solution and then simplify the result for a particular case. This is true even when we consider only the mean equations together with a closure hypothesis, and therefore it is very attractive to try to use some empirical observations to derive a simpler set of equations. Unfortunately, even with very simple closure schemes the thin shear layer equations themselves cannot be solved analytically. It is also widely recognized now that the thin shear layer equations are not a good starting point for a calculation method. In complex flows where, for example, streamline curvature and pressure gradients are present, the approximations used in deriving the thin shear layer equations can lead to errors that are of the same order as the errors introduced by the turbulence model (for a discussion relevant to subsonic flow, see Hunt and Joubert (1979)). Current calculation methods for turbulent shear layers now often use the full equations for the

mean flow, and the approximations are made in the turbulence model, not in the equations themselves. Any prediction method based on the thin shear layer equations will lack generality, and will require various levels of additional modeling to produce a reasonable level of agreement with experiment (see, for example, Bradshaw (1973, 1974)).

Despite these limitations, the thin shear layer equations still play an important role. The equations are derived using empirical input regarding the characteristic scales, which are then used in an order-of-magnitude argument to identify the dominant terms in the original equation. This process helps to provide some physical insight into the behavior of compressible turbulent shear layers by establishing a basis of comparison with the incompressible case, and by identifying the characteristic scales that govern the shear layer behavior.

In what follows, we use order-of-magnitude arguments to derive the thin shear layer equations for compressible turbulent flows. It is useful to derive the equations for the special case of the boundary layer, although the equations also describe the behavior of other thin shear layers such as mixing layers, jets, and wakes. Only zero pressure gradient flows are examined.

3.3.1 Characteristic Scales

To begin the derivation of the thin shear layer equations, we need to define the characteristic scales for the order-of-magnitude analysis. Here we use U and V as the scales for the streamwise and normal velocities, q' for the turbulent fluctuations, ρ^* for the density, and L and δ for the distances in the streamwise direction and the wall-normal direction, respectively. The velocity and density scales are not defined very precisely, but if chosen properly they should be of the same order of magnitude as the primary variables. For example, in the outer part of the layer, we can assume that U could be taken as the freestream velocity. The length scales are equally ill-defined, but again they should be chosen so that the nondimensionalized derivatives are of order unity. Usually, L is taken to be the distance from the origin of the boundary layer (in terms of order-of-magnitude arguments, the difference between the virtual origin of the layer and the beginning of the turbulent flow is not important). For the outer flow, δ is taken as the local boundary layer thickness and the velocity gradients in the direction normal to the wall will, by definition of ΔU, be of order $\Delta U/\delta$, where ΔU, which does not depend on viscosity, will be specified for each particular case. At reasonable Reynolds numbers it is a matter of observation that $\delta/L \ll 1$. Near the wall, where the velocity gradients are large, a new set of scales may be needed. The effects of viscosity dominate, and the appropriate length scale is probably the thickness of the viscous sublayer δ_v. The velocity scale for the mean flow should still be the freestream velocity, or some fraction of it, except perhaps very near the wall where the velocity scale should be defined using the wall stress. Thus there exist two distinct regions

that scale with different similarity variables. In the inner layer, the viscous stress is important, whereas in the outer layer the turbulent frictional stress dominates. Depending on the region of the flow under consideration, one or the other form of friction can become important, and in scaling the turbulence quantities we must look carefully at the contributions of the turbulence and molecular stresses to the total stress. Here, we consider the outer region first. The arguments developed here are similar to the used by Tennekes and Lumley (1972) and Cousteix (1989).

3.3.2 Continuity

For incompressible flow, the continuity equation may be written with the order of magnitude of each term underneath, as follows,

$$\frac{\partial \bar{\rho}\tilde{u}}{\partial x} + \frac{\partial \bar{\rho}\tilde{v}}{\partial y} = 0 \tag{3.16}$$

$$\frac{\Delta U}{L} \qquad \frac{V}{\delta}.$$

We see that the two terms are of the same order of magnitude, and therefore:

$$\frac{V}{\Delta U} \sim \frac{\delta}{L} \ll 1.$$

In compressible flow, two additional questions arise: the effect of the density gradient on the order-of-magnitude argument, and the proper estimate of the velocity gradient $\partial\tilde{u}/\partial x$. The continuity equation (Equation 3.16) can be written in the form

$$\frac{\partial \bar{\rho}\tilde{v}}{\partial y} = -\bar{\rho}\frac{\partial \tilde{u}}{\partial x} - \tilde{u}\frac{\partial \bar{\rho}}{\partial x}.$$

To relate the density and velocity gradients, we need information from the energy equation. Here, we consider the case of adiabatic layers in a perfect gas, where the total temperature gradient is small enough to be neglected for the purpose of order-of-magnitude arguments. That is,

$$\frac{\partial \tilde{T}_0}{\partial x} = \frac{\partial \tilde{T}}{\partial x} + \frac{\tilde{u}}{C_p}\frac{\partial \tilde{u}}{\partial x} = 0.$$

If the pressure is constant, it follows that

$$\frac{\partial \bar{\rho}}{\partial x} = (\gamma - 1)\, M^2 \frac{\bar{\rho}}{\tilde{u}}\frac{\partial \tilde{u}}{\partial x}$$

and

$$\frac{\partial \bar{\rho}\tilde{v}}{\partial y} \approx \bar{\rho}\frac{\partial \tilde{u}}{\partial x}\left(1 + (\gamma - 1)\, M^2\right).$$

Integrating from the outer edge of the layer yields:

$$\bar{\rho}_e \tilde{v}_e - \overline{\rho v} = \int_{\delta}^{y} \bar{\rho} \frac{\partial \tilde{u}}{\partial x} \left(1 + (\gamma - 1) M^2\right) dy,$$

where $\bar{\rho}_e \tilde{v}_e$ is the wall-normal mass flux at the edge of the layer. For the outer part of the layer, the orders of magnitude of both sides of this expression are

$$\rho^* V \sim \rho^* \left(1 + (\gamma - 1) M^2\right) \delta \left(\frac{\partial \tilde{u}}{\partial x}\right).$$

To find the order of magnitude of $\partial \tilde{u}/\partial x$, it is assumed that in the outer layer that the time scales of the mean and turbulent motions, $(\partial \tilde{u}/\partial y)^{-1}$ and δ/q', respectively, are of the same order, as in subsonic flows (Cousteix, 1989). That is,

$$\frac{\partial \tilde{u}}{\partial y} \sim \frac{q'}{\delta},$$

which leads to the conclusion

$$\tilde{u}_e - \tilde{u} \sim q',$$

so that

$$O\left(\frac{\partial \tilde{u}}{\partial x}\right) = \frac{\Delta U}{L} = \frac{q'}{L}.$$

We need to find the magnitude of q'. It is shown in Chapter 5 that Morkovin's hypothesis applies to nonhypersonic boundary layers. As a consequence, we find that the characteristic scale for the velocity fluctuations is $(\rho_w/\rho)^{1/2} u_\tau$, where u_τ is the friction velocity. For an adiabatic plate, the ratio ρ_w/ρ has a magnitude given by $1 + \frac{1}{2}(\gamma - 1) M^2$.

Finally, we obtain an estimate for the order of magnitude of the wall-normal velocity:

$$V \sim u_\tau \frac{\delta}{L} \frac{1 + (\gamma - 1) M^2}{\left(1 + \frac{1}{2}(\gamma - 1) M^2\right)^{1/2}}.$$

So a correction to the incompressible estimate appears that depends on Mach number. However, for Mach numbers less than 5, the incompressible estimate $V/\Delta U \sim \delta/L$ remains valid, and it is used in the rest of the analysis.

3.3.3 Momentum

For the streamwise momentum equation we have:

$$\bar{\rho}\tilde{u}\frac{\partial \tilde{u}}{\partial x} + \bar{\rho}\tilde{v}\frac{\partial \tilde{u}}{\partial y} = -\frac{\partial \bar{p}}{\partial x} + \frac{\partial}{\partial x}\left(-\bar{\rho}\widetilde{u'^2} + \tau_{11}\right) + \frac{\partial}{\partial y}\left(-\bar{\rho}\widetilde{u'v'} + \tau_{12}\right), \qquad (3.17)$$

where $\widetilde{u_i'u_j'} = \overline{\rho u_i'u_j'}/\bar{\rho}$, as before. First, we can show that the two terms in the convective acceleration are of the same order. That is,

$$\bar{\rho}\tilde{u}\frac{\partial \tilde{u}}{\partial x} \sim \rho^* U \frac{\Delta U}{L},$$

and

$$\bar{\rho}\tilde{v}\frac{\partial \tilde{u}}{\partial y} \sim \rho^* V \frac{\Delta U}{\delta} \sim \rho^* \frac{(\Delta U)^2}{L},$$

for moderate Mach numbers. As in the outer part of low-speed boundary layers, we find that the second term in the acceleration is smaller than the first one. Increasing the Mach number will increase the relative importance of the second term, and the analysis suggests that in hypersonic boundary layers both terms are of comparable magnitude. In mixing layers and jets, $\Delta U \sim U$, so that no inertial term can be neglected. In the general case, therefore, both terms on the left-hand side must be retained.

Second, we note that when the friction (that is, the force due to shear stress gradients) is small, the acceleration terms on the left-hand side are counterbalanced by the pressure gradient. In general, the pressure gradient term can be of the same order of magnitude as the acceleration terms and it must be retained.

As a first step in considering the other terms on the right-hand side of Equation 3.17, we can show that the viscous terms τ_{11} and τ_{12} are small in the outer region. With Stokes's hypothesis, we obtain:

$$\tau_{11} = \overline{\mu\left[2\frac{\partial u}{\partial x} - \tfrac{2}{3}\left(\frac{\partial u}{\partial x} + \frac{\partial v}{\partial y}\right)\right]} \tag{3.18}$$

$$\tau_{12} = \overline{\mu\left[\frac{\partial u}{\partial y} + \frac{\partial v}{\partial x}\right]}. \tag{3.19}$$

For boundary layers on an adiabatic flat plate, we can use the approximation

$$\overline{\mu\frac{\partial u_i}{\partial x_j}} \approx \overline{\mu}\frac{\partial \tilde{u}_i}{\partial x_j},$$

where we have neglected terms of the type

$$\overline{\mu\left(\frac{\partial u_i'}{\partial x_j} + \frac{\partial u_j'}{\partial x_i}\right)}.$$

As justification, consider, for example, $\overline{\mu\,(\partial u'/\partial y)}$. Here,

$$\begin{aligned}\overline{\mu\frac{\partial u}{\partial y}} &= \overline{(\overline{\mu}+\mu')\frac{\partial}{\partial y}(\tilde{u}+u')} \\ &= \overline{\mu}\frac{\partial \tilde{u}}{\partial y} + \overline{\mu'}\frac{\partial \tilde{u}}{\partial y} + \overline{\mu}\frac{\partial \overline{u'}}{\partial y} + \overline{\mu'\frac{\partial u'}{\partial y}}.\end{aligned} \tag{3.20}$$

The second term in Equation 3.20 is zero because $\overline{\mu'} = 0$. If the gradients of $\overline{u'}$ and $\tilde{u}$ have comparable length scales (which requires that the density and velocity fluctuations have similar length scales), then the ratio $(\partial\tilde{u}/\partial y)\Big/\left(\partial\overline{u'}\Big/\partial y\right)$ has the same order of magnitude as $\tilde{u}\Big/\overline{u'}$. More precisely:

$$\left(\overline{\mu}\frac{\partial\overline{u'}}{\partial y}\right)\Bigg/\left(\overline{\mu}\frac{\partial\tilde{u}}{\partial y}\right) = \frac{\overline{u'}}{\tilde{u}}.$$

By using the Strong Reynolds Analogy (see Equations 3.4, 3.5 and Section 5.2):

$$\frac{\overline{u'}}{\tilde{u}} = \frac{-\overline{\rho' u'}}{\bar{\rho}\tilde{u}} = -R_{\rho u}\left(\gamma - 1\right)\frac{\overline{u'^2}}{a^2} = -R_{\rho u}\left(\gamma - 1\right){M_t}^2.$$

The term containing u' is therefore negligible if the square of the Mach number of the fluctuating velocity is small; that is, $M_t^2 \ll 1$.

To estimate the order of the last term in Equation 3.20, we use the fact that the viscosity varies with temperature according to $(\mu/\mu_0) = (T/T_0)^{\omega}$, which implies that $\mu'/\overline{\mu} = \omega\left(T'\Big/\overline{T}\right)$ for small fluctuations. If pressure fluctuations are small, then $\mu'/\overline{\mu} = -\omega\left(\rho'/\bar{\rho}\right)$, and by using the same approximations adopted for evaluating the second term in Equation 3.20 we find:

$$\begin{aligned}\left(\overline{\mu'\frac{\partial u'}{\partial y}}\Bigg/\overline{\mu}\frac{\partial\tilde{u}}{\partial y}\right) &\approx \omega R_{\rho u}\left(\gamma - 1\right)M^2\left(\frac{\overline{u'^2}}{\overline{u^2}}\right)\\ \left(\overline{\mu'\frac{\partial u'}{\partial y}}\Bigg/\overline{\mu}\frac{\partial\tilde{u}}{\partial y}\right) &\approx \omega R_{\rho u}\left(\gamma - 1\right)M_t^2.\end{aligned}$$

So this term will also be negligible if the velocity fluctuations are subsonic ($\omega = 0.76$ according to Equation 2.11). In any case, because $\partial\tilde{u}/\partial y$ is $O(\Delta U/\delta)$, and $\partial\tilde{v}/\partial x$ is $O(V/L)$, we can now write $\tau_{12} \sim \overline{\mu}\left(\partial\tilde{u}/\partial y\right)$. From the continuity equation, we know that $\partial\tilde{u}/\partial x$ and $\partial\tilde{v}/\partial y$ are the same order of magnitude, and therefore $\tau_{11} \sim \overline{\mu}\left(\partial\tilde{u}/\partial x\right)$. If the length scales fulfill the conditions noted earlier, then $(\partial\tau_{12}/\partial y) \gg (\partial\tau_{11}/\partial x)$, and

$$\frac{\partial\tau_{12}}{\partial y} \sim \mu^*\frac{\Delta U}{\delta^2} = \rho^*\frac{U\Delta U}{L}\frac{L}{\delta}\frac{\mu^*}{\rho^* U\delta},$$

where μ^* is the characteristic scale for the viscosity.

We see that if the Reynolds number $\rho^* U\delta/\mu^*$ is large enough then the viscous terms are negligible. Such flows are sometimes called "fully turbulent". This means more than simply requiring that the flow must have developed to the point where there are no intermittent periods of laminar flow, as it does in the region where the flow is still transitional. That is, we require the outer flow to be independent of Reynolds number. Specifically, a wake parameter that depends on Reynolds number is not permitted (see Chapter 7).

Now we return to Equation 3.17. As the next step in approximating the right-hand side, consider the turbulent friction, that is, the turbulent shear stress. Experimental results taken in turbulent shear flows have shown that all turbulent stresses have a similar order of magnitude, and the magnitude of $\widetilde{u'^2}$, $\widetilde{v'^2}$, and $\widetilde{w'^2}$ may be represented by q'^2. A typical value of $-\widetilde{u'v'}\big/\widetilde{q'^2}$ is about 0.15, and therefore we can assume that $-\widetilde{u'v'}$ is $O(q'^2)$ for an order-of-magnitude argument. Hence the term $\partial\left(\bar{\rho}\widetilde{u'v'}\right)\big/\partial y$ will be of order $\rho^* q'^2/\delta$, and because $\partial\left(\bar{\rho}\widetilde{u'^2}\right)\big/\partial x$ will be of order $\rho^* q'^2/L$, the shear stress gradient will be the dominant term, as in subsonic flows (note that we need $\delta/L \ll 1$ to be sure of this approximation). Also, the viscous part is of order $\mu^*\tilde{u}/\delta^2$, and the turbulent friction is larger than the viscous term by a factor $(\rho^* U\delta/\mu^*)\left(\widetilde{u^2}\big/\widetilde{u'^2}\right)$, which is always very large in the outer flow.

Finally, in Equation 3.17, because the term involving $-\bar{\rho}\widetilde{u'^2}$ and the first term in the convective acceleration are of the same order, we have

$$\frac{q'^2}{U\Delta U} \sim \frac{\delta}{L}$$

in the outer layer. If $\Delta U \sim q'$, as in boundary layers and wakes, then $q'/U \sim \delta/L$, and if $\Delta U \sim U$, as in mixing layers and jets, $q'/\Delta U \sim (\delta/L)^{1/2}$ as at low speed. It is shown in Chapter 6 that the experimental evidence corroborates this second result.

Subject to the approximations made so far, the boundary layer form of the mean momentum equation for the streamwise direction is given by:

$$\bar{\rho}\tilde{u}\frac{\partial\tilde{v}}{\partial x} + \bar{\rho}\tilde{v}\frac{\partial\tilde{v}}{\partial y} = -\frac{\partial\bar{p}}{\partial x} + \frac{\partial}{\partial y}\left(-\bar{\rho}\widetilde{uv} + \overline{\mu}\frac{\partial\tilde{u}}{\partial y}\right). \tag{3.21}$$

This equation has the same form as for subsonic flows, but of course $\bar{\rho}$ and $\overline{\mu}$ are not constant in supersonic flows.

Consider now the mean momentum equation for the direction normal to the wall, that is, the y-component momentum equation. The pressure gradient across the layer $\partial\bar{p}/\partial y$ is of special interest because all pressure disturbances in a compressible flow propagate only along characteristic directions. If we restrict ourselves to the outer region where the viscous terms can be neglected:

$$\bar{\rho}\tilde{u}\frac{\partial\tilde{v}}{\partial x} + \bar{\rho}\tilde{v}\frac{\partial\tilde{v}}{\partial y} = -\frac{\partial\bar{p}}{\partial y} - \frac{\partial}{\partial x}\bar{\rho}\widetilde{u'v'} - \frac{\partial}{\partial y}\bar{\rho}\widetilde{v'^2} \tag{3.22}$$

$$\frac{\rho^* UV}{L} \qquad \frac{\rho^* V^2}{\delta} \qquad\qquad \frac{\rho^* q'^2}{L} \qquad \frac{\rho^* q'^2}{\delta}.$$

The terms on the left-hand side are all of the same order, and they are smaller than the corresponding terms in the x-component momentum equation by a factor V/U (or δ/L). Also, the first stress gradient is an order of magnitude

smaller than the second, and by considering the estimate for $q'/\Delta U$, the turbulent friction term can be shown to be much larger than the convection term in the y-momentum equation. The reduced equation reads:

$$\frac{\partial}{\partial y}\left(\bar{p} + \bar{\rho}\widetilde{v'^2}\right) = 0,$$

and because

$$\frac{\bar{\rho}\widetilde{v'^2}}{\bar{p}} = \gamma M^2 \frac{\widetilde{v'^2}}{\widetilde{u^2}} = \gamma M_v^2,$$

the pressure is constant across the boundary layer if the Mach number of the normal velocity fluctuations is small (the approximation breaks down at high Mach numbers, as first pointed out by Finley (1977)). This result may be compared to the result for subsonic flows where the pressure is constant if the dynamic pressure associated with the normal velocity fluctuations is small. When $M_t^2 \ll 1$, $M_v^2 \ll 1$, and then the pressure is only a function of streamwise distance: the pressure gradient term in the x-component momentum equation is set by the conditions in the external flow, and, as in subsonic flow, we speak of the pressure gradient being "imposed" on the boundary layer.

Within the viscous sublayer, the viscous terms need to be taken into account. In high-speed flows, we do not have many detailed measurements in this region, but all indications are that for moderate Mach numbers the behavior is similar to that occurring at low speeds: the convection terms are small, the anisotropy of the stresses is modified but the dominant terms are still $\partial\left(\bar{\rho}\widetilde{u'v'}\right)\big/\partial y$ and $\overline{\mu}\partial\tilde{u}/\partial y$. Above all the total stress is constant and equal to the wall stress, and because it may be shown by similar arguments to those given earlier that the viscous terms in the y-momentum equation are an order of magnitude smaller than the wall stress, we arrive at the same conclusion. That is, the pressure is constant across the boundary layer when $M_t^2 \ll 1$.

The condition that $M_t^2 \ll 1$ has now appeared twice. From the results given in Chapter 1, we know that $\bar{\rho}\widetilde{u'^2}\big/\tau_w$ appears to be a nearly universal function of the nondimensional distance y/δ where this function f is apparently independent of Mach number and only weakly dependent on Reynolds number (see Chapter 8 for further discussion). For a constant pressure boundary layer, the maximum value of $\bar{\rho}\widetilde{u'^2}\big/\tau_w$ occurs near the wall, and it is about 8 for an adiabatic wall, as in subsonic flows. That is,

$$\bar{\rho}\widetilde{u'^2} = \tau_w f\left(\frac{y}{\delta}\right)$$

implying that:

$$M_t^2 = \frac{\widetilde{u'^2}}{a^2} = \tfrac{1}{2} C_f M_e^2 \, f\left(\frac{y}{\delta}\right),$$

which gives a maximum value for M_t^2 of about $4C_f M_e^2$. For a boundary layer in a Mach 3 flow with $C_f = 0.001$, we have $M_t^2 = 0.036$, which is very much

less than one. At Mach 5 with the same value of C_f, we get $M_t^2 = 0.10$ and $\gamma M_v^2 = 0.047$ (near the wall $\widetilde{u'^2}\big/\widetilde{v'^2}$ is about 6). This is still small, but at Mach 10, we have $M_t^2 = 0.40$ and $\gamma M_v^2 = 0.18$, which indicates that under these conditions the pressure increases across the layer by about 20% if the anisotropy of the turbulence remains about the same as at lower Mach numbers. This result is interesting in that it implies that by measuring the mean pressure distribution across the layer, we can estimate the Mach number of the fluctuating velocity field and the extent to which compressibility is influencing the turbulence.

3.3.4 Total Enthalpy

Because we know that gradients of a given quantity in the direction of the mean flow are always much less than gradients in the direction normal to the wall, the total enthalpy equation for a steady, two-dimensional boundary layer becomes:

$$\begin{aligned}\frac{\partial}{\partial x}\left(\bar{\rho}\tilde{u}\widetilde{h_0}\right) + \frac{\partial}{\partial y}\left(\bar{\rho}\tilde{v}\tilde{h}_0\right) &= \frac{\partial}{\partial y}\left(-\overline{\rho v' h_0'} + \overline{u\mu\frac{\partial u}{\partial y}} + \overline{k\frac{\partial T}{\partial y}}\right) \\ &= \frac{\partial}{\partial y}\left(\tfrac{1}{2}\mu\overline{\frac{\partial u^2}{\partial y}} - \tilde{u}\overline{\rho u' v'} - \tfrac{1}{2}\overline{\rho u' u' v'}\right) + \frac{\partial}{\partial y}\left(\overline{k\frac{\partial T}{\partial y}} - \overline{\rho h' v'}\right). \quad (3.23)\end{aligned}$$

Clearly, the terms on the right-hand side of the energy equation are considerably more complicated than the corresponding terms in the momentum equation. In the viscous term, we find terms that are quadratic in fluctuating velocity, and the diffusion of kinetic energy contains terms that are cubic in fluctuating velocity. It is possible to neglect certain terms in some regions of the boundary layer, but only at some values of the Reynolds number, and in general all terms must be retained. However, the following approximations appear to be reasonable:

$$\overline{\mu\frac{\partial u^2}{\partial y}} \approx \overline{\mu}\frac{\partial \tilde{u}^2}{\partial y} \quad \text{and} \quad \overline{k\frac{\partial T}{\partial y}} \approx \overline{k}\frac{\partial \tilde{T}}{\partial y}.$$

We can estimate the errors introduced by these approximations for the case of a boundary layer on an adiabatic wall, using the procedure given in the previous section, if we assume that the fluctuations in the total temperature and the pressure are small. This would show that the approximations are valid if $u'/\tilde{u}$, MM_t and M_t^2 are all small compared to one. Thus the condition that $M_t \ll 1$ is necessary to obtain the usual form of the energy equation for a boundary layer (see below).

3.4 Summary

In summary, the equations of motion for a turbulent boundary layer in a steady, two-dimensional, adiabatic supersonic flow are given by:

$$\frac{\partial \bar{\rho}\tilde{u}}{\partial x} + \frac{\partial \bar{\rho}\tilde{v}}{\partial y} = 0, \tag{3.24}$$

$$\bar{\rho}\tilde{u}\frac{\partial \tilde{u}}{\partial x} + \bar{\rho}\tilde{v}\frac{\partial \tilde{u}}{\partial y} = -\frac{d\bar{p}}{dx} + \frac{\partial}{\partial y}\left(-\bar{\rho}\widetilde{u'v'} + \overline{\mu}\frac{\partial \tilde{u}}{\partial y}\right), \tag{3.25}$$

$$\begin{aligned}\bar{\rho}\tilde{u}\frac{\partial \tilde{h}_0}{\partial x} + \bar{\rho}\tilde{v}\frac{\partial \tilde{h}_0}{\partial y} &= \frac{\partial}{\partial y}\left(-\bar{\rho}\widetilde{h_0'v'} + \overline{\mu}\tilde{u}\frac{\partial \tilde{u}}{\partial y} + \overline{k}\frac{\partial \tilde{T}}{\partial y}\right) \\ &= \frac{\partial}{\partial y}\left(-\bar{\rho}\widetilde{h'v'} - \bar{\rho}\tilde{u}\widetilde{u'v'} + \overline{\mu}\tilde{u}\frac{\partial \tilde{u}}{\partial y} + \overline{k}\frac{\partial \tilde{T}}{\partial y}\right),\end{aligned} \tag{3.26}$$

where we have neglected the term $\overline{\rho u'u'v'}$ compared to $\bar{\rho}\tilde{u}\widetilde{u'v'}$.

As we have noted, the condition $M_t^2 \ll 1$ is necessary to write the usual form of the boundary layer equations for supersonic flow. For incompressible flows, the boundary layer equations are often called the thin shear layer equations in that they also apply to free shear layers, mixing layers, jets and wakes, although it should be understood that the approximations involved become less satisfactory for flows that are not bounded by a wall, mainly because the velocity fluctuations are generally larger and the layers grow relatively faster. Similar considerations will apply for compressible flows with the additional constraint that M_t is typically larger in free shear layers than in boundary layers.

It was shown that the continuity and momentum equations for thin shear layers in supersonic flows are identical to those in subsonic flow, as long as the fluctuating Mach number is small compared to one. This formal analogy does not prove that the turbulent fluxes are of the same nature at low and high speeds. In particular, the validity of using turbulence models developed for subsonic flows in calculations of supersonic flows must be verified. Throughout this chapter, the fluctuations in velocity were linked to the fluctuations in mass flux, pressure. and temperature, and therefore it is important to study the behavior of these parameters in compressible flows, as we show in later chapters.

Chapter 4

Fundamental Concepts

Probably the most important question that we need to address when starting a study of compressible turbulence is to determine what is qualitatively different in compressible and incompressible turbulence. Here, we try to define the new elements associated with compressibility, and the links between compressible and incompressible turbulence. We examine if it is possible to characterize these elements quantitatively using simple parameters, at least for some particular flows, and try to decide if the existing approaches are correct. Do they provide the right answers in practice? Do they predict the measured trends? Is it possible to observe the pertinent parameters in the existing experiments, or, conversely, can simple theories predict the measured quantities?

In view of the difficulties in finding general solutions to the Navier-Stokes equations, most research work is confined to finding properties of the solutions under some particular conditions. Two approaches can be taken. First, we can try to find the general properties of the equations, independent of the boundary conditions. Kolmogorov's theory, predicting the $-5/3$ law for the slope of energy spectra for incompressible turbulence at large enough Reynolds number is a good illustration. Unfortunately, this approach is successful only on rare occasions. The second possibility is to investigate the influence of the boundary conditions on the solutions. A classical example in low-speed flows is the analysis of turbulent boundary layers, where the log law exists as a dimensional requirement for matching the viscous region to the high Reynolds number region. The second approach forms the basis for all subsequent chapters, but here we try to summarize the attempts made to characterize compressible turbulence by the first approach, together with some examples to help define and quantify possible trends in the behavior of compressible turbulence. In particular, we consider the linearized equations of motion, which introduce the concept of modes, the interaction of these modes in a higher-order theory (especially with respect to the compressibility of the velocity fluctuations and the role of pressure fluctuations), the effects of rapid distortion of turbulence in compressible flows and the implications for the Reynolds stresses, and, finally,

the physical bases for using different Mach numbers of turbulence and the connections among them.

4.1 Kovasznay's Modes

Kovasznay (1953) suggested that, intuitively, we may expect that sound waves will accompany vorticity fluctuations, and that fluid particles, having passed through different shear regions, may suffer different changes in entropy. To understand how the vortical, compressible, and acoustic motions are connected together, and how the dynamic and thermodynamic aspects are linked, Kovasznay performed a small perturbation analysis for fluctuations developing in a medium at rest ($U_0 = 0$), with uniform temperature T_0, density ρ_0, and pressure p_0. The fluid was assumed to be a perfect gas, with constant specific heats, viscosity, and heat conductivity. More precisely, the conditions on the fluctuations are:

$$\frac{T'}{T_0}, \quad \frac{\rho'}{\rho_0}, \quad \frac{p'}{p_0} \ll 1.$$

The condition on the velocity fluctuations u_i' is not obvious because the reference velocity is zero. However, because the only velocity scale in the problem is the reference sound speed a_0, the condition

$$M_t = \frac{u_i'}{a_0} \ll 1$$

is imposed on the magnitude of the velocity fluctuations. This point is discussed in more detail in what follows. It is important to note that although Kovasznay's analysis does not provide a predictive tool, it is very useful for classifying the mechanisms that operate in compressible turbulent flows.

The continuity equation can be written as:

$$\nabla \cdot \mathbf{V} = -\frac{D \ln \rho}{Dt} = -\frac{1}{\gamma}\frac{D \ln p}{Dt} + \frac{1}{C_p}\frac{Ds}{Dt}, \tag{4.1}$$

where the density has been written in terms of the pressure and entropy. Linearizing Equation 4.1 gives:

$$\frac{\partial u_i'}{\partial x_i} = \frac{1}{C_p}\frac{\partial s'}{\partial t} - \frac{1}{\gamma p_0}\frac{\partial p'}{\partial t}, \tag{4.2}$$

which shows that the divergence of velocity fluctuations (the *fluctuating divergence*) can be changed by pressure and entropy fluctuations.

The linearization of the momentum equation presents no real difficulty: the nonlinear transport terms are neglected, and only the contribution of the mean

viscosity to the viscous stress is retained. Hence:

$$\frac{\partial u_i'}{\partial t} = -a_0^2 \frac{1}{\gamma p_0} \frac{\partial p'}{\partial x_i} + \nu_0 \left(\frac{\partial^2 u_i'}{\partial x_k^2} + \frac{1}{3} \frac{\partial^2 u_i'}{\partial x_i \partial x_k} \right). \tag{4.3}$$

The entropy equation has the usual form:

$$\frac{Ds}{Dt} = \frac{\mathbf{\Phi}}{T} + \frac{1}{\rho T} \frac{\partial}{\partial x_j} \left(k \frac{\partial T}{\partial x_j} \right), \tag{4.4}$$

where $\mathbf{\Phi}$ is the dissipation rate per unit mass and k the coefficient of heat conduction (see Equation 2.24). The transport terms are linearized as in the previous two equations, and only the partial derivative with respect to time is retained. The dissipation is quadratic in velocity gradients, and therefore it is neglected. As a result:

$$\rho_0 \frac{\partial s'}{\partial t} = \frac{k_0}{C_p} \frac{\partial^2 s'}{\partial x_i^2} + \frac{k_0 (\gamma - 1)}{\gamma p_0} \frac{\partial^2 p'}{\partial x_i^2}. \tag{4.5}$$

By taking the curl and the divergence of Equation 4.3, two different forms of the momentum equation can be obtained. Taking the curl leads to an equation for the vorticity where the pressure does not appear because interactions between pressure and density fluctuations are not taken into account. The result has the form of a diffusion equation:

$$\frac{\partial \omega_i}{\partial t} = \nu_0 \nabla^2 \omega_i. \tag{4.6}$$

Taking the divergence of the momentum equation and eliminating the divergence of the velocity using continuity gives an equation for the pressure:

$$\begin{aligned} \frac{\partial^2 p'}{\partial t^2} - a_0^2 \frac{\partial^2 p'}{\partial x_i^2} &= \left(\frac{4\nu_0}{3} + \frac{k_0 (\gamma - 1)}{\rho_0 C_p} \right) \frac{\partial^2}{\partial x_i^2} \left(\frac{\partial p'}{\partial t} \right) \\ &\quad - \frac{\gamma p_0}{C_p} \left(\frac{4\nu_0}{3} - \frac{k_0}{\rho_0 C_p} \right) \frac{\partial^2}{\partial x_i^2} \left(\frac{\partial s'}{\partial t} \right). \end{aligned} \tag{4.7}$$

Equations 4.2, 4.6, 4.7, and 4.5 constitute a complete set of equations for the mass, vorticity, pressure, and entropy.

In fact, determining the velocity field with the present method implies the use of the Helmholtz decomposition in which the velocity field is separated into a solenoidal part with zero divergence and nonzero curl, and an irrotational part with zero vorticity and nonzero divergence. This decomposition is nonunique. In a homogeneous case such as that considered by Kovasznay, a solution can be obtained by specifying the proper boundary conditions at the limits of the domain.

Consider now the form of the equations. The vorticity mode is governed by the same diffusion equation as in incompressible flow, and it produces no

pressure fluctuations. However, the pressure or acoustic mode, the entropy mode, and the velocity divergence are coupled together. Kovasznay (1953) considered the particular case when the Prandtl number $P = \mu_0 C_p/k_0 = 3/4$, which is close to that of air where P is about 0.72 over a wide range of temperatures. The acoustic mode equation then reduces to an equation for a pressure wave propagating at the speed of sound but damped by the action of viscosity. In this case, the equations for the acoustic and entropy modes are independent of each other. Up to first order, the entropy varies only by heat conduction, and velocity divergence follows pressure and entropy variations.

The equation for the vorticity can be solved directly to give:

$$\omega_j(t) = \omega_j(0) e^{-\nu_0 k^2 t}, \tag{4.8}$$

where k is the modulus of the wave number vector. Also, the linear system governing pressure, divergence and entropy can be solved in Fourier space to give the amplitude of sinusoidal fluctuations as a function of time. The influence of the diffusion terms (the viscous decay of the vorticity, entropy, and sound fields) depends on the length and time scales over which the observation is made. Order-of-magnitude arguments can be used to show that for some important cases, such as when a hot-wire is used to measure turbulence in the freestream of a supersonic wind tunnel, these terms are often small. Setting the viscosity and the heat conduction to negligibly small values in the solution shows that the amplitudes of the modes are governed by the following equations:

$$\frac{d\omega_j'(t)}{dt} = 0, \tag{4.9}$$

$$\frac{ds'}{dt} = 0, \tag{4.10}$$

$$\frac{\partial^2 p'}{\partial t^2} = a_0^2 \frac{\partial^2 p'}{\partial x_i^2}, \tag{4.11}$$

$$\frac{1}{\gamma p_0}\frac{\partial p'}{\partial t} = -\nabla.\mathbf{u}'. \tag{4.12}$$

This set of equations represents a consistent zeroth-order approximation for weak fluctuation fields when the time of observation is short. The vorticity and entropy are constant, and the pressure obeys a wave equation with a speed of propagation equal to the speed of sound. Equation 4.9 represents a "frozen pattern" of vorticity (or solenoidal velocity) and when it is applied to homogeneous turbulence in a wind tunnel it predicts an unchanged flow pattern carried by the mean velocity, as suggested by Taylor's hypothesis. Equation 4.10 indicates a similar frozen pattern behavior for temperature spots, and Equation 4.11 is simply the wave equation for propagation of the pressure

field. The only compressibility effect, that is, the creation of velocity divergence, is related to the pressure fluctuations. Because the fluctuating pressure and divergence are in quadrature, the result is the superposition of acoustic waves on an incompressible vortical field, with no coupling.

Kovasznay assumed that the Mach number of the fluctuations was small, which allowed the nonlinear term $u_j' \partial u_i' / \partial x_j$ in the momentum equation to be neglected. Because this nonlinear term is known to be responsible for the energy cascade from large to small scales in three-dimensional turbulence, neglecting it implies some limitations. For example, the characteristic time scale derived for viscous diffusion in Equation 4.8 is several orders of magnitude larger than any turbulent time scale. The only possible conclusion is to assume that the nonlinear term is small compared to the pressure gradient $\partial p' / \partial x_i$. For a given domain size, defined as the volume or time interval over which the small perturbation approximations can be applied, a necessary condition is

$$\frac{\rho_0 u'^2}{p'} \ll 1 \quad \text{or} \quad \frac{\gamma M_t^2 p_0}{p'} \ll 1.$$

It was assumed that $p'/p \ll 1$, so that the condition is $M_t \ll 1$, which is always satisfied by acoustic waves.

Because this is a linear theory the modes do not interact, at least within this domain. An interaction may take place outside the domain, either at solid boundaries or in regions where the fluctuations are not small. If the fluid at some earlier time had passed through a grid, for example, the high-intensity turbulence created by the grid would have produced strong sound waves and the viscous dissipation would have produced entropy spots. The sound waves will propagate away according to the wave equation, but the entropy spots travel with the fluid, diffusing slowly by heat conduction. The small perturbation analysis applies when the modes are sufficiently small for nonlinear interactions between any two modes to be negligible, although nonlinearities may have had an important role in the creation of the modes. Furthermore, if these noninteracting modes pass through a region of strong gradient, such as a shock wave, they may interact with the strong field and then conversion from one mode to another may take place.

Nonlinear interactions between modes were considered in more detail by Chu and Kovasznay (1958). As to the generation of the modes, they found that mass addition produces the sound mode, in that the injected fluid displaces other fluid, and the movement of the displaced fluid generates pressure waves that propagate into the surrounding medium. A body force generates the vorticity and sound modes. The irrotational force component produces only sound, and the solenoidal component produces only vorticity. Heat addition generates the entropy and sound modes, because it increases the temperature of the gas and causes expansion of the heated fluid element. The possible interactions between the modes are summarized in Table 4.1. Several

	Sound source	Vorticity source	Entropy source
Sound–sound	' steepening ' and ' self-scattering ' $\frac{\partial^2(v_{pi}\,v_{pj})}{\partial x_i\,\partial x_j}+$ $+a_0^2\,\nabla^2(P_p^2)+$ $+\frac{\gamma-1}{2}\,\frac{\partial}{\partial t^2}\,P_p^2$	$O(\alpha^2\epsilon)$	$O(\alpha^2\epsilon)$
Vorticity–vorticity	' generation ' $\frac{\partial^2(v_{\Omega i}\,v_{\Omega j})}{\partial x_i\,\partial x_j}$	' self-convection ' $-v_{\Omega j}\,\frac{\partial\Omega_i}{\partial x_j}+\Omega_j\,\frac{\partial v_{\Omega i}}{\partial x_j}$	$O(\alpha^2\epsilon)$
Entropy–entropy	$O(\alpha^2\epsilon)$	$O(\alpha^2\epsilon^2)$	$O(\alpha^2\epsilon)$
Sound–vorticity	' scattering ' $2\,\frac{\partial^2(v_{\Omega i}\,v_{pj})}{\partial x_i\,\partial x_j}$	' vorticity convection ' $-v_{pj}\,\frac{\partial\Omega_i}{\partial x_j}+\Omega_j\,\frac{\partial v_{pi}}{\partial x_j}-$ $-\Omega_i\,\frac{\partial v_{pj}}{\partial x_j}$	$O(\alpha^2\epsilon)$
Sound–entropy	' scattering ' $\frac{\partial^2}{\partial t\partial x_i}\,(S_s\,v_{pi})$	' generation ' $-\alpha_0^2(\nabla S_s)\times(\nabla P_p)$	' heat convection ' $-v_{pi}\,\frac{\partial S_s}{\partial x_i}$
Vorticity–entropy	$O(\alpha^2\epsilon)$	$O(\alpha^2\epsilon)$	' heat convection ' $-v_{\Omega i}\,\frac{\partial S_s}{\partial x_i}$

Table 4.1. Second-order nonlinear interaction between modes of order α. Here, $S = s'/C_p$, $P = p'/\gamma p_0$, and the subscripts p, Ω, and s denote the sound, vorticity, and entropy modes, respectively. The parameter α is a nondimensional measure of the intensity of the disturbance, and $\varepsilon = \nu_0 k/a_0$. (Adapted from Chu and Kovasznay (1958).)

well-known mechanisms are described by these interactions: vortex stretching (the production of vorticity by the interaction of vorticity with itself), the production of vorticity through baroclinic torques (interaction of acoustic and entropy modes, which can sometimes promote early laminar-to-turbulent transition in noisy wind tunnels), the wave-steepening mechanism (interaction between entropy and acoustic modes producing acoustic modes, which can lead to the formation of shock waves), and the scattering of incident sound waves by vorticity fluctuations (the vorticity-sound interaction). As pointed out by Gaviglio (1976), the baroclinic effect is the only generation process in which two modes interact to produce a third one. The other interactions only modify pre-existing modes. The role of pressure fluctuations is discussed in

greater detail in the next section.

4.2 Velocity Divergence in Shear Flows

We saw that in very simple flows with small amplitude fluctuations, pressure fluctuations and compressible turbulence are linked. In general, a non-solenoidal velocity field can have many origins (see, for example, Batchelor (1967)). It can be produced by gravity in a stratified medium, by heat release, viscous dissipation, or pressure gradients, although for pressure gradients to produce significant velocity divergence the turbulence Mach number should be of order unity. Supersonic flows have significant kinetic energy, large enough to produce significant changes in temperature when it is converted into heat. Turbulence is a very dissipative process, and therefore contributions to the fluctuating divergence can come from adiabatic processes, where pressure gradients (and Mach number) are important, and dissipative processes, where entropy production is important. The main concern of this section is to examine if simple order-of-magnitude analyses can give some insight on the importance of compressibility effects on turbulence in known flows. We assume that there are significant compressibility effects when $\nabla \cdot \mathbf{u}'$ becomes large compared to the turbulent velocity gradient $\partial u_i'/\partial x_j$. For the energy-containing motions, this gradient is of order u'/Λ, where Λ is a length scale characteristic of these motions. We begin by deriving simple criteria to assess the importance of compressibility effects, as a function of the flow properties. For most common cases, the criteria can be expressed in terms of pressure fluctuations (isentropic processes), or entropy fluctuations (dissipation or heat conduction), as shown later. For this purpose, we consider the full perturbation forms of the continuity and entropy equations. The approach given by Dussauge et al. (1989) is followed here, in a somewhat expanded form.

If velocity divergence is produced by isentropic pressure variations, the equation for pressure is a wave equation, which is hyperbolic. If the divergence of velocity is produced by entropy variations, the pressure obeys a Poisson equation, and an elliptic problem is obtained (see, for instance, Equation 4.7). This can have many consequences on the overall nature of the flow. For example, for the supersonic flow of a reacting mixture in a nozzle, the heat release will increase the flow entropy, and if the nozzle is not properly designed it can choke. As the flow becomes subsonic there is a transition from hyperbolic to elliptic behavior. Also, if the pressure is governed by a Poisson equation, then it seems likely that in modeling the pressure strain terms in the Reynolds stress equation models similar to the ones used in subsonic flow can probably be used.

By combining the continuity and entropy equations (Equations 4.1 and 4.4)

we have:

$$\nabla \cdot \mathbf{V} = -\frac{1}{\gamma}\frac{d\ln p}{dt} + \frac{\varepsilon}{C_p T} + \frac{1}{\rho C_p T}\frac{\partial}{\partial x_j}\left(k\frac{\partial T}{\partial x_j}\right), \tag{4.13}$$

with $\mathbf{\Phi} = \rho\varepsilon$. The problem is to find reasonable estimates for the amplitude of the pressure fluctuations and the corresponding (Lagrangian) time scale τ.

We can now derive the equation for divergence of the instantaneous velocity fluctuations. The pressure term in Equation 4.13 becomes:

$$\frac{1}{\gamma}\left(\frac{d\,(\ln p)'}{dt} - \overline{u_i'\frac{\partial\,(\ln p)'}{\partial x_i}} + u'\frac{\partial\overline{(\ln p)}}{\partial x_i}\right).$$

Here, the Reynolds decomposition is used, and d/dt denotes the derivative along the instantaneous motion. The last term can be neglected if we restrict ourselves to zero pressure gradient flows. The dissipation and conduction terms are more complicated because they are nonlinear. It is assumed that a sufficient approximation is obtained by assuming small temperature fluctuations, and by linearizing the dissipation and conduction terms with respect to temperature fluctuations. For $T'/T \ll 1$, therefore, the fluctuating part of the dissipation term ε/T becomes:

$$\frac{\varepsilon'}{\bar{T}} - \frac{\bar{\varepsilon}}{\bar{T}}\frac{T'}{\bar{T}}.$$

The bars denote mean quantities. The heat-conduction term can be written as the sum of a flux term and a term that is quadratic in temperature gradients (see Section 3.2.3). That is,

$$\frac{1}{\rho T}\frac{\partial}{\partial x_j}\left(k\frac{\partial T}{\partial x_j}\right) = \frac{1}{\rho}\frac{\partial}{\partial x_j}\left(k\frac{\partial \ln T}{\partial x_j}\right) + \frac{k}{\rho T^2}\left(\frac{\partial T}{\partial x_j}\right)^2.$$

The perturbation form for small temperature fluctuations may now be found, and then we obtain an equation for the fluctuating divergence:

$$\begin{aligned}\nabla.\mathbf{u}' \;=\; & -\frac{1}{\gamma}\left(\frac{d\,(\ln p)'}{dt} - \overline{u_i'\frac{\partial\,(\ln p)'}{\partial x_i}}\right) - \frac{T'}{T}\frac{\bar{\varepsilon}}{C_p T} - \frac{T'}{T}\frac{2\bar{\varepsilon}_\theta}{\gamma T^2} \\ & + \frac{\varepsilon'}{C_p T} + \frac{\varepsilon'_\theta}{\gamma T^2} + \frac{1}{\rho C_p}\frac{\partial}{\partial x_i}\left(k\frac{\partial(T'/T)}{\partial x_i}\right),\end{aligned} \tag{4.14}$$

where $\bar{\varepsilon}$ is the mean rate of dissipation per unit volume, and the term $\bar{\varepsilon}_\theta = \overline{k(\partial T'/\partial x_i)^2}/(\rho C_v)$ is sometimes called the *second dissipation*. It acts as a dissipation for the variance of temperature (energy) fluctuations. Because it represents irreversibility due to molecular effects, it is a local source term for entropy. In Equation 4.14, an approximation for small quantities is obtained. The terms that are cubic in velocity and temperature fluctuations were neglected (terms such as $\epsilon' T' \big/ \bar{\epsilon}\bar{T}$) because at high Reynolds numbers

they involve wave numbers belonging to different domains. Quadratic terms were retained. The reason is that we have linear terms such as $(T'/T)(\bar{\epsilon}/C_pT)$ where $T'/T < 1$, and quadratic terms such as ϵ'/C_pT). It is known (see below) that the fluctuating dissipation can be an order of magnitude larger than the mean dissipation rate, so that the term involving ϵ' has been retained.

We see from Equation 4.14 that divergence fluctuations come from pressure fluctuations, local source terms, and heat fluxes. The sources are proportional to the fluctuations of the dissipation rate, or to the temperature fluctuations themselves. In the following, a primed quantity denotes an *rms* value, rather than the fluctuation itself. The sum of the two pressure terms is assumed to be of order $(p'/p)/\tau$, where the time scale τ depends strongly on whether the pressure wave propagates with respect to the medium. Even if simple estimates can be found for the external flow, the behavior of the near field, or the interaction between the pressure waves and the turbulent field, is not at all clear. Some aspects of the problem are related to problems of wave propagation in a random medium, where the speed of propagation can vary dramatically in amplitude and direction. So two cases are considered: one for which the time scale is acoustic, $\tau_a = \Lambda/a$, and another for which the time scale is turbulent, $\tau_t = \Lambda/u'$, where Λ is a length scale, a the speed of sound and u' the *rms* velocity. The ratio of the two time scales turns out to be the turbulence Mach number:

$$\frac{\tau_a}{\tau_t} = \frac{u'}{a} = M_t.$$

As for the other terms, it is assumed for simplicity that the terms involving the first and second (mean) dissipation rates are all of comparable order, so that only the viscous dissipation needs to be considered. An example is given for supersonic flows without heat sources, which indicates the limits of this approximation. The fluctuating dissipation rates ε' (and ε'_θ) are related to the phenomenon of internal intermittency, according to which the dissipation is distributed randomly in space. This results in a random occurrence in time of strongly dissipative events, at a given fixed point. In subsonic flows, ε' is often an order of magnitude larger than $\bar{\varepsilon}$ (Sreenivasan et al., 1977), so that in Equation 4.14 we expect that the term containing ε' can be larger than the term involving $\bar{\varepsilon}$. An important difference is that the term in ε' probably contains more smaller scales than the term in $\bar{\varepsilon}$, which is proportional to T'/T. The internal intermittency is certainly modified by compressibility because if shock waves appear they introduce regions of strong dissipation with a very particular shape. If the results of recent numerical simulations are a good indication, the shock waves produced by compressible turbulence have a large aspect ratio: they are thin (small-scale), corrugated sheets of long extent (large-scale), located randomly in space, and therefore they are important for the evolution of large and small scales. However, no measurements of the fluctuating dissipation rates are available for supersonic flows, and we need to

assume that their orders of magnitude are not greatly changed by compressibility. Then the contribution of dissipation to the divergence is estimated by considering the fluctuating dissipation rate:

$$\frac{\varepsilon'}{C_pT} \approx 10\,(\gamma-1)\,M_t^2\frac{u'}{\Lambda} = 10\,(\gamma-1)\,\frac{M_t^2}{\tau_t}, \tag{4.15}$$

where it is assumed that, typically, $\varepsilon' \approx 10\bar{\varepsilon}$. For large scales, the important contribution to the divergence is probably the one involving the mean dissipation rate:

$$\frac{T'}{T}\frac{\bar{\varepsilon}}{C_pT} \approx \frac{T'}{T}\,(\gamma-1)\,\frac{M_t^2}{\tau_t}. \tag{4.16}$$

T'/T is generally less than 1, and so the fluctuating dissipation term is probably more important than the mean dissipation term, implying that the major contribution to the velocity divergence occurs at small scales.

The last term, which is related to the fluctuating heat flux, is not considered here. For constant mean temperature at large Reynolds and Peclet numbers it involves no large scales. It is probably not the leading mechanism in flows without heat sources (such as adiabatic or nonreacting flows) or in flows without chemical reactions, because it follows the temperature fluctuations produced by dissipation or pressure fluctuations and just smooths out the smaller scales.

We can now examine some particular situations, beginning with the case of weak compressibility, as found in boundary layers at moderate Mach numbers. Figure 4.1 shows temperature and pressure fluctuation measurements in a zero pressure gradient boundary layer at Mach 1.8. It was possible to measure pressure at only two places: at the wall using a pressure transducer, and in the outer flow using a hot-wire anemometer (where it was assumed that in the freestream the fluctuations were isentropic: see Laufer (1961)). The wall pressure fluctuations measurements are affected by spurious signals such as mechanical vibrations or electronic noise, and they probably underestimate the *rms* level because of spatial integration. For the measurements shown in Figure 4.1, this error was estimated at $\pm 20\%$. Despite these difficulties, the levels at the wall and in the outer flow are comparable, and we expect a smooth variation between these two levels within the layer so that it is clear that adiabatic flows develop temperature fluctuations which are much larger than pressure fluctuations. The entropy fluctuation is $s'/C_p = T'/T$. If the time scales of pressure and entropy are of the same order, Equations 4.14 and 4.15 show that the magnitude of the velocity divergence is given by $10(\gamma - 1)M_t^2/\tau_t$. The divergence can be compared to the order of magnitude of the instantaneous velocity gradients for the energy-containing motions u'/Λ by

$$\frac{\nabla.\mathbf{u}'}{u'/\Lambda} \approx 10(\gamma-1)M_t^2, \tag{4.17}$$

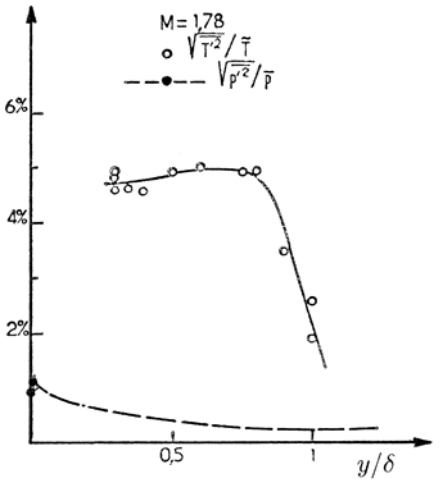

Figure 4.1. Temperature and pressure fluctuation measurements in a zero pressure gradient boundary layer at Mach 1.8. (From Dussauge (1986), with permission.)

which suggests that in the weak compressibility regime, where the dissipation rate is solenoidal, the relative importance of velocity divergence varies according to M_t^2. In a boundary layer at Mach 1.8 with a Reynolds number Re_θ of 5000, M_τ is about 0.07, so that M_t is about 0.1, and the fluctuating divergence is certainly negligible. In a mixing layer with a convective Mach number of 0.6, where compressibility effects are just becoming important, the peak value of M_t is about 0.25, and the ratio in Equation 4.17 is also about 0.25. So $\nabla.\mathbf{u}'$ begins to become significant because of the high dissipation rate. The dissipation rate in the averaged equations, $\bar{\varepsilon}$, may be split into two parts, $\bar{\varepsilon}_s$ and $\bar{\varepsilon}_d$. The solenoidal dissipation rate $\bar{\varepsilon}_s$ is the dissipation in the solenoidal part of the fluctuating motion. In the homogeneous case $\bar{\varepsilon}_s = \nu\overline{\omega_i'\omega_i'}$, where ω_i' is the fluctuating vorticity and $\overline{\omega_i'\omega_i'}$ is the enstrophy. Similarly, the dilatational dissipation rate $\bar{\varepsilon}_d$ is the dissipation in the nonsolenoidal part of the fluctuating motion. In the homogeneous case, $\bar{\varepsilon}_d = \frac{4}{3}\nu\left(\nabla.\mathbf{u}'\right)^2 = \frac{4}{3}\nu\overline{\left(\partial u_i'/\partial x_i\right)^2}$, so that in general, the ratio $\bar{\varepsilon}_d/\bar{\varepsilon}_s$ is something like $\left(\nabla.\mathbf{u}'/(u'/\Lambda)\right)^2$, which suggests that $\bar{\varepsilon}_d$ is not large in this case. Hence, this simple analysis of dilatation produced by solenoidal dissipation indicates the following dependences for the variance of velocity divergence and for the dilatation dissipation:

$$\overline{\left(\nabla\dot{\mathbf{u}}'\right)^2} \propto M_t^4 \qquad \text{and} \qquad \frac{\epsilon_d}{\epsilon_s} \propto M_t^4.$$

More recent studies (Ristorcelli, 1997; Fauchet, 1998; Fauchet and Bertoglio, 1999) have found the same dependence for weak compressibility cases, us-

ing different methods. They both refer to the concept of pseudo-sound used by Ribner (1962). In the regime of pseudo-sound, the acoustic fluctuations (with characteristic velocity scale a) and the turbulent fluctuations (with characteristic velocity scale u') involve distinct ranges of time scales, such as $\tau_a/\tau_t = M_t \ll 1$. Ristorcelli uses the notion of compact sources of sound. The acoustic sources (the turbulent eddies) radiate acoustic waves in the far field, but the near field has a subsonic behavior: for small Mach numbers, information is felt simultaneously in the whole source. Moreover, the "pseudo-pressure" developed in the sources obeys a Poisson equation, as in subsonic flows. The work of Fauchet and Bertoglio (1999) uses simulations of isotropic turbulence with a two-point closure adapted from Kraichnan's DIA model. Their computations reproduce the pseudo sound regime and the M_t^4 dependence. These studies use formulations more elaborate than our simple order-of-magnitude analysis. However, even if the details of the closure are very different in each case, the primary hypotheses are very similar, and the convergence of the results suggests that the scaling in M_t^4 is a rather robust result, which can be used with some confidence.

In flows with temperature inhomogeneities, the magnitude of the second dissipation should be estimated. This implies that we can specify the link between kinetic and thermal energy. We will examine the case of flows without heat sources. Because the flow is adiabatic, it is assumed that the temperature fluctuations are given by the Strong Reynolds Analogy (Equation 5.15), and that ε' and ε'_θ are linked in the same way as usually assumed in models for low-speed flows. That is,

$$\frac{\varepsilon'_\theta}{\varepsilon'} \approx \frac{\bar{\varepsilon}_\theta}{\bar{\varepsilon}} = \frac{r_\varepsilon T'^2}{\frac{1}{2}q'^2},$$

where $q'^2/2$ is the turbulent kinetic energy and $r_\varepsilon = 1.25$ is a constant determined from experiments. For weak compressibility, if the anisotropy of turbulent stresses is not altered,

$$\begin{aligned} \frac{\nabla.\mathbf{u}'}{u'/\Lambda} &\approx 10(\gamma-1)M_t^2\left(1+\frac{r_\varepsilon(\gamma-1)}{\gamma}M^2\right) \\ &\approx 10(\gamma-1)M_t^2\left(1+\frac{M^2}{2\gamma}\right). \end{aligned} \tag{4.18}$$

We can now examine the typical values taken by this ratio in simple flows. If we consider adiabatic supersonic boundary layers for $M < 5$ and mixing layers for $M_c \leq 1$ (see Chapters 6 and 8), maximum values of M_t are at most 0.2. Equation 4.17 indicates that the divergence of fluctuations produced by solenoidal heating is two orders of magnitude lower than the individual component of the fluctuating gradient, and therefore is negligible. A comparison of Equations 4.17 and 4.18 shows that ε'_θ can become the leading term even

under adiabatic conditions (for air), and it can produce significant divergence levels with an elliptic overall behavior if M_t is large enough.

The large-scale estimate of velocity divergence, which is the companion to Equation 4.16, is given by:

$$\begin{aligned}\frac{\nabla.\mathbf{u}'}{u'/\Lambda} &\approx (\gamma-1)^2 M_t^3 M\left(1+\frac{r_\varepsilon(\gamma-1)}{\gamma}M^2\right)\\ &\approx (\gamma-1)^2 M_t^3 M\left(1+\frac{M^2}{2\gamma}\right),\end{aligned}$$

which suggests analogous conclusions: because the ratio is proportional to M_t^3, it remains small for $M_t < 1$ (implying that M remains moderate at the same time).

A second important case is the production of fluctuations by weak shock waves. The entropy increase through the wave is proportional to the cube of the pressure variation (Liepmann and Roshko, 1957; Landau and Lifshitz, 1987):

$$\frac{s'}{C_p} \propto \left(\frac{p'}{p}\right)^3.$$

Because in this case the acoustic and turbulence time scales are the same, the ratio of the pressure and entropy terms in Equation 4.13 is $(p'/p)^2$, which shows that the leading term is the pressure term and in the acoustic approximation it is proportional to M_t. In this case, velocity divergence is produced by quasi-isentropic pressure waves.

Finally, more complicated situations can be considered, with strong pressure fluctuations and high rates of dissipation, by assuming that a typical entropy variation term is given by the fluctuating dissipation rate and that the time scale for pressure is either τ_a or τ_t. The following estimate is obtained,

$$-\frac{1}{\gamma}\left(\frac{d\ln p'}{dt}-\overline{u_i'\frac{\partial \ln p'}{\partial x_i}}\right)+\frac{d\left(s'/C_p\right)}{dt} \approx \frac{p'}{p}\left\{10\left(\gamma-1\right)M_t^n\left(1+C_v r_\epsilon\left(\frac{T'}{T}\right)\left(\frac{T'}{\frac{1}{2}q'^2}\right)\right)\right\}^{-1},$$

where $n = 2$ if $\tau_p = \tau_t$, and $n = 1$ if $\tau_p = \tau_a$, and where T' now denotes the *rms* temperature fluctuation level.

In this case, in the absence of heat sources or chemical reactions, pressure can be an important source of velocity divergence. This is consistent with the results of the previous section, where in simplified cases pressure and divergence fluctuations were found to be strongly linked. Also, the link between T' and p' is crucial, because they both appear in these estimates. There is no general rule to find the magnitude of these terms because they depend on the flow conditions. For the particular case studied by Blaisdell et al. (1993), who

simulated homogeneous turbulence subjected to a shear with constant mean density, pressure, and temperature, it turned out that the fluctuations were produced by nearly isentropic processes, so that $p'/p \approx (\gamma/(\gamma-1))(T'/T)$. They found $p'/p \approx 0.3$ for $M_t \approx 3$. In that extreme case, the ratio of the rates of variation of pressure and entropy is of order 1, so that none of the terms may be neglected. This result is probably not very general, because most of the pressure fluctuations found in these simulations are due to shock waves produced by the interaction of vortices. It is not clear that the time scale for pressure can then be related directly to τ_t or τ_a. Moreover, this case is somewhat far from the more usual case of compressible shear flows where temperature gradients can produce strong temperature fluctuations. For example, with the same values for pressure fluctuations and turbulence Mach number, if the temperature and velocity fluctuations are still linked according to the SRA, then the entropy variations are much larger than the pressure variations. The continuity equation indicates that here the velocity divergence is due to dissipation. Neglecting the pressure terms in the continuity equation leads to a Poisson equation for the pressure fluctuations. The links among T', p', and u' are again important, and in the strongly compressible regimes found in practice they are not clearly identified.

These estimates confirm that turbulence in zero pressure gradient boundary layers at moderate Mach numbers ($M < 5$) may be assumed to be weakly compressible, as long as phenomena such as sound radiation are not of primary interest. Because the divergence of the fluctuating velocity is small, the behavior of the pressure strain terms is found to be similar to that found in the low-speed, variable density case. The fluctuating divergence appears to depend on the turbulence Mach number M_t. In flows where M_t is large, such as in mixing layers, significant levels of fluctuating divergence may be found. If the source of velocity divergence is dissipative heating it seems difficult to produce high levels of the dilatational dissipation, suggesting that significant values of $\bar{\varepsilon}_d$ will be produced by shocklets rather than by viscous heating. If it is possible to produce significant levels of velocity divergence in mixing layers at moderate convective Mach numbers ($M_c \geq 0.5$, say), the equation for the pressure fluctuations and the form of the pressure strain should be changed, and it may be expected that the anisotropy of the Reynolds stresses changes accordingly. This is consistent with an elliptic behavior of the energetic eddies. In addition, it seems difficult to develop significant fluctuations of velocity divergence by the usual levels of dissipation, that is, without shock waves and without heating (or cooling) the flow strongly. If no heat flux is considered, it is clear that the existence of shocklets must be assumed to characterize compressible turbulence.

4.3 Velocity Induced by a Vortex Field

In Chapter 2 we saw that the vorticity transport-equation and the theorems of Kelvin and Helmholtz are easily extended to compressible flows. What is not straightforward is the interpretation of vorticity concentrations in terms of the induced velocity field. In an incompressible flow, we can use the Biot-Savart relation to determine the velocity field induced by concentrated elements of vorticity. When the density is variable (due to the effects of compressibility or stratification), the Biot-Savart relation can strictly no longer be used. The communication among vortex elements is no longer global—it will be confined to directions lying along characteristics (see, for instance, Section 1.3). When the Mach number gradients are severe, the communication paths may have a very complicated geometry. However, in many parts of an otherwise compressible fluid, the mean and instantaneous Mach number gradients may be relatively small. A good example is the outer part of a turbulent boundary layer. Within certain limits, Biot-Savart law may still be used, depending on the importance of the fluctuating divergence.

Formally, we can use the Helmholtz decomposition, in which the velocity field is written as the sum of a rotational part ($\mathbf{V}^\omega$) and an irrotational part ($\mathbf{V}^\phi$) such that $\mathbf{V}^\phi = \nabla\phi$, where ϕ is a potential function (see, for example, Panton (1984)). Hence,

$$\mathbf{V} = \mathbf{V}^\omega + \mathbf{V}^\phi.$$

That is,

$$\begin{aligned} \nabla \times \mathbf{V} &= \boldsymbol{\Omega} = \nabla \times \mathbf{V}^\omega \\ \nabla \times \mathbf{V}^\phi &= 0, \end{aligned}$$

so the vorticity is contained in the rotational part. The appropriate boundary conditions provide the uniqueness of the decomposition. If we require that $\mathbf{V}^\omega$ is solenoidal, then $\nabla \cdot \mathbf{V}^\omega = 0$, and therefore

$$\nabla \cdot \mathbf{V} = \nabla \cdot \mathbf{V}^\phi = \nabla^2\phi,$$

so the dilatation is contained in the irrotational part. For incompressible flow, $\nabla^2\phi = 0$, and ϕ is a harmonic function. For the rotational part, we note that any vector field that is solenoidal can be represented in terms of a vector potential β, so that

$$\mathbf{V}^\omega = \nabla \times \beta.$$

The vector identity $\nabla^{\mathbf{2}}\beta = -\nabla \times (\nabla \times \beta) + \nabla (\nabla \cdot \beta)$ shows that if $\nabla \cdot \beta = 0$, then

$$\nabla^{\mathbf{2}}\beta = -\boldsymbol{\Omega},$$

which can be solved to give the Biot-Savart law for the velocity induced by a vorticity distribution $\mathbf{\Omega}$:

$$\mathbf{V}^{\omega} = -\frac{1}{4\pi}\int \frac{\mathbf{r}\times\mathbf{\Omega}}{|\mathbf{r}|^3}d\upsilon, \tag{4.19}$$

where $\mathbf{r}$ is the position vector measured from the point of interest within the volume υ. This result is general, insofar as the condition $\nabla\cdot\beta = 0$ holds.

To find the velocity $\mathbf{V}$ from a given potential and rotational field, we need V^{ω} and V^{ϕ}. For incompressible flow, $\nabla\cdot\mathbf{V}^{\phi} = 0$, but for compressible flow the dilatation needs to be known. In the particular case of a boundary layer, where the turbulence is relatively weak, compressibility effects are weak and the results of the previous section can be used to determine the magnitude of the fluctuating divergence (Equations 4.17 to 4.19). For low levels of the mean and turbulent Mach number, Biot-Savart can still be used to understand vorticity interactions, and many of the intuitive concepts used in describing structures in boundary layers in subsonic flow carry over unchanged when the flow is supersonic, as long as we are careful in the neighborhood of vorticity sources within the fluid, places where barotropic torques are important (including curved shocks or shocklets).

4.4 Rapid Distortion Concepts

In this section, a particular class of flows is examined where distortions are imposed on the turbulence over a small period of time. The distortions considered here are such that fluid elements are stretched or compressed in some or all directions. A typical example of a "distorting constant area box" used in studies of rapidly distorted subsonic flows is sketched in Figure 4.2. In the experiment by Tucker and Reynolds (1968), for example, the turbulence in the initial section was isotropic and homogeneous. As the flow passed through the box, the spanwise scales were elongated and the vertical ones were compressed. Similar distortions occur frequently in practice, as when turbulence passes through a convergent or a divergent channel, or when a turbulent flow is deformed by the presence of an obstacle or pressure gradient. The characteristic time scale of the energy-containing motions may be estimated by:

$$T_t = \frac{\Lambda}{u'} \qquad \text{or} \qquad T_t = \frac{k}{\varepsilon}.$$

In the first estimate, the scale Λ is some average size of the energetic perturbations, for example, an integral scale, and u' is a characteristic value of the *rms* velocity. The second estimate, due to Townsend (1976), is commonly used in k–ε models, where k is the mean turbulent kinetic energy ($= \frac{1}{2}q'^2$) and ε is its mean dissipation rate per unit mass. As Bradshaw (1973) points out, if the

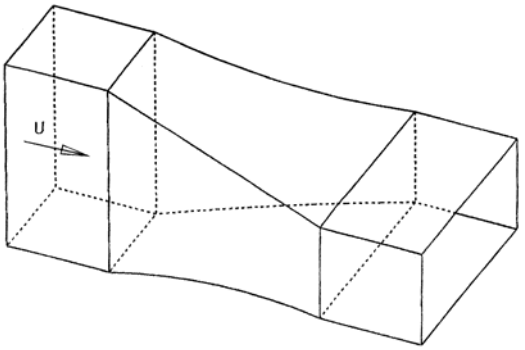

Figure 4.2. An example of a distorting constant area box used in studying rapid distortion effects in subsonic flows.

production were suddenly shut off the turbulent energy initially decays with this time constant. If T_d is the time during which the distortion is applied to turbulence, then if $T_d/T_t \ll 1$ the distortion can be formally classified as a *rapid distortion*.

Most of the work in rapid distortion has been confined to incompressible flows. Yet, compressible flows are potentially very attractive for the application of rapid distortion methods. Changes in the mean field can occur over very short distances, much shorter than is possible in subsonic flows, and the limits of a rapid distortion can often be more easily satisfied. For example, when a boundary layer passes through a Prandtl-Meyer fan or a short region of compression, including the case where the layer interacts with a shock wave, the perturbation can occur over a distance comparable to the boundary layer thickness. Typically, outside the viscous sublayer, the pressure gradients are much stronger than the other stress gradients, and rapid distortion methods become very appealing.

This situation is particularly attractive because analytical solutions can be found for some simple cases where the nonlinear terms in the equation of motion become negligible. The turbulence time scale T_t is related to the nonlinear terms in the momentum equation: after a time T_t, an eddy of size Λ loses its "identity." That is, the nonlinearities are responsible for transferring its energy to smaller scales. For times much smaller than T_t, these nonlinear effects can be neglected, and if the flow is subsonic it obeys a linear set of equations, as long as the mean flowfield is constant and does not depend on the turbulence. These cases represent the field of application of Rapid Distortion Theory (RDT).

The basic theory was developed by Ribner and Tucker (1952) and Batchelor and Proudman (1954) for homogeneous, initially isotropic turbulence in

an irrotational mean flow. The theory was later extended to shear flows (see, for example, Moffatt (1968) and Townsend(1970)) and subsequent developments led to a wide variety of applications. The papers by Hunt (1977); Townsend (1980); Cambon (1982), and the reviews by Savill (1987) and Hunt and Caruthers (1990) provide a comprehensive picture of the current status of RDT for incompressible flows. What seems particularly encouraging is that despite the strict limits on the applicability of RDT, the theory often gives qualitatively useful results outside these bounds, as well as providing guidelines for distorted structure modeling (Savill, 1987).

To solve the linear rapid distortion problem for specific cases, some conditions often need to be satisfied, in addition to the usual rapid distortion criteria. For example, if Fourier transforms of the velocity field are used, the turbulence often needs to be homogeneous. Other solutions may require that the distortion is irrotational, or that the evolution is isentropic along streamlines. In most practical flow realizations these assumptions are not obeyed, and RDT cannot be applied. It is often more attractive to consider instead the Reynolds stress evolution, rather than the associated spectra, especially in supersonic flows where the scope of experimental data is more limited than in subsonic cases. The simplifications of second-order closure needed for rapid distortion approximations to the Reynolds stress equations are not straightforward, as pointed out by Hunt (1977), mainly because terms involving pressure fluctuations must be modeled, giving at best an approximation to the solution. This latter approach, where the scaling arguments and limiting processes employed in RDT are used to approximate the Reynolds stress equations, is what we term the Rapid Distortion Approximation (RDA) and its application to supersonic flows is discussed in Section 4.4.3.

4.4.1 Linearizing the Equations for the Fluctuations

The main consideration in linearizing the equation of momentum comes from the form of the fluctuating acceleration a_i'. That is,

$$a_i' = \underbrace{\frac{\partial u_i'}{\partial t}}_{(1)} + \underbrace{\bar{u}_j \frac{\partial u_i'}{\partial x_j}}_{(2)} + \underbrace{u_j' \frac{\partial \bar{u}_i}{\partial x_j}}_{(3)} + \underbrace{u_j' \frac{\partial u_i'}{\partial x_j}}_{(4)}.$$

Terms 1 and 2 represent the particle derivative of u_i' ($= Du_i'/Dt$), and it is assumed that they are of the same order as the other terms in the acceleration. A necessary condition for the linearization of the acceleration terms is that the second term is much larger than the fourth term. If q' and U are representative scales for u_i' and U_i, respectively, this simply requires that the fluctuations are small:

$$\frac{q'}{U} \ll 1. \tag{4.20}$$

By comparing the third and fourth terms, another condition related to time scales is obtained. If S is the scale for the mean velocity gradient, we require:

$$\frac{q'}{\Lambda S} \ll 1. \tag{4.21}$$

We should also make sure that Du_i'/Dt is large compared to the nonlinear term. If the scale of variation of the fluctuation is the fluctuation itself q', and if the time scale is the transport time L/U, where L is the size of the distorted zone and U a typical mean velocity, we obtain the condition:

$$\frac{q'}{U}\frac{L}{\Lambda} \ll 1. \tag{4.22}$$

This condition may be more stringent than condition 4.21, depending on the flow. Because we have neglected the nonlinear inertial terms, we need to consider only the low wave number part of the spectrum. In this case, the viscous terms in the momentum equation may be neglected, which requires large Reynolds numbers.

The equation for the velocity fluctuation now has the form,

$$\frac{Du_i'}{Dt} + u_j'\frac{\partial U_i}{\partial x_j} = -\frac{1}{\rho}\frac{\partial p'}{\partial x_i}, \tag{4.23}$$

which indicates that the time constant of the linear system is $1/(\partial U_i/\partial x_j)$, and that the nature of the pressure terms depends on the velocity and density fields.

We must also consider the fluctuating continuity equation:

$$\underset{(1)}{\frac{\partial \rho}{\partial t}} + \underset{(2)}{U_i\frac{\partial \rho'}{\partial x_i}} + \underset{(3)}{\bar{\rho}\frac{\partial u_i'}{\partial x_i}} + \underset{(4)}{u_i'\frac{\partial \bar{\rho}}{\partial x_i}} + \underset{(5)}{\rho'\frac{\partial U_i}{\partial x_i}} + \underset{(6)}{\rho'\frac{\partial u_i'}{\partial x_i}} + \underset{(7)}{u_i'\frac{\partial \rho'}{\partial x_i}} = 0.$$

If condition 4.20 is fulfilled, it is clear that the seventh term in this equation is small compared to the second term, and if the density fluctuations are small

$$\frac{\rho'}{\bar{\rho}} \ll 1, \tag{4.24}$$

the sixth term is much less than the third.

The form of the continuity equation is therefore not a problem by itself because the hypothesis of small fluctuations is sufficient to yield a linear equation. The density can be replaced by a function of pressure and entropy. However, as noted in the previous section, there is a contribution of the energy dissipation to the low wave numbers through temperature fluctuations. A linearized form of the energy equation, for example, Equation 4.5, combined with the linearized equation of state, closes the system. This constitutes a complete set of equations for the RDT problem, and a flow case can formally be called a rapid distortion when conditions 4.20 to 4.22 and 4.24 are fulfilled.

4.4.2 Application to Supersonic Flows

As noted earlier, RDT problems for subsonic flows have been studied by many authors. In particular, it is possible to find mean fields that produce homogeneous turbulence fields. Fourier transforms can then be used, and the evolution of the three-dimensional spectra of turbulence can be derived. After integration over all wave numbers, the turbulent stresses can be calculated, analytically if the mean distortion is irrotational.

In trying to formulate a similar approach for compressible flows, a difficulty is encountered with the energy equation. The solution now depends on the source terms in the energy equation, or, if the entropy fluctuation level is constant, from source terms in the distortion. The groundwork for the application of RDT to compressible flows was laid by Ribner and Tucker (1952) who studied the evolution of a solenoidal turbulent field subjected to an irrotational compressible mean field. Another important contribution was made by Goldstein (1978) who separated the velocity fluctuations into vortical and potential parts. He applied this decomposition to the case of isentropic fluctuations with an irrotational mean distortion. This yields a wave equation for pressure, with a source term depending on the vortical part of velocity. Debiève (1986) (reported also in Dussauge et al., 1989) gave a classification of the different possible source terms in this equation.

The applications of RDT to homogeneous flows by Durbin and Zeman (1992) and Jacquin et al. (1993) are of particular interest. Homogeneity makes possible some analytical results, and Fourier transforms can be used. For these particular distortions, the mean velocity gradients, the pressure and the density were spatially uniform but time dependent. Jacquin et al. used the Helmholtz decomposition of the velocity fluctuations into a solenoidal and a dilatational part, while Durbin and Zeman used Goldstein's decomposition into a vortical and a potential part. For the particular case of irrotational distortion they concluded that the nature of the pressure field depends critically on the gradient Mach number $M_g = \lambda S^*/a$. Here Λ is an integral space scale, S^* is a characteristic value of the velocity gradient ($= |\partial U_i/\partial x_j|$), and a is the speed of sound. This Mach number is therefore based on the velocity difference occurring over a distance equal to the integral scale in the distortion. For subsonic velocity differences, the velocity divergence depends only on pressure fluctuations generated by a purely acoustic mode, and it does not depend on the solenoidal part. However, if this velocity difference becomes supersonic, there is a direct coupling with the dilatational mode, without damping by pressure. M_g can also be interpreted as the ratio of the acoustic time scale of the pressure fluctuations Λ/a to the time scale of the distortion $1/S^*$. If M_g is large, the pressure does not have time to develop fully during the distortion. This suggests that in very rapid interactions, such as in shock waves, the effect of pressure can be neglected. For moderate M_g, the contributions of the vortical and potential modes to the pressure variance and to the pressure

divergence term in the turbulent kinetic energy equation are both small. This analysis has recently been extended to the case of a pure shear by Simone and Cambon (1995) and Simone et al. (1997).

4.4.3 Rapid Distortion Approximations

It is usually difficult to apply RDT to shear flows, because in general the distortions of such flows are vortical and inhomogeneous, the entropy fluctuations are not constant, and the initial three-dimensional spectra are not known. The theory has not been developed for such cases. Nevertheless, the analysis of the Reynolds stress equations and the physical hypothesis used in RDT can still provide useful information on practical shear flows. This approach is what we call Rapid Distortion Approximation (RDA).

Consider the Reynolds stress equations. In the equation for the velocity fluctuations (Equation 4.23), it was possible to identify linear and nonlinear interactions with appropriate time scales. This is not so obvious in the Reynolds stress equations, because they are derived by multiplying the equation for the velocity fluctuations by the fluctuations themselves, integrating over all wave numbers and averaging. Consequently, some properties related to the length scales of the fluctuations have been lost. However, we can still apply some of the same physical arguments used in RDT. For example,

(i) The characteristic time scale of turbulent energetic eddies is $T_t = \Lambda/q'$. As noted earlier, after a time T_t the eddies have lost their identity through nonlinear mechanisms and most of their energy has been transferred to smaller scales. A consequence is that for times much less than T_t, the dissipation rate can be considered constant. In the present formulation, Λ is related to the energetic eddies, so that the rate of dissipation can be defined by $\varepsilon = q'^3/\Lambda$ or $\varepsilon = q'^2/T_t$.

(ii) The distortion time is of the order of $T_d = 1/(\partial U_i/\partial x_j) = 1/S^*$. This is the linear response time of the turbulent stresses, which means that after a time T_d a significant evolution of k or the shear stress due to the distortion can be observed. For the cases where the distortion is applied over a time L_d/U that is larger than T_d (L_d is the length of the distorted zone and U an average value of the mean velocity), we must use L_d/U instead of T_d.

It is assumed here that in a rapid distortion the evolution of turbulent fluxes is controlled by the action of the mean distortion, and not by diffusive processes, turbulent or viscous. Only the case of high Reynolds number flow is considered. When the diffusion terms are neglected, the equation for the Reynolds stress $\sigma_{ij} = \widetilde{u_i' u_j'} = \overline{\rho u_i' u_j'} \big/ \bar{\rho}$ can be written in the symbolic form:

$$\frac{D\sigma_{ij}}{Dt} = \quad \text{(production)} + \text{(pressure strain terms)} - \text{(dissipation)}.$$

The pressure strain terms cannot be neglected and need to be modeled. The production terms come in two parts: one from the interaction of the turbulence with mean velocity gradients, and one from the interaction of the turbulence with mean pressure gradients. The second part, in the Favre averaged equations, results from the interaction of turbulent mass fluxes with the mean pressure gradients, whereas for the Reynolds averaged equations it comes from the interaction of the turbulent mass flux with the mean acceleration. This part is sometimes called the *enthalpic production* term, but it is not discussed here because that would not contribute much to the physical understanding of the phenomena (for further details, see Dussauge and Gaviglio (1987)). Both parts of the production can be calculated directly from the mean field. For adiabatic, nonhypersonic Mach numbers, the two parts of the total production are comparable in magnitude and of order $q'^2 S$, and the dissipation terms are of order q'^3/Λ. If the evolution of σ_{ij} is to be independent of the dissipation, we first require that the dissipation be much less than the production and pressure strain terms. That is,

$$\frac{q'^3}{\Lambda} \ll q'^2 S \qquad \text{or} \qquad \frac{q'}{\Lambda S} \ll 1.$$

The result is identical to condition 4.21.

Second, we also require $D\sigma_{ij}/Dt \gg \varepsilon$ because $D\sigma_{ij}/Dt \sim q'^2 U/L$. This gives the same condition as condition 4.22:

$$\frac{q'}{U}\frac{L}{\Lambda} \ll 1.$$

The terms involving pressure fluctuations, that is, the pressure strain terms, need to be evaluated. A linearized equation for the pressure fluctuations can be derived by taking the divergence of the linearized momentum equation (neglecting diffusion), provided $\rho'/\rho \ll 1$ and $u'/U \ll 1$. This is in agreement with the requirements for RDT (in particular, conditions 4.20 and 4.24). The pressure strain terms can be written as the sum of gradients of pressure velocity correlations (the *pressure diffusion* term), and the product of pressure fluctuations and instantaneous velocity gradients (the *redistribution* term). When the initial turbulence is isotropic, exact expressions for the pressure strain terms can be found, but in the general case these terms need to be modeled. The pressure diffusion is simply neglected in RDA, although this may lead to inaccuracies. Hunt (1977) indicated that some rapid distortions may develop pressure fluctuations strong enough to produce significant pressure transport terms, but he suggested that an inhomogeneous version of the RDT could compute this effect. The redistribution term can also be split into two parts: the *return-to-isotropy* part and the *rapid* part. The return-to-isotropy part is of the order of the dissipation, and it is therefore neglected. Dussauge and Gaviglio (1987) developed a model for the rapid part of the pressure strain terms

for solenoidal velocity fluctuations $\nabla \cdot \mathbf{u}' = 0$ and a compressible mean field. For such flows, the pressure fluctuation obeys a Poisson equation, and the mean dilatation does not contribute to p'. This result has two consequences.

First, if the mean distortion is isotropic, that is, a pure dilatation or compression with spherical symmetry, the pressure does not damp the effects of production. The only source term in the equation for σ_{ij} is then the production due to turbulence interacting with the mean velocity gradients. The Reynolds stress equation can be integrated, and as a result the tensor $T_{ij} = \rho^{-2/3}\sigma_{ij}$ is constant along a streamline, and the Reynolds stress σ_{ij} varies with density according to:

$$\sigma_{ij} \propto \rho^{2/3}.$$

This dependence was also proposed from dimensional considerations by Batchelor (1955).

Second, the compressible models for the rapid part of the pressure strain terms can be derived very simply from the subsonic formulations: the rule is that the velocity gradient $\partial U_i/\partial x_j$ should be replaced by its deviatoric $\partial U_i/\partial x_j - \frac{1}{3}\delta_{ij}\,(\partial U_k/\partial x_k)$. In particular, the rapid part can itself be split into two parts, one related to mean velocity gradients, $(\pi_{ij})_u$, and the other to mean pressure gradients, $(\pi_{ij})_p$. Because we assume $\nabla.\mathbf{u}' = \mathbf{0}$, the mean pressure contribution can be modelled according to the incompressible formulation by Lumley (1975, 1978). For the contribution due to mean velocity gradients, several different models are available (see, for example, Launder et al. (1975) and Shih and Lumley (1990)).

Finally, we obtain a Reynolds stress equation that can be solved once the mean field is known. As long as the pressure gradients are much larger than the turbulent stress gradients, the turbulence does not influence the mean field and the mean velocity and pressure gradients can be found using the Euler equation with appropriate boundary conditions. For a supersonic flow, the method of characteristics can be used.

We see that in trying to solve the problem in terms of the Reynolds stresses, the basic concepts developed in RDT were used in RDA. However, in RDA the diffusion processes and the pressure transport are neglected, and the pressure strain terms need to be modeled. The current models were developed for incompressible turbulence and they use the incompressibility condition $\nabla.\mathbf{u}' = 0$ extensively. The discussion in the previous section also showed that the behavior of the pressure may depend strongly on the value of the gradient Mach number. Although these approximations may lead to inaccuracies, the resulting simplifications are attractive because they generally lead to tractable formulations.

4.4.4 Application to Shock-Free Flows

Computations using RDA were performed in expansions and compressions by Dussauge and Gaviglio (1987), Jayaram et al. (1989), Donovan (1989) and Smith et al. (1992). In these experiments, turbulent boundary layers were subjected to expansions and compressions produced by wall deflections, and they are described more fully in Chapter 9. Incoming Mach numbers ranged from 1.8 to 3.0. The pressure gradients were strong, so that the evolution of the supersonic part of the boundary layer could be computed using the Euler equations by the method of characteristics applied to the vortical flow of a perfect gas, together with the boundary conditions given by the experiment. The mean fields determined in this way were used as the input for the computation of the Reynolds stresses. This computation can be performed along streamlines because the diffusion terms were neglected. In all these flows, the gradient Mach number is small, and in any case less always than one. Favre averages were used, so that enthalpic production terms and their counterparts in the pressure strain models were retained.

The results for a 12° expansion at Mach 1.76 are shown in Figure 4.3. The general agreement between experiment and computation was excellent. The main effect on the velocity fluctuations appeared to be due to pure dilatation, but the rest of the mean distortion (due to mean normal strain and mean vorticity) also had a significant influence. The effect of dissipation was always negligible. Near the wall ($y/\delta < 0.4$), the RDA conditions were not fully met, and the predictions underestimate the turbulence damping. For the 20° expansion at Mach 2.89 studied by Smith et al. (1992), the computation also agreed well with the data, at least for $0.2 < y/\delta < 0.8$. In this region the dilatation alone accounted for 90% of the reduction in the streamwise component of the stress.

For the compressions, the task was more difficult. In each case, the compression was produced by a concave wall so that near the wall, where the turnover times are small, the relative length of the distortion increases. For this reason the compression was rapid in the outer flow (where the distortion length is short and the characteristic time scales are large) and slow near the wall. Nevertheless, in the outer layer of an 8° compression at Mach 2.87, Jayaram et al. (1989) found satisfactory agreement between the predictions of RDA and the measurements. Near the wall, the estimate of the nonlinear effects (associated with the neglected return-to-isotropy and dissipation terms) were compatible with the observed discrepancies between measurements and RDA. By including a crude estimate of the dissipation and the return-to-isotropy contributions, the predictions near the wall were improved considerably, as shown by Jayaram et al. (1989) and Donovan (1989). With these corrections, Donovan (1989) found very good agreement between the RDA predictions and the experimental data for the flow over a concavely curved wall with a turning angle of 16° at Mach 2.87, and for the flow over a flat wall with an externally

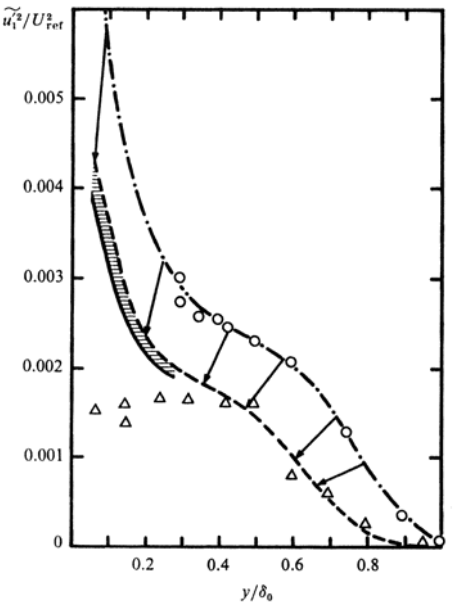

Figure 4.3. Velocity fluctuations in a 12° expansion corner at Mach 1.76. ○, upstream profile; △, along the last Mach wave in the expansion; - - - -, dilatation effect; shaded zone, dissipation effect. Arrows indicate streamline correspondence. (From Dussauge and Gaviglio (1987). Copyright 1987, Cambridge University Press. Reprinted with permission.)

imposed adverse pressure gradient of similar strength.

As we can see, RDA appears to be a useful tool for computing many continuous distortions of turbulent flows, provided the Reynolds number is high enough to satisfy the criteria of rapid distortion. It is also a useful tool to help understand more complex distortions. Smith and Smits (1996a), for example, used RDA to determine the relative importance of several competing distorting influences in the flow over a forward-facing step (see Chapter 9).

4.4.5 Shock Relations for the Turbulent Stresses

Another application of RDA is the case of a turbulent field passing through a shock wave. The main argument for using rapid distortion analysis is that the time of interaction between the shock and a turbulent eddy is very small so that the nonlinear energy cascade has no time to transfer energy. This leads to a linear problem if the strength of the shock does not depend on the incident turbulence. In particular, the shock is assumed to be steady. It was noted

earlier that the nature of the pressure field may depend on the gradient Mach number $M_g = \Lambda S^*/a$. For large values of M_g, pressure fluctuations do not have enough time to propagate, so that there is no damping of the distortion by pressure. If this result still holds in vortical flows with entropy fluctuations, it suggests that the effect of pressure could be neglected for turbulent fluctuations passing through a shock, because the characteristic velocity gradient S^* takes very large values in a thin shock. The Reynolds stresses then experience the whole effect of the production terms. This hypothesis was used by Debiève (1983), who developed relationships for turbulence quantities across a shock (in effect, jump conditions for turbulence). The main difficulty in the analysis, the integration through the discontinuity, was resolved by defining a transport invariant relative to the Reynolds stresses, given by $n_i \sigma_{ij} n_j$, where $\mathbf{n}$ is a unit vector normal to the shock. This quantity is invariant for flows described by $D\sigma_{ij}/Dt =$ production. Turbulence source terms that modify the transport invariant were taken into account if they were either continuous through the shock, or if they varied like a Heaviside function.

The analysis leads to a particularly simple expression for the amplification of turbulence by a shock wave. The result depends on the orientation and strength of the shock wave, and it is given by

$$T_2 = K^* T_1 K \tag{4.25}$$

with $\mathbf{K} = \mathbf{I} - [\tilde{U}](\mathbf{n}^*/U_{2n})$, where T_1 and T_2 are the upstream and downstream Reynolds stress tensors, $\tilde{U}_n$ is the velocity normal to the shock, $[\tilde{U}]$ is the jump in velocity across the shock, and the asterisk denotes a transpose. Figure 4.4 gives a polar representation of the Reynolds stress upstream and downstream of the shock. The vector **OM** has a magnitude equal to the variance of the velocity fluctuation and a direction given by the unit vector $\mathbf{m}$. Note that $\mathbf{OM} = (\mathbf{u}' \cdot \mathbf{m})^2 \, \mathbf{m}$, and $\overline{u'v'} = OP - OQ$. The initial state corresponds to an isotropic tensor and it is represented by a circle. The diagram shows that the amplification through the shock is a maximum in the direction normal to the shock.

In this formulation the enthalpic production terms (which can probably be represented at least approximately as Dirac source terms) are neglected. Comparisons made with experiments in a 6° compression at Mach 1.8 showed good agreement, which suggests that the approximations based on gradient Mach number could also be extended to the rapid distortion of shear flows. However, Smits and Muck (1987) found that in stronger compression corner interactions at Mach 2.9, the agreement was not satisfactory, and for these flows the analysis explains only part of the observed turbulence amplification (see Chapter 10).

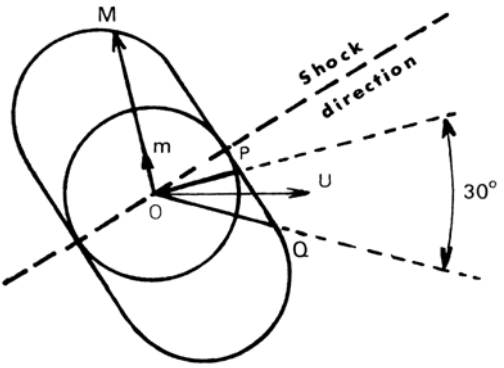

Figure 4.4. Evolution of the Reynolds stress tensor in a 6° compression ramp flow. (From Debiève (1983), with the author's permission.)

4.5 Mach Numbers for Turbulence

We have seen that a variety of Mach numbers has been used to quantify compressible turbulence. Turbulence models in their present form almost exclusively use the turbulence Mach number $M_t^2 = u'^2/a^2$, or $= \frac{1}{2}q'^2/a^2$, which suggests that strong turbulence fluctuations, of the magnitude of the speed of sound, will produce compressibility effects strong enough to change the global turbulence properties. If the velocity fluctuations are of the same order as the speed of sound, we can expect that shocks will be formed in the fluctuating motion. In some situations, however, this Mach number is not very useful. For example, acoustical phenomena are entirely dominated by compressibility, yet M_t is very small for this case. If the *rms* velocity is obtained from the isentropic relationship $p' = \rho a u'$, which can be rewritten as $p'/p = \gamma M_t$, we see that for typical acoustic pressure fluctuation levels it is difficult to obtain an acoustic wave with velocity fluctuations larger than the speed of sound. Another example can be found in direct numerical simulations. In simulating the decay of homogeneous turbulence, Blaisdell et al. (1993) found that the decay cannot be scaled by the turbulent Mach number alone, and that it depended strongly on initial conditions and on the relative importance of the solenoidal and nonsolenoidal parts of the velocity field.

Several other Mach numbers are also commonly used. In Chapter 3, it was shown that for thin shear layers in supersonic flow, the same approximations made in subsonic flows can be used, as long as $M_v \ll 1$, where M_v is the turbulence Mach number based on vertical velocity fluctuations. Some authors have introduced the fluctuating Mach number M', which takes into account the fluctuations in the speed of sound. In the analysis of boundary layers,

and in Preston tube calibrations, a friction Mach number $M_\tau = u_\tau/a_w$ is often used. Finally, a parameter widely used in mixing layer studies is the convective Mach number briefly described in Chapter 1. Its main success is to collapse the data on the spreading rate of mixing layers formed between two different gases at high speed.

It is always puzzling, and certainly a little confusing, to introduce so many different parameters (even though they are all Mach numbers) to characterize situations that appear to be of the same type. Some questions need to be asked. Under what conditions are these Mach numbers defined? What is their physical meaning, and how they are related to each other? Is it possible to represent the properties of turbulence with some generality, as a function of any of these quantities?

We can start with the equations of motion. Dimensionless parameters generally define classes of problems, and they cannot be separated from the equations to which they are related. The momentum equation indicates that each time the magnitude of a turbulent stress is compared to the mean pressure, a Mach number is formed, for example, $M_v = v'/a$, as indicated earlier. This is similar to comparing the turbulent kinetic energy to the mean potential or internal energy, which yields $M_q^2 = \frac{1}{2}q'^2/a^2$. This is fundamentally the case found in the SRA relationship (see Chapter 3), where *rms* temperature fluctuations are proportional to M and M_t. In boundary layer studies, the friction Mach number $M_\tau = u_\tau/a_w$ can also be understood in the same way.

These interpretations are simple, but not very informative. Models for compressible turbulence are more ambitious because they try to scale the ratio of the divergence-free part of the velocity field to the compressible part by a single parameter. A similar attempt was made in Section 4.4, when the order of magnitude of the ratio $(\nabla.\mathbf{u}')/(u'/\Lambda)$ was estimated in terms of M_t. Although the estimates were approximate, this approach is inadequate even in the simplest case because this ratio was a function of both M_t and T'/T. Therefore, the parameter M_t can be a useful parameter to classify phenomena in shear flows only when the flows have a high degree of similarity. For example, Blaisdell et al. (1993) showed in their simulations that the structure of homogeneous sheared turbulence was independent of the initial conditions and could be characterized by either M_t or M'.

Compressibility effects found in acoustic waves are certainly different. In shear flows, intense vortices produce pressure waves such as shock waves or sound waves, which in turn are a powerful mechanism to generate velocity divergence, and therefore "compressible" turbulence. The important point in this case is not so much the Mach number of the (small) velocity fluctuations produced by the waves, but the Mach number of the strong fluctuations generated at the origin of the wave. Because the velocity divergence depends on M_t and T'/T, a representation using M' is therefore probably more appropriate. Because we believe that only relative motions are important, the pressure

fluctuations produced by vortices will be of a different nature if the velocity difference across the layer is subsonic or supersonic, so that the pressure term of Equation 4.14, and consequently $\nabla.\mathbf{u}'$ may depend in general on M' rather than M_t, whereas the entropy term is some function of M_t and T'/T.

These considerations are based on global statistics, rather than a physical view of the flow. More precise descriptions can be obtained by considering some particular cases, and it may be possible that this approach can be applied to other flows as well. For example, the fluctuating Mach number M' represents the magnitude of the local Mach number variation, and it may be the best indication of the effects of compressibility on the distortion of communication paths, and the possible appearance of shocklets. Similarly, the convective Mach number is based on the mean characteristics of the flow, and in simple cases it can be interpreted as the Mach number of the relative motion of the large eddies. This is consistent with the view that the scales of the energy-containing eddies are of the same order as the scales of the mean motion. If M_c is larger than one, compressibility affects these large eddies. The multiple scale aspects of turbulence complicate this approach considerably, and it is not clear that smaller scales, which are less energetic and which have smaller velocity scales, are also directly affected by compressibility. In the general situation, the problem is difficult. In self-similar flows, however, M_c could play the role of a Mach number for turbulence, because all properties will depend only on similarity parameters and only one Mach number is required to describe all compressibility effects. It then becomes possible to derive relationships among M_c, M_t, and M'. For example, in mixing layers it may be assumed that

$$u'/\Delta U = F(M_c),$$

where u' is the peak value of the *rms* velocity fluctuations at a given streamwise location, and F is the normalized spreading rate (see Chapter 5). Introducing the definition valid for mixing layers with the same gas on both sides $M_c = \Delta U/(a_1 + a_2)$, and remarking that $u'/(a_1 + a_2) \approx u'/2a$, we find that $M_t \approx M_c F(M_c)$. Because $F(M_c)$ varies from 1 to about 0.7 when M_c varies from 0 to 2, this relation shows that M_t and M_c are of the same order, and are nearly proportional to each other over a wide range of convective Mach numbers.

The picture would not be complete without referring again to the gradient Mach number $M_g = S\Lambda/a$. Here, $S\Lambda$ is the velocity difference across a distance Λ. If this relative velocity is supersonic, $M_g > 1$, and compressibility effects are expected to become important, in particular with respect to the pressure field. In the simple case of mixing layers, the scale Λ is of the order of δ_ω: $\Lambda = C\,(M_c)\,\delta_\omega$, where C can depend on M_c. In the middle of the layer, $\partial U/\partial y \approx \Delta U/\delta_\omega$, and therefore

$$M_g \approx \frac{\Delta U}{\delta_\omega}\frac{C\delta_\omega}{a} \approx C\,M_c\,.$$

Because C is of order 1, M_g, M_c, and M_t in these shear flows are all of the same order of magnitude, and they are nearly proportional to each other, although they can represent different physical aspects of the flow.

4.6 DNS and LES

Direct Numerical Simulations (DNS) based on the compressible Navier-Stokes equations require that a large number of scales need to be resolved. In many high Reynolds number variable-density flows produced in laboratory experiments, in industrial applications (aerodynamics) and in nature (atmospheric flows), the ratio of the large scales to the small scales is very often greater than 10^6, and a very high accuracy is therefore required. There is also one more variable, the density, and one more equation, the energy equation. Moreover, we have hyperbolic behavior and the equations allow shock solutions that the numerical algorithms must reproduce accurately. The methods also need to make compromises between conflicting requirements: they should have a low numerical viscosity and be able to capture discontinuities such as shock waves without oscillations. These problems remain challenging, and only the most refined numerical methods have these capabilities. At present, three-dimensional computations can have a resolution of 2048^3 (Kaneda and Ishihara, 2004), which means that the ratio of the smallest scales to the largest ones is two thousand. For isotropic flows, this may be enough to establish the high Reynolds number limit (Pearson et al., 2004), but for shear flows, especially wall-bounded flows at large Reynolds number, experiments still remain essential, and several new generations of computers (perhaps two or three) will need to be developed before this situation will change significantly.

There is also the question of which computational techniques can be used. Among the more accurate are spectral methods, usually in Fourier space, which naturally lend themselves to homogeneous or periodic flow conditions. This limits the simulation of compressible flow severely: as pointed out by Lele (1994), there exist only a few possible instances where compressible flows are homogeneous. For steady flow, there is only the case of temporally decaying, homogeneous, compressible turbulence, and the case of pure mean shear with uniform density. It is also possible to compute homogeneous compressions or expansions by balancing the dilatation by a time-varying density. There is obviously a great need to study numerically the behavior of inhomogeneous compressible turbulence, so that, at present, most of the simulations (DNS and LES) are very often performed with finite difference schemes of high accuracy. For reasons of computer power and capacity, it is also often preferred to simulate temporal problems, the longitudinal direction being considered as homogeneous. This indicates the difficulty found in computing fully inhomogeneous, spatially evolving flows. However, this is mostly a question of technical performance, which will probably find a cure in the next generation of com-

puters, and which, it is hoped, does not alter significantly the understanding of the physics of such flows. Current indications are that this holds true, even for relatively low Reynolds number flows (see, for example, Martin (2004)).

These computations are very appealing, despite their limitations, because they can produce results that are very difficult or even impossible to obtain experimentally. First, they can give field properties, because they produce an entire three-dimensional, time-dependent data set, and quantities such as vorticity or velocity divergence can be determined, and the existence of shock waves can be observed or derived. Such data are difficult to obtain experimentally under three-dimensional unsteady conditions such as found in turbulent flows. Second, they provide data on thermodynamic properties such as pressure, density, and temperature. Direct measurements of these quantities in supersonic turbulent flows are very difficult in many respects, and information from simulations, even if it is imperfect or incomplete, can prove to be very useful. Third, some particularly interesting experiments are very difficult to perform at high speed because of experimental difficulties. For example, it is very difficult to produce a homogeneous, decaying turbulence field in a flow of good quality, or to generate grid turbulence subjected to homogeneous shear, or to control the motion of the foot of a shock wave in an experiment. Similarly, because of the small physical size of the flows produced in typical research wind tunnels, and because the Reynolds number is usually high, it is generally more difficult in high-speed flows to take measurements in the near-wall region, or to measure the slope of the spectrum at high frequencies. For such problems, the simulations can play an essential role. The status of the simulations for homogeneous flows and simple shear flows is reviewed in the next section, and the case of inhomogeneous shear flows such as mixing layers, boundary layers, and channel flows is examined in Section 4.6.4. The particular example of the numerical simulation of the interaction of a shock wave with an incoming turbulence field is discussed in Section 4.7. We should also mention the recent simulations of channel flows by Coleman et al. (1995) and Huang et al. (1995). Their results, in particular regarding the pressure and density fluctuations, and the turbulent time scales, are in good agreement with what is known about supersonic wall layers, as described in the following chapters.

4.6.1 Homogeneous Decaying Turbulence

For the case of homogeneous turbulence in a uniform stream with constant mean density, the first simulations were two-dimensional (Passot and Pouquet, 1987). Shock waves were observed, and at the intersection of shock waves vortices were seen forming. In the three-dimensional case, it was more difficult to observe these shock waves, partly because of the problems of spatial resolution. In fact, the formation of shocks depends critically on the amount

of compressible turbulence put in as part of the initial conditions. A useful parameter is χ, the ratio of the kinetic energy of the part of the fluctuations with nonzero divergence to the total kinetic energy. When χ is $O(1)$, nonlinear effects are observed in the acoustic mode and shock waves are produced by wave steepening. However, even with an initial χ of zero, Lee et al. (1991) report the occurrence of shocklets for high enough values of the turbulence Mach number M_t. One of the difficulties in interpreting these simulations is that the observed decay depends on the amount of dilatation dissipation ε_d present at any time, where ε_d itself depends on the initial values of χ, M_t, and the density fluctuations. It also seems that differences occur if the acoustic mode is prescribed independently of the vortical mode (see Sarkar et al. (1991) and Blaisdell et al. (1993)). When the initial conditions of these two modes are specified separately, their superposition is obtained: from Kovasznay's mode theory it is expected that their interaction is weak. Such behavior was confirmed by the work of Kida and Orszag (1990). Moreover, the resolved large scales had a limited statistical ensemble, and the oscillations in the solution obscured the observed trends (Lele, 1994).

Nevertheless, the simulations can give some guidance on the trends that can be expected, and they have been used to calibrate compressible turbulence closure models. In their present state, they are probably not reliable enough because of the ambiguities listed in the previous paragraph, and there is some question as to whether the simulations compute turbulence and the pressure field generated by the eddies, or whether they compute eddies and acoustic waves with weak coupling. In addition, because of insufficient dynamics, the resolved scales are often entirely dominated by viscous effects (Lele, 1994). Even if the functional form of the closure model is correct, therefore, the values of the modeling constants probably have to be treated somewhat skeptically.

4.6.2 Turbulence Subjected to Constant Shear

The situation is brighter for homogeneous turbulence subjected to uniform shear. The simulations are limited to flows with constant mean density, and they can only describe the shear flows found in real life incompletely because they give information on the effect of shear alone. This flow is fundamentally different from an inhomogeneous shear flow, because the latter is bounded and can lose energy by acoustic radiation. In the homogeneous case, the initial conditions are rather quickly forgotten, and after some time the ratio of the solenoidal and dilatational parts of dissipation is nearly constant (Blaisdell et al., 1993). As expected, the amplification of fluctuations is less than at low speeds. Long and thin structures with strong negative velocity divergence have been identified, and they have been interpreted as shocklets developing between zones where the vorticity has concentrated. This supports the notion that shock waves can exist within the turbulent motions present in shear flows.

The simulations also suggest that in practical flows a part of density is related to pressure through nearly isentropic processes, and another part is connected to the turbulent transport of heat, which, at moderate Mach numbers, is nearly isobaric but produces large temperature fluctuations.

Sarkar (1995) has performed simulations for various values of the turbulent Mach number M_t and gradient Mach number M_g. The gradient Mach number was based on the velocity difference occurring over a distance equal to an integral scale (Section 4.4.2), and it was shown that the structure of the pressure field in rapid distortion problems depends critically on this parameter, for both irrotational mean distortions and for shear flows. In these simulations, Sarkar attempted to make M_t and M_g vary independently. The data show that the observed low amplification rate of fluctuations is primarily due to a low level of turbulent friction and to a lesser extent to dilatation dissipation and pressure divergence terms. The amplification rate depends strongly on M_g and it is practically insensitive to variations in M_t. The results suggest that the first signs of compressibility effects are to be found in changes in the anisotropy of the Reynolds stresses. This aspect has been widely ignored in simple compressible turbulence models, and if confirmed, it implies that we are probably just starting to discover the properties of turbulence in high-speed shear flows where compressibility effects are significant.

4.6.3 Spectra for Compressible Turbulence

The form of the spectrum in compressible turbulence is still unknown. A number of theoretical proposals have been made and they were summarized by Passot and Pouquet (1987) and Lian and Aubry (1993). If acoustic waves are superimposed on incompressible turbulence, or if shock waves are present in one-dimensional or two-dimensional turbulence, the shape of the spectrum may be altered. In fact, there is some evidence to suggest that this is possible. In most numerical simulations the number of scales is too small to develop an inertial subrange. Typically, the spectra contain only two decades of wave numbers. However, the first simulations of two-dimensional compressible turbulence showed that there was a dramatic increase in the spectra at high wave numbers when shock waves were produced, suggesting that the slope of the spectrum for small scales could be significantly altered by compressibility. The more recent simulations by Porter et al. (1994, 1995) of forced and decaying turbulence contradict these results. For decaying turbulence, the initial *rms* Mach number was unity, and they reported the existence of a small spectral range with a $-5/3$ slope. Their simulations for turbulence subjected to a shear showed a larger range. When the solenoidal part and the compressible part of the velocity are considered separately, a $-5/3$ range was found for each part. This implies that the part of the motion which is directly controlled by the shocklets can also follow a $-5/3$ law. In a hypersonic boundary layer, Lader-

man and Demetriades (1974) found experimentally a slope close to $-5/3$ in the spectrum at high wave numbers, but these measurements are very difficult: the $-5/3$ slope is found in a frequency range where the frequency compensation of the hot-wire probe is difficult, so that the accuracy of the measurement may be in question.

More recently, Fauchet (1998) and Fauchet and Bertoglio (1998) have explored the shape of the spectra provided by the DIA model adapted for compressible isotropic turbulence. They also found a very robust persistence of the $-5/3$ power law for the solenoidal spectrum, whatever the value of M_t. Their results suggest, for low M_t, a $-3/2$ power law for the compressible part of the motion, and a -3 power law at large M_t. These results are obtained in the high wave number ranges of isotropic turbulence. Existing measurements are restricted to low energetic wave numbers in shear flow turbulence. In this case a distortion of the spectra is observed, the energetic scales being about half the size of their subsonic counterparts. These results are discussed in greater detail in Chapter 8. In summary, although the shape of the spectra appear to be modified, the asymptotic power laws are still observed.

4.6.4 Shear Flows

The computation of simple shear flows has been very successfully developed during the last few years, and an overview of these results in canonical flows such as mixing layers, boundary layers, and channel flows is given in this section. Simulations have been performed with (LES) or without a turbulence model (DNS). Obviously, the LES aim at simulating flows at larger Reynolds numbers. Many models have been used in LES, from the simple MILES (Boris et al., 1992), in which the filtering produced by the truncature at the level of the mesh acts as a sink for the fluctuations of larger scale, to more elaborate subgrid closures such as the dynamic mixed scale model (Sagaut, 2002). The adequacy of these models for high-speed flows is not discussed here, because at the present stage, no specific two-point closure is routinely used in the simulations. However, the discussion presented in Section 4.2 suggests that in flows where M_t is small, the fluctuating field is almost solenoidal. It may therefore be expected that in such flows, typically in channel flows and boundary layers with $M < 4$ or 5, no compressible events are expected. That is, it is probable that no significant singularities such as shocklets occur in the flow, and DNS may be easier. If no compressibility modeling is needed, low-speed formulations can probably be used with success.

Mixing layer simulations are more difficult, in that compressibility effects are important, even for relatively low values of M_c. In Section 6.10, we compare the predicted anisotropy of the Reynolds stresses to the experimental values. The behavior of, for example, $-\overline{u'v'}/\overline{u'^2}$ reveals more or less similar trends (see figure 6.16), but the most striking observations are the discrepancies shown at

low Mach numbers, indicating some serious shortcomings in the computations.

Despite these difficulties, some important results have been uncovered from the computations. There is uniform agreement among the computations quoted here (Vreman et al., 1996; Freund et al., 2000; Pantano and Sarkar, 2002). that the dilatational dissipation and the pressure divergence terms are weak, and that the decrease in the spatial growth rate reflects a change in the structure of the fluctuating pressure. So the computations have already proved their worth by uncovering important physical mechanisms, even if their accuracy remains insufficient to calibrate models.

The predictions seem to be much better for boundary layer and channel flows. Many authors have performed DNS and LES simulations for compressible channel flows, including Coleman et al. (1995), Huang et al. (1995), and Lechner et al. (2001) among others. Their results, in particular regarding the pressure and density fluctuations, and the turbulent time scales, are in good agreement with what is known about supersonic wall layers, as described in Chapter 8. As for flat plate boundary layers, many computations are now available that demonstrate good results, including Guarini et al. (2000), Maeder et al. (2001), Stolz and Adams (2003), Pirozzoli et al. (2004), Sagaut et al. (2004), and Martin (2004), among others. The agreement with measurements in boundary layers at moderate Reynolds numbers is often excellent. An example of LES results obtained by Sagaut et al. (2004) is given in Figures 4.5 and 4.6. The result of the computation is in close agreement with the measurements. Particular hypotheses, such as the assumption of small pressure fluctuations, are well verified.

Recent DNS results obtained by Martin (2003) and (2004) are particularly interesting. The computations covered a Mach number range from 3 to 8, for a constant Reynolds number of $\delta^+ = 400$ (corresponding to a value of $Re_\theta = 2390$ at the lowest Mach number, and $Re_\theta = 13,060$ at the highest). A complementary run at $M = 2.23$ and $Re_\theta = 2390$ allowed comparisons with the experiments of Debiève (1983), at the same Mach and Reynolds number. This body of work is discussed more extensively in Chapter 8, but the initial evaluations show remarkable agreement with the known behavior of high-speed boundary layers, and further analysis of the DNS database will undoubtedly lead to a greatly expanded insight into the underlying physics. What is of equal interest are the DNS results on shock wave-boundary layer interactions obtained by Adams (2000) and Wu and Martin (2004). A preliminary result is shown in Figure 10.9, highlighting the wrinkled character of the shock as it interacts with the incoming turbulent boundary layer. Further consideration of this work is deferred to Chapter 10.

To conclude this short review, it seems that for homogeneous flows and simple wall flows (and possibly even for shock wave-boundary layer interactions), DNS and LES may be accurate enough to predict global properties in a very reliable way. If valid, this conclusion will open up a new era in high-speed

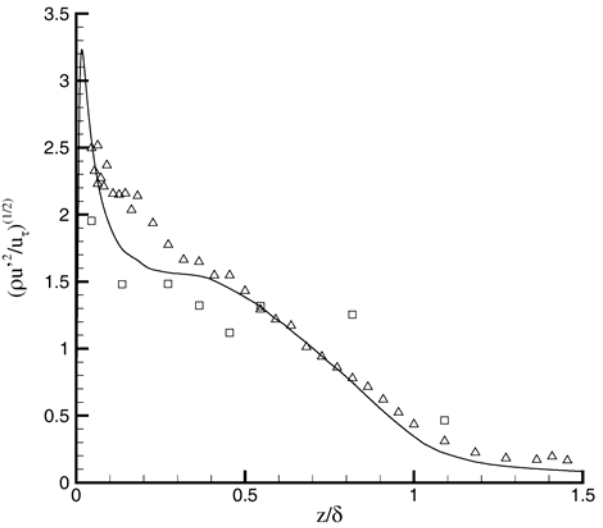

Figure 4.5. Longitudinal velocity variance in a supersonic boundary layer, $M = 2.3$, $Re_\theta = 4500$. □, hot-wire measurements, Debiève (1983); △, LDV measurements, Eléna and Lacharme (1988); ——, LES. (From Sagaut et al. (2004), with permission.)

boundary layer research, where many old questions can be addressed in an entirely new way. For example, numerical results can explore the immediate vicinity of the wall, a zone that is out of reach of most experimental methods. Moreover, time-dependent phenomena can be examined in great detail, such as the three-dimensional deformation of a single large-scale boundary layer motion as it encounters a shock wave. Finally, the computations have already been used for calibrating turbulence models, and they can help significantly in their development. It is not clear, however, that all the pertinent parameters have been systematically examined, and the available results are very often dominated by viscous effects. Whatever the present imperfections, it is expected that future progress in this area will help to improve our understanding of at least some compressibility effects, and it is likely to have a crucial impact on the development of compressible turbulence models.

4.7 Modeling Issues

In developing turbulence models for high-speed shear flows, Morkovin's (1962) hypothesis has often been a starting point. In essence, Morkovin suggested that for moderate Mach numbers compressibility effects did not influence the

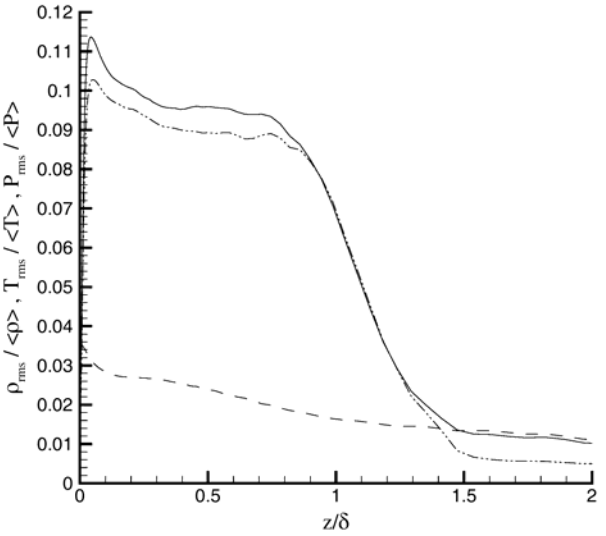

Figure 4.6. Density, pressure, and temperature fluctuations in a supersonic boundary layer, $M = 2.3$, $Re_\theta = 4500$, obtained using LES. ——, *rms* density; - - - -, *rms* pressure; —- · ·, *rms* temperature. (From Sagaut et al. (2004), with permission.)

dynamic behavior of turbulence directly, and the principal effect of high speeds was felt through the change in fluid properties. The next chapter is concerned with the range of validity of this hypothesis, among other topics, and we show that it will be possible to describe some flows, such as nonhypersonic boundary layers with zero pressure gradient, using relatively straightforward extensions of simple low-speed models. In other flows, such as in mixing layers (see, for example, Barre et al. (1994)), or in boundary layers with $M_e > 5$ or with nonzero pressure gradients, there is a need for models taking compressibility effects into account. Here, we discuss some of the difficulties encountered when trying to model compressible turbulence using second-order closures. As we show, this is not a simple task. In contrast to the situation in low-speed flows, no satisfactory model has been found that is general enough to give accurate results over a reasonably extended range of applications. The models for compressible flow are rapidly evolving in as much as this field is relatively new, and we run the risk of making comments that will become obsolete at the same rate. Nevertheless, it is probably a risk worth taking, in order to check that the current proposals are sensible.

It was seen in Chapter 3 that the equation for turbulent kinetic energy does not have the same form in low- and high-speed flows. For compressible flows, there is a pressure velocity divergence term, which represents the power

produced (or lost) by pressure in volume changes. The problem is to determine whether we can keep the modeling of the other terms unchanged (that is, use the models derived for incompressible flows) and add one or more extra terms, appropriately modeled, or whether compressibility modifies several or all of the terms, or even if the pressure divergence term is actually the most important one. Another question of interest is to determine if in models of the k–ε variety, the dissipation equation needs to be modified, and how this should be done.

A useful starting point is the case of subsonic flows with density gradients. These flows are very different from supersonic and hypersonic flows, but they can be considered as a benchmark for defining the action of compressibility as distinct from the departures due to high Mach numbers. At low speed, the degenerate form of a compressible turbulence model should match the variable density form. Somewhat surprisingly, work has been performed in this area only recently. A model accounting for the modification of the turbulent kinetic-energy diffusion was proposed by Shih et al. (1987), and Huang et al. (1994) showed that standard k–ε models have enormous difficulties in computing the equilibrium layer of a subsonic boundary layer with variable density (k–ω models are more successful in this respect).

One of the difficulties comes from the following reason. In the equilibrium, constant stress zone, we have:

$$\rho_w u_\tau^2 = -\overline{\rho u' v'} = \text{constant} \qquad \text{and} \qquad -\overline{u'v'} \propto k.$$

Therefore $\bar{\rho} k$ is constant, but k is not. In the equation for k, if the diffusion term is kept proportional to $\partial k/\partial y$, there exists obviously a diffusion term in the constant stress zone. This term is a function of the density gradient, which alters the balance between production and dissipation. As the constants of these models are linked together, there is a possibility to compensate partially this imbalance by adjusting one of the constants, for example the turbulent Prandtl number for the diffusion of the dissipation rate. Guézengar et al. (1999) and (2000) have used this possibility to compute boundary layers and mixing layers. Catris (2000) and Aupoix (2002, 2004) have explored another way by remarking that the diffusion term in the equation for k should be based on the gradient of $\bar{\rho} k$ to recover equilibrium conditions. Although this modeling brings a clear improvement, modifications to the equation for ϵ are necessary to recover the influence of density gradient on the spreading rate of the mixing layer. They do not reproduce the effect of compressibility on free shear flows.

These adjustments are necessary to cure some pathological aspects of the k-equation in models for incompressible flows. They should not hide more precise compressibility problems, related to the existence of nonzero velocity divergence, that result in two consequences for the k-equation: the existence of a dilatation dissipation and of a pressure divergence term. These terms represent the explicit effects of compressibility, because new terms appear in

the equation. This behavior does not exclude the possibility of implicit effects: compressibility may modify the solenoidal dissipation and the structure of the fluctuating pressure field, even in the pseudo-sound approximation.

The first attempts to model compressible turbulence (Zeman, 1990; Sarkar et al., 1991) concentrated on these explicit aspects. In order to proceed, the source of the divergence terms needs to be identified. Dussauge et al. (1989); Zeman (1990), and Blaisdell et al. (1993) used order-of-magnitude estimates, analysis, and numerical simulations, and their conclusions supported the idea that the strongest sources of velocity divergence are shocklets, not the heating due to viscous dissipation in solenoidal fluctuations (see also Section 4.2). More recent work, however, driven by DNS (Vreman et al., 1996; Freund et al., 2000; Pantano and Sarkar, 2002; Section 4.6), has shown that in many supersonic shear flows, dilatation dissipation and pressure divergence are negligible, and the explicit effects cannot explain the anomalous spatial growth rate of mixing layers. The arguments for a fourth-order scaling in M_t presented in Section 4.2 seem well confirmed, and high-compressibility regimes should be considered to obtain a significant level of $\partial u_k'/\partial x_k$. Moreover, the analysis proposed by Ristorcelli (1997) suggests that pressure divergence scales as $M_t^2(P/\epsilon_s - 1)$. This scaling implies that pressure divergence is important if M_t is not small and if the flow is strongly out of equilibrium ($P/\epsilon_s \neq 1$). This explains probably why subsonic models can often provide reasonable predictions of supersonic boundary layers: in such flows M_t remains small and production balances dissipation over most of the layer, so that dilatation dissipation and pressure-divergence are small. The scaling suggests also that pressure divergence can be important when production and dissipation are very different, that is, in distorted or perturbed flows. This remains a domain that has not been fully explored.

The implicit effects are more puzzling. The work by Aupoix (2004) shows that, before taking compressibility into account, it is necessary to tune the models to reproduce density effects. Equally, it shows that some improvements are still needed to predict accurately the spreading rate of the subsonic, variable density mixing layer. Vreman et al. (1996) have clearly shown that the effect of compressibility in free shear flows is to change the structure of pressure fluctuations and as a consequence, to reduce $-\overline{u'v'}$. This means that taking pressure divergence and dilatation dissipation into account does not solve the central issue, and implies that the modeling of $-\overline{u'v'}$ needs to be revised. In two-equation models such as k–ϵ or k–ω, an eddy viscosity is used, and the formulation of ν_t should probably be modified. One possibility is to make ν_t a function of some local Mach number. Because the evolution of $-\overline{u'v'}$ is, to a large extent, related to the rapid part of pressure, the choice of a gradient Mach number appears as a likely candidate. If more detailed models such as Reynolds stress models, are considered, it is clear that the focus should be put on the modeling of the pressure strain terms. Their rapid

part is again related to the gradient Mach numbers, and the nonlinear part (the return-to-isotropy in incompressible turbulence) depends on the turbulent Mach number. Note that rapid distortion studies for compressible turbulence have already proposed models for the dilatational part of the motion (Durbin and Zeman, 1992; Jacquin et al., 1993; Simone et al., 1997). These models, however, need to be extensively tested.

The previous considerations have dealt mainly with simple shear flows. The problems that were raised are found equally in flows strongly out of equilibrium, as in shock/boundary layer interactions. Such interactions may constitute new sources of vorticity, and of velocity divergence and of sound. They may alter significantly the balance between these various elements, and enhance compressibility effects. The same points as discussed with respect to simple shear flows will need to be addressed again, and the specific problems related to the presence of a shock (production of vorticity, temperature, and pressure fluctuations through the shock, flow separation, and shock unsteadiness) will require extensive further studies. The review paper by Knight et al. 2003 gives a good overview of the ability of the current turbulence models to predict such interactions. We must note that LES may also predict some of these interactions very well, as shown at moderate Mach numbers by Garnier et al. (2002), and that a great deal of new information is coming out of DNS (Adams, 2000; Li and Coleman, 2003; Wu and Martin, 2004).

Chapter 5

Morkovin's hypothesis

One of the more widely used hypotheses for the analysis and computation of boundary layers is Morkovin's hypothesis. This hypothesis was developed in 1962 by Morkovin from an analysis of supersonic boundary layer data, as they were available at that time. He concluded that for moderate Mach numbers "the essential dynamics of these shear flows will follow the incompressible pattern." This assertion is general and rather vague, but the consequences derived from this hypothesis include a scaling for velocity fluctuations and/or for turbulent kinetic energy, and some particular forms of the Reynolds Analogy for boundary layers on adiabatic flat plates. The hypothesis was used and reformulated by Bradshaw (1974) to indicate that high-speed boundary layers can be computed using the same model as at low speeds by assuming that the density fluctuations are weak. This point of view is certainly reasonable for supersonic flows without mass and heat sources. However, the characterization of compressible turbulence depends on the level of fluctuating divergence $\nabla.\mathbf{u}'$ that is proportional to the material derivative of density $D\left(\rho'/\rho\right)/Dt$ rather than to the density fluctuation ρ'/ρ itself. The application of Morkovin's hypothesis is essentially limited to boundary layers. However, it has been widely used in the literature as a basic concept, with the suggestion that it may be extended to other flows, and therefore it is discussed here rather than in Chapters 7 and 8. First, we propose a derivation of the hypothesis in terms of characteristic time scales of turbulent and mean motions, and second we consider different forms of the Reynolds Analogy, and the resulting temperature-velocity relationships.

5.1 Space, Time, and Velocity Scales

In low-speed, equilibrium boundary layers it is usually assumed that the time scales of the mean and turbulent fields are of the same order. It is proposed to generalize these notions to the compressible case. We show that Morkovin's hypothesis assumes that the relationship between time scales is independent

of the Mach number. After some simplification, the scaling suggested by Morkovin is derived.

Consider the characteristic time scales of the turbulent and mean motions. The turbulent time scale t_t can be expressed as a function of mean time scale t_m, flow parameters such as the Reynolds and Mach numbers R and M, the position y, and the length scale L. That is,

$$t_t = g\left(t_m, R, M, y, L, ...\right).$$

We know that the energetic structures and the mean motion have characteristic scales of the same order. This suggests that the previous relationship can be rewritten as

$$t_t = t_m g\left(R, M, y, L, ...\right), \tag{5.1}$$

where the function g is $O(1)$. If we assume Morkovin's hypothesis, then for weak compressibility effects, for example, in boundary layers at moderate Mach numbers, the relation between the scales is the same as at low speeds. Equation 5.1 reduces to:

$$t_t = t_m g\left(R, y, L, ...\right). \tag{5.2}$$

The turbulent time scale is defined as usual by k/ε. This time is a characteristic turbulence decay time, and in the case of compressible turbulence, this also includes the possible dissipation by shocklets, which can change the rate of dissipation and shorten the turbulence decay time. The mean time scale is chosen as $(\partial U/\partial y)^{-1}$, the turnover time of the mean motion, as in low-speed flows. This choice can be justified as follows. The main role of the mean inhomogeneity is to amplify turbulence through linear mechanisms described, for example, by rapid distortion theories. In general, a small fluctuation subjected to mean shear obeys an equation of the form (written in a rather symbolic way):

$$\frac{Du'}{Dt} + u'\frac{\partial u}{\partial y} = f.$$

In this equation, f represents the pressure, nonlinear, and viscous terms. It appears from the linear left-hand side that the amplification of u' by linear mechanisms occurs with a time constant of the order of $(\partial u/\partial y)^{-1}$ (for incompressible turbulence, the role of the pressure terms in f is to reduce $u'\partial u/\partial y$, but the order of magnitude remains unchanged). The mean time scale can therefore be interpreted as a response time of fluctuations to mean inhomogeneity, and it must therefore be of order $(\partial u/\partial y)^{-1}$.

To evaluate the dissipation ε, for example, in the region of constant stress, we follow Morkovin (1962) and assume that the shear stress is constant, and that

$$-\overline{\rho u'v'} \approx -\bar{\rho}\overline{u'v'} = \rho_w u_\tau^2 \ .$$

It is also assumed that, in this region, production and dissipation are equal, and that similarity of the profile is achieved by using either a viscous length

scale, or an external length scale. We denote the scale as L, whatever the choice. Equation 5.2 can then be rewritten as:

$$\frac{\bar{\rho}k}{\rho_w u_\tau^2} = g\left(\frac{y}{L}, R, ...\right). \tag{5.3}$$

We recognize in Equation 5.3 the scaling proposed by Morkovin for the similarity of the Reynolds stresses: similarity is achieved if the local velocity scale in the constant stress region is now $u_\tau \left(\rho_w/\rho\right)^{1/2}$ instead of u_τ.

We can now define a length scale as follows. The turbulent time scale is defined as Λ/u', where u' is a characteristic scale for velocity fluctuations, for example, $\sqrt{k}$. Equating this time to k/ε, and setting ε equal to production gives the relation:

$$\frac{\Lambda}{u'} = \frac{\bar{\rho}k}{\rho_w u_\tau^2 \partial U/\partial y},$$

or, according to Equation 5.3,

$$\Lambda = g\left(\frac{y}{L}, R, ...\right)\frac{u'}{\partial U/\partial y}\ . \tag{5.4}$$

From Equation 5.4, it follows that the length scale is the same in subsonic and supersonic flows when the ratio $u'/(\partial u/\partial y)$ is unchanged. This implies that the scaling for density effects should be the same for u' and $\partial u/\partial y$. We know from experiment and from Equation 5.3 that in supersonic layers u' varies as $\rho^{-1/2}$ (see also Figure 1.2 and the discussion in Section 5.1). We also know that $\partial u/\partial y$ varies as $\rho^{-1/2}$, because, as we show in Chapter 7, the transformed velocity follows a log law with the same von Kármán's constant as in subsonic flows. Therefore, according to Morkovin's hypothesis, the characteristic length scales governing turbulent transport should not change in the supersonic regime (for further details of this argument, see Dussauge and Smits (1995)).

In an expected and consistent way, the normal stress $\overline{u'^2}$ is scaled by $\rho_w u_\tau^2/\bar{\rho}$. The measured behavior of the other normal stresses is not so clear and it is discussed further in Chapter 8. However, measurements of logarithmic mean velocity profiles and of normal stresses are presently the best experimental check on the validity of Morkovin's hypothesis, which apparently can be used with confidence in boundary layers at Mach numbers up to 5. In this range, at least as far as the turbulent transport of momentum is concerned, it can be assumed that the effects of compressibility reduce to the effects of variable fluid properties. When departures from this hypothesis are expected, Equations 5.3 and 5.4 can give some insight into the physical mechanisms involved: first, the relationship between time scales depends on Mach number, because at high Mach numbers the turbulence decay time can be affected by compressibility, and second, the dissipation may no longer balance production if the pressure

divergence terms are large enough. It may be expected that at least close to the wall, the parameter governing these departures is some local Mach number, for example, the friction Mach number.

5.2 Temperature-Velocity Relationships

In Morkovin's original paper (Morkovin, 1962), he also suggested some possible properties of the enthalpy and total enthalpy fluxes. He derived particular relationships between velocity and temperature fluctuations for boundary layers on adiabatic plates, which are known collectively as the Strong Reynolds Analogy (SRA). This is probably the reason why Reynolds analogueies are often considered as part of Morkovin's hypothesis, although the physical mechanisms are not exactly the same as those discussed in the previous section. Of course, if the relations between the heat and momentum fluxes are known, relations between the mean temperature and velocity may be derived from Equations 3.25 and 3.26.

Equation 3.26 determines the temperature field, and considerable efforts have been made to find a solution, or at least an approximate solution. These approximations usually relate the temperature field to the velocity field, and by using the equation of state, allow the density to be eliminated as an unknown in the continuity and momentum equations. Such temperature-velocity relations can only be found by using considerable empirical insight, and therefore we need to review the experimental evidence first.

The temperature in the boundary layer can of course vary significantly, even in the absence of heat transfer at the wall. Because detailed experimental investigations of heated or cooled boundary layers are rare, it is fortunate that a considerable amount of useful information can be obtained from studies of boundary layers on adiabatic walls. Extensive surveys of the available data are given by Fernholz and Finley (1976, 1980, 1981), and further information may be found there.

A useful quantity, at least from a practical point of view, is the turbulent Prandtl number P_t, defined by:

$$P_t = \frac{\widetilde{u'v'}\left(\frac{\partial \tilde{T}}{\partial y}\right)}{\widetilde{v'T'}\left(\frac{\partial \tilde{u}}{\partial y}\right)},$$

and it may be interpreted as the ratio of the turbulent transport of heat to the turbulent transport of momentum.

In what follows, the turbulent Prandtl number is extensively used. It is shown or assumed that, as in boundary layers at low speeds, P_t remains close to unity. This can be considered as another illustration of Morkovin's hypothesis: the links between momentum and heat fluxes are proposed to be independent of the Mach number. At low speeds, temperature fluctuations

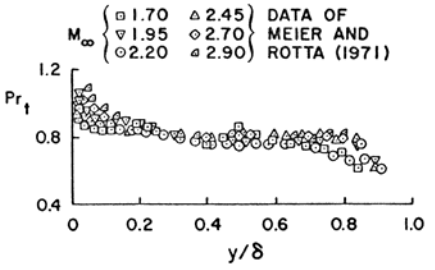

Figure 5.1. Turbulent Prandtl number distribution in a boundary layer. (Figure from Cousteix (1989), after Meier and Rotta (1971). Reprinted with permission of Cépaduès-Éditions.)

are nearly isobaric. At high speed, if there is an increase of the acoustic component of the fluctuating motion, it is clear that the relations among pressure, temperature, and density fluctuations can be affected, and that the turbulent Prandtl number may change. It is consistent with Morkovin's hypothesis to assume that P_t is not significantly altered by compressibility.

5.3 Experimental Results

The variation of the turbulent Prandtl number P_t across a boundary layer at moderate Mach numbers is shown in Figure 5.1. Here, P_t is close to one right across the layer, and for the most part it is constant and equal to 0.8. Therefore the transport coefficients for the turbulent transport of heat and momentum are nearly equal.

The molecular Prandtl number P is defined as $\mu C_p/k$ $(= \alpha/\nu)$, and it may be interpreted as the ratio of the thermal diffusivity to the momentum diffusivity in laminar flow. As indicated in the discussions of Couette flow and laminar boundary layers given in Section 2.5, a molecular Prandtl number of one implies that the total enthalpy is constant in an adiabatic shear layer. Now, the molecular Prandtl number for air is about 0.72, and it is nearly constant across the layer because it is almost independent of temperature, and the recovery temperature of an adiabatic wall is not equal to the total temperature measured in the freestream. The data show that the recovery factor r for a turbulent boundary layer on an adiabatic flat plate is approximately equal to $P^{1/3}$ (Cebeci and Smith, 1974; Cousteix, 1989). For air this gives $r = 0.896$, and the consensus value is close to 0.89 (see Figure 5.2).

If the total enthalpy equation is integrated across the boundary layer, the

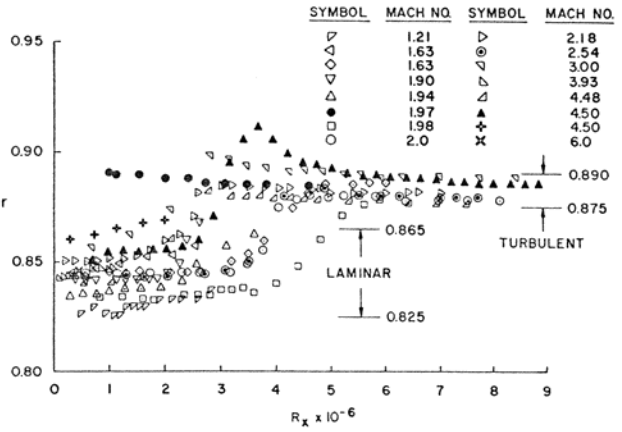

Figure 5.2. Recovery factor distribution in a boundary layer. (Figure from Mack (1954), with the author's permission.)

integral

$$\int_0^\delta \frac{\rho u}{\rho_e u_e}\left(1 - \frac{h_0}{h_{0e}}\right) dy$$

is independent of the streamwise location for adiabatic flows (h_{0e} is the total enthalpy at the outer edge of the layer). When the mass flux and the total enthalpy are functions of y/δ only, the integral must be zero. Because the mass flux is always positive and $h_0/h_{0e} < 1$ near the wall, this result implies that there must be a region where $h_0/h_{0e} > 1$, that is, there must be an overshoot in the total temperature distribution that increases with positive heat flux, as found on a heated wall. In an adiabatic flow, this overshoot is difficult to measure experimentally because it is usually rather small: for the example shown in Figure 5.3 it is less than 1%. The overall variations in total temperature in this example are less than 6%, and even in a strong adverse pressure gradient they are typically less than 10%. A crude, but very useful approximation, is to assume that the total temperature in a boundary layer on an adiabatic wall is constant and equal to its freestream value.

As far as the fluctuations in temperature are concerned, almost all of the measurements have been made using constant current hot-wire anemometry. The data include measurements of $\overline{T_0'^2}$ and $\overline{T'^2}$, as well as the correlations $\overline{u'T_0'}$ and $\overline{u'T'}$. Measurements of $\overline{v'T'}$ and $\overline{v'T_0'}$ are very rare. In supersonic flow, these vertical velocity correlations are sometimes found from a balance of the mean enthalpy equations. The general levels seem to agree reasonably well with subsonic data, and the correlation coefficients for $\overline{u'v'}$ and $\overline{v'T'}$ are approximately the same.

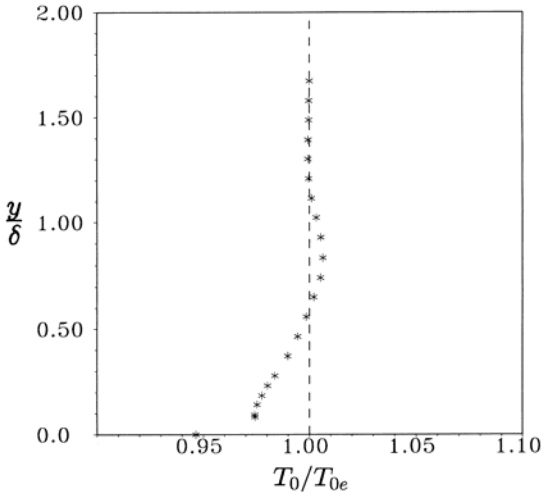

Figure 5.3. Total temperature distributions in an adiabatic boundary layer on a flat plate. Incoming Mach number is 2.3, Reynolds number $R_\theta = 5500$. (From Laurent (1996), with the author's permission.)

The measurements show remarkable agreement in conforming to the following relations:

$$\frac{\sqrt{\overline{T'^2}}}{\tilde{T}} = (\gamma - 1)\, M^2 \frac{\sqrt{\overline{u'^2}}}{\tilde{u}} \tag{5.5}$$

$$R_{uT} = \frac{-\overline{u'T'}}{\sqrt{\overline{u'^2}}\sqrt{\overline{T'^2}}} = \text{constant} \tag{5.6}$$

(see Figures 5.4 and 5.5). Equations 5.5 and 5.6 represent another form of the Strong Reynolds Analogy, and they are identical to Equations 3.4 and 3.5 when the pressure fluctuations are negligible, which is a good approximation in many supersonic shear layers (see, for example, Figure 4.1). The data indicate that $-R_{Tu} > 0.75$. In fact, a comparison of the instantaneous velocity and temperature fluctuations indicates the high degree of (anti-)correlation implied by this result (see Figure 5.6). The data shown in these figures were taken in turbulent boundary layers on isothermal walls, but measurements in free shear layers and mixing layers have confirmed the generality of these relationships.

Equations 5.5 and 5.6 are very close to what would be obtained from a small perturbation form of the one-dimensional energy equation under the assumption that the total temperature fluctuations are negligible. However, as the data given in Figure 5.7 show, this is not a good assumption: although the total temperature fluctuations are smaller than the temperature

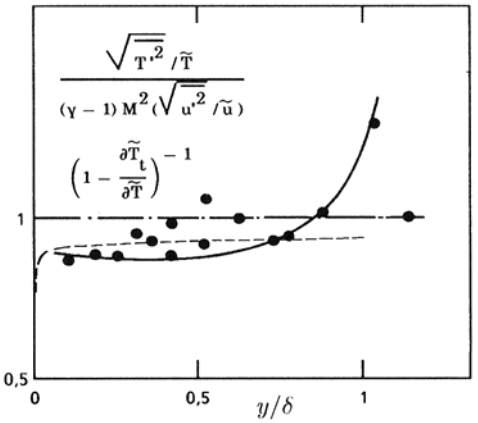

Figure 5.4. Test of the Strong Reynolds Analogy in a supersonic boundary layer ($M_e = 2.32$, $Re_\theta = 5650$). (From Gaviglio (1987). Copyright 1987, Elsevier Science Ltd., Oxford, England. Reprinted with permission. Original data from Debiève (1983).)

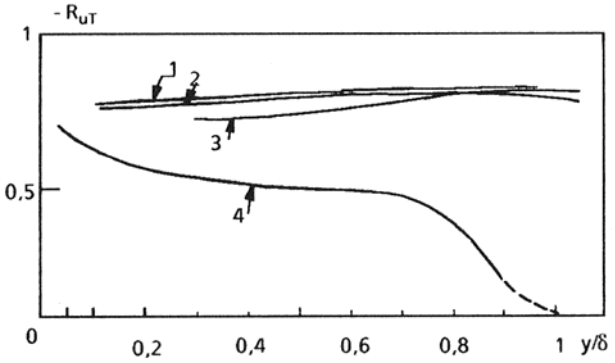

Figure 5.5. Distribution of R_{uT} in boundary layers. Curve 1: $M_e = 2.32$, $Re_\theta = 5650$, from Debiève (1983). Curves 2 and 3: $M_e = 1.73$, $Re_\theta = 5,700$, from Dussauge (1981). Curve 4: $M_e << 1$, $Re_\theta = 5,000$, from Fulachier (1972). (Figure from Eléna and Gaviglio (1993). Reprinted with permission of Éditions Dunod.)

fluctuations themselves, they cannot be considered negligible. In fact, we can use the one-dimensional energy equation to show that we expect $T_0' = \sqrt{2\,(1+R_{uT})}T'$ $(= 0.6T')$. This apparent contradiction is discussed in the next section.

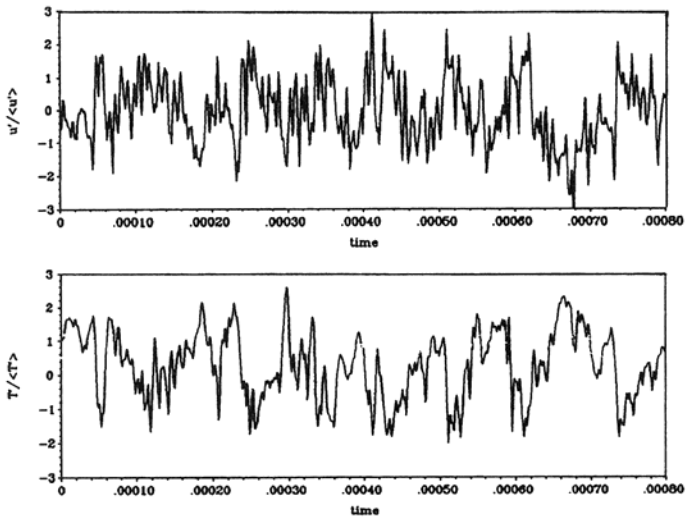

Figure 5.6. Instantaneous temperature and velocity signals in a Mach 2.9 boundary layer at $y/\delta = 0.6$, showing the high level of (negative) correlation. (From Smith and Smits (1993a). Copyright 1993, Elsevier Science Inc. Reprinted with permission.)

5.4 Analytical Results for $\mathbf{P_m = 1}$

We have seen that the molecular Prandtl number and the turbulent Prandtl number are not very different from unity, although we recognize that they are both somewhat less than one. As a first approximation, it is useful to consider flows where all Prandtl numbers are unity because it is possible in this case to obtain some simple analytical results using the boundary layer equations. We begin by defining an eddy viscosity μ_t and an eddy diffusivity k_t, where

$$\mu_t = \frac{-\bar{\rho}\widetilde{u'v'}}{\partial \tilde{u}/\partial y} \tag{5.7}$$

and

$$k_t = \frac{-C_p\bar{\rho}\widetilde{v'T'}}{\partial \tilde{T}\big/\partial y}, \tag{5.8}$$

so that we have a turbulent Prandtl number P_t:

$$P_t = \frac{\mu_t C_p}{k_t} = \frac{-\bar{\rho}\widetilde{u'v'}\left(\partial \tilde{T}\big/\partial y\right)}{-\bar{\rho}\widetilde{T'v'}\left(\partial \tilde{u}/\partial y\right)}, \tag{5.9}$$

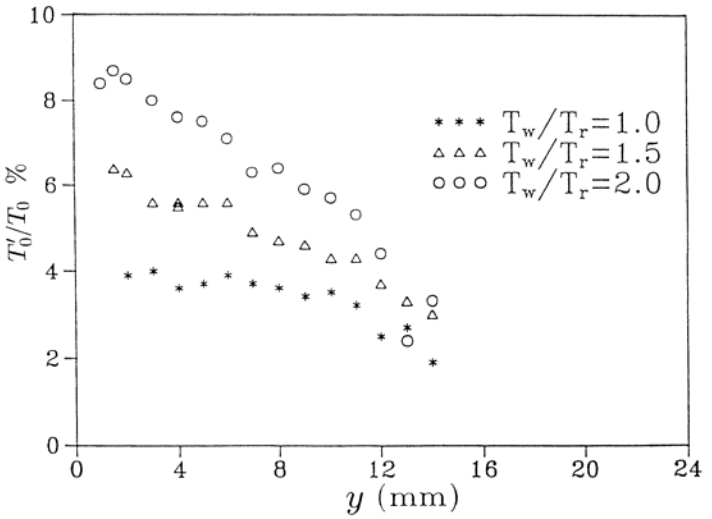

Figure 5.7. Total temperature fluctuation distributions in a boundary layer at Mach 2.3. The adiabatic case is given by $T_w/T_r = 1.0$. The other distributions were measured 48 initial boundary layer thicknesses downstream of a step change in wall temperature. (From Debiève et al. (1997), with the author's permission.)

and a mixed Prandtl number P_m:

$$P_m = \frac{(\mu + \mu_t)\, C_p}{k + k_t}. \tag{5.10}$$

The mixed Prandtl number allows a smooth transition from regions where molecular diffusion dominates to regions where turbulent mixing dominates. If we know P_m and the distributions of $\tilde{u}(y)$ and $\tilde{T}(y)$, the turbulent momentum and heat fluxes may be found (in this approach, the fluctuations in velocity and temperature only appear through their correlations, not through their intensities). For a zero pressure gradient flow, Equations 3.25 and 3.26 become:

$$\bar{\rho}\tilde{u}\frac{\partial \tilde{u}}{\partial x} + \bar{\rho}\tilde{v}\frac{\partial \tilde{u}}{\partial y} = \frac{\partial}{\partial y}\left\{(\mu + \mu_t)\frac{\partial \tilde{u}}{\partial y}\right\} \tag{5.11}$$

$$\bar{\rho}\tilde{u}\frac{\partial \tilde{h}_0}{\partial x} + \bar{\rho}\tilde{v}\frac{\partial \tilde{h}_0}{\partial y} = \frac{\partial}{\partial y}\left\{(\mu + \mu_t)\left[\frac{\partial \tilde{h}_0}{\partial y} + C_p\left(P_m^{-1} - 1\right)\frac{\partial \tilde{T}}{\partial y}\right]\right\}. \tag{5.12}$$

In the particular case where $P_m = 1$, the problem is the same as that studied by Busemann and Crocco for laminar boundary layers (Busemann, 1931; Crocco, 1932). Equations 5.11 and 5.12 become formally identical, and

if there exists a solution $\tilde{u}$ for Equation 5.11 then Equation 5.12 has a solution of the form:

$$\tilde{h}_0 = a\tilde{u} + b \qquad \text{and} \qquad h_0' = au'.$$

By applying the boundary conditions:

$$\begin{array}{llll} y = 0 & u = 0 & h_0 = h_{0w} & (T = T_w) \\ y = \delta & u = u_e & h_0 = h_{0e} & (T = T_e) \end{array}$$

this solution becomes:

$$\tilde{h}_0 = \left(\tilde{h}_{0e} - h_{0w}\right) \frac{\tilde{u}}{u_e} + h_{0w}.$$

That is,

$$\frac{\tilde{h}_0 - h_{0w}}{\tilde{h}_{0e} - h_{0w}} = \frac{\tilde{u}}{u_e}\,. \tag{5.13}$$

Finally:

$$\tilde{T} = \tilde{T}_w + \left(\tilde{T}_{0e} - \tilde{T}_w\right) \frac{\tilde{u}}{u_e} - \left(\tilde{T}_{0e} - \tilde{T}_e\right) \left(\frac{\tilde{u}}{u_e}\right)^2. \tag{5.14}$$

This solution is known as the Crocco relation, or Crocco's law.

For an adiabatic wall $\left(\partial\tilde{T}\big/\partial y\right)_{y=0} = 0$, and using the definition of the total enthalpy we have:

$$\frac{\partial\tilde{h}_0}{\partial y} = C_p \frac{\partial\tilde{T}}{\partial y} + \tilde{u}\frac{\partial\tilde{u}}{\partial y}.$$

At the wall, we see that $\partial\tilde{h}_0\big/\partial y = 0$, and from Equation 5.13 we obtain $\tilde{h}_{0e} = h_{0w}$ and $\tilde{h}_0 = \tilde{h}_{0w}$. As in the Couette flow example given in Section 2.5, the total enthalpy is constant when the Prandtl number (in this case the mixed Prandtl number) equals one.

Consider Equations 5.11 and 5.12 again. Under the condition that the total enthalpy flux $\widetilde{h_0'v'}$ is zero, or at least that $\overline{h_0'v'} \ll \overline{h'v'}$, the two equations become similar. Morkovin (1962) first suggested that this may be a reasonable approximation. If we neglect the differences between Reynolds averaging and Favre averaging, this assumption is equivalent to saying that the correlation between h_0' and v' is negligible throughout the layer. This criterion is satisfied when the total temperature fluctuations are negligible everywhere: this condition is sufficient but it is not necessary. Other solutions are possible, as demonstrated by the solutions obtained for Equation 5.12 for the case of $P_m = 1$.

It is always difficult to say anything rigorous regarding the instantaneous fluctuations using an argument based on mean quantities. The only firm conclusions that can be made are those regarding the quantities which were used to formulate the mixed Prandtl number, that is, the turbulent fluxes. In any

case, if we assume ${h_0}' = 0$, then the one-dimensional energy equation gives $T' = -u'\tilde{u}/C_p$, and:

$$\frac{\sqrt{\overline{T'^2}}}{\tilde{T}} = (\gamma - 1)\, M^2 \frac{\sqrt{\overline{u'^2}}}{\tilde{u}} = (\gamma - 1)\, M M_t \tag{5.15}$$

$$R_{uT} = \frac{\overline{u'T'}}{\sqrt{\overline{u'^2}}\sqrt{\overline{T'^2}}} = -1. \tag{5.16}$$

Also:

$$\widetilde{v'T'} = -\frac{\tilde{u}}{C_p}\widetilde{u'v'} \tag{5.17}$$

$$\frac{\widetilde{v'T'}}{\tilde{T}} = -(\gamma - 1)\, M^2 \frac{\widetilde{u'v'}}{\tilde{u}} \tag{5.18}$$

$$\widetilde{v'T_0'} = \widetilde{v'T'} + \frac{\tilde{u}}{C_p}\widetilde{u'v'} = 0. \tag{5.19}$$

These relations are collectively known as the Strong Reynolds Analogy (SRA) (see Young (1951), Morkovin (1962), and Gaviglio (1987)). The experimental results shown in Figures 5.4 and 5.5, obtained under conditions where the Prandtl numbers are not one and the total temperature fluctuations are not zero, closely follow the SRA. Interestingly, recent DNS results by Wu and Martin (2004), shown in Figure 5.8, demonstrate excellent agreement with experiment. These observations are discussed in more detail in the next section.

5.5 Analytical Results for $\mathbf{P_m \neq 1}$

When the mixed Prandtl number is not one, the energy equation cannot be analytically integrated precisely. However, van Driest (1951, 1956) and Walz (1966) considered approximate solutions for the case where the mixed Prandtl number is close to one, and this is the case for air where $P = 0.72$ and for most turbulent shear flows where $0.6 < P_t < 1$. These analyses are reviewed in detail by Fernholz and Finley (1980), and only the principal results are given here.

In particular, van Driest proposed a form of the enthalpy equation where the enthalpy is assumed to be a function of the velocity $\tilde{h} = h(\tilde{u})$, and most of the streamwise derivatives are neglected on the basis of an order-of-magnitude argument. Hence:

$$\tau\left(\frac{\partial}{\partial u}\left(\frac{1}{P_m}\frac{\partial \tilde{h}}{\partial \tilde{u}}\right) + 1\right) + \left(\frac{1 - P_m}{P_m}\right)\frac{\partial \tilde{h}}{\partial \tilde{u}}\frac{\partial \tau}{\partial \tilde{u}} = 0. \tag{5.20}$$

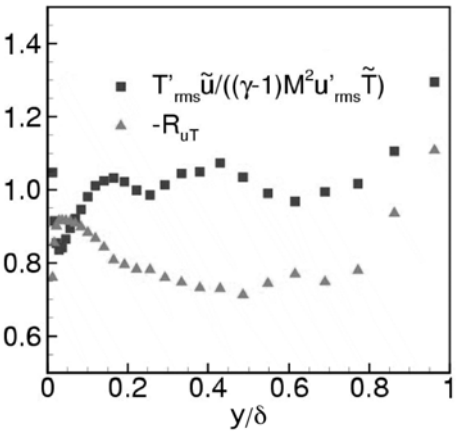

Figure 5.8. Results on the SRA from DNS of a boundary layer at Mach 2.9 with $Re_\theta = 2400$. (Figure from Wu and Martin (2004), with permission.)

When P_m is constant throughout the layer we obtain:

$$\frac{\partial}{\partial u}\frac{\partial \tilde{T}}{\partial \tilde{u}} + (1 - P_m)\frac{\partial \tilde{T}}{\partial \tilde{u}}\frac{1}{\tau}\frac{\partial \tau}{\partial \tilde{u}} = -\frac{P_m}{C_p} \tag{5.21}$$

and

$$\frac{\widetilde{u'v'}}{\widetilde{v'T'}}\frac{\partial \tilde{T}}{\partial \tilde{u}} = P_t = P_m. \tag{5.22}$$

In Equation 5.21, τ is the total stress (viscous plus turbulent). Equation 5.22 is identical to that found by applying the definition of the turbulent Prandtl number outside the viscous sublayer. The advantage of writing the enthalpy equation in this way is that Equation 5.21 can now be integrated to give:

$$\frac{\partial \tilde{T}}{\partial \tilde{u}} = -\frac{P_m}{C_p}\left(\frac{q_w}{\tau_w} + \int_0^u \left(\frac{\tau}{\tau_w}\right)^{1-P_m} du\right)\left(\frac{\tau}{\tau_w}\right)^{P_m - 1},$$

so that

$$\widetilde{v'T'} = \left[\frac{q_w}{\tau_w} + \int_0^u \left(\frac{\tau}{\tau_w}\right)^{1-P_m} du\right]\left(\frac{\tau}{\tau_w}\right)^{P_m-1}\left(\frac{-\widetilde{u'v'}}{C_p}\right), \tag{5.23}$$

where q_w and τ_w are the wall heat flux and the wall shear stress, respectively. This relation represents an extension of the SRA to flows where the Prandtl number is not unity. To derive this result it was necessary to assume that P_m was constant throughout the layer: this can be true near the wall only if the molecular Prandtl number is equal to the turbulent Prandtl number. This difficulty could be resolved by splitting the integration into two parts,

one over the region of the viscous sublayer, and one over the outer layer, and then matching the two solutions at the boundary between the two regions. The most complete approach would be to allow P_m to vary arbitrarily, but this would only complicate the form of the result without adding to our basic understanding.

For an adiabatic wall, $q_w = 0$, and we need to find a way to evaluate the integral:

$$I = \left(\frac{\tau}{\tau_w}\right)^{P_m - 1} \int_0^{\tilde{u}} \left(\frac{\tau}{\tau_w}\right)^{1-P_m} du. \tag{5.24}$$

By assuming a distribution of shear stress similar to that given by Sandborn (1974), and a fixed value of P_m (= 0.9), we obtain the result shown in Figure 5.9, where $A = I/u$ (this result should be independent of Mach number for nonhypersonic values). For $y/\delta < 0.5$, $1.0 < A < 1.05$, so the value of the integral is almost equal to the velocity itself. This is hardly surprising in that the variation of stress only enters the integral with an exponent equal to $1 - P_m$, which obviously weakens the influence of the stress variation.
Finally:

$$\widetilde{v'T'} = A\,(y)\,\frac{\tilde{u}}{C_p}\left(-\widetilde{u'v'}\right).$$

That is,

$$\frac{\widetilde{v'T'}}{\tilde{T}} = A\,(y)\,(\gamma - 1)\,M^2 \frac{-\widetilde{u'v'}}{\tilde{u}}. \tag{5.25}$$

So the earlier analysis, where it was assumed that $P_m = 1$ and that the total temperature fluctuations were negligible, led to a result which is in excellent agreement with this more realistic analysis, especially for $y/\delta < 0.5$. For the outer part of the layer, the approximations are less satisfactory because A continues to increase to a value of about 1.3, but in this region the magnitude of the fluxes diminishes and the errors introduced by the SRA also become significant. In this more general form, the temperature velocity relation is not very attractive from a modeling viewpoint because it involves the stress distribution and not just the velocity itself.

Equation 5.25 can also be used to deduce a relationship between the temperature and velocity fluctuation intensities. We can write

$$\frac{\sqrt{\overline{T'^2}}}{\tilde{T}} = \frac{-R_{uv}}{R_{Tv}} A\,(y)\,(\gamma - 1)\,M^2 \frac{\sqrt{\overline{u'^2}}}{\tilde{u}}, \tag{5.26}$$

where the correlation coefficient R_{Tv} is defined by $R_{vT} = \overline{v'T'} \Big/ \left(\sqrt{\overline{v'^2}}\sqrt{\overline{T'^2}}\right)$. Measurements of T' and u' indicate that the factor $(-R_{uv}/R_{Tv})\,A\,(y)$ takes about the same values as $A(y)$, and this is shown as the solid line in Figure 5.4. Hence we can infer that $0.9 < -R_{uv}/R_{Tv} < 1.1$ for almost the entire boundary layer thickness. The rather limited measurements of this ratio support this conclusion (Bestion et al., 1983; Horstman and Owen, 1972).

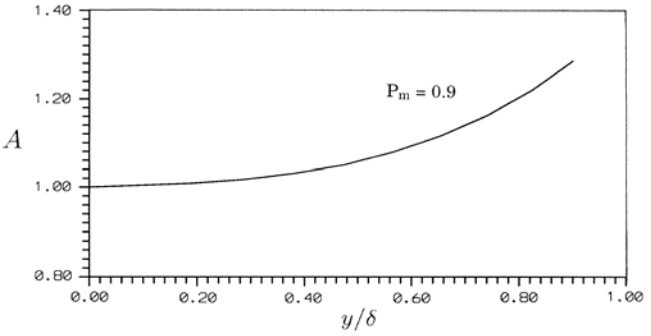

Figure 5.9. Stress integral distribution in a boundary layer. $A = I/u$, and I is given by Equation 5.24.

Gaviglio (1987) used a similar analysis to that given above, in that he used the derivative $\partial\tilde{T}/\partial\tilde{u}$ to establish a relationship between the velocity and temperature fluctuations, but in terms of the intensities rather than the fluxes. In order to do so, he used the length scales ℓ_u and ℓ_T defined by:

$$\ell_u = \frac{\sqrt{\overline{u'^2}}}{\partial\tilde{u}/\partial y} \qquad \text{and} \qquad \ell_T = \frac{\sqrt{\overline{T'^2}}}{\partial\tilde{T}\big/\partial y}$$

so that:

$$\frac{\sqrt{\overline{u'^2}}}{\sqrt{\overline{T'^2}}}\frac{\partial\tilde{T}}{\partial\tilde{u}} = \frac{\ell_u}{\ell_T}.$$

These scales are related to the mixing lengths for the momentum and heat fluxes (ℓ and ℓ_θ, respectively) according to:

$$\frac{\ell_u}{\ell_T} = \frac{\ell}{\ell_\theta}\frac{R_{vT}}{R_{uv}}.$$

Because $\ell/\ell_\theta = P_t$, we know that this ratio is approximately equal to 0.9. Experimental measurements of ℓ_u/ℓ_T indicate that this ratio takes about the same value in the outer part of the layer, which again suggests that the ratio R_{uv}/R_{Tv} is very nearly one. It seems reasonable, therefore, to adopt the form:

$$\frac{\sqrt{\overline{T'^2}}}{\tilde{T}} = A\,(y)\,(\gamma-1)\,M^2\frac{\sqrt{\overline{u'^2}}}{\tilde{u}} = A\,(y)\,(\gamma-1)\,MM_t. \tag{5.27}$$

These considerations can be used to derive modified versions of the earlier relationships where it was assumed that P_m was constant across the layer.

By means of some additional approximations for the values of the integrals appearing in the solution of Equation 5.21, Walz (1966) obtained:

$$\frac{\tilde{T}}{T_e} = \frac{\tilde{T}_w}{T_e} + \frac{\tilde{T}_r - \tilde{T}_w}{T_e}\left(\frac{\tilde{u}}{u_e}\right) - r\frac{\gamma-1}{2}M_e^2\left(\frac{\tilde{u}}{u_e}\right)^2, \tag{5.28}$$

where r is the recovery factor and T_r is the adiabatic wall temperature or recovery temperature. This relationship is called Walz's equation or the modified Crocco relation. It does not describe the overshoot in the total temperature profile observed in the region outside the boundary layer, but it describes the temperature-velocity relationship inside the layer very well, and it is used extensively.

It follows that:

$$\frac{dT}{du} = \frac{T_r - T_w}{u_e} - r\frac{u}{C_p}$$

so that:

$$\frac{\widetilde{v'T'}}{\tilde{T}} = \frac{-\widetilde{u'v'}}{\tilde{u}}\,\frac{(\gamma-1)\,M_e^2}{P_t}\left(r - \frac{C_p\left(\tilde{T}_r - \tilde{T}_w\right)}{u_e^2}\frac{\tilde{u}}{u_e}\right). \tag{5.29}$$

For an adiabatic wall:

$$\frac{\widetilde{v'T'}}{\tilde{T}} = \frac{-\widetilde{u'v'}}{\tilde{u}}\frac{r}{P_t}(\gamma-1)\,M^2. \tag{5.30}$$

Because $r \approx 0.89$ and $P_t \approx 0.9$, the coefficient in Equation 5.30 is nearly one, and we recover the result obtained by Cebeci and Smith (1974) for Crocco's integral. This coefficient is also close to the value of $A(y)$ for $y/\delta < 0.5$. In contrast, for $y\big/\delta > 0.5$, where the temperature-velocity relationship given by Equation 5.28 is not sufficiently accurate to give reasonable values of the derivatives, there is no such agreement with the value of $A(y)$.

In conclusion, it seems that the actual relationships between the turbulent heat and momentum fluxes are very close to those derived for the case where the total temperature fluctuations are negligible. Experimentally, however, we find that the total temperature fluctuations are not negligible, even in adiabatic flow. This is not a contradiction, but simply indicates that the equations of motion have solutions that do not depend strongly on the value of the mixed Prandtl number, as long as it is close to one, which is the case for adiabatic flows.

5.6 Reynolds Analogy for Mixing Layers

To close this chapter, we consider the Reynolds Analogy in mixing layers. Because molecular effects are negligible in this case, we have $P_t = P_m$. For the simple case of of $P_t = 1$, we still have

$$\tilde{h}_0 = a\tilde{u} + b \qquad \text{and} \qquad h_0' = au'$$

(see Section 5.4), but the boundary conditions have changed:

$$\begin{array}{ll} \tilde{u} = u_1 & \tilde{h}_0 = h_{01} \\ \tilde{u} = u_2 & \tilde{h}_0 = h_{02}. \end{array}$$

The derivation of the temperature-velocity relationship is straightforward:

$$T = \frac{u_1 T_{02} - u_2 T_{01}}{\Delta U} + \frac{\Delta T_0}{\Delta U} u - \frac{u^2}{2C_p}, \tag{5.31}$$

where ΔT_0 is the total temperature difference across the layer. Because P_t is unity, the ratio of the fluxes can be deduced from the derivative of temperature with respect to velocity. When $\Delta T_0 = 0$, the momentum flux and heat flux follow the SRA relationships given by Equations 5.15 and 5.16.

The case when $P_t \neq 1$ is more subtle because of the boundary conditions that apply to free shear flows. The results of Section 5.5 can be rewritten as

$$\overline{v'T'} = \frac{-\overline{u'v'}}{C_p} \left[\frac{C_p}{P_t} \left(\frac{\partial \tilde{T}}{\partial \tilde{u}} \right)_{\tilde{u}=\tilde{u}_0} + \int_{\tilde{u}_0}^{\tilde{u}} \left(\frac{\tau}{\tau_0} \right)^{1-P_m} du \right] \left(\frac{\tau}{\tau_0} \right)^{P_m - 1}, \tag{5.32}$$

where the reference velocity $\tilde{u}_0$ is the velocity at a point where the corresponding friction τ_0 is not zero. In practice, $\tilde{u}_0$ is taken to be the velocity at the point where the friction is maximum. The main difference from Equation 5.23 is that $\partial \tilde{T} \big/ \partial \tilde{u}$ is nonzero, even when the total temperature is the same in the two external flows.

Another point is that the turbulent Prandtl number is often smaller in free shear flows than in boundary layers, and therefore we can expect stronger departures from SRA relationships. However, because $\overline{v'T'} = \left(\overline{u'v'}/P_m \right) \partial \tilde{T} / \partial \tilde{u}$, Equation 5.32 can be rewritten as

$$\frac{\partial \tilde{T}}{\partial \tilde{u}} = \left[\left(\frac{\partial \tilde{T}}{\partial \tilde{u}} \right)_{\tilde{u}=\tilde{u}_0} - \frac{P_m}{C_p} \int_{\tilde{u}_0}^{\tilde{u}} \left(\frac{\tau}{\tau_0} \right)^{1-P_m} du \right] \left(\frac{\tau}{\tau_0} \right)^{P_m - 1}$$

This expression can be integrated once again to derive a relation between $\tilde{T}$ and $\tilde{u}$. As in boundary layer flows (see, for example, Fernholz and Finley (1980) or Walz (1959)), we obtain:

$$\tilde{T} = \tilde{T}_0 + \left(\frac{\partial \tilde{T}}{\partial \tilde{u}} \right)_{\tilde{u}=\tilde{u}_0} \int_{\tilde{u}_0}^{\tilde{u}} \left(\frac{\tau}{\tau_0} \right)^{P_m - 1} du - \frac{P_m}{C_p} \int_{\tilde{u}_0}^{\tilde{u}} \left[\int_{\tilde{u}_0}^{\tilde{u}} \left(\frac{\tau}{\tau_0} \right)^{1-P_m} du \right] \left(\frac{\tau}{\tau_0} \right)^{P_m - 1} du$$

To calculate the integrals, the relation $\tau = \tau(u)$ should be known. There remain two unknown coefficients, $\tilde{T}_0$ and $\left(\partial \tilde{T} \big/ \partial \tilde{u} \right)_{\tilde{u}=\tilde{u}_0}$, which are determined by the boundary conditions $\tilde{T} = \tilde{T}_1$ for $\tilde{u} = \tilde{u}_1$, and $\tilde{T} = \tilde{T}_2$ for $\tilde{u} = \tilde{u}_2$.

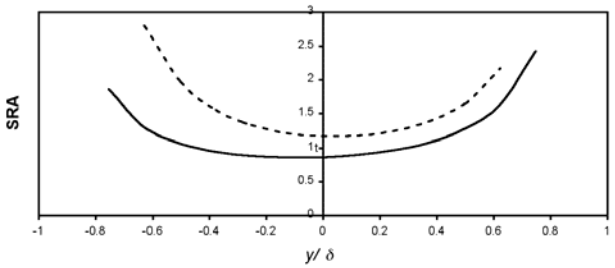

Figure 5.10. The Reynolds analogy for mixing layers. Ratio of heat and momentum fluxes computed from similarity considerations. Solid line: $P_t = 0.8$; dashed line: $P_t = 0.6$.

Because the gradient $\left(\partial\tilde{T}/\partial\tilde{u}\right)_{\tilde{u}=\tilde{u}_0}$ is known, its value may be inserted into Equation 5.32, thereby resolving the difficulty introduced by the nonzero heat transfer at the origin of integration.

It is now possible to discuss the validity of the SRA relationship in mixing layers. It is assumed that the turbulent (or mixed) Prandtl number is constant, and that an appropriate choice for a simple turbulence model in free shear flows is an eddy viscosity assumption. The distribution of $\tilde{u}$ is required. For illustration, we assume that the nondimensional velocity $(\tilde{u} - U_{av})/\Delta U$, where $U_{av} = (u_1 + u_2)/2$, is represented by a cubic. The corresponding distribution for the stress is $\tau/\tau_0 = (1 + y/\delta)(1 - y/\delta)$ inside the layer, a very simple representation that is believed to have only weak consequences on the functional dependence of $\tilde{u}$ on $\tilde{T}$. Under these assumptions, the following relation is obtained,

$$\tilde{T} = \tilde{T}_0 + \left(\frac{\partial\tilde{T}}{\partial\tilde{u}}\right)_{\tilde{u}=\tilde{u}_0} U^* - \frac{P_m}{C_p} U^{**} \tag{5.33}$$

with

$$U^* = \frac{3}{4}\Delta U \int_0^{y/\delta} \left(\frac{\tau}{\tau_0}\right)^{P_m} d\left(\frac{y}{\delta}\right)$$

and

$$U^{**} = \frac{9}{16}(\Delta U)^2 \int_0^{y/\delta} \left[\int_0^{y/\delta} \left(\frac{\tau}{\tau_0}\right)^{2-P_m} d\left(\frac{y}{\delta}\right)\right] \left(\frac{\tau}{\tau_0}\right)^{P_m} d\left(\frac{y}{\delta}\right).$$

We consider the specific mixing layer studied by Barre et al. (1994), Menaa et al. (1996), and Debiève et al. (2000), under approximately the same flow conditions ($M_1 = 1.89$, $M_2 = 0.29$, and $T_{01} \approx T_{02} \approx 300$°K), with a turbulent Prandtl number of about 0.8. This work provides probably the only experimental results on Reynolds Analogy in mixing layers.

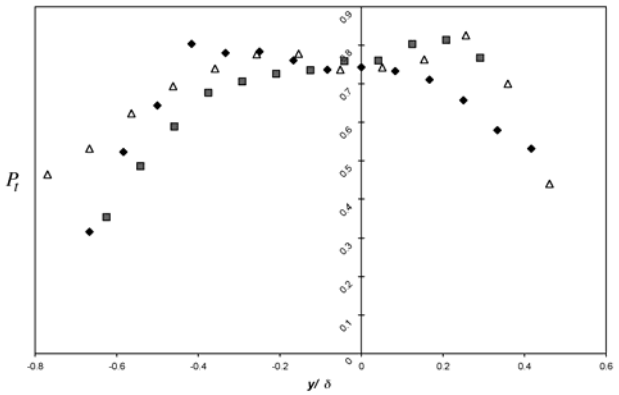

Figure 5.11. Experimental distribution of turbulent Prandtl number in a self-similar mixing layer ($M_c = 0.62$, $M_1 = 1.85$, $M_2 = 0.36$, and $T_{01} \approx T_{02} \approx 300°$K). $\triangle$, $x = 200$ mm; $\square$, $x = 220$ mm; $\diamond$, $x = 240$ mm.

The total temperature distribution derived from Equation 5.33 for this mixing layer is almost constant, with a maximum defect in total temperature of 6%. The measurements show that the total temperature deviates from the external values by 4%. Figure 5.10 shows the ratio $\overline{v'T'}C_p/\left(\overline{u'v'}\tilde{u}\right)$ in a section (denoted SRA in the figure), for two values of the turbulent Prandtl number. It appears that this ratio remains close to unity across most of the flow, and increases near the edges of the layer because the stress goes to zero. For $P_t = 0.6$, the same overall behavior is found with generally higher values, although in the center of the layer the ratio is about 1.1.

Friction and heat fluxes were determined from momentum and total enthalpy budgets. The results for the self-similar part of the mixing layer are given in Figures 5.11 and 5.12.

In this flow, the turbulent Prandtl number is about 0.8 in the center of the layer and is almost constant across the flow except near the boundaries. The ratio of heat and momentum fluxes, shown in Figure 5.12, is close to unity: departures from this value on the centerline are only a few percent, and the profile, which has the shape expected from the previous calculations, is essentially constant in the center of the layer. This agrees well with the measurements of $\overline{u'^2}$ and $\overline{T'^2}$ by Barre et al. (1994), which led to similar conclusions, in spite of greater scatter in the results.

To conclude, it is clear that in mixing layers, despite possibly having smaller values of the Prandtl number, the Reynolds Analogy remains a very robust approximation, which can be used with some confidence for estimating the mean total enthalpy and the ratio of momentum and heat fluxes.

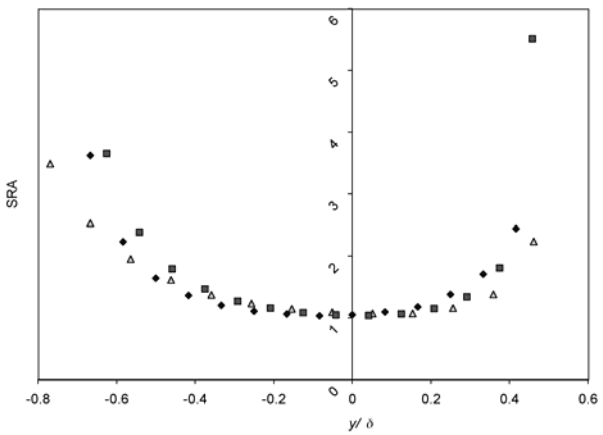

Figure 5.12. The Reynolds analogy for mixing layers. Experimental values for the ratio of heat and momentum fluxes. SRA $= \overline{v'T'}C_p / \left(\overline{u'v'}\tilde{u}\right)$. (Symbols as in Figure 5.11.)

Chapter 6

Mixing Layers

6.1 Introduction

The mixing layer is an example of a inhomogeneous flow that is particularly simple because it is formed by two parallel flows with different velocities, and there is no wall present. It can be considered as an archetype for the development of compressible turbulence in free shear flows at high speeds, such as the shear layer that develops when a boundary layer separates. The interface between the two streams contains an inflection point in the velocity profile, and it is therefore inviscidly unstable. Eddies are formed typical of a Kelvin-Helmholtz-type instability. In subsonic flows the eddies grow rather quickly, and as a result the properties of the two streams mix very efficiently. The Reynolds number of the flow also increases rapidly because, as we show, all the length scales grow linearly with distance (at least for locations far from the origin of the layer). If the velocity difference between the two sides of the layer remains constant, as it is in a zero pressure gradient flow, a rather strong velocity gradient is maintained which leads to high-intensity turbulence levels. Mixing layers are therefore very suitable for studying the properties of compressible turbulence far from the influence of walls, at large Reynolds numbers.

Compressibility effects are important in mixing layers even at moderate Mach numbers, so that the phenomena observed in mixing layers at relatively low Mach numbers can bring some insight into what can be found in boundary layers at much higher Mach numbers. But our experiences do not carry over directly. The absence of a wall means that the scaling for mixing layers is much simpler than for boundary layers: there is only one length scale instead of two. In boundary layers, the wall imposes low Reynolds number features near the wall that must match the high Reynolds number features developing in the outer part of the layer, and turbulence models in their present state are probably not general enough to compute both mixing layers and boundary layers without some fine tuning. Nevertheless, the study of free shear flows can help us to understand the behavior of other inhomogeneous compressible

turbulent flows.

For free shear layers at low speeds, the development of periodic perturbations, the stability and transition process, the effects of variable density, and the effects of initial and boundary conditions have all been studied extensively. The results can be found in a number of recent review articles (see, for example Ho and Huerre (1984) and Dimotakis (1994)). Here, we simply note some properties of subsonic mixing layers, and show how they are connected with the phenomena observed in high-speed mixing layers. First, we consider asymptotic, self-similar mixing layers. In practice, it is very difficult to observe such flows experimentally in the absence of some undesirable perturbations: mixing layers are very sensitive to initial and boundary conditions, and their development can be modified by the presence of acoustic perturbations and state of the initial boundary layers. Acoustic phenomena, for example, may produce phase changes between the energetic eddies by modifying the roll-up process and alter the gross properties of the flow significantly. Bell and Mehta (1990) have demonstrated the almost exquisite sensitivity of the near-field behavior to changes in the inflow conditions, and as a result there can be an order-of-magnitude difference in the initial growth rate among different experiments. Boundary conditions are also difficult to control, particularly when pressure waves reflect off wind tunnel walls and interfere with the mixing layer development. These difficulties make comparisons with computations problematic, partly because the computations are sensitive to similar limitations. For example, an initial disturbance must be specified to trigger the roll-up of the mixing layer, and nonreflective boundary conditions must be used. In addition, direct numerical simulations are currently restricted to Reynolds numbers that are usually much lower than the experiments. Reynolds number effects are expected to be small, at least for fully turbulent flows, but they may not be negligible if the Reynolds number is very low.

As a result of these experimental difficulties, measurements of the spreading rate in low-speed, variable density mixing layers show a scatter of about 25% (Dimotakis, 1991), and therefore we can only draw conclusions on the behavior of these flows if the effects are found to be large enough. To understand the flow behavior more precisely, experimental studies should specify inflow, outflow, and boundary conditions. This is rarely done in experimental work, perhaps because this is a particularly difficult task, and therefore care should be taken when interpreting the results. The scatter in the data also limits the accuracy that we can expect from engineering calculation methods. Turbulence models are often little more than interpolation methods based on experimental data. If the scatter on macroscopic quantities is about 25%, it cannot be expected that the accuracy of predictions will be better than 25%.

Here we consider the global characteristics of mixing layers as a function of Mach and Reynolds number. The Favre averaged equations of motion for this case were derived in Chapter 3 by applying the usual thin shear layer

approximations to the continuity, Navier-Stokes, and energy equations (see Equations 3.24 through 3.26). As an introduction to the scaling behavior of compressible turbulent boundary layers, we first examine the incompressible, uniform-density case.

6.2 Incompressible Mixing Layer Scaling

In a boundary layer, the viscous stress gradients cannot be neglected because the viscous stress terms are necessary to enforce the no-slip boundary condition, and therefore there is always a region near the wall where viscous stresses are important. In a mixing layer there is no wall, and as the Reynolds number Re_δ increases, the magnitude of the viscous stresses relative to the other terms in the momentum equation decreases. Here Re_δ is based on some measure of the thickness of the layer δ, and a velocity scale such as the velocity difference across the layer $\Delta U = U_1 - U_2$ (by convention, U_1 is the velocity on the high-speed side, and U_2 is the velocity on the low-speed side), or $U_1 - U_c$, where U_c is the convection velocity of the large eddies. As we show, the Reynolds number increases rapidly with streamwise distance. In the high Reynolds number limit (that is, far from the origin of the layer), the viscous stresses are negligible and the incompressible mixing layer equations reduce to:

$$\frac{\partial u}{\partial x} + \frac{\partial v}{\partial y} = 0 \tag{6.1}$$

$$u\frac{\partial u}{\partial x} + v\frac{\partial u}{\partial y} = \frac{\partial\left(-\overline{u'v'}\right)}{\partial y}. \tag{6.2}$$

In a self-preserving flow, all parameters scale with local length and velocity scales. For the mixing layer the length scale is δ, although we have not discussed its exact definition. Because the mean velocity and the turbulence must scale in the same way to achieve self-preservation, there can only be one velocity scale (ΔU). In zero pressure gradient, single-stream mixing layers, where ΔU is constant and the velocity on the low-speed side U_2 is zero,

$$u = \Delta U f(\xi), \tag{6.3}$$

$$v = -\int_0^y \frac{\partial u}{\partial x} dy = \Delta U \int_0^\xi \left(\frac{d\delta}{dx}\right) \xi f' d\xi, \tag{6.4}$$

so that

$$v = \Delta U g(\xi), \tag{6.5}$$

and

$$-\overline{u'v'} = (\Delta U)^2 h(\xi), \tag{6.6}$$

where $\xi = y/\delta$ and $\delta = \delta(x)$ (for further details see Tennekes and Lumley (1972) and Lesieur (1987)). Hence,

$$-\frac{d\delta}{dx} f' \int_0^\xi f d\xi = h'. \tag{6.7}$$

Self-preservation can only be obtained if $d\delta/dx =$ constant; that is, the thickness of the layer increases linearly with x, as anticipated earlier (we show in Section 6.7 that this also holds for compressible mixing layers). In addition, if the spreading rate and the mean velocity profile are known, the shear stress can be found by integrating the mean momentum equation.

From Equation 6.6, we see that the nondimensional shear stress distribution in a self-preserving flow has a similarity solution $h(\xi)$, and therefore $u_\tau/\Delta U$ takes a constant value, where $u_\tau = \max\left(\sqrt{-\overline{u'v'}}\right)$. Because all velocity scales must be proportional to each other in a self-preserving flow, this result is self-evident. Similarly, all length scales must be proportional to each other in a self-preserving flow. As an example, if we assume a mixing length hypothesis (Equation 7.28), then

$$\frac{d\ell}{dx}\left(\frac{\ell^2}{2\ell_m^2}\right) \int_0^\xi f d\xi = f'', \tag{6.8}$$

which shows that the mixing length must be proportional to the width of the layer.

The final equation depends on the model used for the turbulent stress. For these simple calculations, a mixing length or an eddy viscosity is commonly used. The eddy viscosity assumption leads to a Falkner-Skan equation that can be solved numerically with standard methods, and the computed profiles generally match the experimental ones well. In particular, they exhibit the same asymmetric shape observed in the experiments. Some experimental results for two-stream mixing layers are shown in Figure 6.1.

Historically, such numerical approaches could not be taken, so that approximate solutions were developed. Although they lead to analytical solutions, or to procedures that can be carried out by hand, they necessitate an oversimplification of the equations. The resulting velocity profiles are symmetric, contradicting the experimental observations, primarily because the inertia terms in the approximate solution are poorly represented. Nevertheless, these symmetric solutions are still often used as reference profiles, especially in stability problems where it is convenient to have the profiles in an analytical form. One of the most commonly used approximations was proposed by Görtler, who found that it is given approximately by an error function (see Schlichting (1979)). That is,

$$\frac{u}{\Delta U} = \frac{U_{av}}{\Delta U}\left(1 + \frac{\Delta U}{U_{av}} \operatorname{erf}\xi\right), \tag{6.9}$$

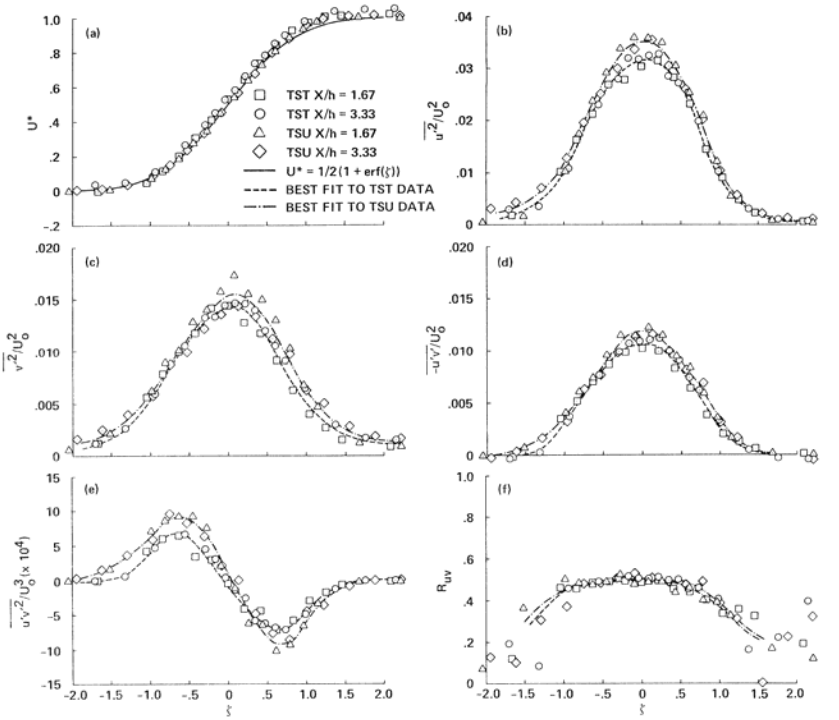

Figure 6.1. Characteristics of subsonic mixing layers. U_0 is the velocity difference across the layer ($= \Delta U$), $U^* = (u - U_1)/\Delta U$, and $\xi = (y - y_0)/\delta_{10}$. TST and TSU stand for *two-stream layer, tripped* and *single-stream layer, not tripped*, respectively. (From Mehta and Westphal (1984). Copyright 1984, AIAA. Reprinted with permission.)

where $U_{av} = (U_1 - U_2)/2$ is the average velocity and $\Delta U = U_1 - U_2$.

To return to the question of a length scale, there exist many possible definitions of the layer thickness. Two of the most common are δ_{10}, the 10% thickness, defined as the distance between the points where the velocity is equal to $U_1 - 0.1\Delta U$ and $U_2 + 0.1\Delta U$, and δ_ω, the vorticity thickness, defined to be the distance given by the ratio of the velocity difference across the layer divided by the maximum slope of the velocity profile ($\delta_\omega = \max(\Delta U/(\partial u/\partial y))$). For an error-function velocity profile, Goebel and Dutton (1990) showed that $\delta_\omega = 1.02\delta_{10}$. A less common definition of the thickness is the Stanford thickness, defined by the distance between the points where the velocity is $U_2 + \sqrt{0.9}\Delta U$ and $U_1 - \sqrt{0.1}\Delta U$.

6.3 Compressible Mixing Layers

In spite of our reservations about the quality of the data, the experiments indicate that low-speed and high-speed mixing layers share some common features. For example, they all grow linearly with distance (as long as we are far enough downstream for the effects of the initial conditions to have become negligible), and large-scale structures are formed with rather high turbulence intensities. However, as indicated in Chapter 1, very significant differences have also been observed. Brown and Roshko (1974) compared their observations of subsonic mixing layers with different density ratios to the properties of supersonic mixing layers with the same density ratios. They found that, in contrast to many of our observations on boundary layers, the behavior of supersonic mixing layers could not be described by simple considerations based on density variations alone, especially with regard to the spreading rate. One obvious question is to what extent the properties of supersonic mixing layers can be described by the effects of variable fluid properties, and at what point changes in the nature of the turbulent perturbations due to compressibility become important. For subsonic mixing layers with zero velocity on the low-speed side (a *single-sided* mixing layer or *half-jet*), Figure 6.2 shows that changing the density ratio $s = \rho_2/\rho_1$ by a factor of 7 changes the growth rate by about 30%. These results may be compared with the behavior of single-sided mixing layers where the high-speed side is supersonic. The abscissa in Figure 6.2 can be read as a density ratio or the equivalent Mach number for a compressible half-jet. It is clear that as soon as the Mach number of a half-jet becomes supersonic, the spreading rate is reduced, and the reduction is much more severe than that based on the density ratio alone. Because the spreading rate and turbulence level are proportional to each other (see below), this macroscopic result on the spreading rate can be considered as the first indication of an important change in the structure of turbulence due to compressibility.

Such results could also have been expected from other studies. In considering the linear stability of a vortex sheet, or of mixing layers of finite size, it is well known that an increasing Mach number has a stabilizing effect (Miles, 1958). The amplification of the fluctuations is reduced, which is consistent with reduced mixing and a smaller spreading rate. It is far from obvious, however, that a linear stability analysis can help to explain the global features of turbulent shear flows, but in free shear flows it seems that the large-scale structures have some qualitative properties which can be described by linear theory, even after nonlinear phenomena such as vortex pairing have occurred. For example, Lele (1994) successfully correlated the maximum linear amplification rate of mixing layers with their spreading rate. This suggests that the growth of large eddies in mixing layers depends significantly on linear mechanisms, even in the turbulent case where nonlinear phenomena are obviously well developed. The similarities may not be sufficient for reliable quantitative

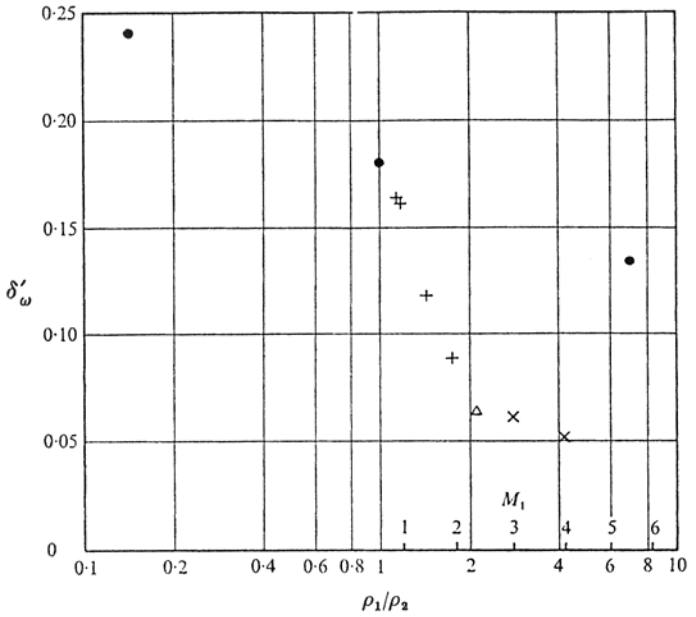

Figure 6.2. Comparison of the spreading rate based on vorticity thickness of mixing layers in subsonic flow with variable density, with mixing layers in supersonic flow. Subsonic flow results: ○, Brown and Roshko (1974). Supersonic flow results: +, Maydew and Reed (1963); △, Ikawa (1973); ×, Sirieix and Solignac (1968). (From Brown and Roshko (1974). Copyright 1974, Cambridge University Press. Reprinted with permission.)

results, but they are useful for understanding how the structures evolve and control mixing as the convective Mach number increases.

Most of these linear theories predict that under some conditions pressure can be radiated away from the layer into the outer flow by Mach waves. It is possible to use a simple example to show how this can happen. Consider a simple vortex sheet formed by the interface between two parallel flows. More precisely, consider the evolution of a sinusoidal perturbation of the interface, and the induced pressure disturbances. For small perturbations, the problem is linear. If the flow is subsonic relative to the interface, the pressure perturbations tend to increase the amplitude of the wavy interface and the flow is unstable (the classic Kelvin-Helmholtz instability). However, if the flow is supersonic, the pressure perturbations act in opposite directions on the leading and trailing edges of the wave so that they cancel out and the flow is marginally stable (Miles, 1958; Papmoschou and Roshko, 1988). It can be shown that the natural parameter appearing in this problem is a Mach num-

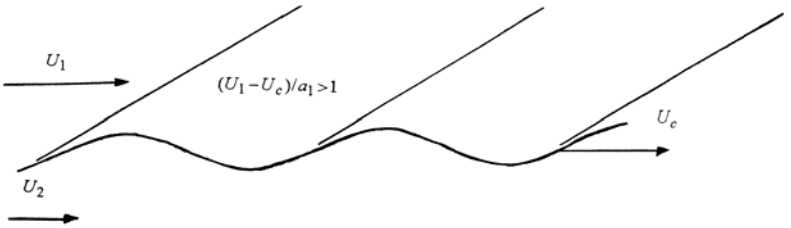

Figure 6.3. Flow over a wavy interface. The motion of the interface is is supersonic with respect to flow 1, and Mach waves are radiated into flow 1.

ber based on the phase velocity of the perturbation. This can be exemplified as follows. We consider the perturbations produced in the external flow by two-dimensional corrugations of the vortex sheet considered as an interface, as sketched in Figure 6.3. The external flows are potential, uniform, and the inviscid approximation will be made: such an assumption is valid for perturbations of large scale (large Reynolds number) for which the effect of viscosity is small. Perturbations can therefore be considered as isentropic, thus the relationship between pressure and density fluctuations is:

$$p' = a^2 \rho'$$

and the equations are the Euler equations. In our example, the perturbations are supposed to be small, so that it is relevant to use linearized equations. Moreover, instead of computing velocity, we consider the displacement field defined by

$$\frac{d}{dt}\vec{\xi} = \vec{u}',$$

where $\vec{u}'$ is the velocity fluctuation. We will write the equations in flow 1 and in flow 2, indicated by the superscripts 1 or 2.

We look for the temporal evolution of a displacement periodic along the x-direction, with amplitude variations according to y. Therefore $\vec{\xi}$ is of the form:

$$\vec{\xi} = \xi_j(y) e^{i(kx-\omega t)}$$

with $j = 1, 2$, k real, and ω complex.

After a straightforward but tedious calculation, equations for the amplitudes ξ_j can be found in flows 1 and 2. For example, the equation for ξ_2 is:

$$\xi_2'' + k^2 \left[\left(\frac{U^{[1]} - \omega/k}{a^{[1]}} \right)^2 - 1 \right] \xi_2 = 0,$$

where the primes denote differentiation with respect to y. A similar equation is found in flow 2, in which the superscript [2] replaces [1]. An interesting

point can be found in the expression in brackets. Firstly, we can recognize that $\omega/k = c$ is the classical phase velocity: its real part is the speed at which the considered perturbation propagates along the interface. The ratio $M_c^{[1]} = \left(U^{[1]} - c\right)/a^{[1]}$ is of course a Mach number. It is based on the velocity difference between the external flow and the phase speed. When this Mach number is smaller than 1, the relative motion between the interface and the external flow is subsonic, and the equation indicates that ξ_2 experiences an exponential decay with respect to y. If the Mach number is larger than unity, ξ_2 has now a periodic distribution in y. Analysis of the solution shows that this corresponds to Mach waves radiated by the interface, without damping in the present formulation, so that perturbations are felt over much larger distances than in the subsonic case. This suggests that in the supersonic case, much more energy is required to transmit the information on the presence of the wavy perturbation.

Therefore, the Mach number, which appears naturally in this problem, is the indicator of compressibility effects in the response of the external flow to the perturbation induced by a wavy vortex sheet, in the limit of the linearized problem. It can be imagined, that in some cases, compressibility effects are felt only by one flow, and not by the second one, so that $M_c^{[1]}$ and $M_c^{[2]}$ may differ significantly. However, without further indication, it is natural to preserve the symmetry of the problem, and to assume that compressibility effects are the same on both sides of the vortex sheet. In this symmetrical case, the Mach numbers defined for each of the external flows are equal:

$$M_c^{[1]} = M_c^{[2]} \quad \text{or} \quad \frac{U^{[1]} - c}{a^{[1]}} = \frac{c - U^{[2]}}{a^{[2]}}.$$

This gives the expression of the symmetrical phase speed:

$$c = \frac{a^{[1]}U^{[2]} + a^{[2]}U^{[1]}}{a^{[1]} + a^{[2]}}.$$

Inserting this value into the previous relations gives:

$$M_c^{[1]} = M_c^{[2]} = M_c = \frac{U_1 - U_2}{a_1 + a_2}.$$

Other properties of such a velocity are given in the next section.

Radiation of Mach waves was also found in direct numerical simulations of two-dimensional mixing layers. It appears that shocklets are produced by the eddies when the convection velocity of the eddies becomes supersonic with respect to the external flow (Lele, 1989). It has been more difficult to find these shocklets in three-dimensional simulations. In experiments, they are also difficult to find, although they can be seen in the visualizations of pulsed supersonic jets by Oertel (1983), in a shear layer between two supersonic counterflows by Papamoschou (1995), in a reattaching shear layer by Poggie (1995), and in

high Mach number shear layers by Rossmann et al. (2002) (see Figure 10.13). Because the net effect of compressibility on supersonic mixing layers can only be explained partly by variable fluid properties, this interpretation helps to show that the effects of compressibility are related to changes in the structure of the flow. It may represent the onset of compressibility effects, because it could well be true that the turbulence contained within the eddies has properties similar to incompressible turbulence, but the eddies themselves produce small shock waves in the outer flows.

Can such Mach or shock waves alter the properties of turbulent shear flows? Their influence can be direct or indirect. The possible sources of direct influence can be listed briefly. Shock waves and shocklets constitute a new source of energy dissipation in fluctuating motions in which $\nabla \cdot \mathbf{u}' \neq 0$. In air, weak shock waves with small entropy steps, close to Mach waves, can still dissipate energy: inside the wave, there is an overshoot of entropy due to dissipation which is imperfectly balanced by heat conduction (see, for example, Landau and Lifshitz (1987)). As discussed in Section 4.7, another element is the pressure divergence correlation term in the equation for k. This term takes a nonzero value as the flow passes through a shock wave, and it can constitute an additional source or sink term for compressible turbulence. Finally, the pressure divergence term in the equation for k is the trace of the pressure strain terms in the equation for the Reynolds stresses. For incompressible turbulence, where the fluctuating field is solenoidal ($\nabla \cdot \mathbf{u}' = 0$), these terms redistribute the energy among the components of the velocity fluctuations. If the fluctuating field is compressible, we may expect that the anisotropy of the turbulent stresses will be modified. Most of the primary work on compressible turbulence modeling considered these direct effects (see Zeman (1990) or Sarkar et al. (1989) among others). Although these effects certainly exist at very high Mach numbers, they appear to be negligible in the supersonic regime, even in mixing layers. The indirect effect is more subtle and is related to modifications of the structure of pressure inside the shear flow itself. For mixing layers, such modifications of fluctuating pressure can happen in the same range of Mach numbers as for the Mach wave radiation. These different points are discussed in more detail in Section 6.10, but first a classification of the effects of compressibility on the turbulence is necessary, together with a description of the available experimental evidence.

6.4 Classification of Compressibility Effects

6.4.1 Convective Mach Number

As indicated in Chapter 1, only relative motions are important. Therefore the Mach number used to characterize compressibility effects must be based on the difference between the convective speed of the large eddies and the velocities

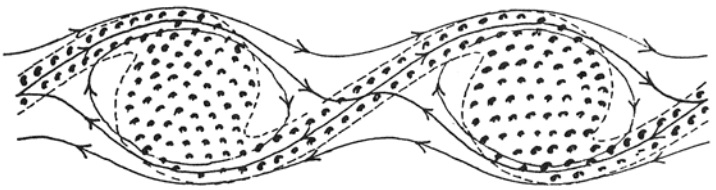

Figure 6.4. Sketch of the flow in a subsonic, two-dimensional, periodic mixing layer with variable density. The solid lines are instantaneous streamlines; the vorticity is concentrated in the shaded area. Note the strain field in the center of the picture. (From Corcos and Sherman (1976). Copyright 1976, Cambridge University Press. Reprinted with permission.)

of the external flows, although it was shown in Chapter 4 that the turbulence and convective Mach numbers are of the same order. If we are to choose M_c in preference to M_t, we need to be sure that it is possible to define a convection velocity, and that the flow is not strongly dispersive. All the scales are then convected at approximately the same speed, and consequently there is no change in the shape of the eddies. This is in direct contradiction to experimental observations that indicate the important role played by vortex pairing (Winant and Browand, 1974). However, measurements in low-speed flows suggest that this can still provide a reasonable description of the large-scale structures between pairing events (Brown and Roshko, 1974). We therefore consider the case of piecewise nondispersive events, that is, the behavior that occurs between two pairings. Because the convection velocity is constant, a frame of reference moving with the eddies is used. For two-dimensional flows it is assumed that a stagnation point occurs between two vortices (see Figure 6.4). If the location of the stagnation point is fixed with respect to the eddies, then the pressure there must be continuous. Furthermore, if the conditions along the streamlines arriving at the stagnation point from the external flows are isentropic, a relation for the convection velocity can be found that gives a single unique value. Because the total pressure is defined with respect to a moving frame of reference, the natural parameters appearing in the equation are convective Mach numbers based on the velocity differences $U_1 - U_c$ and $U_c - U_2$, and the sound speeds a_1 and a_2, not the convection velocity itself (for details, see Bogdanoff (1983), Papamoschou (1986), and Papamoschou and Roshko 1988)). That is,

$$\left(1 + \frac{\gamma_1 - 1}{2} M_{c1}^2\right)^{\gamma_1/(\gamma_1 - 1)} = \left(1 + \frac{\gamma_2 - 1}{2} M_{c2}^2\right)^{\gamma_2/(\gamma_2 - 1)} \tag{6.10}$$

with $M_{c1} = (U_1 - U_c)/a_1$ and $M_{c2} = (U_c - U_2)/a_2$. The low Mach number

limit of Equation 6.10 is

$$M_{c1} = \left(\frac{\gamma_1}{\gamma_2}\right)^{1/2} M_{c2},$$

which gives for $\gamma_1 = \gamma_2$ the low-speed, variable-density value of the convection velocity:

$$\frac{U_c}{U_1} = \frac{1 + (U_2/U_1)\sqrt{s}}{1 + \sqrt{s}}, \tag{6.11}$$

where the density ratio $s = \rho_2/\rho_1$.

In the absence of shock waves, the evolution along the streamlines can be considered isentropic if the time of flight from the external flows to the stagnation point is small compared to the turnover time of the energetic eddies. The only source of entropy is then the viscous dissipation, which is small if the time of flight is short. The time of flight is of the order of $\delta/\Delta U$ and the time scale of turbulence is k/ε or $\Lambda/\sqrt{k}$, where Λ is a characteristic length scale such as an integral scale. For the isentropic assumption to hold, therefore, we require:

$$\frac{\sqrt{k}}{\Delta U}\frac{\delta}{\Lambda} \ll 1,$$

where Λ/δ is $O(1)$. In mixing layers, $\sqrt{k}/\Delta U$ is less than 0.2 in the subsonic regime and probably less than 0.1 in the supersonic regime, so that the proposed approximation seems reasonable (in the absence of shock waves).

In the general case, where $\gamma_1 \neq \gamma_2$ and $s \neq 1$, the two convective Mach numbers are different, and an asymmetric behavior may be expected with compressibility effects occurring more on one side than on the other. If the two external flows have the same γ, simpler relationships may be found. In particular, if the evolution is also isentropic, $M_{c1} = M_{c2} = M_c$, and:

$$M_c = \frac{\Delta U}{a_1 + a_2}, \tag{6.12}$$

and

$$U_c = \frac{a_2 U_1 + a_1 U_2}{a_1 + a_2}. \tag{6.13}$$

Similar expressions were derived in Section 6.3 for the problem of the wavy interface, with symmetric compressibility effects. The result is an indicator of a change of the structure of the pressure field, at least in the outer flow. It can be also understood as the footprint of isentropic external flows, and therefore as a hint of the presence of shock waves radiated by the eddies.

Although these arguments were made with respect to two-dimensional flows, the conclusions are valid for three-dimensional flows because it is only necessary to have a stagnation point. U_c is then the speed of the stagnation point,

rather than the large eddies themselves, although this makes it more difficult to interpret M_c as a Mach number of the large-scale structures.

The apparent simplicity of the result makes it tempting to use M_c as a similarity parameter, where two flows would exhibit the same compressibility effects provided they have the same convective Mach number. This proposition is described and discussed in the following sections, but we can anticipate at least one difficulty. The convective Mach number appeared from considerations regarding the conservation of the momentum flux, and there are no obvious links to problems where other physical mechanisms play a role. For example, acoustic feedback mechanisms can occur if the low-speed side is subsonic. "Screech" tones are formed when pressure waves traveling upstream in the subsonic stream reach the trailing edge of the splitter plate and synchronize the eddy formation to produce coherent eddies at a fixed frequency. It seems likely that mixing layers with one subsonic and one supersonic stream will have properties different from mixing layers with two supersonic streams, even if the value of M_c is the same, and more than one similarity parameter may be required.

6.4.2 Similarity Considerations

For zero pressure gradient turbulent boundary layers in supersonic flow, it appears that the friction coefficient depends on Reynolds number in the same way as it does at low speeds, and it was shown in Chapter 1 that a reasonable value of the wall friction was found if the density and viscosity were evaluated at the wall temperature. Indeed, many of the characteristics of boundary layers in supersonic flow are similar to the properties of a boundary layer in subsonic flow with variable fluid properties. In a similar way, is it possible to deduce the maximum shear stress in a mixing layer from low-speed formulations by choosing the appropriate velocity and density scales (although we have already seen that changes in density are not the only important factor in describing mixing layer behavior)?

To answer this question, we need to examine scaling arguments and the possibility of finding similarity solutions in supersonic mixing layers. For subsonic flows, the scales are unambiguous (see Section 6.2), and they imply that the maximum shear stress scales with the velocity difference $(\Delta U)^2$, and that the ratio $-\overline{uv}\big/(\Delta U)^2$ is constant for sufficiently large Reynolds numbers. In supersonic flows, variable density and other compressibility effects introduce some ambiguities in choosing scaling quantities. For example, Zeman (1992) examined the case of compressible mixing layers with the same mean density and temperature on the high-speed and low-speed sides. Even then the flow depends on Mach number because the "dilatation" dissipation due to eddy shocklets increases with Mach number, thereby changing the distributions of temperature and density within the layer. The shape of the velocity profiles,

however, is not sensitive to Mach number over a wide range, and this follows the same trends as flows with density gradients, as shown in Section 6.7.

The main difficulty is to find a scale for the density. Consider the mean momentum equation for a zero pressure gradient, high Reynolds number, compressible mixing layer:

$$u\frac{\partial u}{\partial x} + v\frac{\partial u}{\partial y} = \frac{1}{\bar{\rho}}\frac{\partial}{\partial y}\left(-\overline{\rho u v}\right) \tag{6.14}$$

We need to define scales for the mean velocity, density, and turbulent shear stress, as well as length scales for the longitudinal and transverse directions. These quantities are denoted U^*, ρ^*, τ^*, L, and δ, where δ is a measure of the shear layer thickness, and U^* is such that the order of magnitude of the velocity gradient $\partial u/\partial y$ is given by U^*/δ. We assume that the spatial scales for velocity and density (and for the mass flux ρU) are the same, which happens to be a good approximation for many common flows. A useful value for τ^* is τ_m, the maximum value of the shear stress in a given cross-section of the flow. According to the order-of-magnitude analysis of Chapter 3, the mean acceleration and friction terms are of the same order. Hence:

$$\frac{\rho^* U^{*2}}{\tau_m}\frac{\delta}{L} \sim 1.$$

As in low-speed flows, this result suggests that if δ/L is constant, the friction coefficient $\tau_m/\rho^* U^{*2}$ is also constant, and that it is of the order of the spreading rate.

We now see if τ_m scales with ρ_1 and U_1, and ρ_2 and U_2, according to the same scaling law. That is, we need to see if

$$\frac{\tau_m}{\rho_1 \left(U_1 - U_m\right)^2} = \frac{\tau_m}{\rho_2 \left(U_m - U_2\right)^2}, \tag{6.15}$$

where U_m is a velocity scale to be defined. Solving Equation 6.15 for U_m we find:

$$U_m = \frac{U_1\sqrt{\rho_1} + U_2\sqrt{\rho_2}}{\sqrt{\rho_1} + \sqrt{\rho_2}}.$$

In the case where the two external flows have the same γ, U_m is the isentropic convection velocity; that is, $U_m = U_c$ (see above). For compressible flows, we define the friction velocity as

$$u_\tau = \sqrt{\tau_m/\rho_m}.$$

We now try to find ρ_m to achieve full similarity with respect to Mach number so that there is a value of ρ_m which will give the friction coefficient defined in Equation 6.15 the same value as in low-speed flows, independent of the Mach

number. For zero Mach number and constant density, the friction coefficient is

$$A = \left(\frac{2u_\tau}{\Delta U}\right)^2_{M=0,\ \rho=cst},$$

where A is a constant. Equation 6.15 becomes:

$$\frac{u_\tau^2}{(U_1 - U_m)^2} = A\frac{\rho_1}{\rho_m}, \tag{6.16}$$

which suggests that full similarity is achieved when for a given value of ρ_1/ρ_m the same level of shear stress per unit mass is obtained. This is unlikely, because experiments show that when the same value of ρ_1/ρ_m is produced either by changing the density ratio $s = \rho_2/\rho_1$, or by changing the convective Mach number, different values of the spreading rate and turbulence level are found. More precisely, the experimental data required to substantiate Equation 6.16 are not available, even in subsonic flows. In the next section, we discuss the empirical correlations that have been developed to give the level of turbulence as a function of the convective Mach number. These empirical interpolation formulae can give unacceptable values of ρ_m when used in Equation 6.16, that is, values larger than the larger value of density in the outer flow, or smaller than the smaller density. So the limited information available at the present time suggests that it is not possible to express the effect of Mach number on the turbulence level by a simple scaling on ρ, even though all the data necessary to explore the question of full similarity are not available. In the general case, therefore, the ratio $\tau_m/\rho_1 (U_1 - U_c)^2$ is a function of the density ratio s, the velocity ratio q $(= U_2/U_1)$, and the convective Mach number M_c. This point is discussed in greater detail in the context of self-similar solutions (Section 6.7).

6.5 Mean Flow Scaling

The shape of the velocity profile is discussed in detail in Section 6.7, but experiments show that in fully developed layers the shape is virtually unaffected by compressibility, especially when the velocity and the density gradients are in the same direction. Papamoschou and Roshko (1988) found that their spreading rate data scaled with the velocity ratio, density ratio, and the Mach number. They assumed that the effect of Mach number can be separated from the other effects, implying that the effects of q and s are the same at low and high speeds and that they may be studied separately. Following Brown and Roshko, they proposed that the spreading rate in subsonic flows, δ_0', has the form:

$$\delta_0' \sim \frac{\Delta U}{U_c}.$$

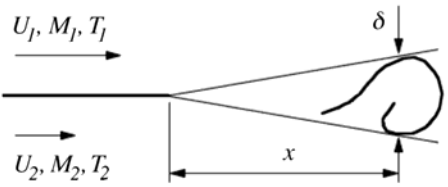

Figure 6.5. Notation for a mixing layer.

This formulation can be interpreted in terms of convection and diffusion times. Suppose that the mixing layer is formed of an array of large eddies of size δ, and in the average, convected a speed U_c. While they are convected, the eddies grow because of turbulent diffusion and entrainment. Their size varies from zero at the origin of the layer to δ at distance x (see Figure 6.5). During a convective time scale $t_c = x/U_c$, the layer thickness grows to δ, that is, the convection time equals the turbulent diffusion time t_t. In general, t_t is evaluated from turbulent quantities, such as the *rms* velocity or an integral scale for the size of the energetic eddies. However, large turbulent eddies have characteristic time scales of the order of the scale of the mean motion, so that the turbulent scale can be estimated by:

$$t_t \propto \frac{1}{\partial u/\partial y}.$$

This definition of the time scale is also convenient, because we consider self-preserving flows, which can be described by only one scale, so that the scales of the turbulent and of the mean motion remain proportional. The mean velocity gradient $\partial u/\partial y$ is of the order of $\Delta U/\delta$, and a simple relation is obtained:

$$\frac{x}{U_c} \propto \frac{\delta}{\Delta U} \quad \text{or} \quad \frac{\delta}{x} = \delta_0' \propto \frac{\Delta U}{U_c},$$

which is Brown and Roshko's proposal. The proportionality to ΔU implies that turbulent momentum transport is proportional to the velocity difference across the layer, which is consistent with Prandtl's eddy viscosity formulation for subsonic free shear flows, where $\nu_t \sim \delta \Delta U$. If we assume instead that the turbulent diffusion rate is constant in a frame of reference convected with the eddies, we find that the spreading rate is *inversely* proportional to the convection velocity.

If U_c is the isentropic approximation for the convection velocity, Equation 6.11 can be used. Then, for subsonic variable density mixing layers:

$$\delta_0' = \delta_{ref}' \frac{(1-q)\,(1+\sqrt{s})}{2\,(1+q\sqrt{s})},$$

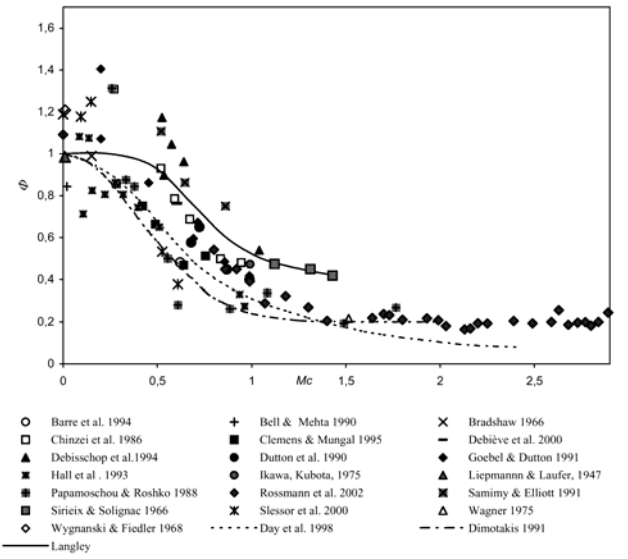

Figure 6.6. Convective Mach number dependence of the normalized spreading rate of supersonic mixing layers.

where $\delta'_{ref} = (d\delta/dx)_{ref}$ is the spreading rate of a subsonic constant density shear layer with $U_2 = 0$.

In order to extend this scaling to compressible mixing layers, Papamoschou and Roshko proposed a correlation of the form:

$$\delta' = \delta'_0 \Phi(M_c) = \delta'_{ref} \frac{(1-q)(1+\sqrt{s})}{2(1+q\sqrt{s})} \Phi(M_c), \tag{6.17}$$

where $\Phi(M_c)$ is a function that must be determined by experiment. This correlation collapsed their data well, supporting the use of the convective Mach number to represent global compressibility effects.

In Figure 6.6 we see how the spreading rates measured by a number of authors vary with the convective Mach number. Only layers formed by co-flowing streams (that is, U_1 and U_2 have the same sign) were considered in this compilation. The plot was derived from Equation 6.17, in which the measured value of the growth rate was employed, together with the experimental values of q and s. The original data were used, and the reassessment proposed in AGARD Fluid Dynamics Panel (1998) was employed. For some data the analysis and the compilation of Aupoix (2004) have been also considered. The same reference value $\delta'_{ref} = 0.16$ was used throughout, δ being the vorticity thickness. In the figure, M_c is the isentropic estimate of the convective Mach number defined by Equation 6.12. Mixing layers between flows with different

values of γ ($\gamma_1 \neq \gamma_2$) were not treated differently. Three reference curves are also plotted: the Langley curve (see also Figure 1.8), the semi-empirical relation

$$\Phi(M_c) = 0.8e^{-M_c^2} + 0.2 \tag{6.18}$$

proposed by Dimotakis (1991), and the amplification rate of the Kelvin-Helmholtz mode obtained by Day et al. (1998) from linear stability theory. This last comparison is discussed further in Section 6.10.

An immediate observation is that the spreading rate decreases with Mach number: compressibility effectively inhibits turbulent mixing and particularly reduces the spreading rate of mixing layers.

A point to be more deeply analyzed is the large scatter in the results. There is still some controversy about the value of δ'_{ref}. The value of 0.16 used here is consistent with the value of 0.115 proposed for the Stanford thickness. It is obvious from Figure 6.6 that even for low-speed layers the value of the spreading rate is not well known. For example, two reference measurements (Wygnanski and Fiedler (1970) and Bell and Mehta (1990)) show a discrepancy of at least 35%. Such large scatter was originally underlined by Dimotakis (1991) who found discrepancies of about $\pm 30\%$ in the experimental determination of spreading rates at subsonic speed. The same scatter of about 50% is observed for all values of M_c. The reason is probably the sensitivity of mixing layers to boundary and incoming conditions: external turbulence, acoustic excitations by wind tunnel resonances, spurious pressure gradients, or effects of confinement. At higher Mach numbers, the situation is still more complicated, because we must evaluate the convective Mach number as a similarity parameter.

The isentropic approximation has been used to evaluate M_c. However, Equation 6.10 clearly indicates that two convective Mach numbers exist when the two gases are of different molecular natures. This would imply that another Mach number should be used. Moreover, in some experiments, an asymmetric behavior has been found, with eddies traveling at a speed close to the velocity of one of the external flows. Such aspects are found in particular conditions, and are discussed in Section 6.9.

More generally, the data must be treated with some caution. First, all compressibility effects are now characterized by one Mach number, corresponding to the case of a frozen pattern where the average shape of the eddies remains unchanged. Second, a given value of M_c can be found in experiments with either one subsonic and one supersonic stream, or with both streams supersonic. As pointed out earlier, in the subsonic-supersonic combination, information can be carried in the upstream direction by pressure waves. The resulting interactions between acoustic and vorticity modes can change the overall organization of the flow dramatically. Clearly, this cannot happen in supersonic-supersonic combinations, and such physical differences cannot be represented by a single Mach number. Third, the use of a convective Mach

number requires that we can determine it accurately. In fact, it is difficult to measure M_c directly, and instead it is often estimated using the isentropic approximation (Equation 6.12), which is probably not valid over the whole range of Mach numbers (see below).

Considering such a large scatter in the data, some authors, such as Lu and Lele (1994) or Slessoret al. (2000), have suggested a different assessment. They consider that the effects of q and s are reasonably well represented by $\Delta U/U_c$, but that the reference value depends on the flow arrangement. This leads to a new expression for the experimental spreading rate for supersonic shear layers δ'_{exp}:

$$\delta'_{exp} = C_\delta\left(M_c\right)\frac{\left(1-q\right)\left(1+\sqrt{s}\right)}{2\left(1+q\sqrt{s}\right)}\Phi\left(M_c\right). \tag{6.19}$$

This result implies that $C_\delta = \delta'_{ref}\Phi\left(M_c\right)$.

On the other hand, it is supposed that, even if δ'_{ref} is different from one set of experiments to another, the evolution of δ'_{ref} versus M_c is independent of each particular experimental arrangement. This is a tempting suggestion. It makes the implicit assumption that for a given set of experiments made in the same wind tunnel, the perturbations are brought to the flow mainly by the machinery and by the set-up, and therefore remain constant. Of course this is only partly true because realizing several values of the convective Mach number implies changing parts of the experimental configuration, so that the layers may be subjected to the different external perturbations, depending on the operating point of the facility. In any case, this suggestion has led to two reassessments of the data, one by Slessoret al. (2000) and a second one by Aupoix (2001, 2004). An example is given in Figure 6.5, which gives C_δ as a function of M_c for most of the available experiments. The formula proposed by Dimotakis (1991) is also presented with an adjustment at zero Mach number to a spreading rate value of 0.135, as measured by Bell and Mehta (1990). Large scatter for low convective Mach numbers is still found but the data points approximately follow the trend suggested by the formula.

In this analysis, only the isentropic estimate M_c has been considered. In the reassessment proposed by Slessoret al. (2000), another formulation is proposed, in which the convective Mach numbers M_{c1} and M_{c2} can be different. For that purpose they define a Mach number Π_c such that:

$$\Pi_c = \max_i \frac{\sqrt{\gamma_i - 1}}{a_i}\Delta U.$$

Compilation of existing data, after revaluating δ'_{ref} for collapsing the results for Mach numbers close to 0.5 leads to the empirical correlation:

$$\delta' = \delta'_0\left(1+4\Pi_c^2\right)^{-\beta}$$

with $\beta = 0.5$. In this case, most of the scatter has been again transferred to δ'_0, for which only a global determination is available with a limited accuracy.

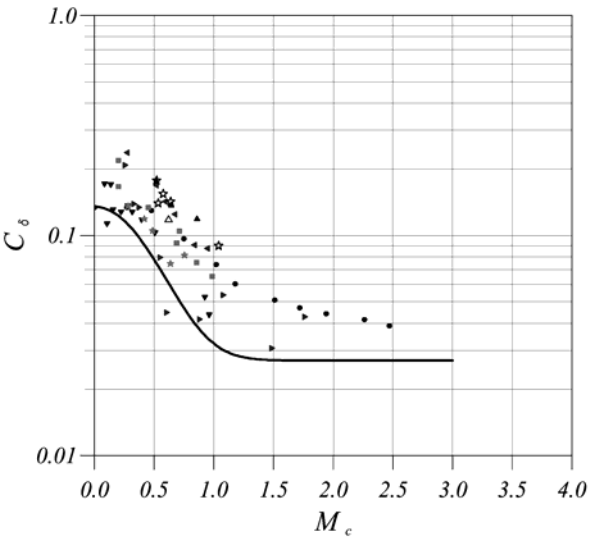

Figure 6.7. Evaluation of C_δ dependence on convective Mach number. ▲, Samimy et al. (1986); ▲, Samimy and Elliott (1990); ◀, Chinzei et al. (1986); ■, Goebel and Dutton (1990); ▶, Papamoschou (1986); ▼, Hall (1991); ★, Clemens and Mungal (1991); ☆, Bonnet et al. (1993); △, Barre et al. (1994); •, Langley curve; ——, Dimotakis (1991). (From Aupoix (2004), with permission.)

This is an alternate possibility, but it does not remove the question of the reference value for zero Mach numbers.

Before concluding this point, a comment should be made on the accuracy of the experimental growth rate. For that, Figure 6.8 is considered, which is the companion of Figure 6.6. Two families of results are identified: the first family encompasses the results obtained from mean velocity profiles, and the second family contains results obtained using flow visualizations and Pitot pressure profiles. Note that the spreading rates for these two methods were tuned on each other. Very clearly most of the data of the first family are grouped around the Langley curve, whereas the second family is in better agreement with Dimotakis' correlation. These two correlations seem to define the limits of likely values of the mixing layer spreading rate. Note, however, that in the first family only air-air combinations were used, whereas all the data using different gases belong to the second family.

These data suggest that our present understanding of the relative effects of compressibility and of density differences probably needs to be revised. As emphasized earlier, the convective Mach number is certainly not the only similarity parameter in the problem. Nevertheless, it is clear that the spreading

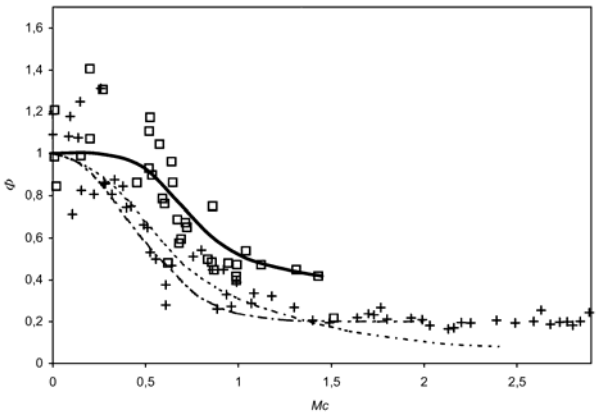

Figure 6.8. Dependence of the spreading rate on experimental method. □, from velocity profiles; +, from visualizations or Pitot pressure profiles. Lines as in Figure 6.6.

rate decreases with Mach number: compressibility inhibits turbulent mixing and in particular it reduces the spatial growth rate of mixing layers. The convective Mach number remains a very reasonable candidate for evaluating such effects in a first approximation, even if it does not represent all the phenomena that can be found in such flows.

The present discussion used formulations valid for temporal mixing layers, for example, for finding the influence of velocity and density ratios on spreading rate. In the case of spatial growth, corrections may be necessary. Dimotakis (1991) proposed the following formulation,

$$\delta' = \delta'_{ref} \frac{(1-q)\,(1+\sqrt{s})}{2\,(1+q\sqrt{s})} \left[1 - \frac{(1-\sqrt{s})\,(1+\sqrt{s})}{1+2.9\,(1+q)\,(1-q)}\right]. \tag{6.20}$$

This correction has not been used in the present assessment of data; although not completely negligible, it does not modify the trends and the conclusions that were drawn.

Another aspect should be discussed. Co-flowing streams produced all the flows under examination. Strykowski et al. (1996) have investigated the behavior of mixing layers produced by counterflowing flows, in particular a supersonic axisymmetric jet with a counterflowing surrounding stream. As for inhomogeneous compressible flows, the Navier-Stokes equations are not invariant by Galilean transformation and different phenomena may be expected when the two streams have opposite directions. Strykowski et al. (1996) found an increase in the growth rate, which they interpreted as the appearance of an absolute instability, leading to a change in the structure of the large eddies.

However they found that for their experiment in which $s = 0.55$, the relation

$$\delta' = \delta'_{ref} \frac{(1-q)\,(1+\sqrt{s})}{2\,(1+q\sqrt{s})}$$

is still well verified for moderate counterflows with $-0.1 < q < 0$.

6.6 Turbulent Shear Stress Scaling

We now see if the results on the scaling of the mean flow can be used to infer the influence of compressibility on the turbulent shear stress and kinetic energy. The anisotropy of the Reynolds stress is also of interest, as well as the effect on the motion of the large eddies and the implications for the relationship between large eddies and turbulent transport.

The behavior of the shear stress $-\overline{u'v'}$ is important, because it has a direct influence on the evolution of the mean velocity profiles and the spreading rate. From an experimental point of view, it is also something that can be measured reasonably accurately, because its value can be checked against the value deduced by integrating the mean momentum equation. To find a dependence between the maximum stress and the parameters characterizing the flow, we use the analysis proposed by Barre et al. (1994). As in Section 6.5, we compare a time of convection and a time of turbulent diffusion, because an eddy grows under the action of turbulence while it is convected. A typical scale for the large scales is δ, and their motion is characterized by the convection velocity U_c. In a frame of reference moving with the large-scale eddies, their growth is assumed to be due to turbulent diffusion only, with an effective viscosity ν_t. From ν_t and δ, we define a diffusion time scale t, which represents the growth rate of the eddies in the convected system of coordinates, by

$$t \sim \frac{\delta^2}{\nu_t}. \tag{6.21}$$

The turbulent viscosity ν_t is assumed to be constant across the shear layer. Because $\nu_t = -\overline{u'v'}\Big/(\partial u/\partial y)$, it is proportional to $u_\tau^2 \delta/\Delta U$, where u_τ^2 is based on the maximum shear stress. Hence:

$$t \sim \frac{\delta \Delta U}{u_\tau^2}.$$

After a time t, the eddies have traveled a distance $x = U_c t$. Eliminating t gives a linear relationship between the longitudinal distance and the size of the eddies. That is, the spreading rate is constant and it is given by:

$$\frac{d\delta}{dx} = \frac{1}{K\,(s,q,M_c)} \frac{u_\tau^2}{U_c\,\Delta U}. \tag{6.22}$$

Here, U_c need not be the isentropic convection velocity. However, in most practical applications, it will need to be so because the actual convection velocity is difficult to measure. The function $K(s, q, M_c)$ reflects the fact that, in general, for a given level of turbulence, the diffusion time can change if the density stratification, the velocity ratio, or the Mach number changes (we have assumed that the convective Mach number is the relevant similarity parameter). Barre et al. (1994) neglected the influence of q, but it is shown in the self-preservation analysis that this parameter should be taken into account. If the relationship proposed by Papamoschou and Roshko (1988),

$$\frac{d\delta}{dx} = \frac{1}{2}\left(\frac{d\delta}{dx}\right)_{ref} \Phi(M_c)\,\frac{\Delta U}{U_c}, \tag{6.23}$$

is accepted, Equation 6.21 becomes

$$\frac{u_\tau^2}{(\Delta U)^2} = \frac{1}{2} K(s, q, M_c) \left(\frac{d\delta}{dx}\right)_{ref} \Phi(M_c)\,. \tag{6.24}$$

Equation 6.22 is consistent with self-preservation because it gives a linear growth of the layer and a maximum shear stress proportional to the spreading rate. More interestingly, Equation 6.24 indicates that if the dependence of K on M_c is weak, the maximum dimensionless shear stress varies with M_c according to $\Phi(M_c)$. An analysis of the dependence of K on s, q, and M_c is given in Section 6.8 for the case of a self-preserving flow. It is shown that K is a function of s and q, but not of the convective Mach number. Moreover, the range of s and q for the experiments considered in Figure 6.9 is such that K does not vary much.

The experimental data and the analysis appear to be in fair agreement. The scatter in the data includes the measurement uncertainty, as well as differences among the experimental conditions. As we noted earlier, the experimental uncertainty in the spreading rate of subsonic mixing layers is about 25%, and it is likely that the level of uncertainty for supersonic mixing layers is in the same range. Difficulties in matching boundary conditions from one experiment to another will contribute to the scatter in measurements of the maximum shear stress, which is also about 25%. As shown in the next section, the effect of the changing density ratio may increase the scatter, because Figure 6.9 contains data from experiments with different values of s, although the data with very different density ratios do not appear to depart significantly from the other data points. Blockage effects may also be important. This effect is discussed in more detail in the next section, but if the mixing layer thickness is not small compared to the height of the test section, then for transonic values of M_c large eddies may produce local regions of supersonic flow where shocklets dissipate energy, causing local blockages and affecting the turbulence level and the spreading rate. Some of the experiments shown in Figure 6.9 are certainly influenced by such effects. Despite all these difficulties, most of the stress

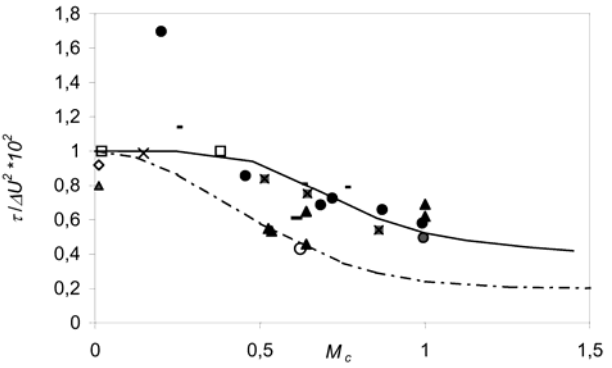

Figure 6.9. Maximum value of the turbulent shear stress in supersonic mixing layers. Symbols as in Figure 6.6, except □ is now Olsen and Dutton (2003), and the symbol - is Urban and Mungal (2001). The Langley curve and Dimotakis' relationship are multiplied by a constant factor of 10^{-2}.

data, as was found for the spreading rates, lie between the Langley curve and Dimotakis' formula. It can still be concluded that for moderate compressibility effects the stress level decreases in a similar way to the decrease in the spreading rate, and we expect that at a value of $M_c = 1.5$ the maximum turbulent shear stress level will be only about 40% of the corresponding low-speed value (this is discussed further in the next section).

Because the shear stress depends on M_c, the eddy viscosity will also depend on M_c. For free shear flows, the eddy viscosity due to Prandtl has the form:

$$\nu_t = C\Phi\left(M_c\right)\Delta U\,\delta\left(x\right), \tag{6.25}$$

where the constant C has the same value as at low speeds (at the same density and velocity ratio), as long as the shape of the velocity profiles does not depend on M_c.

6.7 Self-Preservation Conditions

As in Tennekes and Lumley (1972), we restrict our analysis of self-preservation in flows with temperature or density inhomogeneities to cases where the flow properties at a given point can be described by only one length scale. Strictly speaking, this is possible only if the Prandtl number or the Schmidt number is unity. We restrict our analysis to this case, because self-preserving solutions still give guidelines for the behavior of the mean field if the Prandtl number is not too different from unity.

We need to write the equation in a proper dimensionless form. Because the problem is inviscid, we need a velocity scale and a density scale. The condition

on shear stress scaling suggests we choose $(U_1 - U_c)$ as the velocity scale and ρ_1 for the density scale. The choice of velocity scale is basically similar to the use of ΔU for low-speed layers because the two are linked by the relationship:

$$(U_1 - U_c) = \Delta U \frac{\sqrt{s}}{1+\sqrt{s}},$$

and choosing U_c does not introduce a new variable. We begin by writing the momentum equation for the dimensionless variables f, g, h, and r defined by:

$$\begin{aligned} u &= U_c + (U_1 - U_c) f(\xi), \\ \rho u &= \rho_1 U_c + \rho_1 (U_1 - U_c) g(\xi), \\ \tau &= \rho_1 (U_1 - U_c)^2 h(\xi), \\ \rho &= r(\xi) \rho_1, \end{aligned}$$

where $\xi = y/\delta$, as before. The definition of g is such that $f = g$ when r is constant. Because the Prandtl number is one, the total enthalpy is either constant or a function of velocity only, which implies that there is similarity on r if the velocity profiles are self-similar. For this reason, the energy equation is not considered here.

If self-preservation is achieved, it is expected that all dimensionless quantities depend only on the local variable ξ and not explicitly on x, and that the value of h at its maximum (where $\tau = \tau_m$) is also independent of x; therefore $\tau_m/\rho_1 (U_1 - U_c)^2$ is also expected to be constant, as in the incompressible case. The momentum equation becomes:

$$\begin{aligned} &\left(\frac{U_c}{U_1 - U_c} + g\right) f \frac{\delta}{U_1 - U_c} \frac{\partial (U_1 - U_c)}{\partial x} - \frac{\partial \delta}{\partial x} \left(\frac{U_c}{U_1 - U_c} + g\right) f' \xi \\ &\quad - \frac{\delta}{\rho_1 (U_1 - U_c)} \frac{\partial \rho_1 (U_1 - U_c)}{\partial x} f' \int_0^\xi g d\xi + \frac{\partial \delta}{\partial x} f' \int_0^\xi g' \xi d\xi \\ &\quad = h' - \frac{p_0}{\rho_1 (U_1 - U_c)^2} \frac{\partial p/p_0}{\partial x}. \end{aligned} \tag{6.26}$$

Sufficient conditions for self-preservation are

$$\begin{aligned} \frac{d\delta}{dx} &= \text{cst}, \\ \frac{\tau_m}{\rho_1 (U_1 - U_c)^2} &= \text{cst}, \\ \frac{\delta}{(U_1 - U_c)} \frac{d(U_1 - U_c)}{dx} &= \text{cst}, \end{aligned}$$

$$\frac{\delta}{\rho_1 (U_1 - U_c)} \frac{d\rho_1 (U_1 - U_c)}{dx} = \text{cst},$$

$$\frac{U_1 - U_c}{U_c} = \text{cst}.$$

That is, the spreading rate of the layer is constant, as it is for subsonic flows. Also, the maximum value of the dimensionless shear stress is constant, although the value of the constant will vary with Mach number, as we saw previously. With our choice of U_c, the ratio $(U_1 - U_c)/U_c = \sqrt{s}(1-q)/(1+q\sqrt{s})$ is a function of s and q only.

When the conditions in the external flows do not vary with x, Equation 6.26 reduces to:

$$-f' \frac{\partial \delta}{\partial x} \int_0^\xi r \left(\frac{U_c}{U_1 - U_c} + f \right) d\xi = h'. \tag{6.27}$$

So the spreading rate is proportional to the maximum stress, which was also the case in subsonic flows. Finally, if an eddy viscosity model is used, such that $\tau = \mu_t \partial U/\partial y$, Equation 6.27 becomes

$$-Re_t f' \frac{\partial \delta}{\partial x} \int_0^\xi r \left(\frac{U_c}{U_1 - U_c} + f \right) d\xi = rf'' + r'f', \tag{6.28}$$

where Re_t is the Reynolds number $(U_1 - U_c)\,\delta/\nu_t$. We can expect compressibility effects through the Mach number dependence of the spreading rate, the turbulence Reynolds number Re_t and the density variations. Before we can continue, we need a model for ν_t. The treatment given here is based on the work by Menaa et al. (1996).

By using Equations 6.23 and 6.24, and the relation $u_\tau^2 = \nu_t \Delta U/\delta$, where δ is the vorticity thickness, it can be shown that

$$\frac{U_c}{U_1 - U_c} Re_t \frac{d\delta}{dx} = \frac{1}{K(s, q, M_c)}$$

which depends (possibly) on M_c only through K. Hence:

$$-\frac{1}{K} f' \int_0^\xi r \left(1 + \frac{U_1 - U_c}{U_c} f \right) d\xi = (rf')'.$$

Substituting for U_c, we obtain:

$$-\frac{1}{K} f' \int_0^\xi r \left(1 + \frac{\sqrt{s}(1-q)}{1+q\sqrt{s}} f \right) d\xi = (rf')'. \tag{6.29}$$

So the effect of compressibility can come in only through K, and the rest of the equation is identical to the equation for mixing layers with variable density.

It is clear that K can be absorbed in the definition of the thickness of the layer. Changing ξ for $\eta = \xi\sqrt{K}$ would keep the right-hand side of Equation 6.29 unchanged, and would give the same equation in canonical form ($K = 1$):

$$-f' \int_0^\eta r \left(1 + \frac{\sqrt{s}\,(1-q)}{1+q\sqrt{s}} f\right) d\eta = (rf')', \tag{6.30}$$

where the prime denotes differentiation with respect to η. We see now that the dimensionless velocity profiles depend only on s and q, and not on M_c. Consequently, we have $K = K(s,q)$. In this simple self-preservation analysis, all the effects of compressibility are lumped in the spreading rate, and not in the shape of the velocity profiles. More precisely, the velocity profiles depend only on $(U_1 - U_c)/U_c$ and on $s = \rho_2/\rho_1$.

Menaa et al. (1996) solved the previous equation numerically for the vorticity thickness (the value of K depends on the definition of δ), and the values of $K(s,q)$, for a given distribution of density. To solve Equation 6.30 conditions on the velocity for $\xi \to \pm\infty$ were imposed, as well as the condition that $(rf')' = 0$ for $\xi = 0$. Redundant conditions can then be used to find the value of $K(s,q)$. By definition of the vorticity thickness, the maximum slope of the normalized velocity profile is 1 if the scaling used in Figure 6.10 is adopted. Therefore, the computations were started with an approximate value of K and the exact value of K was deduced by imposing a value of 1 on the maximum slope of the velocity profile. The results shown in Figure 6.11 indicate that K can vary by more than 50% in extreme cases, and that it has a value of about 0.16 for constant density flows. The velocity profiles for $q = 0$ and a constant total temperature are given in Figure 6.10. The range of values of s corresponds to a range of convective Mach numbers up to 1. Here, K varies only by 10%, and therefore the shape of the velocity profile is virtually independent of the Mach number. Similar results were obtained by Samimy and Elliott (1990).

In concluding this section, we should note that because K is not truly constant, the representation of the shear stress in Figure 6.9 cannot collapse the data on a single curve. By using $K(s,q)$ from the previous analysis, the ratio $u_\tau^2/K\,(\Delta U)^2$ can be examined. This is given in Figure 6.12. In light of the somewhat reduced scatter seen in the data, it appears that $u_\tau^2/K\,(\Delta U)^2$ may be a function of M_c only. So the turbulence measurements tend to confirm, indirectly, the validity of the present analysis for $M_c \leq 1$.

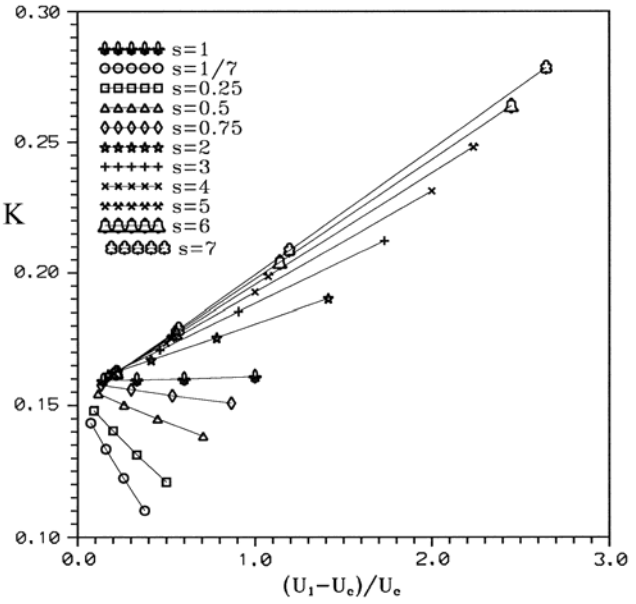

Figure 6.10. Variation of K as a function of s and q. (From Menaa et al. (1996), with the authors' permission.

6.8 Turbulent Normal Stresses

As pointed out in Chapters 3 and 4, changes in the structure of the pressure field may result in modifications of the Reynolds stress anisotropy. This is why it is important, especially for turbulence modeling, to see if the anisotropy of the normal stresses changes when the convective Mach number varies. To see if these changes are significant, we need to consider measurements of the Reynolds stresses and the results of numerical simulations.

Unfortunately, measurements of the complete Reynolds stresses are generally inaccurate. The streamwise component $\overline{u'^2}$ is most easily measured, and a number of data sets are shown in Figure 6.13. There is more scatter than in the measurements of the shear stress, which is surprising because measurements of $\overline{u'^2}$ are generally easier to make, and thought to be more accurate. The scatter is greatest for measurements taken in small wind tunnels, and therefore it may be due to blockage effects. The normalized spreading rate is also shown for comparison. There is a reasonable collapse of most of the data points around this curve, and it seems that $\overline{u'^2}$ varies with M_c according to $\Phi(M_c)$. Therefore, in the range of transonic convective Mach numbers for which data are available, it is likely that the effects of compressibility on

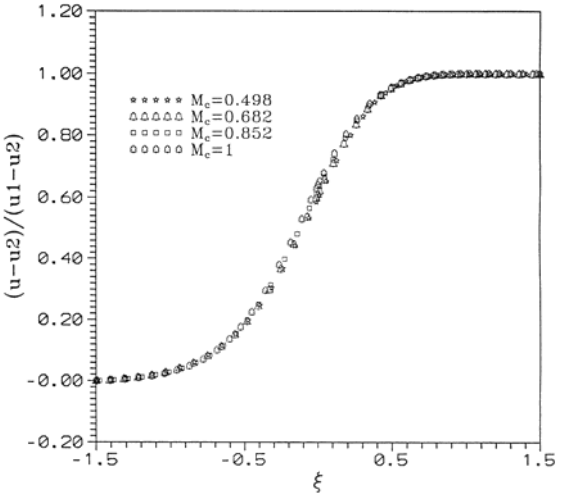

Figure 6.11. Velocity profile in supersonic half jets, for $0 < M_c \leq 1$, $q = 0$ and a constant total temperature, plotted in similarity coordinates. (From Menaa et al. (1996), with the authors' permission.)

$\overline{u'^2}$ remain moderate. Further discussion on the effects of compressibility on Reynolds stress anisotropy is deferred until Section 6.10.

6.9 Space-Time Characteristics

One of the effects of compressibility is to change the shape of the eddies in a mixing layer. This was observed in numerical simulations of two- and three-dimensional mixing layers (Chen, 1991; Lesieur et al., 1992; Lele, 1994). At high convective Mach numbers, shocklets are formed, the eddies become more elongated, and there is a progressive inhibition of pairing. The turbulent structures also become more three-dimensional, which was first inferred from linearized stability theory and numerical simulations (Betchov and Criminale, 1975; Sandham and Reynolds, 1989).

For $M_c \leq 0.6$, the more amplified modes are two-dimensional, but at higher Mach numbers, the more amplified modes are oblique waves and the eddies become more like horseshoes. Chen (1991), for instance, performed a direct numerical simulation of a temporally evolving mixing layer at two convective Mach numbers, 0.4 and 0.8, and showed that compressibility enhanced the three-dimensionality of the flow. What is particularly interesting is the effect on the scalar concentration distributions. At the lower convective Mach number the spanwise rollers bring the fluid from the high- and low-speed sides into

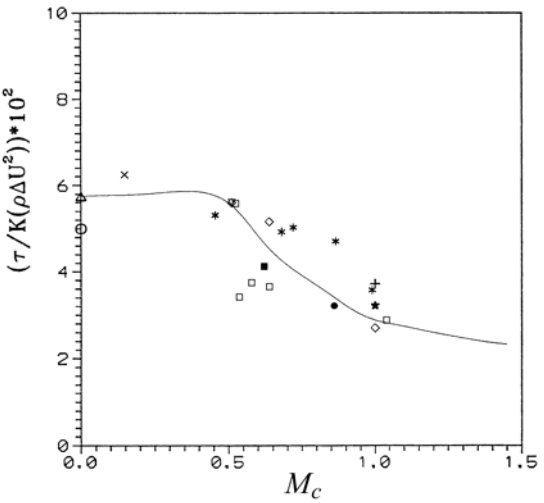

Figure 6.12. Variation of $u_\tau^2/K\left(\Delta U\right)^2$ as a function of s and q. □, Bonnet et al. (1993); ●, Elliott and Samimy (1990); ×, Bradshaw (1966); ○, Liepmann and Laufer (1947); △, Wygnanski and Fiedler (1970); ◇, Samimy and Elliott (1990); +, Ikawa and Kubota (1975); ∗, Dutton et al. (1990); ★, Petrie et al. (1986); ▽, Wagner (1973); ■, Chinzei et al. (1986). ———, Langley curve using $K = 0.17$ in Equation 6.24; (Adapted from Menaa et al. (1996), with the authors' permission.)

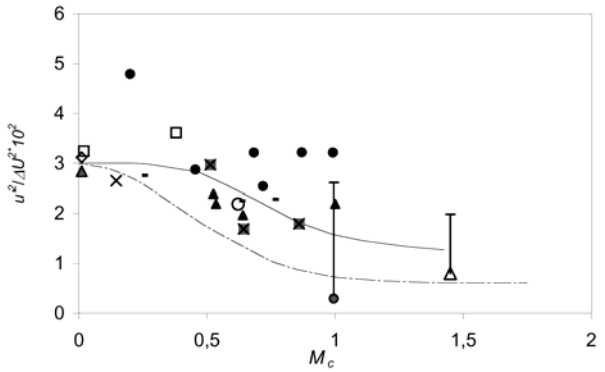

Figure 6.13. Distribution of the maximum value of $\overline{u'^2}\Big/(\Delta U)^2$ as a function of convective Mach number. The bars indicate the measurements as reassessed by Barre et al. (1994). Symbols as in Figure 6.6, except □ is now Olsen and Dutton (2003), and the symbol - is Urban and Mungal (2001). The Langley curve and Dimotakis' relationship are multiplied by a constant factor of 3×10^{-3}.

the center, and the concentration profiles show a well-defined peak at this location. At the higher convective Mach number, the presence of three-dimensional Λ-shaped vortices lead to local upwash and downwash regions that create pockets of partially mixed fluid near the tips of the vortices (Figure 6.14). As a result, the instantaneous concentration profiles show two preferred mixture fractions at a given position in the layer (Figure 1.12). The direct simulations by Fouillet (1991) and Lesieur (1994) confirm that the vortex lines become more three-dimensional, and show that the pressure contours tend to form longitudinal tubes. They also found that pairing is inhibited, which may be one of the causes for the smaller spreading rate and reduced turbulence levels. Flow visualization in turbulent mixing layers does not reveal the obvious horseshoe shapes seen by Chen, but it indicates that at large convective Mach numbers small scales appear on the interface between the eddies and the surrounding flow, suggesting a change in the dynamics of large-scale structures, and also that the large scales experience an increasing loss of coherence, as shown in Figure 1.11 (see also Clemens and Mungal (1992a, 1995), Messersmith et al. (1991), and Samimy et al. (1992)). This seems consistent with some recent spectral measurements by Dussauge and Dupont (1995), where it was found that in supersonic mixing layers the energetic range contained much smaller scales than at low speeds for a given thickness of the layer.

Another important feature is the speed at which the eddies are convected. In our analysis, we used very crude assumptions to represent this property, in that a single convection velocity was used, equal to the speed of the stagnation points, and it was necessary to make an assumption about the variations of entropy in the flow to derive analytical expressions. That is, we assumed a "frozen" row of eddies that move without changing their shape. This crude representation helped classify the global properties of the layers such as the eddy diffusivity, and it was useful in examining self-preserving solutions. How far can the large-scale structures of the shear layer, which control most of turbulent transport, be represented by this parameter? Two approaches can be followed. The first is related to the eddy diffusivity scheme given in Equation 6.25. This relationship shows that if the spreading rate and the maximum shear stress are known, a convection velocity can be determined. In this simple model, the convection velocity represents a transformation between time and space, and it applies to the structures that make the dominant contribution to the diffusion of momentum. The convection velocity appears as the ratio of the temporal growth rate in a convected frame $Ku_\tau^2/\Delta U$ to the spatial growth rate $d\delta/dx$. The most questionable point is the value of K which has not been completely established by experiments. However, this method was believed to give at least qualitative information on the convection velocity of the momentum-diffusing eddies.

The result is given in Figure 6.15, where M_{c1} and M_{c2} were deduced from U_c. The limited accuracy of the method is obvious, because u_τ and $d\delta/dx$ are

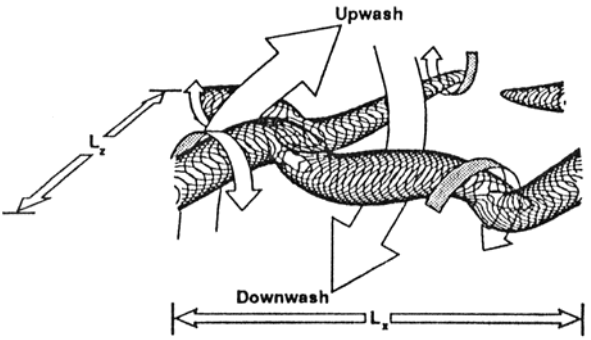

Figure 6.14. Conceptual drawing illustrating the generation of "upwash" and "downwash" regions by the Λ vortices ($M_c = 0.8$). (From Chen (1991), with permission of the author.

probably not known to an accuracy better than 10%. The two solid lines in Figure 6.15 were drawn to correspond to a 10% uncertainty on u_τ. The data points between these two lines represent the cases for which the convection velocity is in agreement with the isentropic estimate, to within the accuracy of the method. Clearly there are some flows in which there are significant deviations from the isentropic approximation, but again these cases were the ones that may have experienced significant blockage effects.

Measurements of the phase and group velocities give information on the speed at which the large-scale structures are convected. Such measurements were performed using hot-wire anemometers by Ikawa and Kubota (1975) and by Dupont et al. (1995) for $M_c \leq 1$ in flows with moderate confinement, over a range of frequencies. For high frequencies, the flow was not dispersive and all the perturbations traveled with the same speed, which was close to the local mean velocity. For low frequencies, that is, for length scales of the order of 5δ, the convection speed of the perturbations was very different from the isentropic convection velocity. In these flows, the increase of entropy is not large, and the shocklets, if present, are not strong. Such asymmetric convective Mach numbers can probably be explained using the results obtained by Si-Ameur (1994) through direct simulations of three-dimensional mixing-layers for transonic convective Mach numbers. He found that for $\delta/h > 0.1$ (where h is the channel height), transonic effects create shocklets on one side of the layer, producing an asymmetric behavior where $M_{c1} \neq M_{c2}$. Such effects are clearly not related to the properties of mixing layers, because they are just a consequence of the relative size of the channel. However, this is an important observation for supersonic mixing applications, in which the shear layers, prior to combustion, fill the entire chamber. These characteristics represent the ef-

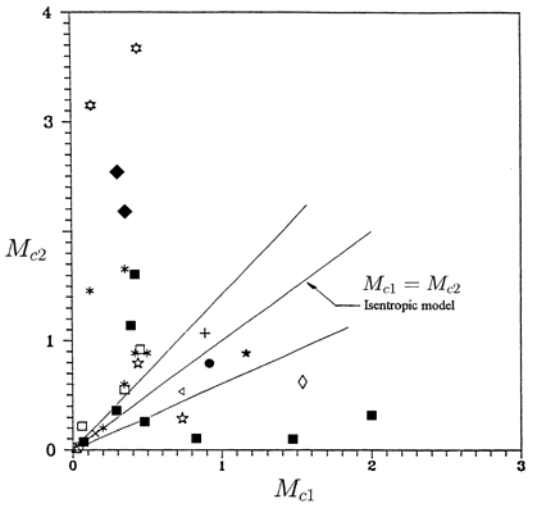

Figure 6.15. Experimental verification of the isentropic approximation for the convection velocity. ◁, Barre et al. (1994). Other symbols as in Figure 6.12, except □ is now Lau (1981). The two outside lines represent ±10% uncertainty limits.

fect of boundary conditions and they are not related to local properties, and therefore they cannot be computed by one-point, turbulence-closure assumptions. At a minimum, large eddy simulations are required to reproduce such effects. Finally, we should note that current models for compressible turbulence emphasize the importance of energy dissipation in shock waves and the losses of energy through acoustic radiation. These assumptions are based on the results of direct numerical simulations, and although it seems likely that these phenomena occur in practice, they have not been checked by direct measurements of the turbulent kinetic energy budgets. One of the few attempts was made by Chambres et al. (1997) for a convective Mach number close to one; his results do not support the idea of a drastic modification of the sum of dissipation and pressure divergence terms.

6.10 Compressibility and Mixing

The previous sections have highlighted the experimental evidence for the decrease in the spreading rate, turbulence level, and Reynolds stresses with increasing Mach number (that is, convective Mach number). This section proposes an interpretation for these observations. The analysis reproduced here is essentially due to Vreman et al. (1996), who used it to interpret direct numerical simulations of temporal mixing layers with the same density in both

external flows. Similar arguments were used by Freund et al. (2000) for annular temporal mixing layers with moderate differences in density, and by Pantano and Sarkar (2002) in a plane mixing layer with either the same or different densities on the two sides of the layer (see also Chassaing et al. (2002)). The analysis is applied to temporal mixing layers, but the arguments are simple enough to be transposed to the case of a steady spatial mixing layer, as is shown.

Vreman et al. (1996) consider the integral (momentum) thickness:

$$\theta = \frac{1}{\rho_\infty \left(\Delta U\right)^2} \int_{\delta_2}^{\delta_1} \bar{\rho} \left(U_1 - \tilde{U}\right) \left(\tilde{U} - U_2\right) dy \tag{6.31}$$

in which δ_1 and δ_2 are the edges of the layer, and $\Delta U = U_2 - U_1$. It is clear that if there exists some relation between U and ρ, this momentum thickness must be proportional to $\delta = \delta_1 - \delta_2$. For example, with a linear velocity profile in the layer and a constant density, $\theta = \delta/6$. In the case of a flow with constant total enthalpy density will affect the results, but its influence can be estimated as follows. First, because U and ρ have the same sense of variation, the weighting introduced by ρ/ρ_1 will give favor zones of larger velocity, and an increase in θ can be expected. This can be estimated in the following way: for one half of a temporal mixing layer:

$$\frac{U}{U_1} = \frac{y}{\delta} \quad \text{and} \quad T_0 = \text{constant}.$$

It follows that

$$\frac{\theta}{\delta} = \frac{1}{(\gamma-1)\,M_1^2} \left[2 + \ln\left(\frac{1}{1 - \frac{(\gamma-1)}{2} M_1^2} \right) - \sqrt{\frac{2}{\gamma-1}} \frac{1}{M_1} \ln\left(\frac{1 + \sqrt{\frac{\gamma-1}{2}} M_1}{1 - \sqrt{\frac{\gamma-1}{2}} M_1} \right) \right], \tag{6.32}$$

where M_1 is the Mach number based on U_1 and T_0. The values of this expression do not vary much: for $M_1 = 0$, this expression is 0.167 ($= 1/6$), and for $M_1 = 1$ (a convective Mach number of about 1.1), it is 0.178. The influence of density is therefore rather weak. Moreover, as θ is larger for high Mach numbers, a decrease of θ with convective Mach number will correspond to a still larger decrease of a thickness based on velocity profiles. Therefore, in cases where the density is the same on both sides of the temporal layer, the variations of the momentum thickness constitute a reasonable indicator of the spreading rate.

Taking the time derivative of Equation 6.31, while taking into account the integrated momentum equation and mean kinetic energy equation, leads to much simplification: the integration in a section removes the diffusion term and the longitudinal derivatives vanish because the fields are statistically homogeneous in the x-direction. The only remaining terms are the volume terms,

that is, the production and the viscous dissipation in the mean motion, which is, as usual, negligible in high Reynolds number flows. The final result shows that the time derivative of the integral thickness (essentially proportional to the spreading rate) is proportional to the integral of production. That is,

$$\frac{d\theta}{dt} = \frac{2}{\rho_\infty (\Delta U)^2} \int \left(-\overline{\rho u' v'} \frac{\partial \tilde{U}}{\partial y} \right) dy. \tag{6.33}$$

This result indicates that the decrease in the spreading rate is directly linked to the decrease in turbulent production. This is not totally surprising. In Section 6.6 a relation between maximum friction and spreading rate was proposed:

$$\frac{d\delta}{dx} = \frac{1}{K} \frac{u_\tau^2}{\Delta U U_c},$$

where $u_\tau^2 = \max(-\overline{u'v'})$, the maximum shear stress per unit mass. Accepting the approximation $U_c(\partial/\partial x) = d/dt$ (see Dimotakis (1991) for a discussion of relations between temporal and spatial shear layers), Equation 6.33 becomes:

$$\frac{d\delta}{dt} = \frac{1}{K} \frac{u_\tau^2}{\Delta U}.$$

Assuming self-similar shapes of profiles and averaging (6.24) over a section, we obtain:

$$\frac{d\theta}{dt} = \frac{C}{\rho_1} \frac{\bar{\rho}}{\Delta U} \frac{u_\tau^2}{\Delta U},$$

which is of the same form as the relation derived in Section 6.6. Therefore Vreman et al. (1996)'s analysis is consistent with the results based on dimensional analysis of a diffusion problem in a convection frame of reference.

Vreman et al. propose further analysis in terms of turbulent kinetic energy and Reynolds stresses. It has been remarked by most of contributors (Vreman et al. (1996), Freund et al. (2000), and Pantano and Sarkar (2002), among others) that the dilatational dissipation and pressure divergence terms in the equation for turbulent kinetic energy k are small compared to solenoidal dissipation and production. The key for the explanation of compressibility effects should therefore be sought in other contributions, such as the turbulent diffusion and/or pressure strain terms. Vreman et al. consider the Reynolds stress equations integrated over a section to remove the diffusion terms. Therefore, their conclusions will be relevant to global levels of turbulence, without respect to modifications of the shape of the profiles, which could happen through a diffusive process.

Equation 6.33 indicates that the reduction of the spreading rate is related to the production of the diagonal stress $R_{11} = (1/\delta) \int \overline{\rho u'^2} dy$, that is, the average of the longitudinal stress over a section. Final elements of understanding are found by examining the anisotropy tensor $b_{ij} = R_{ij}/R_{kk} - \delta_{ij}/3$ and considering

the b_{11} component. By using the DNS result that the anisotropy of dissipation is not significant, it is found to a good approximation that

$$\frac{d\theta}{dt} = -\frac{3}{2\rho_1 \left(\Delta U\right)^2}\Pi_{11} \tag{6.34}$$

in which Π_{11} is the pressure strain term. This simple result is most probably valid because simulations show that the pressure strain is almost proportional to production, as in most incompressible shear layers. This finding is consistent with many simulation results (Vreman et al., 1996; Freund et al., 2000; Pantano and Sarkar, 2002): normalized *rms* pressure decreases with convective Mach number. In any case, although Equation 6.34 is very simple, it suggests an important result. The decrease of the spreading rate of the mixing layer is the footprint of a modification in the structure of pressure fluctuations, and this has dramatic consequences at a macroscopic level: elementary measurements of the growth rate give a global measure of the alteration of pressure strain terms in the Reynolds stress equations.

Is this result general, and can it be applied to the spatial mixing layers we observe in nature and in wind tunnel experiments? In this case a space derivative of some scale directly linked to the layer thickness should be considered, instead of a time derivative. As the relation between space and time involves a velocity, we need either to transform the time derivative into a space derivative through some convection velocity, or directly to define another integral thickness. The second solution is more straightforward. It may be checked that the thickness θ_s defined by:

$$\theta_s \;=\; \frac{1}{\rho_\infty \left(\Delta U\right)^3} \int \bar{\rho}\tilde{U}\left(U_1 - \tilde{U}\right)\left(\tilde{U} - U_2\right) dy$$

shares, for the spatial, statistically steady problem, most of its properties with θ in the temporal homogeneous problem. In particular, it may be verified that, applying the same considerations as in the temporal problem, the companion relation of Equation 6.33 is obtained:

$$\frac{d\theta_s}{dx} = \frac{1}{\rho_\infty \left(\Delta U\right)^3} \int \left(-\overline{\rho u'v'}\frac{\partial \tilde{U}}{\partial y}\right) dy, \tag{6.35}$$

so that the same conclusions can be drawn as for the temporal mixing layer.

The modification of the structure of pressure is consistent with the results of Durbin and Zeman (1992), Jacquin et al. (1993), and Sarkar (1995) for linear and nonlinear analyses. Now, we should examine possible consequences of this result: if the pressure strain terms are modified, their redistribution role may be altered or hampered, and consequently the anisotropy of turbulence may be changed. This conclusion is difficult to verify experimentally because we do not have measurements of the pressure strain terms. Similarly, because of

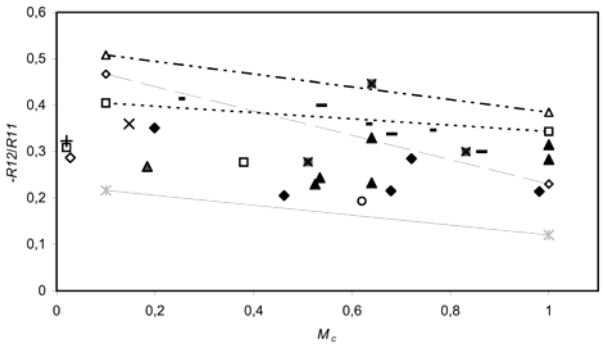

Figure 6.16. Influence of of convective Mach number on stress ratio. Symbols as in Figure 6.6, except □ is now Olsen and Dutton (2003), the symbol – is now Bellaud (1999), and the symbol - is Urban and Mungal (2001). ———, Sarkar (1995); — —, Freund et al. (2000); - - - - -, Pantano and Sarkar (2002); —- - -, Vreman et al. (1996).

the restrictions governing numerical techniques for highly compressible flows, the simulation results may not be conclusive. Considering the scarcity of Reynolds stress measurements and their limited accuracy (see Section 6.8), it also seems difficult to test the anisotropy tensor $\overline{u_i'u_j'}/\overline{u_k'u_k'} - \delta_{ij}/3$ directly. It is more sensible to consider the ratio $\overline{u'v'}/\overline{u'^2}$ and to compare the prediction of simulations with experiments, bearing in mind that such a ratio (as the anisotropy tensor) depends on dissipation and diffusion as well as the pressure terms. The result is given in Figure 6.16.

The experimental results given in Figure 6.16 include one set of measurements in an annular mixing layer (Bellaud, 1999), the numerical simulations an homogeneous shear layer (Sarkar, 1995), and an annular mixing layer (Freund et al., 2000). Note that the data from Vreman et al. (1996) are based only on averages over sections. The overall picture leaves much room for interpretation: the results are somewhat scattered, and no clear trends are apparent. The discrepancies among numerical simulations are probably as large as those that exist among the experiments. Note that it is difficult to define a numerical consensus even for a value at low Mach number. The measurements by Urban and Mungal (2001) are in good agreement with Pantano and Sarkar (2002)'s simulations, and experimental data by Bellaud et al. (1997) and Bellaud (1999) support Freund et al. (2000)'s numerical results in the same geometry. Note that experiments conducted in noisy wind tunnels may lead to small values of the ratio $\overline{u'v'}/\overline{u'^2}$ because potential fluctuations are developed in the external flows. Such fluctuations are known for producing velocity variances but weak fluxes, and thus decrease this ratio. The conclusion is that the overall trend

seems to be a slight decrease of $\overline{u'v'}/\overline{u'^2}$, but nothing spectacular appears from this compilation. Note also that the change in anisotropy due to compressibility appears to be moderate or weak for convective Mach numbers less than 1.

Are there other possible interpretations for the decreases in the growth rate and the turbulence levels? It was conjectured some years ago that the large eddies could induce shock waves in the outer flow, and constitute new sources of energy dissipation. In addition, this shock (or Mach) wave radiation provides an efficient source of aerodynamic noise. The formation of shock waves by the large eddies requires large velocity differences between the turbulent structures and the outer flow: this can occur at sufficiently large convective Mach numbers. Moreover, such waves are obvious in two-dimensional numerical simulations, but not so in the three-dimensional case. Experimentally, they have been observed in very severe circumstances, such as in counterflows by Papamoschou (1995), and in mixing layers at high convective Mach number ($M_c \approx 1.7$) by Rossmann et al. (2002). Large eddy detection was performed by Dupont et al. (1999) at a convective Mach number of 0.62 to determine directly their convection velocity. They found that the convection velocity was close to the isentropic estimate, and therefore, in this case, the existence of shocks of significant strength was not likely. In the supersonic regime, at least at moderate convective Mach numbers, it appears that energy dissipation by shocks radiating into the outer flow is not an attractive scenario to explain the inhibition of mixing.

Another aspect of this question can be examined by considering the generation of noise by mixing layers. The production of noise by Mach waves or shocks requires energy, which is taken from the turbulent flow. Debiève et al. (2000) estimated the energy flux radiated by the acoustic waves in a mixing layer at $M_c = 0.62$ by measuring the level of pressure fluctuations in the outer flow. They showed that this flux was less than 3% of the integral of production in a section. It was concluded that at these moderate convective Mach numbers, acoustic losses could not explain the decrease in the turbulence levels, and consequently the reduced spreading rate of supersonic mixing layers.

Finally, a comment can be made on the rather good agreement between the decrease of the growth rate and the decrease of the amplification rate in linear stability theory. An example, taken from Rossmann et al. (2002), was given in Figure 6.6. Many authors (Ragab and Wu, 1989; Sandham and Reynolds, 1990; Zhuang et al., 1990; Vreman et al., 1996) have noticed that the growth rate follows rather closely the amplification rate of the most unstable mode in linear analysis. Figure 6.6 shows that this is the case, at least up to $M_c \approx 1$. For larger Mach numbers the central mode is not the most important one and supersonic modes become more important. Of course, this does not mean that the growth of a mixing layer is a linear process. Probably the mechanisms leading to the linear spreading rate of the layer, although nonlinear, depend on

the primary development of the Kelvin-Helmholtz instability. Vreman et al. (1996) proposed another interpretation: they remarked that in their simulation and in their linear analyses, the pressure field structurally follows the same trend as in linear analysis at least up to $M_c \approx 0.6$, (which is at the onset of three-dimensional instabilities), and that consequently this can be related to the growth rate of the shear layer.

It can be concluded that the modification of the structure of pressure inside the turbulent shear layer is the key to explaining the observed behaviors, and that this can be parameterized in a first analysis by a convective Mach number. Two comments follow. First, we presented in Sections 6.3 and 6.4 the convective Mach number as an indicator of the organization of the pressure field in the external flows. We now propose that M_c can also characterize the pressure field in the shear layer itself. Second, the models used for the computation of compressible turbulent flows are often a pure extrapolation of incompressible models. The present discussion, however, shows clearly that the level of turbulence is affected by high speeds, and that there is a direct action on turbulent fluxes which cannot be reduced to incompressible, variable density problems. Moreover, the analysis shows that model adaptation should not be made by changing the dissipation rate or the pressure divergence terms, as hypothesized in other attempts at modeling. In terms of practical applications, it is fortunate that the anisotropy of turbulence seems hardly affected by compressibility. Possible adaptations include the modification of the pressure strain terms in Reynolds stress closures, or a direct sensitizing of the eddy viscosity in two-equation models. In this case, because the convective Mach number is not a local parameter, a gradient Mach number could be used. Finally, a set of accurate measurements of turbulence in well controlled conditions is still needed to provide unambiguous tests of these hypotheses.

6.11 Final Remarks

It appears that some further information on low-speed mixing layers is required to help clarify the global effects of compressibility. However, all the results presented in this chapter indicate that the properties of the large-scale eddies are consistent with the global features governing the turbulent transport, and that the convective Mach number concept, although it has a number of limitations, remains a robust concept for classifying the effects of compressibility.

As a final note, we see that the scalar concentration distributions calculated by Chen (Figure 1.12) indicate that considerable mixing still takes place within compressible mixing layers, despite the fact that the growth rate decreases with increasing Mach number. The increased three-dimensionality obviously acts to mix the flows effectively. There have been a number of attempts to increase the mixing layer growth, primarily by efforts to increase the degree of three-dimensionality in the flow. For example, Shau and Dolling (1989) used

vortex generators placed in the upstream boundary layer on the high-speed side to impose a spanwise distortion of the shear layer. Presumably, the vortex generators would be most effective if spaced so as to amplify the "naturally occurring" longitudinal vortices observed by Konrad (1977) in subsonic flows, but of course there is some question whether the same structure is present at high convective Mach number. Instead of vortex generators, Clemens and Mungal (1992b) used a swept shock, generated by a sidewall interaction, to produce kinks in the layer, and mixing was enhanced not so much by an increase in the shear layer growth rate as by an increase in the area of the interface between turbulent and nonturbulent fluid. Similarly, Poggie et al. (1992) used blowing in the direction of the velocity gradient, where the blowing strength varied in the spanwise direction, to kink the shear layer and increase its entrainment area. Similar blowing with constant strength across the shear layer produced only a deflection of the shear layer without enhancing mixing noticeably. This is in accord with the work of Shau and Dolling (1989) who showed that two-dimensional interactions with shocks produced shear layer deflections without enhancing mixing.

More recently, similar ideas were used by Naughton et al. (1997) to enhance mixing by using swirl in axisymmetric jets. Collin (2001) used small cross-jets to control mixing in compressible jets, with the conclusion of the importance of the increase of the area of turbulent/nonturbulent fluid interface.

Chapter 7

Boundary Layer Mean-Flow Behavior

7.1 Introduction

For incompressible flows, the most important parameter in the description of turbulent boundary layer behavior is the Reynolds number. Engineering applications cover an extremely wide range, and Reynolds numbers based on streamwise distance can vary from 10^5 to 10^9. Most laboratory experiments (and all DNS calculations) are performed at the lower end of this range, and to be able to predict the behavior at very high Reynolds numbers it is important to understand how turbulent boundary layers scale.

For compressible flows, the Mach number becomes an additional scaling parameter. Because of the no-slip condition, a significant Mach number gradient exists across the boundary layer at supersonic speeds, and a subsonic region persists near the wall, although the sonic line is located very close to the wall at high Mach number. A strong temperature gradient develops across the layer due to the high levels of viscous dissipation near the wall, exaggerating the variation in the Reynolds number that exists even in subsonic flows. Because the static temperature variation can be very large even in an adiabatic flow, a low-density, high-viscosity region exists near the wall. In turn, this leads to a skewed mass flux profile, a thicker boundary layer, and a region in which viscous effects are somewhat more important than at an equivalent Reynolds number in subsonic flow.

In Chapter 1 we introduced some of the distinguishing characteristics of turbulent boundary layers in supersonic flow. In particular, we discussed the role of temperature variations, and showed some examples of boundary layer profiles on adiabatic, isothermal, and cooled walls (Figures 1.1 and 1.2). It was clear that any comparisons between subsonic and supersonic boundary layers must take into account gradients in Mach number, as well as variations in fluid properties, which may be strong enough to lead to unexpected physical

phenomena. Intuitively, we expect to see significant dynamical differences between subsonic and supersonic boundary layers, but it appears that many of these differences can be explained by simply accounting for the fluid property variations that accompany the temperature variation, as would be the case in a heated incompressible boundary layer.

> The dominating factor in the compressible turbulent-boundary layer problem is apparently then the effect of high temperature on the velocity profile near the wall and therefore on the shear stress. This latter observation was first advanced by von Kármán in 1935 but has been somewhat neglected in favor of interpolation formulae or of elaborate generalizations of the mixing length hypothesis. (Part I of Coles (1953)).

This suggests a rather passive role for the density differences in these flows, most clearly expressed by Morkovin's hypothesis (see Chapter 5), where the dynamics of a compressible boundary layer are expected to follow the incompressible pattern closely, as long as the Mach number associated with the fluctuations remains small. We can interpret that conclusion to mean that the fluctuating Mach number M' remains small, where M' is the fluctuation of the instantaneous Mach number from its mean value, taking into account the fact that both the velocity and the sound speed vary with time. That is, for small fluctuations,

$$M' = M - \overline{M} = \overline{M}\left(\frac{u'}{\overline{U}} - \frac{T'}{2\overline{T}}\right).$$

If the *rms* value of the fluctuating Mach number approaches unity at any point, we expect direct compressibility effects such as local shocklets and pressure fluctuations to become important. If we take $M'_{rms} = 0.3$ as a threshold, we find that for zero pressure gradient adiabatic boundary layers at moderately high Reynolds numbers the freestream Mach number where compressibility effects become important for the turbulence behavior is about 4 or 5 (see Figure 7.1).

In this chapter we consider more fully the characteristics of the mean velocity and temperature distributions in zero pressure gradient, flat-plate boundary layers in steady supersonic flow, under conditions where Morkovin's hypothesis is expected to hold. The Favre averaged equations of motion for this case were derived in Chapter 3 by applying the usual thin shear layer approximations to the continuity, momentum, and energy equations (see Equations 3.24 through 3.26). We are primarily concerned with scaling laws because the equations of motion, even for thin shear layers, cannot be solved without further approximations. Scaling laws are useful because they allow interpolation (and sometimes extrapolation) of our existing knowledge to cases where we have no previous experience. For example, studies of low Reynolds number, incompressible turbulent boundary layers have given a good deal of insight into the

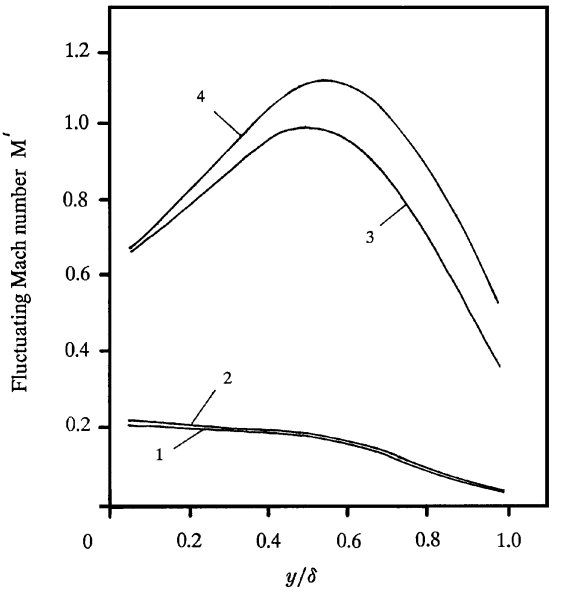

Figure 7.1. Fluctuating Mach number distributions (*rms* value, estimated using SRA and Morkovin's hypothesis). Flow 1: $M_e = 2.32$, $Re_\theta = 4,700$, adiabatic wall (Eléna and Lacharme, 1988); Flow 2: $M_e = 2.87$, $Re_\theta = 80,000$, adiabatic wall (Spina and Smits, 1987); Flow 3: $M_e = 7.2$, $Re_\theta = 7,100$, $T_w/T_r = 0.2$ (Owen and Horstman, 1972); Flow 4: $M_e = 9.4$, $Re_\theta = 40,000$, $T_w/T_r = 0.4$ (Laderman and Demetriades, 1974). (Figure from Spina et al. (1994). Reproduced, with permission, from Annual Reviews, Inc.)

behavior of wall-bounded turbulent flows. The mean flow, the turbulence distributions and their statistical properties have been extensively documented. Furthermore, the nature of the small- and large-scale motions has been studied in detail, and although there is still widespread disagreement on the details of the turbulence dynamics, some consensus on the kinematic behavior seems to be building (see, for example, Robinson (1991a,b)). If we understood the basic scaling laws that apply to boundary layers, we could extend this knowledge to describe flows at much higher Reynolds number, and at supersonic and hypersonic Mach numbers. Scaling laws give a unifying framework to our knowledge, and their derivation and validation is one of the important tasks of turbulence research.

Scaling laws require a set of characteristic scales. In deriving the thin shear layer equations, it was assumed that the shear layer grows slowly, so that all derivatives in the streamwise direction (with the exception of the pressure gradient) are at least an order of magnitude smaller than the derivatives in the

direction normal to the wall, and that the turbulence Mach number M_t (and M') is small. By assuming a set of characteristic length and velocity scales, an order-of-magnitude analysis is then used to simplify the full equations. In order to consider scaling laws, however, we need to examine the characteristic scales in more detail. For boundary layers, there are at least two distinct sets of scales, one for the *inner* flow near the wall where viscous stresses are important, and one for the *outer* flow where the turbulent stresses dominate and viscous stresses can be neglected. We need to consider both incompressible and compressible flow scaling, to try to distinguish between Reynolds number and Mach number dependencies. In general, we assume that Reynolds number variations carry over unchanged from incompressible to compressible flows. This assumption is not entirely justified, because changes in Mach and Reynolds numbers are closely coupled (for example, temperature gradients affect both parameters directly), and care must be taken in interpreting the data. By considering subsonic and supersonic boundary layers together, we also provide a bridge between the incompressible and compressible flow communities. The discussion given here extends the work reported by Fernholz and Finley (1980) and Dussauge et al. (1996). We generally ignore the differences between mass averaged and Reynolds averaged quantities. In all of the remaining chapters, primes denote fluctuating quantities, and the overbars on the mean velocities have been dropped for simplicity.

7.2 Viscous Sublayer

In the viscous sublayer of a compressible boundary layer, the proper velocity scale is $u_\tau\sqrt{\rho_w/\rho}$ and the length scale is ν_w/u_τ, but an order of magnitude analysis leads to the same conclusion as in low-speed flows and as given in Section 3.3 (Equations 3.21 and 3.22). The usual derivation of the velocity distribution in the inner region of a flat plate boundary layer is based on the assumptions:

(1) That the convective terms in the equation of motion are small compared with the viscous term;

(2) That the total stress $\tau = \mu\,(\partial\bar{u}/\partial y) - \bar{\rho}\overline{u'v'}$ is constant in the inner region and equals τ_w;

(3) Morkovin's hypothesis holds, in that the structure of the turbulence does not change significantly due to compressibility effects.

We need a temperature-velocity relationship, and we assume the quadratic profile originally due to Walz (1966) (Equation 5.28):

$$\frac{T}{T_e} = \frac{T_w}{T_e} + \frac{T_r - T_w}{T_e}\left(\frac{u}{u_e}\right) - r\frac{(\gamma-1)}{2}M_e^2\left(\frac{u}{u_e}\right)^2, \tag{7.1}$$

which holds for zero pressure gradient flow. The recovery factor r is given by:

$$\frac{T_r - T_w}{T_e} = 1 + r\frac{(\gamma-1)}{2}M_e^2 - \frac{T_w}{T_e} = -\frac{q_w u_e P_w}{C_p \tau_w T_e},$$

where $P_w = (C_p\mu/k)_w$. Equation 7.1 may also be written as:

$$\frac{T}{T_w} = 1 - P\frac{T_\tau}{T_w}u^+ - rM_\tau^2\frac{(\gamma-1)}{2}u^{+2}, \tag{7.2}$$

where $u^+ = u/u_\tau$, $M_\tau = u_\tau/\sqrt{\gamma R T_w}$ is the friction Mach number, $T_\tau = q_w/\rho_w C_p u_\tau$ is the friction temperature, $u_\tau = \sqrt{\tau_w/\rho_w}$ is the friction velocity, and P is the molecular Prandtl number.

The no-slip condition requires that u, v, u', and v' must approach zero as the wall is approached. If it is assumed that in this viscous sublayer the molecular shear stress $\mu\,(\partial u/\partial y)$ is large compared with the Reynolds shear stress $-\bar{\rho}\overline{u'v'}$, then:

$$\frac{\partial}{\partial y}\left(\mu\frac{\partial u}{\partial y}\right) = -\frac{dp}{dx}, \tag{7.3}$$

because the convective terms become very small as the wall is approached. That is, at the wall, the pressure gradient is balanced by the viscous stress. For a zero pressure gradient flow, the stress is constant in the near-wall region and equal to the skin friction τ_w. Hence,

$$\mu\frac{\partial u}{\partial y} = \tau_w. \tag{7.4}$$

This result for the inner layer is the same for compressible and incompressible flows, to the extent that we can ignore the differences between mass averaged and Reynolds averaged quantities.

When the flow is incompressible, Equation 7.4 can be integrated directly so that

$$u = \frac{\tau_w}{\mu}y, \tag{7.5}$$

which is usually written in the form:

$$\frac{u}{u_\tau} = \frac{y u_\tau}{\nu}. \tag{7.6}$$

Here, ν/u_τ represents the inner layer or viscous length scale. Equation 7.6 is also written as $u^+ = y^+$, where the superscript $(^+)$ denotes normalization with inner variables (u_τ for velocity and ν/u_τ for length). So, for a zero pressure gradient incompressible flow, the velocity near the wall varies linearly with distance from the wall. This result continues to hold in flows with pressure gradients as long as the flow is not accelerating or decelerating very rapidly see also Tennekes and Lumley (1972)). The region where the velocity profile

follows Equation 7.6 is called, naturally enough, the linear region of the viscous sublayer.

In high-speed compressible flows, the increased dissipation rate in the viscous sublayer raises the local temperature so that at a fixed Reynolds number the sublayer thickness increases with increasing Mach number. The same effect is responsible for the observed increase in the thickness of the laminar boundary layer at high Mach numbers (see, for example, van Driest (1951)). Because the temperature affects the viscosity, Equation 7.4 now reads:

$$\frac{\partial u}{\partial y} = \frac{u_\tau^2}{\nu_w} \left(\frac{T_w}{T} \right)^\omega \tag{7.7}$$

in which the variation of the viscosity with temperature was assumed to be given by:

$$\frac{\mu}{\mu_w} = \left(\frac{T}{T_w} \right)^\omega . \tag{7.8}$$

Using the quadratic form of the temperature distribution given by Equation 7.1 (we assume $dp/dx = 0$), Equation 7.7 yields:

$$\frac{U^s}{u_\tau} = \frac{y u_\tau}{\nu_w}, \tag{7.9}$$

where the transformed mean velocity in the sublayer U^s is defined by

$$U^s = \int_0^U \left(\frac{T}{T_w} \right)^\omega du. \tag{7.10}$$

We see that the transformed velocity U^s has a linear distribution similar to that seen for the velocity in the viscous sublayer of an incompressible turbulent boundary layer, and to which it reduces for $T = T_w$. Also, with $\omega = 1$:

$$U^s = u \left[1 + \tfrac{1}{2} a \frac{u}{u_e} - \tfrac{1}{3} b^2 \left(\frac{u}{u_e} \right)^2 \right], \tag{7.11}$$

in which

$$a = \left(1 + r \, \frac{\gamma - 1}{2} M_e^2 \right) \frac{T_e}{T_w} - 1 \tag{7.12}$$

and

$$b^2 = r \, \frac{\gamma - 1}{2} M_e^2 \frac{T_e}{T_w}. \tag{7.13}$$

For air, $\omega \neq 1$, but it is close to one (=0.76) and the trends given by Equations 7.11 to 7.13 are believed to constitute a good approximation.

7.3 Logarithmic Region

Farther from the wall, outside the viscous sublayer, the gradients of turbulent stresses become important but the convective terms remain small, so that, approximately:

$$\frac{\partial}{\partial y}\left(\mu\frac{\partial u}{\partial y} - \rho\overline{u'v'}\right) = \frac{\partial \tau}{\partial y} = \frac{dp}{dx}. \tag{7.14}$$

For a zero pressure gradient flow, we see that the total stress τ is constant in the near-wall region, and equal to the wall stress τ_w. For flows with an adverse pressure gradient ($dp/dx > 0$), the total stress will increase with distance from the wall, and for a favorable pressure gradient ($dp/dx < 0$) it will decrease with distance from the wall. However, if the pressure gradient is not too large and the wall stress not too small, then the total stress is still approximately constant for small distances from the wall.

7.3.1 Incompressible Flow

For incompressible flow, Prandtl (1933) argued that the viscosity and wall shear stress are the important parameters governing the inner, near-wall flow (including the linear part of the sublayer). That is, the velocity must have the following functional dependence:

$$u = f(y, \tau_w, \rho, \mu), \tag{7.15}$$

which simplifies to Equation 7.5 very close to the wall (note that Equation 7.5 is independent of density, whereas Equation 7.15 is not). Because of this asymptotic behavior, in particular that the convective terms are small in the near-wall region, there is little controversy over the mean-flow scaling in the inner region. Moreover, there is a great deal of experimental support for these conclusions.

In the outer layer, viscosity is less important, but the presence of the wall is still felt through the magnitude of the wall shear stress. Thus, von Kármán (1930) suggested that for subsonic flow the velocity defect $u_e - u$ should have the following functional dependence,

$$u_e - u = g(y, \delta, \tau_w, \rho). \tag{7.16}$$

As pointed out by Cousteix (1996), this argument may be flawed. In particular, the inner boundary condition on Equation 7.16 may depend on viscosity. For example, on a rough wall, this boundary condition depends on viscous scales. However, the same functional dependence may be assumed for the velocity gradient,

$$\frac{\partial u}{\partial y} = g'\left(y, \delta, \tau_w, \rho\right),$$

which suggests

$$u_e - u = g''(y, \delta, \tau_w, \rho) + C,$$

where C may depend on viscosity.

Using a different approach, Zagarola and Smits (1998a) argued that the outer layer velocity scale u_0 need not be the same as the inner velocity scale u_τ, although they should become proportional to each other at high Reynolds numbers. This argument permits the appearance of a power law, rather than a log-law in the mean velocity profile near the wall. Their pipe flow data, taken over a very wide Reynolds number range, support these notions, in that the region near the wall showed a power-law scaling (with a constant and exponent independent of the Reynolds number), and a logarithmic region appeared only at very high Reynolds numbers for distances sufficiently far from the wall. Although the differences between the power-law and the log-law representations were not large, they imply that viscous effects on the mean flow persist at distances from the wall greater than previously acknowledged. For pipe flows, u_0 was taken to be $u_{CL} - \langle u \rangle$, and u_{CL} is the centerline velocity and $\langle u \rangle$ is the bulk velocity. For boundary layers, they suggested that $u_0 = (\delta^*/\delta)u_e$ (Zagarola and Smits, 1998b), which has been shown to collapse the outer flow extremely well, over a wide range of pressure gradients (Castillo and George, 2000). Nevertheless, the distinctions between scaling on u_τ or on u_0 are rather fine, and require very accurate measurements over large Reynolds number ranges to become apparent. For the purposes of scaling boundary layers, especially in compressible flows where the data typically display large scatter, these distinctions are ignored, and we assume traditional scaling arguments continue to hold without change.

Accordingly, dimensional analysis of Equations 7.15 and 7.16 leads to

$$\frac{u}{u_\tau} = f\left(\frac{y u_\tau}{\nu}\right), \tag{7.17}$$

or

$$u^+ = f\left(y^+\right), \tag{7.18}$$

and

$$\frac{u_e - u}{u_\tau} = g\left(\frac{y}{\delta}\right), \tag{7.19}$$

or

$$u_e^+ - u^+ = g(\eta), \tag{7.20}$$

where $\eta = y/\delta$. Equation 7.17 is known as the *law-of-the-wall*, and is valid in the inner layer. Equation 7.19 is known as the *defect law* (similar to Coles's concept of a law-of-the-wake), and is valid in the outer layer. Rotta (1950, 1962) suggested that the defect law should be written as

$$\frac{u_e - u}{u_\tau} = g\left(\frac{y}{\delta}, \frac{u_\tau}{u_e}\right), \tag{7.21}$$

where u_τ/u_e indicates a weak or vanishing Reynolds number dependence. The function g in Equation 7.20 has been found to depend strongly on the pressure gradient, whereas the function f in Equation 7.18 is effectively invariant for boundary layers with adverse and slightly favorable pressure gradients (see Patel (1965)), although the extent of the region over which this scaling holds may shrink considerably.

Millikan (1938) proposed that at large enough Reynolds numbers (where the u_τ/u_e dependence is assumed to vanish), there may exist a region of overlap where both the inner and outer similarity laws are simultaneously valid. In this overlap region, where $\nu/u_\tau \ll y \ll \delta$, the velocity gradients given by Equations 7.17 and 7.19 match, so that:

$$y\frac{\partial u^+}{\partial y} = y^+\frac{\partial f}{\partial y^+} \qquad \text{and} \qquad y\frac{\partial u^+}{\partial y} = -\eta\frac{\partial g}{\partial \eta}.$$

Hence,

$$y^+\frac{\partial f}{\partial y^+} = -\eta\frac{\partial g}{\partial \eta} = \frac{1}{\kappa}.$$

This relationship should be valid for $y^+ \to \infty$ and $\eta \to 0$, with a finite, nonzero, constant value of κ. We can now obtain two forms for the (incompressible) law-of-the-wall and defect law in the overlap region:

$$\frac{u}{u_\tau} = \frac{1}{\kappa}\ln\left(\frac{yu_\tau}{\nu}\right) + C, \tag{7.22}$$

and

$$\frac{u_e - u}{u_\tau} = -\frac{1}{\kappa}\ln\left(\frac{y}{\delta}\right) + C', \tag{7.23}$$

where C, C', and κ (called von Kármán's constant) may or may not be Reynolds number dependent. Thus, the velocity profile in the overlap region is logarithmic, and the overlap region is often referred to as the *logarithmic region*.

For the inner layer representation of the log law (Equation 7.22, it is often assumed that the constants are independent of Reynolds number. The von Kármán constant κ is usually taken to be around 0.40, but many different values have been reported in the literature (see Table 7.1). Recently there has been a trend for the boundary layer values to diverge from the pipe flow values, but because a decreasing value of κ is usually associated with a decreasing value of C, the quality of the fit to the data in the overlap region does not vary dramatically, at least at moderate Reynolds numbers, so that in practice small differences in the constants do not have a major impact on the interpretation of the data. This is illustrated in Figure 7.2, where it is shown that for all published values of κ and C the differences in u/u_τ are less than about ± 0.5 over the range $100 \le y^+ \le 10,000$. Here, for purposes of comparison, we adopt the values of 0.40 and 5.1 for κ and C, respectively.

Authors	κ	C	Flow
Coles (1956)	0.40	5.10	Boundary layer
Coles (1962)	0.41	5.0	Boundary layer
Huffman and Bradshaw (1972)	0.41	5.0	Boundary layer
de Brederode and Bradshaw (1974)	0.41	5.2	Boundary layer
Österlund et al. (2000)	0.38	4.10	Boundary layer
Patel (1965)	0.418	5.45	Pipe
Zagarola and Smits (1998a)	0.436	6.15	Pipe
McKeon et al. (2004)	0.421	5.60	Pipe

Table 7.1. Published values of the constants in Equation 7.22. Note that the values given by Zagarola and Smits (1998a) are superseded by the values derived by McKeon et al. (2004).

Before proceeding, we note that the constants of integration, C and C', depend on the inner limit of the integration. For example,

$$C = \frac{u_1}{u_\tau} - \frac{1}{\kappa} \ln \frac{y_1 u_\tau}{\nu}, \tag{7.24}$$

where the suffix 1 indicates the boundary condition at the inner limit of validity of the logarithmic region. Duncan et al. (1970) point out that this inner limit is Reynolds number dependent, and therefore C and C' must also be Reynolds number dependent. Smith (1994) noted that the traditional inner and outer scaling laws cannot both be Reynolds number independent. For example, Equations 7.22 and 7.23 give:

$$C' = -C + \sqrt{\frac{2}{C_f}} - \frac{1}{\kappa} \ln \left(\frac{\delta u_\tau}{\nu} \right). \tag{7.25}$$

Because C_f and δ^+ are both Reynolds number dependent, it is likely that C or C', or C and C' are functions of the Reynolds number. If C and C' are assumed to be constant, C_f and δ^+ must have a very specific relationship, namely that $\sqrt{2/C_f} - (1/\kappa)\ln(\delta^+) = \text{constant}$. The data do not support this relationship: if C is a constant, C' is not, and vice versa. Consequently, if the law-of-the-wall given by Equation 7.22 is universal, then the defect law given by Equation 7.23 is not. Smith (1994) suggested that this may explain the slight Reynolds number dependence seen in the data when the logarithmic region

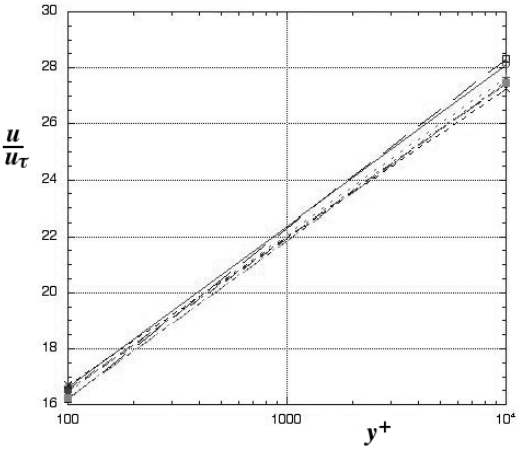

Figure 7.2. Log laws wih different constants, as given in Table 7.1.

is shown using outer scaling. Alternatively, it could indicate the discrepancy between the inner and outer velocity scales at lower Reynolds numbers, as suggested by Zagarola and Smits (1998a).

The velocity profile similarity in the overlap region is commonly indicated using either Equations 7.22 or 7.23. However, the velocity in the overlap region is in fact *independent* of the inner and the outer length scales, and the most useful way to express the velocity behavior is in terms of its gradient. That is,

$$\frac{\partial u}{\partial y} = \frac{\sqrt{\tau_w/\rho}}{\kappa y} = \frac{u_\tau}{\kappa y}. \tag{7.26}$$

Actually, the scaling of the entire mean-velocity profile is best expressed in terms of the mean-velocity gradient $\partial u/\partial y$. That is, $\partial u/\partial y$ in the near-wall region scales with a length scale ν/u_τ and in the outer region the length scale is δ. In the overlap region, the length scale becomes the distance from the wall y. The velocity scales for the inner and outer regions of the incompressible boundary layer are assumed to be the same, and given by u_τ.

Note that the physical boundary layer thickness δ is experimentally ill-defined (this is especially true in supersonic flows; see Fernholz and Finley (1980)), and for scaling purposes it probably ought to be replaced by a well-defined integral thickness, such as the Clauser or Rotta thickness:

$$\Delta = \int_0^\infty \frac{u_e - u}{u_\tau} dy = \delta^* \sqrt{\frac{2}{C_f}}, \tag{7.27}$$

where δ^* is the incompressible displacement thickness.

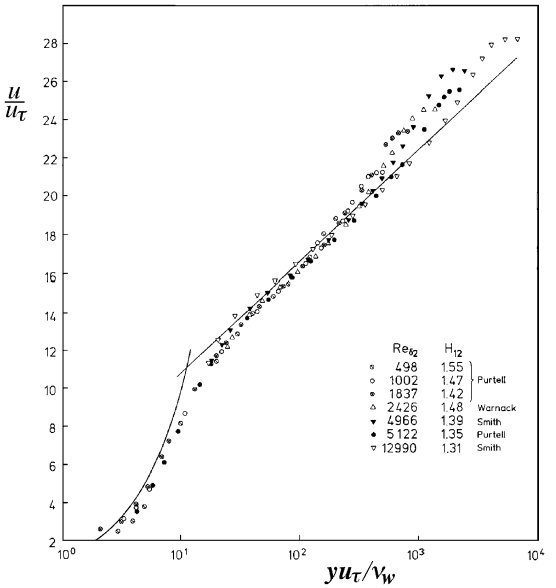

Figure 7.3. Development of the mean velocity in inner layer scaling at low to medium Reynolds numbers. The line is Equation 7.22 with $\kappa = 0.40$ and $C = 5.1$. (Figure from Fernholz and Finley (1996). Reprinted with permission from Elsevier Science Ltd., Oxford, England.)

Fernholz and Finley (1996) recently presented velocity profile data for zero pressure gradient incompressible boundary layers over a wide range of Reynolds numbers. The results are shown in inner layer scaling in Figures 7.3 to 7.5. Over the whole Reynolds number range, the agreement with Equation 7.22 is excellent. Small departures are evident but appear to relate more to differences between investigators than to variations with Reynolds number.

The data are displayed using outer layer scaling in Figures 7.6 to 7.8, using the Rotta thickness as the outer layer length-scale. The data collapse is impressive throughout. Over nearly two decades (for $Re_\theta \geq 2500$), Reynolds number effects are not detectable within the scatter of the data. For the lower Reynolds numbers, the outer velocity scale u_0 suggested by Zagarola and Smits (1998a) does a better job, as shown by Zagarola and Smits (1998b). Further support for the "universal" outer region similarity at higher Reynolds numbers is provided by, for instance, Rotta (1950) and Coles (1962), and by the agreement with transformed supersonic boundary layer profiles found in Fernholz and Finley (1980), where similar low Reynolds number deviations were also observed.

We have already considered mixing length concepts briefly (see, for exam-

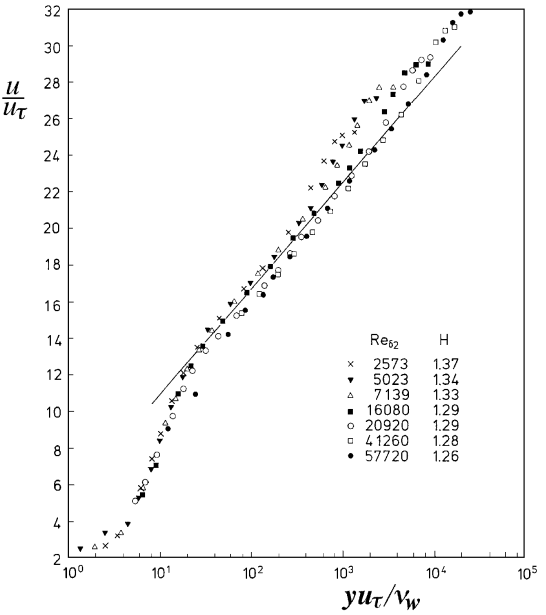

Figure 7.4. Development of the mean velocity in inner layer scaling for medium Reynolds numbers. Data from Bruns et al. (1992) and Nockemann et al. (1994). The line is Equation 7.22 with $\kappa = 0.40$ and $C = 5.1$. (Figure from Fernholz and Finley (1996). Reprinted with permission from Elsevier Science Ltd., Oxford, England.)

ple, Section 5.5 and Chapter 6), but before going on to discuss the scaling of compressible boundary layers it is useful to expand these ideas further. Launder and Spalding (1972) noted that Prandtl's mixing length hypothesis has two distinct parts. First, the turbulent friction is assumed to be proportional to the velocity gradient, with a coefficient of proportionality given by μ_t, the turbulent viscosity or eddy viscosity. By analoguey with the kinetic theory of gases, and the concept of molecular viscosity, μ_t is assumed to be proportional to the product of the density, a turbulence velocity scale, and a mixing length ℓ_m. Second, the turbulence velocity scale is assumed to be proportional to the mixing length times the velocity gradient. Hence,

$$-\rho\overline{u'v'} = \rho\mu_t\frac{\partial u}{\partial y} = \rho\,\ell_m^2\,\frac{\partial u}{\partial y}\left|\frac{\partial u}{\partial y}\right|. \tag{7.28}$$

If either μ_t or ℓ_m is known, the x-momentum equation is closed, and it may be solved. A straightforward application of μ_t to three-dimensional flows gives:

$$-\bar{\rho}\,\widetilde{u_i'u_j'} + \tfrac{2}{3}\bar{\rho}\,\tilde{k}\,\delta_{ij} = \mu_t\left(\frac{\partial\tilde{u}_i}{\partial x_j} + \frac{\partial\tilde{u}_j}{\partial x_i} - \tfrac{2}{3}\frac{\partial\tilde{u}_k}{\partial x_k}\delta_{ij}\right). \tag{7.29}$$

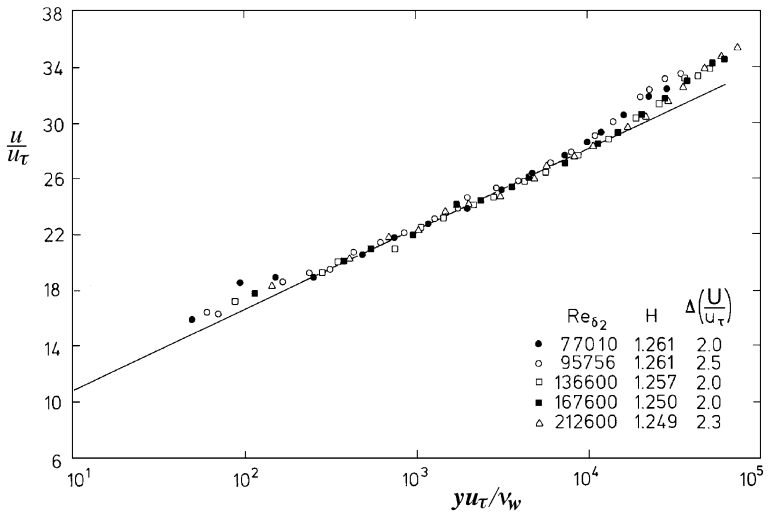

Figure 7.5. Mean velocity profiles in inner layer scaling at high Reynolds numbers. Data from Winter and Gaudet (1973) ($M_e = 0.20$). The line is Equation 7.22 with $\kappa = 0.40$ and $C = 5.1$. (Figure from Fernholz and Finley (1996). Reprinted with permission from Elsevier Science Ltd., Oxford, England.)

The shortcomings of these concepts have been well documented (see, for example, Launder and Spalding (1972) and Cebeci and Bradshaw (1977)). Briefly, Equation 7.29 implies that for parallel, two-dimensional shear flows the magnitude of the turbulence is isotropic; that the shear stress is zero where the mean flow velocity has a maximum or minimum (this contradicts the experimental evidence for wall jets and asymmetric channel flows and wakes; see, for example, Hanjalić and Launder (1972)), and that the turbulence depends only on the local mean velocity gradients (which excludes the possibility of any history or convective effects).

The strength of the mixing-length argument is that it is functionally correct, in that ℓ_m must be proportional to y in the logarithmic region and proportional to δ in the outer layer (Cebeci and Bradshaw, 1977). From its definition, we see that in the logarithmic region, $\ell_m = \kappa y$, and by experiment we find that in the outer flow ℓ_m is approximately equal to 0.085δ (Cousteix, 1989). These aspects of mixing length and eddy viscosity concepts make them a useful starting point for many scaling arguments (as in the next section, for example).

7.3.2 Compressible Flow

When the mean velocity in a supersonic boundary layer is plotted as u/u_e versus y/δ, the profile appears qualitatively similar to that of an incompressible

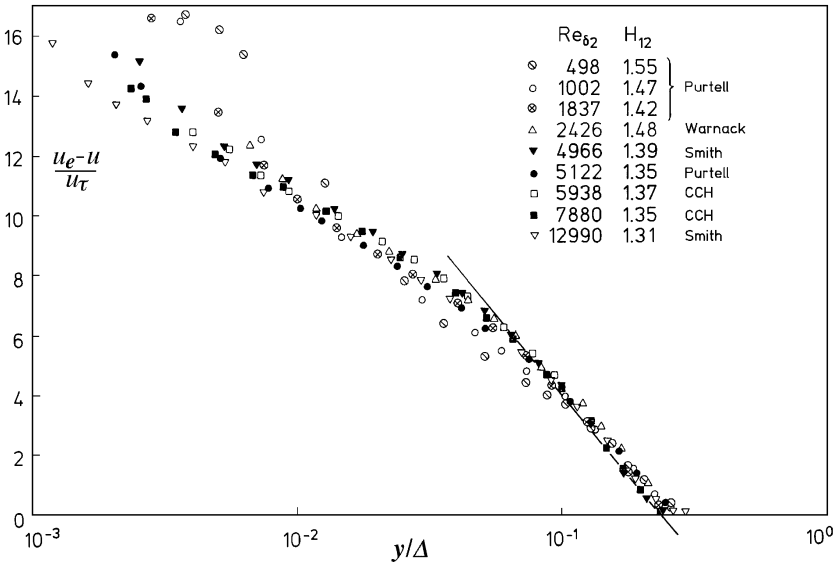

Figure 7.6. Development of the mean velocity in outer layer scaling at low to medium Reynolds numbers. The line is Equation 7.43. (Figure from Fernholz and Finley (1996). Reprinted with permission from Elsevier Science Ltd., Oxford, England.)

flow. However, when the velocity is replotted in classic inner or outer layer coordinates, as described above, the velocity does not follow the incompressible scaling laws. We show that a modified scaling accounting for the fluid property variations collapses much of the compressible mean velocity data on the "universal" incompressible distribution.

Inner Layer

If it is assumed that Prandtl's mixing length theory is also valid for the inner region of the compressible turbulent boundary layer (where viscous stresses are negligible), Equation 7.28 gives:

$$\frac{\partial u}{\partial y} = \frac{\sqrt{\tau_w/\rho}}{\kappa y}, \tag{7.30}$$

where it is assumed that the mixing length is given by κy, as in subsonic flows, and the Reynolds shear stress scales according to Morkovin; that is, $-\overline{u'v'} = \tau_w/\rho$. Although this result is identical to the result for incompressible flows given by Equation 7.26, in compressible flows the density varies with distance from the wall. Cebeci and Bradshaw (1984) argued that a full similarity analysis indicates that T/T_τ, M_τ, and γ should be included in the scaling

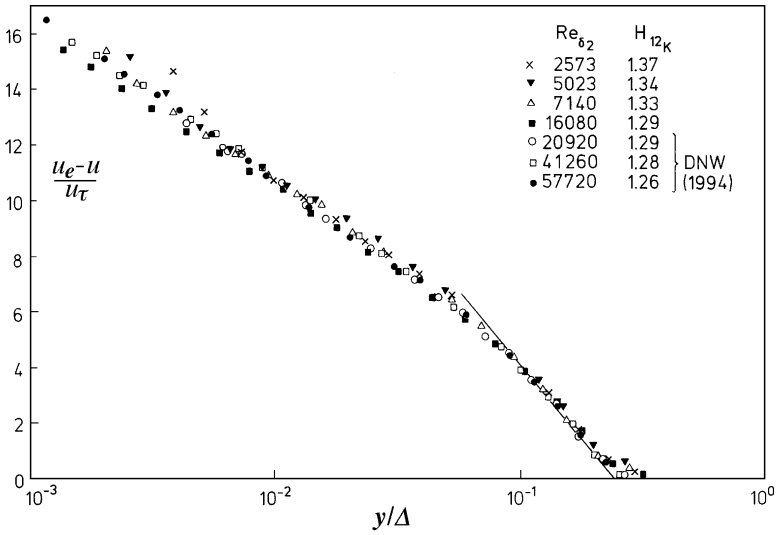

Figure 7.7. Mean velocity profiles in outer layer scaling for medium Reynolds numbers. Data from Bruns et al. (1992) and Nockemann et al. (1994). The line is Equation 7.43. (Figure from Fernholz and Finley (1996). Reprinted with permission from Elsevier Science Ltd., Oxford, England.)

for the velocity and temperature gradients. As they point out, however, the first two parameters represent sources of density fluctuations, and as long as the effect of density fluctuations on the length and velocity scales are small, these can be neglected. Likewise, the assumption that turbulence processes are little affected by density fluctuations implies that γ, which is a measure of the difference between adiabatic and isothermal processes, would also have a negligible effect.

Because the pressure is constant in the wall-normal direction, we have, for a perfect gas:

$$\frac{\partial u}{\partial y} = \frac{u_\tau}{\kappa y}\sqrt{\left(\frac{T}{T_w}\right)}. \tag{7.31}$$

By using Equation 7.1 to substitute for the temperature ratio in Equation 7.31, we obtain

$$\frac{U^{**}}{u_\tau} = \frac{1}{\kappa}\ln\frac{y u_\tau}{\nu_w} + F, \tag{7.32}$$

where

$$U^{**} = \int_{u_1}^{u}\sqrt{\frac{T_w}{T}}\,du, \tag{7.33}$$

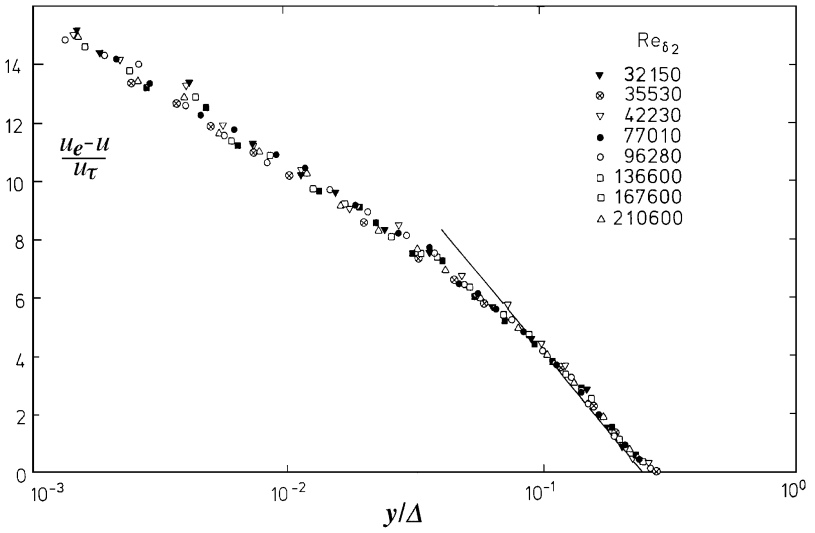

Figure 7.8. Development of the mean velocity in outer layer scaling at high Reynolds numbers. Data from Winter and Gaudet (1973) ($M_e = 0.20$). The line is Equation 7.43. (Figure from Fernholz and Finley (1996). Reprinted with permission from Elsevier Science Ltd., Oxford, England.)

and

$$U^{**} = \frac{u_e}{b}\sin^{-1}\left(\frac{2b^2(u/u_e) - a}{\sqrt{(a^2+4b^2)}}\right) + \frac{u_e}{b}\sin^{-1}\left(\frac{a}{\sqrt{(a^2+4b^2)}}\right). \tag{7.34}$$

Fernholz (1969) pointed out that Equation 7.32 may be written instead as

$$\frac{U^*}{u_\tau} = \frac{1}{\kappa}\ln\frac{yu_\tau}{\nu_w} + C^*, \tag{7.35}$$

where

$$U^* = \frac{u_e}{b}\sin^{-1}\left[\frac{2b^2(u/u_e) - a}{\sqrt{(a^2+4b^2)}}\right] \tag{7.36}$$

and

$$C^* = \frac{1}{\kappa}\ln\frac{y_1u_\tau}{\nu_w} + \frac{u_e}{bu_\tau}\sin^{-1}\left[\frac{2b^2(u_1/u_e) - a}{\sqrt{(a^2+4b^2)}}\right].$$

Here U^* is defined in the same way as U^{**} (Equation 7.33). The parameters a and b are given by Equations 7.12 and 7.13, and the suffix 1 denotes a boundary condition at the lower end of the validity range of the log law. A comparison

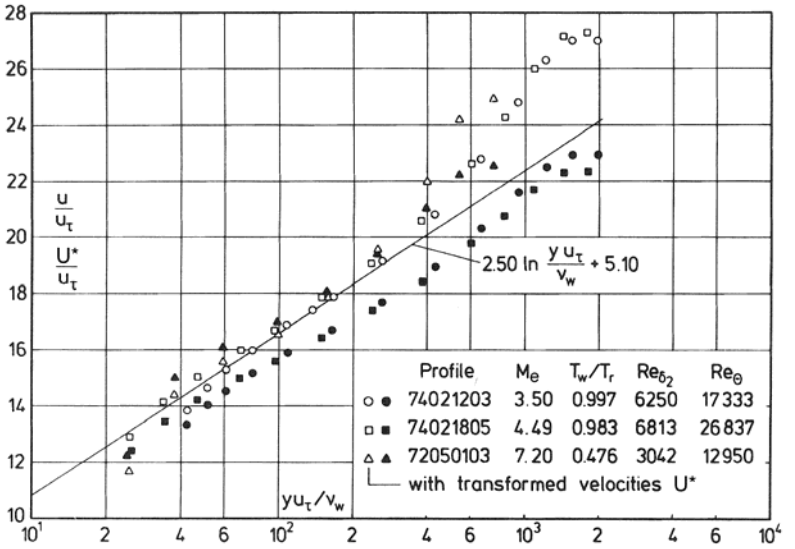

Figure 7.9. Log-linear plots of the velocity profile for a compressible turbulent boundary layer. Natural and transformed velocities (U^*). (From Fernholz and Finley (1980), where catalogue numbers are referenced. Reprinted with permission of the authors and AGARD/NATO.)

between measurements in transformed and untransformed coordinates is given in Figure 7.9.

For an adiabatic wall, T_w becomes the recovery temperature T_r, and $a = 0$. In this case, experiments show that u_1/u_e lies in the range $0.3 \leq u_1/u_e \leq 0.6$. Within this range, the term in $\sin^{-1}$ can be replaced by its argument for Mach numbers up to eight with a relative error of -4% or less. Then C^* reduces to

$$C^*_{ad} \approx \frac{u_1}{u_\tau} - \frac{1}{\kappa} \ln \frac{y_1 u_\tau}{\nu_w} \approx C, \tag{7.37}$$

that is, the same value as for the incompressible case (see Equation 7.24). This result was also confirmed by the measurements discussed by Fernholz and Finley (1980) and by general computational experience (Bushnell et al., 1976). Bradshaw (1977), on an empirical basis, proposed that the additive constant be a function of the friction Mach number M_τ. The scatter in the data is too large to make any firm conclusions regarding this suggestion, because the expected variations in the constant are rather small (when $M_\tau = 0.1$, we might expect $C^* = 6$, instead of 5). In any case, the departure of the additive constant from its low-speed value is probably small.

This mixing length approach can also be used to derive a temperature-

velocity relationship. If we consider the equation for the total enthalpy, and neglect the convective terms in the near-wall region (as we did in the momentum equation), then we obtain for the region of constant stress:

$$\frac{\partial q}{\partial y} = \tau_w \frac{\partial u}{\partial y}. \tag{7.38}$$

By assuming a mixing length for the turbulent heat flux, we obtain:

$$\frac{\partial T}{\partial y} = -\frac{q}{\rho C_p \kappa_H y \sqrt{\tau_w / /\rho}}, \tag{7.39}$$

where κ_H is von Kármán's constant for the thermal boundary layer. Equations 7.30, 7.38, and 7.39 give:

$$\frac{T}{T_w} = c_1 - \frac{\kappa}{\kappa_h}\frac{T_\tau}{T_w}\, u^+ - \frac{\kappa}{\kappa_h} M_\tau^2 \frac{(\gamma - 1)}{2}\, u^{+2} \tag{7.40}$$

where, on the basis of laminar flow analysis, we expect the constant c_1 to be fairly close to unity, although it may depend on T_w/T_τ, M_τ, and P (details of the analysis are given by Cebeci and Bradshaw (1984) and Rotta (1960).) The similarity with Equation 7.2 is clear. In fact, Fernholz and Finley (1980) concluded that velocity profiles in compressible turbulent boundary layers are well represented by Equation 7.35 within the limits set by the assumptions, and the simpler temperature-velocity relationship given by Equations 7.1 or 7.2 seems adequate for the purposes of velocity transformation. We see that the value of the ratio κ/κ_H must lie close to the value of the recovery factor, and/or the Prandtl number.

The first approach to this type of transformation was suggested by van Driest (1951) who derived a relationship similar to Equation 7.34 using $\ell_m = \kappa y$. He assumed Prandtl number unity and a recovery factor equal to one, and determined the constant C so that for the limit $M_e \to 0$ and $(T_w/T_e) \to 1$ the generally accepted relationship for the incompressible case should result. Van Driest's equation for the logarithmic law is then equivalent to Equation 7.34, with $r = 1$ in the definitions of a and b.

The differences likely to appear if this alternative transformation is used can be seen in Figure 7.10. Here three sets of profile data are plotted using Equation 7.36 with $r = 0.896$, and also Equation 7.36 with $r = 1.0$ (which then reduces to van Driest's transformation). The differences, although systematic, are small when compared to experimental error, particularly in finding the value of C_f. Given the uncertainties in the transformation approach and the experimental difficulties, there is little that can be said at the present time for any given set of log-law constants and their possible variation with Reynolds number or Mach number. It is equally difficult to say anything meaningful regarding the existence of power-law similarity, as proposed by George et al.

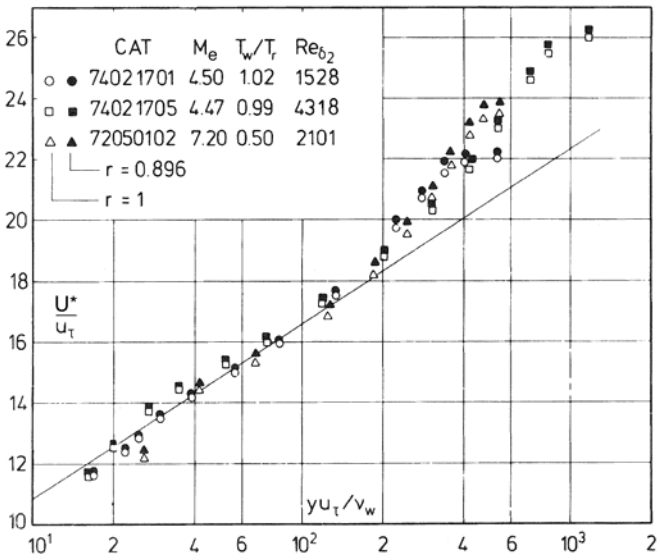

Figure 7.10. Comparison of velocity profiles transformed by using recovery factors of 1 and 0.896 (Mabey et al., 1974; Horstman and Owen, 1972). (From Fernholz and Finley (1980), where catalogue numbers are referenced. Reprinted with permission of the authors and AGARD/NATO.)

(1992), rather than log-law similarity, or the existence of a power-law region near the wall, as discussed in Section 7.3.1.

The empirical validity of Morkovin's hypothesis offers some support for the concept behind the van Driest transform (and similarly that by Fernholz and Finley) by suggesting that multilayer scaling holds in compressible boundary layers. Despite the assumptions inherent to the mixing length hypothesis, the underlying dimensional argument is sound as long as the length scale distributions in supersonic boundary layers follow the same behavior as in subsonic flows. In fact, experimental data taken over a wide Mach number range, with various wall-heating conditions and modest pressure gradients, show good agreement with incompressible data correlations when transformed according to van Driest (see, for example, Kemp and Owen (1972), Laderman and Demetriades (1974), Owen et al. (1975), and Watson (1977)). The systematic discussion given by Fernholz and Finley (1980) is particularly persuasive. Other than strong pressure gradients, the primary constraint is imposed by the fact that similarity requires large values of the Reynolds number, implying universality and independence from upstream history. Fernholz and Finley observe that the low Reynolds number region that begins to dominate the

inner layer at high Mach number may eventually cause the failure of the velocity scaling laws that the transformed data are expected to follow. Hopkins et al. (1972) attribute the poor performance of van Driest at $M_e = 7.7$ to the low Reynolds number of the flow, $Re_\theta \approx 5000$. This result can be compared to a successful application of van Driest at $M_e = 9.4$ and $Re_\theta \approx 37,000$ by Laderman and Demetriades. It also seems reasonable that the transformation suggested by Fernholz and Finley offers a slightly more accurate variation of van Driest, because the temperature distribution is based on a Prandtl number assumption ($0.7 \leq P_m \leq 1.0$) that is more realistic than van Driest's assumption of $P_t = P = 1$.

Three additional observations should be made on the velocity distribution in the constant stress region. First, the logarithmic velocity variation for supersonic flows was not obtained, as in subsonic flows, by constructing an overlap argument between the inner and outer layer scaling. It was derived instead by assuming that the velocity scale is given by the local kinematic stress ($= \sqrt{\tau_w/\rho}$) and that the length scale is the same as in subsonic flows ($= \kappa y$). The validity of these scaling arguments is substantiated by experiment, and it constitutes empirical support for Morkovin's hypothesis. Second, there is no law-of-the-wall, in that there is no single scaling law that describes the velocity distribution in the entire constant stress region because the viscous sublayer and the logarithmic zone use a different velocity transformation: the scaling in the viscous sublayer needs to account for the temperature-dependence of the viscosity, whereas in the fully turbulent zone the scaling needs to account for the temperature dependence of the density. Three, it should be pointed out (as we did for incompressible flows) that the similarity scaling of the compressible boundary layer mean velocity profile is most usefully expressed in terms of the scaling for the mean velocity gradient $\partial u/\partial y$. That is, $\partial u/\partial y$ in the near-wall region scales with a length scale ν_w/u_τ and a velocity scale $u_\tau \left(T_w/T\right)^{\omega/2}$. In the outer region the length scale is δ, and the velocity scale is $u_\tau \left(T/T_w\right)^{1/2}$. In the overlap region, the length scale becomes y, but the velocity scale is still $u_\tau \left(T/T_w\right)^{1/2}$. We see that the mean velocity profile in a compressible boundary layer scales with the same length scales used in scaling incompressible flows, but the velocity scale is modified by the variation in mean temperature.

Outer Layer

For compressible boundary layers, the similarity of the velocity profile in the outer region can be verified by plotting the velocity defect $(U_e^* - U^*)/u_\tau$ versus y/δ' where the characteristic length δ' is yet to be determined. Because the mean velocity approaches the velocity U_e asymptotically the boundary layer thickness is an ill-defined quantity, and Fernholz and Finley (1980) recommend instead the integral length Δ proposed by Rotta (1950) for incompressible

boundary layers (Equation 7.27). The only difficulty in using the reference length Δ is that the velocity profile and the skin friction must be known independently, which is not always possible. In terms of Δ, it is expected that for zero pressure gradient boundary layers the dimensionless velocity defect is given by

$$\frac{U_e^* - U^*}{u_\tau} = f\left(\frac{y}{\Delta^*}\right), \tag{7.41}$$

where

$$\frac{\Delta^*}{\delta} = \int_0^1 \frac{U_e^* - U^*}{u_\tau} d\left(\frac{y}{\delta}\right). \tag{7.42}$$

Equation 7.41 is the proposed defect law, or law-of-the-wake, for boundary layers in a compressible flow. There is no justification for this simple relationship other than verification by experiment. However, an evaluation of a large number of experiments in zero pressure gradient boundary layers, mainly along adiabatic walls, appears to support this particular scaling scheme. The data suggest the following semi-empirical relation (Fernholz, 1971):

$$\frac{U_e^* - U^*}{u_\tau} = -M \ln \frac{y}{\Delta^*} - N \tag{7.43}$$

with $M = 4.70$ and $N = 6.74$ (for the Reynolds number range $1.5 \times 10^3 \leq Re_\theta \leq 4 \times 10^4$). More elaborate relationships of the type:

$$\frac{U_e^* - U^*}{u_\tau} = -\frac{1}{\kappa} \ln \frac{y}{\delta} + \frac{\Pi}{\kappa} g'\left(\frac{y}{\delta}\right) \tag{7.44}$$

were suggested by Coles (1953), Stalmach (1958), Maise and McDonald (1968), and Mathews et al. (1970). Because different methods were used to specify the boundary layer thickness δ, and different transformations were used, there is still considerable uncertainty over the accuracy of this particular relationship (see also Section 7.4). Figure 7.11 illustrates this comparison.

Overlap Region

We noted earlier that the logarithmic velocity variation for supersonic flows was not obtained by using an overlap argument between the inner and outer layer scaling. However, the apparent success of the velocity transformation in the outer layer makes it possible to construct the following a posteriori overlap argument. For the inner region (excluding the viscous sublayer), we write:

$$U_i^* = \int_{u_1^+}^{u^+} \sqrt{\frac{T_w}{T}} du^+ = f\left(y^+\right) \tag{7.45}$$

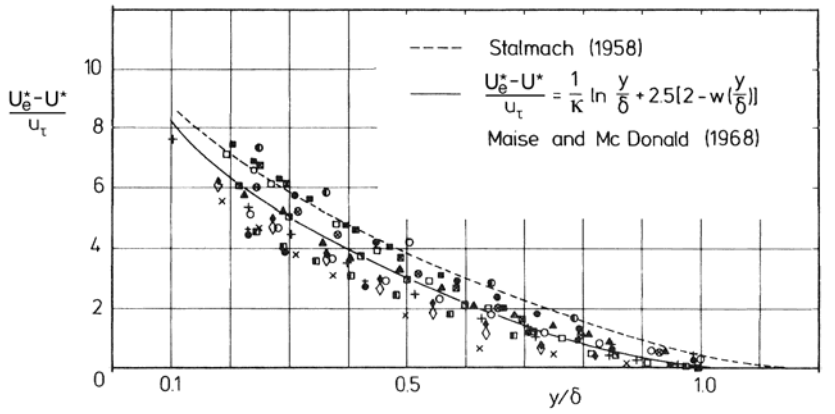

Figure 7.11. Mean velocity profiles in outer layer scaling for zero pressure gradient compressible turbulent boundary layers. (From Fernholz and Finley (1980). The key to the data is given in Fernholz (1969). Reprinted with permission of the authors and AGARD/NATO.)

and for the outer region:

$$U_o^* = \int_{u^+}^{u_e^+} \sqrt{\frac{T_w}{T}} du^+ = g(\eta). \tag{7.46}$$

Hence, in the region of overlap:

$$y^+ \frac{\partial f}{\partial y^+} = -\eta \frac{\partial g}{\partial \eta} = \frac{1}{\kappa},$$

as before. It follows that:

$$U_i^* = \int_{u_1^+}^{u^+} \sqrt{\frac{T_w}{T}} du^+ = \frac{1}{\kappa} \ln y^+ + C^* \tag{7.47}$$

and

$$U_o^* = \int_{u^+}^{u_e^+} \sqrt{\frac{T_w}{T}} du^+ = -\frac{1}{\kappa} \ln \eta + C'^*, \tag{7.48}$$

and the logarithmic forms are recovered.

Finally, we note that the temperature profile can also be expressed in a logarithmic form by using a turbulent total temperature T_i, similar to that suggested by Michel et al. (1969). That is,

$$\frac{T_i}{T_w} = 1 - P \frac{T_\tau}{T_w} u^+,$$

where T_τ is the friction temperature, and

$$T_i = T + \frac{P_m}{2C_p}u^2.$$

Hence

$$\frac{\partial T_i^+}{\partial y^+} = \frac{\partial u^+}{\partial y^+} = \frac{1}{\kappa y^+}\sqrt{\frac{T}{T_w}},$$

and

$$T_i^* = \int_{T_1}^{T_i} \sqrt{\frac{T}{T_w}}\, dT_i = \frac{1}{\kappa}\ln y^+ + C_T, \tag{7.49}$$

where $T_i^+ = -T_i/PT_\tau$, and C_T depends on the inner limit for the integration.

Perturbed Flows

So far, we have only considered flows that scale on local variables, generally called *self-preserving* flows. When a subsonic boundary layer is perturbed by changes in pressure gradient, wall curvature, and wall roughness, logarithmic regions are often still observed, at least over some distance from the wall (see, for example, Smits and Wood (1985)). The time scale for the relaxation of the velocity field downstream of a sudden perturbation, and for the adjustment to slow but continually changing conditions, is given to first order by the ratio of the turbulent kinetic energy to the rate of its production (Townsend, 1976). That is, the time scale varies as $(\partial u/\partial y)^{-1}$. The flow near the wall, therefore, adjusts relatively quickly, and a limited region of self-preserving flow may occur so that a significant region of the velocity profile still follows a logarithmic variation. Carvin et al. (1988) proposed that transformation concepts derived for self-preserving boundary layers can still be applied in the region where the velocity is logarithmic (where, by inference, the stress is constant; see Section 9.3). In that case, the constants in the log law are not known, but if the perturbation is not too strong it seems reasonable to assume that they are unchanged from their usual values.

7.4 Law-of-the-Wake

Coles (1956) proposed a scaling law for velocity profiles in subsonic turbulent boundary layers to include the outer layer as well as the overlap region. He found that the portion of the velocity profile that deviated from the logarithmic formula in all cases shared a similar form, resembling the velocity profile in a wake. Coles thus expressed the departure as a wake function and added it to Equation 7.22 to obtain

$$\frac{u}{u_\tau} = \frac{1}{\kappa}\ln\left(\frac{yu_\tau}{\nu}\right) + C + \frac{\Pi}{\kappa}w\left(\frac{y}{\delta}\right). \tag{7.50}$$

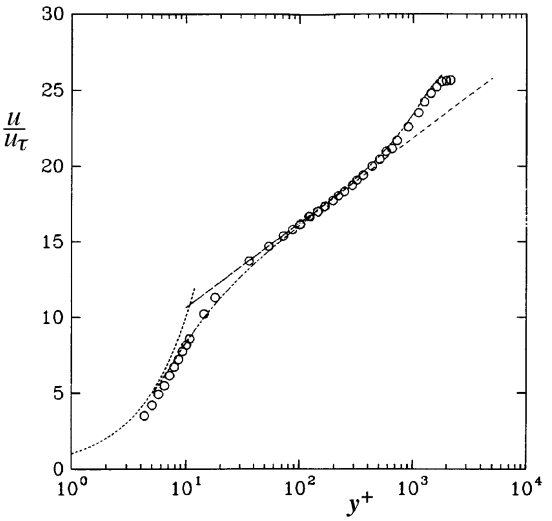

Figure 7.12. Example of a mean velocity profile at $Re_\theta = 5100$ from Purtell et al. (1981) scaled on inner variables, and compared to theoretical and empirical scaling-laws: o data; ---------- linear sublayer; -·-·-·-·- buffer region according to Spalding (1961); - - - - - - - - - logarithmic region (Equation 7.22); ——·-·-—·-·- Coles' law-of-the-wake (Equation 7.50). (Figure from Smith (1994), with the author's permission.)

The parameter Π is set by the maximum deviation of the velocity profile from the log law of Equation 7.22 and it indicates the strength of the wake. The function $w(y/\delta)$ is Coles's wake function $[= 2\sin^2(\frac{\pi}{2}\frac{y}{\delta})]$. Changes in the pressure gradient, and to a lesser extent in the Reynolds number, make themselves felt by changes in the value of the parameter Π, which can be found experimentally. The combined law-of-the-wall and law-of-the-wake describes the velocity profile from the inner edge of the log region all the way to the edge of the boundary layer. Figure 7.12 shows a typical velocity profile scaled with inner variables. The figure also shows the expected linear profile deep in the viscous sublayer, a line corresponding to the logarithmic overlap region, and Coles's wake function. The curve that is used to interpolate the velocity profile between the sublayer and the log region was derived by Spalding (1961), and this region is called the buffer layer.

From an extensive survey of the experimental data, Coles (1962) found that for $Re_\theta < 6000$, Π is a strong function of the Reynolds number, increasing from a value of zero at a Reynolds number of about 500 to an asymptotic value of about 0.55 at high Reynolds numbers (see Figure 7.13). He assumed that κ and C were constant, so that $\kappa = 0.41$ and $C = 5.0$, independent of the Reynolds

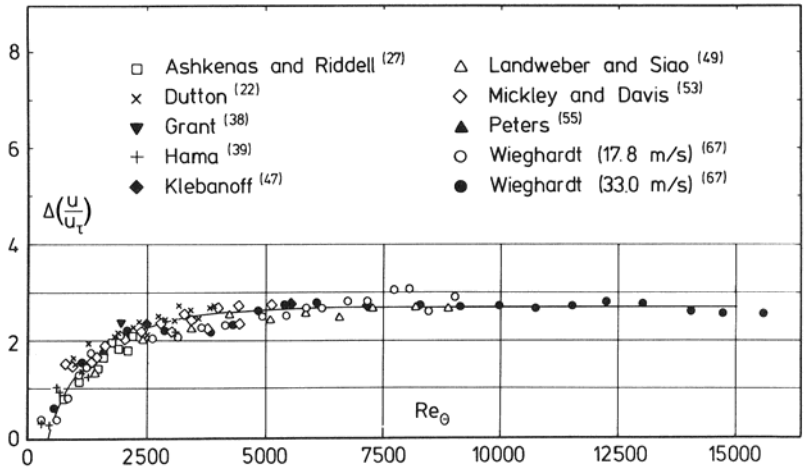

Figure 7.13. Strength of the wake component in zero pressure gradient equilibrium subsonic turbulent flow. Here, $\Delta\left(u/u_\tau\right) = 2\Pi/\kappa$. (From Fernholz and Finley (1980) after Coles (1962). Reprinted with permission of the authors and AGARD/NATO.)

number. In 1968, Coles reanalyzed the data and found the asymptotic value of Π to be about 0.6, as opposed to 0.55 in the earlier study, although the difference may be due to the particular fitting process used to determine u_τ (Erm et al., 1985).

Some more recent data are shown in Figure 7.14, including some very high Reynolds number cases. The low Reynolds number cases are probably affected by relatively high levels of freestream turbulence, and the trend to zero value at $Re_\theta = 500$ is not so clear (see also Smits et al. (1983b)). At high Reynolds numbers, the data suggest that the value of the wake strength may lie below that suggested by Coles on the basis of the Wieghardt and Tillmann (1944) data. Smith (1994) and Fernholz and Finley (1996) pointed out that slight variations in κ and C can have a significant effect on the inferred strength of the wake component because it is always found as the difference between two relatively large quantities. Spalart (1988), in evaluating his own low Reynolds number computational data, found "intolerably large discrepancies between wake strength values consequent upon small variations in the log law constants," and concluded that "very accurate measurements or simulations over a wide Re_θ range, as well as a strong consensus on the value of κ (at least two significant digits) will be needed before definitive results can be obtained for $\Delta\left(u/u_\tau\right)$." At very high Reynolds numbers, where u/u_τ near the edge of the layer takes large values, this problem becomes even more serious, so a high Reynolds number asymptotic value of Π (if one exists) is very difficult

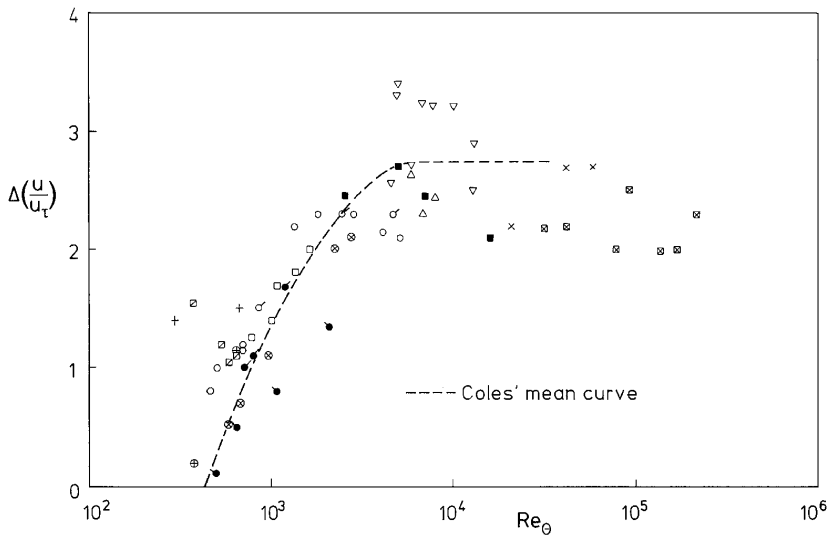

Figure 7.14. More recent data on the Reynolds number dependence of the wake strength in subsonic boundary layers. (Figure from Fernholz and Finley (1996), where the key to the data is given. Reprinted with permission from Elsevier Science Ltd., Oxford, England.)

to establish. Some recent work in pipe and boundary layer flows appears to be making progress towards this goal (Österlund et al., 2000; McKeon et al., 2004).

Libby and Visich (1959), Mathews et al. (1970), and Sun and Childs (1973) extended the Coles (1956) wall-wake velocity profile (Equation 7.50) to compressible turbulent boundary layers in adiabatic flows with pressure gradient and on isothermal walls with zero pressure gradient. A straightforward extension yields:

$$\frac{U^*}{u_\tau} = \frac{1}{\kappa} \ln \frac{y u_\tau}{\nu_w} + C^* + \frac{\Pi}{\kappa} w\left(\frac{y}{\delta}\right). \tag{7.51}$$

This amalgamated velocity profile agrees well with the data, although Cebeci and Bradshaw (1984) pointed out that it may simply be a consequence of the strong constraint on the wake profile, which has to have zero slope and zero intercept at $y = 0$, whereas the profile as a whole needs to have zero slope at $y = \delta$. Actually, Coles's wake function does not satisfy the latter constraint, although a number of modifications exist that do (see, for example, Sun and Childs (1976)). Also, the wake parameter Π and the boundary layer thickness δ can be adjusted to optimize the fit of Equation 7.51, and the success of this relationship does not necessarily prove the validity of the velocity transformation of the outer layer. In that respect, the success of Equation 7.43 is more

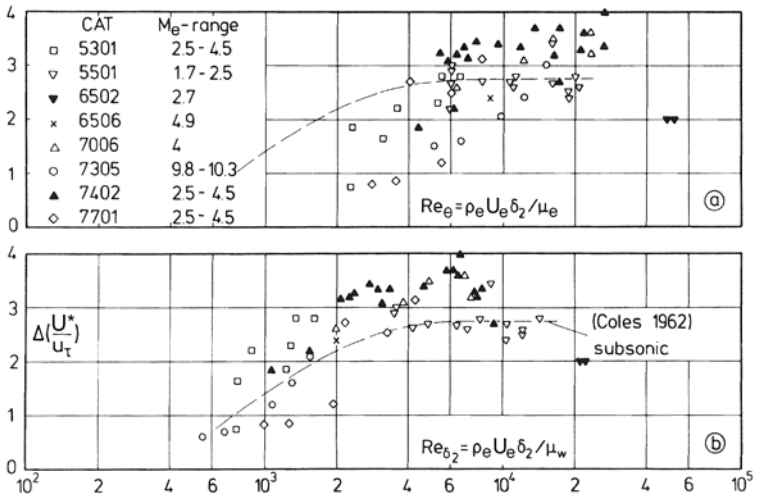

Figure 7.15. Strength of the wake component in compressible turbulent boundary layers. Experiments on adiabatic surfaces, with a defined origin (for example, the leading edge of a flat plate). (From Fernholz and Finley (1980), where catalogue numbers are referenced. Reprinted with permission of the authors and AGARD/NATO.)

persuasive, because the length scale is well defined and if Fernholz's values are accepted there are no adjustable constants.

As can be seen from Figure 7.13, the strength of the wake component of a subsonic zero pressure gradient turbulent velocity profile is a function of the Reynolds number. In the subsonic case the choice of the Reynolds number does not pose a problem, but in supersonic boundary layers there exist many more possibilities, including $Re_\theta = \rho_e u_e \theta / \mu_w$ and $Re_{\delta 2} = \rho_e u_e \theta / \mu_e$ (see also Section 1.2).[1] This ambiguity is well illustrated by a comparison of Figure 7.15a, which shows the development of the strength of the wake component with the Reynolds number Re_θ and Figure 7.15b, which shows the same data as a function of $Re_{\delta 2}$. In Figure 7.15a we see a decrease of the wake component at low Reynolds numbers similar to that observed in the subsonic case. We might expect that the strength of the wake component should be a function of outer edge quantities and should therefore be a function of Re_θ rather than $Re_{\delta 2}$. When plotted versus Re_θ, however, the decay of the wake component at low Reynolds numbers does not agree with the subsonic data trend.

Overall, the scatter of the data shown in Figure 7.15 is such that no ex-

[1] Re_θ and $Re_{\delta 2}$ are, of course, identical in incompressible flows.

plicit influence of the Mach number on the strength of the wake component can be identified. Coles (1962) found that for subsonic boundary layers three-dimensionality in the mean flow, a high freestream turbulence level and inappropriate tripping devices could cause severe anomolies in the strength of the wake component:

> Except possibly at very low Reynolds numbers, the effect of increased free-stream turbulence is to decrease the strength of the wake component. The amount of the decrease may also depend on Reynolds number and on the scale of the turbulence. As for boundary layers with tripping devices it was found that the strength of the wake component sometimes dropped below the normal or equilibrium value following a strong disturbance.

We would expect that similar considerations would apply to compressible boundary layers, and the experimental evidence considered by Fernholz and Finley (1980) supports this conclusion. Three-dimensional effects are commonly encountered in supersonic facilities due to inadequate contraction ratios upstream of the nozzle, and the development of streamwise vorticity in the boundary layers on the nozzle wall due to Taylor-Görtler instabilities associated with concave curvature. A common problem in facilities with rectangular working sections is the presence of lateral pressure gradients that develop because the boundary layers on the nozzle walls and the side walls experience different pressure gradient histories. This leads to a thickening of the boundary layer on the centerline of the side wall. In facilities with circular working sections, all disturbances associated with imperfections in the nozzle tend to focus on the centerline of the tunnel, which can lead to undesirable three-dimensional effects on models and flat plates placed in this region. Many older supersonic wind tunnels have high levels of freestream turbulence, and many facilities exist where the turbulence levels have not been measured (Beckwith et al., 1983; Task Group on Aeronautical research and Development, 1994). Tripping the boundary layer to promote transition and artificially thicken the boundary layer introduces strong upstream disturbances, and this must be done with great care because a boundary layer generally recovers very slowly from the effects of such disturbances. This is especially true at higher Mach numbers where transition can be difficult to promote and relatively large tripping devices are sometimes used. The long turbulence time scales observed at higher Mach numbers aggravate this problem (see Chapter 8).

Additional upstream history effects may also be important. In fact, there was considerable evidence presented in the 1960s and 1970s to show that the temperature-velocity relationships for flat plate flows and tunnel nozzle wall flows were different (see, for example, Spina et al. (1994)), which indicates the severity of the problem. Unfortunately, the strength of the wake at higher Reynolds numbers (Figure 7.16) are usually found by using experiments performed on the walls of the wind tunnel because it is difficult to achieve high

Reynolds numbers on a flat plate with a defined leading edge. The long-lasting influence of the pressure gradient and heat-transfer history experienced by the developing boundary layer may be reflected in the large scatter in the data. However, if a scatter of about ±20% of the wake strength is accepted then an average value of the wake strength of 2.75 ($=\Delta\,(u/u_\tau) = 2\Pi/\kappa$) can be assumed to exist for supersonic boundary layers at $Re_{\delta 2} > 6000$, which agrees with the wake strength for subsonic flow found by Coles (1962) in the range $6000 < Re_{\delta 2} < 15,000$.

Fernholz and Finley (1980) also note that for boundary layers with heat transfer, very few measurements are available, and no satisfactory conclusions can be drawn because of the scatter in the data.

7.5 Skin-Friction Relationships

For incompressible flows, a local friction law is obtained from Equation 7.50 by using the boundary condition $u = u_e$ at $y = \delta$, giving

$$\sqrt{\frac{2}{C_f}} = \frac{1}{\kappa} \ln \left(Re_\delta \sqrt{\frac{C_f}{2}} \right) + C + \frac{2\Pi}{\kappa}, \tag{7.52}$$

where $Re_\delta = \delta u_e/\nu$. Equation 7.52 provides an implicit expression for determining C_f, if Re_δ, Π, and C are all known. To change this into a skin-friction relationship based on Re_x, we use the momentum integral equation for two-dimensional, zero pressure gradient boundary layers:

$$\frac{d\theta}{dx} = \frac{C_f}{2}. \tag{7.53}$$

This expression may be integrated from the point at which the turbulent boundary layer momentum thickness extrapolates to zero (that is, the virtual origin of the boundary layer). The wall-wake formulation can be used to derive a relationship between δ and θ (see, for example Young (1989)), and if we assume that the virtual origin is located at $x = 0$, then, after some approximations, we obtain:

$$\frac{1}{\sqrt{C_f}} = a_1 + a_2 \log C_f Re_x, \tag{7.54}$$

where a_1 and a_2 are constants that are then chosen to obtain the best agreement with experiment (von Kármán used $a_1 = 1.7$ and $a_2 = 4.15$).

The skin-friction coefficients for subsonic flow are shown as a function of Re_θ in Figure 7.17. Agreement with the semi-empirical relations developed by Coles (1962) and Fernholz (1971) is within 5% for the range $600 \leq Re_\theta \leq 220,000$, although with a general tendency for the data to lie systematically

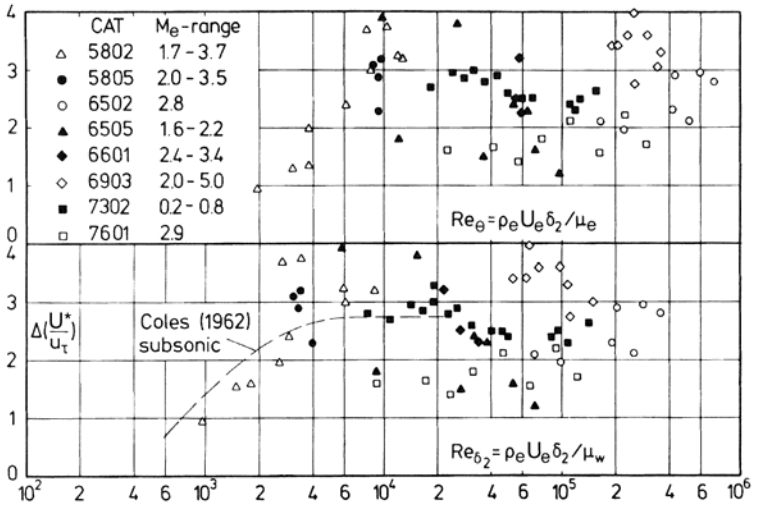

Figure 7.16. Strength of the wake component in compressible turbulent boundary layers. Experiments on adiabatic surfaces, where the origin is not defined (for example, the continuation of a wind tunnel nozzle). (From Fernholz and Finley (1980), where catalogue numbers are referenced. Reprinted with permission of the authors and AGARD/NATO.)

below these correlations at the lower end of the range (see also Smits et al. (1983b)).

In supersonic flows, skin-friction measurements are more difficult to make and interpret. Floating-element gauges are susceptible to inaccuracies stemming from leakage, local variations in heat transfer, flushness, and forces and moments due to streamwise pressure gradients. In addition, Preston-tube data can be analyzed using a variety of calibration schemes, leading to considerable uncertainty in the results. Most schemes for reducing Preston-tube data rely on boundary layer edge conditions (for example, Hopkins and Keener (1966), and this can introduce additional errors, particularly in perturbed flows where the edge properties are often unrelated to the flow behavior near the wall. As Finley (1994) and Finley and Gaudet (1995) point out, calibration equations which involve an empirical intermediate temperature, and/or freestream properties are functionally incorrect, because the Preston-tube pressure should depend on wall variables only, as long as they are used in flows with small or negligible normal pressure gradients. However, in many compressible flows there are significant normal pressure gradients and the calibration equations should be expressed in terms of wall variables. The only calibration that does so is that by Bradshaw and Unsworth (1974). Here, for adiabatic flows and

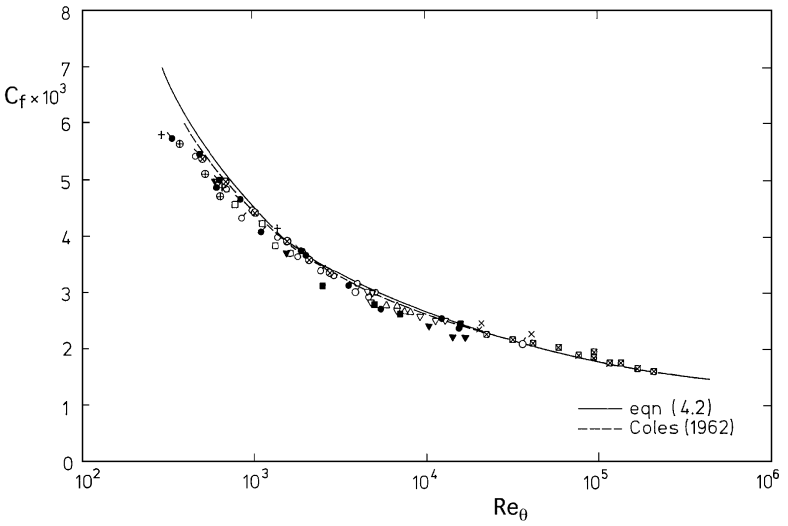

Figure 7.17. Skin-friction coefficient variation with Reynolds number. --------- Coles (1962); ———— Fernholz (1971). (Figure from Fernholz and Finley (1996), where original references are given. Reprinted with permission from Elsevier Science Ltd., Oxford, England.)

for $u_\tau d/\nu_w > 100$:

$$\frac{\Delta p}{\tau_w} = 96 + 60\log_{10}\left(\frac{u_\tau d}{50\nu_w}\right) + 23.7\log_{10}^2\left(\frac{u_\tau d}{50\nu_w}\right) - 10^4 M_\tau^2\left[\left(\frac{u_\tau d}{\nu_w}\right)^{0.26} - 2.0\right], \tag{7.55}$$

which reduces to a very good fit to the calibration data of Patel (1965) for incompressible flows as $M_\tau \to 0$. Allen (1977) suggested that the constants used by Bradshaw and Unsworth were incorrect and proposed that the last term should read:

$$-10^4 M_\tau^2\left[\left(\frac{u_\tau d}{\nu_w}\right)^{0.3} - 2.38\right].$$

However, Finley (1994) concluded that these corrections were based on unreliable balance data, and on the basis of a detailed analysis of the available measurements recommended that the original constants as given in Equation 7.55 are more accurate.

The Clauser method (Clauser, 1954) can also be used as long as a logarithmic region can be found, but the results obviously depend on the validity of the

particular compressibility transformation used. In perturbed flows, the compressibility transformation of Carvin et al. (1988) should be more reliable than that of van Driest because it does not have the additional requirement of a self-preserving boundary layer. In practice, for a wide variety of flows including flows with strong pressure gradients and shock wave-boundary layer interactions, the differences between the Clauser chart results obtained using the two transformations seem to be within about ±15% of the Preston-tube results (Smith et al., 1992). The laser interferometer skin-friction meter (LISF) does not require assumptions about the character of the wall region to deduce the wall shear stress, and can thus provide direct measurement of the skin friction in a perturbed flow. For example, Kim et al. (1991) compared LISF results to Preston-tube measurements in a three-dimensional, shock wave-boundary layer interaction and found encouraging agreement. See also Wideman et al. (1994) and Naughton and Sheplak (2002).

As a result of the increased viscous dissipation in compressible boundary layers the skin-friction coefficient decreases with increasing Mach number at a fixed Reynolds number (see Figure 1.3). The low density of the fluid near the wall indirectly results in a decrease in the slope of the nondimensionalized velocity profile relative to that for an equivalent Reynolds number incompressible boundary layer. Because density has a stronger dependence on temperature than viscosity, the skin-friction coefficient decreases with the Mach number (although the dimensional wall shear increases due to the increase in velocity). As discussed in Chapter 1, the general trends for hot and cold walls can be predicted from these considerations, with heated walls leading to lower C_f (Hinze, 1975; Fernholz and Finley, 1980).

In fact, a variety of experimental correlations, transformations, and finite difference solutions exists for C_f in turbulent compressible boundary layers. Most formulations are based on a compressible form of von Kármán's equation (Equation 7.54). For example, van Driest (1951) used Equation 7.51 and the momentum integral equation for two-dimensional flows (Equation 7.53) to obtain:

$$\frac{0.242}{b\sqrt{C_f\,(T_w/T_e)}}\left[\sin^{-1}\left(\frac{2b^2-a}{\sqrt{(a^2+4b^2)}}\right)+\sin^{-1}\left(\frac{a}{\sqrt{(a^2+4b^2)}}\right)\right]$$

$$=0.41+\log\left(Re_xC_f\right)-\left(\tfrac{1}{2}+\omega\right)\log\left(\frac{T_w}{T_e}\right) \tag{7.56}$$

with $r = 1$ in the definitions of a and b (ω is the exponent in the temperature dependence of the viscosity; see Equation 7.8). This result is based on Prandtl's mixing length model where $\ell = \kappa y$, and it is known as *van Driest I*. In a 1956 paper, van Driest used von Kármán's (1930) mixing length model

$$\ell = \kappa\left|\frac{\partial u/\partial y}{\partial^2 u/\partial y^2}\right|$$

together with Equation 7.1 where the recovery factor was allowed to vary to deduce a new skin-friction formulation, known as *van Driest II*:

$$\frac{0.242}{b\sqrt{C_f\,(T_w/T_e)}}\left[\sin^{-1}\left(\frac{2b^2-a}{\sqrt{(a^2+4b^2)}}\right)+\sin^{-1}\left(\frac{a}{\sqrt{(a^2+4b^2)}}\right)\right]$$

$$=0.41+\log\left(Re_xC_f\right)-\omega\log\left(\frac{T_w}{T_e}\right). \tag{7.57}$$

For adiabatic flows, this may be written as:

$$\frac{0.242}{\sqrt{C_f\,(T_w/T_e)}}\,\frac{U_e^*}{u_e}=0.41+\log\left(Re_xC_f\right)-\omega\log\left(\frac{T_w}{T_e}\right).$$

Bradshaw (1977) critically reviewed the most widely used skin-friction formulas and found that Equation 7.57 is in better agreement with experiment than Equation 7.56, and van Driest II should therefore be used in preference to van Driest I. By using the more general velocity-temperature relationship given by Equation 7.40, Bradshaw derived a transformation that leads to an alternative skin-friction formulation which he called *van Driest III*. This formulation predicts a drop in C_f on very cold walls that results from changes due to heat transfer in the additive constant C^* in the log law, in agreement with the very limited amount of data. The van Driest II and van Driest III formulations exhibited the better agreement with zero pressure gradient data, with less than 10% error for $0.2 \leq T_w/T_{aw} \leq 1$.

7.6 Power Laws

Power-law relations for the boundary layer integral parameters have been used for many years as engineering approximations. They are based on the observation that the velocity profile in a zero pressure gradient boundary layer can be approximated by a relationship such as

$$\frac{u}{u_e}=\left(\frac{y}{\delta}\right)^{1/n}, \tag{7.58}$$

where the value of n depends weakly on the Reynolds number, varying from a value of 7 for $5\times10^5 < Re_x < 10^7$ to a value of 9 for $10^6 < Re_x < 10^8$. As a result, we obtain

$$\frac{\delta^*}{\delta}=\frac{1}{1+n}\qquad\text{and}\qquad\frac{\theta}{\delta}=\frac{n}{(1+n)\,(2+n)}. \tag{7.59}$$

Therefore the shape factor $H\ (=\delta^*/\theta)$ depends on n, and for $n=7$, $H=9/7$. Experiments show that the shape factor is not constant, especially at low

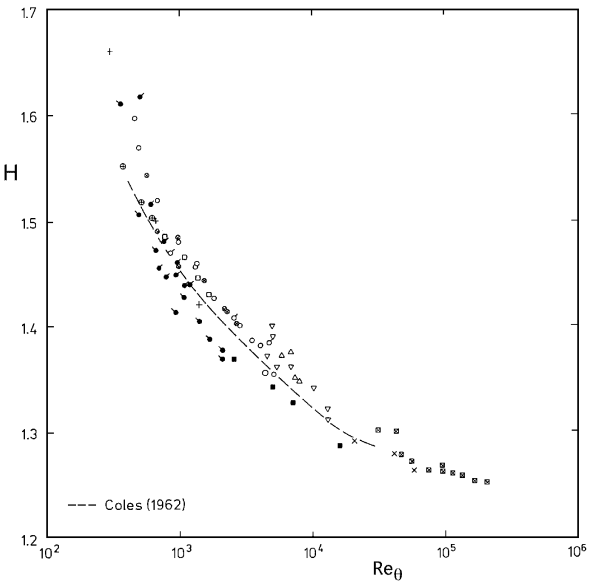

Figure 7.18. Variation of shape factor H with the Reynolds number. (Figure from Fernholz and Finley (1996), where original references are given. Reprinted with permission from Elsevier Science Ltd., Oxford, England.)

Reynolds numbers, indicating to some extent the Reynolds number dependence of n (see Figure 7.18). The agreement with Coles's correlation is generally good, with the Roach and Brierley data, with high freestream turbulence, lying systematically low.

Power-law approximations work reasonably well as a description for the outer-layer velocity distribution, but at the wall $\partial u/\partial y \to \infty$, and they cannot be used to find the skin friction. It is usually assumed instead that the Blasius relationship (derived as a curve fit to pipe flow data) can be used, so that

$$\frac{u_e}{u_\tau} = C_b \left(\frac{u_\tau \delta}{\nu} \right)^{1/n}, \tag{7.60}$$

where C_b is a constant. By using the momentum integral equation (Equation 7.53), we obtain, for $n = 7$,

$$C_{f,i} = \frac{0.0592}{Re_x^{1/5}}, \qquad \left(\frac{\delta}{x} \right)_i = \frac{0.37}{Re_x^{1/5}}, \quad \text{and} \quad \left(\frac{\theta}{x} \right)_i = \frac{0.037}{Re_x^{1/5}}, \tag{7.61}$$

and for $n = 9$,

$$C_{f,i} = \frac{0.0375}{Re_x^{1/6}}, \qquad \left(\frac{\delta}{x} \right)_i = \frac{0.27}{Re_x^{1/6}}, \quad \text{and} \quad \left(\frac{\theta}{x} \right)_i = \frac{0.023}{Re_x^{1/6}}, \tag{7.62}$$

where the constants have been adjusted to fit the experimental data (Young, 1989).

Despite their questionable provenance, these relationships are useful for simple engineering estimates for incompressible flows. They can also be used to estimate the momentum and displacement thickness distributions in compressible boundary layers because the velocity profile also follows a power law, at least approximately. By definition:

$$\frac{\delta^*}{\delta} = \int_0^1 \left(1 - \frac{\rho u}{\rho_e u_e}\right) d\left(\frac{y}{\delta}\right) \quad \text{and} \quad \frac{\theta}{\delta} = \int_0^1 \frac{\rho u}{\rho_e u_e}\left(1 - \frac{u}{u_e}\right) d\left(\frac{y}{\delta}\right).$$

If we assume Walz's form for the temperature-velocity relationship, we find that for an adiabatic wall with $n = 7$, where $M_e \geq 0.2$:

$$\frac{\delta^*}{\delta} = 1 - \frac{7}{2\beta} F\left(M_e\right), \tag{7.63}$$

where

$$F\left(M_e\right) = \alpha^3 \ln \frac{\alpha}{\alpha - 1} - \alpha^2 - \frac{\alpha}{2} - \frac{1}{3},$$

$$\alpha = 1 + 1/\beta,$$

and

$$\beta = r(\gamma - 1)\, M_e^2 \big/ 2.$$

For an adiabatic wall with $n = 6$,

$$\frac{\theta}{\delta} + \frac{\delta^*}{\delta} \;=\; 1 - \frac{3}{\beta} F\left(M_e\right), \tag{7.64}$$

and for $n = 8$,

$$\frac{\theta}{\delta} + \frac{\delta^*}{\delta} \;=\; \alpha - \frac{4\alpha}{\beta} F\left(M_e\right). \tag{7.65}$$

Power laws therefore suggest that the displacement and momentum thicknesses vary with streamwise distance in the same way as they do in subsonic flows, although their magnitudes depend on the freestream Mach number. The experimental data tend to support these conclusions (see, for example, Settles (1975)). The data also show that the boundary layer thickness δ does not depend significantly on the Mach number, and it varies with Re_x approximately as per Equations 7.61 and 7.62. In Chapter 1, Equation 7.61 was used to investigate the influence of compressibility on the skin-friction coefficient. A relationship that lies within $\pm 10\%$ of van Driest II (Equation 7.57) is given by

$$C_f \;=\; \frac{0.024}{Re_\theta} \left(\frac{T_e}{T_w}\right)^{0.56}. \tag{7.66}$$

Some other simple relationships for estimating the skin friction, based on the intermediate temperature concept, were given by Cousteix (1989).

7.7 Summary

Recent experimental work has allowed a new assessment of Reynolds number influences on subsonic turbulent boundary layer mean velocity distributions. The results demonstrate the success of the classic inner and outer scaling arguments over a very large range of Reynolds numbers (approximately $350 \leq Re_\theta \leq 210,000$), and the overlap region is well established over the same range (see Fernholz and Finley (1996)). It may be expected, more by intuition than by hard evidence, that similar Reynolds number variations will hold for supersonic flows. There still exist certain issues, such as the particular values of the constants in the log law, and the evidence for power-law similarity arguments, that cannot be answered on the basis of the existing boundary layer data, primarily because of the difficulty of measuring accurately the friction at the wall. The wake parameter for subsonic and supersonic flows appears to become constant for $Re_\theta > 5000$, and although there have been some previous indications that it may decrease at very high Reynolds numbers, there is probably enough uncertainty in the data (and the values of the log-law constants) to invalidate any strong conclusions regarding the asymptotic behavior.

For supersonic flows at a moderate Mach number, the direct effects of compressibility on the mean profile are rather small: the most notable differences between subsonic and supersonic boundary layers may be attributed to variations in fluid properties across the layer, without explicit reference to "true" compressibility effects such as shocklets, acoustic radiation, and the enhanced redistribution of energy by pressure fluctuations.

Chapter 8

Boundary Layer Turbulence Behavior

8.1 Introduction

In the previous chapter, we found that the classic arguments on inner and outer layer similarity hold well over a very large range of Reynolds numbers, and that the direct effects of compressibility on the mean flow appear to be rather small: the most notable differences between zero pressure gradient subsonic and supersonic boundary layers may be attributed to the variation in fluid properties across the layer. As we show, similar considerations apply to many aspects of the turbulence behavior. However, recent measurements have also indicated some interesting differences between turbulence in subsonic and supersonic boundary layers that do not seem to scale according to fluid property variations. Differences in turbulence length and velocity scales, and the structure of the large-scale, shear-stress-containing motions have been observed, which may indicate that the turbulence dynamics are affected at a lower fluctuating Mach number than previously believed.

"True" compressibility effects, beyond the effects determined by fluid property variations, are usually described in terms of a Mach number representative of the fluctuations. Several candidates were introduced in Chapter 4. It is also possible that some of these apparent changes in the turbulence structure are due to Reynolds number effects, rather than Mach number effects. As pointed out earlier, the characteristic Reynolds numbers encountered in high-speed flow cover a very large range, extending beyond the values typically found in the laboratory. Furthermore, the temperature gradients that are found in the boundary layer in supersonic flow lead to variations in Reynolds number across the layer in addition to the usual variation in the streamwise direction. To understand the effects of Reynolds number on turbulence in supersonic flow, we first need to consider the scaling of turbulence in subsonic flows.

8.2 Scaling Laws

The inner and outer-layer scaling scheme for the mean flow, as expressed by Equations 7.17 and 7.19, appears to be very successful in practice. A similar inner and outer scaling is therefore expected to apply to the time averaged turbulence statistics, and for the inner and outer regions of a subsonic boundary layer we expect, respectively:

$$\frac{\overline{u'^2}}{u_\tau^2} = f\left(\frac{yu_\tau}{\nu}\right), \tag{8.1}$$

and

$$\frac{\overline{u'^2}}{u_\tau^2} = g\left(\frac{y}{\delta}\right). \tag{8.2}$$

That is, we expect that the mean velocity and turbulence intensities scale with the same set of velocity and length scales: more precisely, that the velocity gradient and the turbulence intensities scale in this way. Matching the turbulence intensity in the overlap region leads to the conclusion that $\overline{u'^2}/u_\tau^2$ is constant in the log-law region. As we shall see, this is not observed in experiments. One explanation of this is that the "true" or *active* turbulent motion is overlaid by an irrotational *inactive* motion imposed by the pressure field of the large eddies in the outer part of the layer (Townsend 1956; Bradshaw, 1967, 1994). These eddies have length scales of order δ, and they are large compared to the scale of motions in the inner layer. However, as the wall is approached the v' component of the inactive motion must become small due to the wall constraint (the "splat" effect) so that its influence on the shear stress is minor, and the mean velocity log law is preserved.

Townsend (1976) proposed that

> ... the main eddies of the flow have diameters proportional to the distance of their centers from the wall, because the motion is directly influenced by its presence. In other words, the velocity fields of the main eddies, regarded as persistent, organized flow patterns, extend to the wall and, in a sense they are attached to the wall.

This is commonly known as Townsend's *attached eddy hypothesis*. He also proposed that the interaction between a large eddy and a smaller, viscous-dominated eddy occurs over several intermediate steps. Due to this highly indirect interaction, he proposed that the large-scale motion is essentially inviscid, and thus independent of the Reynolds number. This is known as Townsend's *Reynolds number similarity hypothesis*. Townsend did not regard the main eddies as having any particular shape, but to make his model quantitative, he assumed that the shear stress at a distance y from the wall was due principally to the eddies that have their center at that height. All the main eddies were assumed to be geometrically similar, and subject to the inviscid

boundary conditions at the wall where the normal component of velocity was assumed to be zero, but the other two components were allowed to have slip. If the probability density function of the eddy scales follows an inverse power law, then a constant stress region is obtained. Townsend's model therefore applies to the near-wall, fully turbulent part of the layer, and he found that

$$\frac{\overline{u'^2}}{u_\tau^2} = B_1 - A_1 \ln\left(\frac{y}{\delta}\right), \tag{8.3}$$

$$\frac{\overline{w'^2}}{u_\tau^2} = B_3 - A_3 \ln\left(\frac{y}{\delta}\right), \tag{8.4}$$

$$\frac{\overline{v'^2}}{u_\tau^2} = A_2. \tag{8.5}$$

Note that, by matching the gradients of the turbulence intensity in the inner and outer regions, rather than the intensity levels themselves, Equations 8.1 and 8.2 will also yield a logarithmic term in y/δ, without any recourse to the *pdf* of eddy scales. These relations indicate that the turbulence intensities are independent of the Reynolds number which is again at odds with the data, although Equations 8.3 to 8.5 may represent an infinite Reynolds number limit. The question remains as to what extent the turbulence profiles are similar in the sense that they collapse onto a Reynolds number independent curve, and what is the correct basis for the similarity argument.

8.2.1 Spectral Scaling for Incompressible Flow

It is useful to begin by considering the scaling of the turbulence spectra. For subsonic boundary layer flows, spectral scaling laws were first suggested by Townsend and later developed extensively by Perry and his co-workers. Based upon Townsend's attached eddy hypothesis and the flow visualization results of Head and Bandyopadhyay (1981) (see Section 8.4.2), Perry and Chong (1982) developed a physical model for near-wall turbulence. They assumed that a turbulent boundary layer outside the viscous region may be modeled as a forest of hairpin or Λ-shaped vortices, which originate at the wall and grow outward. Figure 8.1 shows three Λ-shaped vortices of different scales, and indicates their influence on the velocity field sensed by a probe at a position y. The probe will sense contributions to u' and w' from all eddies of scale y and larger. However, only eddies of scale y will contribute to v'. Therefore, u' and w' should follow similar scaling laws, whereas v' may follow a somewhat different scaling law. Using these ideas in conjunction with dimensional analysis, scaling laws can be derived for the energy spectra in the turbulent wall region, defined as $\nu/u_\tau \ll y \ll \delta$ (Perry et al., 1985, 1986). In general, it is the region where direct wall effects such as the damping of the velocity components are unimportant, and where the direct influence of the large-scale flow geometry

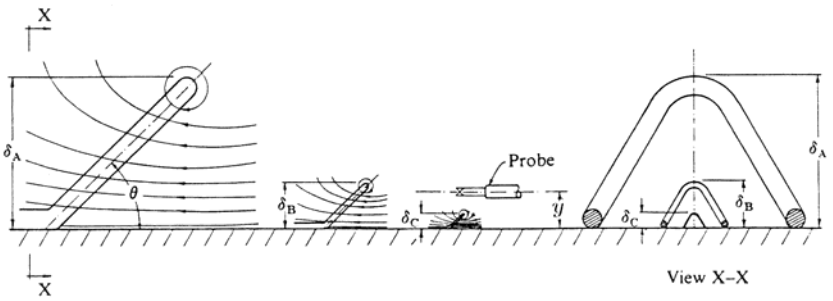

Figure 8.1. Sketch of the streamline patterns and spatial influence of attached eddies at three different scales. (Reproduced from Perry et al. (1986)). Copyright 1986, Cambridge University Press. Reprinted with permission.)

and outer boundary conditions can also be neglected. This region corresponds approximately to the overlap region in the mean velocity profile, that is, the region where the velocity has a logarithmic variation.

First consider the u-component of the turbulence fluctuations in an incompressible flow. Eddies of scale δ will contribute only to the large-scale, low wave number (low frequency) region of the energy spectrum Φ_{11}. For the large-scale eddies, viscosity is less important, and the spectrum in the low wave number region should depend only on u_τ, k_1, y, and δ, where k_1 is the streamwise component of the three-dimensional wave number vector $\mathbf{k}$. From dimensional analysis, the spectrum of u at low wave numbers should have the form

$$\frac{\Phi_{11}(k_1\delta)}{u_\tau^2} = g_1(k_1\delta) = \frac{\Phi_{11}(k_1)}{\delta u_\tau^2}. \tag{8.6}$$

Throughout this section, the argument of Φ_{ii} denotes the unit quantity over which the energy spectral density is measured, following Perry et al. (1986). Equation 8.6 represents an outer flow scaling because it describes the contribution of the large-scale eddies.

Eddies of scale y will contribute to the intermediate wave number range of the spectrum, whereas eddies of scale δ will not. In this range the spectrum should have the following inner flow scaling form,

$$\frac{\Phi_{11}(k_1 y)}{u_\tau^2} = g_2(k_1 y) = \frac{\Phi_{11}(k_1)}{y u_\tau^2}. \tag{8.7}$$

The smallest scale motions, which contribute to the high wave number range of the spectrum, depend on viscosity. Kolmogorov (1961) assumed that these small-scale motions are locally isotropic, and that their energy content depends only on the local rate of turbulence energy dissipation ϵ, and the

kinematic viscosity ν. Dimensional analysis leads to

$$\frac{\Phi_{11}(k_1\eta)}{\upsilon^2} = g_3(k_1\eta) = \frac{\Phi_{11}(k_1)}{\eta\upsilon^2}, \tag{8.8}$$

where η and υ are the Kolmogorov length and velocity scales respectively, defined by

$$\eta = \left(\frac{\nu^3}{\epsilon}\right)^{1/4} \qquad \text{and} \qquad \upsilon = (\nu\epsilon)^{1/4}. \tag{8.9}$$

In the high wave number region, therefore, the spectrum follows a Kolmogorov scaling.

Just as the mean flow exhibited an inner and outer scaling with a region of overlap, it is expected that Equations 8.6 and 8.7 will have a region of overlap (*Overlap Region I*), and that Equations 8.7 and 8.8 will have another region of overlap (*Overlap Region II*). These scalings are illustrated in Figure 8.2. It follows that in Region I the spectrum must have the form:

$$\frac{\Phi_{11}(k_1\delta)}{u_\tau^2} = \frac{A_1}{k_1\delta} = g_1(k_1\delta), \tag{8.10}$$

or

$$\frac{\Phi_{11}(k_1 y)}{u_\tau^2} = \frac{A_1}{k_1 y} = g_2(k_1 y), \tag{8.11}$$

where A_1 is a universal constant. That is, in the turbulent wall layer, the spectrum in Overlap Region I follows a k^{-1} scaling.

In Region II, it follows that

$$\frac{\Phi_{11}(k_1\eta)}{\upsilon^2} = \frac{K_o}{(k_1\eta)^{5/3}} = g_3(k_1\eta), \tag{8.12}$$

or

$$\frac{\Phi_{11}(k_1 y)}{u_\tau^2} = \frac{K_o}{\kappa^{2/3}(k_1 y)^{5/3}} = g_2(k_1 y). \tag{8.13}$$

Equation 8.12 was first derived by Kolmogorov (1961) using entirely different arguments. The region displaying a $k_1^{-5/3}$ scaling is called the *inertial subrange*, and K_o is called the Kolmogorov constant ($\approx$0.5). To derive these $k_1^{-5/3}$ scalings, Perry et al. (1986) imposed the requirement that the spectrum be independent of viscosity in the inertial subrange, and assumed that in the turbulent wall region dissipation equals production, $\varepsilon = -\overline{u'v'}\,(\partial u/\partial y)$, that the velocity profile is logarithmic, and that $-\overline{u'v'} = u_\tau^2$. Some spectra for the turbulent wall region are shown in Figure 8.3. The $k_1^{-5/3}$ and k_1^{-1} regions are evident. At high Reynolds numbers, a very long $k_1^{-5/3}$ range has been observed in the spectrum (Grant et al., 1962), but recent experiments in pipe flow have called into question presence of a k_1^{-1} similarity range at very high Reynolds numbers (Morrison et al., 2004).

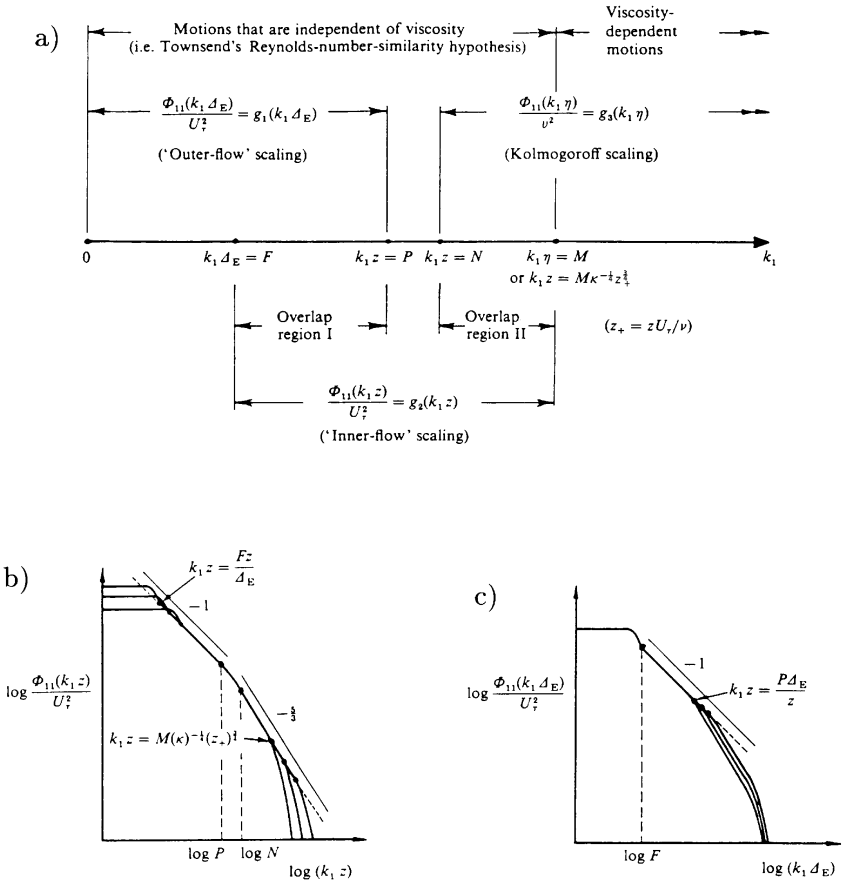

Figure 8.2. Behavior of the energy spectra of the longitudinal and spanwise velocity fluctuations, $\Phi_{11}(k_1)$ according to Perry et al. (see text). $\Phi_{33}(k_1)$ is expected to behave similarly. (a) Chart showing the different scaling regions, (b) inner scaling behavior, and (c) outer scaling behavior. Note that in Perry et al.'s notation, z is distance from the wall, and Δ_E is a boundary layer thickness, similar to δ. (Figure from Perry et al. (1986). Copyright 1986, Cambridge University Press. Reprinted with permission.)

According to these arguments, Φ_{33}, the spectra of w' will follow similar scaling laws, as illustrated in Figure 8.2a. The boundaries of the overlap regions are denoted by P, N, M, and F, where P, N, and M are universal constants, and F is a constant characteristic of the large scales, and likely to be Reynolds number dependent. Figures 8.2b and 8.2c illustrate the deduced

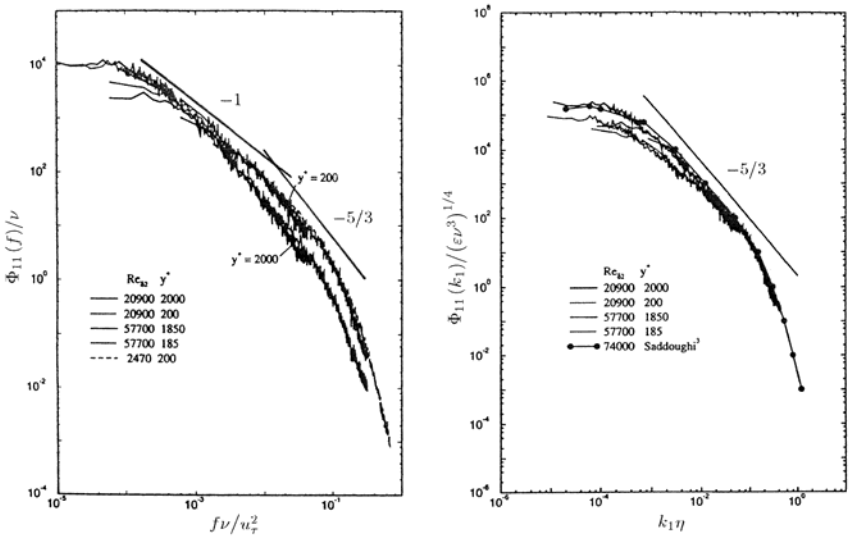

Figure 8.3. Spectra in the inner layer of subsonic boundary layers, plotted using inner layer scales (left), and Kolmogorov scales (right). (Adapted from Fernholz et al. (1995), with permission from Elsevier Science Ltd., Oxford, England.)

form of Φ_{11} and Φ_{33} using inner and outer scaling.

For the wall-normal component, Figure 8.1 suggests that there will be no contributions from δ-scale eddies, and thus there will be no outer flow scaling for Φ_{22}. There will only be inner flow and Kolmogorov scaling, with one region of overlap. Φ_{22} is described by Equations 8.7, 8.8, and 8.12, so that a region of $k_1^{-5/3}$ scaling is expected but not one in k_1^{-1}. Figure 8.4a summarizes the scaling laws for Φ_{22}, and Figures 8.4b and 8.4c illustrate the expected form of the v' spectrum using inner and outer scaling. Energy spectra measured by Perry and Abell (1975, 1977), Perry et al. (1985, 1986) Li (1989); Perry and Li (1990), Erm (1988); Erm et al. (1985), Smith (1994), and Zhao (2005) have all shown good agreement with these spectral scaling laws for the wall-normal component.

By integrating these spectral forms, Li (1989) and Perry and Li (1990) derived the following expressions for the normal stresses in a subsonic boundary layer:

$$\frac{\overline{u'^2}}{u_\tau^2} = B_1 - A_1 \ln\left(\frac{y}{\delta}\right) - V(y^+), \tag{8.14}$$

$$\frac{\overline{w'^2}}{u_\tau^2} = B_3 - A_3 \ln\left(\frac{y}{\delta}\right) - V(y^+), \tag{8.15}$$

$$\frac{\overline{v'^2}}{u_\tau^2} = A_2 - V(y^+), \tag{8.16}$$

where B_1 and B_2 are large-scale characteristic constants, particular to the flow geometry, and A_1, A_2, and A_3 are expected to be universal constants (all the constants are positive). The function $V(y^+)$ is a Reynolds number dependent, viscous correction term that increases with y^+, and it accounts for the dissipation region of the spectrum at finite Reynolds numbers. Equations 8.14 to 8.16 are valid only in the turbulent wall region.

Li (1989); Li and Perry (1989) and Perry et al. (1991) derived an expression for the total stress τ using an assumed form for the mean velocity profile (in this case Coles' combined law-of-the-wall/law-of-the-wake given by Equation 7.50). Figure 8.5 shows several Reynolds shear stress profiles calculated in this way, and the variation with Reynolds number is *not* monotonic because of low Reynolds number effects on the Coles wake factor.

Uddin (1994) and Marušić et al. (1997) extended these scaling laws to include the entire region outside the viscous sublayer. As with the mean flow, the deviation from the logarithmic profile near the wall is attributed to viscous effects, and the deviation in the outer part of the layer is due to wake effects. They suggested a "wall-wake" distribution where, for example,

$$\frac{\overline{u'^2}}{u_\tau^2} = B_1 - A_1 \ln\left(\frac{y}{\delta}\right) - V_{g1}(y^+) - W_{g1}\left(\frac{y}{\delta}\right). \tag{8.17}$$

They called V_{g1} the *viscous deviation*, and W_{g1} the *wake deviation*. Uddin gave empirical forms for V_{g1} and W_{g1} that agreed well with data over the range $6570 \leq Re_\theta \leq 35{,}100$ (V_{g1} was a more accurate version of the earlier function V). An extension of Equation 8.17 that applies across the entire boundary layer including the viscous near-wall layer was proposed by Marušić and Kunkel (2003), and comparisons with the laboratory data of DeGraaff and Eaton (2000) and the atmospheric data of Metzger et al. (2001) showed excellent agreement (Figure 8.6), although the formulation does not reproduce the outer peak in the streamwise intensity observed at high Reynolds numbers (as seen in Figure 8.11). A similar high level of agreement with high Reynolds number pipe flow data was shown by Marušić et al. (2004), despite the absence of a region of k_1^{-1} similarity in the streamwise velocity spectra (Morrison et al., 2004).

8.2.2 Spectral Scaling for Compressible Flow

These spectral arguments for the scaling of the turbulence can be extended to compressible flows, as follows (for further details see Dussauge and Smits (1995)). In the analysis of the mean velocity distributions in supersonic boundary layers it was assumed that the mixing length distribution was the same

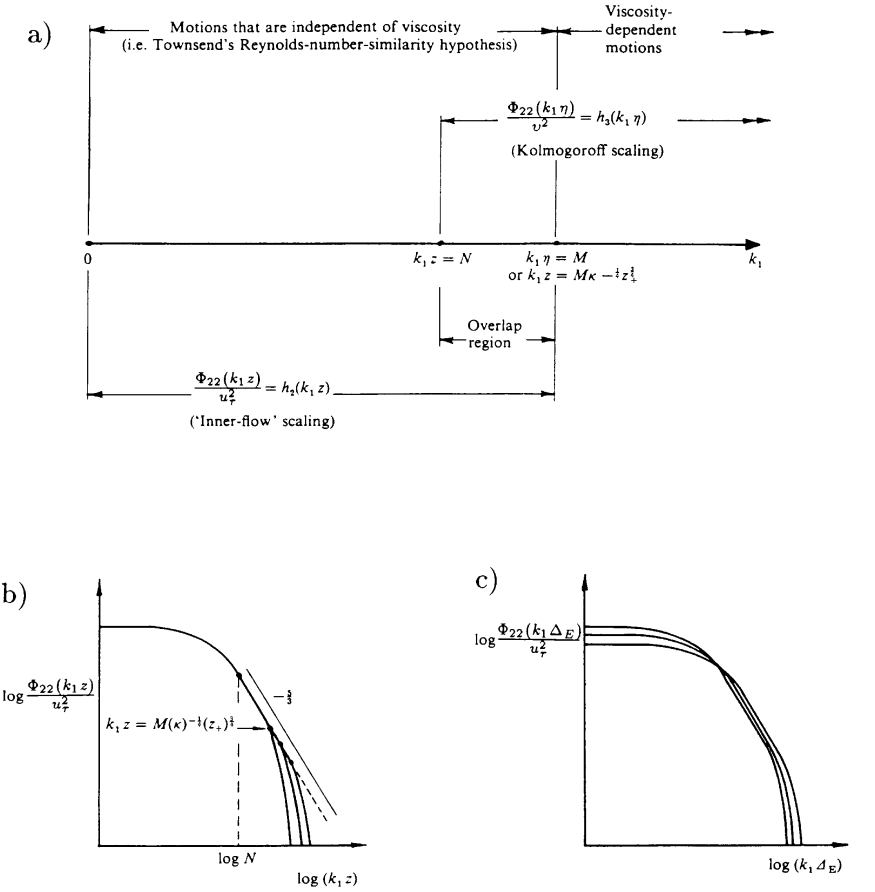

Figure 8.4. Behavior of the energy spectra of the wall-normal velocity fluctuations $\Phi_{22}(k_1)$, according to Perry et al. (see text). (a) Chart showing the different scaling regions, (b) inner scaling behavior, and (c) outer scaling behavior. Note that in Perry et al.'s notation, z is distance from the wall, and Δ_E is a boundary layer thickness, similar to δ. (Figure from Perry et al. (1986). Copyright 1986, Cambridge University Press. Reprinted with permission.)

as in subsonic flows. This comprises essentially a variable fluid property assumption; that is, the mechanisms governing turbulent transport are the same as at low speed, and the variations of density are taken in account by scaling the local stress (see Section 5.1). This hypothesis is quite successful, because, as we have seen, experimental evidence supports that the log law is observed in the transformed velocity profile with the same constants as found at low

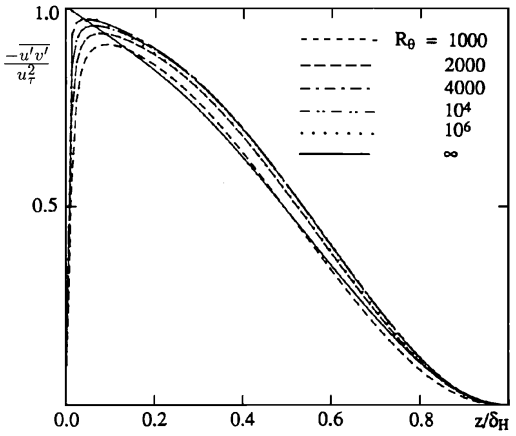

Figure 8.5. Theoretical Reynolds shear stress profiles, $-\overline{u'v'}/u_\tau^2$, derived by Li and Perry (1989), from which this figure is taken, with the authors' permission. In their notation, z is the distance from the wall, and δ_H $(=\Delta_E)$ is a boundary layer thickness similar to δ.

speeds. Therefore it may be expected that the typical size of the energetic eddies producing turbulent transport obeys the same laws as in subsonic flows. Note that this scale is built on the shear stress and that it is a scale related to turbulent diffusion.

Hence, the length scales for the low and intermediate wave number regions in the space $\nu/u_\tau \ll y \ll \delta$ are as in subsonic flow, that is, the boundary layer thickness δ (or equivalently, Δ), and the distance from the wall y, respectively. The velocity scale for both regions is $(\tau_w/\bar{\rho})^{1/2}$. By applying the overlap argument, we find that the k_1^{-1} power law is again obtained in Overlap Region I.

For compressible flow, however, the scaling of the viscous contribution to the spectrum will change because the Kolmogorov scales vary due to temperature gradients. We can define new length and velocity scales by considering the viscosity, the rate of dissipation per unit volume φ (not per unit mass ε), and the density. Dimensional analysis gives:

$$\eta' = \rho^{-1/2}\left(\frac{\mu^3}{\varphi}\right)^{1/4} \qquad \text{and} \qquad v' = \rho^{-1/2}\left(\mu\varphi\right)^{1/4}. \tag{8.18}$$

Equations 8.11 and 8.12 now have the form:

$$\frac{\Phi_{11}\left(k_1 y\right)}{\rho_w u_\tau^2/\rho} = g_2\left(k_1 y\right) = \frac{\Phi_{11}\left(k_1\right)}{y\rho_w u_\tau^2/\rho} \tag{8.19}$$

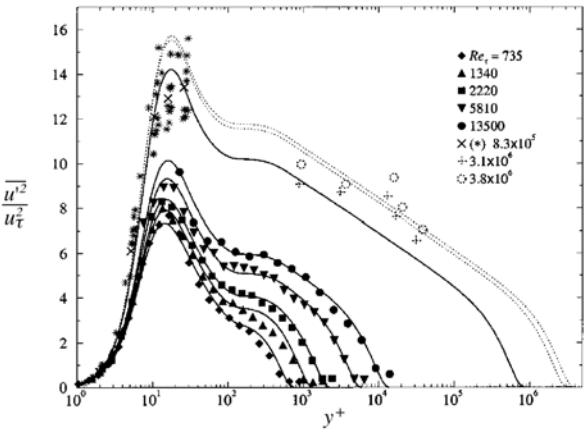

Figure 8.6. Comparison of Marušić and Kunkel (2003) formulation with data. Solid symbols are from DeGraaff and Eaton (2000), and symbols $*$ and $\times$ are from Metzger et al. (2001). Broken symbols are atmospheric surface data, which should be compared with the broken lines. (From Marušić and Kunkel (2003), with permission.)

$$\frac{\Phi_{11}\left(k_1\eta'\right)}{v'^2} = g_3\left(k_1\eta'\right) = \frac{\Phi_{11}\left(k_1\right)}{\eta' v'^2}. \tag{8.20}$$

So the Kolmogorov scales are unchanged as long as $\bar{\nu} \approx \bar{\mu}/\bar{\rho}$ and $\bar{\varepsilon} \approx \bar{\varphi}/\bar{\rho}$. The analysis for the overlap region is the same as for low-speed boundary layers: the Kolmogorov scales are determined in the equilibrium zone where production and dissipation are assumed to balance, where the turbulent shear stress is constant, and where the transformed velocity is logarithmic. It is again found that the spectrum of $\overline{u'^2}$ should have a range in $k_1^{-5/3}$. Because the analysis can be performed using either the incompressible or compressible variables, the changes in the scales due to variations in the mean density are absorbed in the modified dissipation rate because of the density scaling of the velocity gradient. The differences between the incompressible and the compressible definitions of the Kolmogorov scales depend mainly on the link between velocity and density in the part of the layer where dissipation is maximum, and therefore it should scale with the friction Mach number $M_\tau = u_\tau/a_w$.

It may then be inferred that for weak compressibility effects, the spectra for u' and w' have two wave number ranges with power-law variations in k_1^{-1} and in $k_1^{-5/3}$, as at low speeds. This analysis does not indicate where these wave number ranges are placed in the spectrum, that is, if high speeds produce larger or smaller energetic eddies, or induce a change in the orientation of these eddies. Naively, it also seems that the existence of a k_1^{-1} range should be

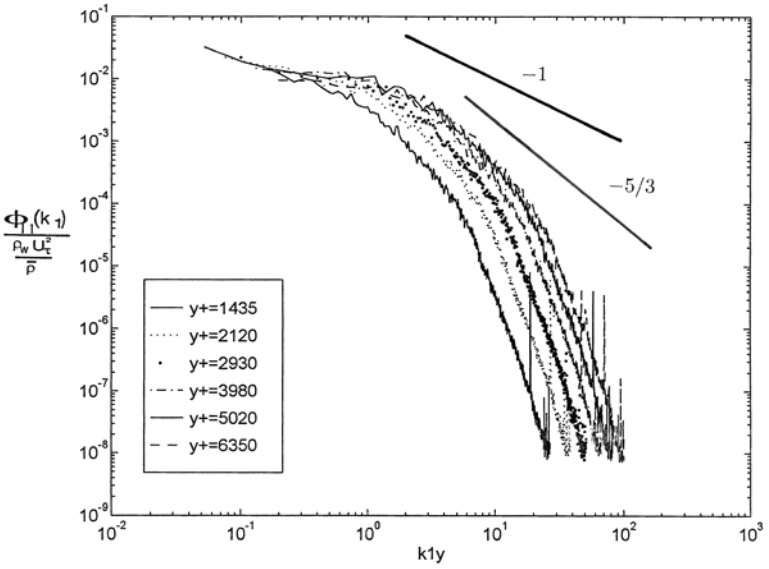

Figure 8.7. Spectra in a Mach 2.9 boundary layer at $Re_\theta = 78,000$. The data for $y^+ \leq 2930$ are in the logarithmic region. (Adapted from Spina (1988), with the author's permission.)

a rather robust feature, because the existence of two domains where the wave numbers scale respectively with δ and y are the only necessary conditions. The $k_1^{-5/3}$ law is expected to have less generality, because the existence of a constant shear stress zone with a logarithmic velocity distribution is postulated, and a balance between production and dissipation is also required. The data are somewhat ambiguous, as shown in Figure 8.7 for a Mach 2.9, high Reynolds number boundary layer: the $k_1^{-5/3}$ range is clearly evident, but the k_1^{-1} region seems to be rather small. These observations agree well with the high Reynolds number data of Morrison et al. (2004) in incompressible, fully developed turbulent pipe flow.

As a last remark, it may be seen that the incompressible and the compressible definitions of the Kolmogorov scales are equivalent for moderate Mach numbers, but in the buffer zone they may differ significantly from each other if the friction Mach number M_τ is close to 1. In this case, however, it may be expected that the hypotheses required for the derivation of the power laws will no longer be valid. In practice, friction Mach numbers are usually small (≤ 0.1), except at hypersonic Mach numbers and very high Reynolds numbers, or on extremely cold walls.

We see that the turbulence spectra give insight into the scaling of the turbulence stresses. There are some obvious shortcomings in the spectral arguments:

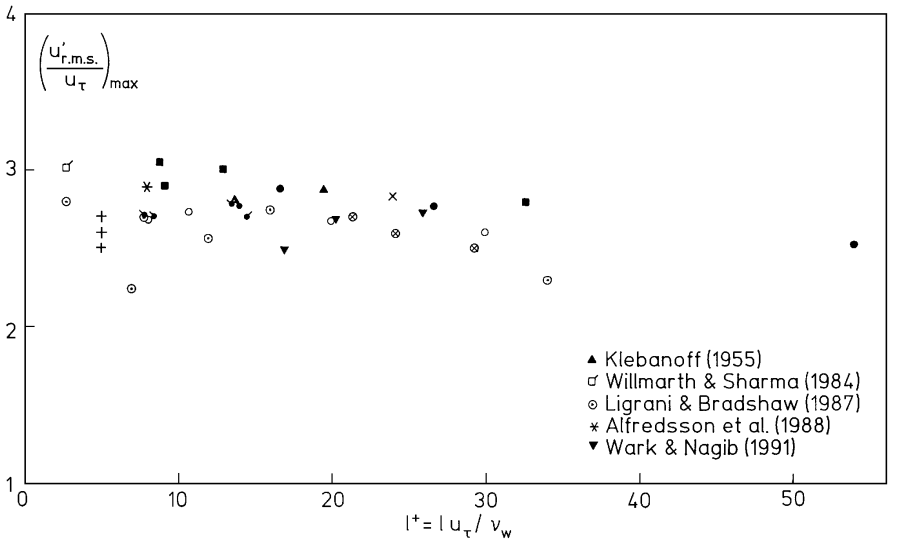

Figure 8.8. The influence of the characteristic dimensionless hot-wire length scale l^+ on the maximum value of $\sqrt{\overline{u'^2}}/u_\tau$ in subsonic boundary layers. $Re_\theta > 700$ and $l/\delta > 180$. (Figure from Fernholz and Finley (1996), where original references are given. Reprinted with permission from Elsevier Science Ltd., Oxford, England.)

in particular, the data are not uniformly supportive of the proposed scaling. Nevertheless, the physical arguments are reasonable, and they provide a starting point for understanding the likely effects of Reynolds and Mach number under conditions where Morkovin's hypothesis is satisfied.

8.3 Turbulence Data

In considering the stress behavior, it is useful to take the approach followed in the previous chapter where we used subsonic flows to try to identify Reynolds number trends, and then went on to examine supersonic flows in order to understand Mach number effects. The discussion given here draws heavily on the earlier reviews by Fernholz and Finley (1996) and Dussauge et al. (1996), although the presentation has been considerably extended. By way of a general comment, we need to be aware of the errors and uncertainties associated with the measurement techniques, particularly the systematic errors. For example, Figures 8.8 and 8.9 show how the finite length of the sensor affects the level of the maximum turbulence intensity measured in the near-wall region of subsonic boundary layers. As the wire length decreases, the level increases. Nevertheless, the data can be extrapolated reasonably unambiguously to zero sensor

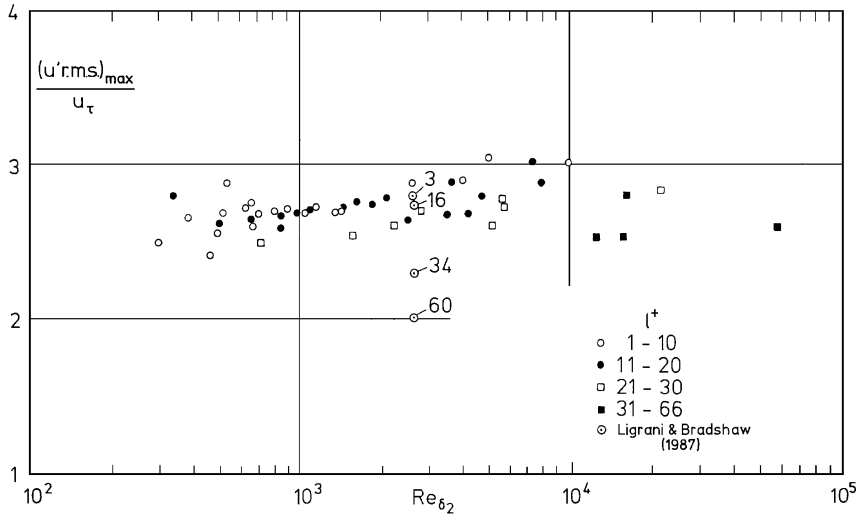

Figure 8.9. The influence of l^+ and Reynolds number on the maximum value of $\sqrt{\overline{u'^2}}/u_\tau$. (Figure from Fernholz and Finley (1996), where original references are given. Reprinted with permission from Elsevier Science Ltd., Oxford, England.)

length, and there is a definite trend where the level increases with Reynolds number, ranging from about 2.8 at $Re_\theta = 1000$ to about 3.2 at $Re_\theta = 10{,}000$. At still larger Reynolds numbers, this ratio can reach a value about 4 (see Figures 8.6 and 8.10). Note that in Figures 8.9 to 8.17, $Re_{\delta 2} = Re_\theta$, because all data shown are for subsonic flow. Marušić and Kunkel (2003) derived the variation of the maximum turbulence intensity with $Re_\tau = \delta u_\tau/\nu$ on the basis of their similarity formulation (Section 8.2.1) and found good agreement with the data. In later work, Marušić (2004) showed that the similarity formulation indicates that the maximum mean square value should follow the functional form:

$$\frac{\overline{u'^2}}{u_\tau^2} = a + b \ln Re_\tau, \tag{8.21}$$

and the agreement with experiment, including very high Reynolds number atmospheric data, is excellent (Figure 8.10).

8.3.1 Incompressible Flow

Figure 8.11 shows the distributions of $\overline{u'^2}$ normalized with wall variables. At all Reynolds numbers, similarity can be observed in the range $3 \leq y^+ \leq 50$, including the cases with high freestream turbulence levels, although the maximum value of $\overline{u'^2}/u_\tau^2$ tends to increase slightly with Reynolds number, as

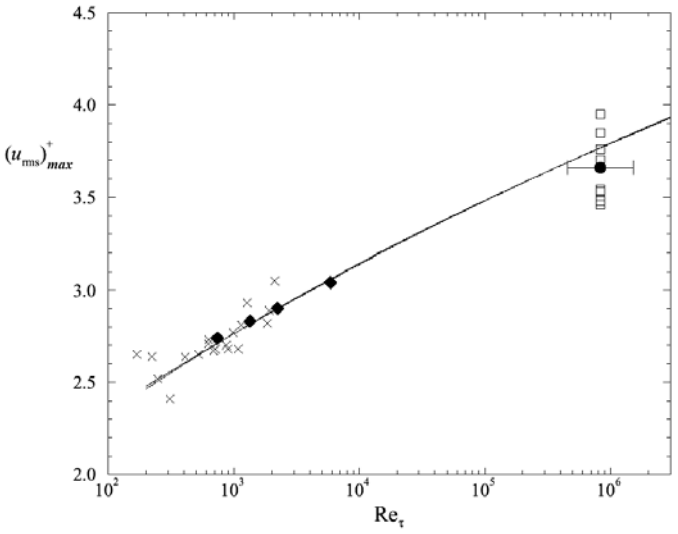

Figure 8.10. The maximum value of $\sqrt{\overline{u'^2}}\big/u_\tau$ in the near-wall region. The solid line is Equation 8.21 with $a = 0.9132$ and $b = 0.9737$. (From Marusic (2004), with permission.)

we noted above. The position where this maximum occurs, however, seems to be fixed at $y^+ \approx 15$ (Sreenivasan, 1988). For values of $y^+ > 100$ large departures are observed in inner scaling, with a tendency for the intensity to form a second maximum in a region corresponding to the mean-profile log law region, which becomes more pronounced as Re_θ increases. Such second peaks are often observed in high Reynolds number compressible boundary layers (Figures 3.1.1 and 3.1.2 in Fernholz and Finley (1981)), although generally not so pronounced.

The $\overline{u'^2}$ data plotted using the Rotta thickness as the outer length scale are shown in Figures 8.12 and 8.13. With this scaling the data collapse well for $y/\Delta > 0.4$ ($y/\delta > 0.1$) for $Re_\theta > 5000$ in the same way as the mean velocity profile (Figures 7.6 to 7.8). The second maximum shown in Figure 8.11 can be seen to represent a further extension of outer similarity toward the wall as Re_θ increases. Figure 8.12 shows the convergence of the $\overline{u'^2}$ profiles toward this universal behavior at lower Reynolds numbers.

At high enough Reynolds number, therefore, the $\overline{u'^2}$ profiles display similarity in the viscous sublayer and buffer layer when expressed in inner scaling, except for a continuing increase of the maximum turbulence intensity at $y^+ \approx 15$, which Morrison et al. (2004) ascribes to the influence of the inactive, outer layer motions on the near-wall turbulence. Morrison et al. suggest that

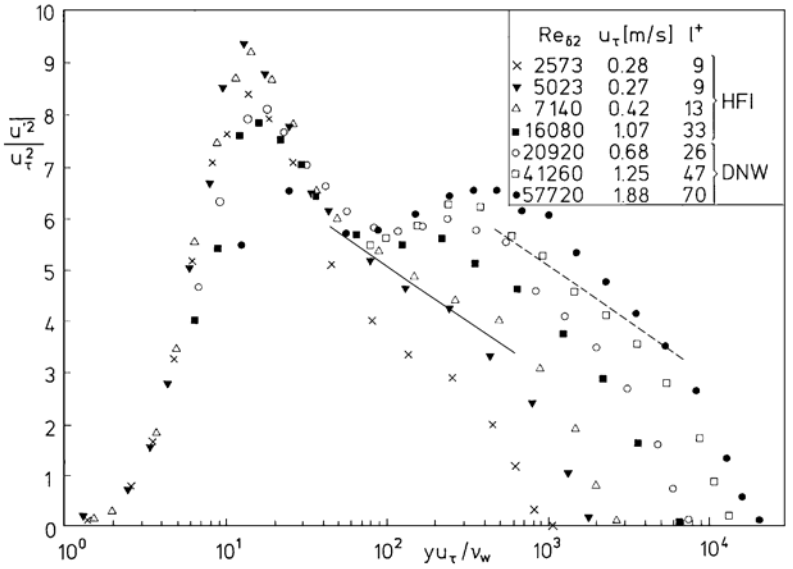

Figure 8.11. Distribution of the longitudinal Reynolds stress in inner layer scaling at medium to high Reynolds numbers. Data from Bruns et al. (1992) and Nockemann et al. (1994). ————, Equation 8.14 for $Re_{\delta 2} = 5023$; ---------, $Re_{\delta 2} = 57{,}720$. (Figure adapted from Fernholz and Finley (1996) with permission from Elsevier Science Ltd., Oxford, England.)

the interaction between inner and outer layer motions are responsible for such departures from strict Reynolds number similarity. In outer scaling, similarity is observed for $y/\delta > 0.4$, approximately. The formulation by Marušić and Kunkel (2003) shows very good agreement with the data at all Reynolds numbers in inner and outer regions, but the appearance of a second maximum in the streamwise component, seen in boundary layer and pipe data, is not reproduced.

The profiles of $\overline{v'^2}/u_\tau^2$ and $\overline{w'^2}/u_\tau^2$ plotted against y^+ (not shown here) display little or no sign of similarity. At least part of this behavior may be due to measurement errors. In particular, measurements of v' and w' using an X-wire probe are subject to errors due to spatial averaging caused by the separation L of the two wires. The dimensionless distance L^+ is likely to have as great an influence as l^+, and as a result v' and w' measurements are usually less precise than u' measurements (see Section 1.7.1).

Figures 8.14 and 8.15 show these data plotted against y/Δ. An orderly similarity behavior is found, although the peak values depend on Reynolds number again, this time quite markedly. The maximum value of $\overline{v'^2}/u_\tau^2$ in-

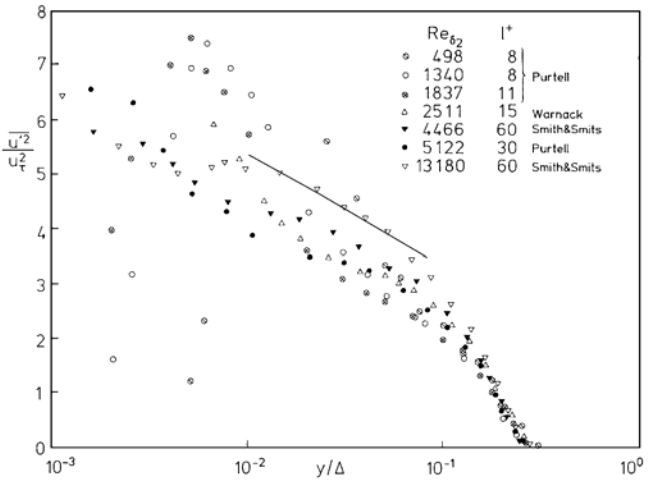

Figure 8.12. Distribution of the longitudinal Reynolds stress in outer layer scaling at low to medium Reynolds numbers. ————, Equation 8.14 for $Re_{\delta 2} = 5023$. (Figure adapted from Fernholz and Finley (1996) with permission from Elsevier Science Ltd., Oxford, England.)

creases from about 1 to 1.6 as Re_θ increases from about 600 to 60,000, and the maximum value of $\overline{w'^2}/u_\tau^2$ increases from about 2 to 3 over a similar Reynolds number range. The y^+ location of the peak for $\overline{v'^2}$ moves away from the wall as Re_θ increases, in agreement with the findings of Sreenivasan (1988). The location of the peak in $\overline{w'^2}$ cannot be determined with sufficient precision to make any meaningful conclusions.

For $\overline{v'^2}$ in the overlap region, comparisons with the predictions according to Equation 8.16 show a similar behavior to that found for $\overline{u'^2}$: good agreement is found with the data at the lower Reynolds numbers, but the increase with Reynolds number is underestimated somewhat. In a parallel study, Smith (1994) found a similar trend, and concluded that the additive constants in Equations 8.14 to 8.16 must be weakly Reynolds number dependent.

In contrast to the observations in boundary layers, recent data taken in a pipe flow indicate the presence of a region of constant v' in the overlap region where $\overline{w'^2}/u_\tau^2 \approx 1.3$, with a peak developing in the near-wall region ($y^+ < 100$ at higher Reynolds numbers (Zhao, 2005). Zhao interpreted this latter observation to demonstrate the increasing effect of the outer layer motions on the inner layer turbulence as the Reynolds number increases.

As far as the Reynolds shear stress is concerned, Sreenivasan (1988) and Sreenivasan and Sahay (1997) suggest "that the location of the peak Reynolds stress in a zero pressure gradient boundary layer is something like a critical

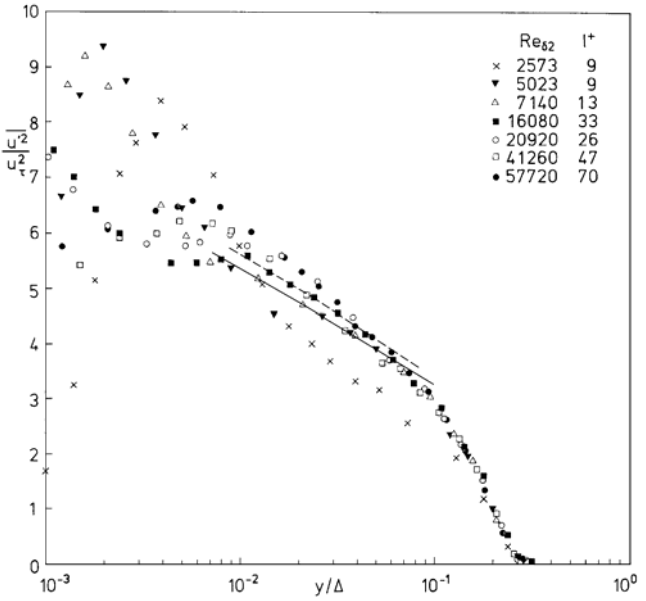

Figure 8.13. Distribution of the longitudinal Reynolds stress in outer layer scaling at medium to high Reynolds numbers. Data from Bruns et al. (1992) and Nockemann et al. (1994). ————Equation 8.14 for $Re_{\delta 2} = 5023$; --------- $Re_{\delta 2} = 57{,}720$. (Figure adapted from Fernholz and Finley (1996) with permission from Elsevier Science Ltd., Oxford, England.)

layer for the flow and that it shares some of the properties of the transitional critical layer." One of these properties is that the velocity of the mean flow in the transitional critical layer appears to be a constant fraction of the freestream velocity. For several wall-bounded shear flows Sreenivasan found $U_{crit} = 0.65U_e$, so that the position of this "critical" layer is in the logarithmic region of the boundary layer.

Similar ideas have been recently proposed by Wei et al. (2005) who derived a new scaling scheme for wall-bounded flows using the streamwise momentum equation and developing arguments based on stress gradients. For the mean flow, they identify two layers that lie between the traditional linear sublayer and the outer wake region: a stress gradient balance layer extending from the viscous-dominated flow near the wall well into the region where the log law is normally assumed to begin, and a viscous-advection balance or "meso-layer" occurring in the region where the maximum Reynolds shear stress is found, corresponding to Sreenivasan's critical layer. The extent of both layers increases with Reynolds number according to $\Delta y^+ \sim \sqrt{\delta^+}$, but of the two layers the stress gradient balance layer is of most interest because its velocity

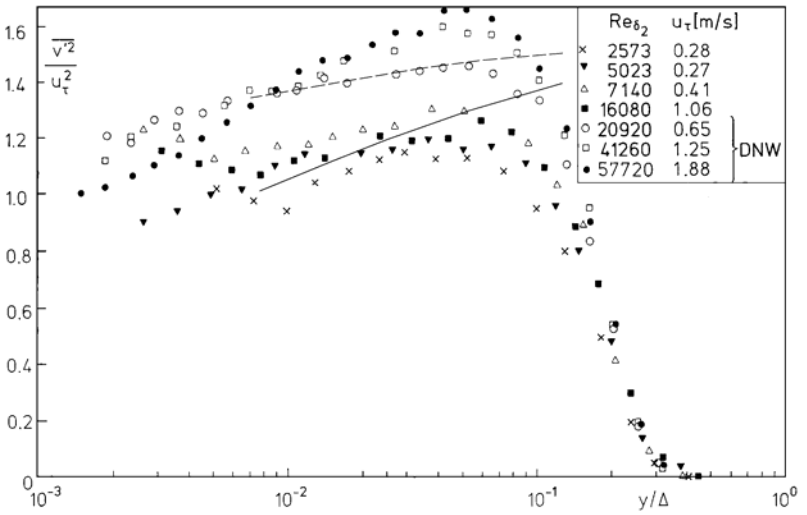

Figure 8.14. Distribution of the wall-normal Reynolds stress in outer layer scaling at medium to high Reynolds numbers. ———— Equation 8.16 for $Re_{\delta 2} = 5023$; - - - - - - - - $Re_{\delta 2} = 57{,}720$. (Figure adapted from Fernholz and Finley (1996), where original references are given, with permission from Elsevier Science Ltd., Oxford, England.)

increment is nearly constant and equal to about $U_e/2$, and it can occupy a substantial fraction of the layer (from $y^+ \approx 3$ to $y^+ \approx 1.6\sqrt{\delta^+}$. These observations may help to explain the power-law variation seen in the near-wall region by Zagarola and Smits (1998a), which blends into a logarithmic variation only for $y^+ > 600$, because it would appear that this power-law region and the stress gradient balance layer occupy similar space.

The scaled shear stress $-\overline{u'v'}/u_\tau^2$ in inner-layer scaling shows a plateau in the vicinity of its peak value of about 0.92 and 0.95 (for details see Fernholz and Finley, 1996). The spatial resolution of X-wire probes near the wall is generally poor, and the near-wall observations are not precise enough to confirm Spalart's (1988) suggestion that the total shear stress approaches the wall with a finite nondimensional slope of order -0.6, with the slope falling to zero only in the buffer layer.

Figure 8.16 shows the shear stress data in outer layer scaling. The data collapse for $y/\Delta > 0.09$. The peak value of the shear stress shows almost no dependence on Reynolds number, but in this scaling the location of the peak moves towards the wall as the Reynolds number increases. When expressed in terms of inner scaling, the peak moves away from the wall with increasing Reynolds number, although the movement of the peak is less pronounced

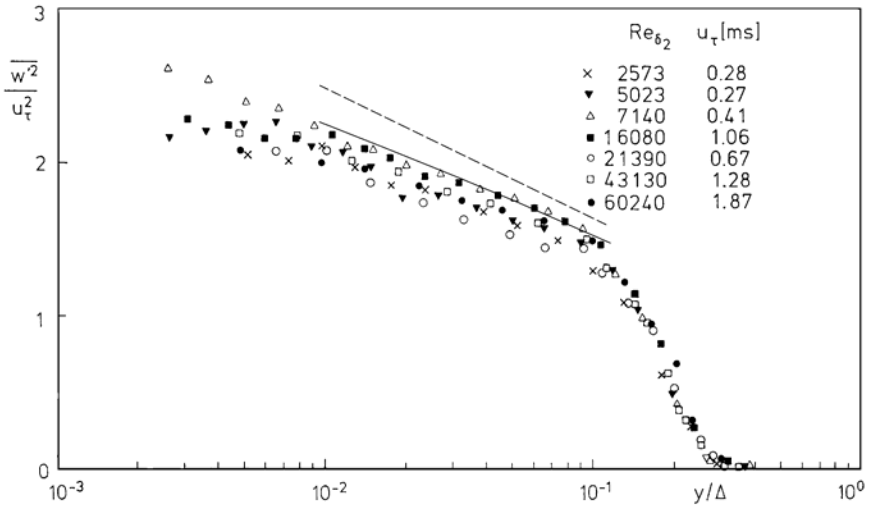

Figure 8.15. Distribution of the spanwise Reynolds stress in outer layer scaling at medium to high Reynolds numbers. Data from Bruns et al. (1992) and Nockemann et al. (1994). ———— Equation 8.15 for $Re_{\delta 2} = 5023$; - - - - - - - - - $Re_{\delta 2} = 57{,}720$. (Figure adapted from Fernholz and Finley (1996), with permission from Elsevier Science Ltd., Oxford, England.)

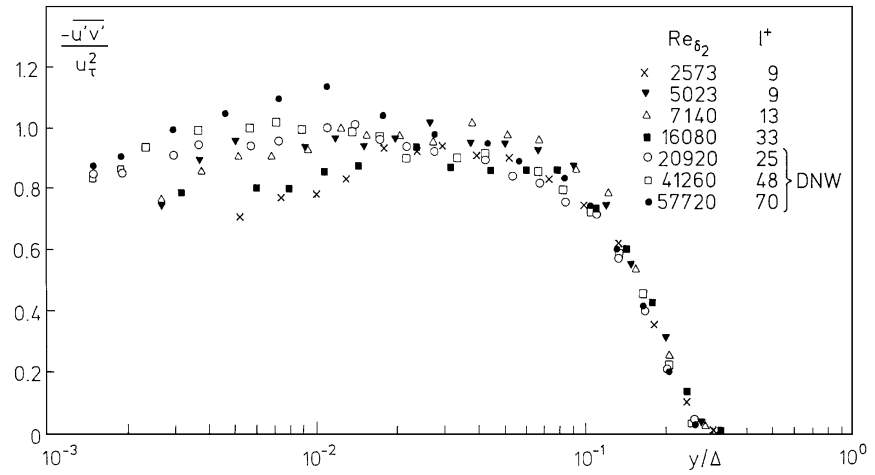

Figure 8.16. Distribution of the Reynolds shear stress in outer layer scaling at medium to high Reynolds numbers. Data from Bruns et al. (1992) and Nockemann et al. (1994). (Figure from Fernholz and Finley (1996). Reprinted with permission from Elsevier Science Ltd., Oxford, England.)

than for $\overline{v'^2}$. This is in qualitative agreement with the results collected by Sreenivasan (1988), who noted that the part of the dynamics contributing to the Reynolds shear stress does not reside either at constant y^+ or at constant y/Δ, again hinting at the influence of outer scales on the inner layer behavior.

Direct numerical simulations give shear stress values near the wall which are generally in good agreement with the experimental values obtained at the same Reynolds number. For example, at $Re_\theta = 670$, Spalart (1988) finds a maximum value of $\overline{u'v'}/u_\tau^2$ of about 0.95 (compared with the experimental value of 0.87 found by Erm and Joubert (1991)), and Yeung et al. (1993) find a maximum value of about 0.89. The position of the maximum value also agrees well with experiment (for further details see Fernholz and Finley (1996)). In other respects, as in the turbulent stress and skewness and flatness distributions, the DNS results agree similarly well with the experimental data (Erm et al., 1994).

Some particular ratios of stresses are also of interest. The "structure parameter" a_1 is the ratio of the Reynolds shear stress to the turbulent kinetic energy, and Klebanoff (1955) found it to be approximately constant in a range $0.1 \leq y/\delta \leq 0.8$, at a Reynolds number $Re_\theta = 7660$. Erm (1988) found similar results in the range $697 \leq Re_\theta \leq 2788$, with a_1 taking values between 0.14 and 0.16. Higher Reynolds number data are shown in Figure 8.17 in outer scaling. The location of the peak value is approximately constant, and the magnitude of the peak value lies between 0.14 and 0.17, increasing slightly with Re_θ.

The correlation coefficient R_{uv} increases from about 0.3 near the wall to about 0.45 in the outer part of the layer (see, for example, Klebanoff's (1955) results in Figure 8.21), and there is a weak tendency for these values to decrease with Reynolds number. The anisotropy ratio $\sqrt{\overline{v'^2}}/\sqrt{\overline{u'^2}}$ increases across the boundary layer from a value of about 0.4 to about 0.8, and shows the same strong Reynolds number dependence as $\overline{v'^2}$ itself (see also Smith (1994)). The ratio $\sqrt{\overline{w'^2}}/\sqrt{\overline{u'^2}}$ is nearly constant at a value of between 0.6 and 0.7 at all y-locations and Reynolds numbers.

As for the higher-order moments, the skewness and flatness of u' (given by $\overline{u'^3}/{u'_{rms}}^3$ and $\overline{u'^4}/{u'_{ms}}^2$, respectively) appear to be independent of Reynolds number when scaled using the appropriate scaling parameters for each region, as found by Smith (1994) and Fernholz and Finley (1996). The behavior of the triple correlations and production terms is discussed by Murlis et al. (1982), Erm (1988), Fernholz and Finley (1996), and Morrison et al. (1992).

8.3.2 Compressible Flow

In Chapter 1 we saw that when the longitudinal velocity fluctuations are normalized by the shear velocity $\overline{u'^2}/u_\tau^2$, there is a decrease in fluctuation level with increasing Mach number (see Figure 1.5). However, when the streamwise normal stress $\bar{\rho}\overline{u'^2}$ is normalized by the wall shear stress, the results are in fair

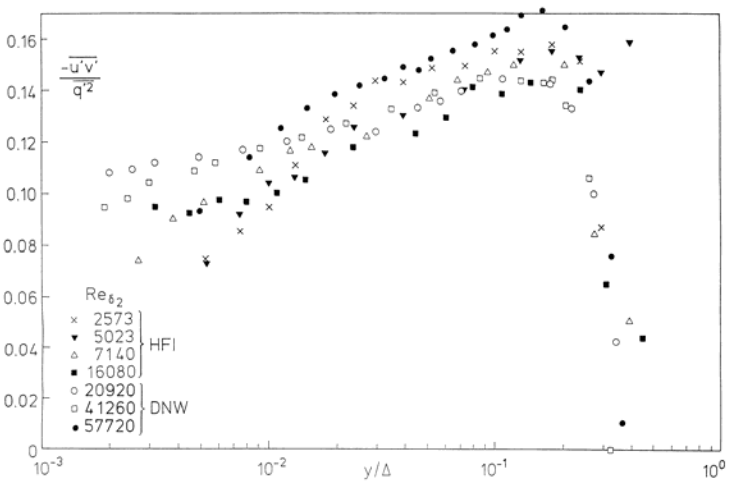

Figure 8.17. Distribution of the structure parameter $a_1 = -\overline{u'v'}/q^2$ in outer layer scaling at medium to high Reynolds numbers. Data from Bruns et al. (1992) and Nockemann et al. (1994). (Figure from Fernholz and Finley (1996). Reprinted with permission from Elsevier Science Ltd., Oxford, England.)

agreement with the incompressible data of Klebanoff (1955), except near the wall where the supersonic measurements are subject to considerable uncertainty (see Figure 1.2). This indicates the success of the scaling suggested by Morkovin (1962) to account for the mean density variation, and provides some support for the discussion given in Section 8.2. It should be mentioned that Fernholz and Finley (1981), in considering an earlier set of data, concluded that the streamwise Reynolds stress did not show a similar behavior in the outer region, no matter which velocity scale was used in the nondimensionalization. It appears that the later data shown in Figure 1.2 display a more regular behavior. Morkovin's scaling appears to be appropriate to at least Mach 5. Measurements by Owen et al. (1975) at $M_e = 6.7$ and Laderman and Demetriades (1974) at $M_e = 9.4$ exhibit damped turbulent fluctuations, particularly near the wall. Because both of the hypersonic data sets are for cold-wall conditions, this may simply indicate the stabilizing effect of cooling.

Measurements of $\overline{v'^2}$ and $\overline{w'^2}$ are less common than those of $\overline{u'^2}$, the data exhibit more scatter, and the conclusions are therefore less certain. Crosswire measurements of both streamwise and wall-normal components of velocity have suggested that some aspects of boundary layer structure depend on Mach number (Smits et al., 1989). In contrast to the streamwise turbulence intensity, $\overline{v'^2}$ and $\overline{w'^2}$ appear to increase slightly with increasing Mach number (Fernholz and Finley, 1981). In this case, Morkovin's scaling does not collapse the data,

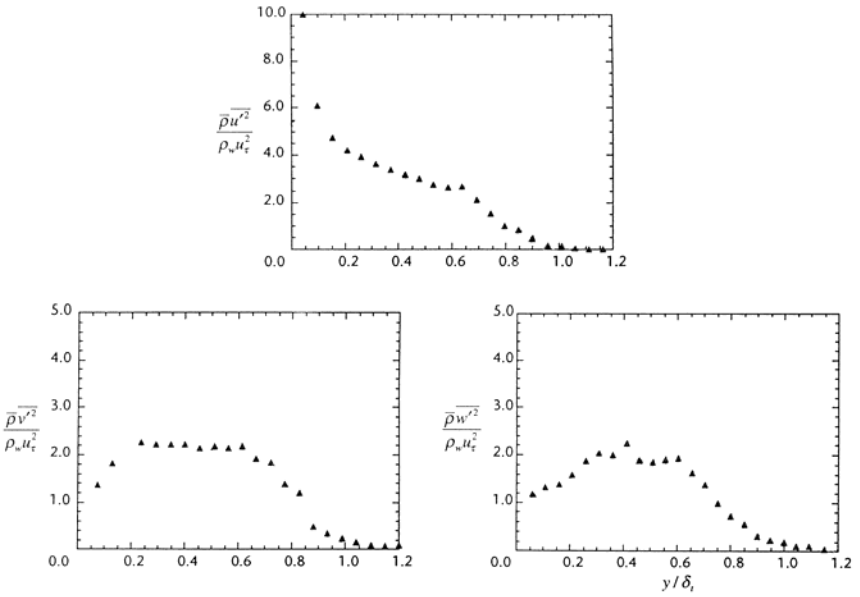

Figure 8.18. Turbulence distributions in a Mach 2.9 boundary layer, measured using hot-wire probes (Re_θ = 65,000). (Adapted from Konrad (1993), with the author's permission.)

and $\overline{\rho v'^2}/\tau_w$ and $\overline{\rho w'^2}/\tau_w$ show no obvious trend toward similarity. Using hot-wire anemometry, Konrad (1993) found that $\overline{w'^2}$ and $\overline{v'^2}$ in a Mach 2.9, high Reynolds number boundary layer were approximately equal throughout the layer (see Figure 8.18). In contrast, the measurements by Eléna and Lacharme (1988) in a Mach 2.3, low Reynolds number boundary layer using laser-Doppler velocimetry indicate that the behavior of $\overline{v'^2}/{u_\tau}^2$ is almost identical to that found in subsonic flows (see Figure 8.19). The behavior of the anisotropy ratio is therefore not clear: Eléna and Lacharme data indicate that the ratio $\overline{v'^2}/\overline{u'^2}$ is almost the same as those found by Klebanoff (1955) in a subsonic boundary layer, whereas the measurements by Fernando and Smits (1990) and Konrad (1993) indicate that this ratio increases with Mach number. As we saw earlier, however, the anisotropy depends strongly on Reynolds number, primarily because of the behavior of $\overline{v'^2}$, and the differences between the two sets of compressible flow data may well be due to the large Reynolds number difference between the experiments. Although the evidence is not conclusive, there may be no significant Mach number influence.

Recent DNS results on a zero pressure gradient boundary layer by Martin (2003, 2004) cover a Mach number range from 3 to 8, where the value of δ^+ was held approximately constant at 400 (corresponding to $Re_\theta = 2390$ at the lowest

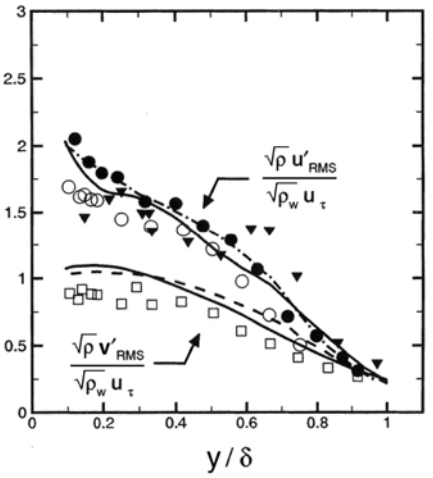

Figure 8.19. Turbulence distributions in a Mach 2.3 boundary layer ($Re_\theta = 4000$ to 4700). Symbols: Experimental results obtained using LDV (Eléna and Lacharme, 1988). Solid lines: DNS; broken lines: subsonic data from Klebanoff (1955). (Figure adapted from Martin (2004), with permission of the author.)

Mach number, and $Re_\theta = 13,060$ at the highest Mach). The wall condition was chosen to be isothermal with a value close to the adiabatic value, and the effect of varying the wall temperature was examined at Mach 5. As reported by Smits and Martin (2004), the DNS results support many of the experimental observations. For example, the mean velocity profiles transformed according to van Driest collapse with the usual scaling using inner and outer variables, and the Reynolds stresses collapse using Morkovin's scaling at about the same level of accuracy as seen in experiment. One of the cases considered by Martin was at $M = 2.23$ and $Re_\theta = 4452$, corresponding to the experiments by Debiève (1983), Eléna et al. (1985), and Eléna and Lacharme (1988), where $Re_\theta = 4000$ to 4700. The comparisons between DNS and experiment are particularly impressive (Figure 8.19).

Sandborn (1974) reviewed direct measurements and indirect evaluations of the Reynolds shear stress $-\overline{\rho}\overline{u'v'}$ in zero pressure gradient flows (a later, more comprehensive study was provided by Fernholz and Finley (1981)). Sandborn constructed a "best fit" of normalized shear stress profiles (τ/τ_w) from integrated mean-flow data taken over a wide Mach number range ($2.5 < M_\infty < 7.2$: extended to Mach 10 for adiabatic and cold walls by Watson (1978)). The data indicate a near-universal shear stress profile that agrees well with the incompressible measurements of Klebanoff (1955) (see Figure 8.20). Direct measurements of the shear stress have exhibited only modest agreement with

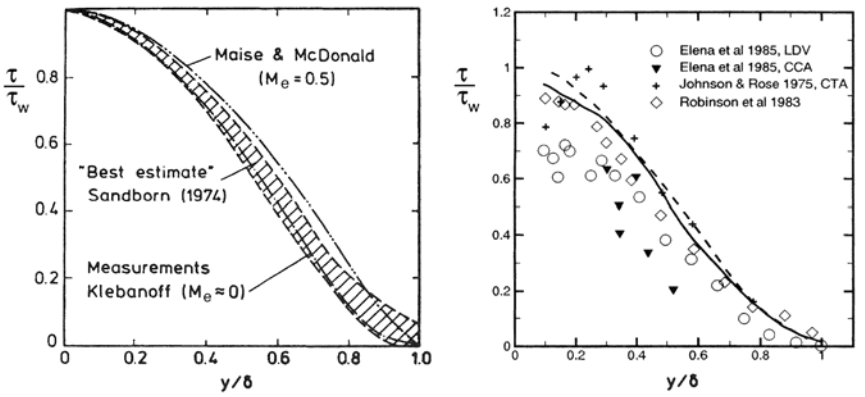

Figure 8.20. Distribution of shear stress in boundary layers at supersonic speed. Left: Figure from Sandborn (1974). Right: Figure from Martin (2004), where the solid line is DNS, and the broken line is subsonic data from Klebanoff (1955). (Figures reprinted with permission of the authors.)

Sandborn's best fit. The agreement is limited to the outer layer, with great scatter in the inner layer and most profiles not tending toward $\tau/\tau_w = 1$ near the wall. The data in the inner layer do not scale with yu_τ/ν_w, almost certainly because of the difficulties with the measurements. In contrast, the DNS results of Martin (2004) shown in Figure 8.20 are in excellent agreement with Sandborn's curve, and the Mach 2.32 LDV data of Eléna et al. (1985).

The shear correlation coefficients obtained by Fernando and Smits (1990) at Mach 2.9, indicated that R_{uv} decreases significantly with distance from the wall, from a value of about 0.45 near the wall to about 0.2 near the boundary layer edge (see Figure 8.21). This is in contrast to most subsonic flows where the correlation coefficient is nearly constant at a value of about 0.45 in the region between 0.1δ and 0.8δ. As can be seen in the figure, the data by Eléna and Lacharme (1988) at Mach 2.3 follow the subsonic distribution closely, and it is difficult to say how compressibility affects the level of R_{uv} without further experiments. However, as noted earlier, there is about a factor of 15 difference in Reynolds number between the results of Fernando and Smits and Eléna and Lacharme, and the differences seen in the distribution of R_{uv} may well reflect that fact, primarily through the Reynolds number dependence of $\overline{v'^2}$ (see Figure 8.14).

In Section 5.2 the Strong Reynolds Analogy was discussed, and some measurements in support of this analoguey were presented in Figures 5.4 and 5.5. It appears that the SRA is closely followed in supersonic boundary layers on adiabatic walls, and that the correlation coefficient R_{uT} is approximately equal to -0.8 throughout the layer. The DNS results of Wu and Martin (2004) at

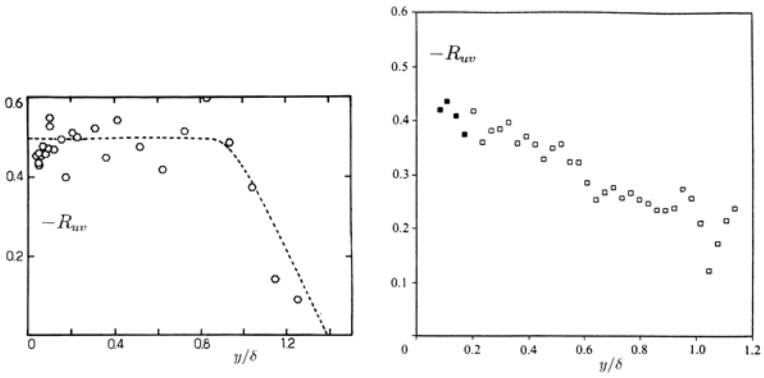

Figure 8.21. Distribution of R_{uv} in subsonic and supersonic boundary layer. Left: Data from Eléna and Lacharme (1988) (the dotted line is the subsonic data of Klebanoff (1955)). (Reprinted with permission of Gauthier-Villars.) Right: Data from Fernando and Smits (1990) (the filled-in symbols are subject to errors due to transonic effects). (Copyright 1990, Cambridge University Press. Reprinted with permission.)

Mach 3 agree very well with these observations (Figure 8.22), as do the computations by Martin (2004) for Mach numbers from 3 to 8. The magnitude of R_{uT} is considerably higher than that found in slightly heated subsonic flows, as seen in Figure 5.5, and the reason is not entirely clear. However, the high level of the correlation makes the SRA a very useful tool in describing the behavior of supersonic turbulent boundary layers, especially in formulating turbulence models. The SRA can also be extended to nonadiabatic flows, as discussed in Chapter 9.

The stagnation temperature fluctuation must be known to evaluate the turbulent heat-flux correlation, $-c_p\overline{\rho}\overline{v'T'}$. Kistler (1959) observed that $T'_{0_{rms}}/\overline{T_0}$ increased with Mach number, with maxima of 0.02 at $M_\infty = 1.72$ and 0.048 at $M_\infty = 4.67$. If Kistler's data are nondimensionalized using T_w (Fernholz and Finley, 1981) or $T_r - T_e$ (Sandborn, 1974), the Mach number dependence appears to be eliminated, but similarity of the stagnation temperature distributions is not achieved. The same conclusions are reached from measurements by Morkovin and Phinney (1958) and Horstman and Owen (1972). The maximum level of stagnation-temperature fluctuations is about 6% (for $M < 7$). Further analysis of these data shows that $T'_{0_{rms}}$ scales according to either $T_{0e} - T_w$ or $T_{0e} - T_r$. The fluctuations in total temperature appear to be produced by the difference in stagnation temperature between the wall and the freestream, and not, for example, by the unsteadiness in pressure through the term $\partial p/\partial t$ in the total enthalpy equation. In these experiments, the maximum of $T_{0_{rms}}/(T_{0e} - T_r)$ is about 0.5, regardless of the Mach number, a rather

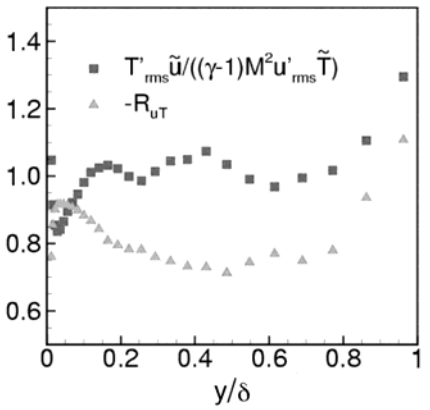

Figure 8.22. DNS results for the SRA in a Mach 3 boundary layer ($Re_\theta = 2400$). (Figure adapted from Wu and Martin (2004), with the authors' permission.)

satisfactory result because it shows that the total temperature fluctuations are of the order of (but less than) the total temperature difference across the boundary layer. Finally, T'_{0rms}/T_o is less than u'_{rms}/U and T'_{rms}/T, but not low enough to satisfy the strict Strong Reynolds Analogy. In fact, as indicated in Section 5.3, the one-dimensional form of the energy equation, together with the empirical results on the SRA, indicate that the ratio $T'_{0_{rms}}/T'_{rms}$ is approximately equal to $\sqrt{2\,(1+R_{uT})}$; that is, $T'_{0_{rms}}$ is about 60% of T'_{rms}, independent of the Mach number (Smits and Dussauge, 1989).

8.4 Organized Motions

Here we describe the organized, spatially correlated motions found in turbulent boundary layers. The interest in such flow structure is driven, at least in part, by the hope that a better understanding of the dynamics of turbulent motions will lead to a better predictive capability. Although we have not yet achieved that objective completely, our studies of organized motions have led to a deep (albeit largely qualitative) understanding of the turbulence production cycle in wall-bounded flows, and a much better understanding of Reynolds number scaling. The presentation given here is based largely on the earlier work by Smith (1994), Spina et al. (1994), Dussauge et al. (1996) and Smits and Delo (2001), and further details are given there. There are several excellent reviews of turbulent flow structure in the literature, including Willmarth (1975); Cantwell (1981), Robinson (1991a), and especially the volume by Panton (1997). More personal interpretations are offered by Hussain (1983), Coles (1987), and Sreenivasan (1989).

The term "structure" has at least two different interpretations. First, it is used to describe the behavior of the mean flow and Reynolds stresses. The scaling of the mean flow and Reynolds stresses, the composition of Reynolds stresses, anisotropy ratios, and the behavior of the shear correlation coefficient, Townsend's structure parameter a_1, and the intermittency profiles, can all be viewed as describing the structure of a turbulent boundary layer. Second, the term is used to describe coherent organized motions occurring in the flow. Robinson (1991a) defines a coherent motion, or structure, as

> a three-dimensional region of the flow over which at least one fundamental flow variable (velocity component, density, temperature, etc.) exhibits significant correlation with itself or with another flow variable over a range of space and/or time that is significantly larger than the smallest local scales of the flow.

This definition is quite general, although as Kline and Robinson (1989) point out, the classification of coherent structures in turbulent boundary layers can be arranged in many ways, and they use the term "quasi-coherent" to emphasize that the structures or motions exhibit significant variation from one experiment to another. More specific versions have been proposed (for instance, Hussain (1983)), but in essence they are just restricted forms of Robinson's definition.

8.4.1 Inner Layer Structure

Klebanoff (1955) found that about 75% of the total turbulence production in the boundary layer occurs in the region where $y/\delta < 0.2$. Most subsequent investigations of turbulent boundary layer structure have therefore focused on the near-wall region, primarily the viscous sublayer and buffer layer. Because of practical considerations, such as the need for adequate resolution of small scales, these studies have been limited to subsonic flows, predominantly at low Reynolds numbers; that is, $Re_\theta < 5000$. In supersonic flows, the scaling of the turbulence in the inner layer undoubtedly becomes more complicated because strong gradients of temperature occur in the near-wall region that can cause major changes in density and viscosity. Almost no near-wall data exist for supersonic boundary layers, and so we must proceed under the assumption that similar mechanisms occur in compressible flows, as long as Morkovin's hypothesis is satisfied. Recent DNS computations help verify this assumption, as discussed below.

Runstadler et al. (1963), Kline et al. (1967), and Bakewell and Lumley (1967) discovered that the viscous sublayer is occupied by alternating streaks of high- and low-speed fluid (relative to the mean), as illustrated in Figure 8.23. The spanwise spacing of the streaks λ_s was found to scale on inner variables and to have a nondimensional mean value of $\lambda_s^+ \approx 100$. The streaks were presumed

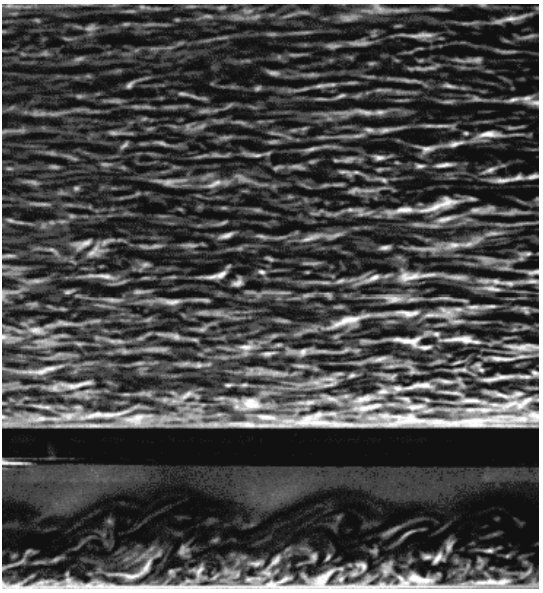

Figure 8.23. Turbulent boundary layer on a flat plate. The water was seeded with aluminum particles and viewed simultaneously from above and the side. Note the large population of meandering near-wall streaks in the top view, and the downstream-leaning, large-scale structure in the side view (Cantwell et al., 1978). (Copyright 1978, Cambridge University Press. Reprinted with permission.)

to be the result of elongated, counter-rotating streamwise vortices very near the wall. Kline et al. observed that the low-speed streaks would gradually lift up from the wall, oscillate, and then break up violently, ejecting fluid away from the wall and into the outer layer. They coined the term *bursting* to describe this sequence of events, and concluded that all the events comprising the bursting process were consistent with a stretched and lifted vortex. Kim et al. (1971) determined that in the wall region $0 < y^+ < 100$, nearly all of the turbulence production occurs during bursting, thus establishing the dynamical significance of the near-wall region and the bursting process.

Similar observations were made by Corino and Brodkey (1969). They found a recurring sequence of events where a large-scale disturbance would frequently impinge upon a near-wall region of low-speed fluid. This would be followed by one or more ejections of low-speed fluid up into the large-scale disturbance, resulting in violent chaotic interaction. Once the ejection(s) had subsided, a large region of high-speed fluid would cleanse the area of the debris of the interaction. Corino and Brodkey called this latter event a *sweep*. As the Reynolds number increased, the frequency and intensity of the ejection events

increased, and at high Reynolds numbers it was difficult to distinguish between individual events.

Cantwell (1981) examined the coherent structures in the inner layer in terms of localized regions of vorticity, and suggested that a fluctuating array of streamwise counterrotating vortices densely covers all parts of the smooth wall. Slightly above the streamwise vortices but still quite close to the wall is a layer that is regularly battered by bursts that involve very intense small-scale motions of energetic fluid, which he termed "energetic near-wall eddies."

The average spanwise spacing of the streaks ($\lambda_s^+ \approx 100$) is one of the few universally accepted aspects of boundary layer structure, although there are large departures from the mean (Smith and Metzler, 1983). In contrast, estimates of the streamwise extent of the streaks vary widely. This is most likely due to the different methods used to make the estimates. The low-speed streaks are seen to extend up to $L_x^+ = Ł_x u_\tau/\nu \approx 2000$ in some cases, when the spanwise meandering of the streaks is taken into account. Marušić (2004) has observed even longer streaks in moderate Reynolds number boundary layers, and recent DNS computations of channel flow support this observation (Iwamoto, 2004). Velocity correlation methods derived from stationary probes tend to underestimate the streamwise length of a meandering streamwise vortex, because only limited portions of such a vortex intersect the probe. The persistence distance of the near-wall vortices is difficult to evaluate for the same reasons. Probably the most complete description of their formation is given by Schoppa and Hussain (1997). As Cantwell points out, even if the low-speed streaks are generated directly by pairs of counterrotating vortices, it does not necessarily follow that the two must have the same streamwise dimension (Smith et al., 1991; Smith and Walker, 1997).

In compressible flow, the only evidence for the behavior of the near-wall structure comes from DNS. Martin (2004), in a study of flat plate boundary layers from Mach 3 to 8, observed a 40% decrease in the streamwise extent of the near-wall streaks with Mach number (as a fraction of δ), and a 20% decrease in spanwise spacing (in terms of ν_w/u_τ). These decreases may be due to the spatial variation in the viscous length, because the rapid variations in temperature near the wall cause significant changes in the local density and viscosity. The fact that an increasing wall temperature had a similar effect on the streaks supports this suggestion.

The convection velocities of the various types of near-wall structures are fairly well established, at least in subsonic flows, and the values represent data from a wide range of studies, primarily correlation based. For example, the average convection velocity of the near-wall streamwise vortices is probably close to the local mean velocity, because the low- and high-speed streaks move at about 50% and 150% of the local mean velocity, respectively (Cantwell, 1981).

In contrast, the scaling of the mean bursting period, T_b (or mean bursting

frequency, $f_b \sim 1/T_b$) is still controversial. Initially, Kline et al. suggested that, because the bursting process is a wall-layer phenomenon, T_b should scale with inner variables. Subsequent research has provided many conflicting results. Rao et al. (1971), working in a turbulent boundary layer in the range $600 < Re_\theta < 9000$, concluded that outer scaling is appropriate, and that $T_b U_e/\delta \approx 5$ (or $T_b U_e/\delta^* \approx 30$), independent of Reynolds number. Alfredsson et al. (1988), working in a fully developed channel flow in the range $13{,}800 < Re_c < 123{,}000$ (Re_c based on channel height and centerline velocity), found that T_b was independent of Reynolds number when nondimensionalized by a mixed time scale equal to the geometric mean of the inner and outer time scales. Thus, three different scalings for T_b (and thus f_b) have been proposed, and the issue has not yet been resolved.

The scaling of T_b is important in its implications for the dynamics of the turbulent boundary layer. If T_b scales on inner variables, it suggests that the inner layer controls the dynamics of the boundary layer, and the outer layer structure may be merely the debris of the bursting process. Alternatively, if T_b follows outer scaling, it implies that the bursting process is controlled or modulated by (and may be responding passively to) the outer layer structure. If T_b scales on mixed variables, it implies an important mutual interaction between the inner and outer structure.

There are many reasons for the discrepancy among the various results. Measurement errors are important, in that spatial-averaging effects will lead to an underestimate of f_b (Blackwelder and Haritonidis, 1983). More important, in order to measure the bursting period, it is necessary to devise a criterion for detecting the bursting process. Visual methods, as used by Kline et al., Corino and Brodkey, and Kim et al., are limited to very low Reynolds numbers. Therefore, Lu and Willmarth (1973) introduced the u'-level method, in which low values of u', relative to the mean, were used to detect ejections, and high levels of u' were used to detect sweeps. Wallace et al. (1972) and Lu and Willmarth (1973) proposed splitting the u'–v' velocity plane into four quadrants, as shown in Figure 8.24. Instantaneous values of $-u'v'$ can then be associated with a certain quadrant and a corresponding event (see also Antonia (1971)).

Blackwelder and Kaplan (1976) developed an alternative method, the Variable Interval Time Averaging (VITA) technique, whereby the variance of the velocity u' is computed over a short time interval. When the short time variance exceeds a preset threshold level, an event is said to have occurred. The goal of these detection schemes is to identify segments of the velocity signal that correspond to events of interest (for example, ejections and sweeps), and to analyze these segments separately from the remaining signal by conditional sampling and averaging.

All detection methods are, to some extent, subjective because they require the user to choose threshold levels and/or averaging times. Willmarth and

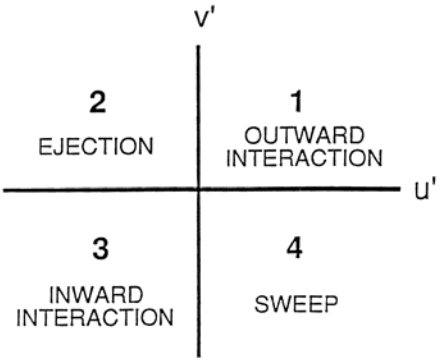

Figure 8.24. The four quadrants of the u'–v' plane, and the common terms for the events corresponding to each quadrant. (Figure from Robinson (1991b), with the author's permission.)

Sharma (1984) found that the bursting period determined using the VITA technique is highly sensitive to the threshold level and the averaging time. When the threshold level was changed by 5%, the measured bursting frequency changed by 40%, and a 20% change in the averaging time resulted in a 15% change in measured bursting frequency. More disturbing is the fact that it is not certain what relationship exists between the detected events and the actual events occurring during the bursting process. Bogard and Tiederman (1986, 1987) evaluated several detection methods and found that different methods could yield values of T_b which differed by an order of magnitude. They also found that different techniques detected different phases of the bursting process. Corino and Brodkey (1969) had already observed that more than one ejection may occur during a single burst, leading to further variations among the reported results. Reynolds number effects may also be important (Shah and Antonia, 1989), and it is possible that the structure of fully developed pipe and channel flows differs from that of turbulent boundary layers because the outer layers have different intermittent characteristics.

8.4.2 Outer Layer Structure

The outer layer is more easily accessible to measurement, and therefore reasonably comprehensive data sets exist for the large-scale structure of subsonic and supersonic flows. The current state of knowledge concerning compressible boundary layer structure is derived largely from studies by Robinson (1986); Spina and Smits (1987); Smits et al. (1989); Fernando and Smits (1990), Spina et al. (1991a,b), Donovan et al. (1994), and Bookey et al. (2005b) of flat-plate layers with freestream Mach numbers of approximately 3, and the work by

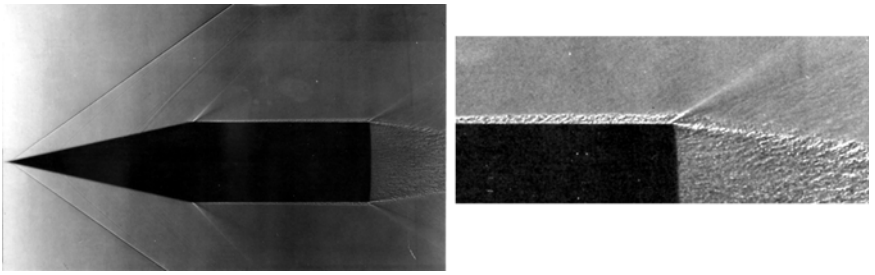

Figure 8.25. Shadowgraph visualizations of the flow over a cone cylinder of 12.5° semi-vertex angle at Mach 1.84. A detail of the flow in the vicinity of the base is shown on the right. (Photograph by A.C. Charters, taken from Van Dyke (1982), with permission.)

Baumgartner et al. (1997) and Bookey et al. (2005a) at Mach 8. These studies were preceded by a pioneering investigation by Owen and Horstman (1972), who made extensive two-point cross-correlation measurements with hot-wires in a Mach 7.2 boundary layer. Most of the results available in the literature were obtained using hot-wire anemometry (with its attendant limitations), with some degree of corroboration at high speed by quantitative flow visualization studies (Smith and Smits, 1988; Cogne et al., 1993; Baumgartner et al., 1997; Bookey et al., 2005a,b).

A characteristic component of the outer layer is the large-scale turbulent *bulge*, also referred to as a *Large-Scale Motion* (LSM). LSMs (Townsend's "main eddies") evolve and decay slowly as they convect downstream, and on average they are inclined to the wall in the downstream direction. Their most identifiable feature is a downstream-sloping shear layer interface between upstream high-speed fluid and downstream low-speed fluid (unfortunately, these structures have been labeled both "fronts" and "backs" in the literature). These interfaces are three-dimensional shear layers that form the upstream side of the largest of the boundary layer eddies, and remain coherent long enough to convect several boundary layer thicknesses downstream. Early shadowgraph images of boundary layers on supersonic bodies of revolution (where the spatial integration is minimized) clearly showed such structures, appearing as marked and regular striations in the layer, leaning downstream at a characteristic angle of 40° to 60° (Figure 8.25). Figure 8.26 shows several LSMs in a subsonic boundary layer, and comparable images for supersonic flow are given in Figure 1.4 and Figure 8.27.

The LSMs are an important feature in that they are responsible for the large-scale transport of turbulence in the outer layer, the growth of the layer by entrainment of initially irrotational flow, and appear to play a role in triggering instabilities in the near-wall region. Up to 40% of the outer layer Reynolds shear stress can be found in the neighborhood of their sloping interfaces (Spina

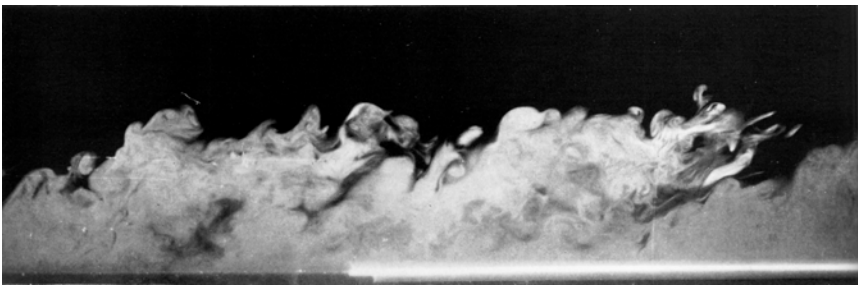

Figure 8.26. Flow visualization of a boundary layer in subsonic flow at $Re_\theta \approx 4000$, obtained by seeding the flow with a fog of oil droplets, and illuminating the flow with a planar laser sheet (Falco, 1977). Flow is from left to right. (Copyright 1977, AIP. Reprinted with permission.)

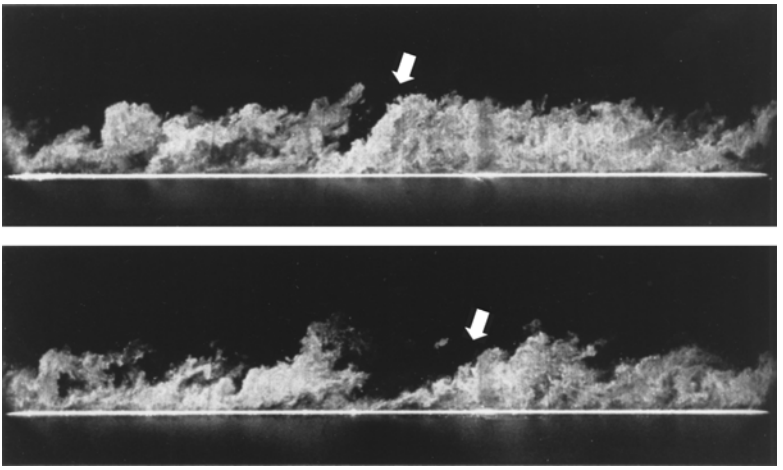

Figure 8.27. Flow visualization of a boundary layer in a Mach 2.82 flow at $Re_\theta = 81{,}190$, obtained by seeding the flow with acetone droplets, and illuminating the flow with a planar laser sheet (the two pictures shown were taken at different times). The flow is from left to right. (Figure from Smith and Smits (1995). Copyright 1995, Springer-Verlag. Reprinted with permission.)

et al., 1991a). Between neighboring bulges, the flow is irrotational, resulting in the intermittent nature of the outer layer. The LSMs vary greatly in size and inclination angle, and their length scales, time scales, convection velocity, and structure angle, as well their characteristic velocity, vorticity, and pressure fields, remain the subject of active research. Furthermore, their Reynolds number and Mach number dependence is not very well understood, although the superficial similarities between the subsonic and supersonic flows is striking

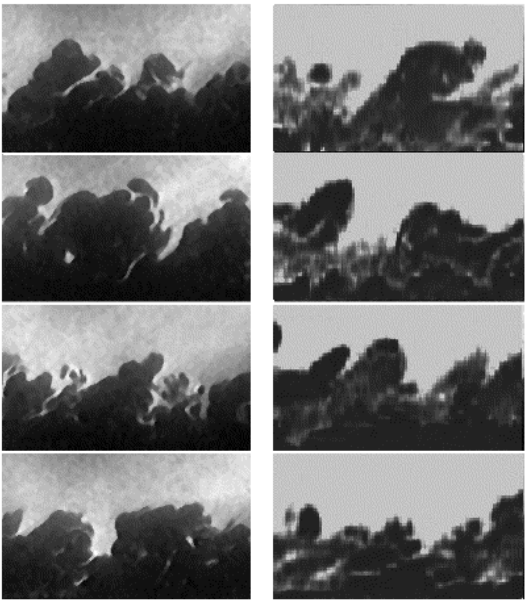

Figure 8.28. Visualizations of flat plate boundary layers. Flow is from left to right. Left: Air at Mach 8, $Re_\theta \approx 3600$ ($\delta^+ \approx 200$), visualized using FRS. Right: Water at Mach 0, $Re_\theta = 700$ ($\delta^+ = 300$), visualized using dye (Delo and Smits, 1997). (Figure from Baumgartner et al. (1997), with the author's permission.)

(compare, for example, Figures 8.26 and 8.27). Even more suggestive is the comparison shown in Figure 8.28, where two low Reynolds number boundary layers, one in a low-speed water channel and the other at Mach 8, are shown side by side.

In contrast to this visual evidence, the hot-wire measurements by Owen et al. (1975) had strongly suggested that the extent of the intermittent zone decreased with Mach number. Part of the difficulty in determining the intermittency (the wallward extent of the entrainment process) is finding an unambiguous criterion for discriminating between turbulent and nonturbulent fluid. Many techniques have been employed, but most methods generate a box-car function by setting a threshold on the turbulence level, or on its first derivative (Antonia, 1971). The most basic output is the intermittency itself, γ, that is, the fraction of the time the flow is turbulent. Another possible method for finding the intermittency is based on the pdf of the turbulence, where γ is measured by the departure of the turbulence from its Gaussian flatness value of 3; that is, $\gamma \equiv 3/F$, where F is the flatness. The flatness distributions for a number of different freestream Mach numbers are shown in

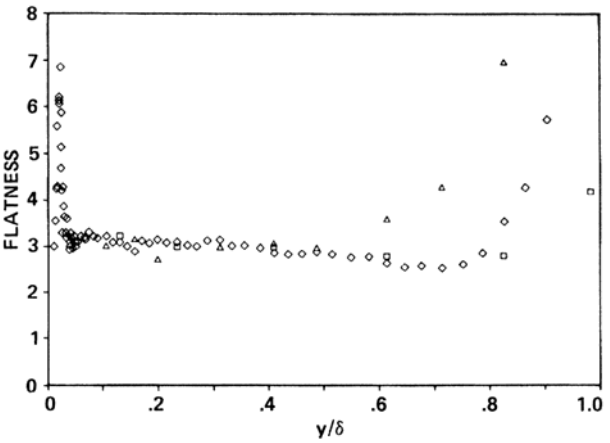

Figure 8.29. Comparison of flatness distributions: □, Owen et al. (1975) (Re_θ = 8500, $M = 7$), based on mass flux; ◇, Robinson (1986) (Re_θ = 15,000, $M = 3.0$, based on mass flux; △, Klebanoff (1955) ($Re_\theta = 7100$, $M \approx 0$), based on velocity. (Figure from Robinson (1986), with the author's permission.)

Figure 8.29. The data display an apparent Mach number dependence, where the onset of intermittency (corresponding to the rise in flatness factor) occurs nearer the boundary layer edge as the Mach number increases. Because the zone of influence of a flow disturbance decreases with Mach number, the intermittent zone could become thinner as the Mach number increases. As already noted, this interpretation is not supported by high-speed flow visualizations, and recent measurements by Baumgartner et al. (1997) and Bookey et al. (2005b), as well as the DNS results of Martin (2004), support the notion that the intermittency does not depend on Mach number to any significant extent (see Figures 8.30 and 8.31).

So far, we have described the LSMs as a unified, large-scale, organized motion. However, considerable evidence now exists to indicate that they possess a rich internal structure, comprising "typical eddies," and horseshoe or hairpin eddies, and that the LSMs may well be formed by well-organized "packets" of hairpin eddies that are originally attached to the wall, and subsequently become detached as vorticity cancellation and viscous effects take place. These eddy structures are discussed in detail in Section 8.7.

8.5 Correlations and Ensemble Averages

A common method for investigating the large-scale structure is multiple-point measurements of one or more flow variables, typically velocity, wall pressure,

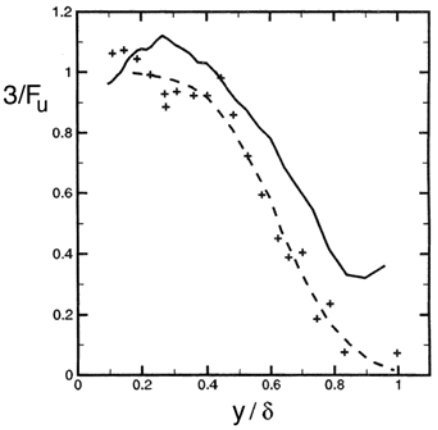

Figure 8.30. Comparison of intermittency distributions based on flatness of the streamwise velocity: +, Eléna and Lacharme (1988) ($Re_\theta = 5650$, $M = 2.32$, LDV); ———, Martin (2004) ($Re_\theta = 4452$, $M = 2.32$, DNS); – – –, Klebanoff (1955) ($Re_\theta = 7100$, $M \approx 0$, HWA). (Figure from Martin (2004), with the author's permission.)

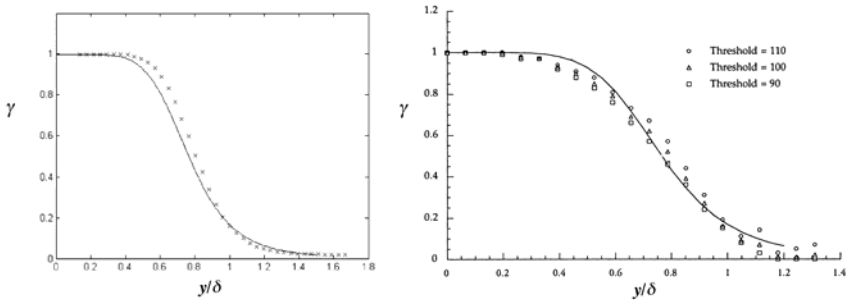

Figure 8.31. Intermittency distributions. Left: ×, Baumgartner et al. (1997) ($Re_\theta = 3600$, $M = 8$, FRS); ———, Klebanoff (1955) ($Re_\theta = 7100$, $M \approx 0$, HWA). Right: Bookey et al. (2005b) ($Re_\theta = 2400$, $M = 2.9$), FRS. (Figures adapted from Baumgartner et al. (1997) and Bookey et al. (2005b), with the authors' permission.)

and wall shear stress. The data are then analyzed in the context of space-time correlations. Space-time correlations generally have a single well-defined peak, which occurs at $\tau = \tau_{max}$, the optimum time delay, which is usually nonzero.

Favre et al. (1957, 1958) pioneered the use of velocity space-time correlations. Their results, for Re_θ values of about 1400 and 2700, showed that the fluctuating velocities in the outer layer are correlated over distances comparable to the boundary layer thickness in the spanwise and wall-normal directions,

and over several boundary layer thicknesses in the streamwise direction. The space-time correlations for optimum time delay also showed that, in the outer layer, structures are convected downstream for a distance of $O(10\delta)$ before decaying. Nearer the wall, the structures decay more rapidly. Sternberg (1967) noted that Favre et al.'s results also indicate that the large eddies are inclined to the wall in the downstream direction.

In a later paper, Favre et al. (1967) used space-time correlations to measure convection velocities of the large-scale motions in a turbulent boundary layer with $Re_\theta \approx 8700$. To complement their broadband results, they bandpass filtered the data to measure the convection velocities of structures within a narrow range of scales. They found that the smallest scales convect at about the local mean velocity throughout the boundary layer. For $y/\delta > 0.2$, large-scale structures convect at speeds less than the local mean velocity, and the convection velocity decreases with scale. For $y/\delta < 0.2$, the opposite behavior is observed. At $y/\delta \approx 0.2$, all scales convect at the local mean velocity. This behavior could be explained as follows. A large structure will extend across a significant fraction of the boundary layer, and will convect at a speed that is a weighted average of the local mean velocity acting over the vertical span of the structure. This convection velocity will be greater than the local mean near the wall, and less than the local mean in the outer layer. The greater the vertical extent of the structure, the greater will be this effect. Based upon space-time correlations of wall pressure fluctuations, Corcos (1963) and Tu and Willmarth (1966) reached similar conclusions regarding the difference in convection velocity between large- and small-scale structures. Spina et al. (1991b) obtained similar results for the convection velocity distribution in a compressible flow (see Figure 8.32).

Using conditional averaging techniques based on the intermittency, Kovasznay et al. (1970) and Blackwelder and Kovasznay (1972) discovered a stagnation point on the back (upstream) side of the turbulent bulges in a subsonic boundary layer. Because the bulges convect at a speed less than the freestream velocity, the high-speed freestream fluid in the regions between the bulges will impinge on the backs of the bulges, resulting in a stagnation point in the convected frame of reference, as shown in Figure 8.33. Similar to the results of Favre et al. (1957, 1958) Kovasznay et al. found that isocontours of the space-time correlations of the streamwise velocity were elongated in the streamwise direction and spanned the entire boundary layer thickness, and that the large eddies lean downstream (see Figure 8.34). The contours were generated by correlating the velocity measured by a probe at a fixed point in the middle of the boundary layer with the velocity measured by a probe that was traversed in both the y- and z-directions while maintaining a constant longitudinal probe separation of 3.8δ. The results indicate that the large eddies are inclined with an average angle of approximately 16°. At the location of the fixed point, the streamwise extent of the correlations is about 0.4δ (based on a minimum

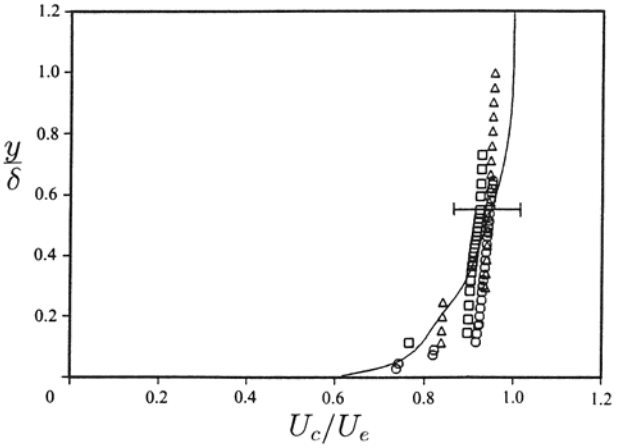

Figure 8.32. Broadband convection velocity in a turbulent boundary layer at $Re_\theta = 81{,}000$ and $M = 2.9$, based on measurements with three different streamwise probe separations. $\xi_x/\delta = 0.11$ □ ; 0.16 ○; 0.18 △. (Figure from Spina et al. (1991a). Copyright 1991, Cambridge University Press. Reprinted with permission.)

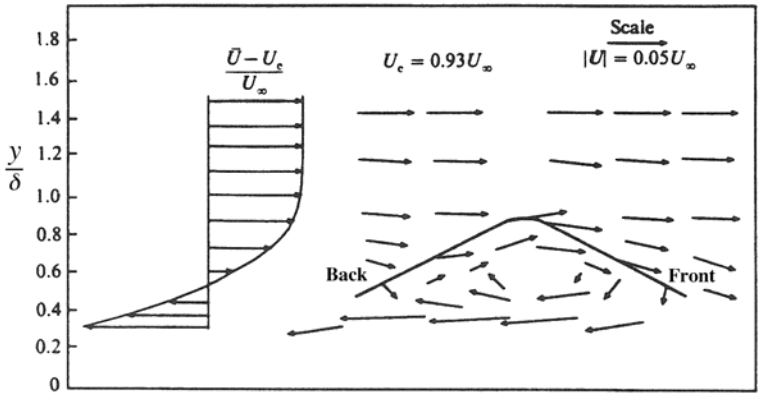

Figure 8.33. Schematic of the flowfield within and surrounding a large-scale motion in a turbulent boundary layer, according to Blackwelder and Kovasznay (1972). (Figure from Spina et al. (1991a). Copyright 1991, Cambridge University Press. Reprinted with permission.)

correlation value of 0.5).

Murlis et al. (1982) used hot-wire anemometry and temperature-tagging methods to study the effect of Reynolds number on boundary layer structure

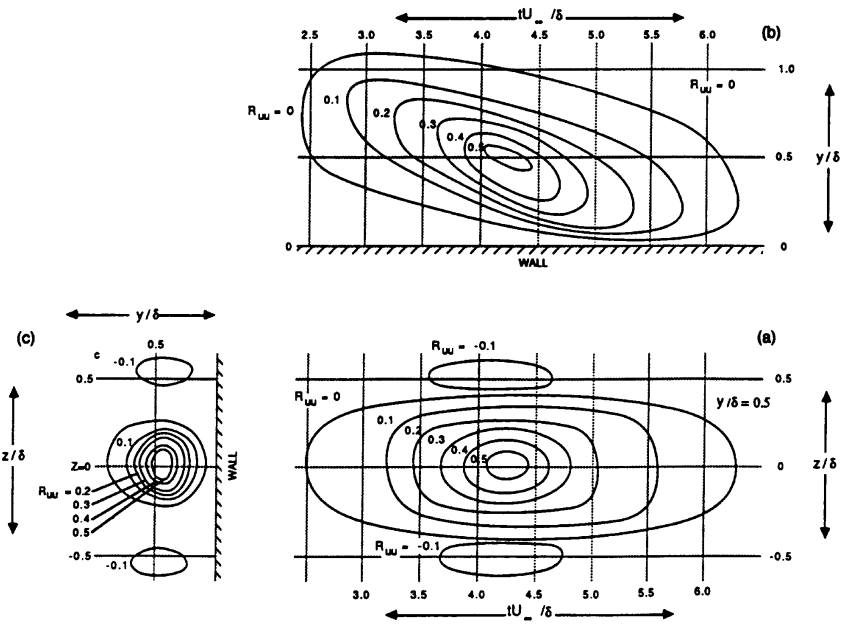

Figure 8.34. Isocorrelation contours of space-time correlations of the streamwise velocity component measured by Kovasznay et al. (1970). (a) x–z plane, (b) x–y plane, and (c) y–z plane. The position of one probe was fixed at $y/\delta = 0.5$. (Copyright 1987, Cambridge University Press. Reprinted with permission.)

for $791 < Re_\theta < 4750$. They found that the intermittency profile is essentially independent of Reynolds number. However, the average length of zones of turbulent motion was found to decrease with increasing Reynolds number up to $Re_\theta \approx 5000$. Their data suggested that, beyond this Reynolds number, the turbulent zone length remained constant. Similarly, Antonia et al. (1990a,b), using what they called a "window average gradient" detection scheme, found that the average period between detected events in the outer layer is independent of Reynolds number when scaled on outer variables, and it has a value of $\approx 2.5\delta/U_e$. This value is similar to that obtained by Corrsin and Kistler (1955) and Ueda and Hinze (1975), as noted by Falco (1977). Conditionally averaged isovorticity contours were observed to extend further from the wall and have a larger inclination angle (they were more upright) at lower Reynolds numbers, and the contribution of the organized motion to the turbulence stresses decreased as the Reynolds number increased.

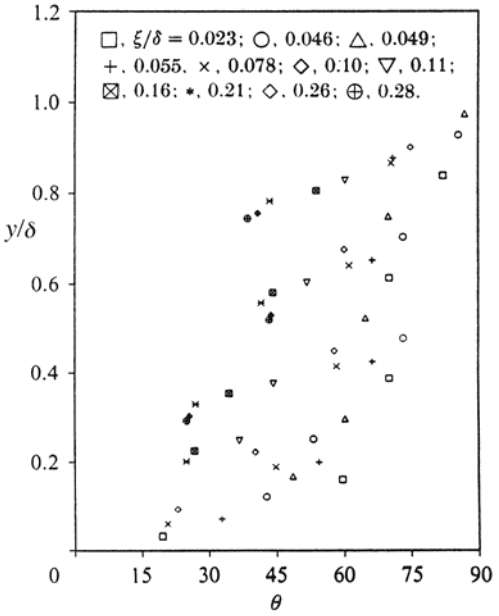

Figure 8.35. Broadband structure angle in a subsonic boundary layer, as a function of probe separation distance. (Figure from Alving et al. (1990). Copyright 1990, Cambridge University Press. Reprinted with permission.)

8.5.1 Structure Angle

Alving and Smits (1990) and Alving et al. (1990) measured the broadband structure angle of the LSMs by using two probes separated by a distance ξ_y in the wall-normal direction. The *structure angle* was defined by $\theta = \tan^{-1}(\xi_y/U_c\tau_{max})$, where U_c is the convection velocity (assumed to be equal to the local mean velocity) and τ_{max} is the time delay to the maximum in the space-time correlation. The results given in Figure 8.35 indicate that θ is a strong function of probe separation when ξ_y is small. It appears, however, that θ reaches a limit as ξ_y increases, where it becomes independent of probe separation. The angles in the middle of the layer are about 30°, considerably higher than the values found by Brown and Thomas (1977) and Kovasznay et al. (1970). Perry et al. (1992) measured structure angles by fixing the wall-normal separation of two probes and varying the streamwise separation until the value of the cross-correlation of the signals from the two probes attained a peak. This method has the advantage of not depending on the validity of Taylor's hypothesis. The results agreed well with the data of Alving et al. (1990), for which the probes were separated in only the wall-normal direction

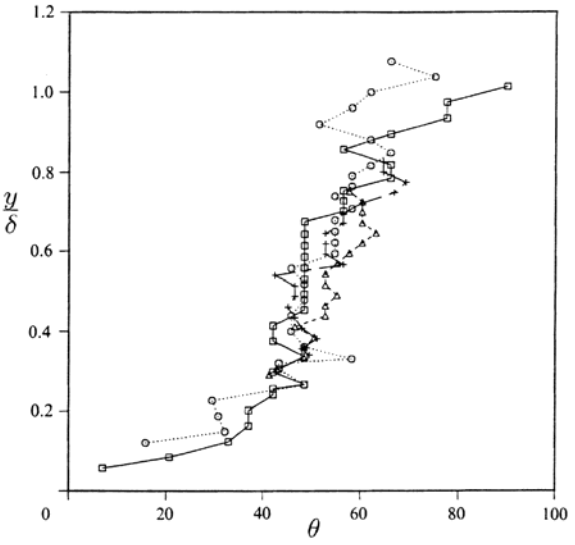

Figure 8.36. Broadband structure angle found using two hot-wire probes with different wall-normal separations. ξ_y/δ = 0.09 ———— □; 0.21 ----------○, 0.30 ---------△; 0.40 ——-——-+. (Figure from Spina et al. (1991a). Copyright 1991, Cambridge University Press. Reprinted with permission.)

and Taylor's hypothesis was used.

Hot-wire and flow visualizations show that the sloping delta-scale structures convect downstream at approximately 90% of the freestream velocity (slightly greater than for similar structures in low Reynolds number, incompressible turbulent boundary layers), and at Mach 2.9 persist for at least four boundary layer thicknesses downstream (and probably much farther) (Spina et al., 1991b). The average angle at which the sharp interfaces lean downstream ranges from 45° to 60° (with a standard deviation of approximately 20°) across most of the boundary layer, with a decrease near the wall and an increase near the boundary layer edge. The measured value of the structure angle is strongly dependent on measurement technique, although one method in current favor employs two hot-wires, separated by a fixed distance in y of 0.1 to 0.3δ, with both traversed across the layer. Structure angles measured using this technique in subsonic, low Reynolds number turbulent boundary layers are somewhat lower than those for Mach 3, high Reynolds number layers (see Figures 8.35 and 8.36). As indicated earlier, it seems likely that increasing Reynolds number decreases the structure angle, and increasing Mach number increases the structure angle.

Space-time correlation measurements by Smith (1994) at Reynolds numbers in the range $4600 \leq Re_\theta \leq 13{,}200$ showed that the broadband convection

velocity and the decay of the large scales with increasing time delay were only weakly dependent on Reynolds number when scaled on outer layer variables (U_e and δ). However, isocorrelation contours indicated that the streamwise length scales increased with Reynolds number, in agreement with the results by Liu et al. (1991) in a fully developed channel flow. Furthermore, space-time correlations in the wall-normal direction revealed that the broadband structure angle *decreased* by about 10° over the same range in Re_θ. Isocorrelation contour maps (Figures 8.37 and 8.38) showed an *increase* of between 30 and 60% in the streamwise length scale over the same Reynolds number range, and this behavior may be related to the decrease in the structure angle. The spanwise length scale showed comparatively little variation.

These subsonic results provide an interesting contrast to the results obtained by Spina et al. (1991a) in a Mach 3 boundary layer with $Re_\theta = 80{,}000$ (see Figure 8.39). In the supersonic flow, the streamwise length scales were two to three times *smaller* than in the subsonic flow, and the structure angles were about 10° *larger*.[1] The spanwise scales were almost independent of the Mach number. Now, the smaller streamwise scale is in accordance with the more upright orientation of the structure, but the trend with Reynolds number for subsonic flows does not seem to hold for supersonic flows. It seems that the streamwise length scale and the structure angle depend on the Mach number and the Reynolds number. This seems to be the most significant structural difference between the two flows yet found, and as indicated earlier Reynolds number and Mach number appear to be important. Increasing Reynolds number will increase the streamwise scales, whereas increasing Mach number will decrease them. Otherwise, the structural model for the large-scale motions in a supersonic flow is very similar to that derived from studies of subsonic flows, as can be seen by comparing Figures 8.33 and 8.40.

Because the influence of compressibility on the large-scale turbulent boundary layer motions seems to be subtle, explanations for the observed differences between low- and high-speed boundary layer structure are mostly speculative. Density gradient effects are known to play a significant role in turbulent shear layers, but these effects are most likely to influence the near-wall region of the wall layer, out of reach of standard measurement techniques. Parallels have also been drawn between the 45-degree slope of the interfacial structures in supersonic boundary layers and that of the hairpin-vortex structure observed in incompressible boundary layers. Insufficient evidence exists to support either side of this comparison, however. More conclusive results concerning compressibility effects on large-scale structure require higher Mach number investigations.

For boundary layers with freestream Mach numbers above 5, the near-wall region is more likely to show significant departures from known incompress-

[1]Baumgartner (1997) found similar results based on FRS measurements in a Mach 8 boundary layer with $Re_\theta = 3600$.

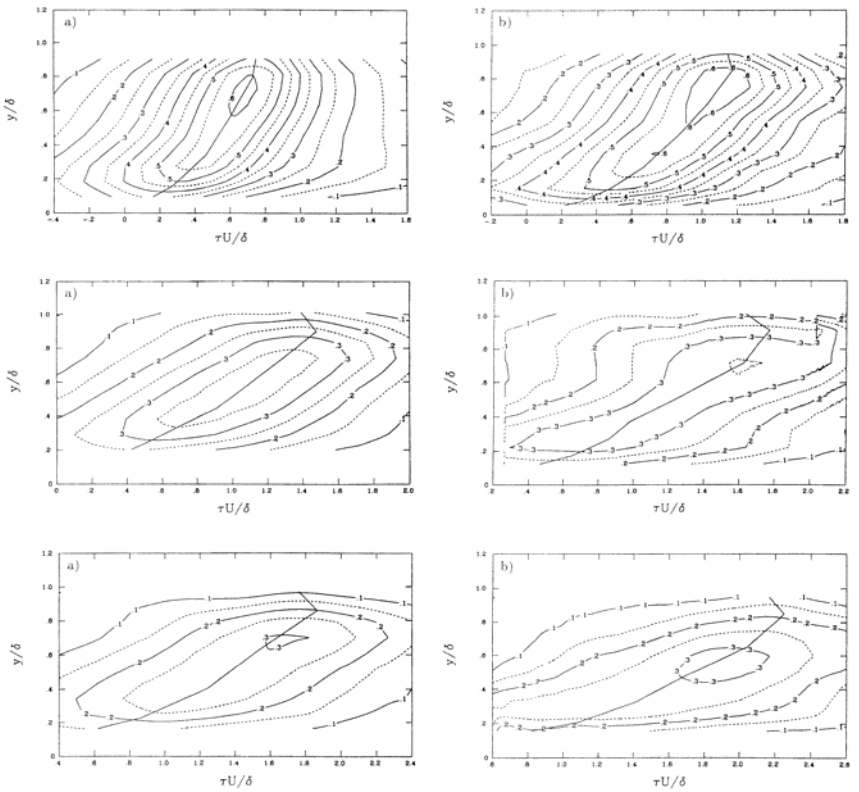

Figure 8.37. Isocorrelation contour maps in the x–y plane, as measured by Smith (1994), in a subsonic turbulent boundary layer at $Re_\theta = 4981$ (left) and 13,052 (right) using different wall-normal probe separations: (a) $\xi_y/\delta \approx 0.1$; (b) $\xi_y/\delta \approx 0.2$; (c) $\xi_y/\delta \approx 0.3$. (Figure from Smith (1994), with the author's permission.)

ible structure. The viscous sublayer for hypersonic boundary layers is likely to be much more quiescent than for incompressible flows (although pressure fluctuations will be imposed from above), and it may not display the familiar streaky structure. Because the mass flux near the wall is very low for high Mach numbers, the buffer region may not be the dominant region for turbulence production, as in subsonic boundary layers (note that hypersonic laminar boundary layers undergo transition by disturbances spreading inward from the outer layer). Further investigation will depend on the development and application of nonintrusive measurement techniques to the near-wall regions of hypersonic boundary layers.

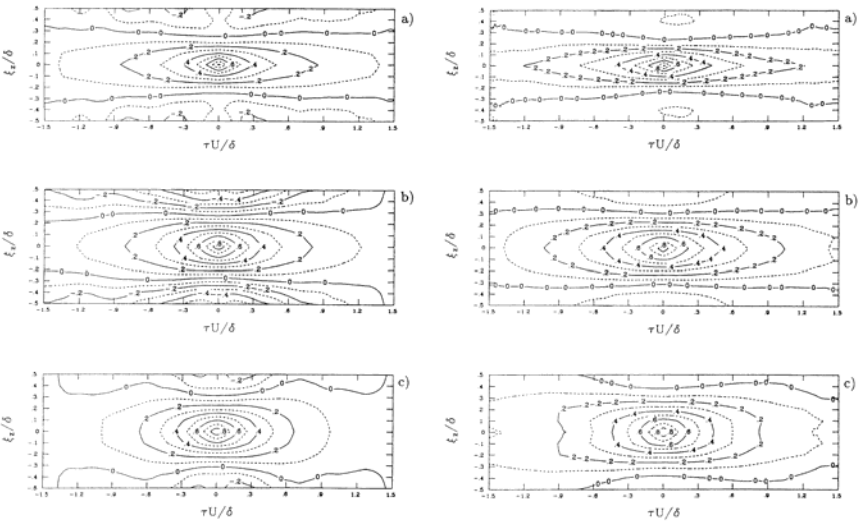

Figure 8.38. Isocorrelation contour maps in the x–z plane, as measured by Smith (1994), in a subsonic turbulent boundary layer at (a) $y/\delta = 0.09$, (b) 0.42, (c) 0.80. Left: $Re_\theta \approx 4600$; right: $Re_\theta \approx 13{,}200$. (Figure from Smith (1994), with the author's permission.)

Finally, we note that the rate of decay of the large-scale motions, as measured by the rate at which the peak in the space-time correlation decays with distance, appears to decrease significantly with the Mach number. For example, the distance over which the peak decreased to half its original level differs by an order of magnitude in the experiments by Favre (1957, 1958) at Mach 0.04 and Owen and Horstman (1972) at Mach 7 when scaled by δ. A better scaling for the rate of decay may be the time scale of the energy-containing eddies, Λ/u'. Λ and u' both decrease with Mach number so that their ratio remains approximately constant. This result may in turn suggest that the decrease in the streamwise length scales with Mach number simply reflects the fact that the time scale of the large eddies remains constant as the absolute fluctuation level decreases. The more complex scaling arguments presented by Smith and Smits (1991b) to explain the experimental observations may therefore not be necessary.

8.6 Integral Scales

Experimentally, the integral scales are usually deduced from one-point hot-wire measurements by using Taylor's hypothesis. Even when measurements of two-point correlations are available in high-speed flows (see, for example,

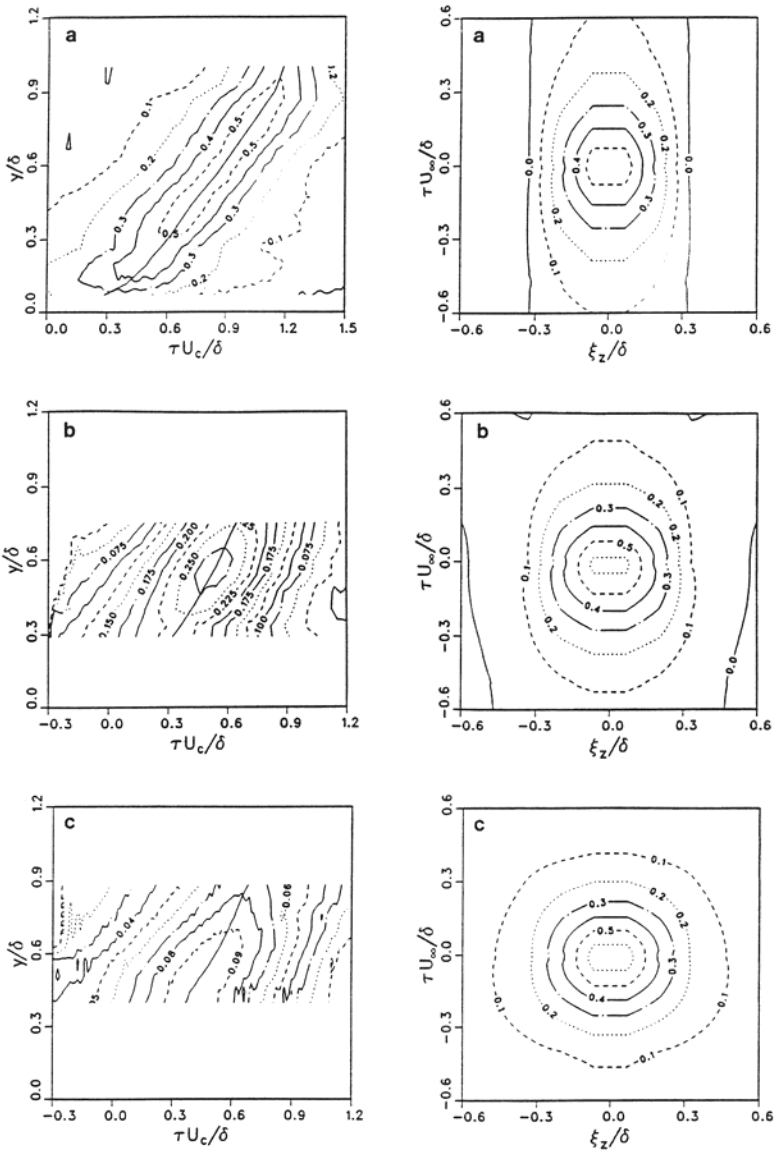

Figure 8.39. Isocorrelation contour maps measured by Spina (1988), in a turbulent boundary layer at $Re_\theta = 81{,}000$ and $M = 2.9$. The figure on the left shows the results in the x–y plane using different wall-normal probe separations: (a) $\xi_y/\delta = 0.09$; (b) $\xi_y/\delta = 0.30$; (c) $\xi_y/\delta = 0.51$. The figure on the right shows the results in the x–z plane at three positions in the boundary layer: (a) $y/\delta = 0.20$; (b) $y/\delta = 0.51$; (c) $y/\delta = 0.82$. (Figure adapted from Spina (1988), with the author's permission.)

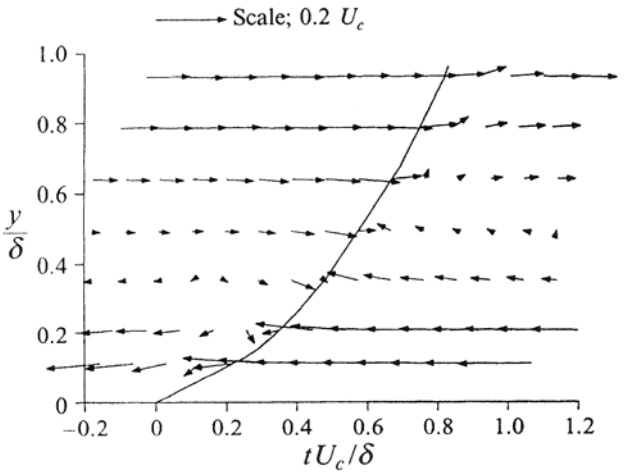

Figure 8.40. Ensemble averaged view of the large-scale motions in a Mach 2.9 boundary layer. (Figure from Spina et al. (1991a). Copyright 1991, Cambridge University Press. Reprinted with permission.)

Spina and Smits (1987) and Robinson (1986)), it is often difficult to determine integral scales from the data. The type of data that is available also depends on the measurement technique. For instance, when Constant Current Anemometers (CCA) are used, time histories are generally not measured, but spectral data for u' and T' can be obtained directly by processing the signal with the fluctuation diagram technique to separate the contributions of u' and T' (see Fulachier (1972), Bestion (1982), Debiève et al. (1982, 1983), Bestion et al. (1983), and Audiffren (1993)). Bestion and Audiffren showed that for an adiabatic flat plate boundary layer at a Mach number of 2.3 the shapes of the spectra of $(\rho u)'$ and u' are practically the same, but they differ considerably from the spectrum of T_0'. Therefore, when anemometers are operated with a single overheat, a sufficiently high value of the resistance should be chosen to minimize the contribution of T_0' and to obtain a signal proportional to $(\rho u)'$. When Constant Temperature hot-wire Anemometers (CTA) are used at a high overheat ratio, the measured signal is almost exactly proportional to $(\rho u)'$, which in turn gives spectral information on u'. Such data can be inaccurate at low wave numbers. The spectral measurements of velocity and temperature performed with a CCA in adiabatic boundary layers by Morkovin (1962), Bestion (1982), and Audiffren (1993) show that the ratio $(u'/U)/(T'/T)$ at low frequencies is not a constant, and that the magnitude of the spectral correlation coefficient $R_{uT}(f)$ increases to unity at zero frequency. This may be the cause for the differences in the shapes of the spectra for u' and $(\rho u)'$ at low frequencies, depending on the Mach number. For higher frequencies, the ratio

$(u'/U)/(T'/T)$ and the correlation coefficient are approximately constant, and the spectra are nearly proportional to each other.

The classical integral scale can be determined from one-point measurements by integrating the autocorrelation coefficient of u'. It is necessary to define the domain of integration, because the autocorrelation can become negative. When using hot-wire anemometry in supersonic flows, this question can be complicated by possible "strain-gauge" effects. These effects can cause peaks in the spectrum, which may be acceptable for measurements of the overall stress or the turbulence energy because the integral contribution is usually small, but they can cause spurious oscillations in the autocorrelations and make the estimates of the integral scale inaccurate.

Alternatively, the integral scale can be determined by finding the value of the energy spectrum at zero frequency. However, because the signal is usually filtered with a highpass filter, it has zero mean and its spectrum has a zero value at zero frequency. The integral scale must then be found by extrapolating the spectrum to zero frequency. In practice, the value at a frequency slightly larger than the limit of the highpass filter is taken as the best estimate. It is generally difficult to measure these low frequencies because the spectra of u' and of $(\rho u)'$ may be different at very low frequencies, the measurements can be affected by noise in the power supply, and by the peculiarities of the wind tunnel, such as acoustic resonances.

For these reasons, an additional scale has also been used. Because we expect that the spectra have a region of k_1^{-1} dependence in the logarithmic zone, $E(k_1)$ varies as k_1^{-1}, and $k_1 E(k_1)$ is constant or presents a maximum. Here we have chosen the wave number for which this maximum occurs as the (inverse of the) characteristic space scale. This probably has a clearer physical meaning than the integral scale, since for the incompressible part of the fluctuating motion it characterizes the eddies extracting energy from the mean field. As indicated earlier, experimentalists commonly measure frequency spectra, so that a characteristic frequency is measured, and then a length scale is deduced using Taylor's hypothesis. There is usually a considerable amount of scatter because the location of the maximum is not always well defined. For the data considered here, a maximum was generally found in the external layer, but in the logarithmic zone of the subsonic boundary layer the spectra were frequently "double-humped" and the maximum was difficult to determine. Such shapes were also mentioned by Perry et al. (1986) who interpreted them to mean that Taylor's hypothesis failed for low frequencies. Uddin (1994) noted that the bump at low wave number became more prominent at higher Reynolds numbers (see also Smith (1994)). These double-humped profiles lead to some difficulty in determining the length scale, and it is sometimes necessary to discard points in the log-law region of the subsonic boundary layer profiles. However, the higher frequency bump typically corresponds to scales comparable to the scales of the outer layer, and the other maximum

Authors	M	$R_\theta - R_{\delta 2}$	Measurement method	Remarks
Klebanoff (1954)	0.044	7000	CCA	
Fulachier (1972)	0.035	4750	CCA	
Fernholz et al. (1994)	0.06 and 0.17	20000 and 60000	CTA	
Spina and Smits (1994)	2.89	80000 – 40000	CTA	Scales estimated from spectra of $(\rho u)'$
Bestion (1982) Debiève (1983)	2.3	4200 – 2900	CCA	Spectra of u' (fluctuation diagram technique)
Bestion et al. (1983)	1.8 and	5000 – 3500	CCA	Spectra of u' (fluctuation diagram technique)
Audiffren (1993) Audiffren and Debiève (1995)	2.2	6300 – 3800	CCA	Spectra of u' (fluctuation diagram technique)
McGinley et al. (1994)	11	12400 – 1115 6500 – 633	CTA	Spectra of $(\rho u)'$

Table 8.1. Sources for spectral data. (Adapted from Dussauge and Smits (1995).)

occurs at frequencies an order of magnitude lower, corresponding to length scales five to ten times larger than the outer layer scales.

The values of the integral scale Λ obtained from the data sets listed in Table 8.1 are given in Figure 8.41. Outer layer scaling was used, because most of the data were obtained in that region. Plotting the data in inner layer variables does not alter the conclusions. The data points from Smits and Dussauge (1989) were deduced from autocorrelations in a way that may underestimate the integral scale, due to a lack of experimental points for large time delays. The boundary layer thickness was found from the profiles of total pressure (as recommended by Fernholz and Finley (1980)). Choosing a boundary layer thickness based on $0.99U_e$ would make some difference in the magnitude of Λ/δ at Mach 3: in this experiment, the integral scale would be a little closer to its subsonic value. It would also significantly increase Λ/δ for the hypersonic experiment by McGinley et al. (1994), but in this case, the mean profiles indicate that the traditional choice based on $0.99U_e$ would be rather unphysical. In any case, a first result appears very clearly: the subsonic data indicate that in the external layer, Λ is about 0.5δ in subsonic flows, but it is only about half that value in supersonic layers. The hypersonic data of McGinley et al. (1994) indicate a very low value, about 0.2δ, for $R_{\delta 2} = 1115$, but larger values at the lower Reynolds number. In this case, the spectra

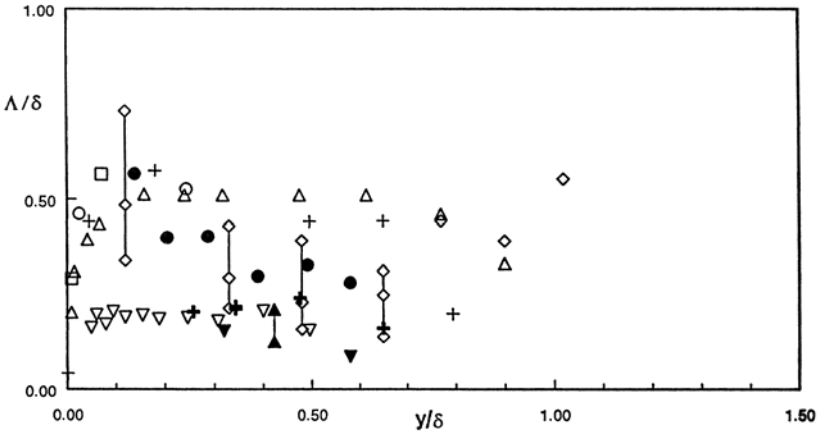

Figure 8.41. Integral scales in turbulent boundary layers. Subsonic data: +, Klebanoff (1955); △, Fulachier (1972); ○ $R_{\delta 2}$ = 20,900, Fernholz et al. (1995); □ $R_{\delta 2}$ = 57,720, Fernholz et al. (1995). Supersonic data: +, Debiève (1983); △, Bestion et al. (1983); ○, Spina and Smits (1987); ▽, Audiffren (1993); ◇ $R_{\delta 2}$ = 633, McGinley et al. (1994); ▽ $R_{\delta 2}$ = 1115, McGinley et al. (1994). (Figure from Dussauge and Smits (1995), with the authors' permission.)

at low frequency reveal peaks and bumps that preclude an accurate estimate of the integral scale. In fact, the lower limit of the error bar overlaps the other high-speed data. The large variation could be due to the remnants of transition. In the data by Spina and Smits, the point at $y/\delta = 0.1$ has an integral scale nearly equal to the subsonic value. This is due to the significant slope in the spectrum, observed at low frequency, where the spectra of u' and $(\rho u)'$ are perhaps not proportional, as discussed above. In spite of this trend, the integral scales at Mach 2.9 in the middle of the layer are significantly below the subsonic results. The results are independent of Reynolds number, within the experimental accuracy. Note that Demetriades and Martindale (1983) in a boundary layer on a flat plate at Mach 3 report measuring an integral scale of 0.28δ, also considerably smaller than that found in subsonic flows.

The production scales L are given in Figure 8.42. The Reynolds numbers in the subsonic and supersonic cases cover comparable ranges, except perhaps for the hypersonic data. It is clear that the production range is shifted to higher frequencies in supersonic flows. It should be emphasized that the limited spatial resolution of the wires probably precludes any accurate determination of the $-5/3$ law in the supersonic data, and tends to shift the maximum of $fE(f)$ to lower frequencies. If such systematic errors are significant, the values measured in high-speed flows are probably overestimated, reinforcing the notion that the scales are reduced with increasing Mach number.

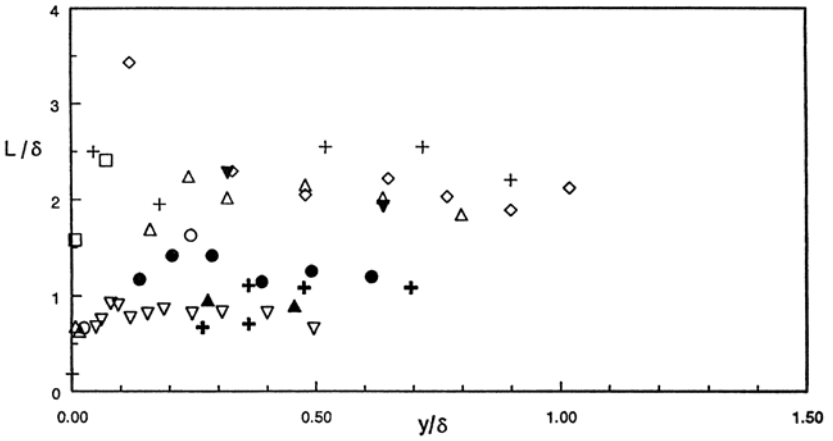

Figure 8.42. Production scales in turbulent boundary layers. Symbols as in Figure 8.41. (Figure from Dussauge and Smits (1995), with the authors' permission.)

It appears that the production scale L follows the same trends as Λ, and that $L \approx 2\Lambda$. That is, L is about 2δ for low-speed boundary layers, and about δ in high-speed boundary layers. The measurements of Morkovin and Phinney, reported by Morkovin (1962), suggested the same trend for the production scales. Again, plotting these data in inner-layer variables does not change the differences between the subsonic and supersonic data. The only discrepancy is found in the Mach 11 boundary layer, but several reasons can be found for this departure. First, the boundary layer is probably not fully turbulent, at least at the lower Reynolds number. Second, it is not clear that the velocity and mass-flux spectra are proportional to each other at this Mach number. Third, the conclusions drawn from the power law analysis are probably not valid if strong compressibility effects are present. Fourth, the change in the shape of the spectra may indicate a modification of the turbulence structure. In hypersonic boundary layers, most of the mass flux occurs near the external edge of the layer and the mass flux profiles have an inflexion point. This suggests that the external layer can behave more like a mixing layer than a classical boundary layer. Such free shear flows are known to contain turbulent structures of large spatial extent, with the production scales being several boundary layer thicknesses in size. This would be consistent with the surprisingly high level of energy observed at low frequencies in the present Mach 11 experiments.

So it seems that the apparent size of the energetic eddies in the longitudinal direction, deduced from measurements of u' or $(\rho u)'$ in zero pressure gradient boundary layers, decreases with increasing Mach number whatever the experimental method. This trend can also be illustrated by using another

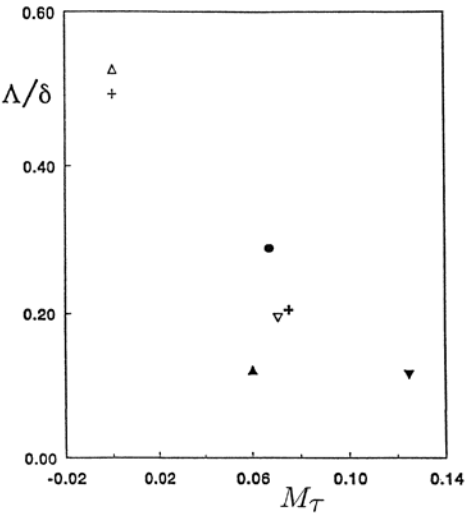

Figure 8.43. Evolution of the integral scale as a function of the friction Mach number. Symbols as in Figure 8.41. (Figure from Dussauge and Smits (1995), with the authors' permission.)

representation. If we assume that the friction Mach number can be used to characterize compressibility in turbulent boundary layers, then we can write $M_\tau^2 = C_f M_e^2/2$. That is, M_τ depends on Mach and Reynolds number. The average value of L/δ in the outer layer is shown as a function of M_τ in Figure 8.43. The results obtained at $M_e = 2.3$ and 2.89 have nearly the same values of M_τ and L/δ, and they agree on the average value of L/δ. The hypersonic results by McGinley et al. have a value of M_τ only a little larger than 0.1, but they indicate a further decrease in the production scale.

This change in typical frequencies or time scales can be attributed either to variations in the convection velocity or variations in the spatial scales. Measurements of convection velocity by Spina and Smits (1987) in a high Reynolds number boundary layer at Mach 2.9 showed that this quantity is not very sensitive to compressibility (see Figure 8.32). This result was confirmed by Cogne et al. (1993), who measured convection velocities directly using double-pulsed Rayleigh scattering flow visualization (see Figure 1.19). This implies that smaller space scales are found in supersonic flows. In contrast, the transverse scales related to turbulent diffusion remain unchanged, and the longitudinal scales determined from u' decrease. Now Spina and Smits (1987) showed that the direction of the maximum space-time correlation in their boundary layer at Mach 2.9 is steeper than at low speeds (see Figures 8.35 and 8.36), so that the streamwise correlation lengths are expected to decrease. As noted earlier,

this purely geometric explanation is not sufficient to explain all the evolution observed in Figure 8.43.

It is expected that the observed modifications in the flow structure and scales are due to compressibility. A possible interpretation can be found in the changes in the potential field induced in the external flow by the boundary layer, and in the generation of acoustic noise by supersonic boundary layers. Can they create smaller scales, and modify the orientation of the lines of maximum correlations? The variation of the angle was interpreted in the previous paragraph as a change in the direction of vortical structures. In fact, the two-point measurements by Spina and Smits did not use conditional statistics, and therefore did not discriminate between the vortical and potential contributions in the intermittent zone. In supersonic flows, the induced pressure field can depend on local conditions (the pressure perturbation induced by a large-scale structure, for instance), but also by the noise radiated by Mach waves. These waves can have low levels of $(\rho u)'$, but they are generally more conservative than ordinary turbulence, and could modify the space-time correlations for large separation distances. The formation of these Mach waves necessitates the velocity difference between the sources and the external flow to be supersonic. In a boundary layer, this condition is always fulfilled, but at moderate supersonic Mach numbers the part of the layer able to radiate Mach waves is very thin and generally confined to the viscous sublayer or the logarithmic zone. In this case, the behavior will be Reynolds and Mach number dependent. The orientation of the Mach waves will depend on this Mach number difference. For example, transonic perturbations would be very steep, and would help to make the maximum space-time correlation locus more vertical.

Another element, as noted by Laufer (1961), is an increase in the radiated field near Mach 3, which could be interpreted as follows. The convection velocity of the large eddies in the logarithmic layer is typically $0.8U_e$, regardless of the Mach number, and so the velocity difference with respect to the external flow is $0.2U_e$. Now, it may be expected that these eddies will start forming eddy shocklets when this relative Mach number is larger than, say, 0.6. This corresponds to an external Mach number of 3, and this criterion would be independent of the Reynolds number because the convection velocity of the large structures appears to be independent of Reynolds number. The measurements taken at a Mach number of 2.9 would then be near the onset of a new regime, and represent the first manifestation, in boundary layers, of compressible turbulence phenomena as observed in mixing layers. Such an interpretation, although speculative in many respects, is tempting because it can explain changes in the structure of u', as long as the radiated noise does not significantly affect the shear stress.

To conclude this section, the spectral data show that there are modifications to the motions which contribute to the energy scales but not to the turbulent transport. This implies that the primary action of compressibility

is to alter inactive motions. As these motions are related to the irrotational part of the fluctuations and to the pressure fluctuations induced by the layer, this explanation may be correct, but a full assessment would require a more complete knowledge of the two-point correlations and conditional statistics of turbulence in these flows.

8.7 Eddy Models of Turbulence

Eddies and coherent structures, particularly their interactions, are an integral part of our understanding of turbulence. Statistical descriptions, however, including correlations and ensemble averages, provide little information on eddy formation, growth, interaction, and dissipation. In this section, we describe some of the prevailing notions that form eddy models of turbulence.

The first physical model of the large-scale structure of turbulent boundary layers was proposed by Theodorsen (1955), who suggested that the basic structure of all turbulent shear flows is the inclined horseshoe vortex, as shown in Figure 8.44. Using the vorticity transport equation, Theodorsen attempted to prove that the only vortical structures which can sustain a nondecaying turbulent field must have a horseshoe shape. As seen in Figure 8.44, the model can certainly account for the generation of Reynolds stress. Between the legs of the vortex, the induced velocity ejects low-speed fluid up, away from the wall, into a region of higher mean velocity, hence $u' < 0$ and $v' > 0$ (a Quadrant II event). On the outboard sides of the legs, high-speed fluid is swept towards the wall, hence $u' > 0$ and $v' < 0$ (a Quadrant IV event).

The flow visualizations by Head and Bandyopadhyay (1981) provide strong support for the concept that at least some of the LSMs are loop-shaped vortical structures, with an aspect ratio that is Reynolds number dependent. Figure 8.45 shows that at $Re_\theta = 600$ the structures have the proposed horseshoe shape, and as Re_θ increases, the structures become elongated and appear more as hairpins. At all Reynolds numbers, the spacing between the legs of the structures is similar to the spacing between the near-wall streaks ($\approx 100\nu/u_\tau$). Note that Smith et al. (1991) and Smith and Walker (1997) present convincing arguments that the low-speed streaks are in fact artifacts of the passage of symmetric and asymmetric hairpin vortices. Head and Bandyopadhyay proposed that the loops extend to the wall, in support of Townsend's (1956) attached eddy hypothesis, although the Reynolds number dependence of their aspect ratio contradicts his Reynolds number similarity hypothesis.

Head and Bandyopadhyay (1981) further suggested that at low Reynolds numbers the LSMs were merely single horseshoe elements, but at higher Reynolds numbers the LSMs were actually agglomerations of many elongated hairpin vortices. They observed the generation of multiple hairpin loops in packets, where the heads of the loops lie along a line that is inclined to the wall at an angle of about 20°, as shown in Figure 8.46.

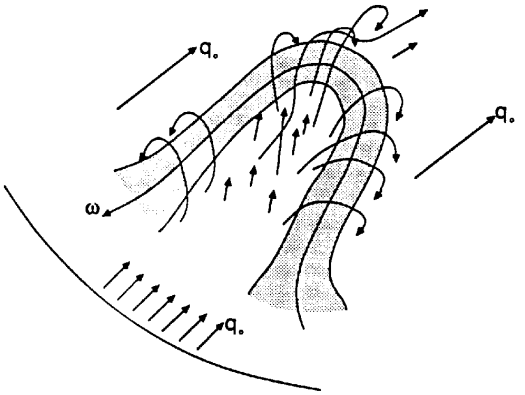

Figure 8.44. The horseshoe vortex proposed by Theodorsen (1955) as the basic structure in wall-bounded turbulent flows. (Figure from Spina (1988), with the author's permission.)

MacAulay and Gartshore (1991) also noted different structure angles using cross-correlations and conditional sampling. They determined that the major contributions to the broadband cross-correlations in a turbulent boundary layer at $Re_\theta = 8390$ came from δ-scale segments of the velocity signals, which encompass many aspects of the flow structure, rather than from individual hairpin eddies, which are an order of magnitude smaller than δ in the streamwise and spanwise directions at this Reynolds number. Using conditional sampling, they were able to measure the inclination angle of the sharp interface at the backs of the large-scale motions. This interface angle is compared to their measurements of the broadband structure angle in Figure 8.47, and the differences are significant.

Work by Zhou et al. (1997, 1999), Liu et al. (2001), and Adrian et al. (2000) has provided insight on the generation of coherent hairpin vortex packets containing a multiplicity of spatially organized hairpinlike vortices in channel and boundary layer flows, confirming and extending Head and Bapadhyay's observations using numerical simulations and PIV experiments. An elegant conceptual model of nested packets of hairpins (or fragments thereof) growing from the wall was developed. This model is illustrated in Figure 8.48. The resulting hierarchy of motions, with changes of scale as a result of vortex pairing, is in the same spirit as the mechanism of wall turbulence proposed by Perry and Chong (1982). Strong confirmation of the statistical significance of coherent hairpin packets has been provided by Marušić (2001) and Christensen and Adrian (2001). Of particular interest is the observation by Adrian et al. (2000) that at low Reynolds number, such packets contain two to three vortices, and that the number of vortices and the range of scales present increases

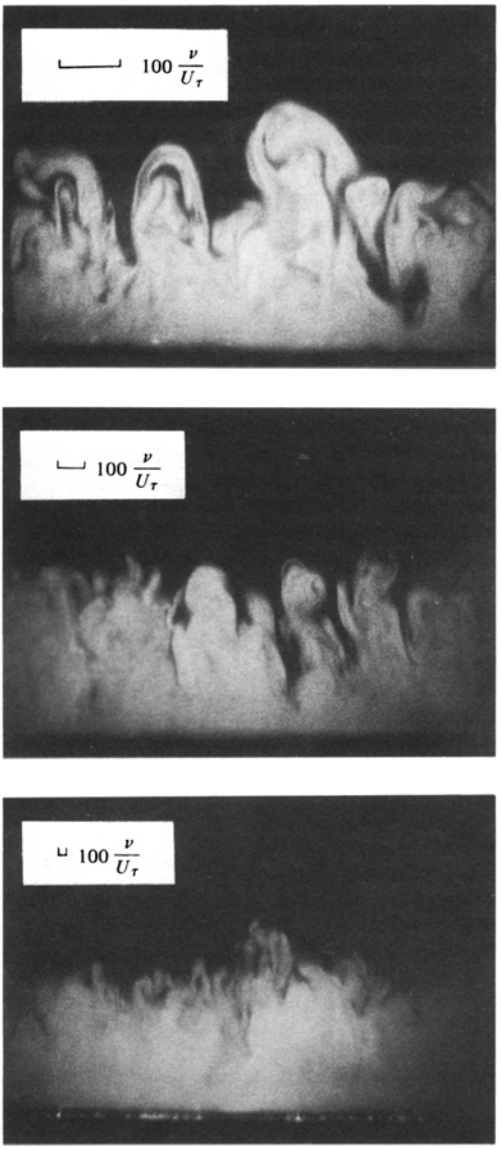

Figure 8.45. Flow visualizations by Head and Bandyopadhyay (1981), showing the Reynolds number dependence of vortex loop structures in a turbulent boundary layer. The visualizations were obtained by filling the boundary layer with smoke, and illuminating the flow with a laser sheet inclined 45° downstream. (a) $Re_\theta = 600$; (b) $Re_\theta = 1700$; (c) $Re_\theta = 9400$. (Figure from Head and Bandyopadhyay (1981). Copyright 1981, Cambridge University Press. Reprinted with permission.)

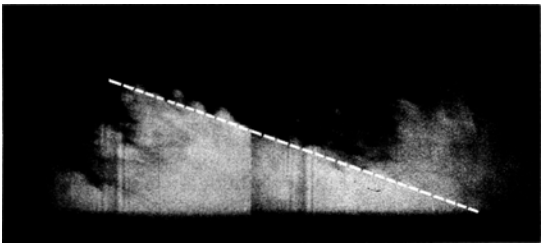

Figure 8.46. Example of 20° interface at R_θ = 17,500. Flow is from right to left. (Figure from Head and Bandyopadhyay (1981). Copyright 1981, Cambridge University Press. Reprinted with permission.)

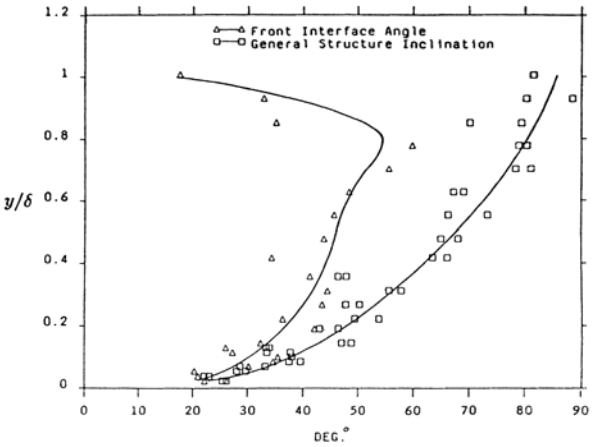

Figure 8.47. Structure angles measured by MacAulay and Gartshore (1991) in a turbulent boundary layer at Re_θ = 8390: □, broadband general structure angle; △, structure angle of the trailing (upstream) interface of the large-scale motions as detected using the VITA technique. (Figure from MacAulay and Gartshore (1991), with the authors' permission.)

with increasing Reynolds numbers.

At low Reynolds numbers, Head and Bandyopadhyay found that the LSMs exhibited a "brisk" overturning motion, and at higher Reynolds numbers they overturned slowly. This suggests that entrainment decreases with increasing Reynolds number, which is in agreement with the observation that the boundary layer grows more slowly with increasing Reynolds number. MacAulay and Gartshore (1991) proposed that at low Reynolds numbers, the horseshoe vortices are of the same magnitude as the boundary layer thickness in the spanwise and wall-normal directions. At high Reynolds numbers, the spanwise

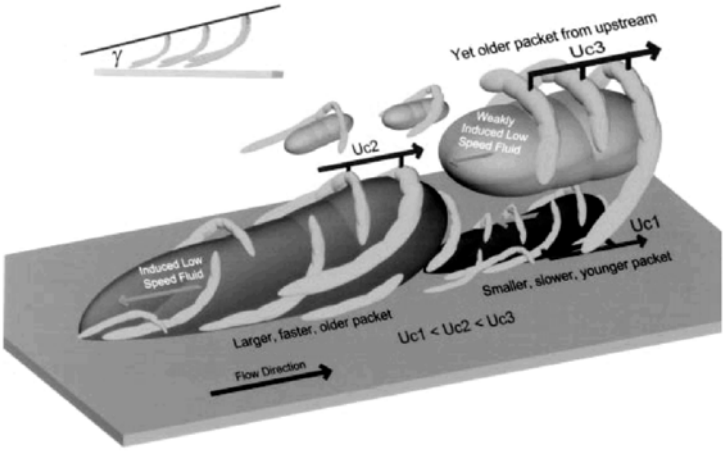

Figure 8.48. Conceptual model of hairpin packets and their evolution. (Figure from Adrian et al. (2000). Copyright 2000, Cambridge University Press. Reprinted with permission.)

scale of the hairpin eddies is much smaller than the boundary layer thickness. Due to their own self-induction, the hairpin vortices will propagate backwards (in a frame of reference moving at the mean velocity) through the low-speed fluid within the turbulent bulges. When they reach the back of a bulge, they encounter a sudden increase in streamwise velocity that balances their self-induced velocity. MacAulay and Gartshore suggest that stronger structures (with higher self-induced velocities) will penetrate the rear interface farther than weaker structures. This results in the appearance of small-scale structures on the backs of the large-scale motions, similar to Falco's typical eddies (see next section). They suggested, in fact, that Falco's eddies may simply be the heads of the hairpin vortices. When the hairpin vortices cease their backward propagation, their self-induction will continue to carry them up, away from the wall, resulting in a slow overturning motion.

8.7.1 Inner-Outer Interactions

Sreenivasan and Sahay (1997) describe the Reynolds number dependence of the peak of the Reynolds shear stress in its location (y_p^+) and maximum value. Combined with the Reynolds number dependence of the peak in the streamwise turbulence intensity (Fernholz and Finley, 1996), these observations indicate that the near-wall region is not entirely independent of the outer layer dynamics. Morrison et al. (2004) and Zhao (2005) have revisited the long-standing notion of active and inactive motions, and they provide compelling evidence to show that the local scaling behavior in fully developed pipe flow is determined

both by inner and outer layer motions. The uncertainty regarding the scaling of the bursting frequency also illustrates the problem.

To this end, Delo and Smits (1997) and Delo et al. (2004) obtained time resolved three-dimensional visualizations of the scalar field in a boundary layer at $Re_\theta = 701$. They noted that groups of the large-scale motions were frequently assembled into agglomerations measuring up to 5δ in length, and suggests that the agglomerations are formed through the merging of adjacent, previously existing individual vortical structures as they convect downstream. Some evidence was found that the large agglomerations actively "build" themselves as they convect downstream, through the addition of near-wall fluid. Most of the ejection events identified in a spatial distribution occurred simultaneously, soon after the passage of the extended, large-scale structures. The fluid ejected by these events generally penetrated through the trailing edges of the structures, growing like Head and Bandyopadhyay's hairpin packets, effectively increasing their streamwise extent. It was tentatively proposed that the addition of energetic near-wall fluid in this manner serves to perpetuate the active nature of the large-scale structures. The structures appear to be "long" enough so that after perturbing the inner layer low-speed streaks and triggering an ejection, the trailing edges of the structures are still in the neighborhood to profit from the addition of the ejected near-wall fluid.

Another example, concerning the relationship between the large-scale motion and the wall shear stress at much higher Reynolds numbers, was given by Brown and Thomas (1977). They found that the large-scale motions were inclined at an angle of 18° to the wall and extended about 2δ in the streamwise direction, similar to Head and Banyopadhyay's observations on hairpin packets. As the structures passed over the wall, they created a characteristic wall shear stress signature. Brown and Thomas suggested that this wall shear stress pattern was related to the bursting process, and concluded that the large-scale, outer layer structure influenced the near-wall structure and dynamics. They found that the results were independent of Reynolds numbers when scaled on outer variables, for $R_\theta = 4940$ and 10,160.

In addition, the flow visualizations by Falco (1977) showed that there may be at least two types of organized motions in the outer layer: LSMs and "typical eddies" (see also Klewicki (1997)). He found that the typical eddies are small-scale motions, which scale on wall variables and are responsible for a significant fraction of the total Reynolds shear stress in the outer layer. The average streamwise extent of the LSMs was about 1.6δ at $R_\theta \approx 1000$. The streamwise length scale of the typical eddies had a constant value of about $200\nu/u_\tau$ for $1000 < R_\theta < 10{,}000$. The vertical length scale varied nearly linearly from $100\nu/u_\tau$ to $150\nu/u_\tau$ over the same range of Reynolds numbers. Falco found that the typical eddies generally appear on the backs of the LSMs, and propagate towards the wall, thus acting as sweeps very near the wall (see Figure 8.49). Cantwell (1981) called these intense small-scale motions

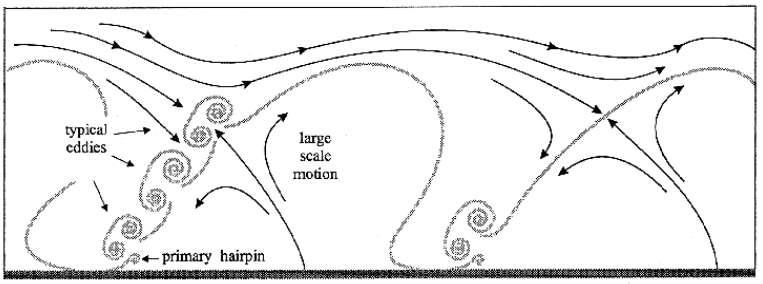

Figure 8.49. Schematic representation of typical eddies grouped on the back of a large-scale motion. (Figure from Falco (1991). Copyright 1991, The Royal Society. Reprinted with permission.)

"energetic outer-flow eddies".

Falco claimed that the typical eddies may be an intermediate link between the inner and outer layers. As discussed by Smith and Smits (1991b), however, if the typical eddies scale on wall variables then at very high Reynolds number, where δ^+ is very large, the typical eddies will become vanishingly small compared to the boundary layer thickness, and they are unlikely to be dynamically significant (that is, they will not carry significant levels of shear stress). Furthermore, flow visualizations at very high Reynolds numbers show features that appear to be very similar to the typical eddies observed by Falco at lower Reynolds numbers, but which are at least an order of magnitude larger (in terms of inner variables), even when the variations in fluid properties, as expressed by the difference between R_θ and R_{δ_2}, are taken into account.

8.7.2 Summary of Boundary Layer Eddy Structure

Here, we describe a unified picture of boundary layer eddy structure that attempts to represent the important kinematic and dynamic behavior in wall-bounded turbulent flows. It is based in large part on the model suggested by Smith and Walker (1997).

The dynamic process of turbulence production and the formation of structure is described as a cycle that begins with the growth of a low-speed streak. The growth continues until the passage of a disturbance of sufficient size and strength impresses a local adverse pressure gradient on the streak causing a local deceleration. This deceleration creates a three-dimensional inflectional profile at the interface between the streak and the higher speed flow in the wall region. The region above the streak is unstable to small local disturbances, and oscillations begin on the top of the streak. The three-dimensional sheet of vorticity above the streak will develop waves due to the oscillations, roll

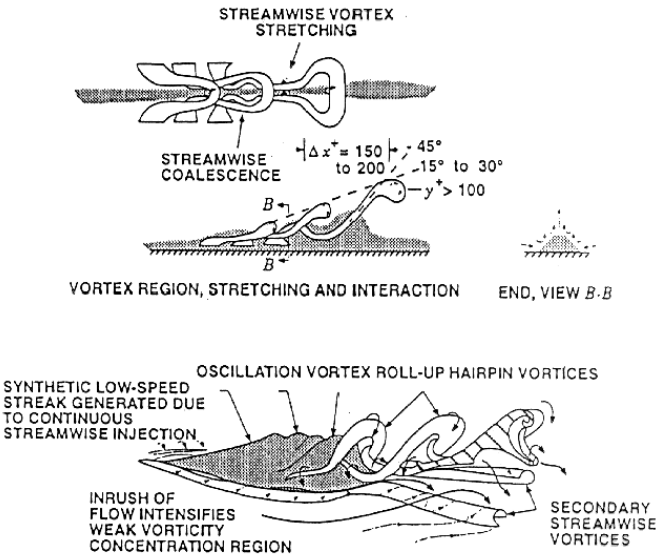

Figure 8.50. Top: Illustration of the breakdown and formation of hairpin loops during a streak-bursting process. Low-speed streak regions are indicated by shading. Bottom: Schematic of breakup of a synthetic low-speed streak generating hairpin vortices. Secondary streamwise vortical structures are generated owing to the inrush of fluid. (From Acarlar and Smith (1987a), with permission.)

up, and concentrate the vorticity in locations on the sheet. This process takes place at a y^+ of between 15 and 20, and there can be between two and five concentrations per streak.

As the roll-up continues, the vortices begin to look like horseshoe vortices (see Figure 8.50). Biot-Savart interactions between various portions of the vortex amplify the distortion. Self-induced movement away from the wall occurs and the vortex is stretched by the steep mean velocity gradient. Legs of the horseshoe, which are a pair of counterrotating vortices oriented in the streamwise direction, develop as the loop is stretched. As the vortex becomes elongated, it begins to look more like a hairpin vortex and the vorticity is increased. The legs tend to pump low momentum fluid away from the wall and thereby perpetuate the low-speed streak. The head or arch creates a streamwise pressure gradient that will cause the liftup and ejection of low-momentum fluid from the low-speed streak as it moves downstream. As the process proceeds, the hairpin continues to be stretched and the head moves farther away from the wall due to self-induction.

As the loops are dragged over the viscous layer near the wall, they help

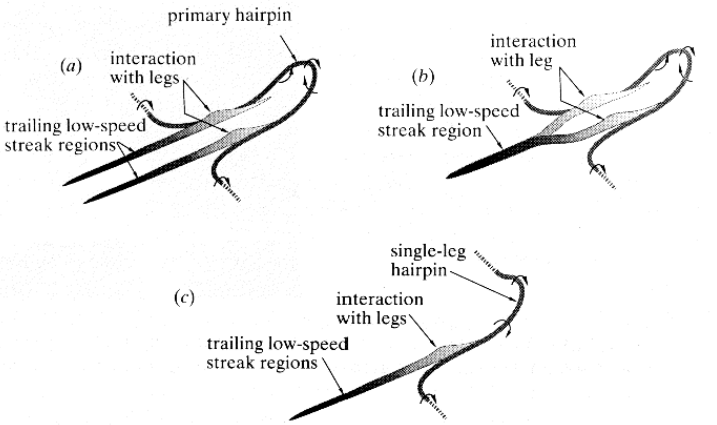

Figure 8.51. Schematic illustrating how advecting symmetric and asymmetric hairpinlike vortices generate low-speed streaks. (Figure from Smith et al. (1991). Copyright 1991, The Royal Society. Reprinted with permission.)

to regenerate new vortices through an interaction with the viscous wall layer (Figure 8.51). The passage of successive loops can tend to focus the streak so that it can continue to grow, or buffet it to weaken it. In either case, the impingement of subsequent vortices creates the appearance of waviness and swaying, a commonly observed behavior.

The timing on the formation of the loops out of the sublayer material appears to be such that as they rise they form the backs of the LSMs, creating a very active shear layer out of the conjunction of the heads of the vortex loops (see also MacAulay and Gartshore (1991), Bernard and Wallace (1997), and Adrian et al. (1998)). The hairpins often align themselves so that their heads lie along a line forming a 15° to 30° angle with the wall, whereas the individual hairpins make an angle of about 45°.

The stretching of the vortex loops by the surrounding flow (viewed either as a background mean velocity gradient, or the summation of the velocity induced by all surrounding vortex loops) requires work to be done. Also, the narrowing of the vortex tube making up the loop will increase the velocity gradients inside the tube, increasing its dissipation rate as the square of the gradients. This dissipation will be greatest near the wall where the velocity gradients are strongest, and diminish in the outer flow where the gradients are relatively weak. According to Smith and Walker (1997):

> ... the process of growth to larger scales in a fully-turbulent boundary layer can be explained by the proximity of multiple hairpin-like vortices in different phases of development, which creates a condition

> conducive to coalescence, or three-dimensional vortex amalgamation. This amalgamation process ... suggest(s) that local collections of hairpin vortices can intertwine and interact to yield essentially a hairpin-like structure of somewhat larger scale... This clearly suggests that the outer region of a turbulent boundary layer can evolve from hairpin vortex structures and that the large, arch-type vortices (Robinson, 1991a) and rollers (Falco, 1977) observed in the outer-region structures directly interface with the freestream flow. The overturning of the structures plays an instrumental part in inducing the flow of higher-speed fluid toward the wall (i.e., intermittent engulfment), which eventually finds its way to the wall along a complex gauntlet of vortex-induced motions, terminating in a "sweep" motion at the wall... However despite the overall size and strength of the outer structures, the stretching mechanism for energy transfer to these larger-scale vortical structures is strongly diminished because of the weak mean velocity gradient in the outer region. Following an initially strong energy input to the initial vortex scales near the wall, these outer structures will basically "evolve" to larger and larger scales, but with no significant additional energy input, eventually succumbing to slow, viscous dissipation. The outer part of the boundary layer of the boundary layer may thus be regarded as a "graveyard" for vorticity, where the cumulative remnants of deformed wall-region vortices pass through a complicated process of dissipation, diffusion and mutual cancellation, similar to the model of Perry and Chong (1982) (Figure 8.52).

We note, however, that the heads of the hairpin loops, being a localized concentration of shear stress, continue to be an active feature of the LSMs. In addition, the viscous diffusion of the legs may free the heads to form vortex loops or rings, with at least two consequences. First, the outer layer motions are no longer attached to the wall, and will look more like that shown in Figure 8.48. Second, at least some of the vortex loops may have an induced velocity that directs them to the wall, as typical eddies (Klewicki, 1997). As the Reynolds number increases, there need to be other levels of organization where very large scale motions emerge because the active motions seen on the backs of the LSM's have a typical dimension of 200 wall units, and these size motions cannot continue to be important in the shear stress budget since the stress in the outer layer scales with outer layer variables. Smits et al. (1989) proposed that as the Reynolds number increases the number of discrete scales of motion also increase. At the lowest Reynolds numbers ($1000 < R_\theta$ and $\delta^+ < 500$), a single scale dominates. This scale must be the same as that of the typical eddy, because they are of the same order as the boundary layer thickness. At higher Reynolds numbers ($1000 < R_\theta < 5000$ and $500 < \delta^+ < 2500$), two scales appear: the large-scale outer layer bulges and Falco's typical eddies. The

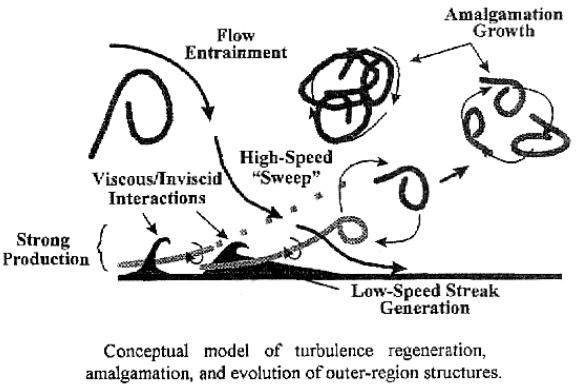

Figure 8.52. Conceptual model of turbulence regeneration, amalgamation, and evolution of outer-region structures. (Figure from Smith et al. (1991). Copyright 1991, The Royal Society. Reprinted with permission.)

typical eddies still make significant contributions to the Reynolds stresses. With a further increase in Reynolds number, the large-scale motions must carry more shear stress owing to the diminishing importance of the typical eddies (see also Murlis et al., 1982). It is possible that a third scale appears, corresponding to the smaller bulges seen at the edges of the large-scale bulges. Falco's typical eddies are now much smaller than the energy-containing range (which scales with δ), so that they are no longer dynamically important (with $Re_\theta = 35{,}000$, $200\nu_w/u_\tau$ corresponds to a frequency of about $100U_e/\delta$). It may be expected that the third scale would scale on outer layer variables, although some form of mixed scaling may also be appropriate. The appearance of new scales with increasing Reynolds numbers at approximately equal intervals in $\log \delta^+$ should be reflected in the behavior of the turbulence, especially the higher-order moments. At present there are insufficient data to support these proposals.

Finally, we address the question of symmetric and asymmetric vortex loops. The horseshoe vortex of Theodorsen (1955), the hairpin loops of Head and Bandyopadhyay (1981), and the Λ-shaped vortices of Perry and Chong (1982), are symmetric structures. It has been widely reported in experimental studies and DNS that the vortex structures observed in boundary layers are only rarely symmetric and asymmetric structures dominate (see, for example, Kline and Robinson (1989) and Kline and Portela (1997)). In the three-dimensional visualizations by Delo et al. (2004), symmetrical structures are rarely seen, although it is readily apparent that legs and arches are always part of the same vortex looplike structure. However, as argued persuasively by Smith and Walker (1997), any kinematic description of the near-wall cycle in terms

of symmetric structures can equally be cast in terms of asymmetric events (see also Figure 8.51). The important point is the sequence of events and their underlying mechanisms, and because the presence of asymmetry does not seem to affect the underlying physics, symmetrical models can be used for simplicity.

8.8 Final Remarks

From our consideration of subsonic flows it appears that, in contrast to the mean flow behavior, the turbulent stresses do not necessarily follow the inner/outer scaling arguments. For example, as found previously by Sreenivasan (1989) and Gad-el-Hak and Bandyopadhyay (1994), the Reynolds number can have a significant effect on the level of the maximum stress, and the location of that maximum in the boundary layer. In other respects, the scaling arguments put forward by Perry and his co-workers (see, for example, Perry and Li (1990)) indicate how the stresses may scale in the overlap region, and the experimental evidence tends to support their arguments, although their proposed constants may need to be adjusted somewhat.

The evolution of the organized motions in the boundary layer also depends on Reynolds number. In particular, the streamwise scaling of the outer layer structure is rather sensitive, where the scale increases with Reynolds number. This was confirmed by direct measurements of the space-time correlations and spectra. In contrast, the spanwise scaling appears to be insensitive to Reynolds number, so that on average the structures become more elongated in the streamwise direction with increasing Reynolds number. The average inclination of the outer layer structures also decreases, which may be related to the increase in the streamwise aspect ratio. It also appears that the spanwise scaling of the sublayer streaks is fixed at a mean value of about $100\nu/u_\tau$ over a very wide Reynolds number range, although the trend with Mach number is unknown.

For supersonic flows with moderate Mach number, it seems that the direct effects of compressibility on wall turbulence are rather small, as was found for the mean velocity distribution. Again, the most notable differences between subsonic and supersonic boundary layers may be attributed to the variation in fluid properties across the layer. Under the assumption that the length scales are not affected by compressibility, the turbulent stresses in the outer region scale on the wall stress, as first suggested by Morkovin (1962), as far as we can tell from the available data. This result is not surprising in some ways because the fluctuating Mach number ($M' = M - \overline{M}$) for moderately supersonic flows is considerably less than one, as illustrated in Figure 7.1.

However, a more detailed inspection of the turbulence properties reveals certain characteristics that cannot be collapsed by a simple density scaling.

For example, the shear correlation coefficient R_{uv} decreases with distance

from the wall in some supersonic flows instead of remaining approximately constant as in subsonic flows. There are other results, however, which indicate that R_{uv} follows the incompressible trend, and there is the possibility that the differences may be caused by a Reynolds number rather than a Mach number dependence. Unfortunately the database is very sparse, and considerable further effort is needed before these issues can be laid to rest. With respect to the streamwise and spanwise length scales of the large-scale motions, and their average inclination to the wall, the effect of Mach number is clear. Even if we account for the change in time scale of the energy-containing eddies Λ/u', we see that the lateral correlations are almost unaffected by changes in Mach and Reynolds number. The streamwise length scales are reduced significantly by increasing Mach number, and the angle of inclination is increased, although in coming to these conclusions we have implicitly assumed that Mach and Reynolds number effects are independent. It is necessary to make this assumption because the data do not overlap to any significant extent, and we are forced to compare experiments in supersonic flow with the results obtained in subsonic flow, usually at a different Reynolds number. In fact, the actual Reynolds number to be used in such a comparison is controversial because there is usually a major difference between the values of Re_θ and $R_{\delta 2}$. Finally, there is an order-of-magnitude decrease in the rate of decay of the large-scale motions as the Mach number increases from low subsonic to high supersonic values (Smits et al., 1989).

How can we explain these differences? Part of the answer may lie in understanding the role of Reynolds number more clearly, but understanding the effects of fluid property variations may be more important. In that respect, we need more direct numerical simulations and more detailed turbulence measurements at higher Mach numbers. We are seeing subtle differences at supersonic speeds that may signal the onset of direct compressibility effects such as the increased importance of pressure fluctuations and pressure-velocity correlations. These effects will become more obvious at hypersonic Mach numbers, and such studies will undoubtedly contribute to our understanding of the supersonic behavior.

Although few specifics are known, the turbulence physics become more complex as the Mach number increases beyond about five. For example, the Strong Reynolds Analogy and Morkovin's hypothesis are staples of boundary layer analysis at moderate Mach number. However, an upper Mach number limit must exist on the applicability of these simplifying assumptions, if only because there is a limit on the magnitude of temperature fluctuations. For instance, the SRA indicates that the standard deviation of the temperature fluctuations becomes comparable to the mean temperature at Mach numbers as low as 5. Indeed, the change in magnitude of the fluctuating Mach number distribution as the flow enters the hypersonic range (see Figure 7.1) points to the possibility of a dramatic alteration of turbulence dynamics due to com-

pressibility effects around Mach 5 (in comparison, the turbulence Mach number M_t is less than 0.3 even for the Mach 7.2 and 9.4 flows). Unlike the distribution of M_t, the fluctuating Mach number develops a peak near the middle of the boundary layer where both the velocity and temperature fluctuations are important. This behavior, when considered together with the large gradients in density and viscosity near the wall, also leads to the conclusion that there may be substantial differences in turbulence dynamics at higher Mach numbers.

At the same time, the near-wall gradients in density and viscosity are strongly dependent on heat transfer, and therefore the thickness of the sublayer will depend on Mach number, Reynolds number, and wall temperature. This raises the issue of how the viscous instability of the sublayer changes when fluid properties vary with distance from the wall (Morkovin, 1992). Because the local Reynolds number increases away from an adiabatic wall faster in supersonic flow than in incompressible flow, we would expect the flow to become less stable as we move away from the wall at a rate that is faster than in an incompressible flow at the same friction velocity. The effect on the near-wall stability and the bursting process in supersonic flows is not clear, but DNS may well provide the answer in the near future.

Chapter 9

Perturbed Boundary Layers

9.1 Introduction

So far we have considered turbulent flows with relatively simple boundary conditions, such as boundary layers on a smooth flat plate, or mixing layers formed at the interface between two parallel, co-flowing streams. Although these studies help to improve our fundamental understanding of compressible turbulence, such canonical flows are rarely encountered in practice. In the aerodynamic design of high-speed vehicles, for example, it is necessary to understand the behavior of turbulence in more complex geometries, and it is not surprising that considerable work has been performed to study the effects of perturbations or distortions on the behavior of turbulent boundary layers in supersonic flows, including the effects of pressure gradients, extra strain rates such as streamline curvature, divergence, and dilatation, and the interaction with shock waves. Reviews of this work were given by Fernholz and Finley (1980, 1981), Smits and Wood (1985), Fernholz et al. (1989), and Spina et al. (1994). Almost all of the relevant work is experimental in nature, because engineering computations cannot provide much insight by themselves, and examples of DNS for perturbed boundary layers in high-speed flow are thus far confined to shock wave-boundary layer interactions, which sre discussed in Chapter 10.

The experiments on perturbed boundary layers have documented the general features of the mean flow behavior in detail, but there are only a few studies where extensive turbulence measurements have been made, most of them quite recently. As we indicated in Chapter 1, reliable and accurate turbulence measurements are difficult to make in any supersonic flow, and the difficulties are usually more extreme in the presence of flow distortions. For example, hot-wire measurements can suffer from many errors in flows with strong pressure gradients. In adverse pressure gradients, transonic effects may become important in large regions of the flow and the flow may separate, whereas in favorable pressure gradients the signal-to-noise ratio degrades because the

turbulence intensities are greatly reduced. In a shock wave-boundary layer interaction, the unsteady shock motion can impose severe loadings on the probe body, greatly increasing the possibility of breaking the hot-wire. In all cases, particular care must be exercised to produce repeatable and reliable measurements, and (as usual) the measurement errors must be taken into account when interpreting the results.

The experiments have covered a broad range of model geometries and flow conditions. To help understand the implications of the results it is useful to classify the existing work according to the type of perturbation(s) that were applied to the flow. One of the major contributions made by Bradshaw (1973) in this area was to provide a classification scheme for the effects of different kinds of extra strain rates e, that is, strain rates additional to the principal shear $\partial u/\partial y$. By identifying the particular extra strain rates associated with streamline curvature ($\partial v/\partial x$), convergence and divergence ($\partial w/\partial z$), and compression and dilatation ($\nabla \cdot \mathbf{V}$), he formulated a general framework for the understanding of such complex flows. Bradshaw included pressure gradients in this classification scheme, in the sense that dp/dx is simply related to du_e/dx for incompressible thin shear layers. See also Smits and Wood (1985) and Spina et al. (1994).

One of the complications encountered in classifying compressible flows is that it becomes difficult to uncouple the effects due to pressure gradient, streamline curvature and bulk dilatation. This coupling occurs in all flows, but in a subsonic flow with streamline curvature, for example, dilatational effects are negligible by definition, and mean radial pressure gradients simply balance the centripetal acceleration, without straining fluid elements. In flows with streamwise pressure gradients there will always be a measure of streamline curvature as well, but for two-dimensional subsonic flows the ratio of $\partial v/\partial x$ to $\partial u/\partial x$ will be of order v/u, and therefore it is always small. In a supersonic flow, a coupling also exists between streamline curvature (that is, radial pressure gradient) and longitudinal pressure gradient, and the degree of coupling depends on the geometry. In simple wave flows, as in the flow over a compression surface, the streamline curvature and pressure gradient are directly coupled through the angle of turn and the Mach number. In reflected wave flows, where the pressure gradients are imposed on the boundary layer by external generated waves, the streamline curvature is (approximately) coupled to the streamwise pressure gradient. This is similar to the case in subsonic flows, but for a given pressure rise the degree of curvature will depend on the decrease in streamtube area, which increases with Mach number. In compressible flows, effects due to streamline curvature, pressure gradients, and mean dilatational are always strongly coupled, regardless of how the pressure gradient is applied.

As seen in Chapters 7 and 8, many of the differences observed between boundary layers on adiabatic walls in subsonic and supersonic flow can be ex-

plained in terms of the fluid property variations that occur as a result of the cross-stream temperature gradients that exist at supersonic Mach numbers. We show that this approach continues to hold when the wall temperature suddenly increases. However, perturbations such as the sudden imposition of a pressure gradient, or longitudinal streamline curvature, or the interaction with a shock wave, produce a boundary layer response that does not have an equivalent subsonic counterpart, and which cannot be explained in terms of fluid property variations. Vorticity can be produced through baroclinic torques. Longitudinal pressure gradients will lead to the compression or dilatation of vortex tubes, enhancing or reducing turbulent velocity and pressure fluctuations. Separation can occur when shock waves are present, if the shock is strong enough (a phenomenon that can be understood from subsonic experience), but even in the absence of separation there exists a strong coupling between the shock and the turbulence, which leads to unsteady shock motion and distortions of the shock sheet. Understanding the shock motion and the resultant unsteady heat transfer and pressure loading is of great importance in many aerodynamic flows. Because the shock motion seems closely connected with the incoming turbulence field and the separation unsteadiness, there is a clear need to understand the nature of the organized motions in the incoming boundary layer, particularly the large scales. Unfortunately, studies of the instantaneous or ensemble averaged turbulent motions in supersonic flows are uncommon, and very few studies have been made in perturbed supersonic flows to try to describe the distortion of the large-scale structure.

The perturbation may originate in a number of different ways. It may be the result of a step change in the flow conditions where, for instance, the wall curvature changes suddenly. Alternatively, the distortion may be produced by an impulsive change, where the impulse consists of two step changes of opposite character, separated by a short streamwise distance. An example of this case would be the flow that develops on a flat plate, passes over a short region of concave curvature, and then relaxes farther downstream over a second flat surface. At some point away from the wall, the compression waves generated by the concave surface curvature will form a shock. For large radii of curvature, the shock will form outside the boundary layer, but for small radii it forms inside the layer. For compression corners, where the radius of curvature is essentially zero, a shock forms immediately outside the sonic layer, and multiple shocks form when the flow separates. The perturbations may also occur successively, as in the case where the surface curvature or the pressure gradient changes sign in the streamwise direction. For example, as the flow passes over a forward-facing step the surface curvature changes sign from concave to convex, and the pressure first rises and then falls.

Here we try to use the extra strain rate classification as a basis for discussing the response of a supersonic turbulent boundary layer to a sudden change in wall temperature, pressure gradient, streamline curvature, or bulk

dilatation, despite the anticipated difficulties. Flows where an additional degree of complexity is introduced by the application of successive perturbations are also considered. At some points in this treatment, it is useful to compare the response to these kinds of perturbations to the strong perturbations produced when a turbulent boundary layer interacts with a shock wave, although a fuller discussion is given in Chapter 10.

9.2 Perturbation Strength

The strength of a perturbation can be difficult to define because it will depend on how rapidly the perturbation is applied, and also because the perturbation may affect different parts of the flow in different ways. The simplest case may be where the wall boundary condition is changing. For instance, when the wall roughness changes suddenly, the ratio of the upstream and downstream equivalent roughness heights is a reasonably obvious parameter to characterize the strength of the perturbation (Smits and Wood, 1985). For a flow where the wall temperature changes suddenly, the ratio of the wall temperatures upstream and downstream serves a similar function (Debiève et al., 1997). The strength of a perturbation in pressure gradient is more difficult to define. In subsonic flows it may be defined in terms of the change in $\beta \equiv \delta^*/\tau_w dp/dx$, Clauser's (1954) pressure gradient parameter. In a supersonic flow where streamwise pressure gradients can be accompanied by significant pressure gradients normal to the wall, additional parameters will be necessary to define the perturbation fully. For instance, it is possible to obtain the same boundary layer wall pressure distribution in two different ways: one by using a curved wall so that the curvature generates the pressure gradient, the other on a flat plate by using a contoured ceiling to generate a reflected wave system (see Figure 9.1). Clearly, the gradients normal to the wall in these two flows will be different. To make this more quantitative, at least for disturbances that are approximately isentropic such as simple wave flows, the ratio of the normal and streamwise pressure gradients is given approximately by $1/(\tan \alpha_M)$, where α_M is the local Mach angle. This ratio is equal to 1.7 at Mach 2, and 5.9 at Mach 6, so that the effects of the cross-stream pressure gradient increase quickly at higher Mach numbers. For reflected wave flows, the analysis is more complicated, but the normal gradients take their maximum values in simple flow regions (in the nonsimple region, where the incident wave system crosses the reflected system, the normal pressure gradients are generally small), so that the simple wave estimate can be taken as an upper bound. This issue is discussed more fully by Finley (1977) and Fernholz and Finley (1980).

As indicated earlier, differences between simple and reflected wave systems also appear in the resulting streamline curvature. For a simple wave system, the curvature can be convex or concave, and for a given overall streamline deflection the pressure rise is fixed by the incoming Mach number. A linearized

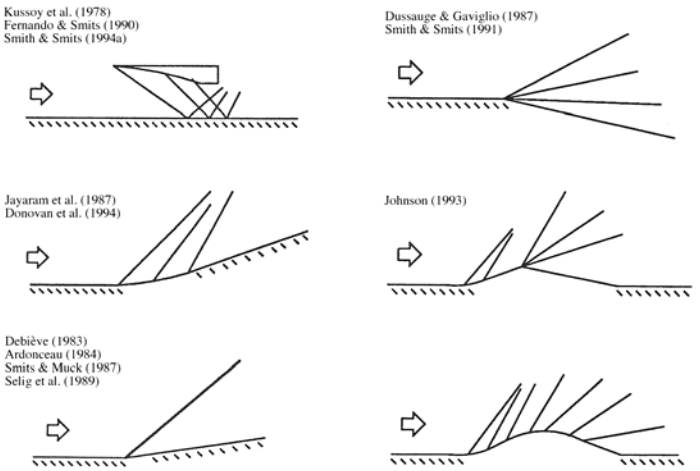

Figure 9.1. Boundary layer flow distortions. Left: Adverse pressure gradients. Right: Favorable pressure gradients. (From Smith and Smits (1994), with the authors' permission.)

analysis gives:

$$\Delta\theta = \frac{\Delta p}{p}\frac{\sqrt{M^2-1}}{\gamma M^2}.$$

In terms of the radius of curvature R_c and the initial boundary layer thickness δ_0,

$$\frac{\delta_0}{R_c} = \frac{\delta_0}{p}\frac{\partial p}{\partial x}\frac{\sqrt{M^2-1}}{\gamma M^2}.$$

Consequently it is not usually possible to discriminate between the individual contributions due to curvature, compression, and pressure gradient to the distortion of the boundary layer without performing the same experiment over a range of Mach numbers, which can in turn introduce additional effects. However, for a reflected wave system with a rising pressure, the curvature is initially convex and then concave, and the overall streamline deflection and pressure rise are independent. For example, in a reflected wave flow such as that shown in Figure 9.1 the overall streamline deflection is zero even though the overall pressure rise is not.

To help resolve these issues of discriminating among perturbations, and to determine the strength of the response in a complex supersonic flow, all perturbations need to be quantified separately, and their interactions need to be determined. For flows where extra strain rates are important, one useful measure is the ratio of each extra strain rate, e, to the principal strain rate, $\partial u/\partial y$ (Bradshaw, 1973, 1974). A distortion is generally classified as weak if

$e/(\partial u/\partial y) \approx 0.01$, and strong if $e/(\partial u/\partial y) \approx 0.1$. The final response of some structure parameter to the prolonged application of a constant, small extra strain rate e can be expressed in a linearized and dimensionless form by an amplification factor $1 + \alpha_o eL/(\partial u/\partial y)$, where α_0 is an empirical constant of order 10 for several types of extra strain rate, and $(\partial u/\partial y)$ can be taken as a measure of the typical *rms* eddy strain rate (following Bradshaw, a better local estimate may be given by $\sqrt{-\overline{u'v'}}\big/L_\varepsilon$, where L_ε is the dissipation length scale). This amplification factor depends only on the local rate of strain rather than the rate-of-strain history. If the extra strain rate is applied over a time comparable to the eddy lifetime, then it might be better to replace $\alpha_0 e$ with an "effective" value I, given by the integral of the extra strain rate over the time which it is applied $(=\int e\,dt)$. For example, a measure of the strength of the impulsive perturbation due to a short region of bulk compression (I_p) is given by $(1/\gamma)\log(p_2/p_1)$ (Hayakawa et al., 1983), where p_2/p_1 is the pressure ratio across the compression, and for an impulse in curvature the strength (I_θ) is given by the angle through which the flow has been turned (Smits et al., 1979b). It is implied that for an impulsive perturbation the overall distortion is the more important parameter, and not the rate at which it is applied.

In the assessment of perturbation strength, it is implicitly assumed that the perturbations are sufficiently small for a linear analysis to be meaningful. That is, the response of the boundary layer can be described in terms of a simple first-order lag equation. When more than one strain rate acts, as in the case of a deflected supersonic flow where streamline curvature and bulk compression act in addition to longitudinal and normal pressure gradients, the linear addition of different perturbation strengths to arrive at some overall measure is unlikely to hold in any quantitative sense. Nevertheless, the linear analysis can still serve as a crude guide for making comparisons among different flow cases, as we hope to show here. For stronger perturbations, we know that Rapid Distortion Approximations (RDA) can give quantitatively useful results. For concavely curved flows this was shown by Jayaram et al. (1989) and Donovan (1989), but the analysis will be valid only for times short compared to the (local) eddy response time. Broadly speaking, the eddy response time scale varies approximately as the turbulent kinetic energy divided by the rate of its production (Townsend, 1976). If we assume that the structure parameter a_1 remains approximately constant, the relaxation time is proportional to $(\partial u/\partial y)^{-1}$, the mean eddy strain rate.

9.3 A Step Change in Wall Temperature

The response of turbulent boundary layers to step changes in boundary conditions has been widely studied in subsonic flows (for a review see Smits and Wood (1985)). The step change may be caused by a sudden change

in wall roughness, surface curvature, pressure gradient, suction/blowing, or heat transfer. The response to the change depends on how the step change is applied, but if the step is caused by a change in the wall boundary condition, such as a sudden change in wall temperature, the boundary layer adjusts to the new boundary condition first at the wall, and then progressively farther from the wall as turbulent diffusion begins to affect the rest of the flow. From a fundamental viewpoint, the initial response of the boundary layer and its subsequent relaxation to the new boundary conditions provides useful information on the time and length scales of turbulent diffusion.

The relaxation process downstream of the step change is often described in terms of the growth of an internal boundary layer, which is the region near the wall where the flow scales with variables based upon the new wall condition (for example, the friction velocity and temperature based on the new level of heat transfer), whereas the rest of the boundary layer continues to scale on the variables based upon the wall conditions that apply in the flow upstream of the step change. Typically, the internal layer grows at a rate similar to that of an undisturbed turbulent boundary layer, that is, at a rate approximately proportional to $x^{0.8}$. The relaxation rate, therefore, decreases with downstream distance, and in some instances the asymptotic state may not be reached for distances of the order of 100 initial boundary layer thicknesses ($\delta_\circ$), if at all (see, for example, the slow relaxation downstream of a prolonged region of convex curvature studied by Alving et al. (1990)).

The response of boundary layers in supersonic flow to step changes in boundary conditions has not been studied so extensively, but a number of interesting experiments have been performed. For example, Kubota and Berg (1977) studied the effects of sudden changes in wall roughness (smooth to rough and rough to smooth) in a Mach 6 turbulent boundary layer. For a step change from smooth to rough, the boundary layer attained a self-preserving state in the mean flow at a distance of about $20\delta_\circ$, and in the fluctuation profiles at about $30\delta_\circ$. The relaxation following a step change from rough to smooth was somewhat slower with the mean flow relaxing over $28\delta_\circ$ and the turbulent field over 40 to $50\delta_\circ$. In essence, their results were not significantly different from similar work in subsonic flow (Antonia and Luxton, 1971, 1972).

Another interesting case is the boundary layer response to sudden changes in heat transfer. Despite the practical significance of such flows, the extensive reviews by Fernholz and Finley (1980, 1981) list only a few experiments where heat transfer was important, and these cases were confined to uniformly cooled walls (Voisinet and Lee, 1972; Laderman and Demetriades, 1974). However, Debiève et al. (1997) studied a Mach 2.3 fully developed turbulent boundary layer experiencing different step increases in wall temperature, and we now consider this experiment in some detail. The ratio of wall temperature to recovery temperature, T_w/T_r, varied from 1.0, to 1.5, to 2.0. To capture the relaxation process, the response was studied over a distance of approximately

$50\delta_\circ$, and many detailed mean flow and turbulence measurements were made.

We expect the step change in heat transfer to be somewhat different from a step change in wall roughness. First, two internal layers will form: one for the temperature field, and the other for the velocity field (because we expect the friction velocity to be affected by the heating). The two internal layers are not coincident because the Prandtl number is not unity. Second, the step change is applied in the temperature field, and we expect to see, at least initially, some differences appearing in the usual relationships between temperature and velocity, that is, Crocco's relation for the mean field, and the Strong Reynolds Analogy for the fluctuations.

In Chapter 5, we showed that in a self-preserving flow a relationship between velocity and temperature may be derived under the conditions that the mixed Prandtl number, P_m [$\equiv (\tau\partial h/\partial y)/(q\partial U/\partial y)$], is constant and $0.7 < P_m < 1.0$ (van Driest, 1955; Walz, 1959). The result is known as the modified Crocco relationship, or sometimes simply as Crocco's law (Equations 3.47 and 5.32). If we consider only the flow in the region where molecular transport processes can be neglected ($y \gg y_v$) and where the stress is constant, dimensional analysis or mixing length arguments give, for zero pressure gradient (Rotta, 1960; Bradshaw, 1977).

$$U_i^* = \int_{U_v^+}^{U^+} \sqrt{\frac{T_w}{T}}\, dU^+ = \frac{1}{\kappa}\log y^+ + C_1 \tag{9.1}$$

(see Equations 5.48 and 5.50). If the temperature variation is known, either by measurement or by assuming the validity of Crocco's law, the integral in Equation 9.1 may be evaluated. Furthermore, because the appropriate velocity scale for the inner and outer regions of the boundary layer is $(\tau_w/\rho)^{1/2}$, we expect from previous considerations that the mean (and fluctuating) velocities scale with this parameter if the flow is self-preserving. For an adiabatic, zero pressure gradient boundary layer, the variation in density is due to the Mach number gradient. For a heated wall, the density variation is also affected by the level of heating.

As noted in Section 9.2, the time scale τ_u for the adjustment of the velocity field to a given perturbation is given by turbulent kinetic energy divided by the rate of its production, that is, $\tau_u = \overline{q^2}/(-\overline{u'v'}\partial u/\partial y)$, which is approximately proportional to $(\partial u/\partial y)^{-1}$. The flow near the wall, therefore, adjusts relatively quickly, and a limited region of self-preserving flow may occur (it is assumed here that, because P_t is close to one, an approximately self-preserving state can occur). A similar argument can be made for the relaxation rate of the temperature field,[1] bearing in mind that the Prandtl number is not unity so that the physical extents of the velocity and temperature layers are not identical. Within this self-preserving part of the boundary layer (the internal

[1]By analoguey with the velocity field, $\tau_T = \overline{T'^2}/(-\overline{v'T'}\partial T/\partial y)$.

layer) the velocity and temperature fields may display a logarithmic variation, and the total stress is then expected to be approximately constant over the same region.

When the mixed Prandtl number is constant, it is possible to obtain for $y < y_s$, where y_s lies in the constant stress region, a temperature-velocity relationship for perturbed flows of the form:

$$\frac{T}{T_s} = \frac{T_w}{T_s} + \frac{T_r - T_s}{T_s}\left(\frac{u}{u_s}\right) - P_m \frac{(\gamma - 1)}{2} M_s^2 \left(\frac{u}{u_s}\right)^2 \tag{9.2}$$

where $M_s = u_s/\sqrt{\gamma R T_s}$, and:

$$\frac{T_r - T_w}{T_s} = 1 + P_m \frac{(\gamma - 1)}{2} M_s^2 - \frac{T_w}{T_s} = -\frac{q_w u_s P}{C_p \tau_w T_s} \tag{9.3}$$

(for details, see Carvin et al. (1988)). Equation 9.2 can be applied to perturbed flows that display a constant stress region. Furthermore, in the region where molecular transport processes can be neglected ($y \gg y_v$) and where the stress is constant, Equation 9.1 still applies as long as the scaling is based on the local wall values. Equations 9.1 and 9.2 then completely define the mean velocity and temperature fields for $y_v \ll y < y_s$.

If we assume that the presence of a logarithmic velocity profile indicates the presence of a constant stress region (this does not necessarily follow, but for the present purpose it may be a reasonable approximation), then Equation 9.2 may be used to determine the heat transfer at the wall by fitting it to the data in the region $y_v \ll y < y_s$. This method for finding the friction temperature $T_\tau (\equiv q_w/\rho_w C_p u_\tau)$ is similar to the Clauser method for finding the friction velocity from the measured velocity profile. The skin-friction and heat-transfer coefficients can then be found from the experimental profiles by an iterative solution of Equations 9.1 and 9.2. In principle, it should also be possible to find P_m using this procedure but the estimates of T_τ and C_h are rather insensitive to the value of P_m, and it difficult to find P_m accurately from the data.

To express the temperature profile in a similar logarithmic form, we note that Equation 9.2 may be rewritten using a turbulent total temperature T_i as indicated in Chapter 7. This leads to

$$T_i^* = \int_{T_1^+}^{T_i^+} \sqrt{\frac{T_w}{T}}\, dT_i^+ = \frac{1}{\kappa} \log y^+ + C_T, \tag{9.4}$$

where $T_i^+ = -T_i/(T_\tau P_m)$, and C_T depends on the inner limits of the logarithmic region (see also Equation 5.64). It will also depend on the Prandtl number and the ratio of the wall temperature to the recovery temperature T_w/T_r (Carvin et al., 1988).

Some results from the experiments by Debiève et al. (1997) are shown in Figures 9.2 to 9.4. From Figure 9.2 we see that the internal thermal layer

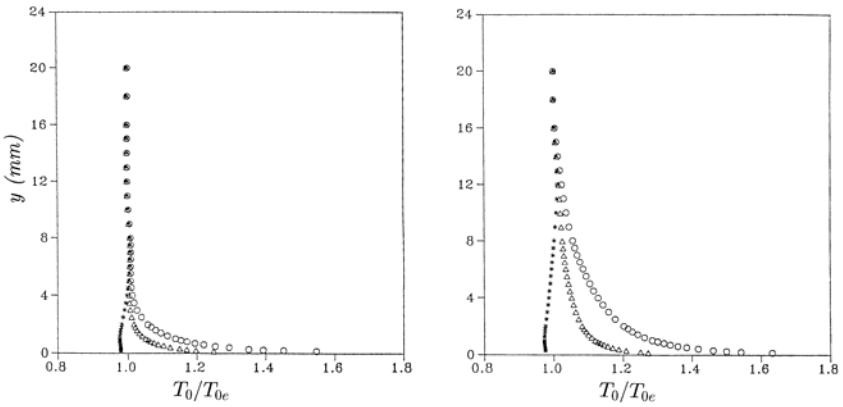

Figure 9.2. Total temperature profiles for step change in wall temperature. Left: $x = 8$ cm; Right: $x = 46$ cm (x is the distance measured from the beginning of the heated wall; the boundary layer thickness at $x = 8$ cm is 10 mm). $*$, $T_w/T_r = 1.0$; $\triangle$, $T_w/T_r = 1.5$; $\circ$, $T_w/T_r = 2.0$. (From Debiève et al. (1997), with the authors' permission.)

grows relatively rapidly: at $x = 8$ cm it fills about half the boundary layer, and by $x = 46$ cm the temperature and the velocity layers are almost coincident. A comparison with Crocco's relation (Equation 5.28) indicated that the boundary layer at $x = 8$ cm is strongly perturbed by the heating, and by $x = 46$ cm has not yet reached equilibrium. In contrast, the velocity profiles demonstrate that the temperature field has only a mild effect on the velocity distribution far from the wall.

To find the variations of wall friction and heat transfer along the plate, the experimental data were fitted to the logarithmic relationships 9.1 and 9.4. Figures 9.3 and 9.4 show the transformed velocity and static temperature data in logarithmic form. In these transformed coordinates, there appears to be little effect of heating. In other words, the variation in density due to the combined effect of compressibility and heating simply alters the velocity scale for the velocity profile without introducing any explicit effects due to the heating. The relaxation of the temperature profile and the large extent of the logarithmic region are clearly evident in Figure 9.4. For this flow, the constant C_T is approximately equal to 3.0, which is a little lower than the value of 3.6 found by Michel et al. (1969).

The coefficients of skin friction C_f $(= 2\tau_w/\rho_e u_e^2)$ and heat transfer C_h $(= q_w/\rho_e u_e C_p(T_r - T_w))$ are shown in Figure 9.5. Although the accuracy of these data is difficult to judge in the absence of an independent measure of τ_w and q_w, the effect of heating appears to reduce the skin-friction and heat-transfer coefficients significantly, regardless of the streamwise location. If we

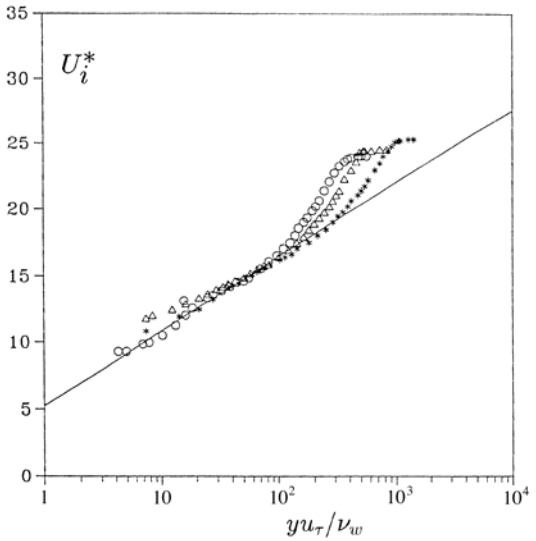

Figure 9.3. Semi-logarithmic representation of transformed velocity profiles at $x = 32$ cm for step change in wall temperature, with u_τ adjusted to give the best fit to Equation 9.1. Symbols as in Figure 9.2. (Figure from Debiève et al. (1997), with the authors' permission.)

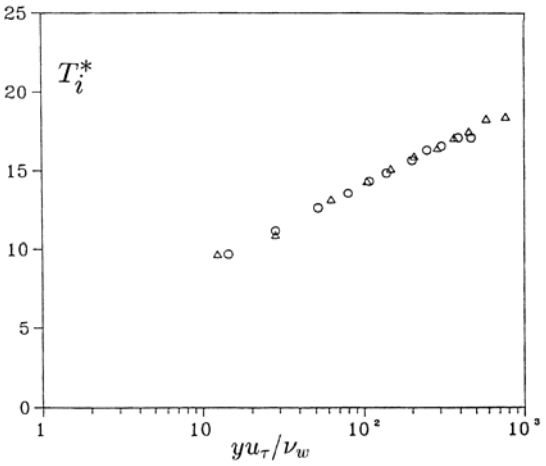

Figure 9.4. Semi-logarithmic representation of temperature profiles $x = 32$ cm for step change in wall temperature, with T_τ adjusted to give the best fit to Equation 9.4. Symbols as in Figure 9.2. (From Debiève et al. (1997), with the authors' permission.)

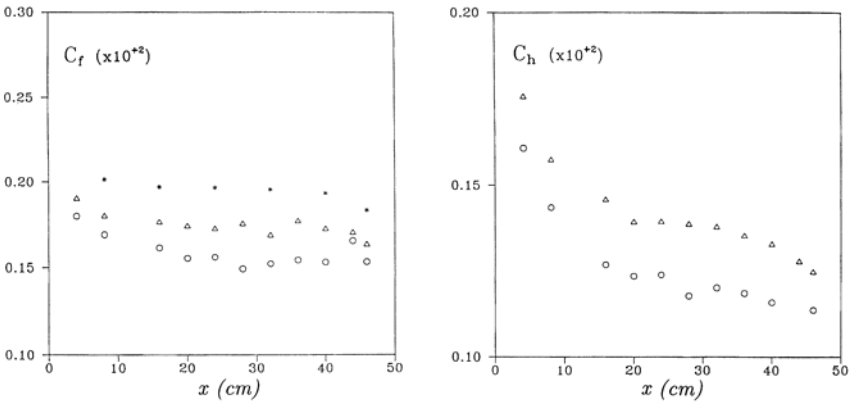

Figure 9.5. Distribution of skin-friction coefficients (left), and heat-transfer coefficients (right) for step change in wall temperature. Symbols as in Figure 9.2. (From Debiève et al. (1997), with the authors' permission.)

assume that the skin-friction coefficient follows the same relation as that found for adiabatic flows, provided that the density and viscosity are evaluated at the wall conditions, we find that most of the differences in C_f observed due to heating are due simply to the change in fluid properties. The argument is similar to that advanced in Chapter 1 to explain the decrease in C_f with Mach number for adiabatic flows. A corresponding argument can also be made for the heat transfer coefficient. However, we can see that the Reynolds Analogy factor s $(=2C_h/C_f)$ appears to be strongly out of equilibrium, approaching a value of about 1.5 near the end of the test section, still well above its equilibrium value of about 1.24.

As for the longitudinal turbulence intensity, Debiève et al. (1997) found that Morkovin's representation appears to take into account the effects of wall heating. That is, the data can be collapsed using a scaling based solely on fluid property variations (within the experimental error). Not unexpectedly, the intensity of the total temperature fluctuations increases with heating. For the turbulent heat transfer, we are more interested in the behavior of the transverse heat flux $\overline{(\rho v)'T'}$. This is a difficult quantity to measure directly, but some indication can be given by examining the behavior of the longitudinal heat flux $\overline{(\rho u)'T'}$. Debiève et al. (1997) found that the correlation coefficient $-R_{uT}$ is not significantly affected by the heating, and it remains almost unchanged from its adiabatic value in a supersonic flow of 0.8 to 0.9 (a typical value in a heated subsonic flow is 0.4 to 0.5). This high degree of correlation between the velocity and temperature (even though the flow is heated) suggests that the instantaneous scales of u' and T' are connected by a relationship such

as $T' = f(u')$. In an adiabatic flow, we have the Strong Reynolds Analogy, but in heated flows where the total temperature fluctuations are significant an alternative analysis is required.

When the distributions $T(y)$ and $u(y)$ are known, a linearization for small fluctuations can be obtained with the aid of a mixing length argument $\sqrt{\overline{u'^2}} = l_u\,\partial u/\partial y$ and $\sqrt{\overline{T'^2}} = l_T\,\partial T/\partial y$, or by a direct linearization of the mean relationship $T = g(u)$. In the case of $l_u(y/\delta) = l_T(y/\delta)$, that is to say when the Prandtl number defined in terms of $\overline{u'^2}$ and $\overline{T'^2}$ is equal to unity, the two methods lead to the same result; the SRA (Gaviglio, 1987). For a direct linearization of the mean relationship $T = g(u)$, similar mixing length arguments are necessary.

To evaluate the influence of wall heating on the SRA, Debiève et al. (1997) linearized Walz's temperature-velocity relationship (Equation 5.28) which explicitly includes the heating parameter, T_w/T_r:

$$\frac{(\gamma-1)M^2\,u'/u}{T'/T} = -\left[r + \left(\frac{T_w}{T_r} - 1\right)\left(\frac{1 + rM_e^2(\gamma-1)/2}{M_e^2(\gamma-1)}\right)\left(\frac{1}{u/u_e}\right)\right]^{-1} \quad (9.5)$$

(a similar approach was followed by Cebeci and Smith (1974), who assumed $r = 1$). Here, the second term on the right-hand side introduces the influence of heating. This term also depends on y/δ through the velocity profile u/u_e which depends only slightly on the heating. In adiabatic flows, the factor in the square brackets reduces to the recovery factor $r = 0.89$. In the case where $T_w/T_r = 2$, we can expect that, for a point located in the middle of the layer, the right-hand side of Equation 9.5 will be reduced by a factor of about two with respect to the adiabatic value. The data given by Debiève et al. (1997) show this decrease from the adiabatic value, but their data are probably not accurate enough to verify the exact form of Equation 9.5.

To summarize, we see the growth of an internal layer in the temperature profile, but the transformed velocity field is relatively unaffected by the wall heating. Near the wall, that is, in the internal layer, logarithmic variations in the mean velocity and temperature profiles were found when the scaling arguments took into account the new values of density and friction velocity. Similarly, the change in fluid properties at the heated wall can explain the observed decrease in the skin-friction and wall heat-transfer coefficients. As for the turbulence, Morkovin's scaling collapses the streamwise Reynolds stress profiles, and the correlation between velocity and temperature fluctuations appear unaffected by the heating at the wall. However, the relationship between the temperature and velocity fluctuations in the SRA is strongly affected by the heating.

9.4 Adverse Pressure Gradients

The response to an adverse pressure gradient depends very much on the external Mach number. Consider a reflected wave flow producing an adverse pressure gradient with little streamline curvature, such as the experiment conducted by Fernando and Smits (1990). As the flow enters a region where the pressure is increasing, the sonic line moves away from the wall because in a decelerating subsonic flow the distance between two adjacent streamlines will increase. In the outer part of the boundary layer where the flow remains supersonic, the distance between adjacent streamlines will decrease as the pressure rises. The overall effect on the boundary layer is not immediately obvious: depending on the external Mach number and the strength of the pressure gradient, the overall boundary layer thickness, for example, may increase or decrease. With respect to the wall stress, at low Mach numbers it decreases in adverse pressure gradients but at higher Mach numbers it can increase. There are two opposing trends at work. As the sonic line moves away from the wall, the velocity gradient at the wall decreases, tending to reduce the wall stress. However, the viscosity increases as the temperature of the fluid rises toward the wall, tending to enhance the wall stress. At lower Mach numbers, the movement of the sonic line is the more important effect, and adverse pressure gradients reduce the wall stress. At higher Mach numbers, the increased viscosity is the dominant effect, and therefore the wall stress increases in an adverse pressure gradient. Because the rising pressure will also increase the velocity gradients in the supersonic part of the flow, the boundary layer thins, and turbulent momentum transport to the wall region will increase, in line with the increase in the wall stress. An example of a rising wall stress with increasing pressure is given in Figure 9.6. We can still expect to see the flow separate at more severe pressure gradients because normal pressure gradients will become important, and the simple analysis given here will break down. The prediction of such flows is understandably difficult, given the complex interactions between the opposing flow response in the subsonic and supersonic zones.

Adverse pressure gradients are often accompanied by significant streamline curvature. The extra strain rate due to streamline curvature ($\partial v/\partial x$) has a profound effect on the turbulence in incompressible flows. When the sense of curvature is concave, the effect on the turbulence in the boundary layer is destabilizing, leading to an increase in wall friction, heat transfer, and the Reynolds stresses. In addition, Taylor-Görtler-like vortices have often been observed to form on concavely curved walls. Convex curvature is stabilizing, and the wall friction, heat transfer, and Reynolds stresses all decrease, and the Taylor-Görtler instability is absent. Von Kármán (1934) considered the equilibrium of a fluid element moving along a curved streamline, and demonstrated that a boundary layer over a curved wall was unstable if the curvature

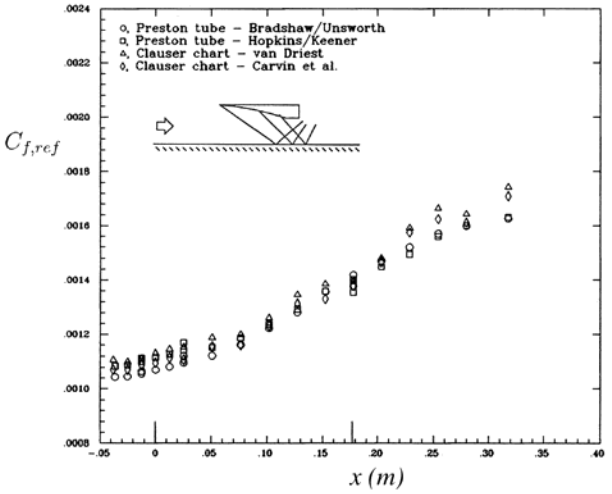

Figure 9.6. C_f versus streamwise distance for adverse pressure gradient flow, with an upstream Mach number of 2.9, decreasing to 2.5 over a distance of about 11 initial boundary layer thicknesses (275 mm). C_f is nondimensionalized using conditions upstream of the pressure rise, so that the figure illustrates the rise in shear stress at the wall. Data from Fernando and Smits (1990) (see Table 9.1). (Figure adapted from Smith et al. (1992). Reprinted with the authors' permission.)

was concave, and stable if it was convex. When the flow is compressible, the stability argument must take into account the effects of density gradients, and the analysis by Bradshaw (1973) suggests that for an adiabatic wall the density gradient will enhance the effect of curvature. In a strongly cooled flow, however, the density gradient changes sign near the wall, and it is possible, at least in principle, for a boundary layer to be unstable in the outer layer and stable in the inner layer, and vice versa.

These arguments provide qualitative descriptions of the flow stability, but experiments show that the effects on the properties of the flow are at least an order of magnitude greater than the analysis would indicate. As may be expected, the effects of streamline curvature in compressible flow are more difficult to determine because, as discussed earlier, curvature in a supersonic flow is always accompanied by pressure gradients and dilatation, and the significance of each individual perturbation can only be found by comparing different experiments where the balance between these effects is changing.

A group of such experiments for impulsive perturbations was performed by Jayaram et al. (1987); Smits and Muck (1987), and Donovan et al. (1994). Two different angles of turning were investigated, 8° (Group One) and 16° (Group Two), and the nondimensional radius of curvature $R_c/\delta_\circ$ varied from

	Group One				
	Smits and Muck	Jayaram *et al.*		Fernando and Smits	Kussoy *et al.*
	Compression corner	Model I Curved wall	Model II Curved wall	Flat wall	Flat wall
M_e	2.9	2.9	2.9	2.9	2.3
R_c	0	$10\delta_\circ$	$50\delta_\circ$	∞	∞
L_i	0	$1.4\delta_\circ$	$7\delta_\circ$	$7\delta_\circ$	$1.5\delta_\circ$
I_θ	0.14	0.14	0.14	< 0.05	—
I_p	0.41	0.46	0.46	0.46	0.40
$\overline{\rho}\overline{u'^2}$	+350%	+240%	+320%	+200%	+370%
$-\overline{\rho}\overline{u'v'}$	+390%	+390%	+200%	+220%	+160%
θ	+8°	+8°	+8°	0	0

Table 9.1. Impulses in adverse pressure gradient cases, Group One. The Flat Wall cases are reflected wave flows. (Adapted from Smith and Smits (1994), with the authors' permission.)

0 (Flat wall), to 10–12 (Models I and IV), to 50 (Model II). The incoming Mach number was fixed at a value of about 2.9. The flow configurations are shown schematically in Figure 9.1, and the estimated strengths of the corresponding impulses of extra strain rates are given in Tables 9.1 and 9.2. Here, δ_0 is the boundary layer thickness of the flow just upstream of the start of the disturbance, and the length of the impulse is L_i.

9.4.1 Flow over Concavely Curved Walls

The experiment by Donovan et al. (1994) illustrates many aspects of flows over concavely curved walls in supersonic flow. The flow conditions are summarized in Table 9.2, under Model IV, Curved wall. The total turning angle was 20°. As the flow passed through the region of surface curvature, the wall pressure rose by a factor of 2.9, the Mach number decreased from 2.86 to 2.10, the density increased by a factor of 2.1, and the velocity decreased by a factor of 0.88. At the same time, the absolute wall shear stress increased by about 125%, and the skin-friction coefficient by about 77%. This increase is counter to that observed in subsonic flows, where an adverse pressure gradient causes the wall shear stress to decrease. Another example of this phenomenon is the Fernando and Smits experiment shown in Figure 9.6. In these flows the sonic layers are very thin, and as the pressure rises the boundary layer thickness decreases. Because the turbulent mixing is strong, the net effect of a thinner

	Group Two		
	Smits and Muck	Donovan *et al.*	Smith and Smits (1981)
	Compression corner	Model IV Curved wall	Flat wall
M_e	2.9	2.9	2.9
R_c	0	$12\delta_\circ$	∞
L_i	0	$3.5\delta_\circ$	$3.5\delta_\circ$
I_θ	0.28	0.28	< 0.09
I_p	0.76	0.78	0.78
$\overline{\rho u'^2}$	+1700%	+900%	+600%
$-\overline{\rho u' v'}$	+650%	+700%	—
θ	+16°	+16°	0

Table 9.2. Impulses in adverse pressure gradient cases, Group Two. The Flat Wall cases are reflected wave flows. (Adapted from Smith and Smits (1994), with the authors' permission.)

layer is to increase the wall stress (see also Figure 9.6). However, the skin friction continues to increase well after the region of wall curvature has ended, and continues to increase even after the pressure gradient has ended.

Figure 9.7 shows the mean velocity profiles in inner layer scaling. The undisturbed boundary layer profile exhibits an extensive logarithmic region (the discrepancies near the wall are almost certainly due to uncertainties in probe position). By the end of the curved region, the profile begins to dip below the logarithmic law near the point where $y^+ = 2000$. The dip grows in size and extends farther into the logarithmic region with increasing streamwise distance. A dip in the logarithmic region is a common feature of flows with concave curvature, and it may indicate that the length scales of the turbulence increase faster with distance from the wall than in the unperturbed boundary layer (Bradshaw, 1973; Smits et al., 1979b; Jayaram, et al., 1987; Smits, et al., 1989). The dip does not become significant until after the curved region ends, suggesting that the inner region of the boundary layer is either exhibiting a delayed response to the curvature, or it is responding relatively quickly to the removal of curvature.

In these measurements, a constant temperature hot-wire anemometer was operated at high overheat ratio to measure the local mass flux fluctuations, $\overline{(\rho u)'^2}/\bar{\rho}^2\bar{u}^2$. The streamwise stress was obtained by using the SRA, according

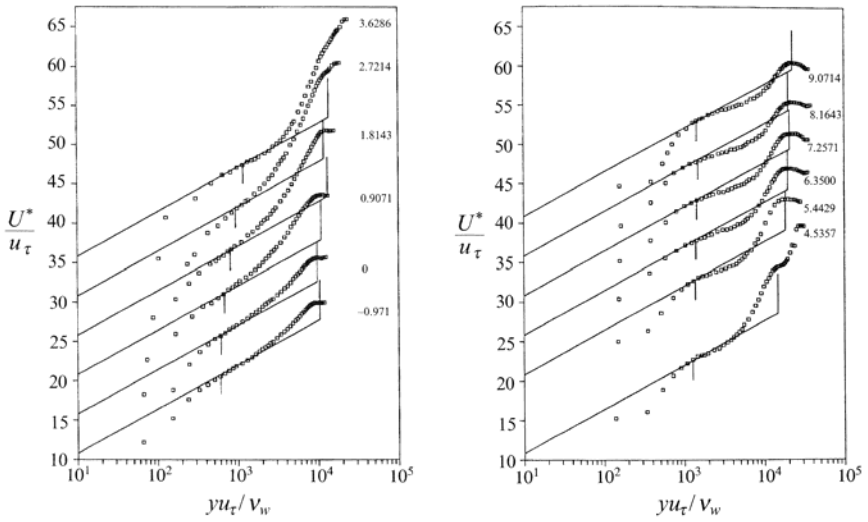

Figure 9.7. van Driest-transformed mean velocity profiles for the Model IV Curved wall impulse experiment (see Table 9.2). The vertical line near 10,000 indicates the boundary layer edge. The x/δ_0 values are indicated to the right of the profiles, where δ_0 is the boundary layer thickness for the incoming boundary layer, and x is measured from the start of the curved wall (the curvature finishes at $x = 3.5\delta_0$). (From Donovan et al. (1994). Copyright 1994, Cambridge University Press. Reprinted with permission.)

to:

$$\frac{(\rho u)'}{\bar{\rho}\bar{u}} = \frac{\rho'}{\bar{\rho}} + \frac{u'}{\bar{u}}.$$

That is,

$$\bar{\rho}\overline{u'^2} = \frac{\overline{(\rho u)'^2}}{\bar{\rho}\left(1 + (\gamma - 1)\, M^2\right)^2}\,. \tag{9.6}$$

The overall increase in the local mass flux fluctuations through the perturbation is only about 60%, but the level of the Reynolds streamwise stress increases considerably more through the perturbation: for instance, at $y/\delta = 0.4$ the level increases by a maximum factor of 6.8. From Equation 9.6, it is clear that the difference in the amplification levels is primarily due to the strong role played by the mean density in the definition of the stress term. The first signs of amplification occur at points close to the wall, where the time scales are small. By the last streamwise station, at $x = 9.1\delta_0$, the relaxation process had begun at points below 0.6δ, but the fluctuations were still growing in the outer 20% of the layer.

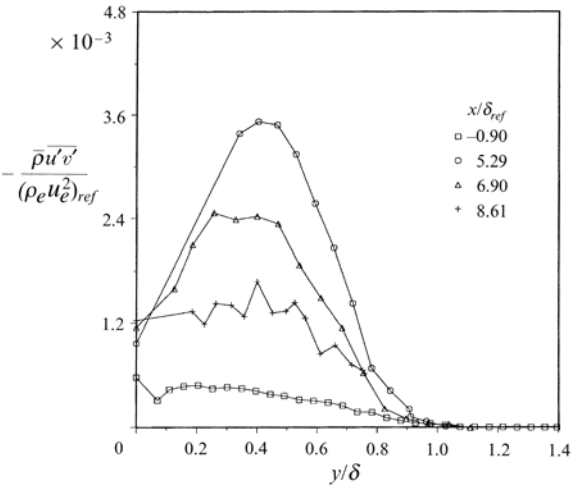

Figure 9.8. Streamwise variation of the Reynolds shear stress profiles for the Model IV Curved wall impulse experiment (see Table 9.2). The values plotted at $y = 0$ correspond to τ_w. (From Donovan et al. (1994). Copyright 1994, Cambridge University Press. Reprinted with permission.)

As the boundary layer exits from the curved region, the profile of the angular momentum $\rho\,(\partial u/\partial y)$ develops an inflection point away from the wall. A generalized inflection point is defined by two conditions:

$$\left(\frac{\partial}{\partial y}\left(\rho\frac{\partial u}{\partial y}\right)\right)_{y_i} = 0 \qquad \text{and} \qquad \left(\frac{u}{u_e}\right)_{y_i} > 1 - \frac{1}{M_e}.$$

In a laminar boundary layer, a generalized inflection point can make the layer unstable to small disturbances (Morkovin, 1992). In the present case, the inflection point is first seen at $x = 4.54\delta_0$, where it is located at $y \approx 0.2\delta$. Downstream, it becomes more exaggerated, and its position moves slowly away from the wall so that at $x = 8.16\delta_0$ it is at $y \approx 0.3\delta$. The Mach numbers at these locations satisfy the second condition, and it seems possible that instabilities associated with the inflectional angular momentum profile contribute to the turbulence amplification downstream of the curved wall region.

The Reynolds shear stress distributions are shown in Figure 9.8. The amplification of the shear stress is largest at $y = 0.4\delta$, where the level has increased by a factor of 5.3, although the shear stress relaxes considerably faster than the streamwise stress. The normal component of the stress $\bar{\rho}\overline{v'^2}$ also increased significantly, by a maximum factor of 6.0 in the middle of the layer. Somewhat surprisingly, the anisotropy ratio u_{rms}/v_{rms} showed little change through the distortion, but the correlation coefficient R_{uv} increased by more than 60%,

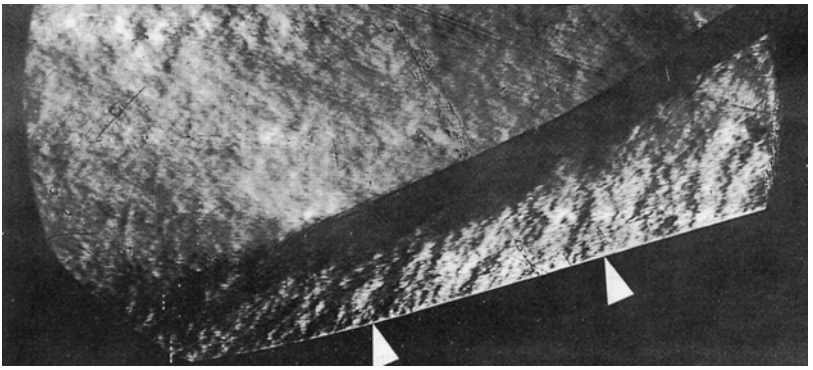

Figure 9.9. Schlieren photograph of a Mach 2.9 boundary layer passing over a short region of concave surface curvature (Model IV in Table 9.2). The flow is from right to left. The first pointer marks the end of curvature and the second marks the $x = 5.4\delta_0$ location. The dark band at the edge of the boundary layer is the compression fan/shock structure. Note the change in the inclination angle of the large-scale structures. (From Donovan et al. (1994). Copyright 1994, Cambridge University Press. Reprinted with permission.)

suggesting that the structure of the organized motions was altered significantly.

Two-point hot-wire measurements were also made to study the behavior of the large-scale motions directly. The convection velocity had decreased by about 5% relative to the local mean velocity at $x = 5.4\delta_0$, and the mean structure angle had increased by about 5°. Farther downstream, the structure angle continued to increase, so that at $x = 9.1\delta_0$ it had increased to about 10° over the undisturbed value.

Schlieren visualization of the boundary layer indicates that the density fronts rapidly change their inclination in the region of curvature (see Figure 9.9). In the beginning stages of the compression, the inclination is considerably less than the upstream value (which is about 50° in the middle of the layer; see Figure 8.36b), but the angles quickly increase so that at $x = 8.9\delta_0$ they increase to about 15° over the undisturbed value, in reasonable agreement with the hot-wire data. This initial decrease in structure angle is also seen in the FRS images of structures passing through a 16° compression corner interaction (Figure 10.7).

Donovan et al. suggested that this behavior may be explained by considering the effect of the compression on the vorticity contained by the large-scale motions. If we assume that the distortion is approximately isentropic, at least as far as the initial response is concerned, and baroclinic torques will not generate significant levels of vorticity, then a simple calculation based on the magnitude of the compression in the plane of curvature (assuming the perturbation to be rapid) suggests that the initial structure angle should decrease

by about 20°, as seen in the visualizations. Alternatively, if we assume the incoming large-scale motions have a vertical scale given by δ, and the overall streamwise extent is given by $\eta\delta$, then $\eta = 1.1$ because the structure angle is about 50° for most of the upstream layer (see Figure 8.36). Furthermore, if we assume that downstream of the curvature the vertical scale is still given by the local boundary layer thickness and the streamwise extent is reduced by the local decrease in mean velocity, we would expect the structure angle to initially decrease by about 15°, as Donovan et al. found. If the structure is assumed to be a large-scale horseshoe vortex, and its circulation remains approximately constant, the initial rotation toward the wall will bring the horseshoe closer to its image vortex. According to Biot-Savart (assuming the gradients of the sound speed are not large in the outer 80% of the boundary layer), the effect of the image vortex is to tend to increase the angle of inclination, restoring it to its original value. These arguments do not explain why the structure angle tends to over-recover in the region downstream of the surface curvature.

In incompressible flows, some investigators (for example, Head and Bandyopadhyay, 1981) have discussed the possibility that the angles of inclination of hairpin vortices and bulge interfaces are related to the principal axis of the rate-of-strain tensor. In any zero pressure gradient boundary layer the inclination of the principal axis is very close to 45°. Donovan (1989) used a rotational method of characteristics to calculate the variation of the rate-of-strain tensor on Model IV. This procedure is valid for rapidly distorted flows where the turbulence has a negligible effect on the mean flow, a condition satisfied reasonably well by the flow for $x = 5.4\delta_0$. The smallest inclination of the principal axis was calculated to be about 40° before relaxing back to its upstream value, which to some extent reflects the behavior observed in the schlieren visualization. However, the causal relation between the principal axis of the mean strain rate and the inclination of the organized motions remains unclear.

Further information on the spatial extent of the outer layer structures was found using two vertically separated wires. By shifting the peak in the space-time correlations along a line corresponding to the mean structure angle, the qualitative picture shown in Figure 9.10 was obtained. This view may be compared to the similar view shown in Figure 8.39 ($\xi_y/\delta = 0.09$) for the undisturbed boundary layer. Both plots illustrate the spatial nature of the organized motions in side view when the horizontal axis is taken as the streamwise direction (using Taylor's hypothesis). The increase in structure angle at $x = 5.4\delta_0$ is evident, as well as the stretched length of the large scales, and the increase in the streamwise correlation length scale. This last observation is somewhat unexpected, but it may indicate that the compression enhances the correlated motions more than the uncorrelated parts.

Finally, by conditionally sampling the fluctuating streamwise and normal velocity signals simultaneously, an approximate view of the average large-scale

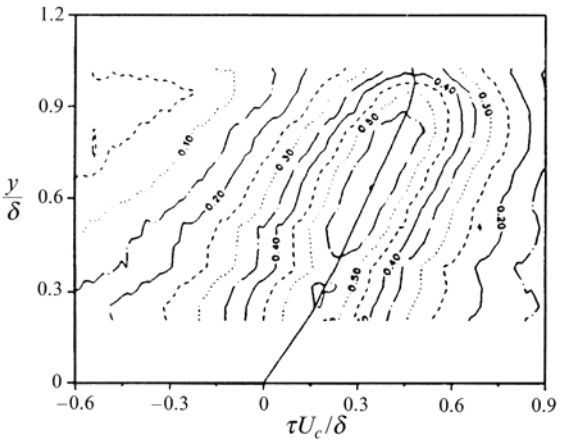

Figure 9.10. Model IV Curved wall impulse experiment (see Table 9.2): correlation contours from hot-wires separated by 0.1δ in a direction normal to the wall at a position $x = 5.4\delta_0$ downstream of the start of curvature. This view may be compared with the corresponding view of the undisturbed boundary layer shown in Figure 8.39a. (From Donovan et al. (1994). Copyright 1994, Cambridge University Press. Reprinted with permission.)

motion can be derived. The VITA technique developed by Blackwelder and Kaplan (1976) was used to identify positive mass flux fronts, and the ensemble averaged flowfields around these fronts are shown in Figure 9.11 (the corresponding view for the upstream boundary layer was shown in Figure 8.40). The clockwise rotation within the large scales is clearly seen, as is the counterclockwise rotation in the region behind the mass flux front (that is, the back of the large-scale structure), and the presence of a stagnation point on the mass flux front itself. Downstream, the rotating motion of the fluid downstream of the back of the structure is not as well defined, and the upward velocity just in front of the back is much larger than in the upstream boundary layer. Throughout the flow, the steeper angle of most of the velocity vectors reflects the amplification of the normal velocity component by the perturbation.

Having described the results of one particular study in some detail, we can now summarize the overall behavior of the curved-wall flows listed in Tables 9.1 and 9.2. In all cases, the Reynolds stresses were found to be amplified downstream of the curvature. The level of amplification depended on the pressure gradient, and the largest amplification was observed in the compression corner flows where the strongest pressure gradients are found. That is, the more rapid the perturbation, the greater the amplification of the turbulence. Changes in the turbulence structure seem to depend therefore on the strength and the rate of application of the perturbation. For the weakest distortion ($R_c/\delta_\circ = 50$) no

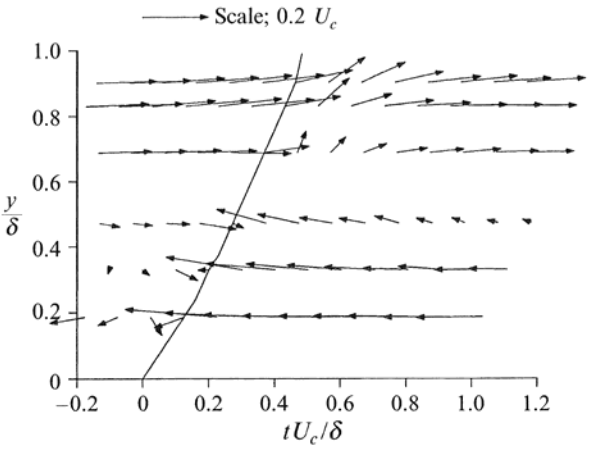

Figure 9.11. Model IV Curved wall impulse experiment (see Table 9.2): average flowfield in the region of instantaneous positive mass flux gradient as seen in a reference frame moving at the convection velocity of the large-scale motions at $x = 5.4\delta_0$ downstream of the start of curvature. This view may be compared with the corresponding view of the undisturbed boundary layer shown in Figure 8.40. (From Donovan et al. (1994). Copyright 1994, Cambridge University Press. Reprinted with permission.)

changes in the structure were observed indicating that the boundary layer was near equilibrium throughout the distortion. For the more rapid distortions at 8° of turning ($R_c/\delta_\circ = 0$ and 10), weak changes in the turbulence structure parameters were observed.

In compression ramp interactions, Debiève (1983); Ardonceau (1984); Kuntz et al. (1987); Smits and Muck (1987), and Selig et al. (1989) found that the amplification of the turbulence increased with the ramp angle, that is, the shock strength. Ardonceau observed that the Reynolds shear stress responded more quickly to the distortions than the streamwise and normal components. For the flow downstream of the interaction, he suggested that the turbulent motions begin to lose their coherence before beginning to dissipate energy. In the experiments by Smits and Muck, the turning of the flow was the same as the turning in the curved wall studies of Models I, II, and IV. A greater amplification of the streamwise Reynolds stress was found when a shock wave was present, but the same trend was not observed in the shear stress, and in the case of an 8° ramp, the boundary layer response was the same with or without the shock wave. As the strength of the perturbation increased from 8° to 16°, the shock wave began to have an influence. For instance, Smits and Muck (1987) found a change in the anisotropy ratio downstream of a 16° shock wave interaction, but as we saw above, there is little change in the anisotropy ratio

in the flow over a 16° curved wall. Initially, it was believed that there was a coupling between the unsteady shock motion and the turbulence which served to amplify the turbulence intensity without directly affecting the shear stress. However, the measurements made by Selig *et al.* using conditional sampling demonstrated that the shock motion had little effect on the amplification of the turbulence intensity. In contrast, there appears to be a strong link between the large-scale motions in the incoming boundary layer and the unsteady motion of the shock wave, at least for attached flows (Gramann and Dolling, 1992; Cogne et al., 1993). Compression ramp interactions are dicussed in more detail in Section 10.2.

9.4.2 Reflected Wave Flows

To study the effects of adverse pressure gradients in the boundary layer with a minimum amount of distortion due to curvature, the pressure gradient can be imposed through a system of reflected waves (see Figure 9.1). The response of the turbulence to this type of perturbation was studied by Kussoy et al. (1978) at Mach 2.3, and by Fernando and Smits (1990) and Smith and Smits (1994) at Mach 2.9. In the first two studies, the pressure rise was approximately equal (in other words, the impulse due to pressure changes was nearly the same), but the pressure gradient occurred over a shorter distance in the first ($1.5\delta_\circ$) than in the second ($7\delta_\circ$). The strength of the perturbation in the third study was stronger and more rapid (see Tables 9.1 and 9.2), but in all three flows the Reynolds stresses were strongly amplified. Fernando and Smits found that the turbulence stress ratios varied less than the stresses themselves, indicating that the structure of the turbulence remained largely unchanged in their flow. This conclusion was confirmed by measurements of the space-time correlations which were essentially unchanged from the correlations in the undisturbed boundary layer. These observations were not unexpected because the distortion was comparatively weak and relatively slow. However, a frequency shift was observed in the energy spectra of the turbulence, suggesting an increase in the turbulence length scale. This change was more obvious in the velocity profiles that exhibited the dip below the logarithmic law characteristic of subsonic flows experiencing concave streamline curvature, and it may indicate the effect of the small but perhaps significant amount of streamline curvature found in the reflected wave flows of Fernando and Smits (and Smith and Smits). Of course, if we assume that the concept of an impulsive perturbation holds in this case, $I_\theta = 0$ because the incoming and outgoing flow directions are the same. However, the region over which the pressure rises is rather long (of the order of the large-eddy turnover distance $\approx 10\delta_0$) and the appearance of curvature-related effects may signal the limit of the impulse approximation. In that case, the approximation will also break down for the flow over Model II where $R_c = 50\delta_0$.

The pressure gradients in the flat plate studies by Fernando and Smits and Smith and Smits were designed to match the pressure gradients on curved walls with 8° and 16° of turning, respectively, where the nondimensional radius of curvature was $R_c/\delta_\circ = 50$, and 10 to 12 (Jayaram, et al., 1987; Donovan et al., 1994). For 8° of turning, the presence of curvature was found to enhance the increase in the streamwise Reynolds stress, and although it did not change the total amplification in the shear stress, the rate at which the shear stress changed was faster for the flow with curvature. For 16° of turning, a similar behavior in the streamwise stress was observed. Structural changes in the turbulence appear to be directly linked to the presence of substantial amounts of streamline curvature and the rate at which the perturbation is applied. For example, changes in the turbulence structure were noted by Jayaram *et al.* on an 8° curved wall, but Fernando and Smits found no structural changes in a flow with the same adverse pressure gradient on a flat wall. The more rapid the distortion, the greater the change observed in the turbulence structure, suggesting that these changes may be described using the total strain rate and the slower distortions should be described using local strain rates.

9.4.3 Taylor-Görtler Vortices

In subsonic turbulent boundary layers, concave curvature in the streamwise direction introduces longitudinal vortices according to a mechanism similar to that responsible for producing Taylor-Görtler vortices in laminar flows (Tani, 1962). These longitudinal roll-cells tend to be spaced in the spanwise direction with a reasonably regular spacing of one to two boundary layer thicknesses, and once established they are very stable in location and strength. Although their tangential velocity is at least an order of magnitude smaller than the freestream velocity, they can have strong effects on the turbulence. For example, Smits et al. (1979b) found that downstream of an impulse in concave curvature the shear stress differed by up to a factor of two in the spanwise direction, where the low level was found in the region where the secondary flow was towards the wall (that is, a "crest" in the spanwise C_f distribution), and the high level was found where it was away from the wall (a "trough" in the C_f distribution). The corresponding C_f values differed by about 20% from the crest to the trough.

In some flows with concave curvature, Taylor-Görtler vortices have not been observed. In the study by Smits et al. (1979a), where the flow developed on a cylindrical forebody before diverging on a cone, the boundary layer experienced the combined effects of concave curvature and divergence, and steady vortices were not detected. It is possible that the roll-cells did not form at all because of a nonlinear interaction between concave curvature (which amplifies longitudinal vorticity) and divergence (which amplifies spanwise vorticity). It is also possible that unsteady vortices were formed, without a preferred spanwise position, or that the vortices originated intermittently at different spatial

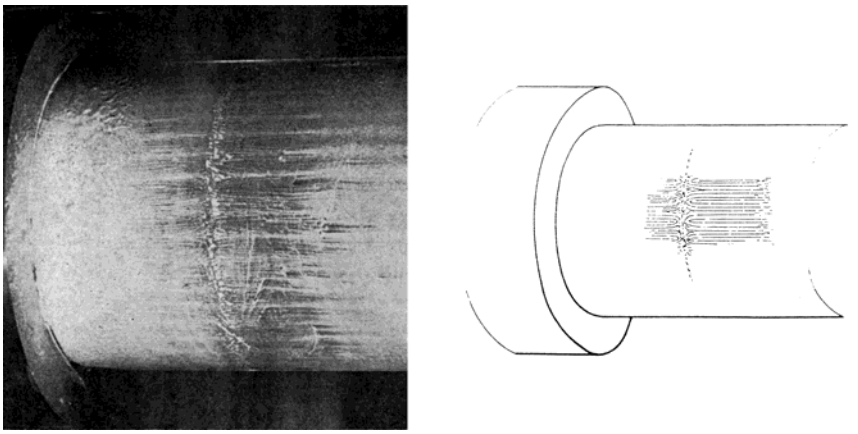

Figure 9.12. Reattachment flow patterns downstream of a backward-facing step on an axisymmetric body. Left: Roshko and Thomke (1966) at $M = 3.20$. Right: Shamroth and MacDonald (1970). (Copyright 1966, 1970, AIAA. Reprinted with permission.)

locations. The measurements were not designed to detect such unsteady motions, and so we can only speculate.

In separated supersonic flows, surface oil flow visualizations in the region of reattachment suggest that steady Taylor-Görtler vortices also occur in compressible flows (Roshko and Thomke, 1966; Shamroth and MacDonald, 1970). Visualizations of the separation and reattachment lines in compression corner flows similarly suggest the existence of longitudinal vortices, with a spanwise spacing similar to that seen in incompressible flows (see Figure 10.14). Selig et al. (1989) suggested that longitudinal vortices could be the cause for a bimodal pdf in the mass flux fluctuations downstream of a 24° compression corner, because they are an effective mechanism for sweeping low-momentum fluid up from the near-wall regions. However, no evidence of steady Taylor-Görtler-like vortices was found in any of the attached flows listed in Tables 9.1 to 9.3. It is again possible that nonlinear effects may have prevented their appearance. For example, it was suggested by Green (see Bradshaw (1973) and Smits et al. (1979a)) that bulk compression acts in many respects similarly to lateral divergence. If it is true that Taylor-Görtler vortices do not form in subsonic boundary layer flows when concave curvature and divergence act together, then by extension it may not be surprising that when concave curvature and dilatation occur together, Taylor-Görtler vortices may also be absent.

A criterion for the onset of steady Taylor-Görtler vortices in compressible flows with concave curvature may be developed as follows. According to Schlichting (1979), Taylor-Görtler vortices first appear in a laminar, incom-

pressible boundary layer on a concavely curved wall when the characteristic parameter, the Görtler number G_T,

$$G_T = \frac{U_e \theta}{\nu} \sqrt{\frac{\theta}{R}},$$

exceeds a certain value. Stability calculations give the neutral curve as a function of Görtler number and nondimensional wavelength.

Tani (1962) suggested that this criterion could be applied to turbulent flows by using the same characteristic length scale θ and simply replacing the molecular viscosity by the eddy viscosity. If we assume that the eddy viscosity in the outer layer is given by

$$\nu_t = 0.018 U_e \delta^* \tag{9.7}$$

(Clauser, 1956), then

$$G_T = \frac{\theta}{0.018 \delta^*} \sqrt{\frac{\theta}{R}}, \tag{9.8}$$

which indicates that the appearance of longitudinal vortices in a turbulent flow is a weak function of Reynolds number because the shape factor varies somewhat with Reynolds number (see Figure 7.18). Bradshaw (1973) pointed out that the direct use of the neutral curve for the Blasius profile is not realistic, but Tani's measurements agreed reasonably well with this simple proposal. Note that the Görtler number for turbulent flow can also be written as

$$G_T = \frac{(\theta/\delta)^{1.5}}{0.018\,(\delta^*/\delta)} \sqrt{\frac{\delta}{R}}. \tag{9.9}$$

We can extend the analysis to compressible flow by assuming that the length scale remains unchanged and that the eddy viscosity is still given by Equation 9.7. In other words, the Görtler number for a compressible turbulent flow is given by Equation 9.9, where we recognize that the momentum and displacement thicknesses are a strong function of Mach number (see Equations 7.63 to 7.65). Some typical values may then be found for the lower limit on δ/R where we expect to find longitudinal vortices, corresponding to the neutral curve calculated by Smith (1955) and a fixed wavelength of 2δ. For the present purpose, we ignore the weak dependence of the Görtler number on Reynolds number. As the freestream Mach number increases from 0, to 1, to 3, to 5, we find $(\delta/R)_s$ increases from 0.003, to 0.005, to 0.03, to 0.11. That is, the analysis predicts a strong increase in stability with increasing Mach number. Most of the Mach 3 curved wall cases listed in Tables 9.1 and 9.2 exceed this rather crude criterion, but not by very much, and it seems likely that the absence of Taylor-Görtler vortices in these attached flows is at least partly due to the stabilizing influence of Mach number. For the separated flows, the distortion of the mean velocity profile will influence the stability calculation, and the appearance of an inflection point will obviously make the layer more unstable in every sense.

	Group Three			
	Dussauge and Gaviglio	Smith and Smits (1991)	Johnson	
	Expansion corner	Expansion corner	Expansion corner	Curved wall
M_e	1.76	2.9	2.5	2.5
R_c	0	0	0	$15\delta_\circ$
L_i	$0-1\delta_\circ$	$0-6\delta_\circ$	$0-3\delta_\circ$	$3\delta_\circ$
I_θ	–0.21	–0.35	–0.26	–0.26
I_p	–0.50	–1.02	–0.78	–0.78
$\overline{\rho u'^2}$	–78%	–85%	–72%	–72%
$-\overline{\rho u'v'}$	—	—	—	—
θ	-12°	-20°	-15°	-15°

Table 9.3. Impulses in favorable pressure gradient cases, Group Three. (Adapted from Smith and Smits (1994), with the authors' permission.)

9.5 Favorable Pressure Gradients

When the sense of the curvature is convex, the effect on the boundary layer turbulence is stabilizing, and the wall friction, heat transfer, and the Reynolds stresses are expected to decrease. If the flow is supersonic, then the convex curvature will generally be accompanied by a favorable pressure gradient that will enhance the stabilizing effect. With the exception of Morkovin (1955) and Johnson (1993), all of the studies in supersonic flows of convex curvature effects have been made in expansion corner flows ($R_c = 0$) where the curvature and pressure gradient are stabilizing (see Figure 9.1). Turbulence measurements in expansion corners by Dussauge and Gaviglio (1987) at Mach 1.76, and Smith and Smits (1991a) at Mach 2.9, show a substantial reduction in the streamwise Reynolds stress downstream of the corner (see Group Three, Table 9.3).

Some results of the experiments by Dussauge and Gaviglio (1987) and Smith and Smits (1991a) were discussed in Chapter 4 in the context of RDA. The strong stabilizing influence of expansion can be seen in Figure 4.3. The good agreement between the measured and calculated stress profiles suggests that the evolution of the mean flowfield was essentially independent of the turbulence field, and that the turbulence field evolved in direct response to the changes in the mean velocity gradients. Smith and Smits also found that 90% of the reduction in the streamwise stress was due to the effect of bulk dilatation, that is, the change in mean density. Curvature appeared to play a very small role even though the flow was turned through a relatively large angle of 20°.

If the favorable pressure gradient is strong enough, it seems possible that the boundary layer will *relaminarize*, as in subsonic flow, although it might be more accurate to say that pressure forces can become large enough to dominate the nearly frozen Reynolds stresses, and over a large part of the boundary layer the Reynolds stresses then have little influence on the mean flow (see Narasimha and Sreenivasan (1979)). That is, the turbulent fluctuations may not be absent, but they no longer contribute appreciably to the momentum or energy transport. Johnson (1993) made turbulence measurements downstream of a convex wall to study the possibilities for relaminarization in supersonic flow. In his experiments, the nondimensional radius of curvature of the wall $R_c/\delta_\circ$ was varied from 0 to 15 and the overall turning angle remained at 15° (see Table 9.3). The incoming flow was recovering from the distortion presented by a 10° concavely curved wall placed some distance upstream, but the incoming flow was the same for each case so that the effect of varying R_c could still be determined to some degree. Johnson found a strong suppression of the longitudinal velocity fluctuations with the suppression being remarkably similar in all four cases, suggesting that in his flow the dominating influence was the overall pressure rise (or, equivalently, the total turning angle) rather than the strength of the pressure gradient. Here again, the distortions were rapid, with the slowest distortion occurring over $4\delta_\circ$.

Unfortunately, the limitations of wind tunnel testing usually prevent the study of the full relaxation behavior in expansion corner flows, simply because it is difficult to follow the flow far downstream in a wind tunnel of fixed geometry. For example, the measurement region downstream of the expansion corner in the study by Dussauge and Gaviglio was $11\delta_\circ$ long, and in the experiment by Smith and Smits it was only just over $5\delta_\circ$ in length. Because these flows have large and rapid decreases in pressure, it is clear that only the initial response of the boundary layer to the pressure distortion could be observed before the end of the measurement section was reached.

9.6 Successive Distortions

Studies of boundary layers experiencing successive distortions can give new insight into the relaxation of a distorted boundary layer. In the investigations by Zheltovodov et al. (1990) and Smith and Smits (1993b), the boundary layer experienced successive impulses in curvature of opposite sign such that the direction of the flow upstream and downstream of the curved wall regions was the same (see Figure 9.13, and Group Four, Table 9.4). In the study by Zheltovodov *et al.* the flow passed over a 25° forward-facing step, and a remarkable relaxation behavior was found in the streamwise turbulence intensity. After the second impulse, that is, on the flat plate downstream of the step, the turbulence intensity levels initially returned to the upstream levels, but farther downstream the stress levels in the middle of the boundary layer continued to

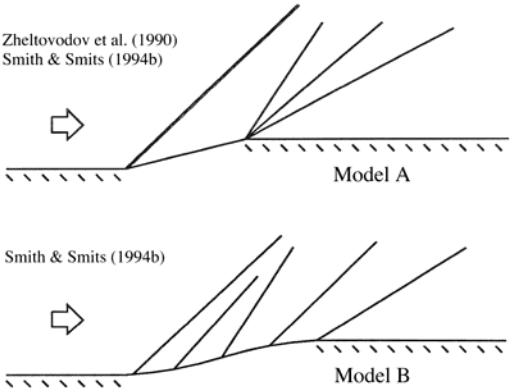

Figure 9.13. Successive distortion flow geometries. (From Smith and Smits (1994), with authors' permission.)

decrease. Unfortunately, the limited spatial resolution of the probes in this experiment makes it difficult to gauge the response quantitatively.

In the study by Smith (1993) and Smith and Smits (1993b), two different flows over forward-facing ramps were studied, each with 20° of turning. In the first case (Model A), the turning was produced by sharp corners as in the Zheltovodov flow, but in the second case (Model B) the turning was produced by curved walls. As the flow passed over these steps, the boundary layer was

	Group Four					
	Zheltovodov *et al.*		Smith and Smits (1993b)			
	Compression corner	Expansion corner	Compression corner A	Expansion corner A	Curved compression B	Curved expansion B
M_e	2.9	2.9	2.9	2.9	2.9	2.9
R_c	0	0	0	0	$15\delta_\circ$	$15\delta_\circ$
L_i	$0-10\delta_\circ$	—	$0-6.5\delta_\circ$	—	$0-12\delta_\circ$	—
I_θ	+0.44	–0.44	+0.35	–0.35	+0.35	–0.35
I_p	+1.1	–1.1	+0.92	–0.92	+0.92	–0.92
θ	+25°	−25°	+20°	−20°	+20°	−20°

Table 9.4. Impulses in successive distortion cases, Group Four. Here, δ_0 is the boundary layer thickness of the flow just upstream of the start of the disturbance. (Adapted from Smith and Smits (1994), with the authors' permission.)

subjected first to an adverse pressure gradient combined with concave streamline curvature and bulk compression, followed by a favorable pressure gradient combined with convex streamline curvature and bulk dilatation. On Model A, the initial turning at the compression corner resulted in a shock wave-boundary layer interaction, and the subsequent expansion occurred through a centered expansion fan. On Model B, the concave and convex streamline-curvatures were distributed over longer streamwise distances than on Model A, and therefore the pressure gradients were less severe. In particular, the shock associated with the concave curvature did not form until well outside the boundary layer, and within the boundary layer the compression occurred through a compression fan rather than a shock wave-boundary layer interaction. On Models A and B, however, there was no net change in flow direction across the successive distortions and therefore the upstream and downstream freestream conditions were effectively the same except for a small shock loss on Model A.

The overall response corresponded closely to that seen by Zheltovodov. The streamwise Reynolds stress profiles first show a strong amplification downstream of the compression surface (a factor of 10 for Model A), followed by a large decrease just downstream of the expansion (see Figure 9.14: the large initial amplification downstream of the compression corner is not shown in this figure, only the relaxation behavior on the flat plate downstream of the expansion). In the profiles farther downstream, this region of reduced stress grows in size and the shape of the stress profile suggests the presence of an internal layer. There is no detectable relaxation towards a self-preserving state, in agreement with the results obtained by Johnson (1993) in a similar flow configuration at Mach 2.45.

Over most of the boundary layer immediately downstream of the distortions, the shear stress appeared to change sign. A subsequent recovery of the shear stress was observed in the lower 60% of the boundary layer, but in the remaining part of the layer the shear stress remained at very low values.

Despite the differences between Models A and B—different distortion lengths, and the presence of a shock wave in the first case compared to an isentropic compression in the second case—the general response of the boundary layer was very similar. In both cases, the distortions occurred rapidly, suggesting that the perturbation rate was not important and that the distortion can be described qualitatively using the appropriate impulse levels (see Table 9.4). However, it is not suggested that the overall response of the boundary layer can be described as a linear sum of the two successive impulses: this would indicate that the overall perturbation is zero (assuming that α_o is the same for all perturbations). Remarkably, the stress levels at the exit from the second perturbation were almost unchanged from their upstream values, but farther downstream the undershoot in the turbulence levels suggests a second-order response of an underdamped system. The turbulence is strongly out of equi-

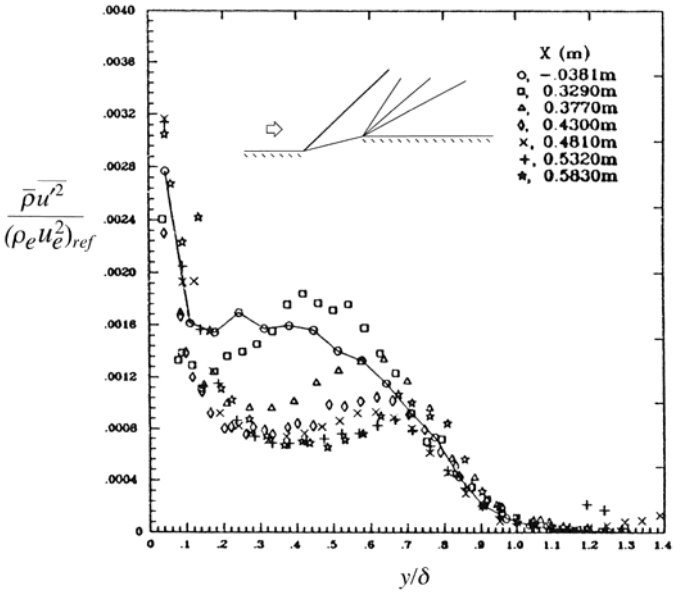

Figure 9.14. Longitudinal Reynolds stress profiles for the flow over a compression corner followed by an expansion corner (Model A in Table 9.4). The distance x is measured from the start of the compression ramp, and the ramp is 149 mm long (about $4\delta_0$). Only the profiles upstream of the compression corner and downstream of the expansion corner are shown. (From Smith and Smits (1993b). Reprinted with permission of Kluwer Academic Publishers.)

librium, and the production, dissipation, and anisotropy are out of balance.

An RDA Reynolds stress calculation similar to the ones discussed in Chapter 4 was used to help understand the response of the turbulence over Model A. In the expansion, estimates of the production terms in the Reynolds stress equations revealed that negative production can occur and this may be largely responsible for the change of sign in the shear stress, and the complex nature of the relaxation process. Not unexpectedly, this indicates that the conventional eddy viscosity approaches to turbulence modeling have severe limitations for these strongly perturbed flows. A number of factors combined to inhibit the turbulence production mechanisms in the relaxing boundary layer. These factors included a fuller velocity profile, a decay of the streamwise stress, and a collapse of the shear stress in the expansion fan. As a result, a long recovery period may be expected. Qualitatively, it appeared that the streamline curvature in the second impulse combined with the amplified streamwise Reynolds stress on the ramp to exaggerate the stabilizing effect of the expansion corner. In the flows over a simple expansion corner (Group Three), the dominant effect

is that of bulk dilatation, whereas in the flows where a compression precedes the expansion (Group Four), curvature plays a more important role within the expansion.

The shape of the streamwise Reynolds stress profiles suggested three zones of response: a recovery zone near the wall where the turbulence recovers quickly from the perturbations; a zone of strong response in the middle of the boundary layer where the turbulence levels eventually undershoot the equilibrium distributions sharply in response to the combined effects of the perturbations (second-order response); and a zone of advection near the edge of the boundary layer where the turbulence appears to be unchanged by the integrated effects of the perturbations (linear response). This latter observation supports the conclusion of Selig and Smits (1991) that at this Mach number shock wave oscillation does not contribute appreciably to turbulence amplification in shock wave-boundary layer interactions.

9.7 Summary

For the cases with both adverse pressure gradients and concave streamline curvature, the changes in the turbulence structure (as inferred from the trends in the Reynolds shear stress) appear to be strongly tied to the magnitude of the impulses due to curvature. If the radius of curvature of the turning is small enough, a shock wave forms in the boundary layer, and the streamwise stress increases with increasing shock strength. If the pressure gradients are not strong enough to separate the layer, the shock wave seems to exert no additional effect on the shear stress over and above the changes that could be attributed to streamline curvature (or the equivalent compression).

In the flows with rapid, favorable pressure gradients and convex curvature, it appears that the initial response of the boundary layer turbulence is dominated by the effects of the bulk dilatation, and the effects of convex curvature are always small. That is, the turbulence initially changes in response to the pressure gradient as would be expected using the conservation of circulation (we can largely ignore the effects of compressibility on relative motions because the Mach number gradients in the outer layer are usually small). The effect of bulk dilatation on the turbulence (expressed as an impulse) is not a strong function of the pressure gradient, indicating that it is the overall pressure change which is important. In contrast, the relaxation behavior appeared to be largely controlled by the streamline curvature history. However, these observations were made in a boundary layer downstream of two successive distortions where the effect of curvature appeared to be greatly augmented by the amplification of the stresses downstream of the first distortion. The relaxation behavior is similar to the second-order response seen by Smits et al. (1979b) in an incompressible turbulent boundary layer downstream of an impulse of curvature. In addition, the behavior of the shear stress was similar to that ob-

served by So and Mellor (1973) in a boundary layer developing over a surface with prolonged surface curvature in incompressible flow. What has not been explained is the observation that in the outermost part of the boundary layer there was no change in the streamwise stress from its undisturbed profile even though it is in this region where the principal strain rate $\partial U/\partial y$ is small and the effects of the extra strain rates should be felt most strongly.

Overall, it appears that the boundary layer response to curvature in a supersonic flow is similar to the response in subsonic flow, even to the appearance of a dip below the log law in the mean velocity profile as a response to any significant amount of concave streamline curvature. More specifically, in the case of a single impulse of curvature, we expect to observe the same counter-intuitive trends in the Reynolds stress behavior as observed by Smits *et al.* in subsonic flow, where a stabilizing distortion (an impulse in convex curvature) caused an increase in turbulence activity far downstream and a destabilizing distortion (an impulse in concave curvature) caused a decrease.

Compressibility effects on the turbulence appear to be small, at least at supersonic Mach numbers. In flows with concave or convex streamline curvature, Reynolds stress calculations using subsonic turbulence models by Degani and Smits (1990) were found to give reasonable predictions of Reynolds stress behavior, at least for distortions where the boundary layer did not depart too far from equilibrium. For these flows, the limitations of the calculation are probably due to the turbulence modeling, rather than any specific influence of compressibility, and the observations tend to support the turbulence structure similarity suggested by Morkovin's hypothesis. For strong distortions, our predictive capability is confined to the initial response where linear theories such as RDA become useful. This situation should improve considerably with the application of DNS to this class of problems, bearing in mind that the relaxation behavior is typically slow and DNS studies will require large computational domains. No results are currently available.

Chapter 10

Shock Wave-Boundary Layer Interactions

10.1 Introduction

Shock-turbulence interactions are a common occurrence in supersonic flow because compression and flow deflection are almost always accompanied by the formation of a shock. The characteristics of the interaction depend on the Mach number, the nature of the incoming flow, the shock angle, the source of the shock, and the flow geometry. The shock may interact with freestream turbulence (Figure 1.14), with a free shear layer (Figure 1.13), or with a boundary layer (Figure 10.1). The earliest experiments studied transonic interactions, to make possible flight at supersonic speeds (Liepmann, 1946; Ackeret et al., 1946; Liepmann et al., 1951). Once the sound barrier was broken, attention shifted to supersonic and hypersonic interactions, and to date a large number of experiments have been performed. Green (1970); Stanewski (1973); Sirieix (1975); Adamson and Messiter (1980); Délery (1985), and Viswanath (1988) give detailed surveys of interactions which are two-dimensional in the mean, and Green (1970); Korkegi (1971); Peake and Tobak (1980); Settles and Dolling (1990); Dolling (1990); Settles and Dolling (1992), and Dolling (1993) provide a similarly comprehensive treatment for three-dimensional interactions. The most recent overview is given by Dolling (2001). Rather than attempting to summarize these reviews, we instead focus on some of the salient features of shock-wave turbulence interactions, with an emphasis on the underlying mechanisms controlling the scaling of the interaction, the possibility of flowfield separation, modifications to the incoming turbulence, and the unsteadiness of the shock. We also consider the contributions of DNS to our understanding of these flows.

Shock wave interactions are usually classified according to how the shock is generated. For shock wave-boundary layer interactions, the shock may impinge on the layer from an external source (an *incident shock interaction*), or

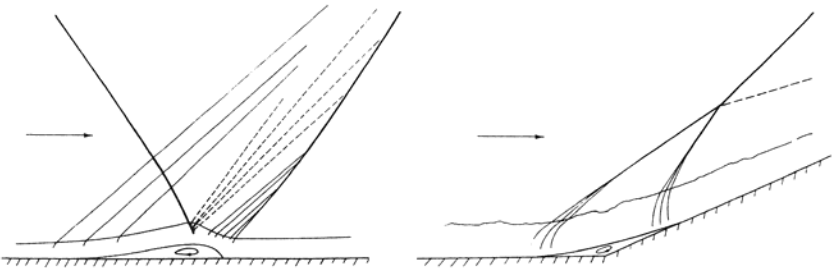

Figure 10.1. Typical interactions between shock waves and boundary layers: (a) incident oblique shock; (b) compression corner interaction. (From Adamson and Messiter (1980). Reproduced, with permission, from Annual Reviews, Inc.)

the shock may be generated by the same surface that generated the boundary layer (a compression surface or *compression corner interaction*). In most practical flows the interaction is three-dimensional, in that the shock sheet is swept at some angle to the boundary layer (which in itself may be two- or three-dimensional). Some of the more common configurations used to study shock wave-boundary layer interactions in the laboratory are illustrated in Figure 10.2. In three-dimensional interactions, the shock may be generated by a sharp fin placed at an angle of attack to the incoming flow, by a blunt fin where the leading edge has a finite radius of curvature, or by a cone or other protrusion rising from the surface. The fins may also be swept in the streamwise direction, so that the shock sheet in the freestream is angled in two directions with respect to the upstream flow. The geometries of these interactions have many degrees of freedom, and they can become quite complex. Further complexities are introduced when shocks interact with each other, as in crossing-shock interactions (see Figure 10.30). In addition, the Mach number plays a crucial role in governing the inviscid flowfield. For example, as the Mach number increases for a given shock generator configuration, the inviscid shock may change from being detached to being attached, producing large changes in the near field. Even if the inviscid shock is attached, the reduced Mach number within the boundary layer may cause detachment at some point, and this can change the entire flow pattern. Variations in Reynolds number will also play a role, but for fully-turbulent flows its influence appears to be relatively minor because most interactions are pressure dominated.

We start by considering shock-turbulence interactions far from walls, and shock wave-boundary layer interactions where the incoming boundary layers are two-dimensional in the mean. We first consider interactions with a boundary layer, even though they are more complicated, because the boundary conditions are better defined. Shock-turbulence interactions away from walls are

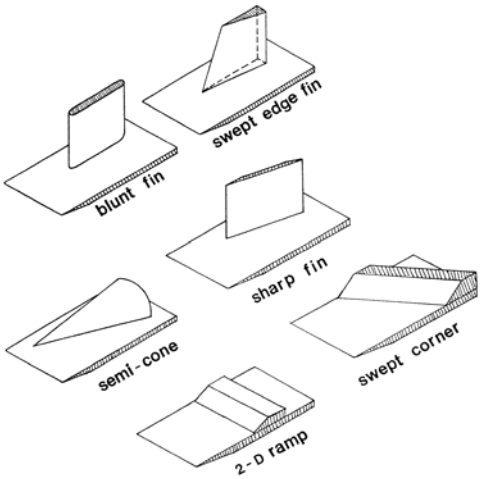

Figure 10.2. Examples of two- and three-dimensional shock wave-boundary layer interaction geometries studied in the laboratory. (From Tran (1987). Copyright 1987, AIAA. Reprinted with permission.)

considered in Section 10.3 in the context of RDA and other linear methods. Three-dimensional interactions are discussed in Section 10.6, and flows produced by multiple shock interactions are considered briefly in Section 10.7.

10.2 Compression Corner Interactions

Two-dimensional compression ramp flows have been extensively studied (see, for example, Settles et al. (1979), Debiève (1983), Ardonceau (1984), Smits and Muck (1987), Dolling and Murphy (1983), Selig et al. (1989), and Evans and Smits (1996)). The experiments at Mach 2.9 by Settles et al. and Smits and Muck are particularly revealing because they cover a wide range of turning angles, and detailed mean flow and turbulence data are available. As an illustration, we consider the 24° case (see Figure 10.3). In this flow, the incoming boundary layer is turbulent. The 24° corner produces a shock wave with an initial turning of about 10°. The rest of the deflection is produced more gradually downstream through a series of unsteady compression waves. The pressure rise is strong enough to separate the layer, and there is a considerable increase in the turbulence level across the interaction. The velocity fluctuations are amplified by passing through the shock, and vorticity is generated by interaction between entropy spots and the shock, in agreement with the second-order modes theory discussed in Chapter 4.

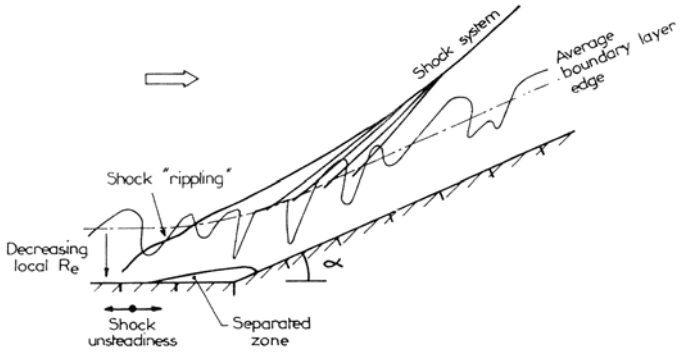

Figure 10.3. Sketch of the Mach 2.9, 24° compression ramp flow. (From Dussauge et al. (1989). Reprinted with permission of the authors and AGARD/NATO.)

The whole flow is unsteady: the shock moves over a significant distance, its motion is three-dimensional, and it occurs at low frequencies. It seems that the shock unsteadiness by itself makes a negligible contribution to the turbulence amplification (Selig and Smits, 1991). However, the separated zone is the source of large-scale fluctuations that are convected downstream, and these large-scale structures are probably related to low-frequency mechanisms. If the flow over the separated zone has features in common with mixing layers, we can expect this part of the flow to be very sensitive to compressibility effects, as free shear flows are. These aspects of the flow properties can be at the heart of couplings in the interaction, because they impose unsteady outlet conditions on the shock and can make it move. Because the incoming turbulence imposes an unsteady inlet condition, coupling with the incoming flow can also occur.

In terms of the extra strain rate terminology adopted in the previous chapter, the boundary layer experiences the combined effects of an adverse pressure gradient, concave streamline curvature, bulk compression, shock unsteadiness, and, if the pressure rise is strong enough, flow separation. The wall stress typically decreases sharply near the start of the interaction, but quickly recovers as the boundary layer thins in response to the overall compression, overshooting the upstream level before eventually recovering to its undisturbed level appropriate to the new Reynolds number on the ramp. At the same time, the turbulence levels increase dramatically through the interaction and appear to relax only slowly. The shear stress is generally affected less than the normal stresses, and as a result structure parameters, such as $a_1 \equiv -\overline{u'v'}/q^2$, are strongly distorted. Because the flow responds to the combined effects of many distortions, it is difficult to conclude from the available data what the specific contributions are of, say, concave streamline curvature and bulk compression.

It was apparent from Chapter 9 that when the flow is compressed rapidly on a curved wall with a short radius of curvature, the boundary layer turbulence is amplified to a significantly larger degree than when the compression occurs more slowly, regardless of the curvature of the surface.

In the following discussion, we try to infer the phenomena controlling the evolution of turbulence in shock wave-boundary layer interactions by reviewing these different elements.

10.2.1 Skin Friction

For the compression corner interaction shown in Figure 10.3, the mean pressure distributions begin to develop a *plateau* region for turning angles greater than 16° (see Figure 1.16), which indicates the onset of mean flow separation: the condition at 16° is called *incipient* separation (Settles et al., 1979). The terms *weak* and *strong* are sometimes used to describe attached and separated interactions, respectively, but these terms can mean different things in different contexts, and they are avoided here. The instantaneous flow will show signs of reversal at smaller turning angles, but at 16° the mean skin friction becomes zero at some point (see Figure 10.4). Both the 20° and 24° corners exhibit regions of separated flow, and the mean velocity profiles (Figure 10.5) display a region of reversed flow that agrees in location and extent with the skin-friction measurements shown in Figure 10.4. We noted earlier (Section 9.4) that adverse pressure gradients in a compressible boundary layer flow can cause the skin friction to increase because of the thinning of the layer. Here we see that if the pressure gradients are strong enough, the skin friction can decrease suddenly, and the flow can separate. Downstream, however, the overall increase in pressure can still cause the skin friction to rise above its usual value at the same Reynolds number, again because of the thinning of the layer.

10.2.2 Separation

An important aspect of shock wave-boundary layer interactions is the prediction of the onset of separation. However, we need to distinguish between mean flow separation, and instantaneous flow separation, especially for these inherently unsteady flows. There is evidence to indicate that the motion of the instantaneous separation point is closely tied to the instantaneous position of the shock (Gramann and Dolling, 1990; Beresh et al., 2002), so that the probability that the flow is separated at any position is similar to the probability that the shock is located upstream of that location. Mean flow separation can then be defined as the point where the flow is separated for 50% of the time Simpson (1981). This location is often found using surface flow visualization such as the kerosene-graphite technique (Settles and Teng, 1984), but it should be noted that the line of accumulation seen in the visualization is

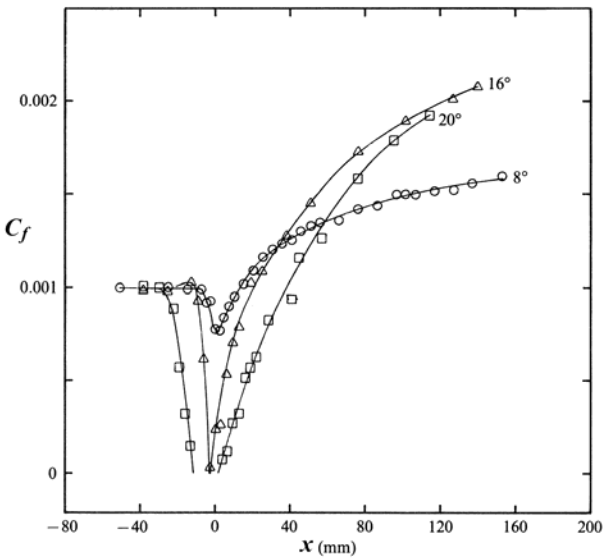

Figure 10.4. Distributions of C_f in compression corner interactions at Mach 2.9. The wall stress is nondimensionalized using "effective" edge conditions based on tunnel stagnation and local static pressures. (Figure adapted from Smits and Muck (1987), showing data by Settles et al. (1979) with permission from Cambridge University Press.)

located typically downstream of the line of separation, because the mixture accumulates by the action of the wall shear stress which is higher upstream of the instantaneous separation point than it is downstream, so that the flow visualization results are biased towards a position downstream of the mean separation location (Gramann and Dolling, 1990).

Chapman et al. (1957) used order-of-magnitude arguments to describe the similarity of the mean pressure distribution for separated flows. From an extensive series of experiments in laminar and turbulent flow, they argued that if the separated zone is large enough, the interaction in the vicinity of separation is local, independent of the underlying cause of separation. That is, the pressure rise to the point of separation, for example, should be similar for compression ramps and forward-facing steps, and it should scale with the Mach number and the incoming boundary layer characteristics. This *free-interaction* concept seems to hold well for laminar flows, but for turbulent flows the collapse of the data is not impressive, indicating a more significant dependence of the pressure distribution on the downstream boundary conditions. A mean flow concept such as free interaction theory does not take into account the unsteady motion of the shock. However, because the pressure distribution is

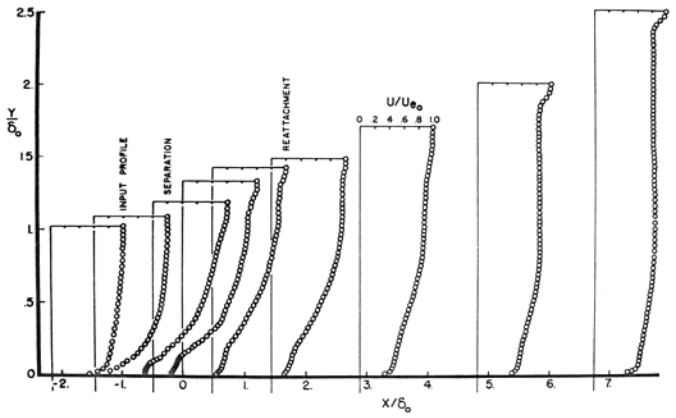

Figure 10.5. Development of the mean velocity profiles through a 24° compression corner interaction at Mach 2.9, with $Re_\theta = 72{,}100$. Distances and velocities normalized by upstream values. (Figure adapted from Settles et al. (1976). Copyright 1976, AIAA. Reprinted with permission.)

a result of the averaging due to the unsteady shock motion, the breakdown of this criterion can be taken as further evidence to indicate that the unsteadiness depends to some extent on the downstream flow conditions, at least for separated flows.

10.2.3 Upstream Influence

Figure 1.16 demonstrates that the wall pressure does not rise sharply in the region of separation. Instead, it rises gradually, levels off somewhat in the fully separated zone (the "pressure plateau"), and then starts to rise again in the region of reattachment, eventually reaching its maximum value some distance downstream of the mean reattachment line. The region of *upstream influence* is defined as the distance from the corner to the point where a straight line drawn to fit the slope of the initial pressure rise intersects the pressure level corresponding to the incoming boundary layer. Now, even in a perfectly steady (laminar) interaction, we expect there to be an upstream influence. The pressure rise generated by the flow deflection can propagate upstream through the subsonic part of the flow near the wall, causing the streamtubes below the sonic line to thicken, and producing a flow deflection upstream of the corner. However, the upstream propagation distance depends on the thickness of the subsonic layer (Schneider, 1974), and the sonic line rapidly approaches the wall as the Mach number increases. For the case shown in Figure 1.16, the sonic line for the incoming boundary layer is located at a distance less than 0.01δ

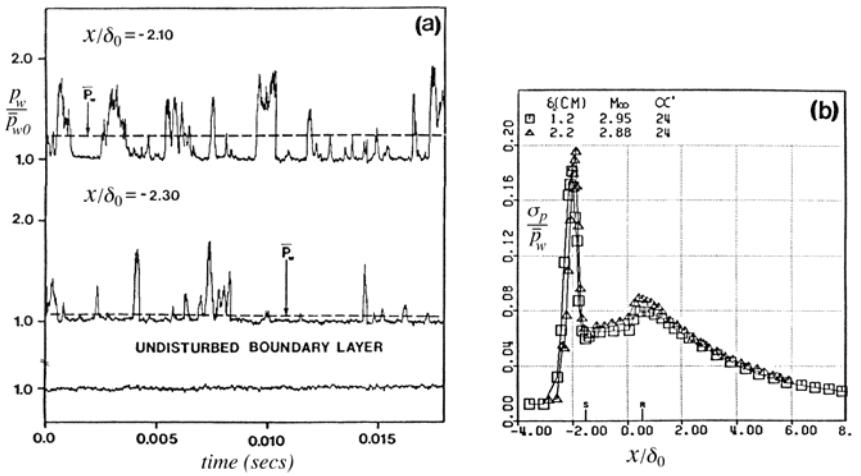

Figure 10.6. (a) Wall pressure time histories, and (b) *rms* wall pressure levels, in a 24° compression ramp at Mach 3. The lines of mean separation and reattachment are marked by S and R, respectively. The pressures were nondimensionalized using the upstream mean wall pressure, $\overline{p_{w0}}$; σ_p is the *rms* wall pressure level. (From Dolling and Murphy (1983). Copyright 1983, AIAA. Reprinted with permission.)

from the wall, and the steady upstream propagation distance is expected to be very short. Indeed, measurements of the instantaneous wall pressure show that the shock appears as a very rapid rise in the pressure signature: there is no sign of an instantaneous upstream propagation of pressure. However, the unsteady motion of the shock occurs over a much greater distance than the steady upstream propagation distance, and it is this unsteady motion that is primarily responsible for the upstream influence seen in the wall pressure distributions. The mechanism is illustrated in Figure 10.6. Note that the extent of the upstream influence is a strong function of Reynolds number (see Settles et al. (1976) and Bookey et al. (2005b)).

Within the region of shock motion, the wall pressure signal is intermittent, as seen in the figure. The values of pressure upstream and downstream of the shock are consistent with the pressure rise through the mean shock at its foot. The local mean wall pressure at a given location is simply the result of the pressure rise across the shock foot, weighted by the time the shock is upstream of that location.

10.2.4 Shock Motion

The strong shock oscillation that is seen in separated flows creates perturbations with new time and length scales. Such perturbations typically have a

large characteristic time, and contribute to the slow recovery of the boundary layer downstream of separation. If a shock is considered as an interface matching upstream and downstream flow condition, what are the possible sources of these low frequency motions? Here, we present some experimental observations, and discuss the properties of the motions.

The shadowgraphs of the instantaneous flowfields given in Figure 1.15 show qualitatively that the turbulent mixing appears to be considerably enhanced across the shock and the trend is more pronounced as the shock strength increases. The distortion of the shock front is also clearly shown. Visualizations using Rayleigh scattering in a 24° compression ramp flow at $M = 3$ confirmed that large-scale eddies are energetic enough to distort the shock (Smith et al., 1989). High-speed movies using filtered Rayleigh scattering reveal how the large-scale motions in the boundary layer interact with the shock, and how they are subsequently distorted by the compression (Figure 10.7). Furthermore, wall pressure signals obtained simultaneously using a spanwise row of transducers reveal that the shock has spanwise ripples, because some perturbations were not measured by all the transducers (Muck et al., 1988). The shock not only translates back and forth, but also experiences large-scale spanwise perturbations. These spanwise "wrinkles" are clearly visible in the flow visualizations shown in Figure 10.8. Similar three-dimensional distortions of the shock sheet were observed by Wu and Martin (2004) using DNS (see Figure 10.9).

A detailed description of the shock motion near the wall was obtained from wall pressure fluctuation measurements in compression ramp flows by Dolling and Murphy (1983); Muck et al. (1988); Bonnet (1988), and Selig et al. (1989) (for a review, see Dolling and Dussauge (1989)). Around the mean position of the shock, low-frequency wall pressure fluctuations of large amplitude are present. The spatial extent of these oscillations is a function of the strength of the shock, as shown in Figure 10.10. Muck et al. (1985) and Debiève and Lacharme (1985) used these observations to propose a reasonable approximation for the maximum *rms* value of the pressure fluctuation level across an oscillating shock from simple intermittency considerations: the maximum level is obtained when the intermittency coefficient is 0.5, and the maximum *rms* pressure p' is given by the simple relation $p'/\Delta p = 0.5$, where Δp is the mean pressure rise through the shock. This relation works well when the upstream and downstream levels of pressure fluctuations are not too high, and when the shock motion is not correlated with these fluctuations: in practice, it does not work well in strongly separated cases.

At Mach 2.9, incipient separation occurs at a ramp angle α of 16°. For lower values of α, the part of the flow affected by shock oscillation is limited and varies slowly with α, so in this regime it appears that the shock moves mainly under the action of incoming turbulence. However, there is a significant increase in the range of shock motion when $\alpha > 16°$, suggesting that the

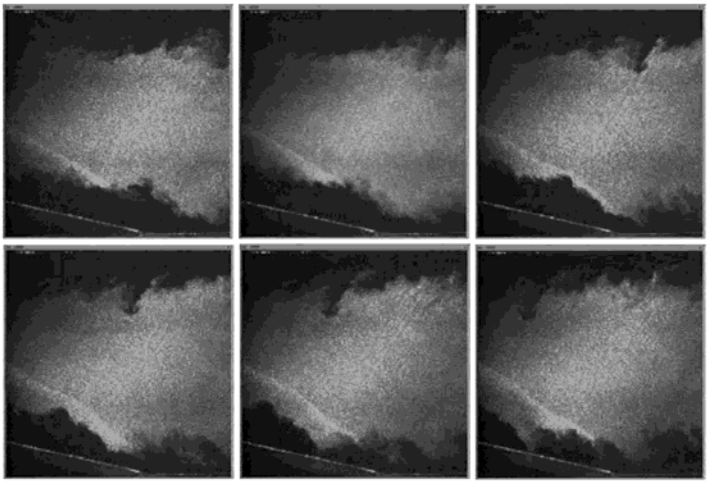

Figure 10.7. Successive frames from a movie using filtered Rayleigh scattering to visualize a 12° Mach 2.5 compression corner interaction. The time delay is 4 μs between images. The flow is from right to left. Note the undisturbed boundary layer on the upper wall of the tunnel. Plan view images are shown in Figure 10.8. (Adapted from Wu et al. (2000). Copyright 2000, AIAA. Reprinted with permission.)

wall pressure fluctuations are influenced by the unsteadiness of the separation bubble. The shock motion in these separated flows has an amplitude of the order of the boundary layer thickness, but its mean frequency is an order of magnitude below the characteristic frequency of the boundary layer u_e/δ. This indicates that the average value of the shock speed $\dot{x}$ is given by $\dot{x}/u_e \approx 0.1$.

Time-resolved flow visualization data and conditional sampling of wall pressure measurements indicate that the separation bubble undergoes a coherent, large-scale expansion and contraction (Kussoy et al., 1988; Gramann and Dolling, 1990; Thomas et al., 1994). Smaller scale distortion of the shock system by δ-scale boundary layer turbulence structures has also been identified using wall pressure measurements (Muck et al., 1985; Marshall, 1990) and planar laser visualization methods (Wu et al., 2000). Conditional averages of pressure fluctuations in the incoming boundary layer, based on shock motions downstream, have shown that δ-scale organized structures are responsible for small-scale motions of the separation shock foot, but no direct link has been found between the boundary layer structures and large-scale shock motions (Erengil and Dolling, 1991).

The dynamics of the shock motion is still a field of investigation, even in two-dimensional configurations. Important contributions to the stability of two-dimensional shock waves have been obtained, often applied to transonic flows and buffeting (see, for example, Chen et al. (1979), Bogar et al. (1983),

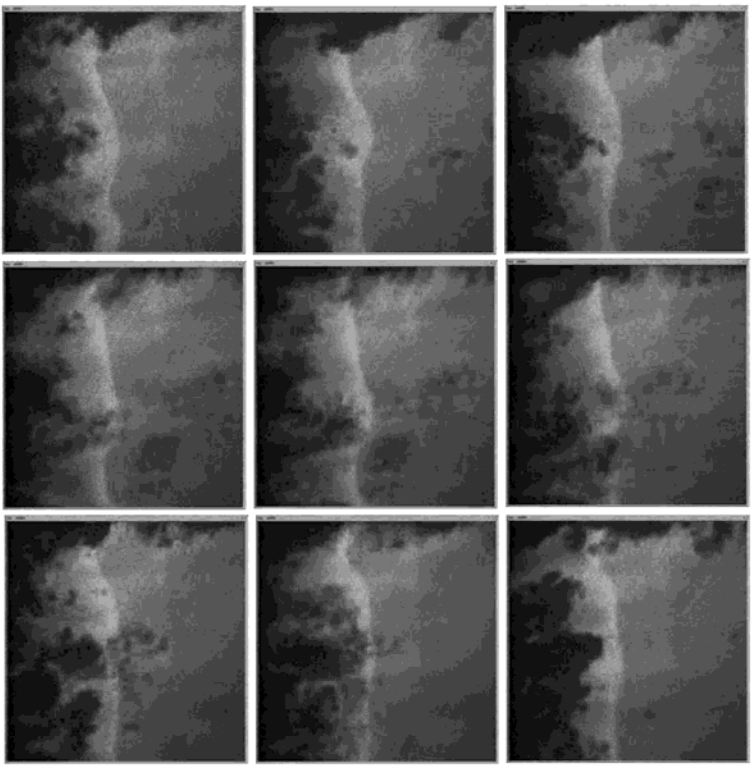

Figure 10.8. Successive frames from a movie using filtered Rayleigh scattering to visualize a 12° Mach 2.5 compression corner interaction (plan view, taken at a height close to the incoming boundary layer thickness). The time delay is 4 μs between images. The flow is from right to left. Note the side-wall boundary layer in the upper part of each frame. Side-view images shown in Figure 10.7. (Adapted from Wu et al. (2000). Copyright 2000, AIAA. Reprinted with permission.)

Culick and Rogers (1983), Robinet and Casalis (1999), and Robinet (1999, 2001)). The overall results are briefly summarized here. In general, if some singular behaviors such as shock "carbuncles" are not considered, shocks are stable, and weak shocks are more stable than strong shocks. It is often difficult to determine the transfer function of a shock wave. The response of a shock to a perturbation depends of course on the upstream conditions, but also, and perhaps more importantly, on some integral of the downstream flow. A shock acts generally as a lowpass filter, but depending on the nature of the flow downstream of the interaction, it may or may not be frequency selective (Chen et al., 1979; Bogar et al., 1983; Culick and Rogers, 1983; Robinet and Casalis, 1999). Another important property, one that can be derived from the

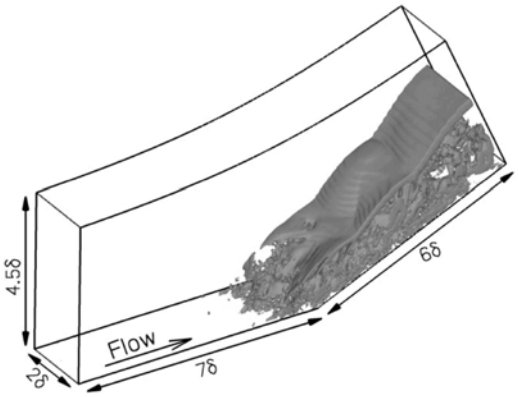

Figure 10.9. DNS of a 24° compression corner interaction, with an incoming boundary layer at $M = 2.9$, $Re_\theta = 2400$. Shock structure made visible by the isosurface $|\nabla p| = 3 \times 10^8$ N/m^3. (From Wu and Martin (2004), with the authors' permission.)

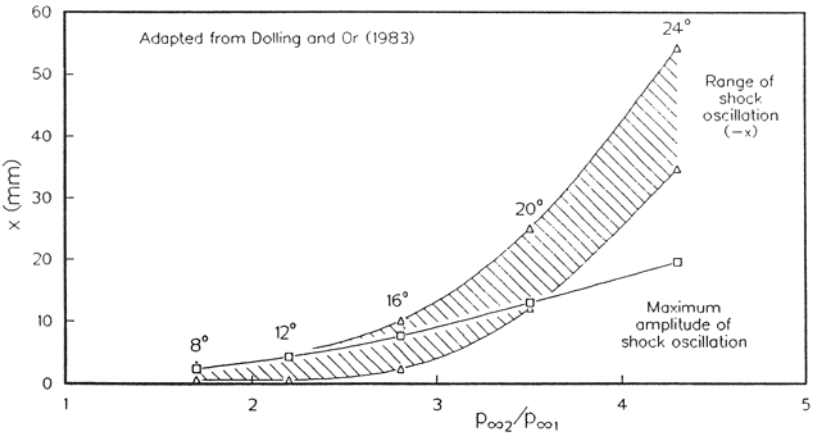

Figure 10.10. Range and amplitude of the shock oscillation for the Mach 2.9 compression corner interactions examined by Dolling and Murphy (1983). (From Selig et al. (1989). Copyright 1989, AIAA. Reprinted with permission.)

linear analysis of oblique shock waves, is that oblique shocks are stable, but the perturbations propagate along the shock sheet with the direction of the tangential velocity of the upstream flow (Robinet, 2001). This behavior is what is usually observed in shock wave-boundary layer interactions: the boundary layer perturbs the foot of the shock and the perturbations propagate along

the shock into the external flow, although the amplitude of the perturbation decreases with increasing distance from the shock stem. As a consequence, in the external flow far from the layer, and for weak shock intensities, the shock can often be considered as steady. This behavior is observed in experiments (Haddad (2005) for shock reflection experiments), and in LES simulations (Knight et al. (2003) for compression ramp flows or Garnier et al. (2002) for a shock reflection configuration). A precise description of the transfer function still remains to be determined.

The linear analysis quoted above shows that shocks can often be considered as lowpass filters. Therefore, it is not very surprising to find that their motion occurs predominantly at lower frequencies than the rest of the flow. A more detailed analysis was suggested by Plotkin (1975), who developed what is probably the only simple global model along these lines (for further details, see Poggie and Smits (2001)). The shock velocity $\dot{x}$ was taken to be the superposition of a random forcing function u and a restoring velocity that is proportional to the displacement x of the shock from its equilibrium position:

$$\dot{x} = u(t) - x/\tau_R. \tag{10.1}$$

Here t is time, and τ_R is a time constant specifying how rapidly the shock recovers from a perturbation. The variables x and u are defined to have zero mean. The random function u represents convection of the shock by velocity fluctuations in the boundary layer, and the restoring term x/τ_R represents the shock velocity induced by changes in the local conditions with displacement from the equilibrium shock location.

For a given history of velocity perturbations, Equation 10.1 can be solved to give the time history of shock position. Assuming that $x(0) = 0$, the solution can be set in the form

$$x = e^{-t/\tau_R} \int_0^t u(\xi) e^{\xi/\tau_R} \, d\xi. \tag{10.2}$$

Plotkin used Equation 10.2 to relate the statistical properties of the shock motion to those of the velocity fluctuations in the turbulent boundary layer, noting an analoguey to linearly damped Brownian motion. Assuming that the shock response is much slower than the turbulent fluctuations ($\tau_R \gg \tau_u$, where $\int_0^\infty R_u(t)dt$ is the integral time scale of the autocorrelation of the forcing function u), and that the pressure distribution induced by the oscillating shock can be approximated by the mean pressure distribution translated to the instantaneous shock position, Plotkin derived the following simplified form for the autocorrelations of the shock position and wall pressure fluctuations:

$$R_x(t) = R_p(t) = e^{-t/\tau_R}. \tag{10.3}$$

At this level of approximation, the autocorrelations are independent of the detailed statistical properties of the boundary layer turbulence, and the integral

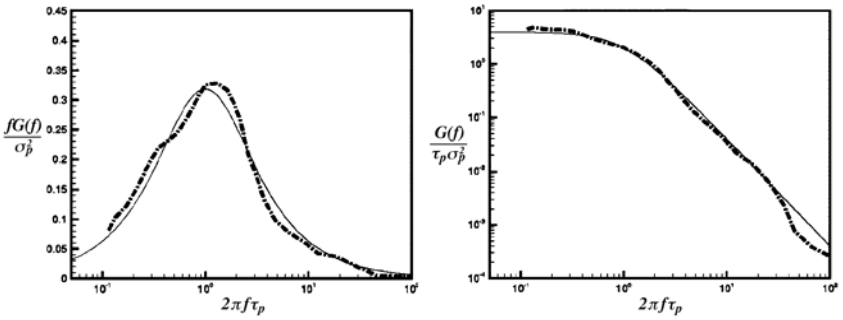

Figure 10.11. Blunt fin pressure fluctuation spectra at Mach 5: – - –, experiment (Gonsalez and Dolling, 1993); ——-, Equation 10.4. Left: Semi-log plot. Right: Log-log plot. (From Poggie and Smits (2005). Copyright 2005, AIP. Reprinted with permission.)

time scales of the shock position and wall pressure are the same as the time constant of the restoring velocity, $\tau_p = \tau_x = \tau_R$. The corresponding one-sided power spectra follow from the Fourier transform of the autocorrelations:

$$\frac{G_x(f)}{\overline{x^2}\tau_R} = \frac{G_p(f)}{\overline{p'^2}\tau_R} = \frac{4}{1 + (2\pi f\tau_R)^2}, \tag{10.4}$$

where f is the frequency, and the approximation requires that $f \ll 1/(2\pi\tau_u)$.

Plotkin's model requires two experimentally determined quantities as input: the integral time scale of the autocorrelation τ_p and the mean square pressure fluctuation $\sigma_p^2 = \overline{p'^2}$. Given these quantities, it predicts the form of the autocorrelation, Equation 10.3, and power spectrum, Equation 10.4, of the pressure fluctuations.

Poggie and Smits (2001) compared Plotkin's model to their measurements in a reattaching shear layer, and Poggie and Smits (2005) compared the model to experimental data obtained in blunt fin flows at Mach 3 and Mach 5 by Evans et al. (1990); Gonsalez and Dolling (1993); Erengil and Dolling (1993), and Brusniak and Dolling (1994). The model was found to give an excellent fit to the autospectrum and autocorrelation of pressure fluctuations and shock position fluctuations in the region of separation shock unsteadiness (see, for example, Figure 10.11). For the Mach 3 flow, a relatively good fit was also obtained for the region corresponding to the motion of the rear leg of the λ-shock system, but over a more limited range of frequencies and time scales. The results suggest that shock motion in the blunt fin flow can be described with good accuracy with this model.

This rather good agreement may be obtained from other reasons than the hypothesis used in Plotkin's model. We know that in many cases, and if

the turbulence level is small enough (see, for example, Figure 10.6), the wall pressure time history resembles a random boxcar signal. Such a signal, with normal distributions for the length of the high and low states, has an autocorrelation given by $R(t) = e^{-t/\tau}$, where τ is the integral scale. This relationship is identical to Equation 10.3, and therefore it has a spectrum $G(f)$ of the form given by Equation 10.4, and $fG(f)$ should have a maximum for $f = t/2\pi$.

We have claimed that the linear analysis finds that shock waves act as lowpass filters. Equation 10.4 also represents the amplitude response as a simple lowpass filter. Although this response is consistent with the data, it does not provide proof for the assumptions used by Plotkin, such as Brownian forcing and a linear restoring force. It also does not imply that the autocorrelation of the shock location is identical to the autocorrelation of the pressure. An important parameter for the formulation is the integral scale of pressure fluctuations (which depends either on the upstream or downstream conditions), which cannot be derived from Plotkin's analysis. Hence, the model is more ad hoc than fully predictive. It is therefore useful to derive a pertinent Strouhal number to characterize these motions, if that is possible. The cases considered here refer to interactions where the downstream flow is mainly supersonic, so that acoustic coupling as found in buffeting or screech are not expected to be significant. The first attempts to find a characteristic frequency tried to correlate this frequency with a characteristic time scale of the incoming boundary layer turbulence. This was found not to work in the general case (see, for example, Beresh et al. (2002)). Simple flow experiments show that the geometry of the interaction is a key parameter. For example, Dolling and Smith (1989) have shown that in the case of an interaction produced by a blunt fin the frequency scales with the size of bluntness rather than with the thickness of the incoming boundary layer. Erengil and Dolling (1991) suggested that the extent of the interaction (or the length of the separated zone) could be a pertinent length scale L, and found that in the case of a 28° compression ramp flow at Mach 5 the Strouhal number $St = fL/u_\infty \approx 0.03$, where u_∞ is the external velocity of the upstream flow. Dupont et al. (2005) and Haddad (2005) applied the same scaling to shock reflection cases at Mach 2.3, and found that the Strouhal number was also close to 0.03. In a three-dimensional interaction produced by a circular cylinder normal to a wall, the measurements by Dolling and Smith (1989) lead again to about the same value for the Strouhal number. It seems that such a value has some generality, at least for relatively simple interactions in the supersonic regime.

Is it possible to rely on such a result? It seems surprising to find similar Strouhal number values under significantly different conditions. We should note first that such values are not very accurate: the characteristic frequency of the shock motion is typically evaluated using the maximum value of a bump in the wall pressure spectrum, which can only be done with an accuracy of no more than 20 or 30%. Moreover, determining the separation length is always

difficult. A second comment may bring more insight to this question. It may be assumed that the shock motion depends strongly on the fluctuations in the separated zone (that is, of the vortical structures characteristic of separation). It is shown in Section 10.6 that a possible scenario for many cases is that large eddies, associated with the reversed flow, are produced in the separated zone in a fashion resembling mixing layers. For such convective phenomena, the separation length seems to be the pertinent scale introduced by the existence of separation, as suggested by Kiya and Sasaki (1983) in subsonic conditions. For this reason, it may be expected that the fluctuations produced by the separated zone, and felt by the shock system, should scale with the length of the interaction. Similarly, in the absence of a leading shock, the convection velocity of the structures is nearly proportional to the external velocity, at least for small values of backflow velocity. If the external velocity above the recirculating bubble is not too different from the upstream one, U_∞ may appear as a reasonable scale for the convection velocity of the large structure, and therefore may scale with the shock frequency. Finally, even if some insight into the physics of the shock motion in boundary layer interactions has been obtained, it appears that the question of their frequency and amplitude of motion is still an open question. Further discussion on the influence of downstream conditions is given in Sections 10.2.6 and 10.4.

10.2.5 Turbulence Amplification

Rose (1973) and Kussoy and Horstman (1975) were the first to measure the strong amplification of turbulence levels in shock wave-boundary layer interactions, a result that is in agreement with the observations from freestream turbulence-shock interactions. Both investigations were performed in incident shock interactions. Compression corner studies confirmed that interactions produce a large increase in turbulence activity: for a 20° deflection at Mach 2.9, Smits and Muck (1987) found that the maximum level of $\overline{u'^2}$ increased by a factor of about 12. The unsteady shock motion smears the region over which the amplification occurs, and it sometimes produces a local peak in the intensity profiles. The results given in Figure 10.12 show this behavior clearly. It appears that the region directly affected by the shock has a thickness of about 0.1δ for the 8° case, and 0.2δ for the 16° case. The extent of the unsteady shock motion at the wall measures approximately 0.15δ and 0.3δ for these two cases, respectively, as indicated in Figure 10.10. Clearly, the shock motion extends throughout the layer, and the amplitude of the motion is approximately constant with distance from the wall.

The level of turbulence intensity in the separated zone takes a maximum away from the wall, near the edge of the separation bubble. Selig et al. found that this level matches the high levels of turbulence found in mixing layers. Therefore, it seems possible that the separated zone can produce large-

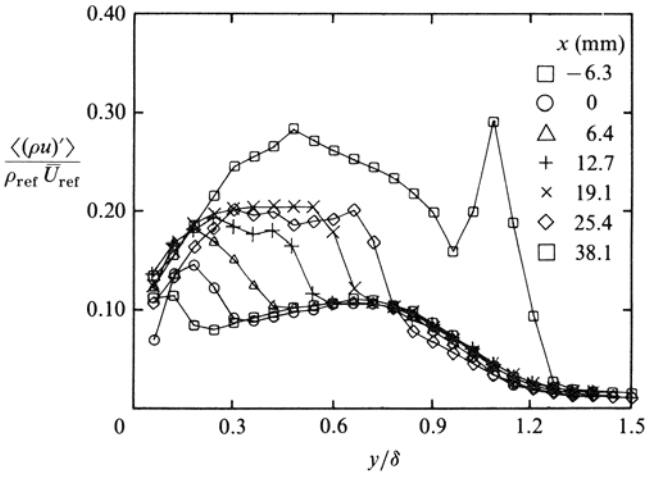

Figure 10.12. Distributions of $(\rho u)'$ in 16° compression corner interaction, in the region near the corner. (From Smits and Muck (1987). Copyright 1987, Cambridge University Press. Reprinted with permission.)

scale perturbations that are convected downstream. Such structures have been found from computations in laminar flows at low and high speeds (Daghsstani, 1993; Ripley and Pauley, 1993), and have some features in common with the perturbations seen in mixing layers. In particular, they involve low frequencies, or at least frequencies much lower than the characteristic frequency of a boundary layer of the same thickness. Other experimental evidence favors this picture also. For example, measurements of turbulence downstream of the reattachment revealed a strongly perturbed outer layer intermittency, and schlieren images triggered by a hot-wire detecting the occurrence of sharp fronts in the mass flux signal have very clearly shown the presence of radiation by Mach waves (Smith, 1989). Again, these visualizations are perhaps among the few that suggest the emission of shocklets in a distorted boundary layer at supersonic speeds. In recent unpublished work at Princeton, shocklets have been seen emanating from the large-scale motions in a Mach 8 boundary layer, but the evidence for their presence in wall-bounded flows at lower Mach numbers is scarce. Because the space-time characteristics of equilibrium boundary layers indicate that the large-scale structures in this flow produce only weak Mach waves at supersonic speeds, we have to suppose that there are eddies with large velocity fluctuations which are convected at a speed that is supersonic with respect to the external flow. This is consistent with the conjecture that large-scale perturbations are produced in the mixing zone over the separated bubble (see also Selig and Smits (1991)). The low-frequency

unsteadiness that they produce is the downstream condition imposed on the shock and thereby makes it move. This could explain why the shock motion occurs at frequencies typically an order of magnitude below the characteristic frequency of the boundary layer. Selig and Smits have also supposed that Taylor-Görtler vortices produced by the concave streamline contribute to the perturbation. Ünalmis and Dolling (1996) in a Mach 5 blunt-fin interaction found a significant level of correlation between the shock foot position and the ensemble averaged total pressure well upstream of the interaction. The frequency of these events was lower than the typical frequency content of the large-scale motions, and suggest some long-term variations in the incoming boundary layer. They proposed that these variations are consistent with the presence of unsteady Taylor-Görtler vortices, possibly produced by the concave curvature in the nozzle, because the measurements were made in the nozzle wall boundary layer. The last conclusion is that the return to equilibrium of the boundary layer downstream of reattachment probably depends on the way that the perturbations shed by the separated bubble into the wall layer lose their identity, through the process by which they lose energy through acoustic losses and interact with the new structures generated near the wall.

To study the reattachment region more closely, Settles et al. (1982), Hayakawa et al. (1984), Poggie et al. (1992); Shen et al. (1993), and Poggie (1995) conducted experiments in a backward-facing step flow where the separation point was fixed, and a relatively large recirculation zone was formed. The freestream Mach number was 2.9. The reattachment occurred on a 20° ramp, and the ramp was adjusted so that the upstream boundary layer separated without deflection. The pressure fluctuations on the ramp reached very high levels, and a peak value equal to about 11% of the local mean wall pressure was found just downstream of the mean reattachment line. Multiple shocks were observed in this region, interacting in complex patterns. Shocks typically formed at the upstream edges of the large-scale structures in the reattaching shear layer and redeveloping boundary layer. Double-pulsed Rayleigh scattering images showed the formation and progressive strengthening of these shocks as the structures convected through the reattachment zone (Figure 10.13). The spectra of the wall pressure did not display the low-frequency peak commonly observed in compression corner interactions, supporting the notion that it is the expansion and contraction of the separation bubble that is responsible for low-frequency shock motion in those flows. In the case of the reattaching shear layer, it is the incoming turbulence that is the primary cause for the shock motion and the intense levels of fluctuating pressure that occur near the mean reattachment line.

Finally, measurements of the heat transfer in a 16° compression corner interaction at Mach 2.84 demonstrate that the Reynolds Analogy factor s, the ratio of the Stanton number to the skin-friction coefficient, strongly deviates from a constant value in the region downstream of the interaction. Evans and

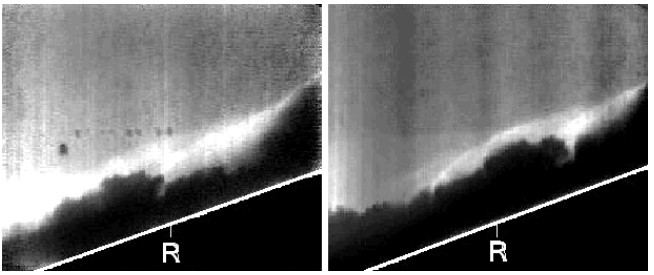

Figure 10.13. Rayleigh scattering flow visualization of a reattaching shear layer. The incoming flow is a free shear layer formed by a backward-facing step, with a freestream Mach number of 2.9. The visualization is just downstream of attachment which takes place on a 20° ramp. The flow is along the ramp, from left to right, and the average position of reattachment is indicated by the letter R. The right image was taken 20 μs after the left image. The shocklets are visible as bright fronts, shrouding the darker large-scale features in the boundary layer. (From Poggie (1995) with the author's permission.)

Smits (1996) found that s initially increased by a factor of about three, relaxed quickly to a value equal to twice its upstream value at a distance $3\delta_0$ from of the corner, and then showed no obvious signs of further relaxation further downstream.

10.2.6 Three-Dimensionality

So far we have focused on interactions that are two-dimensional in the mean. Of course, the turbulence is always three-dimensional, leading to three-dimensional distortions of the shock sheet. Furthermore, three-dimensional features often appear in nominally two-dimensional separated flows. This often takes the shape of spanwise irregularities, which are most likely associated with Taylor-Görtler-like vortices formed in regions of concave streamline curvature. As noted in Section 9.4.3, such features are often seen in the reattachment region of laminar and turbulent flow over backward-facing steps (Ginoux, 1971; Roshko and Thomke, 1966; Shamroth and MacDonald, 1970). Roshko's experiment was performed on a body of revolution, and showed that these streamwise structures occur independent of the side wall boundary condition (see Figure 9.12). In planar flows, there is a complex interaction between the streamwise structures and the effects of the side walls, which depends on the ratios δ/W, and δ/H, where δ is the incoming boundary layer thickness, W is the width of the step, and H is the height of the step). This complex interaction was recently studied in detail by Poggie (1995) for the case of a reattaching flow downstream of a backward-facing step. Similar streamwise structures are believed to be responsible for the spanwise variations seen in

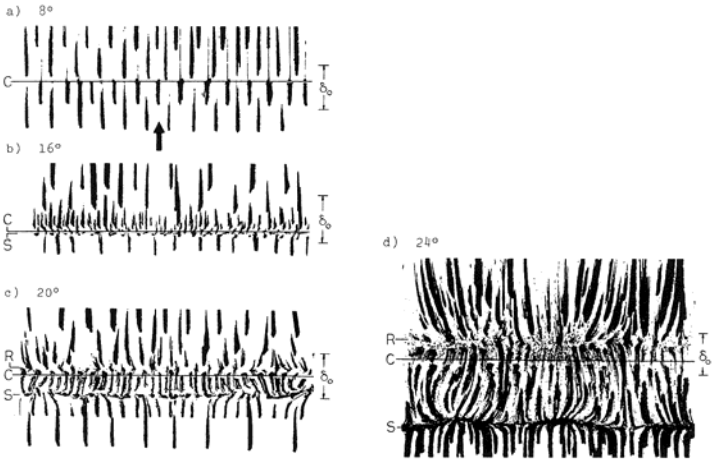

Figure 10.14. Surface streak patterns for compression corner flows at Mach 2.9 (the line S indicates the mean separation line, line R the mean reattachment line, and line C the position of the corner). The flow is from top to bottom, and the incoming boundary layer thickness is shown for comparison. (From Settles et al. (1979). Copyright 1979, AIAA. Reprinted with permission.)

the mean separation line (as indicated by surface flow visualization) of two-dimensional compression corner flows (see Figure 10.14).

10.3 Rapid Distortion and Linear Methods

The first hypothesis that can be tested is to determine if the amplification of turbulent fluctuations in a shock wave-boundary layer interaction may be described by RDT. It should be noted immediately that the incoming flow is a boundary layer, that is, a flow with a viscous sublayer in which the Reynolds number is low. Clearly RDT cannot be applied in this zone. A second consideration is the existence of a region near the wall (at about $y^+ \approx 15$, say), where the turbulence intensity can be very large, so that the small velocity fluctuation hypothesis fails. Hence, only the evolution of the outer part of the layer can be analyzed using rapid distortion concepts.

The time of distortion through the leading shock is very small, so that the ratio $(q'/U)\,(L/\Lambda)$ is much smaller than one. The mean distortion is not properly speaking irrotational, but the physical arguments developed in Section 4.4 for irrotational distortions can probably be retained as a guide to the phenomena that can occur. If the gradient Mach number is large, that is, if $M_g = (\partial U/\partial x)\,(\Lambda/a) \gg 1$, there is not enough time for pressure perturbations

to be fully developed: pressure is no longer a limiting factor for the changes of anisotropy, as at low speeds. When the flow is separated, a more-or-less continuous compression fan follows the leading shock. In this case, the interaction length is increased, and the distortion becomes slower. A typical value for $(q'/U)\,(L/\Lambda) = T_d/T_t$ at a position $y/\delta = 0.4$ in the 24° compression corner flow studied by Selig et al. (1989) is about 0.4, where T_d is taken over the whole of the interaction. This corresponds to the limit of application of the RDT, but the distortion of turbulence through the leading shock is of course much faster than that. The use of such an estimate is questionable because the rate of dissipation can be modified by the distortion. In the case of a compression, the effect of mean compression is to transfer part of the energy to small scales, because a large scale becomes smaller in the direction normal to the shock. This linear transfer brings the energetic range closer to the dissipative one. Consequently, the time scale of the energetic range may decrease through the interaction and the continuous distortion downstream of the shock is probably slower than expected from estimates where the time scale of turbulence is determined from upstream conditions. Note also that if $\partial U/\partial x = U/L = 1/T_d$, then $M_g T_d = M_t T_t$. In the present case, this leads to the value $M_g \approx 0.1$, which is small, so that in this interaction the rapid distortion, if relevant, is expected to have a behavior similar to the subsonic one.

A second contribution to the increase in turbulence through linear mechanisms is the generation of vorticity by interaction of fluctuating entropy through the mean shock. From a technical point of view, cases where the variations of density occur in space are generally not compatible with the homogeneity conditions required by the Fourier representation of the fluctuations. Analytical tools appropriate to inhomogeneous situations have to be used. However, Goldstein (1978, 1979) proposed a solution for the case of irrotational distortion and frozen entropy fluctuations, for which an analysis can be developed. Even if detailed analysis is not available for the action of this term in the general case, it is possible to examine the Reynolds stress equations. The corresponding source terms in these equations are the production terms involving the mean pressure gradient, and sometimes called "enthalpic production" terms, $\left(\overline{\rho' u_i'}\big/\bar{\rho}\right)(\partial\bar{p}/\partial x_j) + \left(\overline{\rho' u_j'}\big/\bar{\rho}\right)(\partial\bar{p}/\partial x_i)$. The difficulty is that we do not know the turbulent mass flux $\overline{\rho' u_i'}$ in the vicinity of the mean location of the shock. However, for distortions without discontinuities in adiabatic flows at nonhypersonic Mach numbers, these production terms are of the same order, or smaller, than the other production terms, so that in considering only the amplification due to mean velocity, inhomogeneity is a useful and significant indication for the overall evolution of the turbulent quantities.

An estimate of the increase of turbulence through the shock can be made from the shock formulae given in Section 4.4.5. For the 20° compression corner flow at Mach 3, $\overline{u'^2}$ along a streamline starting at $y/\delta_0 = 0.4$, this predicts an increase by a factor of about 3.6, which is half the observed amplification.

Rapid distortion alone cannot explain the total evolution. RDT assumes that the distortion is imposed on the turbulence, and that the distortion itself is independent of the turbulence. In the case of a shock, this implies that its strength and geometry are independent of the incoming turbulence, and that it is steady. It turns out that the shock motion is an important feature.

Two sorts of shock unsteadiness may be defined: the shock motion due to the incoming turbulence which can distort the shock locally, and motions imposed independently of the local turbulent condition, for example, by some unsteady boundary condition at the foot of the shock. These possible actions have been illustrated by a number of studies, for example, the work by Hussaini et al. (1985) who note that an oscillating shock wave exhibits some curvature, and therefore it is a source of vorticity. They considered a two-dimensional vortex suddenly inserted into a supersonic flow. A bow shock formed upstream of the vortex and the baroclinic production of vorticity was sufficient to reverse the sign of the vorticity in the upper half of the vortex. As a result, the vortex appeared to split into two parts with an attendant reduction in the characteristic length scale. Baroclinic torques generated by shocklets may be an important source of vorticity (with a sign opposite to that of the main shear), particularly in free shear layers.

The coupling between a shock wave and an incident turbulent field has been studied mainly by Ribner (1953); McKenzie and Westphal (1968), and Anyiwo and Bushnell (1982). In this work, a linear coupling between turbulent field and shock motion is used: assuming small fluctuations, the Rankine-Hugoniot relations are linearized and the shock motion is deduced. Some simulations of the same flow have been performed by Zang et al. (1984) for computations based on the two-dimensional Euler equation, and for isotropic quasi-incompressible turbulence interacting with a weak shock wave using direct simulations of the Navier-Stokes equations by Lee et al. (1993). In the linearized theories, homogeneous flows in infinite space were considered on both sides of the shock, and the shock was assumed to be rippled in phase with the incident turbulence. This work gives the amplification in the linear coupling approximation or Linear Interaction Approximation (LIA). As noticed by Jacquin et al. (1993) and Lee et al. (1992), the LIA gives an amplification significantly smaller than the RDT based on an irrotational one-dimensional deformation with the same mean velocity difference through the distortion. The LIA was compared to the two-dimensional Euler computations by Zang et al. (1984), which showed a very good agreement between both methods in most situations for a large range of Mach numbers ($M < 8$), because the only discrepancies were found for waves with an orientation close to the critical angles found by the linear theory. Lee et al. (1993) demonstrated that, for isotropic incident turbulence and constant mean temperature, LIA predicts that the velocity of the shock is of the order of the *rms* velocity of incoming turbulence, and that the radius of curvature is of the order of the

Taylor microscale. Their direct simulations were limited to transonic Mach numbers ($M < 1.2$), and the results probably represent only weak effects of compressibility. The evolution of the longitudinal velocity fluctuation intensity $\overline{u^2}$ displayed a rapid increase followed by a rapid decrease downstream of the shock, whereas linear theory predicts a monotonic decay. The difference arises because of the redistribution of the turbulence kinetic energy in the relaxation downstream of the shock. The overall amplification rates, after the initial oscillations in the relaxation region, were in reasonable agreement with the prediction of the LIA. They also found that the shape of the shock is sensitive to the level of incoming turbulence, so that for large M_t the strength of the compression through the shock is smaller than through a laminar shock. In addition, the vorticity downstream of the shock occurs at smaller scales than in the upstream flow, and that in agreement with the LIA, the Taylor microscale is smaller than that in the upstream flow. An important effect of the shock, taking into account the coupling with the incident turbulence, seems to be to produce scales of smaller length.

This picture is the one for a shock far from solid walls, and for which the shock corrugations are in phase with the incoming fluctuations. The situation is very different if the shock is forced to start at a given point. Duck et al. (1993) considered the case of the shock attached to the sharp leading edge of the shock generator. They required the shock to remain attached to the leading edge, and a perfect fluid condition (zero normal velocity) was imposed along the plate. For a sinusoidal incident wave, the shock location was not sinusoidal, and for a single mode upstream of the shock, broadband fluctuations developed downstream.

Another source of turbulence is the "externally driven" shock: it corresponds to the case when the shock motion is not correlated with the incident turbulence. This case was explored analytically for two-dimensional perturbations by Anyiwo and Bushnell (1982). For zero incoming turbulence they found that the turbulent fluctuations u' produced by such a mechanism are of the order of $0.8u'_s$ for large Mach numbers, where u'_s is the *rms* shock velocity, and as high as $1.6u'_s$ in the transonic range. These motions can contribute to the increase of turbulence in shock wave-boundary layer interactions because the shocks move without any noticeable correlation when the layer is separated. In some cases, as in the experimental examples that follow, the ratio u'_s/U_1 can be about 10%, and these fluctuations occur at low frequencies: this can be a significant mechanism to produce turbulence in the transonic zone, if the shock moves back and forth with a velocity constant throughout the layer. In the 24° interaction that was considered to illustrate the problem, the externally driven shock motions probably contribute to the increase of turbulence close to the wall, but not significantly to the large amplifications in the external part of the flow, where very large turbulence intensities are observed.

The experimental results on shock wave turbulence or shock wave-turbulent

boundary layer interactions do not always match the previous analytical description, perhaps because of the measurement difficulties. Experimental work on quasi-homogeneous turbulence subjected to a shock wave has been performed by Debiève and Lacharme (1985); Honkan and Andreopoulos (1992); Jacquin et al. (1991); Barre et al. (1995); Agui et al. (2005), and recently reviewed by Andreopoulos et al. (2000). In the experiment by Debiève and Lacharme, the shock was produced by a shock generator at the wall of the wind tunnel at Mach 2.3. The experiment was first discussed in Chapter 1, where some of the principal aspects of the interaction of a shock with freestream turbulence were introduced. The turbulence caused the shock to oscillate, waves were propagated along the shock, and the scales of the shock distortion were similar to the scales of the incoming turbulence, whereas the turbulence levels were significantly amplified. These features seem to be characteristic of all shock wave interactions. In the second study, turbulence interacting with a shock in a shock tube was considered at $M = 1.62$; in Jacquin et al.'s experiment turbulence was subjected to a nearly-normal shock in a nozzle at $M = 1.4$, and in Barre et al.'s experiment, grid turbulence experienced a compression through a shock at Mach number 3. In all experiments, the incoming turbulence was quasi-homogeneous and was decaying. The turbulence level was very small, because the turbulent Mach number was typically 0.01 or 0.03. Concerning the amplification through the shock, contradictory results were found. Debiève and Lacharme found a slight increase of the level of turbulence, consistent with the shock formula of Section 4.4.5, but the increase was so small it was at the limit of measurement uncertainty. Similarly, Jacquin et al. found practically no change of turbulence level through the shock; instead they observed that the rate of decrease of turbulence downstream of the shock was significantly increased, suggesting that turbulence was out of equilibrium or that new mechanisms (involving probably pressure) were involved. It is possible that the decay rate was high enough to mask the expected rise in turbulence intensity level.

In contrast, Honkan and Andreopoulos (1992) and Agui et al. (2005) observed a much larger increase through the shock, although the amplification factor was not the same for different length scales and different turbulence intensities. In the more recent study, rectangular grids of various mesh sizes were used to generate turbulence with Reynolds numbers based on the Taylor microscale ranging from 260 to 1300. Estimates of dilatation, compressible dissipation, and dilatational stretching were obtained. The *rms* values of the lateral vorticity components indicate a 25% amplification on average, with only a very weak dependence on shock strength, M_s (see Figure 10.15), but the longitudinal vorticity fluctuations were less affected. Integral length scales and Taylor's microscales were reduced after the interaction in all cases, whereas the integral length scales in the lateral direction increased at low Mach numbers and decreased at higher Mach numbers. Their results suggest that in

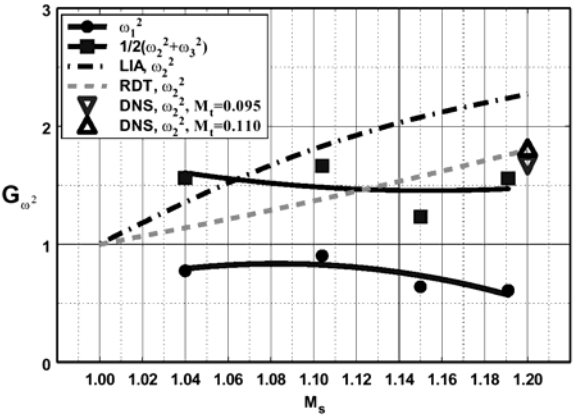

Figure 10.15. Amplification of vorticity fluctuations in shock-turbulence interactions. Experiments by Agui et al. (2005). Computations: LIA by Lee et al. (1993); RDT by Jacquin et al. (1993); DNS by Lee et al. (1993). (From Agui et al. (2005), with authors' permission.)

the weakest of the present interactions, turbulent eddies are compressed in the longitudinal direction drastically and their extent in the normal direction remains relatively the same. As the shock strength increases the lateral integral length scales increases whereas the longitudinal decreases. At the strongest interaction studied, turbulent eddies are compressed in both directions. They noted, however, that even in the highest Mach number case the issue is more complicated because amplification of the lateral scales has been observed in flows with fine grids. Thus the outcome of the interaction appears to depend strongly on the initial conditions.

In the work by Barre et al., the increase in level is in satisfactory agreement with the predictions of the LIA. In particular, the small scales were amplified more than the large ones. All the other experiments found the opposite trend. Although the conditions for these experiments were not identical, the initial levels of turbulence were quite similar, and all the turbulence Mach numbers were small. However, none of the experiments reported the proportion of compressible turbulence in the incoming fluctuations. Depending on the manner used to generate the incoming turbulence, it may be possible to have shocklets present in the fluctuations, as shown by the schlieren visualizations of Alem (1995) in the experimental configuration used by Barre et al. A regular diamond-shaped pattern was observed coming from the multinozzle array used to generate the supersonic flow and the grid turbulence. Moreover, because the turbulence levels were small, the fluctuations induced by the acoustic radiation from the wall layers may constitute a nonnegligible fraction of the *rms*

velocity. This is a major limitation in interpreting these results, because the linear theories quoted in the previous section show that the transfer function is not the same for vorticity waves and acoustic waves, and that the shock wave may be subjected to a pressure perturbation that is periodic in space.

The other differences among the flows probably come from the conditions on the shock itself. In Debiève and Lacharme, the shock was rather weak, because the change in ρU through the shock was comparable (or smaller) than the *rms* value of $(\rho u)'$. The shock was produced by a deflection of the wall, so that its motion may have been partly driven by the turbulent boundary layer on the wall. Whatever the source of the motion, the experiment proved that the shock was oscillating, and that the amplitude of its motion was of the order of the integral scale of the freestream turbulence. As mentioned earlier, the increase of turbulence through the shock was rather small, so that it is difficult to draw conclusions on the validity of RDT or of the LIA in this case. The incoming turbulence increased the amplitude of the shock oscillation, so that the shock motion was assumed to be due mainly to the local action of turbulence, and not to the unsteady motion of the shock foot. However, the experiment provided no information on the phase relationship between the shock motion and the incoming fluctuations. In the other experiments, the shocks were stronger, so that the incoming fluctuations are probably not strong enough to make the shock move appreciably. In the experiments by Honkan and Andreopoulos and Jacquin et al., it is very likely that the interactions between the shock and the walls produce shock motions that are not controlled and not described by the experiments. From this point of view, the experiment by Barre et al. seems to be free from such effects, and it is consistent with the qualitative agreement between their results and the LIA predictions.

As concluding remarks on this description of two-dimensional interactions, it must be emphasized that many unknown features remain. Analytical work has been useful for identifying some of the important physical mechanisms responsible for enhancing turbulence. In general, these interactions cannot be predicted by simple RDT, mainly because of the shock motions that often seem to be important, although the experiments are by no means conclusive. Among the points that need to be studied by experiments, we can note the curvature of the shock produced by incoming turbulence. Because the variations in the shape of the shock depend on the incoming Mach number, the fluctuating Mach number is probably a relevant parameter for these effects, together with the spatial scale of the incoming turbulence. Other experimental verifications that are needed are the measure of the level of turbulence produced by the shock motion (shock "flapping" and shock curvature), and the rate of energy lost by Mach wave radiation downstream of reattachment. These are effects of compressibility that still need to be investigated and which are beyond the present capability of the models for compressible turbulence.

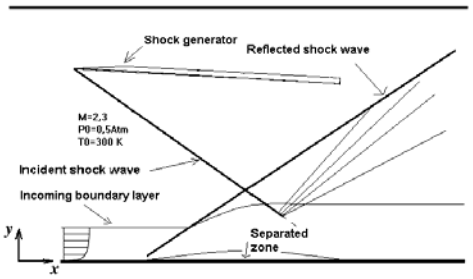

Figure 10.16. Sketch of the interaction produced by the reflection of an oblique shock wave on a wall. The Mach number is 2.3, the Reynolds number of the incoming boundary layer is $R_\theta = 5000$. (From Dussauge et al. (2005), with the authors' permission.)

10.4 Incident Shock Interactions

Incident shock interactions in supersonic flows, as illustrated in Figure 10.1, were studied by Law (1975), Délery (1992), Audiffren (1993), and Deleuze and Eléna (1995). Three-dimensionality is observed in many two-dimensional interactions, as illustrated for compression corner flows in Figure 10.14, where multiple streamwise vortices seem to form as a result of a Taylor-Görtler instability. In experiments with a plane incident shock by Bourgoing and Reijasse (2001), Doerffer and Szwaba (2004), and Bookey et al. (2005b), however, surface visualizations have suggested that two vortices are embedded in the separated zone. Their position is symmetric with respect to the axis; the separation line and the leading shock waves show spanwise curvature, suggesting strong three-dimensionality. Such features have not been reproduced in recent DNS of incident shock interactions, mainly because of the limited spanwise domain and the use of reflecting boundary conditions (see Li and Coleman (2003) and Wu and Martin (2004)).

Similar evidence of large scale three-dimensionality was obtained by Haddad (2005) and Dussauge et al. (2005) in the case of an incident oblique shock wave at a Mach number of 2.3. The flow arrangement is given in Figure 10.16. When the shock generator was set at 9.5° of incidence, a large separated zone was observed. On the centerline of the tunnel, the wall pressure spectra showed bumps at frequencies about an order of magnitude higher than the frequencies typical of the shock motion. These frequencies decrease with downstream distance, as they would do in a mixing layer, until the middle of the separation zone is reached where they begin to increase. Then, in the region close to reattachment, they become constant (Dupont et al., 2005).

To study the spanwise structure of the interaction, PIV measurements were performed in planes parallel to the wall. The mean velocity vectors in this

plane showed two points of streamline convergence, symmetric with respect to the centerline of the wind tunnel, with features similar to the visualizations shown by Bourgoing and Reijasse (2001), Doerffer and Szwaba (2004), and and Bookey et al. (2005b). By investigating several parallel planes, the three-dimensional mean flowfield was constructed, as shown for one half in Figure 10.17. Here, x, y, z are the longitudinal, vertical, and spanwise directions, respectively; x is normalized by the length of interaction L; and the longitudinal axis of the wind tunnel is located at $z = 0$. In the separated zone, tornado-shaped vortices are evident. Their height is about one half of the initial boundary layer thickness, indicating strong three-dimensionality in the recirculating zone. The mean time scale inside the vortices (the inverse of the mean velocity gradient in the part of the vortex showing solid body rotation) is of the same order of magnitude as the inverse of the shock frequency, suggesting that in this sort of interaction the unsteadiness may be controlled by the three-dimensional structure of the recirculation zone. This suggestion is preliminary, because there may exist other motions with comparable time scales. It is often supposed, for example, that the time scale of large turbulent eddies is of the same order as the time scale of the mean motion. However, this turbulent time scale should be understood as a Lagrangian time scale, and an estimate based on the mean flow may not be appropriate. Also, as hypothesized by Jacquin (2005), there may exist a mutual induction between the two vortices that could produce low-frequency motions. Clearly, the question of how important such eddies are in explaining the interaction unsteadiness remains a question for further study.

10.5 Isentropic Three-Dimensional Flows

Here, we consider three-dimensional boundary layers in supersonic flow in the absence of a shock wave, that is, "isentropic" three-dimensional interactions. Such flows have been studied by Hall (1965); Demetriades and McCullough (1985); Konrad (1993), and Konrad et al. (1994), where the three-dimensionality was generated by a curved fin, or a curved wall (see, for example, Figure 10.18). In the experiment by Konrad, the curvature was chosen so that the compression waves focused to a point well away from the surface of the fin, so that no shock wave was present in the region of interest. The strength of the spanwise and streamwise gradients increased progressively through the interaction, so that the degree of three-dimensionality (that is, the level of yaw) increased in the same way. A line of convergence appeared in the surface flow visualization, and it conveniently divided the flowfield into two regions. The upstream region could be further subdivided into a *small crossflow region* and an *upstream convergence region*. The small crossflow region was defined as the region where the velocity profiles followed the Johnston triangular model for the spanwise velocity component (Johnston, 1960). The Johnston model

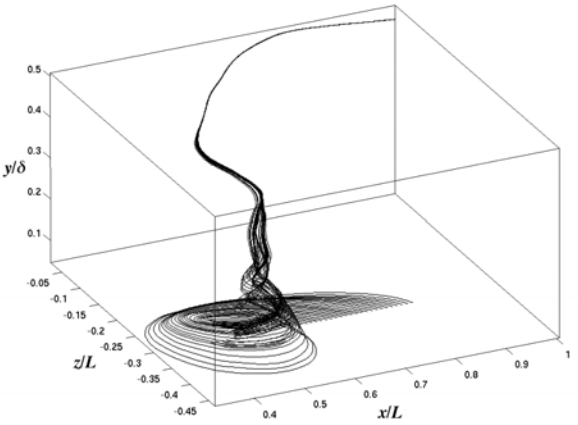

Figure 10.17. Tornado vortex in the separation in the oblique shock reflection sketched in Figure 10.16. One half of the interaction is shown. The upstream Mach number is 2.3; the angle of the shock generator is 9.5°. (From Dussauge et al. (2005), with the authors' permission.)

works well for mildly three-dimensional subsonic flows, and the yaw angles did not exceed 10° in this region, so this conclusion is in agreement with subsonic experience. In the upstream convergence region, the crossflow angles increased to about 20°, and the flow near the wall experienced near-wall retardation similar to that seen in other adverse pressure gradient flows. Pitch angles were very small everywhere, and the local boundary layer thickness remained almost constant throughout the interaction. The streamline curvature is virtually confined to horizontal planes ("in-plane curvature").

The turbulence response is most easily seen in the trends for the velocity fluctuations, as given in Figure 10.19. Here, u' is the component measured along the mean streamline, and v' is in the wall-normal direction and w' is in the mutually orthogonal direction. The absolute level of the streamwise intensity $\overline{u'^2}$ is almost unchanged in the outer part of the layer, but $\overline{v'^2}$ and $\overline{w'^2}$ display a strong attenuation initially, especially in the region $0 < y/\delta < 0.5$, before relaxing slowly toward the upstream undisturbed levels. A decrease in the u' component is not seen until the downstream convergence region, where a sharp drop occurs in the region near the wall, again related to the influx of high-momentum, low-turbulence fluid from the outer parts of the upstream boundary layer. The strongest effects of three-dimensionality were seen in the *downstream convergence region.* The velocity in the outer part of the layer is decreased due to the pressure gradients along the mean streamline, whereas the near-wall velocity profile is much fuller because high-momentum fluid from the upstream boundary layer is drawn closer to the wall as the low-momentum

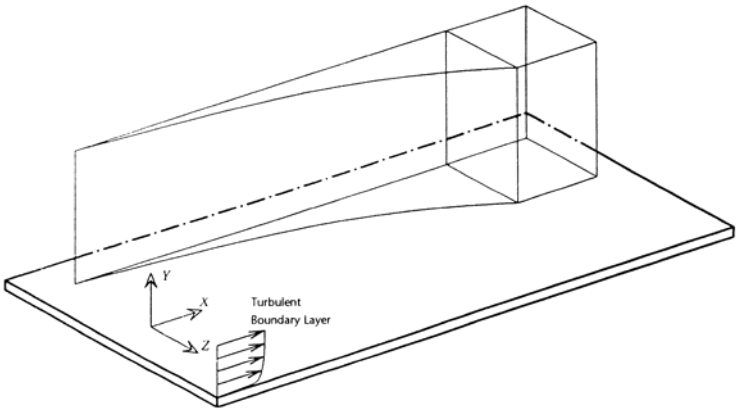

Figure 10.18. The isentropic 20° compression formed by a curved fin at Mach 2.9. (From Konrad (1993), with the author's permission.)

fluid originally near the wall is removed by the action of the spanwise pressure gradients.

The results could also be used to evaluate the importance of in-plane curvature as a stabilizing extra strain rate. By tracing out mean streamlines, a streamline was identified where the pressure gradient history matched the experiment by Fernando and Smits (1990) (see Section 9.4.2 and Table 9.1). The Fernando and Smits experiment was an experiment to study the effects of pressure gradient on a boundary layer that was two-dimensional in the mean. By comparing their results with the evolution of the turbulence intensities along the matched streamlines in Konrad's experiment, where the curvature was confined almost completely to planes parallel to the wall, the strong stabilizing effects of in-plane curvature could be identified. In the middle of the layer, $\overline{u'^2}$ and $\overline{v'^2}$ were lower in the three-dimensional flow by a factor of more than two when compared to the two-dimensional flow, but the shear stress $-\bar{\rho}\overline{u'v'}$ only showed significant in-plane curvature effects in the lower half of the layer. This indicates some level of agreement with the subsonic study of the flow over an infinitely swept wing by Bradshaw and Pontikos (1985), who suggested that the Reynolds shear stress was reduced because the eddies were tilted out of their preferred direction.

10.6 Three-Dimensional Interactions

In three-dimensional shock wave interactions, similar effects to those seen in isentropic compressions will occur, except that the effects of compression and

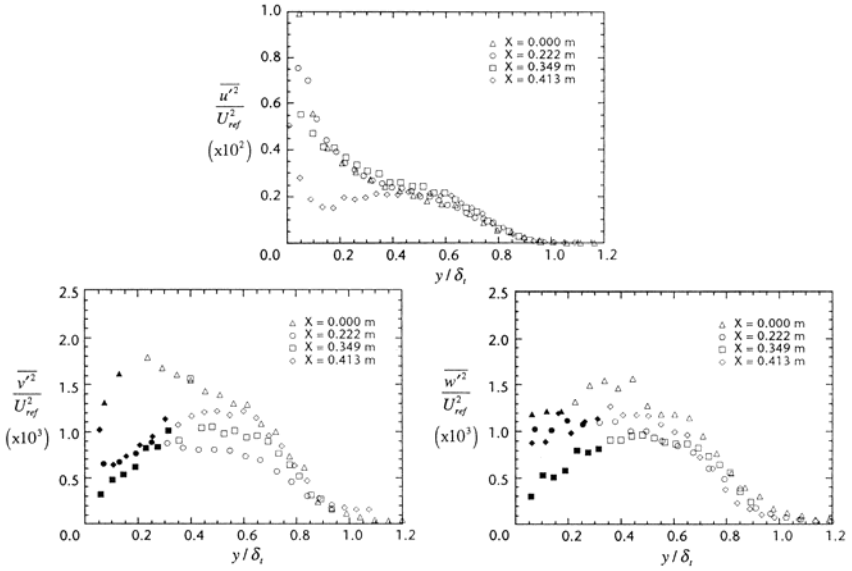

Figure 10.19. Turbulence distributions in an isentropic 20° compression formed by a curved fin at Mach 2.9. (From Konrad (1993), with the author's permission.)

pressure gradients are expected to be dominant because the pressure rise occurs over a very much shorter distance.

Most three-dimensional interactions can be classified according to four basic types: sharp-fin, swept-corner, swept-step, and blunt-fin. These in turn can be broken into two classes: the first two types are in the class of being "nondimensional" interactions in that there is no characteristic dimension associated with the shock generator, and the second two types are in the class of "dimensional" interactions in that the shock generator has a characteristic dimension, such as the diameter of the fin or the height of the step. In all cases, apart from a small inception region (located either near the upstream extent of the compression corner, or near the leading edge of the fin), the flow develops a helical flow with its axis closely aligned with the shock.

Two relatively simple examples of nondimensional interactions are shown schematically in Figure 10.20. In the first view, the interaction is generated by a swept compression corner, and in the second view it is generated by a sharp fin placed at an angle of attack to the incoming flow. Both examples display lines of accumulation of dye upstream and downstream of the inviscid shock location: the *line of convergence* is sometimes called the line of separation, and the *line of divergence* is sometimes called the reattachment line. These figures illustrate relatively weak interactions: as the strength of the shock increases,

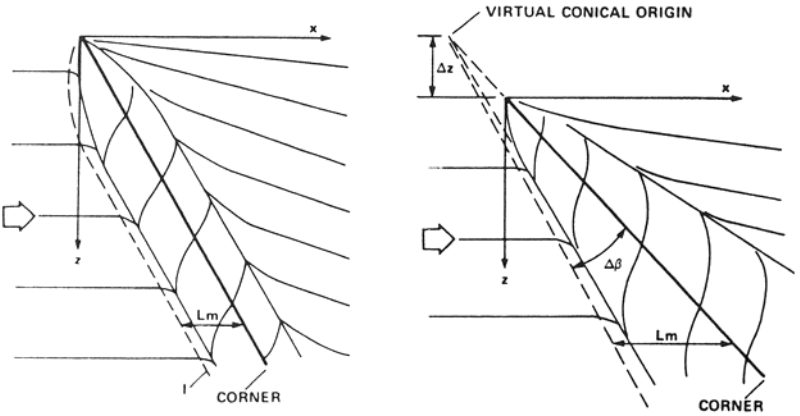

Figure 10.20. Schematic representations of the surface flow patterns produced by (a) swept compression, and (b) sharp-fin interactions. (From Settles and Teng (1984). Copyright 1984, AIAA. Reprinted with permission.)

multiple secondary flows can be observed.

Settles and Teng (1984) suggested that the nondimensional interactions represent examples of *cylindrical* similarity and the dimensional interactions display *conical* similarity. For example, in the compression corner flow the cross-section of the secondary flow becomes constant (cylindrical similarity), whereas for the sharp-fin flow it scales with distance from the virtual origin of the flowfield (conical similarity). The flows become two-dimensional when viewed in the appropriate coordinate system, similar to what happens in the inviscid flow over an infinitely swept wing, or a cone. We consider briefly two examples of nondimensional flows (the swept compression corner and sharp-fin interactions) and one example of a dimensional flow (the blunt-fin interaction).

10.6.1 Flow Field Topology

The instantaneous streamline pattern can often give a qualitative understanding of the flow behavior, and this becomes particularly important in the investigation of three-dimensional flows. There is, generally, some difficulty in visualizing and interpreting three-dimensional flowfields, and the topology of separated flows has received considerable attention (see, for example, Maskell (1955), Legendre (1956), Oswatitsch (1958), Lighthill (1963), Perry and Fairlie (1974), Tobak and Peake (1982), and Perry and Chong (1987)). A description of flow patterns using critical point concepts provides a framework and methodology for overcoming this difficulty. Just as importantly, *critical point* theory (also known as *phase-plane* or *phase-space* theory) provides a termi-

nology for describing complicated three-dimensional flow patterns unambiguously. Phase-plane analysis, combined with topological rules and the laws of vortex motions allows us to deduce physically plausible flow patterns from flow visualization results, or from limited flowfield measurements. In addition, phase-plane analysis uses the terminology of nonlinear dynamics, and it provides an unambiguous language for describing fluid flow behavior. For example, in two-dimensional flows, separation is a relatively clear concept, and a separation line is where the skin friction is instantaneously zero and the stream surface leaves the body. In sideview, the surface streamlines are joined at a *saddle point*. In three-dimensional flows, separation is often a more imprecise concept, and a separation bubble may have only two points where the skin friction is zero, or the bubble may appear only in a given coordinate system or direction of viewing. Terms such as separation and reattachment lose their traditional meanings, and phase-plane analysis gives us a better terminology, one that is closely connected with the equations of motion.

Phase-plane analysis is the analysis of nonlinear dynamical systems, and obviously fluid flow systems belong to this general class. In this analysis, critical points are identified in the governing equations. Critical points are points in the flow where the streamline slope is indeterminate and the velocity is zero relative to an appropriate observer. Hornung and Perry (1984) and Perry and Chong (1987) classify critical points into two major types: *no-slip* critical points, such as separation points on a no-slip boundary, and *free-slip* critical points which occur within the fluid away from no-slip boundaries. If the governing equations are regular, as for an incompressible, constant density flow or a compressible flow in the absence of shock waves, no discontinuities exist, and the equations may be linearized in the neighborhood of the critical points. Expanding the solution about the critical point allows us to identify the nature of the critical point, whether it be centers, saddles, nodes, or logarithmic spirals. Given the classification of critical points, the topologically correct pattern of, for example, surface streamlines, or more accurately, the lines of surface shear stress, can be determined to give a qualitative solution of the flowfield. In joining up the critical points, phase trajectories of limiting streamlines may be identified, and other features such as limit cycles may be revealed. Clearly, phase-plane analysis can be very useful for helping to understand complicated fluid dynamical systems.

Very briefly, we see that at any point in the flow where the solution is regular the velocity field can be expanded in terms of the space coordinates in a Taylor series with coefficients that are a function of time if the flow is unsteady. Close to a critical point, the velocity u_i is a linear function of x_i. If the eigenvalues and eigenvectors of the coefficient matrix are real, three planes containing solution trajectories (instantaneous streamlines) exist, defined by the eigenvectors, but if they are complex, only one solution plane exists. In these planes simple phase-plane methods can be used to classify the critical

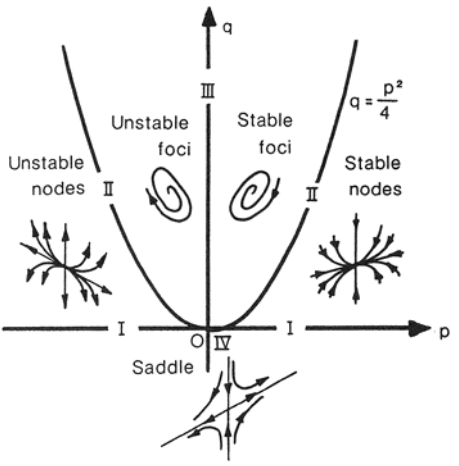

Figure 10.21. Classification of critical points on the p–q chart. For critical points on the boundaries I, II, and II, and at the origin IV, see Figure 10.22. (From Perry and Chong (1987). Reproduced, with permission, from Annual Reviews, Inc.)

point patterns. That is, by defining a new coordinate system in each plane $[y_1, y_2]$, we can write:

$$\dot{\mathbf{y}} = \overline{\overline{\mathbf{F}}}\mathbf{y},$$

where $\overline{\overline{F}}$ is the matrix of coefficients in the linearized equation. The types of critical points can be classified on a p–q chart, where $p = -\text{trace } \overline{\overline{F}}$, and $q = \det \overline{\overline{F}}$ (see Figure 10.21).

As pointed out by Perry and Chong (1987), if all the eigenvalues are real, either nodes or saddles are obtained. These patterns will in general be in noncanonical form; that is, the eigenvectors are nonorthogonal. If the eigenvalues are complex and the $[y_1, y_2]$-plane contains trajectories, a focus is obtained. If the pattern occurs on the boundaries of the p–q chart (that is, when $p^2 = 4q$, $p = 0$ or $q = 0$), we have *degenerate* critical points (see Figure 10.22). So, complicated flow patterns can be broken down into simpler components according to the nature of the critical points. For example, Figure 10.23 shows irrotational free-slip critical points. Here, the critical point is a local maximum or minimum in pressure. This is not true when vorticity is present. If the eigenvalues are complex, then a vortexlike pattern is formed, one that is often seen in three-dimensional separation from a surface, as in Figure 10.17. These are sometimes called "complex eigenvalue" critical points. It is also possible to have bifurcation lines (see Figure 10.24). These are lines in the flow toward which other trajectories are asymptotic (Hornung and Perry, 1984; Perry and Hornung, 1984). On a surface with three-dimensional separation, bifurcation

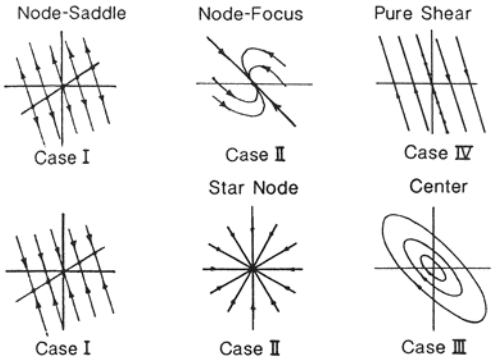

Figure 10.22. Degenerate critical points, or borderline cases. Case numbers refer to Figure 10.21. (From Perry and Chong (1987). Reproduced, with permission, from Annual Reviews, Inc.)

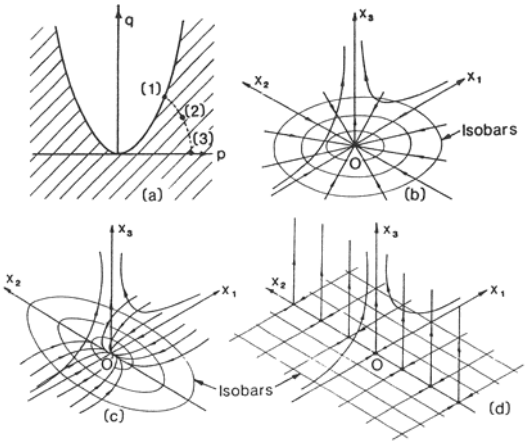

Figure 10.23. Critical points resulting from linear irrotational flow analysis. (a) Shaded zone shows allowable region for such points on the p–q chart for the $[x_1, x_2]$-plane; (b) Case 1; (c) Case 2; (d) Case 3. (From Perry and Chong (1987). Reproduced, with permission, from Annual Reviews, Inc.)

lines are often called separation or reattachment lines, but they can also occur within the fluid away from the boundaries.

In a compressible flow, especially in shock wave-boundary layer interactions, we must allow the possibility of discontinuities in velocity gradient. This does not affect the interpretation of surface flow patterns because the shock cannot

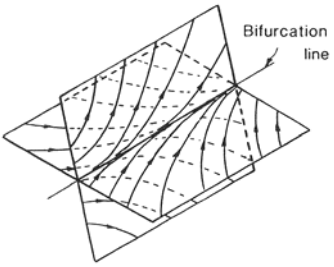

Figure 10.24. A bifurcation line. (From Perry and Chong (1987). Reproduced, with permission, from Annual Reviews, Inc.)

extend to the surface in a viscous fluid. However, the interpretation of the flow away from the wall becomes more difficult. The limiting streamlines that originate from the no-slip critical points may not persist very far from the wall, and there is no unambiguous way to join the free-slip critical points without additional information. Nevertheless, it seems that in many cases the shocks form on the outer surface of the interaction region, and critical point analysis can still be useful to describe the flow away from the wall, even within the interaction.

10.6.2 Swept Compression Corner Interactions

In the experiments on two-dimensional compression corners, side wall fences are typically used to simulate the infinite-span condition. As shown in Figure 10.14, the surface flow pattern usually displays a cellular character in the separated zone, which may indicate the presence of longitudinal roll-cells that are known to develop in concavely curved shear layers. The presence of three-dimensional features in nominally two-dimensional flows underlines the now widely accepted notion that there are no "truly" two-dimensional flows, especially when the flow is separated.

Consider the Mach 2.9, 24° compression corner interaction, with zero sweep angle. We saw that at this deflection angle, the flow was separated with a separation bubble length of about one boundary layer thickness. As the sweepback is increased from zero, fluid begins to flow along the corner line, and because of the finite length of the model the infinite-span condition immediately breaks down. The model becomes semi-infinite, and the inviscid shock shape is now conical in the sense that it is described only by an angle, and not by a dimension. Within the viscous flow, an inception region appears near the apex of the model, and this region is particularly noticeable when the upstream fence is removed (Settles et al., 1980).

With increasing sweep, the size of the inception region grows. This growth

is caused by the spreading influence of the pressure disturbances initiated at the apex. At this point, the boundary layer first encounters the swept shock wave, and the pressure rise across the shock sets up a lateral pressure gradient that abruptly turns the flow in the subsonic separated region near the wall. The turning angle of the freestream flow, however, is approximately equal to the yaw angle, and it is always smaller than the flow near the wall. These differences in flow direction generate secondary motions. Away from the wall, the flow is supersonic and pressure disturbances can only propagate in the downstream direction along characteristics. Hence, the growth of the inception region is a function of Mach number.

At small angles of sweep, there remains a substantial region of subsonic flow. As the sweep angle is increased, the secondary flow becomes stronger under the action of the increased lateral pressure gradient, and the region of subsonic flow must therefore decrease in size and ultimately shrink to negligible proportions. However, for sweep angles up to 10°, the wall pressure distribution does not significantly change, suggesting that the region of subsonic flow is not changed significantly.

As indicated in Section 10.6.1, it is not clear what connection exists between the surface features and the flow a small distance away from the wall. From continuity, we expect that above the lines of convergence and divergence fluid is transported either away from or towards the surface. The magnitude of the pitch angle, however, is unknown. The simplest possible interpretation of the flowfield structure suggests the presence of a significant vortical motion aligned in the direction of the corner. This interpretation is supported by the flow visualization of Settles and Teng (1984), and the calculations by Horstman (1984). Outside the inception zone, the experiments by Settles indicate that many of the flow features follow conical similarity, including the wall pressure distribution and the total pressure distribution in the flowfield. For low angles of sweep the far field is nearly cylindrical, despite the apparent conical nature of the inviscid shock wave. An asymptotic state is expected but it is likely to scale with the local boundary layer thickness, rather than the thickness measured near the apex. A truly cylindrical interaction will only occur when the size of the boundary layer thickness is small compared to the scale of the interaction.

Significant unsteadiness in two-dimensional flows has been associated with the presence of large subsonic regions, as found in separated flows. Thus, the interaction at large angles of attack and small angles of sweep should also display significant unsteadiness. As the angle of sweep increases from zero, and the subsonic region shrinks in size, we may expect that the unsteadiness will be reduced. The unsteadiness of swept compression ramp flows was first demonstrated by Tran (1987) at Mach 3. A more detailed study was made by Erengil and Dolling (1992) in a 28° swept compression corner at Mach 5 over a range of sweepback angles. For angles greater than 25°, the *rms*

wall pressure distributions were found to be conically symmetric, as were the mean distributions. In general, the amplitude of the wall pressure fluctuations decreased, as expected, and the frequencies increased with increasing sweep but the shock position was unsteady at all sweep angles. The separation shock characteristics, as determined from multiple-point wall pressure signals, were found to be essentially the same in all cases considered. The mean velocity of the separation shock was nearly constant, and therefore the higher frequencies seen with increasing sweep simply reflect the fact that the length over which the separation shock moves decreases as the sweep increases.

10.6.3 Sharp-Fin Interactions

As an example of a three-dimensional interaction, consider the case of a swept shock interaction generated by a sharp fin placed at an angle of attack to the incoming flow. Here the oblique shock sweeps across the incoming boundary layer, and strong secondary flows can be produced by the spanwise pressure gradients. Typically, one or more large-scale vortical motions are induced that sweep the low-momentum fluid from the near-wall region of the incoming boundary layer in the direction along the shock (see Figure 10.25). The high momentum fluid in the outer part of the boundary layer passes over the vortex with a turning angle more typical of the inviscid deflection associated with the shock, and it is then swept close to the wall. The skin-friction and heat-transfer levels seem largely unaffected by the strong secondary motions, but the values rise sharply in the region closer to the fin where the high momentum fluid "scours" the wall. The turbulence response is not well understood. Very few experimental results are available, but measurements by Tan (reported by Konrad (1993)) suggest that the turbulence levels are strongly amplified, and Tran et al. (1985) found that the shock is unsteady, leading to strong wall pressure fluctuations. In these respects, three-dimensional interactions appear to be similar to their two-dimensional counterparts, but the detailed response of the turbulence is clearly quite different. In particular, the turbulence amplification and the unsteady pressure loading are weaker.

In the interaction generated by a sharp fin, the shock sweeps across the incoming flow at an oblique angle to the upstream flow direction. In contrast to the swept compression corner interaction, the shock in the freestream is normal to the wall over which the incoming boundary layer is developing. However, the response of the flow is very similar in the two interactions. A streamtube encountering the shock is turned, compressed, and decelerated. When the pressure gradient is strong compared to the entering momentum flux, the flow is turned in a direction away from the direction of the pressure gradient. The degree of turning increases as the Mach number decreases. Therefore, for a boundary layer entering a pressure gradient, the gradient in Mach number will cause the flow near the wall to turn through a greater angle than the flow away

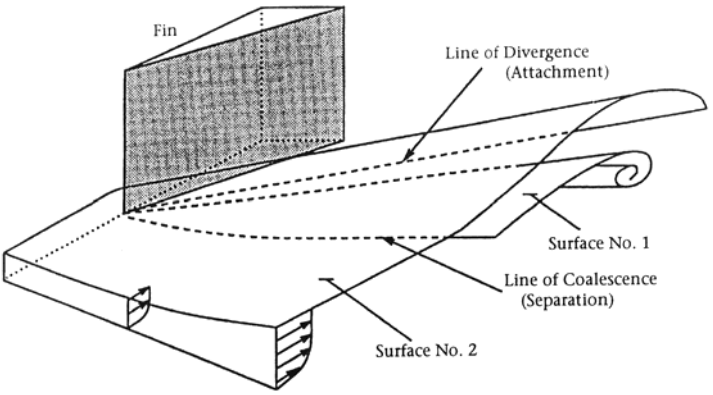

Figure 10.25. Structure of three-dimensional shock wave-boundary layer interaction generated by a sharp fin at an angle of attack. (From Knight et al. (1987). Copyright 1987, AIAA. Reprinted with permission.)

from the wall (as long as the pressure gradient dominates). The differential turning leads to a helical secondary flow, as illustrated in Figure 10.25.

The shock bifurcates in response to the formation of this secondary flow, in a manner very similar to that seen in two-dimensional separated compression corner flows. There is an initial turning and compression by a well-defined shock which is slanted forward (the "separation" shock), and a stronger trailing shock, where broadly speaking the two shock structures encompass the large-scale vortical flow. When the flow is viewed along the axis of the helix it appears similar to the cross-section of a two-dimensional separated flow (see Figure 10.26). In that view, a bubble-type separated flow is observed, and the flow characteristics typically scale in conical coordinates. The detailed flowfield model is shown in Figure 10.27. The experiments show that the wall pressure distribution and the total pressure distribution can be collapsed in conical coordinates. One feature that deserves particular attention is the "impinging jet", found in close proximity to the fin itself. As the model by Garg and Settles (1993) makes clear, the jet is formed by high-momentum fluid from the outer regions of the incoming layer (including the freestream) curved towards the surface as the low-momentum fluid near the wall is removed in the spanwise direction by the main vortical flow. This phenomenon is quite similar to that seen in the isentropic interaction discussed earlier (Konrad, 1993; Konrad et al., 1994). Not surprisingly, the maximum skin-friction and heat-transfer rates occur near the jet impingement location.

The unsteadiness of the sharp-fin interaction was first studied by Tan et al. (1985); Tran et al. (1985), and Tran (1987). Although these studies were con-

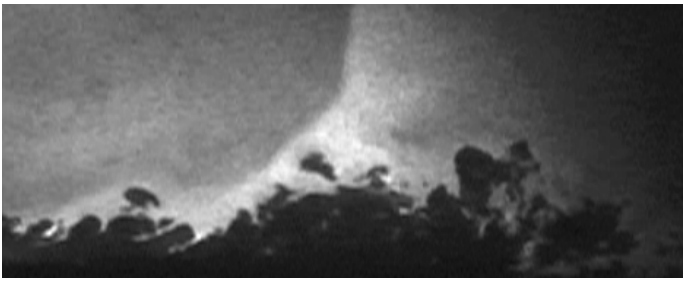

Figure 10.26. Filtered Rayleigh scattering image of a sharp-fin interaction at Mach 8, with $Re_\theta = 2400$. The view is in a plane aligned with the incoming flow direction. Incoming flow is from left to right. Within the interaction, the flow is out of the page at approximately 16°. (From Bookey et al. (2005a), with the authors' permission.)

fined to a single Mach and Reynolds number, they discovered many of the same features seen in two-dimensional interactions, particularly the intermittency of the pressure signal in the upstream influence region. The Rayleigh scattering visualizations by Smith et al. (1991) showed the movement of the separation shock clearly, and also revealed the motion of the triple point where the separation shock meets the main shock. Later work by Gibson and Dolling (1991); Schmisseur and Dolling (1992), and Garg and Settles (1993) demonstrated that the mean and *rms* pressure distributions scale in conical coordinates. The wall pressure signals near separation were clearly intermittent and qualitatively similar to those in two-dimensional flows. As expected, the amplitude of the *rms* pressure fluctuations increased with the fin angle, and in agreement with the data from the swept compression corners, the shock frequencies increased with the sweep angle of the separation line, at least up to an angle of about 25 to 30°.

One of the few investigations to make turbulence measurements in three-dimensional interactions was performed by Tran and Tan (unpublished) in a 10° sharp-fin interaction at Mach 2.9. Their results are shown in Figure 10.28. The inviscid shock position in the freestream is evident through the local maximum in the distributions at $x = 0.165$ m and 0.177 m. The turbulence levels in the outer flow increase substantially, and there is little sign of the start of a relaxation process. Near the wall, the levels are strongly attenuated, and at first sight it appears as though an internal layer has formed. This is misleading in that it neglects the three-dimensionality of the flow: in fact, the lower turbulence levels indicate that high-momentum, low-turbulence fluid has been brought into the region near the wall. The maximum amplification of the *rms* mass flux intensity for this 10° fin is about 30%, which may be compared to the case of the unswept 8° compression corner at the same Mach number where an increase of about 35% was observed. The small decrease

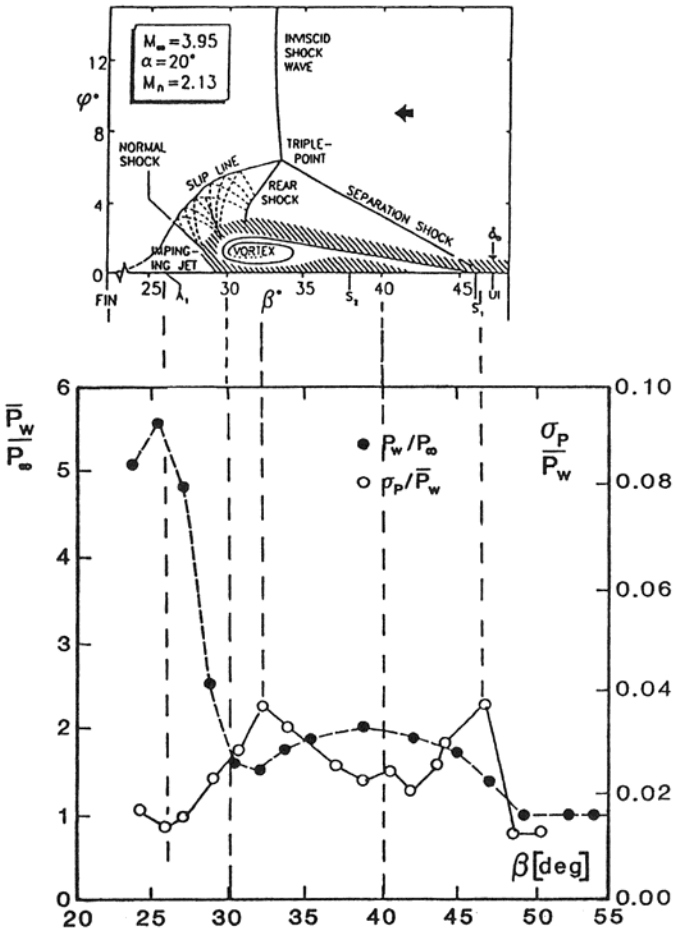

Figure 10.27. Flowfield structure, together with the mean and *rms* wall pressure distributions ($\overline{p_w}$ and σ_p, respectively) for a 20° sharp-fin interaction at Mach 4. The angle β is the conical coordinate, measured from the upstream flow direction. UI marks the location of the upstream influence, S_1 and S_2 mark the primary and secondary separation lines, and A_1 marks the mean reattachment line. The view is in a plane normal to the inviscid shock sheet. (From Garg and Settles (1993). Copyright 1993, AIAA. Reprinted with permission.)

observed in the amplification level may be due to the three-dimensionality, but the uncertainties in the data are too large to be sure.

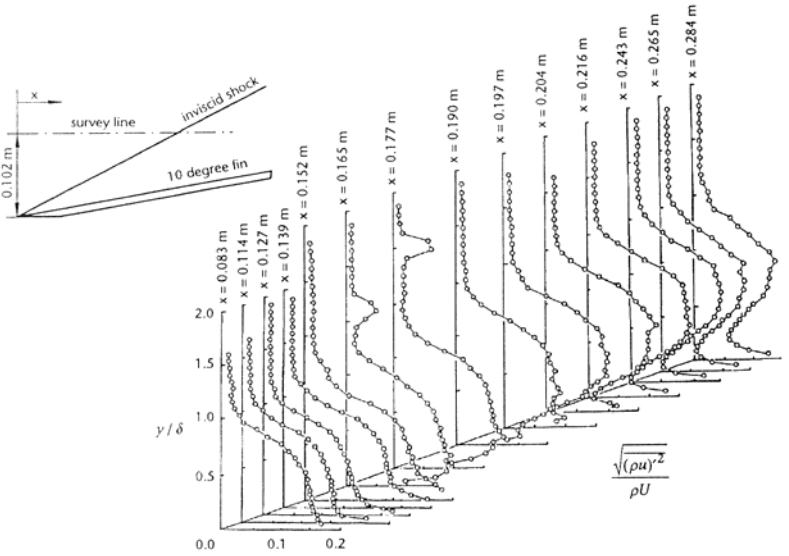

Figure 10.28. The evolution of the *rms* mass flux intensities for a 10° sharp-fin interaction at Mach 2.9. Data from Tran and Tan (unpublished). (Figure from Konrad (1993), with the author's permission.)

10.6.4 Blunt-Fin Interactions

When a boundary layer in supersonic flow encounters a blunt fin or another kind of cylindrical obstruction, the boundary layer typically separates at a distance of two or three fin diameters upstream of the leading edge. A vortical structure forms in the nature of a horseshoe vortex system, and the vortices are stretched as they wrap around the fin. Rayleigh scattering visualizations by Smith et al. (1991) on the centerline of the interaction produced very similar images to those seen in the sharp-fin visualizations: the movements of the separation shock and the triple point were clearly shown. The vortices generate strong pressure gradients, and combined with the usual unsteadiness of the flowfield, they produce intense pressure fluctuations (up to 184 dB near the root of the fin; Dolling (1990)). Away from the centerline the levels falloff, but not too rapidly, and the maximum level generally lies in the direction of the inviscid bow shock (see Figure 10.29).

The blunt fin produces a dimensional interaction, in that the diameter D of the rounded leading edge of the fin sets a length scale for the interaction. Generally, the scale of the interaction flowfield depends largely on D and only weakly on the incoming boundary layer thickness δ_0 (Dolling and Bogdonoff,

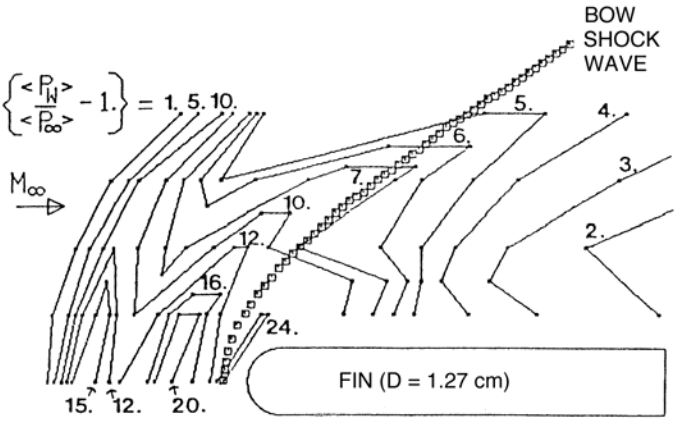

Figure 10.29. Blunt-fin interaction. (Figure from Dolling and Bogdonoff (1982). Copyright 1982, AIAA. Reprinted with permission.)

1982). For small values of D/δ_0, the separated flowfield is contained inside the boundary layer, but as this ratio increases the shock structure forms outside the layer, and as the diameter increases further, the interaction becomes independent of the boundary layer thickness. For example, the pressure fluctuation intensity near the point of separation on the centerline asymptotes to a constant value for $D/\delta_0 > 6$. The unsteadiness of the blunt fin interaction was discussed in Section 10.2.4. Further information can be found in the works by Gonsalez and Dolling (1993), Brusniak and Dolling (1994), Wang et al. (1998), Mukund et al. (2003), and Poggie and Smits (2005).

10.7 Crossing-Shock Interactions

Lastly, we briefly consider crossing-shock interactions, first studied by Mee et al. (1986). These interactions are formed when two sharp-fin shock generators are used so that the shocks cross (see Figure 10.30). The resulting interaction is a laboratory model for the interactions generated inside high-speed inlets, and it produces some interesting flow phenomena. In the symmetric case, where the two shocks are of equal strength, the flowfield is broadly as follows. The two vortical flows meet along the centerline, and they turn in the "streamwise" direction, that is, the direction corresponding to the upstream flow. Their induced velocity fields cause them to rise up, as well as transport fluid away from the wall in the region between them. The interaction size grows quickly with streamwise distance, and intense mixing appears to take place within the vortical regions. Farther downstream, depending on the

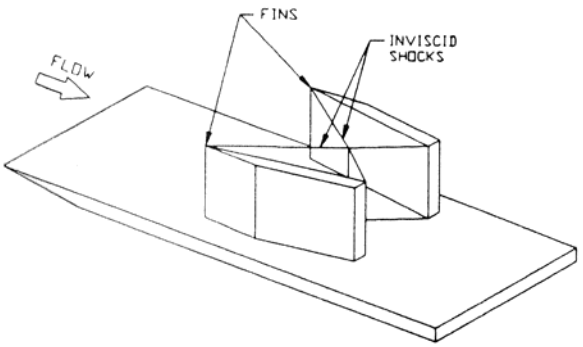

Figure 10.30. Crossing-shock interaction. (Figure from Garrison and Settles (1992). Copyright 1992, AIAA. Reprinted with permission.)

width of the passage, it is possible for each shock to reflect off its opposing fin, creating an additional interaction with the boundary layer on that fin. Flow visualizations using planar Mie scattering (Garrison and Settles, 1992) and filtered Rayleigh scattering (Forkey et al., 1993) reveal a complicated interaction structure that rapidly develops with streamwise distance. Computations have been very useful in revealing this structure, because the results presented by Narayanswami et al. (1993) and Garrison et al. (1993) indicate a high level of agreement between the computation and the experiment. Of course, the computations do not capture the flowfield unsteadiness, and preliminary measurements of the wall pressure fluctuations by Bogdonoff and Poddar (1991) show that crossing-shock interactions exhibit the same unsteadiness found in every other type of shock wave-boundary layer interaction.

10.8 Concluding Remarks

We have seen that all nondimensional interactions (swept and unswept compression corners, and sharp fins) behave similarly: there is the unsteady shock motion, the appearance of separated flow regions that are aligned with the inviscid shock direction, the presence of strong wall pressure fluctuations, and strongly amplified turbulence levels. As the three-dimensionality increases, the pressure fluctuation levels and the amplification of the turbulence decreases. A simple scaling on normal Mach number seems to be called for, but the database is not extensive enough to test this hypothesis fully. A common feature of three-dimensional interactions is the appearance of an impinging jet, where the skin friction, heat transfer, and pressure loading reach a maximum. The strength of the jet seems directly related to the strength of the pressure rise in the spanwise direction because this dictates the mass flux induced along

the axis of the vortical flow and the resulting transport of the low-momentum fluid near the wall.

By way of a final comment, we can make some remarks on the mechanism of the flowfield unsteadiness. As discussed earlier, the large-scale motions in the incoming boundary layer provide an unsteady upstream boundary condition on the separation shock. Conversely, the unsteady separated flow provides an unsteady downstream boundary condition. The wall pressure signal has low- and high-frequency content. As suggested by Brusniak and Dolling (1994), the incoming turbulence appears to be responsible for shock distortion and some small flapping motion, but it is not on a large scale. Its effect is most clearly seen in the wall pressure signals and the instantaneous flow visualizations of unseparated compression corner flows. When the flow is separated, the separation bubble unsteadiness can lead to larger excursions in the shock position, and the extent of the upstream influence seen in the mean pressure distribution grows considerably. There is still some question regarding the mechanism that drives the unsteadiness of the bubble. The free shear layer forming the edge of the bubble is undoubtedly very sensitive to external disturbances. These disturbances could come from, for instance, outer layer turbulence which may provide a trigger for a flowfield instability similar to that seen in the supersonic flow over a spiked body. It may also be possible that the low-frequency oscillations of the separation bubble are tunnel-specific, in that they are related to meandering Taylor-Görtler-like vortices formed in the upstream flow, convecting into the interaction, as suggested by Ünalmis and Dolling (1996).

The discussions in this chapter have noted that a shock depends on upstream and downstream conditions. We can tentatively propose two kinds of interactions and shock motion. The first kind is composed of flows with free downstream conditions, so that there would be only weak feedback from the downstream flow, and shock motion is determined mainly by the inflow. An example can be found in the shock-turbulence interaction experiment performed by Debiève and Lacharme (1985), in which homogeneous turbulence is subjected to an oblique shock. The second kind of flow is characterized by strong downstream constraints, such as compression ramp flows, flows around blunt obstacles, normal shock interactions, and oblique shock reflections. In such cases, separation bubbles are present that impose their own time and length scales as downstream conditions. For both kinds, we may speculate that transonic or subsonic downstream conditions would allow strong acoustic feedback, whereas supersonic outflow would reduce this effect to a narrow zone, enhancing the influence of fluctuations with a convective character, produced, for example, in the separated zone. The properties of the second kind of flow will depend, of course, on particular geometrical conditions, and should be analyzed for each particular case. Therefore, the onset and the properties of fluctuations in separated bubbles and their consequence on shock motions remains an open and challenging question.

References

Acarlar, M.S. and Smith, C.R. 1987a. A study of hairpin vortices in a laminar boundary layer. Part 1. Hairpin vortices generated by hemisphere protuberances. *Journal of Fluid Mechanics*, **175**, 1–41.

Acarlar, M.S. and Smith, C.R. 1987b. A study of hairpin vortices in a laminar boundary layer. Part 2. Hairpin vortices generated by fluid injection. *Journal of Fluid Mechanics*, **175**, 43–83.

Ackeret, J., Feldman, F. and Rott, N. 1946. Investigations of compression shocks and boundary layers in gases moving at high speed. *NASA TM 1113*.

Adams, N. 2000. Direct simulation of the turbulent boundary layer along a compression ramp at $M = 3$ and $Re_\theta = 1685$. *Journal of Fluid Mechanics*, **420**, 47–83.

Adamson, T.C. and Messiter, A.F. 1980. Analysis of two-dimensional interactions between shock waves and boundary layers. *Annual Review of Fluid Mechanics*, **12**, 103–138.

Adrian, R. J., Christensen, K. T., Soloff, S. M., Meinhart, C. D. and Liu, Z.-C. 1998. Decomposition of turbulent fields and visualization of vortices. 9th Int'l Symp. Applications of Laser Techniques to Fluid Mechanics, Lisbon.

Adrian, R.J., Meinhart, C.D. and Tomkins, C.D. 2000. Vortex organization in the outer region of the turbulent boundary layer. *Journal of Fluid Mechanics*, **422**, 1–54.

AGARD Fluid Dynamics Panel 1998. A selection of test cases for the validation of large-eddy simulations of turbulent flows. *AGARD AR 345*, Neuilly, France.

Agui, J., Briassulis, G. and Andreopoulos, Y. 2005. Studies of interactions of a propagating shock wave with decaying grid turbulence: Velocity and vorticity field. *Journal of Fluid Mechanics*, to appear.

Alem, D. 1995. *Analyse expérimentale d'une turbulence homogène en écoulement supersonique soumise à un choc droit*. Thèse de Doctorat, Université de Poitiers.

Alfredsson, P.H., Johansson, A.V., Haritonidis, J.H. and Eckelmann, H. 1988. The fluctuating wall shear stress and the velocity field in the viscous sublayer. *Physics of Fluids*, **31**, 1026–1033.

Alkislar, M. B., Krothapalli, A. and Lourenco, L. M. 2003. Structure of a screeching rectangular jet: A stereoscopic particle image velocimetry study. *Journal of Fluid Mechanics*, **489**, 121–154.

Alkislar, M.B., Lourenco, L.M. and Krothapalli, A. 2000. Stereoscopic PIV measurements of a screeching supersonic jet. *Journal of Visualization*, **3**, 2, 135–143.

Allen, J.M. 1977. Reevaluation of compressible flow Preston tube calibrations.

NASA TM X-3488.

Alving, A.E. and Smits, A.J. 1990. Correlation measurements and structure angles in a turbulent boundary layer recovering from convex curvature. *In:* Kline, S.J. and Afgan, N.H. (eds), *Near-Wall Turbulence*. Hemisphere.

Alving, A.E., Smits, A.J. and Watmuff, J.H. 1990. Turbulent boundary layer relaxation from convex curvature. *Journal of Fluid Mechanics*, **211**, 529–556.

Ames Research Staff. 1953. Equations, tables and charts for compressible flow. *NASA Report 1135*. Reprinted by TechPress Publishing Co., North Olmsted, Ohio, 1992.

Andreopoulos, Y., Agui, J.H. and Briassulis, G. 2000. Shock wave turbulence interactions. *Annual Review of Fluid Mechanics*, **32**, 309–345.

Antonia, R.A. 1981. Conditional sampling in turbulence measurement. *Annual Review of Fluid Mechanics*, **13**, 131–156.

Antonia, R.A. and Luxton, R.E. 1971. The response of a boundary layer to a step change in surface roughness. Part 1 – Smooth to rough. *Journal of Fluid Mechanics*, **48**, 721–761.

Antonia, R.A. and Luxton, R.E. 1972. The response of a boundary layer to a step change in surface roughness. Part 2 – Rough to smooth. *Journal of Fluid Mechanics*, **53**, 737–757.

Antonia, R.A., Bisset, D.K. and Browne, L.W.B. 1990a. Effect of Reynolds number on the topology of the organized motion in a turbulent boundary layer. *Journal of Fluid Mechanics*, **213**, 267–286.

Antonia, R.A., Browne, L.W.B. and Bisset, D.K. 1990b. Effect of Reynolds number on the organized motion in a turbulent boundary layer. *In:* Kline, S.J. and Afgan, N.H. (eds), *Near Wall Turbulence*. Hemisphere.

Anyiwo, J.C. and Bushnell, D.M. 1982. Turbulence amplification in shock wave boundary layer interactions. *AIAA Journal*, **20**, 893–899.

Ardonceau, P.L. 1984. The structure of turbulence in a supersonic shock-wave/boundary-layer interaction. *AIAA Journal*, **22**, 1254–1262.

Arzoumanian, E. and Debiève, J.F. 1990. Un processus programmé en anémométrie à fil chaud en écoulement supersonique. *L'Onde Electrique*, **70**, 54.

Aubry, N., Holmes, P. Lumley, J.L. and Stone, E. 1988. The dynamics of coherent structures in the wall region of a turbulent boundary layer. *Journal of Fluid Mechanics*, **192**, 115.

Audiffren, N. 1993. *Turbulence d'une couche limite soumise à une variation de densité due à une onde de choc ou à un chauffage pariétal*. Thèse d'Université, Université d'Aix-Marseille II.

Aupoix, B. 2001. Recherche de modèles de turbulence adaptés à la prévision des jets et couches de mélange. *RT 6/05284, DMAE, ONERA*, Toulouse.

Aupoix, B. 2002. Introduction to turbulence modelling for compressible flows. *VKI Lecture Series*, VKI, Rhodes St Genèse, Belgium.

Aupoix, B. 2004. Modelling of compressibility effects in mixing layers. *Journal of Turbulence*, **5**, 7.

Auvity, B., Etz, M.R. and Smits, A.J. 2001. Effects of transverse helium injection on hypersonic boundary layers. *Physics of Fluids*, **13**, 10, 3025–3032.

Bakewell, H.P. Jr. and Lumley, J.L. 1967. Viscous sublayer and adjacent wall region

in turbulent pipe flow. *The Physics of Fluids*, **10**.

Barre, S., Alem, D. and Bonnet, J.P. 1995. Experimental study of a normal shock/homogeneous turbulence interaction. *AIAA Paper 95-0579*.

Barre, S., Dupont, P. and Dussauge, J.P. 1992. Hot wire measurements in turbulent transonic flows. *European Journal of Mechanics B/Fluids*, **28**, 439–454.

Barre, S., Quine, C. and Dussauge, J.P. 1994. Compressibility effects on the structure of supersonic mixing layers: Experimental results. *Journal of Fluid Mechanics*, **259**, 47–78.

Batchelor, G.K. 1955. The effective pressure exerted by a gas in turbulent motion. *Vistas in Astronomy*, **1**.

Batchelor, G.K. 1967. *An Introduction to Fluid Dynamics*. Cambridge University Press.

Batchelor, G.K. and Proudman, I. 1954. The effect of rapid distortion of a fluid in turbulent motion. *Quarterly Journal of Mechanics and Applied Mathematics*, **7**, 83–103.

Baumgartner, M.L. 1997. Turbulence structure in a hypersonic boundary layer. Ph.D. Thesis, Princeton University.

Baumgartner, M.L., Erbland, P.J., Etz, M.R., Yalin, A., Muzas, B., Smits, A.J., Lempert, W.R. and Miles, R.B. 1997. Structure of a Mach 8 turbulent boundary layer. *AIAA Paper 97-0765*.

Beckwith, I.E., Creel, T.R., Chen, F.J. and Kendall, J.M. 1983. Freestream noise and transition measurements on a cone in a Mach 3.5 pilot low disturbance tunnel. *NASA TD 2180*.

Bell, J.H. and Mehta, R.D. 1990. Development of a two-stream mixing layer with tripped and untripped boundary layers. *AIAA Journal*, **28**, 2034–2042.

Bellaud, S. 1999. Mesures détaillées des champs turbulents en couches de mélange annulaires supersoniques. Thèse de Doctorat, Université de Poitiers.

Bellaud, S., Barre, S. and Bonnet, J.P. 1997. Obtention des composantes du tenseur de Reynolds dans une couche de mélange axisymétrique. *13ème Congrès Français de Mécanique, Poitiers, France*.

Beresh, S.J., Clemens, N.T., Dolling, D.S. 2002. Relationship between upstream turbulent boundary layer velocity fluctuations and separation shock unsteadiness. *AIAA Journal*, **40**, 12, 2412–2422.

Bernal, L.P. and Roshko, A. 1986. Streamwise vortex structure in plane mixing layers. *Journal of Fluid Mechanics*, **170**, 499–525.

Bernard, P.S. and Wallace, J.M. 1997. Vortex kinematics, dynamics, and turbulent momentum transport in wall bounded flows. *In: Self-Sustaining Mechanisms of Wall Turbulence.* Advances in Fluid Mechanics Series, **15**, 65–82. Computational Mechanics Publications, Southampton, UK and Boston, USA.

Bestion, D. 1982. *Méthodes anémomètriques par fil chaud: Application à l'étude d'interactions turbulence-gradient de pression élevé en couches limites à vitesse supersonique*. Thèse de Docteur-Ingénieur, Université d'Aix-Marseille II.

Bestion, D., Debiève, J.F. and Dussauge, J.P. 1983. Two rapid distortions in supersonic flows: Turbulence/shock wave and turbulence/expansion. *In:* Dumas, R. and Fulachier, L. (eds), *Structure of Complex Turbulent Shear Flow*. Springer Verlag.

Betchov, R. and Criminale, W.O. 1967. *Stability of Parallel Flows.* Academic Press.

Birch, S.F. and Eggers, J.M. 1972. A critical review of the experimental data for developed free turbulent shear layers. *NASA SP-321*, 11–40.

Blackwelder, R.F. and Haritonidis, J.H. 1983. Scaling of the bursting frequency in turbulent boundary layers. *Journal of Fluid Mechanics*, **132**, 87–104.

Blackwelder, R.F. and Kaplan, R.E. 1976. On the wall structure of the turbulent boundary layer. *Journal of Fluid Mechanics*, **76**, 89–112.

Blackwelder, R.F. and Kovasznay, L.S.G. 1972. Time scales and correlations in a turbulent boundary layer. *The Physics of Fluids*, **15**, 1545–1554.

Blaisdell, G.A., Mansour, N.N. and Reynolds, W.C. 1993. Compressibility effects on the growth and structure of homogeneous turbulent shear flow. *Journal of Fluid Mechanics*, **256**, 443–485.

Bogar, T.J., Sajben, M., Kroutil, J.C. 1983. Characteristic frequencies of transonic diffuser flow oscillations. *AIAA Journal*, **21**, 9, 1232–1240.

Bogard, D.G. and Tiederman, W.G. 1986. Burst detection with single-point velocity measurements. *Journal of Fluid Mechanics*, **162**, 389–414.

Bogard, D.G. and Tiederman, W.G. 1987. Characteristics of ejections in turbulent channel flow. *Journal of Fluid Mechanics*, **179**, 1–20.

Bogdanoff, D.W. 1983. Compressibility effects in turbulent shear layers. *AIAA Journal*, **21**, 926–927.

Bogdonoff, S.M. and Poddar, K. 1991. An exploratory study of a three-dimensional shock wave turbulent boundary layer interaction. *AIAA Paper 91-0525.*

Bonnet, J.P. 1988. Space-time correlations of wall-pressure fluctuations in shock-induced separated flows. *Physics of Fluids A*, **31**, 2821–2833.

Bonnet, J.P. and Alziary de Roquefort, T. 1980. Determination and optimization of frequency response of constant temperature hot-wire anemometers in supersonic flows. *Review of Scientific Instruments*, **51**, 234–239.

Bonnet, J.P. and Knani, M. 1986. Mesures par anémométrie à fil chaud incliné dans un sillage turbulent supersonique. *In: Proc. Colloque DRET–ONERA Écoulements Turbulents Compressibles.* DRET–ONERA, Poitiers, France.

Bonnet, J.P., Debisschop, J.R. and Chambres, O. 1993. Experimental studies of the turbulent structure of supersonic mixing layers. *AIAA Paper 93-0217.*

Bookey, P., Wu, M., Smits, A. J. and Martin, P. 2005a. New experimental data of STBLI at DNS/LES accessible Reynolds numbers. *AIAA Paper 2005-0309.*

Bookey, P. Wyckham, C. M. and Smits A. J. 2005b. Experimental Investigations of Mach 3 shock-wave turbulent boundary layer interactions. *AIAA Paper 2005-4899.*

Boris, J.P., Grinstein F.F., Oran E.S. and Kolbe R.L. 1992. New insights into large eddy simulation. *Fluid Dynamics Research*, **10**, 199.

Bourgoing, A. and Reijasse, P. 2001. Experimental analysis of unsteady separated flow in a planar nozzle. *In: Proceedings of the International Symposium on Shock Waves (ISSW 23).* The University of Texas Fort Worth, Texas.

Bradshaw, P. 1966. The effect of initial conditions on the development of a free shear layer. *Journal of Fluid Mechanics*, **26**, 225–236.

Bradshaw, P. 1967. 'Inactive' motion and pressure fluctuations in turbulent boundary layers. *Journal of Fluid Mechanics*, **30**, 241–258.

Bradshaw, P. 1973. Effects of streamline curvature on turbulent flow. *AGARDograph 169*.

Bradshaw, P. 1974. The effect of mean compression or dilatation on the turbulence structure of supersonic boundary layers. *Journal of Fluid Mechanics*, **63**, 449–464.

Bradshaw, P. 1977. Compressible turbulent shear layers. *Annual Review of Fluid Mechanics*, **9**, 33–54.

Bradshaw, P. 1994. Turbulence: The chief outstanding difficulty of our subject. *Experiments in Fluids*, **16**, 203–216.

Bradshaw, P. and Pontikos, A.S. 1985. Measurements in the turbulent boundary layer on an "infinite" swept wing. *Journal of Fluid Mechanics*, **159**, 105–130.

Bradshaw, P. and Unsworth, K. 1974. Comment on "Evaluation of Preston tube calibration equations in supersonic flow." *AIAA Journal*, **12**, 1293–1296.

Brown, G.L. and Roshko, A. 1974. On density effects and large structure in turbulent mixing layers. *Journal of Fluid Mechanics*, **64**, 775–816.

Brown, G.L. and Thomas, A.S.W. 1977. Large structure in a turbulent boundary layer. *The Physics of Fluids*, **20**, S243–S252.

Browne, L.W.B., Antonia, R.A. and Shah, D.A. 1988. Selection of wires and wire spacing for X-wires. *Experiments in Fluids*, **6**, 286–288.

Bruns, J., Dengel, P. and Fernholz, H.H. 1992. Mean flow and turbulence measurements in an incompressible two-dimensional turbulent boundary layer. Part I: Data. *Institutsbericht Nr. 02/92, Hermann-Föttinger-Institut für Thermo- und Fluiddynamik, Technische Universität Berlin.*

Brusniak, L. and Dolling, D.S. 1994. Physics of unsteady blunt-fin-induced shock wave/turbulent boundary layer interactions. *Journal of Fluid Mechanics*, **273**, 375–409.

Busemann, A. 1931. *Handbuch der Physik.* Vol. 4. Geest und Portig, Leipzig.

Bushnell, D.M., Cary, Jr., A.M. and Harris, J.E. 1976. Calculation methods for compressible turbulent boundary layers. State of the art. *NASA SP-422.*

Bushnell, D.M., Johnson, C.B., Harvey, W.D. and Feller, W.V. 1969. Comparison of prediction methods and studies of relaxation in hypersonic turbulent nozzle-wall boundary layers. *NASA TN D-5433.*

Cambon, C. 1982. *Étude spectrale d'un champ turbulent incompressible soumis à des effets couples de deformation et de rotation.* Thèse de Doctorat d'Etat, Université Claude Bernard, Lyon.

Cantwell, B.J. 1981. Organized motion in turbulent flow. *Annual Review of Fluid Mechanics*, **13**, 457–515.

Cantwell, B.J., Coles, D. and Dimotakis, P. 1978 Structure and entrainment in the plane of symmetry of a turbulent spot. *Journal of Fluid Mechanics*, **87**, 641–672.

Carvin, C., Debiève, J.F. and Smits, A.J. 1988. The near-wall temperature profile of turbulent boundary layers. *AIAA Paper 88-0136.*

Castillo, L. and George, W.K. 2000. Boundary layers with pressure gradient: Similarity of the velocity deficit region. *AIAA Paper 2000-0913.*

Catris, S. and Aupoix, B. 2000. Density corrections for turbulence models. *Aerospace Science and Technology*, **4**, 1–11.

Cebeci, T. and Bradshaw, P. 1977. *Momentum Transfer in Boundary Layers*. Hemisphere.

Cebeci, T. and Bradshaw, P. 1984. *Physical and Computational Aspects of Convective Heat Transfer*. Springer-Verlag.

Cebeci, T. and Smith, A.M.O. 1974. *Analysis of Turbulent Boundary Layers*. Academic Press.

Chambres, O., Barre, S. and Bonnnet, J.P. 1997. Flows with density variations and compressibility: Similarities and differences. *Pages 279–302 of:* Fulachier, L., Lumley, J.L., and Anselmet, F. (eds), *IUTAM Symposium on Variable Density Low-Speed Turbulent Flows, Marseille, France*. Kluwer. *Fluid Mech. and its Applications*, **12**.

Chapman, D.R., Kuehn, D.M. and Larson, H.K. 1957. Investigation of separated flows in supersonic and subsonic streams with emphasis on the effect of transition. *NASA TN 3869*. Also NACA Rep. 1356, 1958.

Chassaing, P., Antonia, R.A., Anselmet, F., Joly, L. and Sarkar, S. 2002. *Variable Density Fluid Turbulence*. Kluwer Academic Publishers.

Chen, C.P., Sajben, M., Kroutil, J.C. 1979. Shock-wave oscillations in atransonic diffuser flow. *AIAA Journal*, **17**, 10, 1076–1083.

Chen, J.H. 1991. The effect of compressibility on conserved scalar entrainment in a plane free shear layer. *In: Proceedings of the Eighth Symposium on Turbulent Shear Flows*. Technical University of Munich.

Chinzei, N., Masuya, G., Komuro, T., Murakami, A. and Kudou, K. 1986. Spreading of two stream supersonic turbulent mixing layer. *The Physics of Fluids*, **29**, 1345–1347.

Christensen, K.T. and Adrian, R.J. 2001. Statistical evidence of hairpin vortex packets in wall turbulence. *Journal of Fluid Mechanics*, **431**, 433–443.

Chu, B.T. and Kovasznay, L.S.G. 1958. Non-linear interactions in a viscous heat-conducting compressible gas. *Journal of Fluid Mechanics*, **3**, 494–514.

Clauser, F.H. 1954. Turbulent boundary layers in adverse pressure gradients. *Journal of the Aeronautical Sciences*, **21**, 91–108.

Clauser, F.H. 1956. The turbulent boundary layer. *In: Advances in Applied Mechanics*, **4**. Academic Press.

Clemens, N.T. and Mungal, M.G. 1991. A planar Mie scattering technique for visualizing supersonic mixing layers. *Experiments in Fluids*, **11**, 175–185.

Clemens, N.T. and Mungal, M.G. 1992a. Two- and three-dimensional effects in the supersonic mixing layer. *AIAA Journal*, **30**, 973–981.

Clemens, N.T. and Mungal, M.G. 1992b. Effects of sidewall disturbances on the supersonic mixing layer. *Journal of Propulsion and Power*, **8**, 249–251.

Clemens, N.T. and Mungal, M.G. 1995. Large-scale structure and entrainment in the supersonic mixing layer. *Journal of Fluid Mechanics*, **284**, 171–216.

Cogne, S., Forkey, J., Miles, R.B. and Smits, A.J. 1993. The evolution of large-scale structures in a supersonic turbulent boundary layer. *In:* Stock, D.E., Smits, A.J. and Sheriff, S.A. (eds), *Proc. of the Symposium on Transitional and Turbulent Compressible Flows*. ASME Fluids Engineering Division.

Coleman, G.N., Kim, J. and Moser, R.D. 1995. A numerical study of turbulent supersonic isothermal-wall channel flow. *Journal of Fluid Mechanics*, **305**, 159–

183.
Coles, D. 1953. Measurements in the boundary layer on a smooth flat plate in supersonic flow. *J.P.L. CalTech Reports 20-69, 20-70, 20-71.*
Coles, D. 1956. The law of the wake in the turbulent boundary layer. *Journal of Fluid Mechanics*, **1**, 191–226.
Coles, D. 1962. The turbulent boundary layer in a compressible fluid. *Report R-403-PR, The Rand Corporation, Santa Monica, California.*
Coles, D. 1987. Coherent structures in turbulent boundary layers. *Pages 93–113 of:* Meier, H.U. and Bradshaw, P. (eds), *Perspectives in Turbulence Studies.* Springer-Verlag.
Collin, C. 2001. Etude de l'injection radiale de fluide dans une couche de mélange annulaire supersonique. Application à l'augmentation du mélange. Thèse de Doctorat, Université de Poitiers.
Corcos, G.M. 1963. The structure of the turbulent pressure field in boundary-layer flows. *Journal of Fluid Mechanics*, **18**, 353–378.
Corcos, G.M. and Sherman, F.S. 1976. Vorticity concentration and the dynamics of unstable free shear layers. *Journal of Fluid Mechanics*, **73**, 241–264.
Corino, E.R. and Brodkey, R.S. 1969. A visual investigation of the wall region in turbulent flow. *Journal of Fluid Mechanics*, **37**, 1–30.
Corrsin, S. and Kistler, A.L. 1955. Free-stream boundaries of turbulent flows. *NACA Report 1244.*
Cousteix, J. 1989. *Turbulence et Couches Limites.* Cépaduès-Éditions, Toulouse.
Cousteix, J. 1996. Private communication.
Crocco, L. 1932. Sulla trasmissione del calore da una lamina piana a un fluido scorrente ad alta velocita. *L'Aerotecnica*, **12**, 181–197. Translated as NACA TM 690.
Culick, F.E.C. and Rogers, T. 1983. The response of normal shocks in diffusers. *AIAA Journal*, **21**, 10, 1382–1390.
Currie, I.G. 1974. *Fundamental Mechanics of Fluids.* McGraw-Hill.
Daghsstani, K. 1993. *Rôle des fluctuations de pression dans les interactions onde de choc/couche-limite.* Thèse de Doctorat, Université de Poitiers.
Davis, M.R. and Davies, P.O.A.L. 1972. Factors influencing the heat transfer from cylindrical anemometer probes. *International Journal of Heat Mass Transfer*, **15**, 1659–1677.
Day, M.J., Reynolds, W.C. and Mansour, N.N. 1998. The structure of the compressible reacting mixing layer: Insights from linear stability analysis. *Physics of Fluids*, **10**, 993–1007.
Debiève, J.F. 1983. *Étude d'une interaction turbulence/onde de choc.* Thèse de Doctorat d'État, Université d'Aix-Marseille II.
Debiève, J.F. 1986. Problèmes de distortion rapide en écoulement compressible. *In: Proc. Colloque DRET–ONERA Écoulements Turbulents Compressibles.* DRET–ONERA, Poitiers, France.
Debiève, J.F. and Lacharme, J.P. 1985. A shock wave/free turbulence interaction. *In:* Délery, J. (ed), *Turbulent Shear-Layer/Shock-Wave Interactions.* Springer Verlag.
Debiève, J.F., Dupont, P., Laurent, H., Menaa, M. and Dussauge J.P. 2000. Com-

pressibility and structure of turbulence in supersonic shear flows. *European Journal of Mechanics B: Fluids*, **19**, 673–694.

Debiève, J.F., Dupont, P., Smith, D.R. and Smits, A.J. 1997. *The response of a supersonic turbulent boundary layer to a step change in wall temperature. AIAA Journal*, **35**, 51–57.

Debiève, J.F., Gouin, H. and Gaviglio, J. 1981. Momentum and temperature fluxes in a shock wave-turbulence interaction. *In: Proc. ICHM/IUTAM Symp. Structure of Turbulence and Heat and Mass Transfer*, Dubrovnik.

Debiève, J.F., Gouin, H. and Gaviglio, J. 1982. Evolution of the Reynolds stress tensor in a shock-turbulence interaction. *Indian Journal of Technology*, **20**, 90–97.

Debisschopp, J.R., Chambres, O. and Bonnet, J.P. 1994. Compressibility and structure of turbulence in supersonic shear flows. *Experimental Thermal and Fluid Science*, **9**, 147–155.

de Brederode, V. and Bradshaw, P. 1974. A note on the empirical constants appearing in the logarithmic law for turbulent wall flows. *I.C. Aero Report 74-03*. Imperial College, London.

Degani, D. and Smits, A.J. 1990. Effect of short regions of surface curvature on compressible turbulent boundary layers. *AIAA Journal*, **28**, 113–119.

DeGraaff, D.B. and Eaton, J.K. 2000. Reynolds number scaling of the flat plate boundary layer. *Journal of Fluid Mechanics*, **422**, 319–346.

Délery, J.M. 1985. Shock wave/turbulent boundary-layer interaction and its control. *Progress in Aerospace Sciences*, **22**, 209–280.

Délery, J.M. 1992. Étude expérimentale de la réflexion d'une onde de choc sur une paroi chauffée en présence d'une couche limite turbulente. *La Recherche Aérospatiale*, **1**, 1–23.

Délery, J.M. and Marvin, J.G. 1986. Shock-wave boundary layer interactions. *AGARDograph 280*.

Deleuze, J. and Eléna, M. 1995. Quelques caractéristiques de la turbulence en aval d'une interaction onde de choc couche limite. *12ème Congrès Français de Mécanique, Strasbourg, France*.

Delo, C.J. and Smits, A.J. 1997. Volumetric visualization of coherent structure in a low Reynolds number turbulent boundary layer. *International Journal of Fluid Dynamics*, **1**.

Delo, C.J., Kelso, R.M. and Smits, A.J. 2004. Three-dimensional structure of a low Reynolds number turbulent boundary layer. *Journal of Fluid Mechanics*, **512**, 47–83.

Demetriades, A. and Martindale, W.R. 1983. Determination of one dimensional spectra in high speed boundary layers. *The Physics of Fluids*, **26**, 397–403.

Demetriades, A. and McCullough, G. 1985. Mean-flow measurements in a supersonic three-dimensional turbulent boundary layer. *Journal of Fluid Mechanics*, **156**, 401–418.

Dimotakis, P.E. 1991. Turbulent free shear layer mixing and combustion. *In:* Murthy and Curran (eds), *Progress in Astronautics and Aeronautics, Vol. 137*. AIAA, Washington DC.

Doerffer, P. and Szwaba, R. 2004. Shock wave/ boundary layer interaction control

by streamwise vortices. *In: Proceedings of ICTAM XXI.* Warsaw, Poland.

Dolling, D.S. 1990. Unsteady phenomena in shock wave/boundary layer interaction. *Pages 4.1–4.46 of: Special Course on Shock Wave/Boundary Layer Interactions in Supersonic and Hypersonic Flows.* AGARD Report 792.

Dolling, D.S. 1993. Fluctuating loads in shock wave/turbulent boundary layer interaction: Tutorial and update. *AIAA Paper 93-0284.*

Dolling, D.S. 2001. Fifty years of shock wave/boundary layer interaction research: What next? *AIAA Journal*, **39**, 8, 1517–1531.

Dolling, D.S. and Bogdonoff, S.M. 1982. Blunt fin-induced shock wave turbulent boundary layer interaction. *AIAA Journal*, **20**, 1674–1680.

Dolling, D.S. and Dussauge, J.P. 1989. Fluctuating wall pressure measurements. *Chapter 8, AGARDograph 315.*

Dolling, D.S. and Murphy, M.T. 1983. Unsteadiness of the separation shock wave structure in a supersonic compressible ramp flowfield. *AIAA Journal*, **21**, 1628–1634.

Dolling, D.S. and Smith, D.R. 1989. Unsteady shock-induced separation in Mach 5 cylinder interactions. *AIAA Journal*, **27**, 12, 1598–1706.

Donovan, J.F. 1989. *The structure of supersonic turbulent boundary layers subjected to concave surface curvature.* Ph.D. Thesis, Princeton University, Princeton, NJ.

Donovan, J.F., Spina, E.F. and Smits, A.J. 1994. The structure of a supersonic turbulent boundary layer subjected to concave surface curvature. *Journal of Fluid Mechanics*, **259**, 1–24.

Dorrance, W.H. 1962. *Viscous Hypersonic Flow.* McGraw-Hill.

Duck, P.W., Lasseigne, D.G. and Hussaini, M.Y. 1993. On the interaction between the shock wave attached to a wedge and freestream disturbances. *ICASE Report No. 93-61, NASA Langley Research Center, Hampton, Virginia.*

Duncan, W.J., Thom, A.S. and Young, A.D. 1970. *Mechanics of Fluids.* 2 edn. Edward Arnold.

Dupont, P. and Debiève, J.F. 1992. A hot wire method for measuring turbulence in transonic and supersonic heated flows. *Experiments in Fluids*, **13**, 84–90.

Dupont, P., Haddad, C. and Debiève, J.F. 2006. Space and time organization in a shock-induced separation. *IUSTI, UMR CNRS-Université de Provence Report No. 6595.*

Dupont, P., Muscat, P. and Dussauge, J.P. 1995. Space and space-time statistics in a supersonic mixing layer. *In: Symposium on Transitional and Turbulent Compressible Flows, ASME Fluids Engineering Conference, Hilton Head Island, SC.*

Dupont, P., Muscat, P. and Dussauge, J.P. 1999. Localisation of large scale structures in a supersonic mixing layer: A new method and first analysis. *Turbulence and Combustion*, **62**, 335–358.

Durbin, P.A. and Zeman, O. 1992. Rapid distortion theory for homogeneous compressed turbulence with application to modelling. *Journal of Fluid Mechanics*, **242**, 349–370.

Dussauge, J.P. 1981. *Évolution de transferts turbulents dans une détente rapide, en écoulement supersonique.* Thèse de Doctorat d'État, Université d'Aix Marseille.

Dussauge, J.P. 1986. Rapport Convention. *ONERA/IMST 20.352/SAT/CDC.*

Dussauge, J.P. and Dupont, P. 1995. Experimental evidences of compressibility on turbulence in high speed flows. *Symposium on Transitional and Turbulent Compressible Flows, ASME Fluids Engineering Conference, Hilton Head Island, SC.*

Dussauge, J.P. and Gaviglio, J. 1987. The rapid expansion of a supersonic turbulent flow: Role of bulk dilatation. *Journal of Fluid Mechanics*, **174**, 81–112.

Dussauge, J.P. and Smits, A.J. 1995. Characteristic scales for energetic eddies in turbulent supersonic boundary layers. *In: Proceedings of the Tenth Symposium on Turbulent Shear Flows.* Pennsylvania State University.

Dussauge, J.P., Debiève, J.F. and Smits, A.J. 1989. Rapidly distorted compressible boundary-layers. *Chapter 2, AGARDograph 315.*

Dussauge, J.P., Dupont, P., and Debiève, J.F. 2005. Unsteadiness in shock wave boundary layer interactions with separation. *In: AAAF 40th Colloquium on Applied Aerodynamics.* Toulouse, March 21-23.

Dussauge, J.P., Fernholz, H., Finley, P.J., Smith, R.W., Smits, A.J. and Spina, E.F. 1996. Turbulent boundary layers in subsonic and supersonic flow. *AGARDograph 335.*

Dutton, J.C., Burr, R.F., Goebel, S.G. and Messersmith, N.L. 1990. Compressibility and mixing in turbulent free shear layers. *In: Proceedings of the Twelfth Biennial Symposium on Turbulence.*

El Baz, A.M. and Launder, B.E. 1994. Second-moment modelling of compressible mixing layers. *In:* Rodi, W. and Martelli, M. (eds), *Engineering Turbulence Modelling and Experiments 2.*

Eléna, M. 1989. Laser Doppler anemometry in supersonic flows: Problems of seeding and angular bias. *Chapter 7, AGARDograph 315.*

Eléna, M. and Gaviglio, J. 1993. La couche limite turbulente compressible: Méthodes d'étude et résultats, synthèse. *La Recherche Aérospatiale*, 1–21.

Eléna, M. and Lacharme, J.P. 1988. Experimental study of a supersonic turbulent boundary layer using a laser Doppler anemometer. *Journal Mécanique Théorique et Appliquée*, **7**, 175–190.

Eléna, M., Lacharme, J.P. and Gaviglio, J. 1985. Comparison of hot-wire and laser Doppler anemometry methods in supersonic turbulent boundary layers. *In:* Dybb, A. and Pfund, P.A. (eds), *International Symposium on Laser Anemometry.* ASME.

Elliott, G.S. and Samimy, M. 1990. Compressibility effects in free shear layers. *Physics of Fluids A*, **2**, 1231–1240.

Erbland, P.J. 2000. *Development and application of carbon dioxide enhanced Filtered Rayleigh Scattering for high speed low density flows.* Ph.D. Thesis, Princeton University.

Erengil, M.E. and Dolling, D.S. 1991. Unsteady wave structure near separation in a Mach 5 compression ramp interaction. *AIAA Journal*, **29**, 5, 728–735.

Erengil, M.E. and Dolling, D.S. 1992. Effects of sweepback on unsteady separation in Mach 5 compression ramp interactions. *AIAA Journal*, **31**, 302–311.

Erengil, M.E. and Dolling, D.S. 1993. Physical causes of separation shock unsteadiness in shock wave/turbulent boundary layer interactions. *AIAA Paper 93-3134.*

Erm, L.P. 1988. *Low-Reynolds-number turbulent boundary layers.* Ph.D. Thesis, University of Melbourne.

Erm, L.P. and Joubert, P.N. 1991. Low-Reynolds-number turbulent boundary layers. *Journal of Fluid Mechanics*, **230**, 1–44.

Erm, L.P., Joubert, P.N. and Spalart, P.R. 1994. *Low-Reynolds-number turbulent boundary layers: Experimental data compared with numerical simulations.* Unpublished report.

Erm, L.P., Smits, A.J. and Joubert, P.N. 1985. Low Reynolds number turbulent boundary layers on a smooth flat surface in a zero pressure gradient. *In: Proceedings of the Fifth Symposium on Turbulent Shear Flows.* Cornell University.

Evans, T.T. and Smits, A.J. 1996. Measurements of the mean heat transfer in a shock wave-turbulent boundary layer interaction. *Experimental Thermal and Fluid Science*, **12**, 87–97.

Evans, T.T., Poddar, K. and Smits, A.J. 1990. Compilation of wall pressure data for a shock wave boundary layer interaction generated by a blunt fin. *MAE Report 1908 T, Department of Mechanical and Aerospace Engineering, Princeton University.*

Ewing, D., Hussein, H.J. and George, W.K. 1995. Spatial resolution of parallel hot-wire probes for derivative measurements. *Experimental Thermal and Fluid Science*, **11**, 155–173.

Falco, R.E. 1977. Coherent motions in the outer region of turbulent boundary layers. *The Physics of Fluids*, **20**, S124–S132.

Falco, R.E. 1991. A coherent structure model of the turbulent boundary layer and its ability to predict Reynolds number dependence. *In:* Walker, J.D.A. (ed), *Turbulent Flow Structure Near Walls.* The Royal Society. First published in *Phil. Trans. R. Soc. London A*, 1991, **336**, 35–65.

Fauchet, G. 1998. *Modélisation en deux points de la turbulence isotrope compressible et validation à l'aide de simulations numériques.* Thèse de Doctorat, Université Claude Bernard-Lyon I, Lyon.

Fauchet, G. and Bertoglio, J.P. 1998. An analytical expression for the spectrum of compressible turbulence in the low Mach number limit. *Pages 317–332 of:* Frisch, U. (ed), *Advances in Turbulence VII, Proc. of the 7th European Turb. Conf., St Jean Cap Ferrat, France.* Kluwer. *Fluid Mech. and its Applications*, **46**.

Fauchet, G. and Bertoglio, J.P. 1999. Régimes pseudo-son et acoustique en turbulence compressible. *C.R. Acad. Sc. Paris*, **327**, Série Ib, 665–671.

Favre, A. 1965. Equations des gaz turbulents compressibles. *Journal de Mécanique*, **4**, 361–421.

Favre, A. 1976. Équations fondamentales des fluides à masse volumique variable en écoulements turbulents. *Pages 24–78 of:* Favre, A., Kovasznay, L.S.G., Dumas, R., Gaviglio, J. and Coantic, M. (eds), *La Turbulence en Mécanique des Fluides.* CNRS.

Favre, A., Gaviglio, J. and Dumas, R. 1967. Structure of space-time correlations in a boundary layer. *The Physics of Fluids*, **10**, S138–S145.

Favre, A.J., Gaviglio, J.J. and Dumas, R.J. 1957. Space-time double correlations and spectra in a turbulent boundary layer. *Journal of Fluid Mechanics*, **2**,

313–342.

Favre, A.J., Gaviglio, J.J. and Dumas, R.J. 1958. Further space-time correlations of velocity in a turbulent boundary layer. *Journal of Fluid Mechanics*, **3**, 344–356.

Fernando, E.M. and Smits, A.J. 1990. A supersonic turbulent boundary layer in an adverse pressure gradient. *Journal of Fluid Mechanics*, **211**, 285–307.

Fernholz, H.H. 1969. Geschwindigkeitsprofile, Temperaturprofile und halbempirische Gesetze in kompressiblen turbulenten Grenzschichten bei konstantem Druck. *Ing. Archiv*, **38**, 311–328.

Fernholz, H.H. 1971. Ein halbempirisches Gesetz für die Wandreibung in kompressiblen turbulenten Grenzschichten bei isothermer und adiabater Wand. *ZAMM*, **51**, T148–T149.

Fernholz, H.H. and Finley, P.J. 1976. A critical compilation of compressible turbulent boundary layer data. *AGARDograph 223*.

Fernholz, H.H. and Finley, P.J. 1980. A critical commentary on mean flow data for two-dimensional compressible turbulent boundary layers. *AGARDograph 253*.

Fernholz, H.H. and Finley, P.J. 1981. A further compilation of compressible turbulent boundary layer data with a survey of turbulence data. *AGARDograph 263*.

Fernholz, H.H. and Finley, P.J. 1996. Incompressible zero-pressure-gradient turbulent boundary layers: An assessment of the data. *Progress in Aerospace Sciences*, **32**.

Fernholz, H.H., Krause, E., Nockemann, N. and Schober, M. 1995. Comparative measurements in the canonical boundary layer at $Re_{\delta_2} \leq 6\text{x}10^4$ on the wall of the German-Dutch windtunnel. *The Physics of Fluids*, **7**, 1275–1281.

Fernholz, H.H., Smits, A.J., Dussauge, J.P. and Finley, P.J. 1989. A survey of measurements and measuring techniques in rapidly distorted compressible turbulent boundary layers. *AGARDograph 315*.

Finley, P.J. 1977. Static pressure in hypersonic nozzle boundary layers. *AIAA Journal*, **15**, 878–881.

Finley, P.J. 1994. The Preston tube in adiabatic compressible flow. *Report 94-02, Imperial College of Science and Technology, Department of Aeronautics*.

Finley, P.J. and Gaudet, L. 1995. The Preston tube in adiabatic compressible flow. *Experiments in Fluids*, **19**, 2, 133–135.

Forkey, J.N., Cogne, S., Smits, A.J., Bogdonoff, S.M., Lempert, W.R. and Miles, R.B. 1993. Time-sequenced and spectrally filtered Rayleigh imaging of shock wave and boundary layer structure for inlet characterization. *AIAA Paper 93-2300*.

Forkey, J.N., Finkelstein, N.D., Lempert, W.R. and Miles, R.B. 1996. Demonstration and characterization of filtered Rayleigh scattering for planar velocity measurements. *AIAA Journal*, **34**, 442–448.

Forkey, J.N., Lempert, W.R., Bogdonoff, S.M. and Miles, R.B. 1994. Volumetric imaging of supersonic boundary layers using filtered Rayleigh scattering background suppression. *AIAA Paper 94-0491*.

Fouillet, Y. 1991. *Contribution à l'étude par expèrimentation numérique des écoulements cisaillés libres: Effets de compressibilité*. Thèse de l'I.N.P., Université de Grenoble.

Freund, J.B., Lele, S.K. and Moin, P. 2000. Compressibility effects in a turbulent annular mixing layer. Part 1. Turbulence and growth rate. *Journal of Fluid Mechanics*, **421**, 229–267.

Fulachier, L. 1972. *Contribution à l'étude des analogies des champs dynamiques et thermiques dans une couche limite turbulente. Effet de l'aspiration.* Thèse de Doctorat ès Sciences Physiques, Université de Provence, Aix-Marseille.

Gad-el-Hak, M. and Bandyopadhyay, P. 1994. Reynolds number effects in wall-bounded flows. *Applied Mechanics Reviews*, **47**.

Garg, S. and Settles, G.S. 1993. Wall pressure fluctuations beneath swept shock/boundary layer interactions. *AIAA Paper 93-0384.*

Garg, S. and Settles, G.S. 1998. Measurements of a supersonic turbulent boundary layer by focusing schlieren deflectometry. *Experiments in Fluids*, **25**, 254–264.

Garnier, E., Sagaut, P. and Deville, M. 2002. Large eddy simulation of shock/boundary layer interaction. *AIAA Journal*, **40**, 1935–1944.

Garrison, T.J. and Settles, G.S. 1992. Flowfield visualization of crossing shock-wave/boundary layer interactions. *AIAA Paper 92-0750.*

Garrison, T.J., Settles, G.S., Narayanswami, N. and Knight, D.D. 1993. Structure of crossing shock-wave/turbulent boundary layer interactions. *AIAA Journal*, **31**, 2204–2211.

Gaviglio, J. 1976. La turbulence dans les écoulements compressibles des gaz. *Pages 232–297 of:* Favre, A., Kovasznay, L.S.G., Dumas, R., Gaviglio, J. and Coantic, M. (eds), *La Turbulence en Mécanique des Fluides.* CNRS.

Gaviglio, J. 1978. Sur les méthodes de l'anémométrie par fil chaud des écoulements turbulents compressibles de gaz. *Journal de Mécanique Appliqueé*, **2**, 449–498.

Gaviglio, J. 1987. Reynolds analogies and experimental study of heat transfer in the supersonic boundary layer. *International Journal of Heat and Mass Transfer*, **30**, 911–926.

Gaviglio, J., Anguillet, J.P. and Eléna, M. 1981. On the application of hot-wire anemometry to the solution of problems arising in variable temperature turbulent flows. *Recherche Aerospatial*, **1**, 59–66.

George, W.K., Knecht, P. and Castillo, L. 1992. The zero-pressure gradient turbulent boundary layer revisited. *In: Proceedings of the Thirteenth Biennial Symposium on Turbulence.*

Gibson, B.G. and Dolling, D.S. 1991. Wall pressure fluctuations near separation in a Mach 5, sharp fin-induced turbulent interaction. *AIAA Paper 91-0646.*

Ginoux, J.J. 1971. Streamwise vortices in reattaching high-speed flows: A suggested approach. *AIAA Journal*, **9**, 759–760.

Goebel, S.G. and Dutton, J.C. 1990. An experimental investigation of compressible, turbulent mixing layers. *Department of Mechanical and Industrial Engineering, University of Illinois at Urbana-Champaign, Technical Report ENG 90-4005.*

Goldstein, J.E. and Smits, A.J. 1994. Flow visualization of the three-dimensional, time-evolving structure of a turbulent boundary layer. *Physics of Fluids*, **6** (2).

Goldstein, M.E. 1978. Unsteady vortical and entropic distortions of potential flows round arbitrary obstacles. *Journal of Fluid Mechanics*, **89**, 433–468.

Goldstein, M.E. 1979. Turbulence generated by the interaction of entropy fluctuations with non-uniform mean flows. *Journal of Fluid Mechanics*, **93**, 209–224.

Goldstein, S. 1938. Note on the conditions at the surface of contact of a fluid with a solid body. *In: Modern Developments in Fluid Dynamics.* Clarendon Press, Oxford. Compiled by the Fluid Motion Panel of the Aeronautical Research Committee and Others, edited by S. Goldstein. Dover edition, 1965.

Gonsalez, J.C. and Dolling, D.S. 1993. Correlation of interaction sweepback effects on the dynamics of shock-induced turbulent separation. *AIAA Paper 93-0776.*

Gramann, R.A. and Dolling, D.S. 1990. Detection of turbulent boundary layer separation using fluctuating wall pressure signals. *AIAA Journal*, **28**, 1052.

Gramann, R.A. and Dolling, D.S. 1992. A preliminary study of turbulent structures associated with unsteady separation shock motion in a Mach 5 compression ramp interaction. *AIAA Paper 92-0744.*

Grant, H.L., Stewart, R.W. and Moilliet, A. 1962. Turbulence spectra from a tidal channel. *Journal of Fluid Mechanics*, **12**, 241–268.

Green, J.E. 1970. Interaction between shock waves and turbulent boundary layers. *Progress in Aerospace Sciences*, **11**, 235–340.

Guarini, S.E., Moser, R.D. and Shariff, K. 2000. Direct numerical simulation of supersonic turbulent boundary layers at Mach 2.5. *Journal of Fluid Mechanics*, **414**, 1–33.

Guézengar, D., Francescatto, J., Guillard, H. and Dussauge, J.P. 1999. Variations on a k-ϵ model for supersonic boundary layer computations. *European Journal of Mechanics B/Fluids*, **18**, 713–738.

Guézengar, D., Guillard, H. and Dussauge, J.P. 2000. Modelling the dissipation equation in supersonic turbulent mixing layers with high density gradients. *AIAA Journal*, **38**, 1650–1655.

Haddad, C. 2005. *Instationnarités, mouvements d'onde de choc et tourbillons à grandes échelles dans une interaction onde de choc/couche limite avec décollement.* Thèse de Doctorat en Mécanique-Energétique, Université de Provence, Marseille, France.

Hall, J.L. 1991. *An experimental investigation of structure, mixing and combustion in compressible turbulent shear layers.* Ph.D. Thesis, California Institute of Technology, Pasadena, CA.

Hall, M.G. 1965. Experimental measurements in a three-dimensional turbulent boundary layer in supersonic flow. *In: AGARDograph 97.*

Hanjalić, K. and Launder, B.E. 1972. Fully developed asymmetric flow in a plane channel. *Journal of Fluid Mechanics*, **51**, 301–335.

Hanratty, T.J. and Papavassiliou, D.V. 1997. The role of wall vortices in producing turbulence. *In: Self-Sustaining Mechanisms of Wall Turbulence.* Advances in Fluid Mechanics Series, **15**, 83–108. Computational Mechanics Publications, Southampton, UK and Boston, USA.

Hayakawa, K., Smits, A.J. and Bogdonoff, S.M. 1983. Turbulence measurements in two shock-wave/shear-layer interactions. *In:* Dumas, R. and Fulachier, L. (eds), *Structure of Complex Turbulent Shear Flow.* Springer Verlag.

Hayakawa, K., Smits, A.J. and Bogdonoff, S.M. 1984. Turbulence measurements in a compressible reattaching shear layer. *AIAA Journal*, **22**, 889–895.

Head, M.R. and Bandyopadhyay, P.R. 1981. New aspects of turbulent boundary-layer structure. *Journal of Fluid Mechanics*, **107**, 297–338.

Hill, F.K. 1956. Boundary layer measurements in hypersonic flow. *Journal of Aeronautical Sciences*, **23**, 35–42.

Hinze, J.O. 1975. *Turbulence*. 2 edn. McGraw-Hill.

Ho, C.M. and Huerre, P. 1984. Perturbed shear layers. *Annual Review of Fluid Mechanics*, **16**, 365–424.

Honkan, A. and Andreopoulos, J. 1992. Rapid compression of grid-generated turbulence by a moving shock wave. *Physics of Fluids A*, **4**, 2562–2572.

Hopkins, E.J. and Keener, E.R. 1966. Study of surface Pitots for measuring turbulent skin friction at supersonic Mach numbers — Adiabatic wall. *NASA TN D-3478*.

Hopkins, E.J., Keener, E.R., Polek, T.E. and Dwyer, H.A. 1972. Hypersonic turbulent skin-friction and boundary-layer profiles on nonadiabatic flat plates. *AIAA Journal*, **10**, 40–48.

Hornung, H.G. and Perry, A.E. 1984. Some aspects of three-dimensional separation. Part I. Streamwise bifurcations. *Zeitschrift für Flugwissenschaften und Weltraumforschung*, **8**, 77–87.

Horstman, C.C. 1984. A computational study of complex three-dimensional compressible turbulent flow fields. *AIAA Paper 84-1556*.

Horstman, C.C. and Owen, F.K. 1972. Turbulent properties of a compressible boundary layer. *AIAA Journal*, **10**, 1418–1424.

Horstman, C.C. and Rose, W.C. 1977. Hot wire anemometry in transonic flows. *AIAA Journal*, **15**, 395–401.

Hou, Y.X., Clemens, N.T. and Dolling, D.S. 2003. Wide-field PIV study of shock-induced turbulent boundary layer separation. *AIAA Paper 2003-0441*.

Huang, P.G., Bradshaw, P. and Coakley, T.J. 1994. Turbulence models for compressible boundary layers. *AIAA Journal*, **32**.

Huang, P.G., Coleman, G.N. and Bradshaw, P. 1995. Compressible channel flows: DNS results and modelling. *Journal of Fluid Mechanics*, **305**, 185–218.

Huffman, G.D. and Bradshaw, P. 1972. A note on von Kármán's constant in low Reynolds number turbulent flows. *Journal of Fluid Mechanics*, **53**, 45–60.

Hunt, I.A. and Joubert, P.N. 1979. Effect of small streamline curvature on turbulent duct flow. *Journal of Fluid Mechanics*, **91**, 633–659.

Hunt, J.C.R. 1977. A review of the theory of rapidly distorted turbulent flows and its applications. *Pages 121–152 of: Fluid Dynamics Transactions*, vol. 9. Thirteenth Biennial Fluid Dynamics Symposium, Warsaw, Poland.

Hunt, J.C.R. and Caruthers, D.J. 1990. Rapid distortion theory and the "problems" of turbulence. *Journal of Fluid Mechanics*, **212**, 497–532.

Huntley, M. and Smits, A.J. 2000. Transition studies on an elliptic cone in Mach 8 flow using filtered Rayleigh scattering. *European Journal of Mechanics B — Fluids*, **19**, 5, 695–706.

Hussain, A.K.M.F. 1983. Coherent structures — Reality and myth. *The Physics of Fluids*, **26**, 2816–2850.

Hussaini, M.Y., Collier, F. and Bushnell, D.M. 1985. Turbulence alteration due to shock motion. *In:* Délery, J. (ed), *Turbulent Shear-Layer/Shock-Wave Interactions*. Springer Verlag.

Ikawa, H. 1973. *Turbulent mixing layer experiments in supersonic flow*. Ph.D.

Thesis, California Institute of Technology, Pasadena, CA.

Ikawa, H. and Kubota, T. 1975. Investigation of supersonic turbulent mixing layer with zero pressure gradient. *AIAA Journal*, **13**, 566–572.

Ivanov, M.S. and Gimelshein, S.F. 1998. Computational hypersonic rarified flows. *Annual Review of Fluid Mechanics*, **30**, 469–505.

Iwamoto, K. and Nobu Kasagi, N. 2004. Private communication.

Jacquin, L. 2005. Private communication.

Jacquin, L., Blin, E. and Goeffroy, P. 1991. Experiments on free turbulence/shock wave interaction. *In: Proceedings of the Eighth Symposium on Turbulent Shear Flows*. Technical University of Munich.

Jacquin, L., Cambon, C. and Blin, E. 1993. Turbulence amplification by a shock wave and rapid distortion theory. *Physics of Fluids A*, **5**, 2539–2550.

James, C.S. 1958. Observations of turbulent-burst geometry and growth in supersonic flow. *NASA TN 4235*.

Jayaram, M., Donovan, J.F., Dussauge, J.-P. and Smits, A.J. 1989. Analysis of a rapidly distorted, supersonic turbulent boundary layer. *Physics of Fluids A*, **1**, 1855–1864.

Jayaram, M., Taylor, M.W. and Smits, A.J. 1987. The response of a compressible turbulent boundary layer to short regions of concave surface curvature. *Journal of Fluid Mechanics*, **175**, 343–362.

Johnson, A.W. 1993. *Laminarization and retransition of turbulent boundary layers in supersonic flow*. Ph.D. Thesis, Yale University, New Haven, CT.

Johnson, D.A. 1989. Laser Doppler anemometry. *Chapter 6, AGARDograph 315*.

Johnson, D.A. and Rose, W.C. 1975. Laser velocimeter and hot-wire anemometer comparison in a supersonic boundary layer. *AIAA Journal*, **13**, 512–515.

Johnston, J.P. 1960. On the three-dimensional turbulent boundary layer generated by secondary flow. *Journal of Basic Engineering, Series D, Transactions of the ASME*, **82**, 233–248.

Kaneda, Y. and Ishihara, T. 2004. High resolution direct numerical simulation of turbulence: Spectra of fourth-order velocity moments. *Pages 155–162 of:* Smits, A.J. (ed), *IUTAM Symposium on Reynolds Number Scaling in Turbulent Flow, Princeton, NJ*. Kluwer. *Fluid Mech. and its Applications*, **74**.

Kegerise, M.A. and Spina, E.F. 2000a. A comparative study of constant-voltage and constant-temperature hot-wire anemometers: Part I — The static response. *Experiments in Fluids*, **29**, 2, 154–164.

Kegerise, M.A. and Spina, E.F. 2000b. A comparative study of constant-voltage and constant-temperature hot-wire anemometers: Part II — The dynamic response. *Experiments in Fluids*, **29**, 2, 165–177.

Kemp, J.H. and Owen, F.K. 1972. Nozzle wall boundary layers at Mach numbers 20 to 47. *AIAA Journal*, **10**, 872–879.

Kida, S. and Orszag, S.A. 1990. Energy and spectral dynamics in forced compressible turbulence. *J. Sci. Comput.*, **5**, 1–34.

Kim, H.T., Kline, S.J. and Reynolds, W.C. 1971. The production of turbulence near a smooth wall in a turbulent boundary layer. *Journal of Fluid Mechanics*, **50**, 133–160.

Kim, K.S., Lee, Y. and Settles, G.S. 1991. Laser interferometry/Preston tube skin-

friction comparison in a shock/boundary layer interaction. *AIAA Journal*, **29**, 1007–1009.

Kistler, A.L. 1959. Fluctuation measurements in a supersonic turbulent boundary layer. *Physics of Fluids*, **2**, 290–296.

Kiya, M. and Sasaki, K. 1983. Structure of a turbulent separation bubble. *Journal of Fluid Mechanics*, **137**, 83–113.

Klebanoff, P.S. 1955. Characteristics of turbulence in a boundary layer with zero pressure gradient. *NACA Report 1247*.

Klewicki, J.C. 1997. Self-sustaining traits of near-wall motions underlying boundary layersstress transport. *In: Self-Sustaining Mechanisms of Wall Turbulence.* Advances in Fluid Mechanics Series, **15**, 135–166. Computational Mechanics Publications, Southampton, UK and Boston, USA.

Klewicki, J.C. and Falco, R.E. 1990. On accurately measuring statistics associated with small-scale structure in turbulent boundary layers using hot-wire probes. *Journal of Fluid Mechanics*, **219**, 119–142.

Kline, S.J. and Portela, L.M. 1997. A view of the structure of turbulent boundary layers. *In: Self-Sustaining Mechanisms of Wall Turbulence.* Advances in Fluid Mechanics Series, **15**, 167–180. Computational Mechanics Publications, Southampton, UK and Boston, USA.

Kline, S.J. and Robinson, S.K. 1989. Quasi-coherent structures in the turbulent boundary layer. Part 1. Status report on a community-wide summary of the data. *In:* Kline, S.J. and Afgan, N.H. (eds), *Near-Wall Turbulence.* Hemisphere.

Kline, S.J., Cantwell, B.J. and Lilley, G.M. (eds). 1981. *The 1980-81 AFOSR-HTTM-Stanford Conference on Complex Turbulent Flows: Comparison of Computation and Experiment.* Thermosciences Division, Mechanical Engineering Department, Stanford University, Stanford, CA.

Kline, S.J., Reynolds, W.C., Schraub, F.A. and Runstadler, P.W. 1967. The structure of turbulent boundary layers. *Journal of Fluid Mechanics*, **30**, 741–773.

Knight, D.D., Horstman, C.C., Shapey, B. and Bogdonoff, S.M. 1987. Structure of supersonic flow past a sharp fin. *AIAA Journal*, **25**, 1331–1337.

Knight, D.D., Yan, H., Panaras, A.G. and Zheldotovodov, A. 2003. Advances in CFD prediction of shock wave turbulent boundary layer interactions. *Progress in Aerospace Sciences*, **39**, 121–184.

Kolmogorov, A.N. 1961. The local structure of turbulence in incompressible viscous fluid for very large Reynolds numbers. *In:* Friedlander, S.K. and Topper, L. (eds), *Turbulence: Classic Papers on Statistical Theory.* Interscience.

Konrad, J.H. 1977. *An experimental investigation of mixing in two-dimensional turbulent shear flows with applications to diffusion-limited chemical reactions.* Ph.D. Thesis, California Institute of Technology, Pasadena, CA.

Konrad, W. 1993. *A three-dimensional supersonic turbulent boundary layer generated by an isentropic compression.* Ph.D. Thesis, Princeton University, Princeton, NJ.

Konrad, W., Smits, A.J. and Knight, D.D. 1994. A combined experimental and numerical study of a three-dimensional supersonic turbulent boundary layer. *Experimental Thermal and Fluid Science*, **9**, 156–164.

Korkegi, R.H. 1971. Survey of viscous interactions associated with high Mach num-

ber flight. *AIAA Journal*, **9**, 771–784.

Kovasznay, L.S.G. 1953. Turbulence in supersonic flow. *Journal of the Aeronautical Sciences*, **20**, 657–674 (cont. 682).

Kovasznay, L.S.G. 1954. Hot-wire method. *In: High Speed Aerodynamics and Jet Propulsion*. Princeton University Press.

Kovasznay, L.S.G., Kibbens, V. and Blackwelder, R.F. 1970. Large-scale motion in the intermittent region of a turbulent boundary layer. *Journal of Fluid Mechanics*, **41**, 283–325.

Kubota, T. and Berg, D.E. 1977. Surface roughness effects on the hypersonic turbulent boundary layer. *Report AD A 042141, California Institute of Technology, Pasadena, California*.

Kuethe, A.M. and Schetzer, J.D. 1967. *Foundations of Aerodynamics*. 2 edn. John Wiley and Sons.

Kuntz, D.W., Amatucci, V.A. and Addy, A.L. 1987. Turbulent boundary-layer properties downstream of the shock-wave/boundary-layer interaction. *AIAA Journal*, **25**, 668–675.

Kussoy, M.I. and Horstman, C.C. 1975. An experimental documentation of a hypersonic shock-wave/turbulent boundary layer interaction flow — With and without separation. *NASA TMX-62412*.

Kussoy, M.I., Brown, J.D., Brown, J.L., Lockman, W.K. and Horstman, C.C. 1978. Fluctuations and massive separation in three-dimensional shock-wave/boundary-layer interactions. *In:* Hirata, M. and and Kasagi, N. (eds), *Transport Phenomena in Turbulent Flows: Theory, Experiment, and Numerical Simulation*. Hemisphere, NY.

Kussoy, M.I., Horstman, C.C. and Acharya, M. 1978. An experimental documentation of pressure gradient and Reynolds number effects on compressible turbulent boundary layers. *NASA TM 78488*.

Kutateladze, S.S. and Leont'ev, A.I. 1964. *Turbulent Boundary Layers in Compressible Gases*. Academic Press. Translated by D.B. Spalding. Originally published in Russian in 1962 by the Academy of Sciences of the USSR, Siberian Division.

Lacharme, J.P. 1984. *Vèlocimétrie laser Doppler bidimensionnelle pour écoulement turbulent supersonique: Quelques aspects spécifiques des processus de mesure*. Thèse de Docteur Ingénieur, Université d'Aix-Marseille II.

Laderman, A.J. and Demetriades, A. 1974. Mean and fluctuating flow measurements in the hypersonic boundary layer over a cooled wall. *Journal of Fluid Mechanics*, **63**, 121–144.

Landau, L.D. and Lifshitz, E.M. 1987. *Course of Theoretical Physics*. 2nd edn. Fluid Mechanics, vol. 6. Pergamon Press. First edition, Mir, Moscow 1959.

Lau, J.C. 1981. Effects of exit Mach number and temperature on mean flow and turbulence characteristics in round jets. *Journal of Fluid Mechanics*, **105**, 193–218.

Laufer, J. 1961. Aerodynamic noise in supersonic wind tunnels. *Journal of the Aerospace Sciences*, **28**, 685–692.

Launder, B.E. and Spalding, D.B. 1972. *Mathematical Models of Turbulence*. Academic Press.

Launder, B.E., Reece, G.J. and Rodi, W. 1975. Progress in the development of a

Reynolds stress turbulent closure. *Journal of Fluid Mechanics*, **68**, 537–566.

Laurent, H. 1996. *Turbulence d'une interaction onde de choc/couche limite sur une paroi plane adiabatique ou chauffée.* Thèse de Doctorat, Université de la Méditerranée, France.

Law, C.H. 1975. Two-dimensional compression corner and planar shock wave interactions with a supersonic, turbulent boundary layer. *Rep. ARL 75-0157, Aerospace Research Laboratories, Wright-Patterson AFB.*

Lechner, R., Sesterhenn, J. and Friedrich, R. 2001. Turbulent supersonic channel flow. *Journal of Turbulence*, **2**, 1.

Lee, S., Lele, S.K. and Moin, P. 1991. Eddy shocklets in decaying compressible turbulence. *Physics of Fluids A*, **3**, 657–664.

Lee, S., Lele, S.K. and Moin, P. 1993. Direct numerical simulation of isotropic turbulence interacting with a weak shock wave. *Journal of Fluid Mechanics*, **251**, 533–562.

Lee, S., Moin, P. and Lele, S.K. 1992. Interaction of isotropic turbulence with a shock wave. *Rep. TF-52, Department of Mechanical Engineering, Stanford University, Stanford, CA.*

Legendre, R. 1956. Séparation de l'écoulement laminaire tridimensionel. *La Recherche Aerospatiale*, 327–335.

Lele, S.K. 1989. Direct simulations of compressible free shear flows. *AIAA Paper 89-0374.*

Lele, S.K. 1994. Compressibility effects on turbulence. *Annual Review of Fluid Mechanics*, **26**, 211–254.

Lempert, W.R., Wu, and Miles, R.B. 1997. Filtered Rayleigh scattering measurements using a MHz rate pulse-burst laser system. *AIAA Paper 97-0500.*

Lesieur, M. 1987. *Turbulence in Fluids.* Martinus Nijhoff Publishers, Dordrecht, The Netherlands.

Lesieur, M. 1994. *La Turbulence.* Presses Universitaires de Grenoble, Grenoble.

Lesieur, M., Comte, P. and Normand, X. 1992. The vortex lattice structure of turbulent shear flows. *In:* Gatski, T.B., Sarkar, S. and Speziale, C.G. (eds), *Studies in Turbulence.* Springer-Verlag.

Li, J.D. 1989. *The turbulence structure of wall shear flow.* Ph.D. Thesis, University of Melbourne.

Li, J.D. and Perry, A.E. 1989. Shear stress profiles in zero-pressure-gradient turbulent boundary layers. *In: Proceedings of the Tenth Australasian Fluid Mechanics Conference.*

Li, Q. and Coleman, G. 2003. DNS of an oblique shockwave impinging upon a turbulent boundary layer. *In: Proceedings of DLES-5.* Garching, Germany.

Lian, W. and Aubry, N. 1993. Self similarity of compressible turbulence. *In: Proceedings of the Transitional and Turbulent Compressible Flows Symposium, FED-Vol. 151.* ASME Fluids Engineering Division.

Libby, P.A. and Visich, M. 1959. The law of the wake in compressible turbulent boundary layers. *Journal of the Aeronautical Sciences*, **26**, 541–542.

Liepmann, H.W. 1946. The interaction between boundary layer and shock waves in transonic flow. *Journal of the Aeronautical Sciences*, **13**, 623–637.

Liepmann, H.W. and Laufer, J. 1947. Investigation of free turbulent mixing. *NACA*

TN 1257.

Liepmann, H.W. and Roshko, A. 1957. *Elements of Gasdynamics*. John Wiley and Sons. GALCIT Aeronautical Series.

Liepmann, H.W., Roshko, A. and Dhawan, S. 1951. On reflection of shock waves from boundary layers. *NACA TN 2334*. Also NACA Report 1100, 1952.

Lighthill, M.J. 1963. Attachment and separation in three-dimensional flow. *Pages 72–82 of:* Rosenhead, L. (ed), *Laminar Boundary Layers*. Oxford University Press. Reprinted by Dover Publications, 1988.

Ligrani, P.M. and Bradshaw, P. 1987. Spatial resolution and measurement of turbulence in the viscous sublayer using subminiature hot-wire probes. *Experiments in Fluids*, **5**, 407–417.

Liu, Z., Adrian, R.J. and Hanratty, T.J. 2001. Large-scale modes of turbulent channel flow: Transport and structure. *Journal of Fluid Mechanics*, **448**, 53–80.

Liu, Z., Landreth, C.C., Adrian, R.J. and Hanratty, T.J. 1991. High resolution measurements of turbulent structure in a channel with particle image velocimetry. *Experiments in Fluids*, **10**, 301–312.

Lou, H., Shih, C. and Alvi, F.S. 2003. A PIV study of supersonic impinging jet. *AIAA Paper 03-3263*.

Lu, J.F. and Lele, S.K. 1994. On the density effects on the growth rate of compressible mixing layer. *Physics of Fluids*, **6**, 1073–1075.

Lu, S.S. and Willmarth, W.W. 1973. Measurements of the structure of the Reynolds stress in a turbulent boundary layer. *Journal of Fluid Mechanics*, **60**, 481–511.

Luchik, T.S. and Tiederman, W.G. 1987. Timescale and structure of ejections and bursts in turbulent channel flows. *Journal of Fluid Mechanics*, **174**, 529–552.

Lumley, J.L. 1975. Prediction methods for turbulent flows: Introduction. *Von Kármán Institute, Rhodes-Saint-Genèse, Belgium*.

Lumley, J.L. 1978. Computational modeling of turbulent flows. *Advances in Applied Mechanics*, **18**, 124–176.

Mabey, D.G., Meier, H.U. and Sawyer, W.G. 1974. Experimental and theoretical studies of the boundary layer on a flat plate at Mach numbers from 2.5 to 4.5. *RAE TR 74127*.

MacAulay, P. and Gartshore, I.P. 1991. A tentative model of outer-region structure in a turbulent boundary-layer developing on a smooth-wall. *In:* Keffer, J.F., Shah, R.K. and Ganić, E.N. (eds), *Experimental Heat Transfer, Fluid Mechanics, and Thermodynamics 1991*. Elsevier Science.

Mack, L.B. 1954. An experimental investigation of the temperature-recovery factor. *Jet Propulsion Lab., Report 20–80, California Institute of Technology, Pasadena, California*.

Mack, L.M. 1984. Boundary-layer linear stability theory. *NATO AGARD Report R-709*.

Maeder, T., Adams, N.A. and Kleiser, L. 2001. Direct simulation of turbulent supersonic boundary layers by an extended temporal approach. *Journal of Fluid Mechanics*, **429**, 187–216.

Maise, G. and McDonald, H. 1968. Mixing length and kinematic eddy viscosity in a compressible boundary layer. *AIAA Journal*, **6**, 73–80.

Marshall, T.A. and Dolling, D.S. 1990. Spanwise properties of the unsteady separation shock in a Mach 5 unswept compression ramp interaction. *AIAA Paper 90-0377*.

Martin, M.P. 2003. Preliminary DNS/LES database of hypersonic turbulent boundary layers. *AIAA Paper 03-3726*.

Martin, M.P. 2004. DNS of hypersonic turbulent boundary layers. *AIAA Paper 04-2337*.

Marušić, I. 2001. On the role of large-scale structures in wall turbulence. *Physics of Fluids*, **13**, 735–743.

Marušić, I. 2004. Private communication.

Marušić, I. and Kunkel, G.J. 2003. Streamwise turbulence intensity formulation for flat-plate boundary layers. *Physics of Fluids*, **15**, 2461–2464.

Marušić, I, Kunkel, G. J., Zhao, R. and Smits, A. J. 2004. Turbulence intensity similarity formulations for wall-bounded flows. *In:* Andersson, H.I. and Krogstad, P.-A. (eds), *Advances in Turbulence X*, Proc. of the 10th European Turb. Conf., CIMNE, Barcelona, Spain.

Marušić, I., Uddin, A.K.M. and Perry, A.E. 1997. Similarity law for the streamwise turbulence intensity in zero-pressure-gradient turbulent boundary layers. *Physics of Fluids*, **9**, (12) 3718–3726.

Maskell, E.C. 1955. Flow separation in three dimensions. *RAE Rep. Aero. 2565*.

Mathews, D.C., Childs, M.E. and Paynter, G.C. 1970. Use of Coles' universal wake function for compressible turbulent boundary layers. *Journal of Aircraft*, **7**, 137–140.

Maydew, R.C. and Reed, J.F. 1963. Turbulent mixing of compressible free jets. *AIAA Journal*, **1**, 1443–1444.

McGinley, C.B., Spina, E.F. and Sheplak, M. 1994. Turbulence measurements in a Mach 11 helium boundary layer. *AIAA Paper 94-2364*.

McGregor, I. 1961. The vapor-screen method of flow visualization. *Journal of Fluid Mechanics*, **11**, 481–511.

McKenzie, J.F. and Westphal, K.O. 1968. Interaction of linear waves with oblique shock waves. *Physics of Fluids*, **11**, 2350–2362.

McKeon, B.J., Li, J., Jiang, W., Morrison, J.F. and Smits, A.J. 2004. Further observations on the mean velocity in fully-developed pipe flow. *Journal of Fluid Mechanics*, **501**, 135–147.

Mee, D., Stalker, R. and Stollery, J. 1986. Glancing interactions between single and intersecting oblique shock waves and a turbulent boundary layer. *Journal of Fluid Mechanics*, **170**, 411–433.

Mehta, R.D. and Westphal, R.V. 1984. Near-field turbulence properties of single and two-stream plane mixing layers. *AIAA Paper 84-0426*.

Meier, H.U. and Rotta, J.C. 1971. Temperature distributions in supersonic turbulent boundary layers. *AIAA Journal*, **9**, 2149–2156.

Menaa, M., Dupont, P. and Dussauge, J.P. 1996. Self similar solutions for the velocity profiles in supersonic mixing layers. *IRPHE Report*, IRPHE Marseille.

Merzkirch, W. 1988. *Flow Visualization*. 2nd edn. Academic Press.

Messersmith, N.L., Dutton, J.C. and Krier, H. 1991. Experimental investigation of large scale structures in compressible mixing layers. *AIAA Paper 91-0244*.

Metzger, M.M., Klewicki, J.C., Bradshaw, K.L. and Sadr, R. 2001. Scaling the near-wall axial turbulent stress in the sero pressure gradient boundary layer. *Physics of Fluids*, **13**, 1819–1821.

Michel, R., Quemard, C. and Durand, R. 1969. Application d'un schéma de longueur de mélange à l'étude des couches limites turbulentes d'équilibre. *ONERA NT.154*.

Mieghem, J. van. 1949. Les équations générales de la mécanique et de l'énergétique des milieux turbulens en vue des applications à la météorologie. *Mémoires Institut Royal Météo. de Belgique, No. 34*.

Miles, J.W. 1958. On the disturbed motion of a plane vortex sheet. *Journal of Fluid Mechanics*, **4**, 538–551.

Miles, R.B. and Nosenchuck, D.M. 1989. Three-dimensional quantitative flow diagnostics. *Pages 33–107 of:* Gad-el-Hak, M. (ed), *Lecture Notes in Engineering, Advances in Fluid Mechanics Measurements*, vol. 45. Springer-Verlag.

Miles, R.B., Cohen, C., Connors, J., Howard, P., Huang, S., Markowitz, E. and Russell, G. 1987. Velocity measurements by vibrational tagging and fluorescent probing of oxygen. *Optics Letters*, **12**, 861–863.

Miles, R.B., Connors, J., Markowitz, E., Howard, P. and Roth, G. 1989. Instantaneous supersonic velocity profiles in an underexpanded sonic air jet by oxygen flow tagging. *Physics of Fluids A*, **1**, 389–393.

Miles, R.B., Forkey, J.N. and Lempert, W.R. 1992. Filtered Rayleigh scattering measurements in supersonic/hypersonic facilities. *AIAA Paper 92-3894*.

Miles, R.B., Lempert, W.R., Forkey, J.N., Finkelstein, N.D. and Erbland, P. 1994. Quantifying high speed flows by light scattering from air molecules. *AIAA Paper 94-2230*.

Millikan, C.B.A. 1938. A critical discussion of turbulent flows in channels and circular tubes. *Pages 386–392 of: Proceedings of the Fifth International Congress of Applied Mechanics*.

Moffatt, H.K. 1968. The interaction of turbulence with a strong wind shear. *Pages 139–150 of:* Yaglom, A.M. and Tatarskii, V. (eds), *International Colloquiem on Atmospheric Turbulence and Radio Wave Propagation, Moscow 1965*. Nauka Press, Moscow.

Moin, P. and Spalart, P.R. 1987. Contributions of numerical simulation data base to the physics, modeling, and measurement of turbulence. *NASA TM 100022*.

Monaghan, R.S. 1955. The behaviour of boundary layers at supersonic speeds. *IAS Preprint No. 557*.

Morkovin, M.V. 1955. Effects of high acceleration on a turbulent supersonic shear layer. *In: Proceedings of the 1955 Heat Transfer and Fluid Mechanics Institute*. Stanford University Press.

Morkovin, M.V. 1956. Fluctuations and hot-wire anemometry in compressible flows. *AGARDograph 24*.

Morkovin, M.V. 1962. Effects of compressibility on turbulent flows. *Pages 367–380 of:* Favre, A.J. (ed), *Mécanique de la Turbulence*. CNRS.

Morkovin, M.V. 1987. Transition at hypersonic speeds. *NASA-CR-178315, ICASE Interim Report 1*.

Morkovin, M.V. 1992. Mach number effects on free and wall turbulent structures in

light of instability flow interactions. *Pages 269–284 of:* Gatski, T.B., Sarkar, S. and Speziale, C.G. (eds), *Studies in Turbulence*. Springer Verlag.

Morkovin, M.V. and Phinney, R.E. 1958. Extended applications of hot wire anemometry to high-speed turbulent boundary layers. *Johns Hopkins University, Baltimore, MD, Report AFOSR TN-58-469*.

Morrison, J.F., Subramanian, C.S. and Bradshaw, P. 1992. Bursts and the law of the wall in turbulent boundary layers. *Journal of Fluid Mechanics*, **241**, 75–108.

Morrison, J. F., McKeon, B. J., Jiang, W. and Smits, A. J. 2004. Scaling of the streamwise velocity components in turbulent pipe flow. *Journal of Fluid Mechanics*, **508**, 99–131.

Mougnangola, H. 1986. *Influence de la conduction thermique sur la réponse en fréquence de l'anémomètre à fil chaud en écoulement supersonique*. Thèse Docteur, Université d'Aix-Marseille II, France.

Muck, K.C., Andreopoulos, J. and Dussauge, J.P. 1988. Unsteady nature of shock wave/turbulent boundary layer interaction. *AIAA Journal*, **26**, 179–197.

Muck, K.C., Dussauge, J.P. and Bogdonoff, S.M. 1985. Structure of the wall pressure fluctuations in a shock-induced separated turbulent flow. *AIAA Paper 85-0179*.

Mukund, R., Viswanath, P.R., Prabhu, A. and Vasudevan, B. 2003. Study of glancing and blunt fin shock-boundary layer interactions at low supersonic Mach numbers. *National Aerospace Laboratories, Report PD EA 0316, Bangalore, India*.

Murlis, J., Tsai, H.M. and Bradshaw, P. 1982. The structure of turbulent boundary layers at low Reynolds numbers. *Journal of Fluid Mechanics*, **122**, 13–56.

Nagakawa, H. and Nezu, I. 1974. On a new eddy model in turbulent shear flow. *Proc. of J.S.C.E.*, **231**, 61–70.

Narasimha, R. and Sreenivasan, K.R. 1979. Relaminarization of fluid flows. *Advances in Applied Mechanics*, **19**, 221–301.

Narayanswami, N., Horstman, C.C. and Knight, D.D. 1993. Numerical simulation of crossing shock/turbulent boundary layer interaction at Mach 8.3 — Comparison of zero- and two-equation turbulence models. *AIAA Paper 93-0779*.

Nau, T.-A. 1995. *Rayleigh scattering as a quantitative tool in compressible turbulent boundary layers*. MSE Thesis, Princeton University.

Naughton, J.W. and Sheplak, M. 2002. Modern developments in shear-stress measurement. *Progress in Aerospace Science*, **38**, 515–570.

Naughton, J.W., Cattafesta, L.N. III and Settles, G.S. 1997. An experimental study of compressible turbulent mixing enhancement in swirling jets. *Journal of Fluid Mechanics*, **330**, 271–305.

Nockemann, M., Abstiens, R., Schober, M., Bruns, J. and Eckert, D. 1994. Vermessung der Wandgrenzschicht im Deutsch-Niederländischen Windkanal bei hohen Reynolds-zahlen. *Institutsreport DNW 1994, Aerodynamisches Institut RWTH Aachen*.

Norman, M.L. and Winkler, A. 1985. Supersonic jets. *Los Alamos Science, Spring-Summer Issue*.

Oertel, H. 1983. Coherent structures producing Mach waves inside and outside of the supersonic jet. *In:* Dumas, R. and Fulachier, L. (eds), *Structure of Complex Turbulent Shear Flow*. Springer Verlag.

Olsen, M.G. and Dutton, J.C. 2003. Planar velocity measurements in a weakly compressible mixing layer. *Journal of Fluid Mechanics*, **486**, 51–77.

Österlund, J.M., Johansson, A.V., Nagib, H.M. and Hites, M.H. 2000. A note on the overlap region in turbulent boundary layers. *Physics of Fluids*, **12**, 1–4.

Oswatitsch, K. 1958. Die Ablösungsbedingung von Grenzschichten. *Pages 357–367 of:* Görtler, H. (ed), *Grenzschichtforschung*. Springer Verlag.

Owen, F.K. 1990. Turbulence and shear stress measurements in hypersonic flow. *AIAA Paper 90-1394*.

Owen, F.K. and Horstman, C.C. 1972. On the structure of hypersonic turbulent boundary layers. *Journal of Fluid Mechanics*, **53**, 611–636.

Owen, F.K., Horstman, C.C. and Kussoy, M.I. 1975. Mean and fluctuating flow measurements of a fully-developed, non-adiabatic, hypersonic boundary layer. *Journal of Fluid Mechanics*, **70**, 393–413.

Pantano, C. and Sarkar, S. 2002. A study of compressibility effects in the high-speed turbulent shear layer using direct simulation. *Journal of Fluid Mechanics*, **452**, 329–371.

Panton, R.L. 1984. *Incompressible Flow*. John Wiley and Sons.

Panton, R.L. (ed) 1997. *In: Self-Sustaining Mechanisms of Wall Turbulence*. Advances in Fluid Mechanics Series, **15**, Computational Mechanics Publications, Southampton, UK and Boston, USA.

Papamoschou, D. 1986. *Experimental investigation of heterogeneous compressible shear layers*. Ph.D. Thesis, California Institute of Technology.

Papamoschou, D. 1990. Sound propagation issues in compressible turbulence. *AIAA Paper 90-0155*.

Papamoschou, D. 1991. Effect of Mach number on communication between regions of a free shear layer. *In: Proceedings of the Eighth Symposium on Turbulent Shear Flows*. Technical University of Munich.

Papamoschou, D. 1993. Zones of influence in the compressible shear layer. *Fluid Dynamics Research*, **11**, 217–228.

Papamoschou, D. 1995. Evidence of shocklets in a counterflow supersonic shear layer. *Physics of Fluids*, **7**, 233–235.

Papamoschou, D. and Roshko, A. 1988. The compressible turbulent shear layer: An experimental study. *Journal of Fluid Mechanics*, **197**, 453–477.

Park, S.-R. and Wallace, J.M. 1993. The influence of instantaneous velocity gradients on turbulence properties measured with multi-sensor hot-wire probes. *Experiments in Fluids*, **16**, 17–26.

Passot, T. and Pouquet, A. 1987. Numerical simulation of compressible homogeneous flows in the turbulent regime. *Journal of Fluid Mechanics*, **181**, 441–466.

Patel, V.C. 1965. Calibration of the Preston tube and limitations on its use in pressure gradients. *Journal of Fluid Mechanics*, **23**, 185–208.

Peake, D.J. and Tobak, M. 1980. Three-dimensional interactions and vortical flows with emphasis on high speeds. *NASA TM 81169*.

Pearson, B.R., Krogstad, P.-Å. and Johnson, G.R. 2004. R_λ dependence of the Kolmogorov constant and scaling. *Pages 229–236 of:* Smits, A.J. (ed), *IUTAM Symposium on Reynolds Number Scaling in Turbulent Flow*, Princeton, NJ. Kluwer. *Fluid Mech. and its Applications*, **74**.

Perry, A.E. 1982. *Hot-Wire Anemometry*. Oxford University Press.

Perry, A.E. and Abell, C.J. 1975. Scaling laws for pipe-flow turbulence. *Journal of Fluid Mechanics*, **67**, 257–271.

Perry, A.E. and Abell, C.J. 1977. Asymptotic similarity of turbulence structures in smooth- and rough-walled pipes. *Journal of Fluid Mechanics*, **79**, 785–799.

Perry, A.E. and Chong, M.S. 1982. On the mechanism of wall turbulence. *Journal of Fluid Mechanics*, **119**, 173–219.

Perry, A.E. and Chong, M.S. 1987. A description of eddying motions and flow patterns using critical-point concepts. *Annual Review of Fluid Mechanics*, **19**, 125–155.

Perry, A.E. and Fairlie, B.D. 1974. Critical points in flow patterns. *Advances in Geophysics*, **18B**, 299–315.

Perry, A.E. and Hornung, H.G. 1984. Some aspects of three-dimensional separation. Part II. Vortex skeletons. *Z. Flugwiss. Weltraumforsch.*, **8**, 155–160.

Perry, A.E. and Li, J.D. 1990. Experimental support for the attached-eddy hypothesis in zero-pressure-gradient turbulent boundary layers. *Journal of Fluid Mechanics*, **218**, 405–438.

Perry, A.E., Henbest, S. and Chong, M.S. 1986. A theoretical and experimental study of wall turbulence. *Journal of Fluid Mechanics*, **165**, 163–199.

Perry, A.E., Li, J.D. and Marušić, I. 1991. Towards a closure scheme for turbulent boundary layers using the attached eddy hypothesis. *In:* Walker, J.D.A. (ed), *Turbulent Flow Structure Near Walls*. The Royal Society. First published in *Phil. Trans. R. Soc. London A*. 336, 1991.

Perry, A.E., Lim, K.L. and Henbest, S.M. 1985. A spectral analysis of smooth flat-plate boundary layers. *In: Proceedings of the Fifth Symposium on Turbulent Shear Flows*. Cornell University.

Perry, A.E., Lim, T.T. and Teh, E.W. 1981. A visual study of turbulent spots. *Journal of Fluid Mechanics*, **104**.

Perry, A.E., Smits, A.J. and Chong, M.S. 1979. The effects of certain low frequency phenomena on the calibration of hot wires. *Journal of Fluid Mechanics*, **90**, 415–431.

Perry, A.E., Uddin, A.K.M. and Marušić, I. 1992. An experimental and computational study on the orientation of attached eddies in turbulent boundary layers. *In: Proceedings of the Eleventh Australasian Fluid Mechanics Conference*.

Petrie, H.L., Samimy, M. and Addy, A.L. 1986. Compressible separated flows. *AIAA Journal*, **24**, 1971–1978.

Pirozzoli, S., Grasso, F. and Gatski, T.B. 2004. Direct numerical simulation and analysis of a spatially evolving supersonic turbulent boundary layer at $M = 2.25$. *Physics of Fluids*, **16**, 3, 530–545.

Plotkin, K.J. 1975. Shock wave oscillation driven by turbulent boundary-layer fluctuations. *AIAA Journal*, **13**, 1036.

Poggie, J. 1991. *Quantitative flow visualization applied to the study of compressible turbulent flow*. MSE Thesis, Princeton University.

Poggie, J. 1995. *On the control of a compressible, reattaching shear layer*. Ph.D. Thesis, Princeton University.

Poggie, J. and Smits, A.J. 2001. Shock unsteadiness in a reattaching shear layer.

Journal of Fluid Mechanics, **429**, 155–185.

Poggie, J. and Smits, A.J. 2005. Experimental evidence for Plotkin model of shock unsteadiness in separated flow. *Physics of Fluids*, 018107.

Poggie, J., Erbland, P.J., Smits, A.J. and Miles, R.B. 2004. Quantitative visualization of compressible turbulent shear flows using condensate-enhanced Rayleigh scattering. *Experiments in Fluids*, **37**, 3, 438–454.

Poggie, J., Smits, A.J. and Glezer, A. 1992. The dynamics and control of fluctuating pressure loads in the reattachment region of a supersonic free shear layer. *AIAA Paper 92-0178*.

Porter, D.H., Pouquet, A. and Woodward, P.R. 1995. Compressible flows and vortex stretching. *In:* Meneguzzi, M., Pouquet, A. and Sulem, P.L. (eds), *Proceedings*. Springer Verlag.

Porter, D.H., Woodward, P.R. and Pouquet, A. 1994. Inertial range structures in compressible turbulent flows. *University of Minnesota Supercomputer Institute Report 94/197*.

Prandtl, L. 1933. Recent results of turbulence research. *Zeitschrift des Vereines Deutscher Ingenieure*, **77**. English translation NACA TM 720 (1933).

Purtell, L.P., Klebanoff, P.S. and Buckley, F.T. 1981. Turbulent boundary layer at low Reynolds number. *Physics of Fluids*, **24**, 802–811.

Ragab, S.A. and Wu, J.L. 1989. Linear instabilities in two-dimensional compressible mixing layers. *Physics of Fluids A*, **1**, 957–966.

Rao, K.N., Narasimha, R. and Narayanan, M.A. 1971. The bursting phenomenon in a turbulent boundary layer. *Journal of Fluid Mechanics*, **48**, 339–352.

Reshotko, E. and Beckwith, I.E. 1958. Compressible laminar boundary layers over a yawed infinite cylinder with heat transfer and arbitrary Prandtl number. *NACA Report 1379*.

Ribner, H.S. 1953. Convection of a pattern of vorticity through a shock wave. *NACA TN 2864*.

Ribner, H.S. 1962. Aerodynamic sound from fluid dilatation. *UTIA Rep. 68*; also *AFOSR TN 3430*.

Ribner, H.S. and Tucker, M. 1952. Spectrum of turbulence in a contracting stream. *NACA TN 2606*.

Ripley, M.D. and Pauley, L.L. 1993. The unsteady structure of two-dimensional steady laminar separation. *Physics of Fluids A*, **5**, 3099–3106.

Ristorcelli, J.R. 1997. A pseudo-sound constitutive relationship for the dilatational covariances in compressible turbulence. *Journal of Fluid Mechanics*, **347**, 37–70.

Robinet, J.C. 1999. *Stabilité linéaire d'un écoulement présentant une onde de choc*. Thèse de Doctorat, ENSAE, Toulouse, France.

Robinet, J.C. 2001. Étude des instabilités dans une couche limite décollée incompressible et compressible, et réponse d'une onde de choc oblique à une perturbation. *Rapport Post-Doctoral, CNES, IUSTI, UMR CNRS-Université de Provence, Marseille, France, Report No. 6595*.

Robinet, J.C. and Casalis, G. 1999. Shock oscillations in a diffuser modelled by a selective noise amplification. *AIAA Journal*, **37**, 4, 1–8.

Robinson, S.K. 1986. Space-time correlation measurements in a compressible turbulent boundary layer. *AIAA Paper 86-1130*.

Robinson, S.K. 1991a. Coherent motions in the turbulent boundary layer. *Annual Review of Fluid Mechanics*, **23**, 601–639.

Robinson, S.K. 1991b. The kinematics of turbulent boundary layer structure. *NASA TM 103859*.

Rong, B.S., Tan, D. K. M. and Smits, A. J. 1985. Calibration of the constant-temperature normal hot-wire anemometer in transonic flow. *Department of Mechanical and Aerospace Engineering Report 1696, Princeton University, Princeton, N.J.*

Rose, W.C. 1973. The behavior of a compressible turbulent boundary layer in a shock wave induced adverse pressure gradient. *NASA TN D-7092*.

Roshko, A. and Thomke, G.J. 1966. Observations of turbulent reattachment behind an axisymmetric downstream-facing step in supersonic flow. *AIAA Journal*, **4**, 975–980.

Rossmann, T., Mungal, M.G. and Hanson, R.K. 2002. Evolution and growth of large-scale structures in high compressibility mixing layers. *Journal of Turbulence*, **3**.

Rossmann, T., Mungal, M.G. and Hanson, R.K. 2003. Nitric-oxide planar laser-induced fluorescence applied to low-pressure hypersonic flow fields for the imaging of mixture fraction. *Applied Optics*, **42**, 33, 6682–6695.

Rotta, J.C. 1950. Über die Theorie der turbulenten Grenzschichten. *Mitteilung Max Planck Institut für Strömungs Forschung, No. 1.* English translation NACA TM 1344.

Rotta, J.C. 1960. Turbulent boundary layers with heat transfer in compressible flow. *NATO AGARD 281*.

Rotta, J.C. 1962. Turbulent boundary layers in incompressible flow. *Pages 5–219 of:* Küchemann, D. (ed), *Progress in Aeronautical Science*, vol. 2. Pergamon Press.

Rubesin, M.W. and Johnson, H.A. 1949. A critical review of skin-friction and heat-transfer solutions of the laminar boundary layer of a flat plate. *Transactions of the ASME*, **71**, 4, 383–388.

Runstadler, P.W., Kline, S.J. and Reynolds, W.C. 1963. An experimental investigation of flow structure of the turbulent boundary layer. *Mechanical Engineering Department, Stanford University Report MD-8*.

Sagaut P. 2002. *Large Eddy Simulations for incompressible flows: An introduction*. 2nd edn. Springer-Verlag, Berlin.

Sagaut P., Garnier E., Larchevêque L., Tromeur E. and Labourasse E. 2004. Turbulent inflow condition for LES of compressible wall-bounded flows. *AIAA Journal*, **42**, 3, 469–477.

Samimy, M. and Elliott, G.S. 1990. Effects of compressibility on the characteristics of free shear layers. *AIAA Journal*, **28**, 439–445.

Samimy, M., Petrie, H.L. and Addy, A.L. 1986. A study of compressible turbulent reattaching free shear layers. *AIAA Journal*, **24**, 261–267.

Samimy, M., Reeder, M.F. and Elliott, G.S. 1992. Compressibility effects on large structures in free shear flows. *Physics of Fluids A*, **4**, 1251–1258.

Sandborn, V.A. 1974. A review of turbulence measurements in compressible flow. *NASA TR X-62337*.

Sandham, N.D. and Reynolds, W.C. 1989. Growth of oblique waves in the mixing layer at high Mach number. *In: Proceedings of the Seventh Symposium on Turbulent Shear Flows*. Stanford University.

Sandham, N.D. and Reynolds, W.C. 1990. Compressible mixing layer: Linear theory and direct simulation. *AIAA Journal*, **28**, 618–624.

Sandham, N.D. and Reynolds, W.C. 1991. Three-dimensional simulations of large eddies in the compressible mixing layer. *Journal of Fluid Mechanics*, **224**, 133–158.

Sarkar, S. 1995. The stabilizing effect of compressibility in turbulent shear flow. *Journal of Fluid Mechanics*, **282**, 163–186.

Sarkar, S., Erlebacher, G. and Hussaini, M.Y. 1992. Compressible homogeneous shear: Simulation and modeling. *ICASE Report 92-6*.

Sarkar, S., Erlebacher, G., Hussaini, M.Y. and Kreiss, H.O. 1989. The analysis and modeling of dilatational terms in compressible turbulence. *ICASE Report 89-79*.

Sarkar, S., Erlebacher, G., Hussaini, M.Y. and Kreiss, H.O. 1991. The analysis and modeling of dilatational terms in compressible turbulence. *Journal of Fluid Mechanics*, **227**, 473–493.

Savill, M. 1987. Recent developments in rapid distortion theory. *Ann. Rev. Fluid Mech.*, **19**, 531–575.

Scarano, F. and Haertig, J. 2003. Application of non-isotropic resolution PIV in supersonic and hypersonic flows. *5th International Symposium on Particle Image Velocimetry, Paper 3125*, Busan, Korea.

Schetz, J.A. 1972. *Foundations of Boundary Layer Theory for Momentum, Heat, and Mass Transfer*. Prentice-Hall.

Schewe, G. 1983. On the structure and resolution of wall pressure fluctuations associated with turbulent boundary-layer flow. *Journal of Fluid Mechanics*, **134**, 311–328.

Schlichting, H. 1979. *Boundary-Layer Theory*. 7th edn. McGraw-Hill.

Schmisseur, J.D. and Dolling, D.S. 1992. Unsteady separation in sharp fin-induced shock wave/turbulent boundary layer interaction. *AIAA Paper 92-0748*.

Schneider, W. 1974. Upstream propagation of unsteady disturbances in supersonic boundary layers. *Journal of Fluid Mechanics*, **63**, 465–485.

Schoppa, W. and Hussain, F. 1997. Genesis and dynamics of coherent structures in near-wall turbulence: A new look. *In: Self-Sustaining Mechanisms of Wall Turbulence*. Advances in Fluid Mechanics Series, **15**, 385–422. Computational Mechanics Publications, Southampton, UK and Boston, USA.

Selig, M.S. and Smits, A.J. 1991. Effect of periodic blowing on attached and separated supersonic turbulent boundary layers. *AIAA Journal*, **29**, 1651–1658.

Selig, M.S., Andreopoulos, J., Muck, K.C., Dussauge, J.P. and Smits, A.J. 1989. Turbulence structure in a shock wave/turbulent boundary-layer interaction. *AIAA Journal*, **27**, 862–869.

Settles, G.S. 1975. *An experimental study of compressible turbulent boundary layers at high Reynolds numbers*. Ph.D. Thesis, Princeton University.

Settles, G.S. and Dodson, L.J. 1991. Hypersonic shock-boundary layer interaction database. *NASA CR 177577*.

Settles, G.S. and Dolling, D.S. 1990. Swept shock/boundary layer interactions — Tutorial and update. *AIAA Paper 90-0375.*

Settles, G.S. and Dolling, D.S. 1992. Swept shock wave boundary layer interaction. *AIAA Progress Series: Volume on Tactical Missile Aerodynamics*, **141**, 505–74.

Settles, G.S. and Teng, H.Y. 1984. Cylindrical and conical upstream influence regimes of three-dimensional shock/turbulent boundary layer interactions. *AIAA Journal*, **22**, 194–200.

Settles, G.S., Baca, B.K., Williams, D.R. and Bogdonoff, S.M. 1982. Reattachment of a compressible turbulent shear layer. *AIAA Journal*, **20**, 60–67.

Settles, G.S., Bogdonoff, S.M. and Vas, I. 1976. Incipient separation of a supersonic turbulent boundary layer at high Reynolds numbers. *AIAA Journal*, **14**, 50–56.

Settles, G.S., Fitzpatrick, T.J. and Bogdonoff, S.M. 1979. Detailed study of attached and separated compression corner flowfields in high Reynolds number supersonic flow. *AIAA Journal*, **17**, 579–585.

Settles, G.S., Perkins, J.J. and Bogdonoff, S.M. 1980. Investigation of three-dimensional shock/boundary layer interactions at swept compression corners. *AIAA Journal*, **18**, 779–785.

Shah, D.A. and Antonia, R.A. 1989. Scaling of the bursting period in turbulent boundary layer and duct flows. *Physics of Fluids A*, **1**, 318–325.

Shamroth, S.J. and MacDonald, H. 1970. A new solution of the turbulent near wake recompression problem. *AIAA Paper 70-0228.*

Shau, Y.R. and Dolling, D.S. 1989. Experimental study of spreading rate enhancement of high Mach number turbulent shear layers. *AIAA Paper 89-2458.*

Shen, Z.H., Smith, D.R. and Smits, A.J. 1993. Wall pressure fluctuations in the reattachment region of a supersonic free shear layer. *Experiments in Fluids*, **14**, 10–16.

Shih, T.H. and Lumley, J.L. 1990. Modeling of pressure correlation terms in Reynolds stress and scalar flux equations. *Report FDA–85–3, Sibley School of Mechanical and Aerospace Engineering, Cornell University, Ithaca, NY.*

Shih, T.H., Lumley, J.L. and Janicka, J. 1987. Second-order modelling of variable density mixing layer. *Journal of Fluid Mechanics*, **180**, 93–116.

Si-Ameur, M. 1994. *Simulations numériques de mélanges turbulents dans les écoulements cisaillés supersoniques.* Thèse de Doctorat, Université Joseph Fourier, Grenoble, France.

Simone, A. 1995. *Étude et simulation numerique de la turbulence compressible en presence de cisaillement où de variation de volume à grande échelle.* Thèse de Doctorat, École Centrale de Lyon, Écully.

Simone, A. and Cambon, C. 1995. Rapid distortion and direct simulation approach to compressibility in turbulent shear flow. *In: Proceedings of the Tenth Symposium on Turbulent Shear Flows.* Pennsylvania State University.

Simone, A., Coleman, G.N. and Cambon, C. 1997. The effect of compressibility on turbulent shear flow: A rapid distortion theory and direct-simulation-study. *Journal of Fluid Mechanics*, **330**, 307–338.

Simpson, R.L. 1981. A review of some phenomena in turbulent flow separation. *Journal of Fluids Engineering*, **102**, 520–533.

Sirieix, M. 1975. Décollement turbulent en 'ecoulement bidimensionnel. *In: Flow*

Separation. AGARD CP-168, Paper 12.

Sirieix, M. and Solignac, J.L. 1968. Contribution à l'étude expérimentale de la couche de mélange turbulente isobare d'un écoulement supersonique. *Pages 241–270 of: Symposium on Separated Flows.* AGARD CP-4(1).

Slessor, M.D., Zhuang, M. and Dimotakis, P. 2000. Turbulent shear layer mixing: Growth-rate compressibility scaling. *Journal of Fluid Mechanics*, **414**, 35–45.

Smith, A.M.O. 1955. On the growth of Taylor-Görtler vortices along highly concave walls. *Quarterly Journal of Applied Mathematics*, **13**, 233–262.

Smith, C.R. and Metzler, S.P. 1983. The characteristics of low-speed streaks in the near-wall region of a turbulent boundary layer. *Journal of Fluid Mechanics*, **129**, 27–54.

Smith, C.R. and Walker, J.D.A. 1997. Sustaining mechanisms of turbulent boundary layers: The role of vortex development and interactions. *In: Self-Sustaining Mechanisms of Wall Turbulence.* Advances in Fluid Mechanics Series, **15**, 13–48. Computational Mechanics Publications, Southampton, UK and Boston, USA.

Smith, C.R., Walker, J.D.A., Haidara, A.H. and Sobrun, U. 1991. On the dynamics of near-wall turbulence. *In:* Walker, J.D.A. (ed), *Turbulent Flow Structure Near Walls.* The Royal Society. First published in *Phil. Trans. R. Soc. London A.* 336, 1991.

Smith, D.R. 1993. *The effects of successive distortions on a turbulent boundary layer in a supersonic flow.* Ph.D. Thesis, Princeton University.

Smith, D.R. and Smits, A.J. 1991a. The rapid expansion of a turbulent boundary layer in a supersonic flow. *Theoretical and Computational Fluid Dynamics*, **2**, 319–328.

Smith, D.R. and Smits, A.J. 1993a. The simultaneous measurement of velocity and temperature fluctuations in the boundary layer of a supersonic flow. *Experimental Thermal and Fluid Science*, **7**, 221–229.

Smith, D.R. and Smits, A.J. 1993b. Multiple distortions of a supersonic turbulent boundary layer. *Applied Scientific Research*, **51**, 223–229.

Smith, D.R. and Smits, A.J. 1994. The effects of streamline curvature and pressure gradient on the behavior of turbulent boundary layers in supersonic flow. *AIAA Paper 94-2227.*

Smith, D.R. and Smits, A.J. 1997. The effects of successive distortions on the behavior of a turbulent boundary layer in a supersonic flow. *Journal of Fluid Mechanics*, **351**, 253–288.

Smith, D.R., Fernando, E.M., Donovan, J.F. and Smits, A.J. 1992. Conventional skin friction measurement techniques for strongly perturbed supersonic turbulent boundary layers. *European Journal of Mechanics, B/Fluids*, **11**, 719–740.

Smith, D.R., Poggie, J., Konrad, W. and Smits, A.J. 1991. Visualization of the structure of shock wave turbulent boundary layer interactions using Rayleigh scattering. *AIAA Paper 91-0651.*

Smith, M.W. 1989. *Flow visualization in supersonic turbulent boundary layers.* Ph.D. Thesis, Princeton University.

Smith, M.W. and Smits, A.J. 1988. Cinematic visualization of coherent density structures in a supersonic turbulent boundary layer. *AIAA Paper 88-0500.*

Smith, M.W. and Smits, A.J. 1995. Visualization of the structure of supersonic

turbulent boundary layers. *Experiments in Fluids*, **18**, 288–302.

Smith, M.W., Smits, A.J. and Miles, R.B. 1989. Compressible boundary-layer density cross sections by UV Rayleigh scattering. *Optics Letters*, **14**, 916–918.

Smith, R.W. 1994. *Effect of Reynolds number on the structure of turbulent boundary layers*. Ph.D. Thesis, Princeton University.

Smith, R.W. and Smits, A.J. 1991b. Effect of Reynolds number on the large structure of turbulent boundary layers. *AIAA Paper 91-0526*.

Smits, A.J. 1974. *Further development of hot-wire and laser methods in fluid mechanics*. Ph.D. Thesis, University of Melbourne, Melbourne, Australia.

Smits, A.J. and Delo, C.J. 2001. Self-sustaining mechanisms of wall turbulence *In:* Reguera, D., Bonilla, L.L. and Rubi, J.M. (eds), *Coherent Structures in Complex Systems*. Lecture Notes in Physics, 17–38, Springer.

Smits, A.J. and Dussauge, J.-P. 1989. Hot-wire anemometry in supersonic flow. *Chapter 5, AGARDograph 315*.

Smits, A.J. and Lim, T.T. 2000. *Flow Visualization: Techniques and Examples*. Imperial College Press.

Smits, A.J. and Martin, P. 2004. Turbulence structure in supersonic and hypersonic turbulent boundary layers. *IUTAM Symposium on One Hundred Years of Boundary Layer Research*, DLR-Göttingen, Germany.

Smits, A.J. and Muck, K.-C. 1984. Constant-temperature hot-wire anemometer practice in supersonic flows. Part 2: The inclined wire. *Experiments in Fluids*, **2**, 33–41.

Smits, A.J. and Muck, K.-C. 1987. Experimental study of three shock wave/turbulent boundary layer interactions. *Journal of Fluid Mechanics*, **182**, 291–314.

Smits, A.J. and Wood, D.H. 1985. The response of turbulent boundary layers to sudden perturbations. *Annual Review of Fluid Mechanics*, **17**, 321–358.

Smits, A.J., Eaton, J.A. and Bradshaw, P. 1979a. The response of a turbulent boundary layer to lateral divergence. *Journal of Fluid Mechanics*, **94**, 243–268.

Smits, A.J., Hayakawa, K. and Muck, K.C. 1983a. Constant temperature hot-wire anemometry practice in supersonic flows. Part 1: The normal wire. *Experiments in Fluids*, **1**, 83–92.

Smits, A.J., Matheson, N. and Joubert, P.N. 1983b. Low-Reynolds-number turbulent boundary layers in zero and favorable pressure gradients. *Journal of Ship Research*, **27**, 147–157.

Smits, A.J., Perry, A.E. and Hoffmann, P.H. 1978. The response to temperature fluctuations of a constant-current hot-wire anemometer. *Journal of Physics E: Scientific Instruments*, **11**, 909–914.

Smits, A.J., Spina, E.F., Alving, A.E., Smith., R.W., Fernando, E.M. and Donovan, J.F. 1989. A comparison of the turbulence structure of subsonic and supersonic boundary layers. *Physics of Fluids A*, **1**, 1865–1875.

Smits, A.J., Young, S.T.B. and Bradshaw, P. 1979b. The effect of short regions of high surface curvature on turbulent boundary layers. *Journal of Fluid Mechanics*, **94**, 209–242.

So, R.M.C. and Mellor, G.L. 1973. Experiment on convex curvature effects in turbulent boundary layers. *Journal of Fluid Mechanics*, **60**, 43–62.

Spalart, P.R. 1988. Direct simulation of a turbulent boundary layer up to $R_\theta = 1410$. *Journal of Fluid Mechanics*, **187**, 61–98.

Spalding, D.B. 1961. A single formula for the law of the wall. *Transactions of the ASME, Series E: Journal of Applied Mechanics*, **28**, 455–458.

Spina, E.F. 1988. *Organized structures in a supersonic turbulent boundary layer.* Ph.D. Thesis, Princeton University.

Spina, E.F. and Smits, A.J. 1987. Organized structures in a compressible turbulent boundary layer. *Journal of Fluid Mechanics*, **182**, 85–109.

Spina, E.F., Donovan, J.F. and Smits, A.J. 1991a. On the structure of high-Reynolds-number supersonic turbulent boundary layers. *Journal of Fluid Mechanics*, **222**, 293–327.

Spina, E.F., Donovan, J.F. and Smits, A.J. 1991b. Convection velocity in supersonic turbulent boundary layers. *Physics of Fluids A*, **3**, 3124–3126.

Spina, E.F., Smits, A.J. and Robinson, S.K. 1994. The physics of supersonic turbulent boundary layers. *Annual Review of Fluid Mechanics*, **26**, 287–319.

Sreenivasan, K.R. 1988. A unified view of the origin and morphology of the turbulent boundary-layer structure. *In:* Liepmann, H. and Narasimha, R. (eds), *Turbulence Management and Relaminarization.* Springer Verlag Berlin.

Sreenivasan, K.R. 1989. The turbulent boundary layer. *In:* Gad-el-Hak, M. (ed), *Frontiers in Experimental Fluid Mechanics*, 159–210. Springer-Verlag.

Sreenivasan, K.R. and Johnson, A.W. 1989. Private communication.

Sreenivasan, K.R. and Sahay, A. 1997. The persistence of viscous effects in the overlap region, and the mean velocity in turbulent pipe and channel flows. *In: Self-Sustaining Mechanisms of Wall Turbulence.* Advances in Fluid Mechanics Series, **15**, 253–272. Computational Mechanics Publications, Southampton, UK and Boston, USA.

Sreenivasan, K.R., Antonia, R.A. and Danh, H.Q. 1977. Temperature dissipation fluctuations in a turbulent boundary layer. *Physics of Fluids A*, **4**, 2062–2069.

Stalmach, C.J. 1958. Experimental investigation of the surface impact probe method of measuring local skin friction at supersonic speed. *Univ. of Texas Report DRL-410, CF 2675.*

Stanewski, E. 1973. Shock-boundary layer interaction in transonic and supersonic flow. *In: Transonic Flows in Turbomachinery.* Von Kármán Institute, Rhodes-Saint-Genèse, Belgium, Lecture Series 59.

Sternberg, J. 1967. On the interpretation of space-time correlation measurements in shear flow. *The Physics of Fluids*, **10**, S146–S152.

Stolz, S. and Adams, N.A. 2003. Large eddy simulation of high-Reynolds number supersonic boundary layers using the approximate deconvolution model and a rescaling and recycling technique. *Physics of Fluids*, **15**, 8, 2398–2412.

Strykowski, P.J., Krothapalli, A. and Jendoubi, S. 1996. The effect of counterflow on the development of compressible shear layers. *Journal of Fluid Mechanics*, **308**, 63–96.

Sun, C.C. and Childs, M.E. 1973. A modified wall-wake velocity profile for turbulent compressible boundary layers. *Journal of Aircraft*, **10**, 381–383.

Sun, C.C. and Childs, M.E. 1976. A wall-wake velocity profile for compressible non-adiabatic flows. *AIAA Journal*, **14**, 820–822.

Tan, D.K.M., Tran, T.T. and Bogdonoff, S.M. 1985. Surface pressure fluctuations in a three-dimensional shock wave/turbulent boundary layer interaction. *AIAA Paper 85-0125.*

Tani, I. 1962. Production of longitudinal vortices in the boundary layer along a concave wall. *Journal of Geophysical Research*, **67**, 3075.

Task Group on Aeronautical Research and Development Facilities. 1994. *National Facilities Study.* Available from National Facilities Office, NASA Lewis Research Center, Cleveland, OH.

Tedeschi, G. 1993. *Analyse théorique et expérimentale du comportement de particules à la traversée d'une discontinuité de vitesse (onde de choc).* Thèse d'Université, Université d'Aix-Marseille II.

Tennekes, H. and Lumley, J.L. 1972. *A First Course in Turbulence.* The MIT Press.

Theodorsen, T. 1955. The structure of turbulence. *In:* Görtler, H. and Tollmien, W. (eds), *50 Jahre Grenzschichtforschung.* Friedr. Vieweg and Sohn.

Thomas, F.O., Putnam, C.M. and Chu, H.C. 1994. On the mechanism of unsteady shock oscillation in shock wave/turbulent boundary layer interactions. *Experiments in Fluids*, **18**, 69–81.

Thompson, P.A. 1972. *Compressible Fluid Dynamics.* McGraw-Hill.

Thurow, B., Jiang, N., Lempert, W.R. and Samimy, M. 2004. Narrow-linewidth megahertz-rate pulse-burst laser for high-speed flow diagnostics. *Applied Optics*, **43**, 26, 5064–5073.

Thurow, B., Lempert, W.R. and Samimy, M. 2000. MHz rate imaging of large-scale structures within a high speed axisymmetric jet. *AIAA Paper 00-0659.*

Tobak, M. and Peake, D.J. 1982. Topology of three-dimensional separated flows. *Annual Review of Fluid Mechanics*, **14**, 61–85.

Townsend, A.A. 1956. *The Structure of Turbulent Shear Flow.* Cambridge University Press.

Townsend, A.A. 1970. Entrainment and the structure of turbulent flow. *Journal of Fluid Mechanics*, **41**, 13–46.

Townsend, A.A. 1976. *The Structure of Turbulent Shear Flow.* 2 edn. Cambridge University Press.

Townsend, A.A. 1980. The response of sheared turbulence to additional distortion. *Journal of Fluid Mechanics*, **98**, 171–191.

Tran, T.T. 1987. *An experimental investigation of unsteadiness in swept shock wave/turbulent boundary layer interactions.* Ph.D. Thesis, Princeton University.

Tran, T.T., Tan, D.K.M. and Bogdonoff, S.M. 1985. Surface pressure fluctuations in a three-dimensional shock wave/turbulent boundary layer interaction at various shock strengths. *AIAA Paper 85-1562.*

Tu, B.-J. and Willmarth, W.W. 1966. An experimental study of the structure of turbulence near the wall through correlation measurements in a thick turbulent boundary layer. *University of Michigan ORA 02920-3-T.*

Tucker, H.J. and Reynolds, A.R. 1968. The distortion of turbulence by irrotational plane strain. *Journal of Fluid Mechanics*, **32**, 657–673.

Uberoi, M.S. and Kovasznay, L.S.G. 1953. On mapping and measurement of random fields. *Quarterly of Applied Mathematics*, **10**.

Uddin, A.K.M. 1994. *The structure of a turbulent boundary layer.* Ph.D. Thesis, University of Melbourne.

Ueda, H. and Hinze, J.O. 1975. Fine-structure turbulence in the wall region of a turbulent boundary layer. *Journal of Fluid Mechanics*, **67**, 125–143.

Ünalmis, Ö.H. and Dolling, D.S. 1996. On the possible relationship between low frequency unsteadiness of shock-induced separated flow and Görtler vortices. *AIAA Paper 96-2002.*

Ünalmis, Ö.H. and Dolling, D.S. 1998. Experimental study of causes of unsteadiness of shock-induced turbulent separation. *AIAA Journal*, **36**, 371.

Urban, W.D. and Mungal, M.G. 2001. Planar velocity measurements in compressible mixing layers. *Journal of Fluid Mechanics*, **431**, 189–222.

van Driest, E.R. 1951. Turbulent boundary layer in compressible fluids. *Journal of the Aeronautical Sciences*, **18**, 145–160.

van Driest, E.R. 1955. The turbulent boundary layer with variable fluid properties. *In: Meeting. of the Heat Transfer and Fluid Mechanics Institute.*

van Driest, E.R. 1956. On turbulent flow near a wall. *Journal of the Aeronautical Sciences*, **23**, 1007–1011 and 1036.

Van Dyke, M. 1982. *An Album of Fluid Motion.* Parabolic Press.

van Oudheusden, B.W. 1997. A complete Crocco integral for two-dimensional laminar boundary layer flow over an adiabatic wall for Prandtl numbers near unity. *Journal of Fluid Mechanics*, **353**, 313–330.

Viswanath, P.R. 1988. Shock-wave-turbulent-boundary-layer interaction and its control: A survey of recent developments. *Sādhanā, Indian Academy of Sciences, Proceedings in Engineering Sciences*, **12**, 45–104.

Voisinet, R.L.P. and Lee, R.E. 1972. Measurements of a Mach 4.9 zero pressure gradient boundary layer with heat transfer. *Nav. Ord. Lab. TR 72-232.*

von Kármán, T. 1930. Mechanische Ähnlichkeit und Turbulenz. *Nachrichten der Akademie der Wissenschaften Göttingen, Math. Phys. Klasse*, **58**. *Proc. 3rd Int. Congr. Appl. Mech.,* Stockholm, Pt. I, 1930, p. 85; English trans. NACA TM 611 (1931).

von Kármán, T. 1934. Turbulence and skin friction. *Journal of the Aeronautical Sciences*, **1**.

Vreman, A.W., Sandham, N.D. and Luo, K. 1996. No title. *Journal of Fluid Mechanics*, **320**, 235–258.

Wagner, R.D. 1973. Mean flow and turbulence measurements in a Mach 5 free shear layer. *NASA TN D7366.*

Wallace, J.M., Eckelmann, H. and Brodkey, R.S. 1972. The wall region in turbulent shear flow. *Journal of Fluid Mechanics*, **54**, 39–48.

Walz, A. 1959. Compressible turbulent boundary layers with heat transfer and pressure gradient in flow direction. *Research Journal, National Bureau of Standards*, **63 B**, 53.

Walz, A. 1966. *Strömungs- und Temperaturgrenzschichten.* Braun Verlag, Karlsruhe. English translation *Boundary Layers of Flow and Temperature*, MIT Press, 1969.

Wang, S.F., Ren, Z.Y. and Wang, Y. 1998. Effects of Mach number on turbulent separation behaviours induced by blunt fin. *Experiments in Fluids*, **25**, 347–351.

Watmuff, J.H. 1995. An investigation of the constant-temperature hot-wire anemometer. *Experimental Thermal and Fluid Science*, **11**, 117–134.

Watson, R.D. 1977. Wall cooling effects on hypersonic transitional/turbulent boundary layers at high Reynolds numbers. *AIAA Journal*, **15**, 1455–1461.

Watson, R.D. 1978. Characteristics of Mach 10 transitional and turbulent boundary layers. *NASA TP-1243*.

Watson, R.D., Harris, J.E. and Anders, J.B. 1973. Measurements in a transitional/turbulent Mach 10 boundary layer at high Reynolds number. *AIAA Paper 73-165*.

Wegener, P.P. and Stein, G.D. 1968. Light-scattering experiments and theory of homogeneous nucleation in condensing supersonic flow. *12th International Symposium on Combustion*, 1183–1191.

Wei, T., Fife, P., Klewicki, J. and McMurtry, P. 2005. Properties of the mean momentum balance in turbulent boundary layer, pipe and channel flows. *Journal of Fluid Mechanics*, **522**, 303–327.

Weinstein, L.M. 1993. Large-field high brightness focusing schlieren system. *AIAA Journal*, **31**, 1250–1255.

White, F.M. 1991. *Viscous Fluid Flow*. 2 edn. McGraw-Hill.

Wideman, J.K., Brown, J.L., Miles, J.B. and Özcan, O. 1994. Surface documentation of a 3-D supersonic, shock-wave/boundary-layer interaction. *NASA TM 108824*, 1994.

Wieghardt, K. and Tillmann, W. 1944. Zür turbulenten Reibungsschicht bei Druckansteig. *Z.W.B. K.W.I., U. and M. 6617*. Translated as 'On the turbulent friction layer for rising pressure', NACA TM 1314, 1951.

Willmarth, W.W. 1975. Structure of turbulence in boundary layers. *Advances in Applied Mechanics*, **15**, 159–254.

Willmarth, W.W. and Sharma, L.K. 1984. Study of turbulent structure with hot wires smaller than the viscous length. *Journal of Fluid Mechanics*, **142**, 121–149.

Winant, C.D. and Browand, F.K. 1974. Vortex pairing: The mechanism of turbulent mixing-layer growth at moderate Reynolds number. *Journal of Fluid Mechanics*, **63**, 237–255.

Winter, K.G. and Gaudet, L. 1973. Turbulent boundary-layer studies at high Reynolds numbers and Mach numbers between 0.2 and 2.8. *ARC Reports and Memoranda No. 3712*.

Wu, M. and Martin, M.P. 2004. Direct numerical simulation of two shock-wave/turbulent boundary layer interactions at Mach 2.9 and $Re_\theta = 2400$. *AIAA Paper 04-2145*.

Wu, P. 2000. *MHz-rate pulse-burst laser imaging system: Development and application in high speed flow diagnostics*. Ph.D. Thesis, Princeton University.

Wu, P., Lempert, W.R. and Miles, R.B. 2000. MHz pulse-burst laser system and visualization of shock-wave/boundary-layer interaction in a Mach 2.5 wind tunnel. *AIAA Journal*, **38**, 4, 672–679.

Wygnanski, I. and Fiedler, H.E. 1970. The two-dimensional mixing region. *Journal of Fluid Mechanics*, **41**, 327–362.

Wyngaard, J.C. 1968. Measurement of small-scale turbulence structure with hot

wires. *Journal of Scientific Instruments: Journal of Physics E*, **1 (Series 2)**, 1105–1108.

Wyngaard, J.C. 1969. Spatial resolution of the vorticity meter and other hot-wire arrays. *Journal of Scientific Instruments: Journal of Physics E*, **2 (Series 2)**, 983–987.

Yanta, W.J. and Crapo, B.J. 1976. Applications of the laser Doppler velocimeter to measure subsonic and supersonic flows. *AGARD CP No. 193*.

Yeung, P.K., Brasseur, J.G. and Bell, D.M. 1993. Evolution of passive scalar sources in a numerically simulated boundary layer. *In:* So, R.M.C., Speziale, C.G. and Launder, B.E. (eds), *Near-Wall Turbulent Flows*. Elsevier.

Young, A.D. 1951. The equations of motion and energy and the velocity profile of a turbulent boundary layer in a compressible fluid. *Report No. 42, College of Aeronautics, Cranfield*.

Young, A.D. 1989. *Boundary Layers*. AIAA Education. AIAA¡ Washington, DC.

Zagarola, M.V. and Smits, A.J. 1998a. Mean flow scaling of turbulent pipe flow. *Journal of Fluid Mechanics*, **373**, 33–79.

Zagarola, M.V. and Smits, A.J. 1998b. A new mean velocity scaling for turbulent boundary layers. *ASME paper FEDSM98-4950*.

Zang, T.A., Hussaini, M.Y. and Bushnell, D.M. 1984. Numerical computations of turbulence amplification in shock-wave interactions. *AIAA Journal*, **22**, 13–21.

Zeman, O. 1990. Dilatation dissipation: The concept and application in modeling compressible mixing layers. *Physics of Fluids A*, **2**, 178–188.

Zeman, O. 1992. Similarity in supersonic mixing layers. *AIAA Journal*, **30**, 1277–1283.

Zeman, O. 1993. A new model for super/hypersonic turbulent boundary layers. *AIAA Paper 93-0897*.

Zhao, R.W. 2005. *High Reynolds number turbulent pipe flow*. Ph.D. Thesis, Princeton University.

Zheltovodov, A.A., Trofimov, V.M., Shilein, E.H. and V.N., Yakovlev. 1990. An experimental documentation of supersonic turbulent flows in the vicinity of sloping forward and back facing steps. *TPM Report 2013, Institute of Theoretical and Applied Mechanics, Siberian Division of the USSR Academy of Sciences, Novosibirsk, USSR*.

Zhou, J., Adrian, R.J., Balachandar, S. and Kendall, T.M. 1999. Mechanisms for generating coherent packets of hairpin vortices in channel flow. *Journal of Fluid Mechanics*, **387**, 353–396.

Zhou, J., Meinhart, C.D., Balachandar, S. and Adrian, R.J. 1997. Formation of coherent hairpin packets in wall turbulence. *In: Self-Sustaining Mechanisms of Wall Turbulence*. Advances in Fluid Mechanics Series, **15**, 109–134. Computational Mechanics Publications, Southampton, UK and Boston, USA.

Zhuang, M., Kubota T. and Dimotakis, P.E. 1990. Instability of inviscid, compressible free shear layers. *AIAA Journal*, **28**, 1728–1733.

Zimmermann, M. and Miles, R.B. 1980. Hypersonic-helium-flow-field measurements with the Resonant Doppler Velocimeter. *Applied Physics Letters*, **37**, 885–887.

Index